Karlsruhe Institute of Technology

Electron Microscopic Investigation of Superconducting Fe- and Cu-based Thin Films

Zur Erlangung des akademischen Grades eines
Doktors der Naturwissenschaften (Dr. rer. nat.)

von der KIT-Fakultät für Physik des
Karlsruher Instituts für Technologie (KIT)
angenommene

Dissertation

von

M. Sc. Lukas Grünewald

Tag der mündlichen Prüfung: 06. Mai 2022

Referentin: Prof. Dr. Dagmar Gerthsen
Korreferent: Prof. Dr. Bernhard Holzapfel

Contents

List of Variables

A	Atomic mass / Wave amplitude (HRTEM)
$a_\mathrm{f}, a_\mathrm{s}$	Lattice parameters of the film and substrate in heteroepitaxy
α_t	Thermal expansion coefficient
a_i, c_i	Atomic/weight fractions of elements in a material
α	Convergence semi-angle
A_p	Projected area of a measured particle or precipitate
b	Electron-beam broadening in a sample
β	Collection semi-angle
β_gun	Electron-gun brightness
$\vec{b}$	Burgers vector
C_c	Chromatic aberration coefficient
χ	Aberration function
C_s	Spherical aberration coefficient
D	Data matrix / Dislocation spacing
d	Lattice-plane spacing in a crystal
d_0	Smallest probe size, HAADF-STEM resolution
ΔE	Energy spread of electrons
d_e	Area-equivalent diameter
δ_D	Defocus spread of a microscope
Δ	Spatial sampling (TEM/STEM) / Energy interval (EELS)
δ	Secondary electron yield
$\hat{\delta}$	Dirac delta function
Δf	Defocus
ΔR	Contrast delocalization
Δs	Minimum resolvable distance between two points
D_m	Moiré-fringe spacing
d_PLD	Sample-target distance (PLD)
E	Energy
E_0	Primary electron energy
C	Elemental concentration
E_c	Ionization energy of an atomic shell
n_{e^-}	Number of electrons per second
E_FEG	Electric field at the tip of a field-emission gun
E_PLD	Laser energy (PLD)
ϵ_d	EDXS detector collection efficiency
ϵ	Lattice mismatch
η	Backscattered electron yield

f	Focal length / Secondary fluorescence factor
f_{PLD}	Laser frequency (PLD)
γ	Superconductor anisotropy / Angle between surface normal and incident beam / Angle between crystalline facets
z	Sample depth
g_{ck}	Factor for Coster-Kronig transitions
H	Magnetic field / Hurst exponent
h, k, l	Miller indices of a crystal lattice
I	Intensity of a signal
I_{p}	Probe current
J_{c}	Critical current density
H_{c}	Critical magnetic field
j_{c}	Critical current density (Cooper-pair depairing)
k	Spatial frequency / Number of relevant components for PCA
k_{AB}	Cliff-Lorimer factor for two elements A and B
κ	Ginzburg-Landau parameter
κ_{AB}	Scaling factor for two elements A and B for EELS quantification
k_{EDXS}	Input x-ray count rate for STEM-EDXS
λ	Relativistic electron wavelength / Laser wavelength (PLD)
λ_{L}	London penetration depth
M	Mode of a distribution
m	Relativistic electron mass
μ	Absorption factor
n	Exponent of Z^n HAADF-STEM intensity / Number of values for arithmetic mean
J	Mean ionization energy of a material
$N_{\mathrm{PE}}, N_{\mathrm{SE}}, N_{\mathrm{BSE}}$	Number of primary, secondary, and backscattered electrons
$\varepsilon_{\mathrm{SE}}$	Average required energy to produce a secondary electron
$N_{\mathrm{tot/px}}$	Total x-ray counts per pixel in a STEM-EDXS spectrum image
$N_x, N_y, N_{\mathrm{m}}, N_c$	Number of $(x \times y) = \mathrm{m}$ measurement positions and energy channels
Ω	Detector solid angle in EDXS
ω	Fluorescence yield
P	Loading matrix
p	Impulse / Transition probability between atomic shells
ϕ	Phase of an electron wave
ϕ_0	Magnetic flux quantum
$\phi(\rho z)$	Depth distribution function of x-rays
$d_{\mathrm{p}}, d_{\mathrm{s}}, d_{\mathrm{d}}, d_{C_{\mathrm{s}}}, d_{C_{\mathrm{c}}}$	Total, geometric, diffraction-limited, C_{s}-, and C_{c}-limited probe sizes
ψ	Wave function
$p_{\mathrm{survey}}, p_{\mathrm{mapping}}$	Pixel sizes for survey-image and spectrum-image acquisition
Q	Ionization cross-section
R	Percentage of electrons in a defined probe size / Size of the interaction volume
r	Tip radius of a field-emission gun / Ratio of elemental concentrations
ρ	Material density
s	Scattering parameter [Yam+18]
σ	(Partial) ionization cross-section

σ_i	Interaction constant
σ_x	Sample standard deviation
T	Temperature / Score matrix
V	Acceleration voltage / Specimen potential
t	Thickness (TEM sample / amorphous surface layer)
T_c	Critical temperature
t_EDXS	Mapping duration for STEM-EDXS
θ	Scattering angle
θ_d	EDXS detector take-off angle
θ_GB	Grain-boundary angle
$\theta_\mathrm{GB,c}$	Critical grain-boundary angle
θ_TB	Twin-boundary angle
T_m	Melting temperature of a material
T_sub	Substrate temperature (PLD)
U_ext	Extractor voltage of a field-emission gun
ξ	Superconducting coherence length
$\overline{x}, \mu_x$	Arithmetic mean
Z	Atomic number
$\overline{Z}$	Average atomic number

List of Akronyms

μP	Microprobe mode (Mini condenser lens optically on)
ABSF	Average background subtraction filter
ACTF	Amplitude contrast-transfer function
ADF	Annular dark-field
APB	Antiphase boundary
Ba122	$Ba(Fe_{0.92}Co_{0.08})_2As_2$
BF	Bright field
BFP	Back-focal plane
BHO	$BaHfO_3$
BLU	Bayesian linear unmixing
BMO	$BaMO_3$ (M = Zr, Hf, Ti, Sn, Nb)
BNO	$BaNb_2O_6$
BSCCO	$Bi_2Sr_2Ca_{n-1}Cu_nO_{2n+4+x}$
BSE	Backscattered electron
BSO	$BaSnO_3$
BSS	Blind source separation
BTO	$BaTiO_3$
BW	Butterworth (filter)
BZO	$BaZrO_3$
C1	First condenser lens
C2	Second condenser lens
C3	Third condenser lens
CBED	Convergent beam electron diffraction
CBS	Concentric backscatter detector
CCD	Charge-coupled device
CCS	Cleaning cross-section
CMOS	Complementary metal–oxide–semiconductor
CSD	Chemical solution deposition
CTEM	Conventional transmission electron microscopy (parallel sample illumination)
CTF	Contrast-transfer function
DCFI	Drift-corrected frame integration

DM	DigitalMicrograph (software)
DP	Diffraction pattern
DQE	Detective quantum efficiency
EBID/IBID	Electron-/ion-beam-induced deposition
EDXS	Energy-dispersive x-ray spectroscopy
EELS	Electron energy loss spectroscopy
EFSTEM	Energy-filtered scanning transmission electron microscopy
EFTEM	Energy-filtered transmission electron microscopy
ELNES	Energy-loss near-edge structure
EPQ	Electron Probe Quantification
ETD	Everhart-Thornley detector
FEG	Field-emission gun
FEI	Field Electron and Ion Company
FFP	Front-focal plane
FFT	Fast Fourier transform
FIB	Focused ion beam
FT	Fourier transform
FWHM	Full width at half maximum
GIF	Gatan Imaging Filter
GIS	Gas-injection system
GOS	Generalized oscillator strength
HAADF	High-angle annular dark-field
HRSTEM	High-resolution scanning transmission electron microscopy
HRTEM	High-resolution transmission electron microscopy
IBS	Iron-based superconductor
ICA	Independent component analysis
ICE	In-chamber electron detector
ICP-MS	Inductively coupled plasma mass spectrometry
ICSD	Inorganic Crystal Structure Database
ITEP	Institute for Technical Physics
KIT	Karlsruhe Institute of Technology
LAADF	Low-angle annular dark-field
LAO	$LaAlO_3$
LEM	Laboratory for Electron Microscopy
LMIS	Liquid metal ion source
LN_2	Liquid nitrogen
MAADF	Medium-angle annular dark-field
MAC	Mass-absorption coefficient
MC	Mini condenser lens

MCR	Multivariate curve resolution
MLLS	Multiple linear least squares
MOD	Metal-organic deposition
MSA	Multivariate statistical analysis
MTF	Modulation transfer function
NBED	Nanobeam electron diffraction
NCSI/PCSI	Negative/Positive-C_s imaging
NLLS	Non-linear least squares
NMF	Non-negative matrix factorization
NP	Nanoparticle
nP	Nanoprobe mode (Mini condenser lens optically off)
OL	Objective lens
PACBED	Position-averaged convergent beam electron diffraction
PC	Principal component
PCA	Principal component analysis
PCTF	Phase contrast-transfer function
PIPS	Precision ion polishing system
PLD	Pulsed laser deposition
PSF	Point-spread function
RE	Rare-earth element
RE123	Same as REBCO
RE124	$REBa_2Cu_4O_8$ (RE = Y, Sm, Dy, Gd, Er, Ho)
RE247	$RE_2Ba_4Cu_7O_{15-\delta}$ (RE = Y, Sm, Dy, Gd, Er, Ho)
REBCO	$REBa_2Cu_3O_{7-\delta}$ (RE = Y, Sm, Dy, Gd, Er, Ho)
ROI	Region of interest
S/TEM	Combined scanning transmission electron microscope
SAED	Selected-area electron diffraction
SDD	Silicon drift detector
SE	Secondary electron
SEM	Scanning electron microscope
SF	Stacking fault
STEM	Scanning transmission electron microscopy
STO	$SrTiO_3$
TB	Twin boundary
TEM	Transmission electron microscopy
TFA	Trifluoroacetate
TFS	Thermo Fisher Scientific
TKD	Transmission Kikuchi diffraction
TLD	Thru-lens detector
TWS	Trainable WEKA Segmentation

UHV	Ultra-high vacuum
VCA	Vertex component analysis
WEKA	Waikato Environment for Knowledge Analysis
XRD	X-ray diffraction
YAG	Yttrium aluminium garnet
YAP	Yttrium aluminium perovskite

Physical and Mathematical Constants[1]

c	=	$2.99792458 \times 10^{8}\,\mathrm{ms}^{-1}$	Speed of light in vacuum
e	=	$1.602176634 \times 10^{-19}\,\mathrm{C}$	Elementary charge
h	=	$6.62607015 \times 10^{-34}\,\mathrm{J\,Hz}^{-1}$	Planck's constant
m_0	=	$9.1093837015(28) \times 10^{-31}\,\mathrm{kg}$	Electron (rest) mass
N_A	=	$6.02214076 \times 10^{23}\,\mathrm{mol}^{-1}$	Avogadro's constant
ϕ_0	=	$2.067833848\cdots \times 10^{-15}\,\mathrm{Wb}$	Magnetic flux quantum
e	=	$2.7182818\ldots$	Euler's number
i	=	$\sqrt{-1}$	Imaginary number
π	=	$3.1415926\ldots$	Pi (Archimedes's constant)

[1] Based on the values of Tiesinga et al. Tie+21.

1. Introduction

Superconducting materials are capable of lossless transmission of large electrical currents. This property makes superconductors attractive for technical applications. For example, superconducting coils can generate large magnetic fields, which are used in magnetic resonance imaging [CP11], particle colliders [dOud+97; Amb15; BZ16], magnetic levitation for transportation [Wer+11], or fusion reactors [Mit+08]. Superconducting wires are also promising candidates in the sustainable-energy sector [JM19]. Application-relevant superconductors must be kept at cryogenic temperatures, which adds technical difficulties and cost. High-temperature superconductors, such as the rare-earth barium copper oxides (REBCOs, discovered in 1986 [BM86]), become superconducting at critical temperatures above 77 K and can be cooled with liquid nitrogen with much less cost and effort than superconductors that require expensive liquid-helium cooling. Still, the search for novel superconducting materials with higher critical temperatures that require even less cooling and have better properties is an ongoing scientific endeavor. In this process, the family of iron-based superconductors (IBSs) was discovered in 2006 [Kam+06] (and more recently also the nickelate superconductors [Li+19]). Most known IBSs require lower temperatures than REBCOs. Nevertheless, IBSs have other promising superconducting properties for technical applications, such as a lower anisotropy of the superconducting properties and higher resilience against grain-boundary misorientations [Hos+18; HI20]. Whole "zoos" of materials have emerged for REBCOs and IBSs in the pursuit of better superconducting properties and this trend is still ongoing. Besides technical applications, these novel materials will undoubtedly provide new insights for the development of an improved microscopic theory of superconductivity.

Regarding technical applications, state-of-the-art high-temperature superconducting tapes are fabricated as "coated conductors". The superconducting material is deposited as a highly textured or even epitaxial film on a substrate [OP14; MW21]. This aspect alone requires optimization of several fabrication parameters for each superconducting material. In addition, non-superconducting nanoscale defects in the superconducting film are desired for "flux (or vortex) pinning" [Bla+94], which increases the current-carrying capabilities of a superconductor. The effectiveness of such pinning centers depends not only on their size and shape, but also on external factors such as the temperature or the orientation of the superconductor in an external magnetic field [FKM17]. The addition of non-superconducting nanoparticles into the superconducting material is an popular method to create such pinning centers [Mac+04]. The controlled addition of pinning centers with optimal size and shape during (or after) film fabrication is desired but challenging. Optimization of the fabrication requires a detailed understanding of the formation of crystalline defects and secondary phases in superconducting materials. Another aspect is the optimization of the cost-effectiveness of superconducting-tape fabrication. Many research groups study the fabrication of superconducting films under well-controlled conditions (e.g. the deposition rate) to understand and improve the growth process.

Electron microscopy is a powerful technique for the investigation of superconducting materials, because it provides information on the structure and chemical composition between the atomic and micrometer scale. This is essential because the microstructural features, that determine the superconducting properties, require often atomic-scale resolution.

It was therefore the goal of this thesis to apply a large variety of electron-microscopic techniques to study in detail the structural and chemical properties of IBS and REBCO thin films grown under different conditions.

- Thin $Ba(Fe,Co)_2As_2$ (Ba122) films have already been intensively studied. For example, secondary phases such as Fe [Lee+10; Hän+11; Kat+12; Kat+13; Yoo+16; Dai+19] and BaF_2 [Kur+13b], and the formation of planar defects [Yua+17; Zhe+19] were observed in earlier studies. Growth of Ba122 on CaF_2 substrates typically results in high-quality films with high critical temperatures and current densities [Kur+13b; INM17; Hän+19]. Still, further optimization of the superconducting properties and, hence, the Ba122 microstructure is desired by optimizing the growth conditions. Therefore, Ba122 films grown on CaF_2 substrates by pulsed laser deposition with different growth rates were investigated in this work. A preliminary study [Lan+19b] on these films was performed, which showed an influence of the growth rate on secondary-phase formation (BaF_2, Fe). However, more detailed information on the secondary-phase formation is desirable, which motivates the detailed electron microscopy investigations in this work.
  Another set of experiments focuses on a multilayer-deposition approach [Mey+20], where different nanoparticle materials ($BaHfO_3$, $BaZrO_3$, and InAs) are introduced into the superconductor to generate pinning centers (nanocomposite films). Multilayer deposition has been employed for REBCO nanocomposite films [Cai+05a; Kie+11; Aye+21], but was tested only recently for IBSs with the aim of introducing pinning centers [Mey+20; Mey21]. Detailed electron microscopy studies on these materials are not available yet and were performed in this work.

- REBCO is the second class of materials studied in this thesis. REBCO films were prepared by pulsed laser deposition and a chemical solution deposition. The latter is a cost-effective fabrication method since it is a non-vacuum process [Obr+12]. The first set of GdBCO samples is analyzed to gain insights into the oxygenation process, which is a necessary step to form the superconducting phase. Associated defects and secondary phases can form (or vanish) during the oxygenation process and affect the superconducting properties. This process was studied earlier for YBCO, but only recently for GdBCO with a focus on defect formation [Oh+18; Oh+20; Par+18a; Par+18b; Lee+16]. This thesis adds to the existing studies by a detailed comparison of the microstructure of oxygenated and non-oxygenated GdBCO films.
  Another investigation focuses on REBCO films with a mixture of different rare-earth elements (REs). Such films have enhanced low-temperature and low-field pinning performance [Mac+06; Fei+21]. The use of multiple REs complicates REBCO growth since each RE has an optimal growth window [Erb+20]. In addition, a recent study observed the formation of individual REBCO clusters instead of a homogeneous RE mixture [Ara+18]. The latter is desired for point-defect formation. Here, mixed-RE films with up to five different REs were analyzed. A further complication arises by incorporating additional nanoparticles (for enhanced flux pinning), which can interact chemically with the surrounding REBCO matrix [Maj+21]. Even though this was noted already in 2004 [Mac+04], only a few studies mention or investigate this problem, e.g. for $BaNb_2O_6$ [Yam+08] or $BaZrO_3$ [Maj+21; Díe+21]. Therefore, detailed studies were performed in this thesis on RE intermixing by analyzing the chemical composition of $BaHfO_3$ nanoparticles in single- and mixed-RE REBCO films.

Besides these material-related questions, this thesis also aims to raise and solve method-related issues. This concerns detailed investigations of artifacts induced by TEM-sample preparation or electron-beam-induced damage. Even though very important, such artifacts are rarely reported in the literature, especially for the more novel IBSs [Hai+19; Grü+21a]. Being aware of artifacts and finding solutions is essential for the interpretation of experimental results and the correlation of the structural and electrical properties.
Furthermore, new data-analysis approaches are constantly emerging, which can significantly enhance the information obtained from experimental results. For example, image segmentation can be partly automated with random-forest classifiers [Arg+17; Arz+22], which enables good statistics to accurately measure image features (e.g. the size of precipitates). Blind source separation methods such as non-negative matrix factorization [MS20] or independent component analysis [BN05] are useful for exploratory data analysis in high-dimensional electron-microscopy datasets (e.g. to detect chemical [Grü+21d] or crystalline phases [Vas+15] with small volume fractions). These novel data-analysis approaches will not only be applied on (scanning) transmission electron microscopy ((S)TEM) analyses but also on scanning electron microscopy (SEM) data, for which fewer studies exist in which these techniques were applied [JJK17; TG20]. The application of scanning electron microscopes – compared to transmission electron microscopes – is interesting because they are widely available in materials science research laboratories. Method development and the application of novel data-analysis strategies mentioned above for SEM will significantly enhance the quality of microstructural (surface) analyses and increase sample throughput. The latter aspect is essential for superconducting materials since many fabrication parameters need to be optimized. For this reason, this thesis describes and applies recent data-analysis methods to substantially enhance the information obtained from electron microscopic and electron spectroscopic data from superconducting thin films.
This thesis contains six chapters. After the introduction, the second chapter provides basic information on superconducting materials and electron microscopy. The methods and used experimental procedures are explained in chapter three. Here, details are also given on the used data-acquisition and data-analysis methods. Chapters four and five are concerned with the experimental results and discussion of the two analyzed material systems (IBS and REBCO). A literature overview on the investigated materials is also provided in these chapters. The results and conclusions are summarized in chapter six.

2. Fundamentals

This chapter explains fundamental concepts relevant for this thesis. The working principle and critical materials aspects of superconducting thin films are presented in the first part. Electron microscopy is then introduced (Section 2.2 on page 12), starting with transmission electron microscopy. This section also contains related experimental techniques such as scanning electron microscopy (Page 32), the description of the operation principle of a focused-ion-beam instrument (Page 36), and aspects of chemical analysis with analytical electron microscopy (Page 39). A brief introduction to multivariate statistical analysis (Section 2.3 on page 47) is given at the end of this chapter.

2.1 Superconducting Thin Films

This section introduces basic concepts, critical material properties and the commonly used fabrication techniques of superconducting thin films. The following explanations are based on the textbooks by Sharma [Sha21] and Mangin and Kahn [MK17].

The discovery and concept of superconductivity. The term "superconductivity" describes a state of matter where the electrical resistance vanishes and magnetic field lines are expelled from a material (perfect diamagnetism). Superconductivity was discovered in 1911 by Kamerlingh Onnes and Holst [MK17, p 2] for Hg. An essential prerequisite for this finding was the liquefaction of He only three years earlier by the same group, which - for the first time - enabled experiments at extremely low temperatures of a few K. The transition of Hg to the superconducting state occurs at a temperature of 4.15 K. This transition temperature is denoted as "critial temperature" T_c and was the first discovered physical property related to superconductivity. The requirement for low temperatures was (and is still) partially limiting the broader use of superconductors for commercial, technical applications. The search for a room-temperature superconductor is an ongoing scientific endeavor. In 2020, Snider et al. [Sni+20] reported superconductivity in CSH_x at 15 °C. However, not only are the experimental findings still under debate [HM21] at the time of writing, but superconductivity only occurred under extreme pressure conditions (267 GPa[1]). For commercial applications, the goal would be a superconductor under ambient conditions. Still, the room-temperature superconductivity for CSH_x exemplifies that temperature alone is not the only important property for superconductivity. Indeed, an important property for comparing superconducting materials is the "critical current density" J_c, which specifies how much current can be passed through a superconductor before superconductivity breaks down.

[1] For reference, the pressure in the earth's core is 360 GPa to 400 GPa [Boe+21].

Another property is related to (external or self-induced [TT15]) magnetic fields. Analogous to T_c and J_c, superconductivity is lost when a magnetic field increases above a critical (external) magnetic field H_c. The interaction of a superconductor with an external magnetic field H can be used to classify a superconducting material into two different groups:

- For a **type-I superconductor**, magnetic field lines are fully expelled from the superconductor ("perfect" Meißner-Ochsenfeld effect) and superconductivity vanishes entirely at a H_c. Elemental superconductors (such as Hg) are mostly type-I superconductors.
- For a **type-II superconductor**, two critical magnetic fields, H_{c1} and H_{c2} with $H_{c1} < H_{c2}$, are observed (Fig. 2.1a). Below H_{c1} and above H_{c2}, a type-II superconductor behaves like a type-I superconductor and is superconducting (Meißner phase, i.e. fully expels and external magnetic field) and non-superconducting (normal phase), respectively. Magnetic flux lines can penetrate a type-II superconductor in the intermediate regime $H_{c1} < H < H_{c2}$. This phase is commonly called mixed phase or Shubnikov phase. Most importantly, the material is still superconducting in this phase.

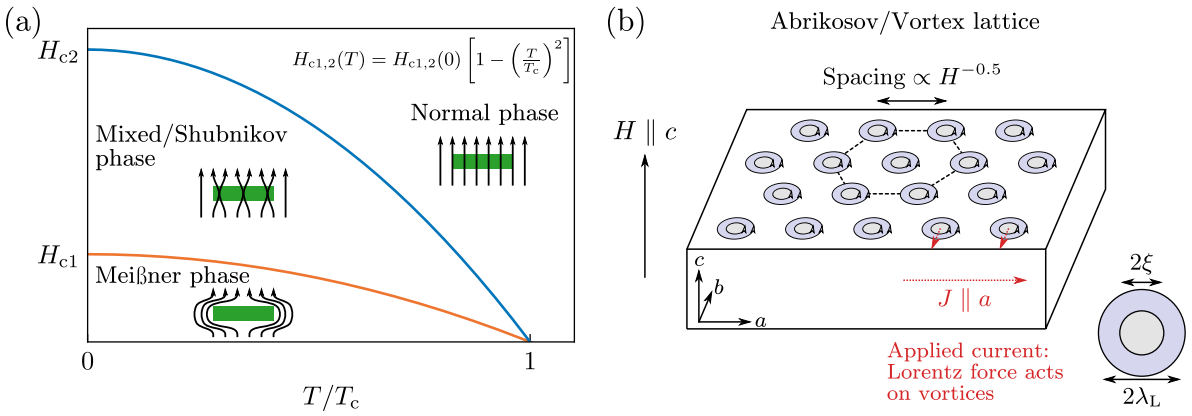

Figure 2.1: Schemes of a typical phase diagram of type-II superconductors and the vortex lattice. (a) H-T-phase diagram according to Tuyn's law (top right) of a type-II superconductor. The arrows schematically show the behavior of an external magnetic field H. Magnetic fluxes penetrate a type-II superconductor in the mixed (or Shubnikov) phase. (b) Scheme of the Vortex (or Abrikosov) lattice in the mixed state shown in (a). The vortices penetrate a superconductor parallel to the external field (here $H \parallel c$) and align in a hexagonal lattice (indicated by a dashed hexagon in the top region). Their spacing depends on the external magnetic field. The characteristic length scale ξ and λ_L describe the extensions of the non-superconducting region and the magnetic field strength, respectively, inside a vortex (see scheme on the bottom right). A Lorentz-type force acts on the vortices if a current J is passed through a superconductor in the mixed state (marked in red). The resulting vortex movement can lead to a macroscopic electrical resistance. The schemes are based on reference [MK17, pp 112, 128, 137, 148].

Each magnetic flux line carries a magnetic flux quantum $\phi_0 = h/2e$, with Planck's constant $h = 6.626 \times 10^{-34}\,\mathrm{JHz}^{-1}$ and the elementary charge $e = 1.602 \times 10^{-19}\,\mathrm{C}$. The concentration and density of these flux lines increase with increasing H as the system maximizes the "surface area" covered by flux lines[2] until $H > H_{c2}$, where superconductivity breaks down. The region at a magnetic flux line is non-superconducting and shielded by induced currents from the surrounding superconducting matrix. This can be seen as a "whirlpool" of currents [MK17], hence these structures are also called (magnetic) vortices. The vortices form a hexagonal (or

[2]For type-II superconductors, the free enthalpy (Gibbs free energy) associated with vortex formation is negative [MK17, p 123]. The system tries to minimize its free enthalpy by generating vortices. However, the magnetic field in a vortex cannot be indefinitely small, i.e. limited by ϕ_0, so the system cannot create indefinitely many vortices.

triangular [Abr57]) vortex lattice (cf. scheme in Fig. 2.1b and see Träuble and Essmann [TE67] for an early experimental visualization). The phenomena of type-II superconductors were first described by Abrikosov in 1952 [Abr04], based on earlier theoretical work by Ginzburg and Landau [GL09].

The London penetration depth λ_L [LLL35] and the superconducting coherence length ξ are two characteristic length scales of a superconducting material. The variable λ_L is a measure of how far an external magnetic field can penetrate a superconductor and is in the range of a few ten to a few hundred nm [MK17, p 26]. Introduced by Pippard and Bragg [PB53], the coherence length ξ "is regarded as determining the width of the interface between superconducting and normal regions" [PB53]. It estimates the length over which superconductivity can be fully restored from a non-superconducting region and shows that such a transition is not fully abrupt. Such a non-superconducting region exists in the core of each vortex (Fig. 2.1b). Superconducting currents (depicted by small arrows at each vortex in Fig. 2.1b) around the core shield the non-superconducting region from the surrounding superconducting matrix. Hence, superconductivity in the surrounding matrix is preserved in the mixed phase between $H_{c1} < H < H_{c2}$. The density of superconducting electrons rises from 0 to the surrounding bulk value over a distance ξ [MK17, p 122], so that the diameter of a magnetic vortex (regarding its non-superconducting properties) can be roughly approximated by 2ξ. Similarly, the magnetic flux is shielded over a distance λ_L (cf. bottom right scheme in Fig. 2.1b). The value of ξ is important for flux pinning, discussed further below. The Ginzburg-Landau parameter $\kappa = \lambda_L/\xi$ relates both characteristic length scales and mathematically defines the two types of superconductors. Type-I superconductors have $\kappa < 1/\sqrt{2}$, whereas type-II superconductors have $\kappa > 1/\sqrt{2}$ [Abr57]. Table 2.1 lists properties of some superconductors. Al has a large value $\xi = 550\,\text{nm}$ compared to its $\lambda_L = 40\,\text{nm}$ [MK17, p 124] and is a type-I superconductor. Nb_3Sn is currently used for low-T high-field magnets (e.g. at the LHC particle accelerator [dOud+97] or at the ITER fusion reactor [Mit+08]) thanks to the well-established fabrication process of Nb_3Sn wires. Compared to Al, Nb_2Sn has ξ in the nm range (with $\lambda_L = 65\,\text{nm}$ [MK17, p 124]), typical for type-II superconductors.

Table 2.1: Superconducting properties for some materials. The given values for the (upper) critical fields H_{c2} are given for $T = 0\,\text{K}$. The values of ξ and γ also depend on T.

	Type	T_c (K)	$\mu_0 H_{c1}$ (T)	$\mu_0 H_{c2}$ (T)	ξ / nm	γ	Reference
Al	I	1.1	–	0.011 (H_c)	550	–	[MK17]
Nb_3Sn	II	18.2	0.44	23	3–4.5	–	[MK17; PLH15]
YBCO	II	93	0.005	140 (ab)	~ 1.3 (ab)	5–7	[MK17]
			0.5	29 (c)	~ 0.2 (c)		
Ba122	II	22	–	70 (ab)	2.4 (ab)	1–2	[Yam+09]
			–	50 (c)	1.2 (c)		

High-temperature superconductivity. Even though significant progress was made in a better understanding of superconductors, the superconducting-material diversity and critical temperatures did not increase dramatically for about 75 years after the first discovery in 1911. The highest critical temperature observed then was 23.2 K for Nb_3Ge [MK17, p 9]. The situation changed drastically in 1986, when Bednorz and Müller [BM86] reported a T_c near 30 K for the layered oxide $La_{2-x}Ba_xCuO_4$. This led to a renewed interest in the scientific community for superconducting materials. One year later, a compound containing Y-Ba-Cu-O reached $T_c = 93\,\text{K}$ [Wu+87]. The composition was identified as $YBa_2Cu_3O_{7-\delta}$ (yttrium barium copper

oxide, YBCO) and was the first superconductor to be cooled with liquid N_2 (LN_2, 77 K), which is cheaper than He cooling. The layered structure and the CuO_2 planes are important for this class of superconductors termed "cuprates". Substitution of Y^{3+} in YBCO with other elements from the lanthanide series (La^{57} to Lu^{71}) with similar ionic radii leads to the more general class of $REBa_2Cu_3O_{7-\delta}$ compounds (rare-earth barium copper oxide, REBCO). These materials are studied as one part of this thesis and a model of the crystalline structure is shown in Fig. 2.2a. The compound is also commonly denoted as "RE123" according to the stoichiometry of RE, Ba, and Cu. Another example for cuprate superconductors is the $Bi_2Sr_2Ca_{n-1}Cu_nO_{2n+4+x}$ (BSCCO) family [Mae+88]. To this date, cuprate superconductors have the highest T_c at ambient pressures and a few technical applications are already available. A recent review was published by MacManus-Driscoll and Wimbush [MW21]. For example, Bergen et al. [Ber+19] built a REBCO-based wind-turbine generator and around a dozen companies [MW21] offer commercial superconducting tapes based on "coated conductor" technology [XS03; OP14], for which epitaxially grown superconducting thin films are used.

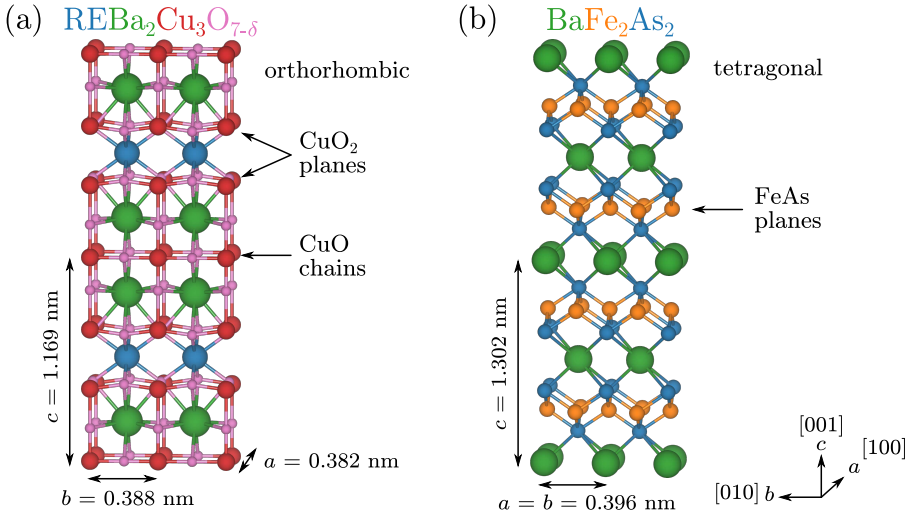

Figure 2.2: Crystal structures of $REBa_2Cu_3O_{7-\delta}$ and $BaFe_2As_2$. Both structures are viewed along the a (or [1 0 0]) direction. The shown structures and unit-cell parameters were taken from ICSD code 56 507 (YBCO) and 169 555 ($BaFe_2As_2$).

Another class of superconductors based on Fe was discovered in 2006 by Kamihara et al. [Kam+06] in LaFeOP with $T_c = 4$ K with an iron-pnictide plane $Fe^{2+}P^{3-}$. The compound has a layered structure similar to the cuprates. Broader interest in the scientific community for these iron-based superconductors (IBS) only rose two years later with another publication by the same group [Kam+08], where a comparably high $T_c = 26$ K was found for $LaFeAsO_{1-x}F_x$. These discoveries mark the beginning of the "iron age" of superconductivity [Hai21] (which appropriately follows the "bronze age" of the cuprate superconductors). Like cuprates, a whole "zoo" of IBS materials of different compositions has emerged over the following years. The reader is referred to the book by Haindl [Hai21] for a chronological overview. The compound $BaFe_2As_2$ (Ba122, with 122 describing the stoichiometry, cf. Fig. 2.2b) with a slight Co-substitution for Fe, typically $Ba(Fe_{0.92}Co_{0.08})_2As_2$ [Kat+12], is a widely studied IBS thanks to its phase stability and easier synthesis compared to other IBS. Ba122 thin films grown on CaF_2 show $T_c \approx 26$ K [Kat+12; Lan+19a] (higher than the value for bulk samples listed in Table 2.1), even though K-substituted (for Ba) Ba122 has reached $T_c = 38$ K [RTJ08]. Naturally, there are fewer technical applications yet when compared with cuprate superconductors. However, IBS are promising candidates for low-T high-field applications (e.g. for particle accelerator magnets [Zha+21a]). A great advantage of IBS is the reduced anisotropy γ of their superconducting properties compared to cuprate superconductors [Hos+18] (cf. Table 2.1). The anisotropy in IBS and cuprate superconductors

arises due to their layered structure (cf. unit cells in Fig. 2.2), where, e.g., the values for H_{c2} are different parallel to the superconducting planes ($\parallel ab$) compared to the orthogonal direction ($\parallel c$) [Hos+18]:

$$\gamma = \frac{H_{c2\parallel ab}}{H_{c2\parallel c}} = \frac{\xi_{ab}}{\xi_c} \tag{2.1}$$

The temperature-dependent anisotropy values are $\gamma = 1$ to 2 for 122-type IBS versus $\gamma = 5$ to 7 for REBCO [Hos+18], meaning that, e.g., IBS are less affected by the direction of an external field H. Another advantage of IBS is the higher critical grain-boundary angle $\theta_{\mathrm{GB,c}} \approx 8°$ for Ba122 compared to $\theta_{\mathrm{GB,c}} \approx 5°$ for REBCO [IHY20]. In general, J_c drops exponentially for increasing θ_{GB} when an angle between two crystalline structures at a grain boundary exceeds $\theta_{\mathrm{GB,c}}$. This means that IBS are less susceptible to grain misorientations than cuprate superconductors. Both types of superconductors show high critical fields H_{c2} (cf. Table 2.1, note that the values are extrapolated for $H_{c2}(0\,\mathrm{K})$) and cuprates have an advantage regarding T_c. This short introduction shows that both types are promising materials for technical applications. A goal for all superconducting materials is to better understand the superconducting properties and optimize the growth conditions to maximize J_c for technical applications. Epitaxially grown thin films on single crystalline substrates are an ideal model platform to control and study the influence of different growth parameters [Hai+14; Hän+19], e.g. the growth rate.

Vortex Pinning. A fundamental research interest for type-II superconductors is the controlled addition of so-called "pinning centers" into the microstructure of a superconductor. All application-relevant superconductors operate in the mixed regime ($H_{c1} < H < H_{c2}$), where a superconductor is partially penetrated by magnetic vortices (Fig. 2.1b). When a current J is applied through a superconductor, a Lorentz force acts on the vortices and causes them to move through a material. This creates a macroscopic resistance and ultimately causes a transition to the normal-conducting state at a critical current density J_c[3]. However, magnetic vortices tend to get "pinned" or trapped by non-superconducting regions in a superconductor. Such regions are called pinning centers. Crystalline defects (e.g. stacking faults or dislocations) often result in non-superconducting regions in the superconducting matrix, making them act as pinning centers. As a result, a pinning landscape with ideal-sized defects [Fol+07; FKM17] in the microstructure of a superconductor leads to a higher J_c, which is beneficial for applications and a main goal of current research. The *controlled* and *reproducible* fabrication of pinning centers is a challenging task due to several reasons:

- The optimal size of a pinning center is in the order of the coherence length ξ, i.e. in the range of a few nm (cf. Table 2.1). Since $\xi_{ab} \neq \xi_c$ (especially for REBCO), a pinning center can be more efficient for $H \parallel c$ or $H \parallel ab$. More isotropic pinning is achieved as a compromise between the two optimal sizes (e.g. a round nanoparticle).

- The direction of an external field H influences the pinning efficiency. For example, a non-superconducting planar defect in the ab plane is efficient for $H \parallel ab$, whereas a grain-boundary oriented parallel to the c direction is efficient for $H \parallel c$. In general, the dimensionality (0D–3D) of a pinning center is essential.

[3] The here discussed J_c is related to a critical current limited by vortex movement. A more fundamental critical current density j_c ($> J_c$) is related to a depairing of Cooper pairs in a superconductor (Silsbee effect). The value j_c can be seen as the theoretical maximum current density for a superconductor. However, the value J_c is (still) limiting the possible critical current density J for real-world superconductors.

- The efficiency of a pinning center depends on the operating temperature, since ξ depends on T, $\xi(T) \propto (1 - T/T_c)^{-0.5}$ [MK17, p 125]. The value of $\xi(T)$ increases with increasing T, and the ideal size (and pinning efficiency) of a vortex-pinning center, therefore, depends on the operating temperature [MW21]. For example, zero-dimensional point defects (e.g. atomic disorder) become effective pinning centers at very low temperatures $T < 30\,\mathrm{K}$ [Cay+20; Fei+21; MW21].
- The growth conditions and kinetics are different for different fabrication methods [MW21].
- For each fabrication method, several fabrication parameters (e.g. growth rate, substrate temperature, purity of the source materials, oxygenation conditions for REBCO, ...) influence the final microstructure. It is challenging to identify these parameter-structure relationships.
- Experimental investigation of the microstructure, e.g. by electron microscopy, may not represent the as-synthesized bulk material. In the case of electron microscopy, thin samples may be altered structurally by ion- or electron-beam bombardment. Superconducting samples can also degrade structurally during sample storage.

Besides *intrinsic* pinning centers such as stacking faults (2D) or atomic disorder (0D), external stimuli (e.g. addition of nanoparticles or ion bombardment) can be used to modify the microstructure. This defect type is often denoted as an *artificial* pinning center. For example, the addition of barium oxide perovskite nanoparticles (3D) such as $BaHfO_3$ or $BaZrO_3$ is a popular method to enhance pinning and subsequently J_c [Ant+20; MW21]. Despite the challenges mentioned above, the controlled addition of pinning centers into the structure of a superconductor has already increased J_c compared to pristine superconducting films.

Thin-Film Fabrication. Superconducting thin films of Ba122 and REBCO in this work are prepared either by pulsed laser deposition (PLD) or chemical solution deposition (CSD). In the following, the basic principles are explained. In PLD [CE08] (Fig. 2.3a), a clean substrate is placed into a vacuum chamber with its surface facing a target material[4] (on-axis PLD) consisting of the desired thin-film material. Laser pulses are directed at the target material and locally evaporate it. A plasma plume forms and the target material condenses on the opposing substrate. Epitaxial growth of the target material on the substrate surface is then possible for an optimized set of fabrication parameters (e.g. substrate temperature, deposition rate, ...) and matching lattice parameters between the target and the substrate materials. Multiple different target materials can be loaded into the vacuum chamber and switched during PLD, enabling complex sample mixtures. The chamber can be pumped to ultra-high vacuum conditions (e.g., for Ba122 deposition) or exposed to a constant gas flow (e.g., O flow for REBCO deposition). An important property of PLD is (in a first approximation [CE08]) the preservation of the target composition (or stoichiometry) for the thin-film composition. This feature enables the growth of complex materials as thin films. For a more detailed explanation about the plasma formation and PLD, the reader is referred to literature [Eas06; CE08].

Chemical solution deposition is a cost-efficient method to prepare REBCO thin films since it is a non-vacuum process. More specifically, metal-organic deposition (MOD) using trifluoroacetate (TFA) precursor solutions [Erb+20] was used in this work which can be considered a subset of CSD [AH03; Obr+04]. The method was introduced by Mankiewich et al. [Man+87] and Gupta et al. [Gup+88] and consists of three steps (Fig. 2.3b):

[4] The substrate surface can also be tilted by 90° with respect to the target surface in *off-axis* PLD [Hol+92].

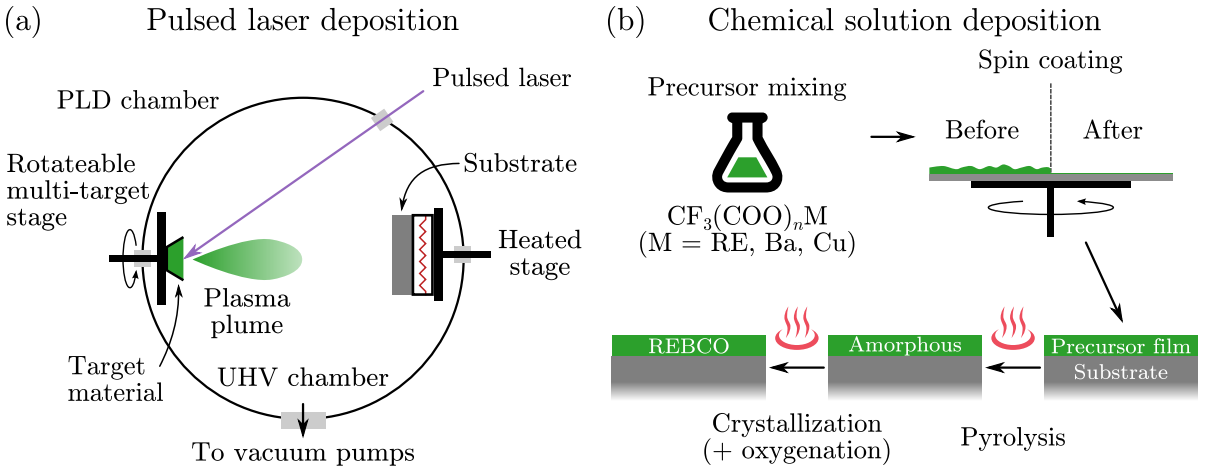

Figure 2.3: Schemes of pulsed laser deposition (PLD) and chemical solution deposition (CSD) for thin-film fabrication. (a) Basic components of a PLD setup in an ultra-high vacuum chamber. A pulsed laser evaporates a target material and generates a plasma plume with the desired film composition. A heated substrate facing the target material is hit by the evaporated material, which condenses on the surface and forms an epitaxial film for optimized PLD parameters. (b) Basic steps for REBCO film growth by CSD (TFA-MOD). Precursor solutions are prepared, mixed and then spin coated on a single-crystalline substrate. A pyrolysis heating step removes the organic material from the precursor solution. A second heating step at higher temperatures forms the crystalline REBCO structure. O is supplied to form the superconducting $REBa_2Cu_3O_{7-\delta}$ phase.

1. Precursor solutions from metal acetates $CF_3(COO)_nM$ (M = RE, Ba, Cu) [AH03] are prepared and mixed.

2. A clean substrate is coated with the precursor solutions. This work used spin-coating to spread the solution evenly over a substrate. The film thickness can be tuned by the rotation speed.

3. The precursor solution and the substrate are treated in an oven. The organic molecules are removed first at a lower temperature (pyrolysis). This step results in an amorphous RE-Ba-O-F matrix with CuO crystals [AH03]. The amorphous structure crystallizes (at a higher temperature) and forms a REBCO film in a second heating step.

For REBCO, an oxygenation step is additionally required independent of the fabrication method. This step changes the non-superconducting compound $REBa_2Cu_3O_6$ (tetragonal) to the desired superconducting compound $REBa_2Cu_3O_{7-\delta}$ ($\delta \approx 0$, orthorhombic, cf. Fig. 2.2a). Oxygenation can be performed *in-situ* during film deposition (e.g., PLD under an O atmosphere) or *ex-situ* after film deposition in an oven with an O atmosphere. Controlling (and preserving) the optimal O stoichiometry is important for cuprate supercondcutors [Cay16]. For example, Lu et al. [Lu+21] found pronounced O out-diffusion from REBCO during heating which worsens the superconducting properties. Heating of a REBCO film can appear during soldering of REBCO tapes, as required for technical applications. A thin passivation layer (e.g. Au) is often deposited on REBCO films to preserve the film integrity from air and prevent O out-diffusion [Kum+94]. A better understanding of O in-diffusion (out-diffusion) into (out of) the REBCO structure is desired to optimize REBCO fabrication.

This brief introduction to high-temperature superconductors, vortex pinning and the fabrication methods shows the complexity of film fabrication of superconducting films. A delicate balance of a high-quality film texture combined with ideal-sized non-superconducting inclusions (in

the range of the coherence length ξ) is desired. This requires a detailed understanding of the microstructure and the fabrication process. Electron microscopy is a versatile tool to study the resulting microstructure with the required spatial resolution in the nm range.

2.2 Electron Microscopy

This section introduces basic concepts of electron microscopy. Electron microscopy exploits the smaller wavelength λ and stronger interaction of electrons with matter than (visible) light. Abbe [Abb73] showed that the resolving power of an optical microscope is ultimately limited by the illumination wavelength, i.e. $\Delta s \propto \lambda$ with the distance Δs between two points, which can still be resolved. The wavelength of visible light is in the range of 380 nm to 780 nm. In 1905, Einstein [Ein05] showed that some phenomena concerning light waves can only be explained when light is assumed as (quantized) particles, i.e. photons. Based on this idea, De Broglie [dBro25] proposed that the same wave-particle duality also holds for particles, e.g. that electrons (then seen as particles) can also behave as a wave with a wavelength $\lambda = h/p$, with the impulse p. The relativistic wavelength for electrons accelerated by a voltage V (i.e. with an energy $E_0 = eV$) is given by [WC08, p 14]

$$\lambda = \frac{h}{\sqrt{2m_0 eV\left(1 + \frac{eV}{2m_0c^2}\right)}} \tag{2.2}$$

with the electron's rest mass $m_0 = 9.109 \times 10^{-31}\,\mathrm{kg}$, the elementary charge $e = 1.602 \times 10^{-19}\,\mathrm{C}$, and the speed of light in vacuum $c = 299\,792\,458\,\mathrm{m\,s^{-1}}$. For example, the electron wavelengths for typical energies E_0 used in electron microscopy range from 27.4 pm (2 keV), 2.5 pm (200 keV), or 2.0 pm (300 keV), which is at least a factor 10 000 smaller compared to visible light. Another important aspect of an electron microscope is the usage of electromagnetic lenses (analogous to glass lenses in light microscopy) to control and focus an electron beam. Busch [Bus27] noticed in 1927 that magnetic fields produced by narrow electric coils focus electrons similar to convex glass lenses. Multiple lenses of this kind were combined five years later by Knoll and Ruska [KR32] for imaging, leading to the invention of the electron microscope. A higher spatial resolution of an electron microscope compared to light microscopes was reported only two years later [Rus34].

In transmission electron microscopy (TEM), a thin sample is illuminated with a high-energy electron beam (typically $\geq 60\,\mathrm{keV}$). Typical thicknesses of electron-transparent specimens are between a few 10 nm and a few um depending on the average atomic number of the material and on the specific electron energy. Two basic operation modes can be distinguished by the geometry of the illumination (Fig. 2.4a). A broad, parallel illumination of a sample region (similar to light microscopy) is used in conventional TEM (CTEM), whereas a focused electron probe is scanned over a sample region in scanning transmission electron microscopy (STEM). Electrons interact with the specimen structure and different signals are generated, which can be used to obtain structural and chemical information about a specimen (Fig. 2.4a). The scattering events can be separated into *elastic* (scattering at atomic nuclei without energy loss) and *inelastic* (scattering at electrons with energy loss) scattering. Coherently and elastically scattered electrons are used for diffraction imaging and in high-resolution TEM (Page 21). Incoherently scattered electrons with high scattering angles are used for high-angle annular dark-field STEM imaging (Page 30). Inelastic scattering events include an energy loss of an incoming electron in the sample. Such electrons are mainly scattered into small angles [Ege11, p 125] and provide chemical and

electronic information by electron energy loss spectroscopy (Page 44). Similarly, x-rays also provide chemical information and are generated isotropically in all directions (Page 40).

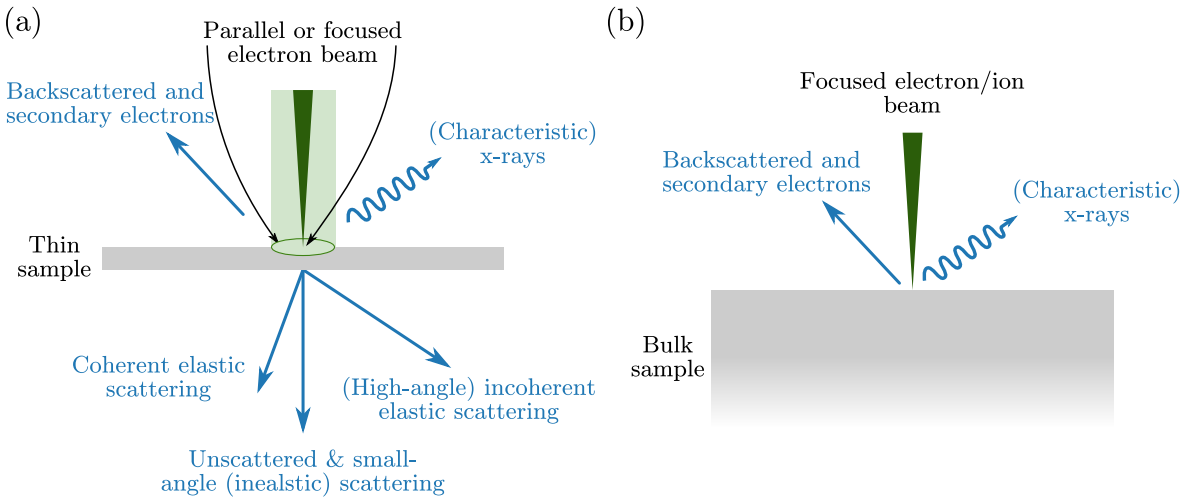

Figure 2.4: Typical signals arising from electron-matter interactions. (a) Selected signals generated in an electron-transparent sample in TEM. The incident illumination can be parallel (CTEM) or focused (STEM). The transmitted signals are typically used for TEM analyses. (b) A focused electron probe is scanned over a bulk-sample (electron-transparent-sample) surface in scanning (transmission) electron microscopy (or with a focused ion beam). Different signals emerging near the sample surface are used for materials analysis. The schemes mostly show typical signals used in this work and are based on Williams and Carter [WC08, p 25].

.

Bulk samples can be investigated with scanning electron microscopy (Page 32) and structurally modified with a focused-ion-beam instrument (Page 36), as shown in Fig. 2.4b. Secondary or backscattered electrons are used for imaging and x-rays can be used for chemical analysis. The following sections introduce the mentioned techniques and the working principles of electron microscopes.

2.2.1 Operation Principle of a (Scanning) Transmission Electron Microscope

This section explains the basics of combined (scanning) transmission electron microscopes (S/TEM). A S/TEM can illuminate an electron-transparent sample with a parallel beam (as used in CTEM) or with a focused electron probe (as used in STEM). This is achieved by a symmetrical objective-lens design, where the sample is embedded in the strong magnetic field between the two lens pole-pieces. Figure 2.5 schematically shows the electron optics of the used FEI Titan^3 80–300 S/TEM. The main components are briefly explained from top to bottom in the following. The information is taken from literature [HS19; WC08; RK08]

Electron source

The two fundamental characteristics of an electron gun are the brightness β_{gun}, which is given by the current density per area and solid angle in units of $\text{Am}^{-2}\text{sr}^{-1}$ (higher is better), and the energy spread ΔE of the emitted electrons (smaller is better). Modern electron microscopes are equipped with so-called *field-emission guns* (FEGs) to generate the electron beam. FEGs provide higher β_{gun}/smaller ΔE values than thermionic sources such as a simple W filament or a LaB_6 tip. In addition, the temporal coherence (related to ΔE) and spatial coherence (related to the virtual source size at the first beam cross-over) is important for high-resolution imaging

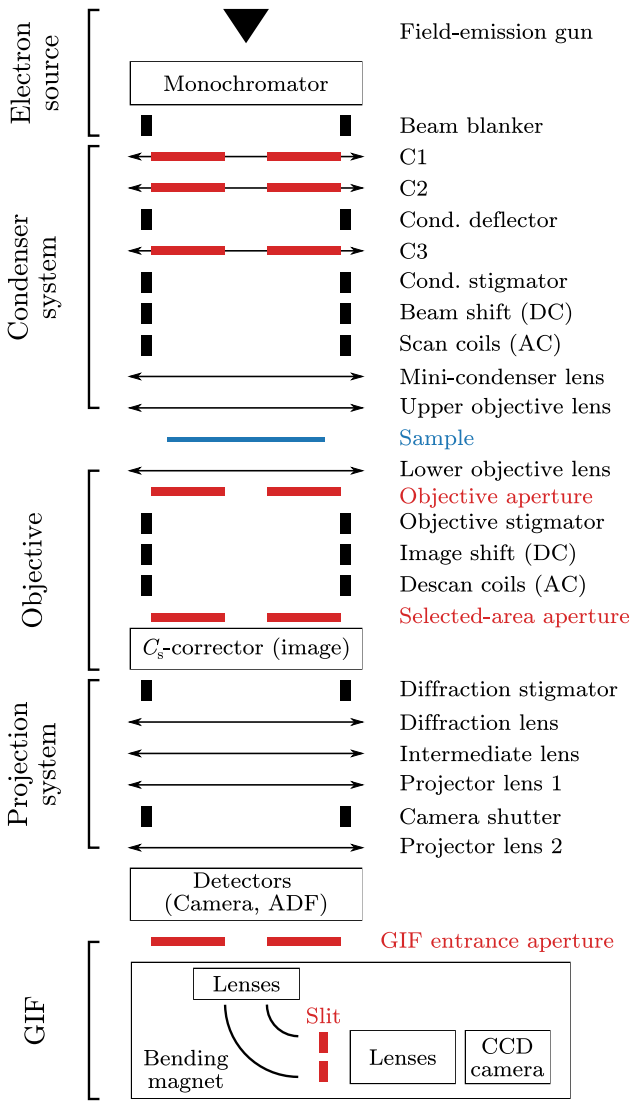

Figure 2.5: Schematical view of the electron optical parts of the FEI Titan³ 80–300 microscope. Lenses are drawn as horizontal arrows (↔), beam deflection coils and stigmator coils are shown as vertical bars, and apertures are shown as red horizontal bars. The shown distances are not to scale.
A S/TEM instrument can be summarized as a condenser system (sample illumination), an objective (image formation in CTEM), a projection system (image magnification), and a set of detectors (alignment screen, camera). Each section contains a set of lenses (condenser lenses are abbreviated as "CX"), physical apertures, and beam deflectors to control the beam. The sample (blue) is embedded in the magnetic field between two symmetrical objective pole-pieces.
The used Titan microscope is additionally equipped with a monochromator, an image-side C_s-corrector, and a Gatan Imaging Filter (GIF) for EELS analysis.
Some special notes about the Titan electron optics: (i) The C_s-corrector corrects the lower objective lens, the upper objective lens is used for probe formation with $C_s = 1.2\,\mathrm{mm}$. (ii) An additional third condenser lens (C3) allows for variable parallel illumination settings and convergences angles for STEM. (iii) Additional descan coils work in tandem with the scan coils to keep the beam stationary in the detector plane during STEM imaging at low magnification or small camera lengths.

in CTEM and probe formation in STEM and scanning electron microscopy.
As the name suggests, a FEG uses an effect called field emission, which is caused by a strong electric field E_{FEG} at a thin tip made of W. To extract electrons from the tip, the energetic barrier (as defined by the work function of the material) must be overcome. In the case of field emission, this barrier is lowered by the applied external field E_{FEG} due to the Schottky effect. If E_{FEG} is large enough (in the order of $1 \times 10^8\,\mathrm{V\,m^{-1}}$), electrons can tunnel through the reduced potential barrier and escape from the tip. The electric field at the tip is given by

$$E_{\mathrm{FEG}} = \frac{U_{\mathrm{ext}}}{r} \tag{2.3}$$

with the extraction voltage U_{ext} and the tip radius r. Larger E_{FEG} can be realized by using a sharp tip, e.g., $E_{\mathrm{FEG}} = 1 \times 10^{10}\,\mathrm{V\,m^{-1}}$ for $U_{\mathrm{ext}} = 1\,\mathrm{kV}$ and $r = 100\,\mathrm{nm}$. In practice, FEGs are made of W because they must withstand high mechanical stress in this operating condition. The work function of the emitting surface should be as small as possible. Furthermore, the tip must be kept free of contamination which is achieved by running the tip in an ultra-high vacuum environment ($< 1 \times 10^{-9}\,\mathrm{Pa}$). The electron source has the highest vacuum requirements in an electron microscope. A FEG is isolated from the rest of the column by a valve when the

microscope is not used or during a sample exchange. Two types of FEGs are currently used in electron microscopes:

- The *thermally-assisted FEG* (or *Schottky FEG*) is heated to around 1700 K for thermionic emission and to remove adsorbed contamination on the tip. In addition, a ZrO_2-coating on the W-tip is used to reduce the work function from 4.5 eV to 2.7 eV [RK08, p 84]. The strong electrical field at the tip reduces the potential barrier. As pointed out in [RK08, p 88], the Schottky FEG is technically a thermionic emitter and *not* a FEG such as the cold FEG below. Still, the properties of a Schottky FEG are better than other thermionic emitters (W filaments or a LaB_6 emitters): The energy spread ΔE of the emitted electrons is around 0.7 eV and the brightness is around $5 \times 10^{12}\,\mathrm{Am^{-2}sr^{-1}}$. The virtual source size is about 15 nm resulting in high spatial coherence.

- The *cold FEG* is not heated during operation and the electrons are emitted by tunneling through a thin potential barrier. The required E_{FEG} for tunneling is roughly ten times higher than the Schottky FEG [RK08, p 88]. The cold FEG has a smaller energy spread of $\Delta E \approx 0.3\,\mathrm{eV}$ and a higher brightness of $1 \times 10^{13}\,\mathrm{Am^{-2}sr^{-1}}$ compared to the Schottky FEG. The virtual source size is only a few nm. Because of contamination, the cold FEG has higher vacuum requirements than the Schottky FEG. In addition, the current decreases continuously during usage because of surface contamination. After a while (around every few hours), the contamination is removed from the tip by quickly heating it ("flashing").

To summarize, the cold FEG provides better performances with the drawbacks of higher vacuum requirements and less stable beam currents. The latter must be considered in analytical and quantitative analysis, where constant beam currents are typically assumed [Hor+10]. All microscopes used in this work are equipped with a Schottky FEG.
The used FEI Titan^3 80–300 and Thermo Scientific Helios G4 FX microscopes also have a monochromator after the FEG, which can be switched on ("excited") to decrease the energy spread ΔE in the beam at the expense of beam current. In the case of the FEI Titan^3 80–300, the monochromator was not actively used in the experiments. Still, even in the unexcited state the monochromator gives the operator fine control of the gun lens, which can be used to quickly adjust the beam current to prevent irradiation damage of the sample.

Condenser system

The condenser system controls the electron beam illumination on the sample. Different types of illumination settings can be set up depending on the experiment. In this regard, a modern S/TEM uses 4 to 5 lenses in the condenser system to offer the required flexibility. Understanding the different possibilities of sample illumination is one of the critical aspects of applying different electron-microscopy techniques in a S/TEM. Therefore, this paragraph aims to give a brief overview of the condenser system and the basic operation modes.
The two basic illumination settings are a (i) parallel illumination of an extended sample region (for CTEM) and (ii) the formation of a focused electron probe on the sample (for STEM). These modes are discussed in context with the schematic ray diagrams shown in Fig. 2.6. The C3 lens was removed in the ray diagrams for simplicity compared to Fig. 2.5.

The explanation starts with two microscope modes for parallel illumination (Fig. 2.6a and b). The difference between the "Microprobe" and "Nanoprobe" mode (terminology by the microscope manufacturer FEI) is the excitation of the so-called "mini-condenser" lens (MC lens):

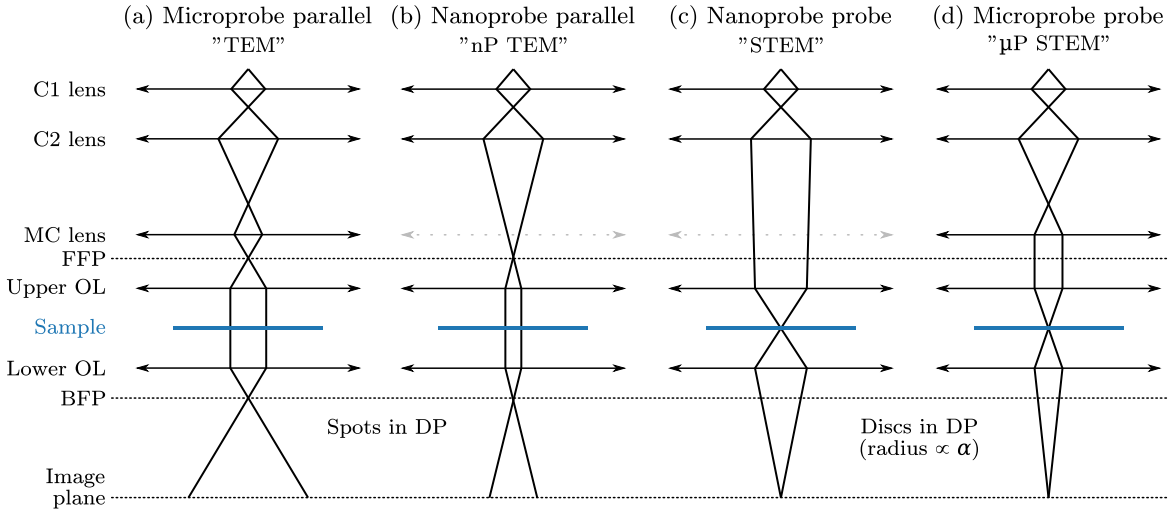

Figure 2.6: Simplified ray diagrams for different illumination settings. Parallel sample illumination for (a) large areas in microprobe and (b) small areas in nanoprobe mode. A spot diffraction pattern (SAED pattern) is observed in the BFP. An electron probe can be formed with (c) large (nanoprobe) or (d) small (microprobe) convergence semi-angle α. A diffraction disc pattern (CBED pattern) is observed in the BFP. The mini-condenser (MC) lens is optically on/off in microprobe/nanoprobe mode.

In microprobe mode, the MC lens is on and in nanoprobe, it is off[5], i.e. in the off-state, it does not focus the electron beam. In the symmetrical objective-lens design of a combined S/TEM, the highly excited upper objective lens is the final lens of the condenser system and defines the shape of the beam. As in light optics, electron lenses have special focal planes. Parallel rays entering a lens will be focused to a spot in the *back-focal plane* (BFP). *Vice versa*, rays emerging from a point in the *front-focal plane* (FFP) will continue in a parallel path behind a lens. The latter aspect is used in a S/TEM to create a parallel beam on the sample. When the beam is focused to a cross-over in the FFP of the upper objective lens, the sample illumination will be parallel. The FFP and BFP are conjugate, meaning that in a ray diagram, a point in the FFP of the upper OL will result in a point in the BFP of the lower OL. The point pattern in the BFP under parallel sample illumination is called the *(selected-area) electron diffraction* (SAED) or simply *diffraction* pattern.

As visible in the ray diagrams in Fig. 2.6a and b, an electron beam can be focused in the FFP of the upper objective lens in microprobe ("TEM" mode) mode as well as in nanoprobe mode ("nP TEM" mode). The benefits of the microprobe mode are that larger sample areas can be illuminated with parallel incidence. In addition, for high-resolution imaging at very high magnification, the beam sometimes has to be condensed to increase the intensity on a camera to record an image. In this case, the convergence angle for the non-parallel illumination is roughly five times smaller than in nanoprobe mode. This results in better spatial coherence for HRTEM. The benefit of using the nanoprobe mode for parallel illumination is the possibility to form smaller parallel beams compared to the microprobe mode. For example, in the FEI Titan^3 80–300 microscope, it is possible to illuminate an area with a diameter of roughly 200 nm with a parallel beam in nP-TEM mode (using a small 50 µm C2 aperture). The smaller beam diameter can be exploited to minimize the illuminated area on the sample by using a small parallel beam that just fills the camera's necessary area for acquisition. Because of this reason, the nP-TEM mode is often used in cryo-electron microscopy for imaging beam-sensitive biological samples,

[5]In practice, the current is reversed to prevent thermal drift. The MC lens is only "optically" switched off.

e.g. in references [Chu+16; Sug+18; Yip+20]. In a similar fashion, the nP-TEM mode was primarily used for HRTEM imaging in this work to minimize irradiation damage to adjacent sample regions. The microprobe TEM mode was used at (i) lower magnification for overview imaging or (ii) at very high magnification when the beam could no longer be kept parallel.

The condenser system can form a focused probe in the sample plane for STEM (Fig. 2.6c and d). Similar to the discussion for parallel illumination, electron probes can be formed in nanoprobe (MC lens off) and microprobe mode (MC lens on). The nanoprobe setup will be discussed first because it is the default mode for STEM imaging. As visible in Fig. 2.6c, the C2 lens is weakly excited and a nearly parallel beam enters the upper OL. The beam is then focused into the BFP of the upper OL. The S/TEM manufacturer aligns and sets a specific excitation of the OL for best microscope performance, which also defines the aforementioned BFP with the optimal probe. The sample is physically moved to this plane with the sample holder during coarse focusing. Effectively, an image of the source is imaged onto the sample and the condenser system demagnifies the source image. A stronger excitation of the C1 lens results in a stronger demagnification at the expense of beam current. The C1 excitation is changed in fixed steps denoted as *spot-size* values (1 to 11). A higher spot-size value corresponds to a stronger C1 lens excitation. The upper OL focuses the beam under a convergence semi-angle α on the sample. Due to lens aberrations, an optimal value for α can be found for the smallest possible electron probe in nanoprobe mode. This will be discussed in Section 2.2.3.
A convergent illumination (instead of parallel illumination) will result in diffraction discs (instead of sharp diffraction spots) in the BFP of the lower OL. Such diffraction patterns are called *convergent beam electron diffraction* (CBED) patterns. The radius of the diffraction discs is given by α. For typical microscope conditions and crystalline samples, the large α used to form the smallest possible probe in nanoprobe mode will cause an overlap of the diffraction discs in the BFP. This is shown exemplarily in Fig. 2.7a, where the electron probe was continuously scanned during CBED pattern acquisition to average the CBED pattern over a small CaF_2 sample area, i.e. a position-averaged CBED (PACBED) pattern [LeB+10]. For phase identification of crystalline samples by diffraction patterns, the disc positions the angles between different discs must be evaluated. The substantial overlap of the diffraction discs in nanoprobe mode hinders precise analysis of these properties.

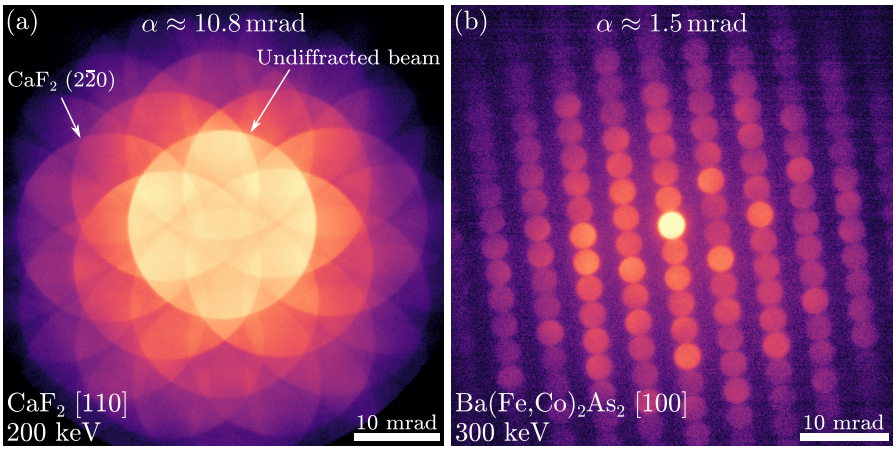

Figure 2.7: PACBED patterns for nanoprobe and microprobe STEM modes. (a) A large α in nanoprobe mode leads to overlapping diffraction discs. (b) In microprobe STEM mode the discs are separated and easier to analyze. Experimental setups and samples are shown in the images.

To overcome this problem, α must be smaller than the characteristic distances between Bragg reflections for a given sample. Such conditions can be realized in microprobe STEM mode ("µP-STEM", Fig. 2.6d). Figure 2.7b shows an exemplary PACBED pattern of the Ba122[1 0 0]

zone-axis orientation with a small convergence semi-angle $\alpha \approx 1.5\,\mathrm{mrad}$ where adjacent diffraction discs touch each other but do not overlap. The probe diameter in this configuration is about 1 nm, which is suited for diffraction analysis at the nanoscale. The technique is called *nanobeam electron diffraction* (NBD or NBED). In comparison, SAED using a parallel illumination is limited to a spatial resolution of around 100 nm to 500 nm [WC08, p 323].
Independent of the chosen STEM mode, the generated electron probe is scanned over the samples by a set of scan coils to form STEM images (Fig. 2.5). The pivot points of the scan coils are aligned with the FFP of the upper OL, which results in a stationary CBED pattern in the BFP of the lower OL [RK08, p 98]. The CBED pattern in the BFP is then imaged (and (de)magnified) onto the plane of the STEM detectors by the projection system (not shown in Fig. 2.6). Another set of coils can translate the beam electronically over small distances ("beam shift"). The beam shift is used for parking the beam on a selected sample region (e.g. to collect spectral data or diffraction patterns) or as an alternative to stage movements at high STEM magnification to prevent stage drift. The beam position can be synchronized with the acquisition of electron energy-loss spectra, energy-dispersive x-ray spectra, or CBED patterns.
At this point it is worth mentioning that a third condenser lens (C3) is used in modern S/TEMs to further increase the condenser system's flexibility (but also complexity). With a C3 lens, α can be freely adjusted in an angular range for STEM and the beam is kept parallel for a variable range of beam sizes in CTEM.

Sample holder, objective lens, and aberration corrector

After the condenser system, the electron beam hits the sample, which is mounted on a TEM grid (3.05 mm diameter) in a TEM holder. In this work, double-tilt holders were used to allow for tilting the sample along two perpendicular directions (normally called α and β tilt, not be confused with the convergence and collection semi-angle). The two tilt directions are required to align crystalline TEM samples precisely with respect to the incident beam. The TEM holder is fixed in a stage, allowing fine movements in three dimensions (x, y, z, with z being parallel to the beam direction by convention) with minimal stage drift.
The beam enters the lower OL after transmission through an electron-transparent sample area. Parallel rays emerging from the sample are focused into a spot in the BFP and form the diffraction pattern. Bragg's law, $\theta \propto d^{-1}$, shows that higher spatial frequencies (smaller crystalline plane distances d) correspond to higher scattering angles θ. In the BFP, θ is directly proportional to the radial distance from the undiffracted beam. An objective aperture can be introduced into the beam path in the BFP to select the range of scattering angles θ contributing to the image. One can select (i) the undiffracted beam (for bright-field CTEM), (ii) a specific diffraction spot (dark-field CTEM), (iii) or a set of Bragg reflections for HRTEM.
A first image of the sample is formed in the image plane of the lower OL. Here, one can introduce a *selected-area aperture* to indirectly select the sample area which contributes to the diffraction pattern (or EELS signal in CTEM-EELS). The objective lens magnifies the image by a factor of 20 to 50 [RK08, p 103]. Therefore, the angular range of the electron trajectories entering the following lens is demagnified by the same factor. This means that the lens aberrations (mainly the spherical aberration coefficient C_s) of the lower OL determine the attainable resolution in CTEM.
An aberration corrector (or C_s-corrector) is used in modern S/TEMs to correct for such lens aberrations in the objective lens. This technology has been available since the late 90s [Kri+97; Hai+98b; Hai+98c; Hai+98a] and is seeing a widespread use today. In the used FEI Titan^3 80–300 microscope, the aberrations of the lower OL (and CTEM image) are corrected. Hence,

the used FEI Titan^3 80–300 is an *image-corrected* S/TEM. Alternatively (or additionally), the aberrations of the upper OL can be corrected to form a smaller STEM probe with higher probe currents in a *probe-corrected* S/TEM. Aberration correctors consist of a complicated stack of hexa- or octopole lenses combined with quadrupole transfer lenses [Kir20, p 27] to effectively introduce negative C_s, which cannot be achieved by round lenses according to Scherzer's theorem [Sch36]. This balances the intrinsic, positive C_s of the OL [Sch36]. Spherical aberration correctors enable sub-Å-resolution imaging.

Figure 2.5 shows that beam deflectors are implemented in the objective similar to the condenser system. The *image shift* coils can electronically translate the field of view to a different sample region without stage movements (analogous to the *beam shift* in STEM). This is useful to prevent stage drift in atomic-resolution imaging. The *descan* coils work (when activated) in tandem with the scan coils to tilt the beam back to the optical axis. Descanning is necessary for STEM imaging at low magnifications and/or when working at small camera lengths (e.g. for electron energy loss spectroscopy in STEM mode), where the differential pumping aperture can obstruct part of the STEM image [Ott91].

Projection system

The projection system is responsible for the magnification of (i) the first image from the lower OL or (ii) the diffraction pattern of the BFP onto a suitable detector (camera or STEM detectors). The first projection lens (diffraction lens in Fig. 2.5) is used for switching between the "Imaging" and "Diffraction" modes by using (i) the first image plane or (ii) the BFP as the object plane. In diffraction mode, the magnification of a diffraction pattern (i.e., the angular field of view) is termed *camera length*. The following projection lenses in the beam path (intermediate lens, projection lenses 1 & 2) perform a stepwise magnification of an image (or diffraction pattern) from the diffraction lens. The excitation of the projection lenses for a given magnification setting is calibrated by the manufacturer (a so-called *lens series*) and not normally accessible by the microscope user.
The FEI Titan^3 80–300 microscope has a special projection lens mode called "EFTEM", a magnification series with a 14.85 times smaller magnification than the normally available projector lens settings. It is often used in conjunction with the EELS spectrometer to form images with electrons that have undergone a specific energy loss (*energy-filtered* TEM, EFTEM). The additional demagnification of the projection system in EFTEM mode is used to counteract the intrinsic magnification of the energy-loss spectrometer optics to enable larger field of views in the EFTEM technique. EFTEM is typically performed with a parallel illumination. However, the EFTEM projection-lens series can also be used in conjunction with STEM to increase the collection angle (EFSTEM mode).

Image-signal detection

Viewing screen. A retractable fluorescent viewing screen is used for general sample navigation and beam alignments. The viewing screen is coated with ZnS (or CdS), which is excited by the electron beam (cathodoluminescence). The viewing screen is directly visible through a Pb-glass window or recorded by a camera (termed *Flucam* in TFS/FEI microscopes). The latter is used in modern microscopes, where the operator controls the microscope from a remote location to minimize environmental influences.

Camera. A (retractable) camera can record the magnified image or diffraction pattern. Different types of camera detection hardware are currently used in electron microscopy: charge-

coupled device (CCD) [RCM82], complementary metal-oxide-semiconductor (CMOS) [Tie08], and (CMOS-based) direct electron detectors. The incoming electrons are converted to photons in a scintillator (e.g. yttrium aluminium garnet, YAG) for CCD and CMOS cameras because the energetic electron beam can damage the sensor electronics under direct exposure. The photons are guided via fiber optics to the CCD/CMOS chip, where the image signal is registered. In contrast, direct electron detectors can tolerate direct electron-beam exposure.
One metric for detection devices is the detective quantum efficiency (DQE), which measures the noise amplification of the camera (lower is better) in the signal for each electron [FH07]. Another metric is the point spread function (PSF), which relates to the signal spread of a single electron event over several physical camera pixels (smaller is better) [FH07]. The modulation transfer function (MTF) is the Fourier transform of the PSF and is more commonly used to evaluate the camera performance. The MTF modifies the original image intensity described in spatial-frequency space $I_0(k)$ to yield the detected image intensity $I_\mathrm{d}(k)$ [Thu09]:

$$I_\mathrm{d}(k) = I_0(k) \cdot \mathrm{MTF}(k) \tag{2.4}$$

Effectively, the MTF acts as a damping/envelope function in frequency space with a value ranging from 1 (full information transfer) to 0 (no information transfer). Typically, the MTF at lower frequencies is 1 ($\mathrm{MTF}(0) = 1$) and continuously falls off towards the Nyquist frequency k_max. The latter is given by

$$k_\mathrm{max} = \frac{1}{2\Delta} \tag{2.5}$$

with the magnification-dependent pixel size Δ (Nyquist-Shannon sampling theorem). The MTF depends on camera hardware (fiber-optic coupling, physical pixel size), electron energy, and read-out mode (e.g. binning increases the effective pixel size). Exact knowledge of the MTF for a given camera is necessary for quantitative image simulations for HRTEM [Thu09]. In practice, the magnification is used to control the information transfer: a high spatial sampling (small Δ) moves the spatial frequencies of interest to smaller k and, therefore, to higher $\mathrm{MTF}(k)$. The trade-off for using high magnifications is a smaller field of view. Another practical aspect for modern cameras are the comparably large values of $\mathrm{MTF}(k_\mathrm{max}) > 0$. A high enough spatial sampling (small Δ) must be chosen experimentally to avoid aliasing ("undersampling") depending on the sample. For conventional imaging, the largest resolved spatial frequency of the sample must be within the Nyquist limit, i.e. $k_\mathrm{sample} < k_\mathrm{max}$.

STEM detectors. Retractable STEM detectors are used to detect electrons that are scattered in a specific angular range. A circular detector placed in the path of the unscattered beam is used for bright-field imaging. Dark-field imaging is done with one or more annular detector rings, which are concentrically placed around the unscattered beam. Depending on the angular range, the detectors provide different information about the sample. These imaging modes and the detectors will be discussed in section Section 2.2.3.

Gatan Imaging Filter (GIF). An energy filter can be attached to a S/TEM for electron energy loss spectroscopy. A commonly used filter is the post-column "Gatan Imaging Filter" (GIF), which consists of several electron-optical elements, slits, apertures, and a camera for spectroscopy and imaging. More details on this technique are given in Section 2.2.5.

2.2.2 (High-resolution) Transmission Electron Microscopy

This chapter introduces the image-formation principles of high-resolution transmission electron microscopy (HRTEM) and lattice-fringe imaging. In these techniques, the periodic structure of a crystalline TEM sample creates a complicated interference pattern. Exact knowledge of the electron-optical parameters of the OL and the sample thickness are required for the interpretation of HRTEM images.

The specimen as a phase object. The interaction of an incoming electron beam with a specimen can be described in a wave-optical treatment. In general, a specimen alters the amplitude and the phase $\phi(x, y, z)$ of the incoming (plane) wave $\psi_0(x, y)$. A specimen is often modeled as a pure *phase object*, i.e. the amplitude is assumed to be unaffected in the following. After interaction with a specimen, the scattered wave (or exit-wave function) ψ_s is described as [HS19, p 7]

$$\psi_\mathrm{s}(x, y) = |\psi_0(x, y)| \cdot \mathrm{e}^{\mathrm{i}\phi(x,y)} \tag{2.6}$$

This approximation is valid for thin samples (and weakly scattering materials). The phase shift $\phi(x, y, z)$ can be rewritten as a projected potential $V_\mathrm{p}(x, y)$ (projected along the z- or beam direction) of a specimen of thickness t and an energy-dependent interaction constant σ_i:

$$\phi(x, y) = \sigma_\mathrm{i} \int_0^t V(x, y, z)\mathrm{d}z = \sigma_\mathrm{i} V_\mathrm{p}(x, y) \tag{2.7}$$

with

$$\sigma_\mathrm{i} = \frac{2\pi m e \lambda}{h^2} \quad , \tag{2.8}$$

where m and λ are the relativistic electron mass and wavelength. A homogeneous illumination is assumed and the amplitude is set to 1 for clarity, i.e. $|\psi_0(x, y)| = 1$. The scattered wave function ψ_s then reads

$$\psi_\mathrm{s}(x, y) = \mathrm{e}^{\mathrm{i}\sigma_\mathrm{i} V_\mathrm{p}(x,y)} \quad . \tag{2.9}$$

For small phase shift Eq. (2.9) can be expanded as a power series (weak phase-object approximation)

$$\psi_\mathrm{s}(x, y) \approx 1 + \mathrm{i}\sigma_\mathrm{i} V_\mathrm{p}(x, y) \tag{2.10}$$

For a perfect lens without aberrations, a weak-phase object does not produce significant contrast in an image, i.e., it is invisible. This can be understood by noting that the recorded intensity of a wave is given by the squared modulus of a wave ψ_x. Following the description by Reimer and Kohl [RK08, p 211], the intensity of the incident, unscattered wave is given by

$$I_0 = |\psi_0|^2 = 1 \quad . \tag{2.11}$$

Consideration of the scattered wave ψ_s in the image intensity yields the image intensity I_s in the complex plane

$$I_\mathrm{s} = |1 + \mathrm{i}\sigma_\mathrm{i} V_\mathrm{p}(x, y)|^2 \quad . \tag{2.12}$$

For small phase shifts $\sigma_\mathrm{i} V_\mathrm{p}(x, y)$ follows $I_0 \approx I_\mathrm{s} = 1$, i.e. no contrast is produced for weak phase objects. An additional $\pm 90°$ phase shift for the scattered wave ψ_s is desirable to "convert" the phase shift into a measureable change in I_s, i.e.

$$I_{\mathrm{s},90°} = |1 \mp \sigma_\mathrm{i} V_\mathrm{p}(x, y)|^2 \quad . \tag{2.13}$$

In light optics, Zernike introduced a phase-shifting plate into the BFP of the objective lens to convert the phase difference between scattered and unscattered beam into a measureable intensity difference (phase-contrast microscopy). In recent years, such phase plates were also realized for electron microscopes and are used in CTEM of biological (or other weakly scattering) specimens [ND08]. However, the aberrations of the objective lens also introduce phase shifts. These aberrations can be exploited to generate phase contrast in CTEM, as described in the following.

The contrast-transfer function of the objective lens. So far, it was shown that an ideal objective lens would produce no phase contrast for a weak phase object. However, a real OL has aberrations (lens imperfections) such as, e.g., defocus Δf and spherical aberration. Aberrations introduce additional phase shifts, which can be exploited in CTEM to generate phase contrast [Sch49]. The phase-shifting action of the OL aberrations is described by an *wave-aberration function* χ. The scattered wave at the BFP can be calculated by a Fourier transform ($\mathcal{F}$). The actions of lenses can be described by Fourier transforms $\mathcal{F}$ as known from Fourier optics [BW69]. A Fourier transform describes the propagation of a wave from the FFP (real-space) to the BFP (k-space), here for the scattered wave ψ_s

$$\psi_\mathrm{s}(k_x, k_y) = \mathcal{F}\left[\psi_\mathrm{s}(x, y)\right] \tag{2.14}$$

$$= \hat{\delta}(k_x, k_y) + \mathrm{i}\sigma_\mathrm{i}\mathcal{F}\left[V_\mathrm{p}(x, y)\right] \quad , \tag{2.15}$$

where the variables ($k_x = 1/x, k_y = 1/y$) are the coordinates (i.e. spatial frequencies) of (x, y) in reciprocal space (or k-space) after the Fourier transform. Note that the weak phase-object approximation from Eq. (2.10) was used for ψ_s and that $\mathcal{F}[1] = \hat{\delta}(k_x, k_y)$ with the Dirac delta function. This k-space representation is useful since convolutions in real-space are transformed to multiplications in k-space (convolution theorem). Mathematically, the phase shift of χ can now be expressed as a multiplication in k-space, i.e.

$$\psi_\mathrm{s}(k_x, k_y) = \left(\hat{\delta}(k_x, k_y) + \mathrm{i}\sigma_\mathrm{i}\mathcal{F}\left[V_\mathrm{p}(x, y)\right]\right) \cdot \mathrm{e}^{-\mathrm{i}\chi(k_x, k_y)} \quad . \tag{2.16}$$

For an uncorrected microscope, the most important aberrations are the defocus Δf and the spherical aberration with the spherical aberration coefficient C_s. With $k^2 = k_x^2 + k_y^2$, χ is typically written as

$$\chi(k) = \pi\Delta f\lambda k^2 + \frac{1}{2}\pi C_\mathrm{s}\lambda^3 k^4 \quad . \tag{2.17}$$

The intensity in the BFP is calculated by $I = |\psi|^2$ with ψ_s from Eq. (2.16). Neglecting higher-order terms of σ_i yields [FH08, p 546]

$$I_\mathrm{BFP} \approx \hat{\delta}(k) + 2\sigma_\mathrm{i}\mathcal{F}\left[V_\mathrm{p}(x, y)\right]\sin\left(\chi(k)\right) \quad . \tag{2.18}$$

Therefore, the information transfer by the objective lens is described by a complicated sine-function, which depends on the spatial frequency k, the defocus Δf, and the spherical aberration coefficient C_s. The values for the latter are in the order of mm, e.g. 1.2 mm for a Philips CM200 with a SuperTWIN objective lens, that was also used in this work. The effects of the sine function on the image contrast will be discussed further below.

Partial coherence. In addition to $\sin(\chi(k))$, the effect of partial coherence of the electron beam has to be taken into account to better describe the contrast transfer through the OL. Instabilities in lens current and accelerating voltage (temporal envelope function, E_t) and the effect of non-perfectly parallel illumination of the specimen (spatial envelope function, E_s) damp the

information transfer of a microscope and ultimately limit the achievable spatial resolution. This limit is called the information limit. Specimen drift/vibration ($E_{\mathrm{drift}}/E_{\mathrm{vibration}}$) and detection efficiency of the camera (E_{MTF}) can further dampen the information transfer but are neglected in the following discussion for simplicity. The combined effect of phase-shifting and dampening is described by the *phase contrast transfer function* (PCTF):

$$I_{\mathrm{BFP}} \approx \hat{\delta}(k) + 2\sigma_{\mathrm{i}}\mathcal{F}\left[V_{\mathrm{p}}(x,y)\right] \cdot \mathrm{PCTF}(k) \quad \text{with} \tag{2.19}$$

$$\mathrm{PCTF}(k) = \sin(\chi(k)) \cdot E_{\mathrm{t}} \cdot E_{\mathrm{s}} \cdot \underbrace{E_{\mathrm{drift}} \cdot E_{\mathrm{vibration}} \cdot E_{\mathrm{MTF}}}_{\approx 1 \text{ for simplicity}} \tag{2.20}$$

The *spatial envelope function* $E_{\mathrm{s}}(k)$ describes the effect of finite beam convergence α (non-parallel illumination) on the coherence and is given by

$$E_{\mathrm{s}}(k) = \exp\left(-\left(\frac{\pi\alpha}{\lambda}\right)^2 \left(C_{\mathrm{s}}\lambda^3 k^3 + \Delta f \lambda k\right)^2\right) \quad . \tag{2.21}$$

Because dampening due to $E_{\mathrm{s}}(k)$ depends strongly on C_{s}, a too strong beam convergence α in an uncorrected microscope (e.g. $> 0.2\,\mathrm{mrad}$ for a CM200) can reduce information transfer at higher spatial frequencies more significantly than the dampening due to $E_{\mathrm{t}}(k)$. In contrast, for a C_{s}-corrected TEM $E_{\mathrm{s}}(k)$ becomes negligible and $E_{\mathrm{t}}(k)$ determines the information limit.
The *temporal envelope function* $E_{\mathrm{t}}(k)$ depends on the microscope-specific *defocus spread* δ_{D} describing the root-mean-square variations of beam current I_{p} and acceleration voltage V, and the finite energy-spread ΔE of electrons in the beam multiplied by the chromatic aberration coefficient C_{c}:

$$E_{\mathrm{t}}(k) = \exp\left(-0.5\left(\pi\lambda\delta_{\mathrm{D}}\right)^2 k^4\right) \quad \text{with} \tag{2.22}$$

$$\delta_{\mathrm{D}} = C_{\mathrm{c}}\left(\left(\frac{\Delta E}{E}\right)^2 + \left(\frac{2\Delta I_{\mathrm{p}}}{I_{\mathrm{p}}}\right)^2 + \left(\frac{\Delta V}{V}\right)^2\right)^{0.5} \tag{2.23}$$

Because $E_{\mathrm{t}}(k)$ often limits the ultimate resolution in a FEG-TEM, the information limit k_{max} is defined as the the drop-off of $E_{\mathrm{t}}(k)$ to a value of $1/\mathrm{e}^2$ (or $13.5\,\%$), i.e. $E_{\mathrm{t}}(k_{\mathrm{max}}) = \mathrm{e}^{-2}$. For a given defocus spread, the information limit k_{max} can be approximated (or *vice versa*):

$$k_{\mathrm{max}} = \left(0.25\left(\pi\delta_{\mathrm{D}}\lambda\right)^2\right)^{0.25} \tag{2.24}$$

$$\delta_{\mathrm{D}} = \left(4\left(\pi\lambda\right)^{-2} k_{\mathrm{max}}^4\right)^{0.5} \tag{2.25}$$

The non-C_{s}-corrected microscope. The CTF can be visualized for different microscope settings. Exemplary, PCTF(k) is plotted in Fig. 2.8a for $\lambda = 2.51\,\mathrm{pm}$ ($200\,\mathrm{keV}$), $C_{\mathrm{s}} = 1.2\,\mathrm{mm}$, $\delta_{\mathrm{D}} = 7.5\,\mathrm{nm}$, and $\Delta f = \Delta f_{\mathrm{Scherzer}}$ (see below). Specimen structures in an image appear dark on a white background for $\sin(\chi(k)) < 0$ and bright on a dark background for $\sin(\chi(k)) > 0$. Due to the oscillations of $\sin(\chi(k))$ different spatial frequencies in an image appear dark/bright and an image cannot be interpreted intuitively. An ideal information transfer would be constant ($\sin(\chi(k)) = \pm 1$) for all k. In practice, Δf is varied to modify $\sin(\chi(k))$ and, therefore, the objective lens's information transfer. Some special defocus values are:

- **Extended Scherzer defocus**: For $\Delta f_{\mathrm{Scherzer}} = -1.2\left(\lambda C_{\mathrm{s}}\right)^{0.5}$ the information transfer is maximized up until a first cross-over of $\sin(\chi(k))$ at $k_{\mathrm{ps}} = 1.51(\lambda^3 C_{\mathrm{s}})^{-0.25}$ (Fig. 2.8b). After

k_{ps} contrast reversals appear and higher spatial frequencies (smaller image features) cannot be interpreted easily anymore. The spatial frequency k_{ps} defines the point-resolution of an uncorrected microscope. For the example of a CM200 microscope one finds $\Delta f_{\mathrm{Scherzer}} = -66\,\mathrm{nm}$ and $k_{\mathrm{ps}} = 4.07\,\mathrm{nm}^{-1}$ (or $k_{\mathrm{ps}}^{-1} = 0.246\,\mathrm{nm}$). In practice, an aperture is placed in the BFP to cut off image information above k_{ps} to prevent contrast oscillations from higher spatial frequencies contributing to the image.
The PCTF for a CM200 microscope under Scherzer conditions is plotted in Fig. 2.8a with the spatial and temporal dampening functions. Atoms appear dark on a white background in this condition (PCTF < 0). The passband up to k_{ps} is visible. The gray area shows the $1/\mathrm{e}^2$-value defining the information limit.

- **Minimum contrast defocus**: For $\Delta f_{\mathrm{mc}} = -0.44\,(\lambda C_{\mathrm{s}})^{0.5}$ (phase) contrast is minimized in the image. This defocus is important for practical use, as it is the only one that can be recognized during HRTEM imaging (with a systematic error of roughly $\pm 5\,\mathrm{nm}$). It acts as a reference defocus to set up other defocus values. For a CM200 one finds $\Delta f_{\mathrm{mc}} = -24\,\mathrm{nm}$.

- **Lichte defocus**: For $\Delta f_{\mathrm{Lichte}} = -0.75 C_{\mathrm{s}}\,(k_{\mathrm{max}}\lambda)^2$, with the maximum possible transmitted spatial frequency of a microscope k_{max} defined by the information limit, delocalization of image information is minimized. This defocus is used for electron holography.

Indeed, information delocalization is an unwanted phenomenon in HRTEM and a consequence of aberrations. It delocalizes image information from its true origin in a specimen, which significantly impedes the analysis of interfaces and defects. The amount of delocalization ΔR depends on the spatial frequency and is given by [WC08, p 498]

$$\Delta R(k) = \lambda k \left(\Delta f + C_{\mathrm{s}}\lambda^2 k^2\right) \quad . \tag{2.26}$$

For a CM200 microscope at Scherzer defocus, the delocalization at the point resolution k_{ps} is about 0.6 nm, enough to obscure details at an interface or a crystalline defect. A reduction or a full correction of C_{s} leads to a strongly reduced delocalization.

The C_{s}-corrected microscope. In a C_{s}-corrected microscope, the corrector introduces negative C_{s} value to compensate for the positive C_{s} of the lower OL. The values Δf and C_{s} in Eq. (2.17) can *both* be adjusted for different imaging conditions. In this work, the following modes were used:

- **Amplitude-contrast imaging**: For $C_{\mathrm{s}} \approx 0$ and Gaussian focus $\Delta f = 0$, i.e. full compensation of C_{s}, the PCTF becomes 0 and no phase contrast is visible in the image. Instead of phase contrast, the amplitude contrast transfer function (ACTF) given by $\cos(\chi(k))$ instead of $\sin(\chi(k))$ in Eq. (2.20) will become important[6], especially for samples containing heavier elements in materials science. Conversely, phase objects (e.g. biological samples) that do not create much amplitude contrast will be hardly visible. The delocalization ΔR vanishes under these conditions. The ACTF and PCTF are plotted in Fig. 2.8b for a exemplary residual value $C_{\mathrm{s}} \approx 1\,\mu\mathrm{m}$ and $\Delta f_{\mathrm{mc}} = -0.6\,\mathrm{nm}$.

- **Negative-C_{s} imaging (NCSI)**: A small C_{s}-value with a corresponding defocus Δf can be set up to maximize phase contrast in a C_{s}-corrected microscope [Sch49]. Lentzen et al. [Len+02] showed conditions to maximize phase contrast up to the information limit at k_{max}

[6] Absorption, typically described in the form of a dampening $\exp(-\mu(x,y))$, was neglected here, so the ACTF was not derived. See, e.g., Fultz and Howe [FH08, pp 545 sq.] for a detailed description.

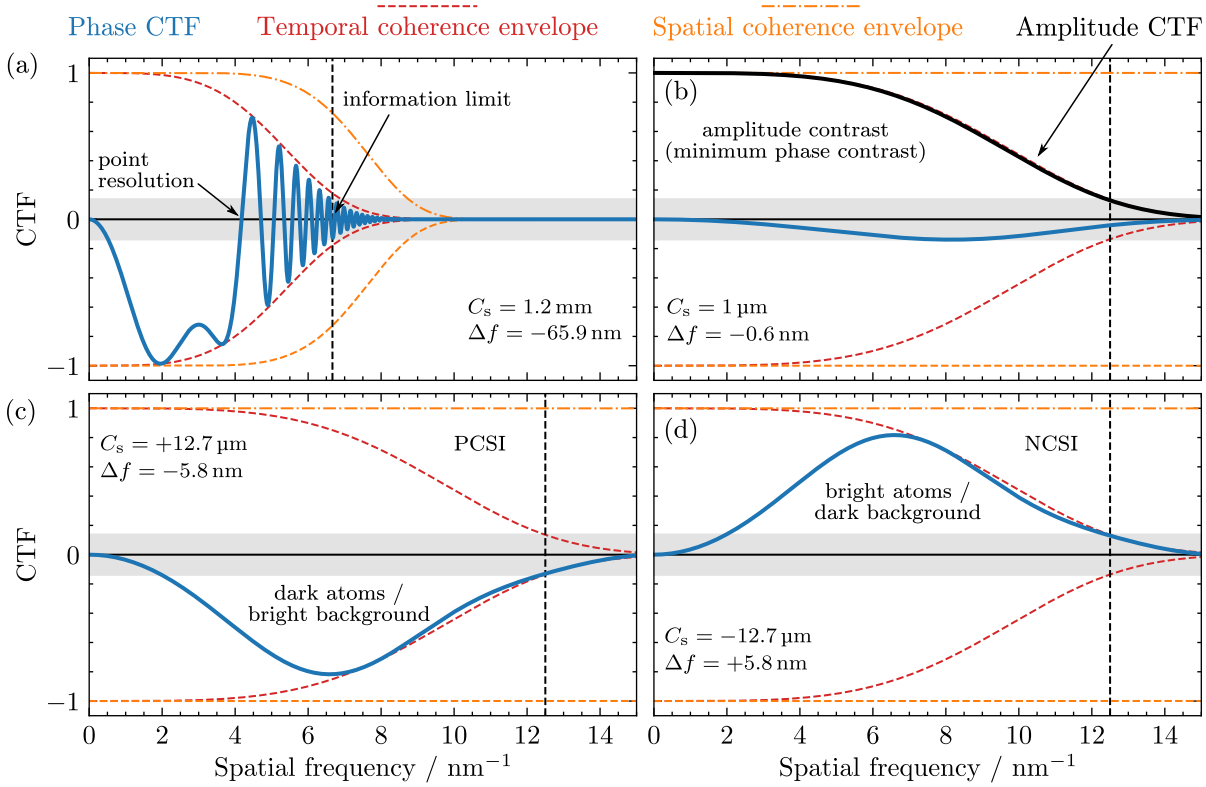

Figure 2.8: Exemplary objective lens contrast transfer functions (CTFs) in HRTEM. (a) PCTF for an uncorrected microscope at 200 keV and Scherzer defocus (e.g. for a Philips CM200 microscope). No contrast reversals are observed up to the point resolution (here 245 pm). Afterwards, the CTF oscillates rapidly until the information limit is reached (vertical dashed line, here 145 pm as calculated from $\delta_D = 7.5\,\mathrm{nm}$). The spatial coherence of the illumination does not limit the PCTF in the shown case ($\alpha = 0.1\,\mathrm{mrad}$). (b–d) Typical C_s-corrected HRTEM imaging parameters for the FEI Titan^3 80–300 microscope (300 keV, 80 pm = $12.5\,\mathrm{nm}^{-1}$ nominal information limit shown as vertical dashed line, $\alpha = 0.1\,\mathrm{mrad}$). (b) Tuning the corrector to $C_s \approx 0\,\mu\mathrm{m}$ leads to vanishing phase- and maximum amplitude contrast. Image delocalization is minimized. The PCTF is plotted for $C_s \approx 1\,\mu\mathrm{m}$ (typical residual value) to better visualize the PCTF, which would be 0 for $C_s = \Delta f = 0\,\mu\mathrm{m}$. (c–d) Lentzen conditions for (c) positive and (d) negative C_s-corrected imaging (PCSI/NSCI) leads to optimum phase contrast with small residual delocalization. Both settings results in a PCTF without phase contrast reversals up to the information limit. The NCSI mode can visualize light elements for very thin samples (typcially $< 10\,\mathrm{nm}$).

with small residual delocalization by equating the Scherzer and Lichte defocus conditions:

$$C_{s,\mathrm{NCSI}} = -\frac{64}{27}\left(\lambda^3 k_{\max}^4\right)^{-1} \quad , \tag{2.27}$$

$$\Delta f_{\mathrm{NCSI}} = +\frac{16}{9}\left(\lambda k_{\max}^2\right)^{-1} \quad . \tag{2.28}$$

For the used FEI Titan^3 80–300 with a nominal information limit $k_{\max} = 12.5\,\mathrm{nm}^{-1}$ (80 pm) at 300 keV ($\lambda = 1.97\,\mathrm{pm}$) this results in $C_{s,\mathrm{NCSI}} = -12.7\,\mu\mathrm{m}$ with an overfocus of $\Delta f_{\mathrm{NCSI}} = 5.8\,\mathrm{nm}$. The residual contrast delocalization is $\frac{16}{27} k_{\max}^{-1} = 47\,\mathrm{pm}$ under these imaging conditions [HTU06]. The CTF is shown in Fig. 2.8d, where atoms appear as white objects on a dark background. In principle, the signs of $C_{s,\mathrm{NCSI}}$ and Δf_{NCSI} can be flipped to invert contrast, which is shown in Fig. 2.8c as positive-C_s imaging (PCSI). However, NCSI is advantageous and even enables direct imaging of light elements (such as O in YBCO [JLU04; HTU06]) for very thin TEM samples where the weak phase-object

approximation holds (typically $< 10\,\mathrm{nm}$). See the literature for more information [JLU04; Len06; Urb+09; Jia+10].

It is worth mentioning that in actual practice, C_s (Δf) can only be adjusted to a precision of around $\pm 3\,\mu\mathrm{m}$ ($\pm 5\,\mathrm{nm}$). In addition, higher-order aberrations which were neglected in Eq. (2.17) due to the presence of C_s become important.

This section introduced the concept of HRTEM imaging. A precise knowledge and setup of experimental parameters are required to (i) maximize image contrast and (ii) to associate the observed image contrasts to the underlying specimen structure. Multiple images at different Δf are typically acquired to account for uncertainties in determining Δf. Image simulations are then required to interpret HRTEM images in terms of actual specimen structures. This is especially problematic for defects and interfaces, where (often complicated) samples models have to be assumed for simulation. Because of these reasons, high-resolution STEM imaging is currently preferred over HRTEM in materials science.

2.2.3 (High-resolution) Scanning Transmission Electron Microscopy

In STEM and in scanning electron microscopy, a (sub-)nanometer-sized electron probe is scanned over a sample. Various signals can be detected at each scan position and subsequently used to form images or extract chemical information. In particular, high-angle annular dark-field (HAADF) STEM resulting in atomic number (Z-)contrast images is a popular imaging mode in materials science due to the (often) straightforward interpretation of the measured image intensity, provided that the TEM-sample thickness does not change significantly. In high-resolution STEM (HRSTEM), atomic resolution is reached by scanning an electron probe with a diameter of about 0.2 nm or less over a thin TEM sample. In this section, the basic principles of electron-probe formation and STEM imaging are explained. For more details, the reader is referred to textbooks [WC08; Kir20; HS19] and the recent review by Liu [Liu21].

Probe formation

In general, the aim in S(T)EM is to focus an electron probe (i) as small as possible on a sample to maximize the spatial resolution and with (ii) enough beam current for an experimental task. The spatial resolution is (mostly) determined by the probe size d_p in STEM. One can approximate d_p for a non-probe-corrected microscope by modeling the contributions of the finite source size (d_s), diffraction effects of the probe-forming aperture (d_d), as well as spherical (d_Cs) and chromatic (d_Cc) aberrations from the probe-forming lens (upper objective lens) as Gaussian functions and adding them in quadrature [RK08, p 94]:

$$d_\mathrm{p}^2 = \underbrace{\left(\left(\frac{4I_\mathrm{p}}{\pi^2\beta_\mathrm{gun}}\right)^2 \frac{1}{\alpha}\right)^2}_{d_\mathrm{s}} + \underbrace{\left(0.61\frac{\lambda}{\alpha}\right)^2}_{d_\mathrm{d}} + \underbrace{\left(\frac{1}{2}C_\mathrm{s}\alpha^3\right)^2}_{d_\mathrm{Cs}} + \underbrace{\left(C_\mathrm{c}\frac{\Delta E}{E_0}\alpha\right)^2}_{d_\mathrm{Cc}} \tag{2.29}$$

This equation can be simplified depending on the operating conditions. For example, a beam current I_p of a few pA may be sufficient for high-resolution STEM imaging, whereas spectroscopic techniques can require a few hundred pA or even nA to generate enough signal in a reasonable time frame. This means that the contribution of d_s is primarily relevant for analytical STEM. A high-brightness electron source with a large β_gun such as the "X-FEG" in the used FEI Tecnai Osiris is beneficial for applications requiring high beam currents such as EDXS.

Another example is the contribution of chromatic aberration d_{Cc}. Because $\Delta E \approx 0.7\,\mathrm{eV}$ is the same for a Schottky FEG independent of the accelerating voltage, the term d_{Cc} becomes negligible at high beam energies (e.g. $E_0 = 300\,\mathrm{keV}$) (compared to d_{Cs}) but important at lower beam energies (e.g. 10 keV and lower). In particular, the resolution in scanning electron microscopes (Page 32) is often limited by the chromatic aberration at low beam energies ($< 1\,\mathrm{keV}$). State-of-the-art SEMs such as the TFS Helios G4 FX tackle this problem by implementing a monochromator after the FEG to reduce ΔE (so-called "UC (unicolor)" mode).
In the µP-STEM mode the probe is set up with a small α to acquire diffraction patterns with non-overlapping diffraction discs. The used beam current is often relatively small to avoid damage of the camera and to maximize the spatial resolution. Therefore, the probe is limited by diffraction effects and the probe size can be approximated by d_{d}. For typical conditions used in this work (50 µm C2 aperture, $\alpha = 0.6\,\mathrm{mrad}$, $\lambda = 1.97\,\mathrm{pm}$ at the FEI Titan^3 80–300) one can form a probe of about 2 nm in diameter (full width at half maximum, FWHM). The operator can adjust the probe conditions using the gun lens (or monochromator excitation/focus), spot size, the size of the beam-limiting condenser aperture, and the setup of the C2-C3 lenses in a 3-condenser-lens system as used in the FEI Titan^3 80–300 microscope.
In the following, the optimal conditions for probe formation for high-resolution STEM (HRSTEM) imaging are described. Here, the probe alignment and the chosen beam parameters are critical to achieving the highest possible resolution, thereby reaching atomic resolution in modern S/TEMs. The most important parameters are the convergence semi-angle α and the defocus Δf. Similar to HRTEM, a slight underfocus (here defined as negative defocus Δf) is necessary to compensate for the positive C_{s} of the upper OL. In Eq. (2.29), the lens aberrations contributions are assumed to be independent (or incoherent) with each other. This assumption is invalid for FEGs with high coherency [HS19, p 354] and will underestimate the achievable probe size under optimal imaging conditions. Using a wave-optical treatment, one can find optimal values for the convergence semi-angle α and the defocus Δf for STEM imaging with an uncorrected microscope [CS82; WM05]:

$$\alpha_{\mathrm{opt}} = 1.41 \left(\frac{\lambda}{C_{\mathrm{s}}}\right)^{0.25} \quad , \tag{2.30}$$

$$\Delta f_{\mathrm{opt}} = -(\lambda C_{\mathrm{s}})^{0.5} \quad \text{(Scherzer defocus)} \tag{2.31}$$

The used microscopes have $C_{\mathrm{s}} \approx 1.2\,\mathrm{mm}$ for the probe-forming upper OL which results in $\alpha_{\mathrm{opt},300} = 9\,\mathrm{mrad}$ with $\Delta f_{\mathrm{opt},300} = -49\,\mathrm{nm}$ ($\alpha_{\mathrm{opt},200} = 9.5\,\mathrm{mrad}$ with $\Delta f_{\mathrm{opt},200} = -55\,\mathrm{nm}$) for 300 keV (200 keV). After setting up the probe with α_{opt}, the optimal defocus Δf_{opt} is found "intuitively" by finding the sharpest image in incoherent annular dark-field imaging [Pen89; WM05], which will be discussed in the next paragraph. This makes focusing in HRSTEM easier and more intuitive than focusing for HRTEM. As shown by Weyland and Muller [WM05], if the used α deviates too much (roughly 2 mrad or more) from the optimal value, other defocus values may also give sharp images, but not with the highest attainable resolution of the microscope. The FWHM of the resulting probe using the parameters in Eq. (2.30) and Eq. (2.31) corresponds to the attainable STEM point resolution d_0 which can be calculated as [WM05]

$$d_0 = 0.43 \left(C_{\mathrm{s}} \lambda^3\right)^{0.25} \quad , \tag{2.32}$$

which results in $d_{0,300} = 0.133\,\mathrm{nm}$ ($d_{0,200} = 0.160\,\mathrm{nm}$) for 300 keV (200 keV). For example, the optimal probe for 300 keV is calculated using *Dr Probe* [Bar18] and shown in Fig. 2.9a. Besides

the main lobe in the center, unwanted side maxima (or probe tails) are visible, resulting from phase-shift errors and diffraction from the probe-forming aperture. The concentric-ring pattern is typical for an Airy disc, i.e. the probe formed by a circular aperture [BW69, p 396]. It should be noted that one can achieve a smaller probe size d_0 at the expense of larger probe tails. This leads to slightly different definitions for (the prefactors of) $\alpha_{\text{opt}}/\Delta f_{\text{opt}}$ in literature than shown in Eq. (2.30)/Eq. (2.31) [MCC87; HS19; Kir20].

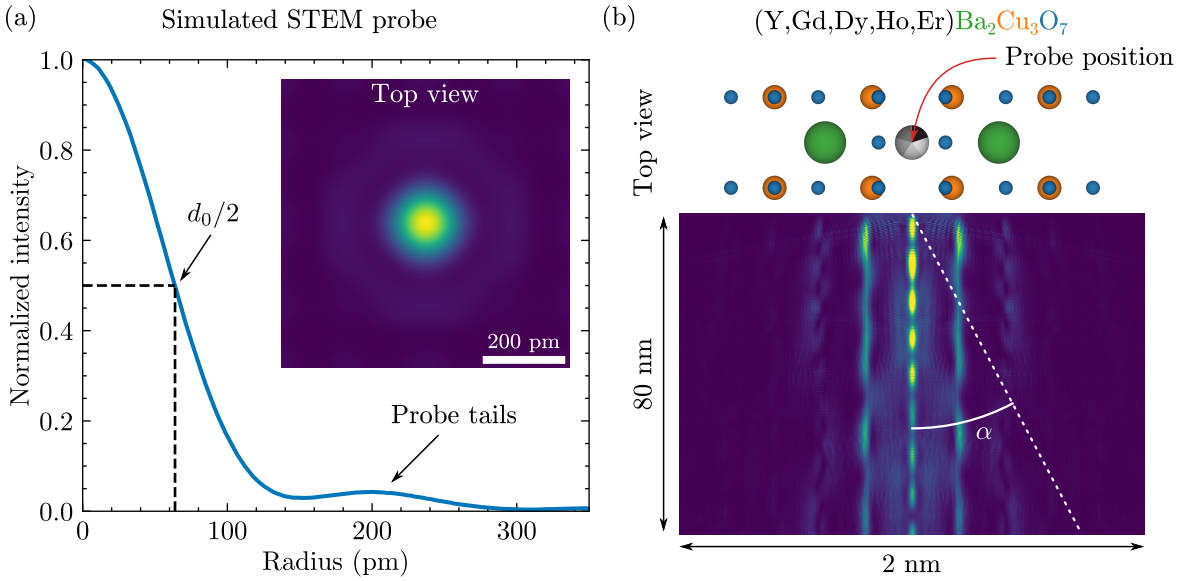

Figure 2.9: Simulated STEM probe and propagation in a crystalline sample. (a) Radial profile and top view (inset) of the optimal probe for the FEI Titan^3 80–300 microscope at 300 keV ($\lambda = 1.97$ pm, $C_s = 1.2$ mm, $\alpha = 9$ mrad, $\Delta f = -48.6$ nm). (b) Simulated propagation of the probe shown in (a) through 80 nm (Y,Gd,Dy,Ho,Er)$Ba_2Cu_3O_7$. The probe is placed on the rare-earth atomic column. In such an on-axis condition of the sample with respect to the incident beam, the probe channels down along the atomic columns. Periodic intensity variations of the probe along the sample thickness are observed.

So far, the probe formation in vacuum was explained. The next part explains the beam-sample interaction in STEM and image formation. Exemplary, the propagation of a stationary probe through an 80 nm thin crystalline REBCO sample is shown in 2.9b. The scheme in the top part of the figure shows the unit cell as seen from the entering probe, which was placed onto the atomic column of the RE column (marked by an arrow). The bottom part of the figure shows a slice through the lateral dimension (horizontal) and the sample depth (vertical). The dotted line displays the convergence semi-angle α of the incident probe when focused on the sample surface. Neglecting any beam-sample interaction, the beam would broaden again after the focus point to a diameter of $2 \tan(9\,\text{mrad}) \cdot 80\,\text{nm} = 1.4\,\text{nm}$. For an amorphous sample, the probe diameter at the exit surface would be even larger because the beam broadens due to scattering events in the material. Assuming an amorphous sample for 2.9b, the diameter of the probe after traversing the sample can be approximated from the contributions of the incident probe diameter d_0, beam broadening in the sample b [GR16; Dre+18; HMG19], and the convergence semi-angle α as [GR16]

$$d_{\text{max}} = \sqrt{d_0^2 + b^2 + (2t \tan \alpha)^2} = 2.38\,\text{nm}. \tag{2.33}$$

The beam broadening term b was calculated with equation (9) in [HMG19] with a Hurst exponent $H = 1$ (assuming ballistic scattering regime [Dre+18]), $R = 0.76$ (corresponding to the percentage of electrons contained within the FWHM of a Gaussian probe), an average atomic number

$\overline{Z} = 24.3$, calculated density $\rho = 7\,\mathrm{g\,cm^{-3}}$, and an average atomic mass $A = 55.8\,\mathrm{Da}$. The beam at the exit surface for an amorphous sample would be larger than the shown horizontal field of view (2 nm) in 2.9b. This drastic broadening of the probe for amorphous samples greatly reduces the spatial resolution in STEM imaging. At first glance, the only solution to this problem seems to be the use of very thin samples ($< 10\,\mathrm{nm}$). However, a complex beam-sample interaction called "channeling" alleviates this problem for crystalline materials.
The simulation in 2.9b for a crystalline REBCO sample exemplarily shows the reason that atomic-resolution STEM images are possible from thicker TEM samples ($> 10\,\mathrm{nm}$). The positively charged atomic nuclei attract the propagating electron beam and a complex pattern with an oscillating behavior for the simulated probe-intensity distribution inside the sample is visible. This effect is called "channeling" and is helpful for HRSTEM imaging by effectively pinning the probe onto the atomic columns [Pen+96; LKS88], when the sample is aligned with the atomic columns parallel to the incident beam (i.e. in a low-index zone-axis orientation). The typical broadening of the electron probe with increasing sample thickness t in an (amorphous) sample can be described by a $t^{1.5}$ dependence, which is reduced by channeling to $t^{0.5}$ [Pen89]. The oscillatory behavior of the probe intensity can complicate image interpretation in (quantitative) STEM imaging [VMK04]. In this work, STEM images were only evaluated qualitatively, e.g. by assigning heavier atomic columns to higher image intensity in annular dark-field STEM images. For further details on the consequences of channeling and also other aspects in quantitative STEM imaging the reader is referred to the literature, e.g. [VMK04; Jon16; Wu+17].
Channeling is only present for crystalline samples. In amorphous materials, the electron probe broadens due to the beam convergence α in addition to scattering events in the sample. This has important consequences for TEM sample preparation. Any amorphous surface layers on a TEM sample surfaces will broaden the incident probe before it can "lock" onto the atomic columns. Amorphous surface layers can result from (i) amorphization of the TEM sample due to ion bombardment during TEM sample preparation (cf. Fig. 2.10) or (ii) contamination of the sample during storage and interaction of organic molecules adsorbed on the sample surface with the electron beam. The latter results in a C-rich contamination layer that forms during S(T)EM imaging. The scheme in Fig. 2.10a visualizes the typical situation during the final TEM-sample thinning steps for a TEM sample prepared with a focused ion beam (FIB). Here, a low-energy Ga^+-FIB is scanned at grazing incidence with respect to the sample surface. Ga^+-ions penetrate the material and deposit their energy step-by-step until they lose all their kinetic energy. Crystalline surface regions are often amorphized by these interactions. Simulations using *SRIM 2013* [ZB85; ZZB10] can be used to approximate the range of the impinging Ga^+-ions (Fig. 2.10b, 5000 Ga^+-ions simulated). A study on amorphous surface layers on GaN by Mehrtens et al. [Meh+12] showed that the thickness of the damaged layer is slightly larger than the peak position in the simulated ion ranges by *SRIM*, i.e. $\approx 10\,\mathrm{nm}$ for 30 keV and $\approx 2\,\mathrm{nm}$ for 2 keV for REBCO.
Low Ga^+-ion energies are typically used during the final steps of FIB preparation to reduce surface damage ($\approx 10\,\mathrm{nm}$ at 30 keV vs. $\approx 2\,\mathrm{nm}$ at 2 keV). Equation (2.33) can be used to approximate the beam diameter after the beam has passed through such an amorphous layer. For $d_0 = 0.133\,\mathrm{nm}$ and $\alpha = 9\,\mathrm{mrad}$ results $d_{\mathrm{max}} \approx 0.138\,\mathrm{nm}$ (thickness of amorphous layer $t = 2\,\mathrm{nm}$) vs. $d_{\mathrm{max}} \approx 0.225\,\mathrm{nm}$ ($t = 10\,\mathrm{nm}$) for the exemplary REBCO sample (neglecting effects of implanted Ga^+ on the material density). Therefore, HRSTEM resolution is (often) degraded by sample quality and contamination, even when the probe is optimally aligned. The mitigation of amorphous surface layers during sample preparation is important and will be discussed in the experimental section (Page 59).

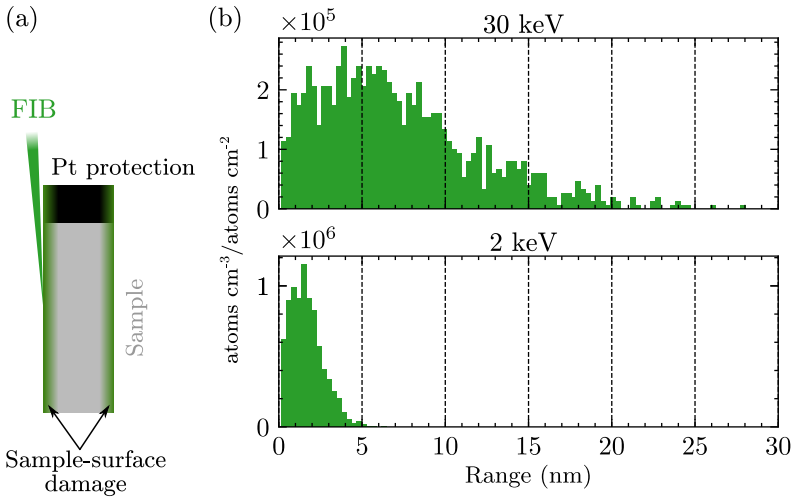

Figure 2.10: SRIMulation of sample-surface damage during TEM-sample preparation. (a) Scheme showing final FIB milling of the sample, which results in amorphous sample surfaces (sidewall damage). (b) Simulated range of Ga^+-ions in REBCO for 30 keV (top) and 2 keV (bottom) for a beam incidence angle of 1°. The thickness of the damaged surface layer is reduced at lower FIB energies ($\approx$ 10 nm at 30 keV vs. $\approx$ 2 nm at 2 keV).

Annular dark-field imaging

The annular dark-field (ADF) imaging mode is probably the most widespread STEM imaging technique. As shown schematically in Fig. 2.11a, an annular detector collects electrons, which have been scattered into a specific angular range. The inner detector edge is often denoted as the inner collection semi-angle β. The detector is made of a scintillator (e.g. Y-Al perovskite, YAP, for the Fischione Model 3000 detector), which converts the incoming electrons into photons. A photomultiplier tube registers the photons as a signal [KT96]. At each scan position, the integrated ADF signal is recorded and digitized. The measured values are displayed as an image. The unscattered direct beam propagates through a central hole (hence the term "dark field") and further traverses along the microscope column, where it can be detected by a camera or give chemical information by entering a post-column energy filter for electron energy loss spectroscopy.
The beam must be stationary in the ADF detector plane to achieve a fixed collection angle for all scan positions. In a S/TEM instrument, this is achieved by running the microscope in "Diffraction" mode, where the projector lenses image the BFP onto the ADF plane. The camera length (effective distance between the ADF detector and the sample) can be altered by changing the excitation of the projector lenses (cf. Fig. 2.11b-d). In these images, the shadow of the ADF detector is imaged together with the undiffracted beam by a camera below the ADF detector. The displayed image intensity is inverted (direct beam is dark) for better visibility of the ADF detector edge. Different angular ranges of the scattered electrons can be used for imaging, giving different sample information.

For example, Fig. 2.11b shows typical high-angle annular dark-field (HAADF) STEM imaging conditions. At a nominal camera length of 115 mm, only electrons scattered to high angles ($\beta \approx 40$ mrad or higher at 300 keV) contribute to the image. At such high angles, coherently scattered electrons by diffraction from crystalline planes do not contribute to the image and only the incoherently scattered electrons are used to form an HAADF-STEM image. This gives rise to Z-contrast images, where (in most cases) the local image intensity is correlated with higher atomic numbers Z for sample regions with similar thickness and material density [Pen89; Pen+96; NP00]. Because of the Z-contrast, image interpretation in HAADF-STEM imaging is relatively straightforward, especially compared to HRTEM. In addition, the optimal defocus is found by intuitively making the HAADF-STEM image as sharp as possible. For large β, a Z^2-dependence for the HAADF intensity is expected as suggested by the (unscreened) Rutherford scattering

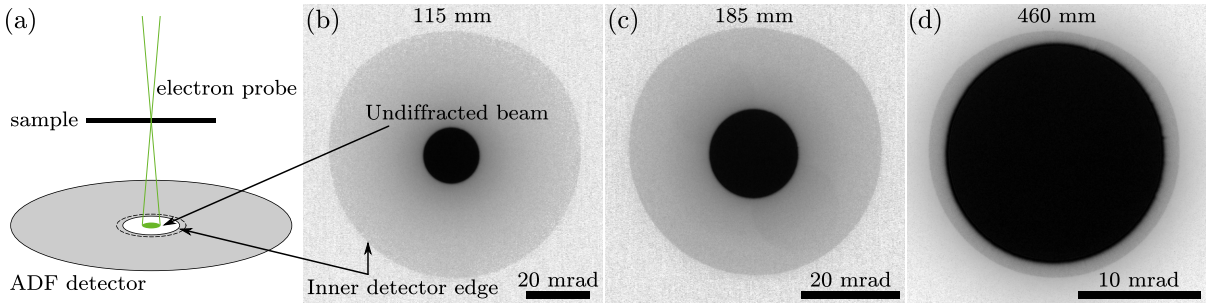

Figure 2.11: Experimental setups for annular dark-field imaging in STEM. (a) Scheme of an annular dark-field (ADF) detector in STEM. The direct beam propagates through a hole in the center. The inner detector edge can be imaged by a camera below the ADF detector, defining the inner collection angle β. Note: The actual sensor area starts slightly away from the edge (schematically shown by the dotted circle). (b–d) Experimental images of the undiffracted beam (black circle) and the inner detector edge for different camera lengths. Images are displayed with inverted lookup tables (white to black) for better visibility. The setups can be classified as (b) high-, (c) medium-, and (d) low-angle annular dark-field STEM imaging modes. In all three cases, the beam convergence is $\alpha \approx 9\,\mathrm{mrad}$.

cross-section from Coulomb scattering of the atomic nuclei. Deviations from the Z^2-dependence are observed in practice depending on the collection angle and screening of the nucleus by outer-shell electrons. This leads to different exponents $n \neq 2$ in the Z^n-dependence, which are mostly important for quantitative HAADF-STEM and exact image simulations. For typical collection angles used in HAADF-STEM ($\beta \geq 3\alpha$), a $Z^{1.7}$-dependence can be approximated [HS19]. Still, even for qualitative HAADF-STEM imaging, β must be chosen large enough to avoid diffraction contrast and establish a power-law Z^n-dependence for the HAADF signal so that atomic columns in a high-resolution HAADF-STEM image can be unambiguously assigned by their image intensity. A simple rule of thumb is that $\beta \geq 3\alpha$ for incoherent HAADF-STEM imaging [Mul09]. The formula by Yamashita et al. [Yam+18] can also be used to calculate the scattering parameter s (in Å) in dependence of the primary electron energy E_0 (in eV) and the collection angle β (in rad) by

$$s(E_0, \beta) = \frac{\beta E_0^{0.5} \left(1 + 0.9785 \cdot 10^{-6} E_0\right)}{24.52} \quad . \tag{2.34}$$

The results by Yamashita et al. [Yam+18] show that – as a rule of thumb – an experimental setup with $s \geq 1\,\text{Å}$ should be used to obtain the desired power-law Z^n-dependence in (qualitative) HAADF imaging. For the experimental setup in Fig. 2.11b with $\beta \approx 40\,\mathrm{mrad}$ (or 2.3°) at $E_0 = 300\,\mathrm{keV}$ one finds $s = 1.16\,\text{Å}$. It is noteworthy that the actual β is slightly larger than the value measured by the shown HAADF detector shadow images because the active sensor area (scintillator) does not directly start at the detector edge [LS08]. However, these subtle differences in β are mostly relevant for detailed image simulations and quantitative ADF STEM [Jon16]. The main drawback of using large β is a reduced signal, because fewer electrons are scattered at higher angles. In practice, this can lead to noisy, unusable images and subsequently, the electron dose must be increased by changing the imaging parameters (dwell time, beam current). The latter can lead to irradiation damage or problems with sample drift during slower image acquisition. Therefore, a trade-off between HAADF-STEM signal (and also the tolerable electron dose on the sample) and β has to be found in practice.

Another useful ADF imaging mode is an experimental setup with small β (but still $\beta > \alpha$) as displayed in Fig. 2.11d. Here, the undiffracted beam nearly fills the detector hole. The resulting STEM image stems from electrons that are scattered under low angles. Hence, this imaging mode is called low-angle annular dark-field (LAADF) STEM [YMS04; GR11; Bau12].

In LAADF-STEM, low-order diffraction discs are sampled by the ADF detector giving rise to diffraction contrast in the image. In addition, strain fields arising at interfaces and near structural defects cause a change in LAADF-STEM image intensity. This is explained by a dechanneling of the electron probe from atomic columns due to a distortion of the crystalline lattice near defects [Phi+12]. Therefore, LAADF-STEM is a useful imaging mode for detecting grain boundaries, crystalline defects, nanoparticles, and strained regions.
The intermediate regime between HAADF and LAADF is termed medium-angle annular dark-field (MAADF, Fig. 2.11c). In this case, one must be careful with interpreting STEM image intensities due to possibly convoluted contributions from (coherent) diffraction contrast and (incoherent) Z-contrast. In this work, the shown MAADF-STEM condition (resulting in $s = 0.75\,\text{Å}$ with $\beta \approx 26\,\text{mrad}$ for Eq. (2.34)) was partially used to increase the collected signal in high-resolution Z-contrast imaging. In practice, no noticeable difference for qualitative Z-contrast imaging was observed for the investigated samples, meaning that atomic columns could be assigned equally well by their MAADF-STEM intensity and their HAADF-STEM intensity. However, special care must be taken when interpreting Z-contrast near crystalline defects: slight strain contrast in MAADF can be misinterpreted as Z-contrast. In doubt, "stronger" Z-contrast conditions (i.e. larger β) should be used to double-check experimental results.

2.2.4 Scanning Electron Microscopy and Focused-Ion-Beam System

This section explains the basic working principles of scanning electron microscopy and focused-ion-beam (FIB) instruments. If not cited explicitly, the following explanations are taken from [Rei98; Gol+18] (scanning electron microscopy) and [GS05; Cox15; Sez16] (FIB).

Scanning Electron Microscopy. Scanning electron microscopy is an electron-microscopy technique that is usually applied to study electron-opaque bulk samples. Unlike TEM, which has many analogies to the optical microscope, the image in a scanning electron microscope (SEM) is not generated from the transmitted electrons[7]. Instead, different detectors of an SEM collect the signals emerging from the sample surface caused by an incident electron probe (the so-called primary beam). The primary beam is scanned over the sample surface and the collected signal(s) at each probe position are used to generate an SEM image. Due to this mode of operation, the surface of bulk samples can be examined in an SEM, which saves the time-consuming preparation of thin TEM samples. Some examples for the generated (and collected) signals are secondary electrons (SEs), backscattered electrons (BSEs), and x-rays (characteristic and bremsstrahlung). The FWHM of the incident electron probe is in the range of $\sim 1\,\text{nm}$ for typical imaging conditions but can be larger for low electron energies or analytical scanning electron microscopy, where a high beam current is required. However, it is essential to note that the spatial resolution of an SEM image is primarily given by the excitation volume of a collected signal (SEs, BSEs, x-rays) and *not* the diameter of the incident electron probe. This is in contrast to HAADF-STEM imaging, where the size of the electron probe limits the spatial resolution (for an ideally prepared TEM sample).

The basic design of an SEM's electron column is similar to Fig. 2.5 on page 14 for the electron source, condenser system (albeit typically fewer condenser lenses are used), (upper) OL and a sample. However, there are no lenses and detectors below the sample in a conventional SEM. Detectors are located above the sample instead (Fig. 2.12a). The electron source used in modern instruments is a FEG. All used SEMs in this work are equipped with Schottky FEGs.

[7] An exception to this is STEM-in-SEM imaging, which will be explained further below.

The maximum electron energy is 30 keV, which is smaller than the energies used in a S/TEM instrument. In addition, the electron energy can be freely adjusted between 0.35 keV to 30 keV (for the TFS Helios G4 FX) within a few seconds. In this way, it is possible to optimize the primary energy for a specific experiment. For example, low primary beam energies (< 5 keV) generally lead to a higher surface sensitivity [JJ96] and better spatial resolution in SE-SEM surface imaging. However, at low energies (below about $E_0 < 2$ keV) and depending on the SEM's electron optics, the probe diameter rapidly becomes larger with decreasing E_0 due to chromatic aberration (cf. d_{C_c} term in Eq. (2.29) on page 26). In this regime, the spatial resolution is then limited by the probe size and not by the interaction volume of the signal.

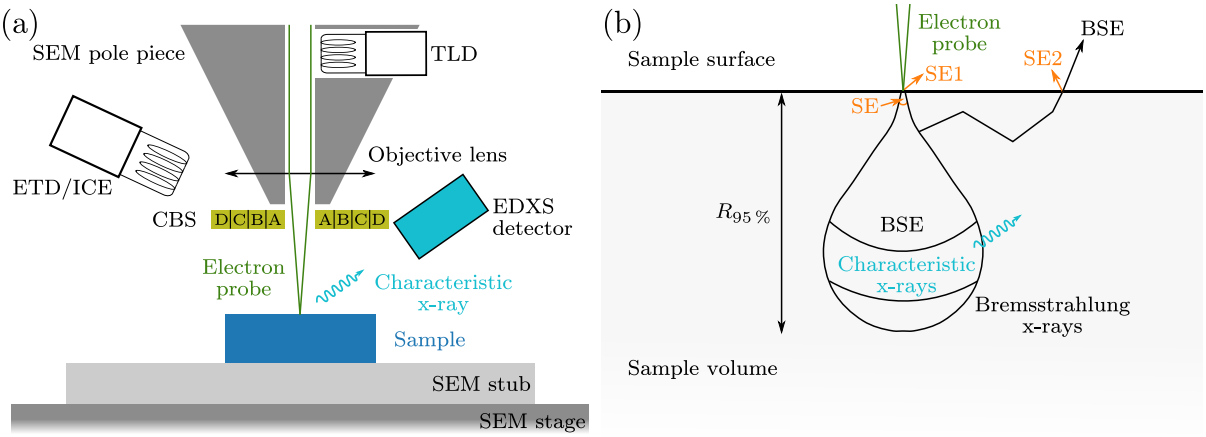

Figure 2.12: Schemes of typical detectors in an SEM and an interaction volume. (a) Scheme of typical detectors used for SEM imaging. A focused electron probe is scanned over the sample surface. The ETD, ICE, and TLD detectors have a filter grid, which can be biased to detect only SEs or BSEs. The TLD is built into the pole piece. A CBS detector is used for BSE detection and consists of four concentric segments (A–D), which collect BSEs scattered in different angular ranges. For chemical analyses characteristic x-rays are detected in energy-dispersive x-ray spectroscopy (EDXS). (b) Scheme of the pear-shaped interaction volume with marked depth distribution of different signals (not to scale). SEs can be produced close to the primary beam (SE1) and from remote sample areas (SE2).

A set of condenser lenses demagnifies the first cross-over of the electron source and focuses the electron probe onto a sample surface. Apertures in the beam path control the beam convergence and beam current. The final lens is called OL, similar to the upper objective-lens pole piece in a combined S/TEM instrument. The aberrations of the OL determine how finely the electron probe can be focused. Critical instrument parameters for achieving the smallest electron probe are given in Eq. (2.29) on page 26. However, an exact calculation of the probe size (especially for $E_0 < 5$ keV) is not trivial [JJ96]. Like in STEM, the electron probe is scanned over a rectangular area with defined step size and the signal at each position forms an SEM image.

Primary electrons hit the sample and interact with the sample atoms through elastic (e.g. backscattered electron generation) and inelastic scattering processes (e.g. secondary electron and x-ray generation) with the atoms and electrons of the sample. This happens until a primary electron has deposited all its energy in the sample by inelastic scattering (Bethe range [Gol+18, p 2]) or if it leaves the sample by elastic scattering processes (e.g. for BSEs). The area from which these different signals originate typically has the shape of a pear (or a "half-pear" shape for strongly scattering materials) and is schematically shown in Fig. 2.12b. The interaction volume size (or depth R_x) depends on the signal type x. The Kanaya–Okayama formula gives an estimate of the size of the interaction volume for *all* elastic and inelastic scattering events,

including 95 % of all electrons [Gol+18, p 12]:

$$R_{95\,\%}(\mathrm{nm}) = 27.6 A E_0^{1.67} / \left(Z^{0.89}\rho\right) \tag{2.35}$$

with the atomic weight A ($\mathrm{g\,mol^{-1}}$), the atomic number Z, the material density ρ ($\mathrm{g/cm^3}$), and the primary electron-beam energy E_0 (keV). As an example, the formula yields $R_{95\,\%}(10\,\mathrm{keV}) = 673\,\mathrm{nm}$ for 10 keV electrons and $R_{95\,\%}(2\,\mathrm{keV}) = 46\,\mathrm{nm}$ for 2 keV electrons in $Ba(Fe_{0.92}Co_{0.08})_2As_2$. This shows that using lower beam energies leads to smaller interaction volumes and higher surface sensitivity in an SEM. The interaction volume for characteristic x-rays $R_{\text{x-ray}}$ can be approximated by modifying the Kanaya–Okayama formula by the atomic shell ionization energy E_c (keV) [Gol+18, p 365]

$$R_{\text{x-ray}}(\mathrm{nm}) = \left(27.6 A / \left(Z^{0.89}\rho\right)\right)\left(E_0^{1.67} - E_\mathrm{c}^{1.67}\right) \quad . \tag{2.36}$$

For example, the Fe L_3 shell with $E_\mathrm{c} = 0.7081\,\mathrm{keV}$ can only be excited down to a sample depth of about $R_{\text{x-ray}}(2\,\mathrm{keV}) = 38\,\mathrm{nm}$ for $E_0 = 2\,\mathrm{keV}$ in $Ba(Fe_{0.92}Co_{0.08})_2As_2$ due to energy losses. Such formulas can give a quick estimation of the size of the interaction volume. More sophisticated approximations and experiment planning can be carried out with Monte Carlo simulations (described in more detail on Page 44).

Secondary electrons. Secondary-electron (SE) imaging is the most important imaging mode in an SEM. The SEs are generated when an incident primary electron scatters inelastically at a valence or conduction band electron. The SEs have a low energy (by convention $< 50\,\mathrm{eV}$) and move on a random trajectory within the sample. SEs that reach the sample surface and manage to overcome the work function of the material (typically a few eV) leave the sample and can be detected. However, similar to the electrons from the primary electron beam, an SE loses energy by inelastic scattering processes along its path through the material. For this reason and the low energies of SEs, the detected SEs must be generated close to the surface. SEs generated deeper within the sample have already lost too much energy during the scattering processes and cannot reach the surface (or overcome the work function). As a result, the SE signal contains mainly information about the surface topography. This behavior can be expressed mathematically by the SE yield δ, which is the ratio of produced SEs (N_SE) and the number of primary electrons (N_PE) [Rei98, p 158]:

$$\delta = \frac{N_\mathrm{SE}}{N_\mathrm{PE}} = \frac{1}{2\varepsilon_\mathrm{SE}} \underbrace{E_0^{-1} \ln\left(\frac{E_0}{J}\right)}_{\text{Bethe stopping power}} \sec\gamma \int_0^\infty \mathrm{e}^{-\frac{z}{R_\mathrm{SE}}}\,\mathrm{d}z \tag{2.37}$$

with the average energy required to produce one SE ε_SE, the mean ionization energy of the sample material J, the angle between the surface normal and the primary beam γ, the depth in the sample z, and the size of the interaction volume of SEs R_SE for a given sample. The Bethe formula describes how much energy a primary electron loses per distance traveled in the sample. The integral calculates the exit probability of an SE generated at depth z. Due to the sec-dependence, the SE yield depends strongly on the sample's topography. If the electron beam passes over a slope or edge, the angle γ is large and so is the factor $\sec\gamma$. At such positions, many SEs are generated, which is visible in an SEM image as a bright contrast at edges.

The SEs can be further differentiated (Fig. 2.12b). SEs, which are generated in the vicinity of the beam provide the highest spatial resolution and are designated as SE1. Due to its small

excitation volume, the SE1 signal contains high-resolution information in the range of the size of the electron probe. A primary electron can leave the sample at another location on its random path through the sample. At this location, further SEs can be generated (denoted as SE2), thereby contributing to the signal and reducing the spatial resolution. Secondary electrons are also generated from hardware components inside the microscope chamber if a BSE strikes such a component (not shown in Fig. 2.12b). Such SEs are referred to as SE3. For conventional SE-SEM imaging, a high contribution of SE1 to the image signal is desired.

Backscattered electrons. Electrons emerging from the sample with an energy of more than 50 eV are called backscattered electrons (BSEs). BSEs partially result from elastic backscattering of the primary electrons at the atomic nuclei. Since almost no energy is lost during this process, the detected BSEs can originate from deeper sample layers than SEs. The topographic contrast is lower compared to SE-SEM imaging, especially when only BSEs from a small angular range away from the incident primary beam are collected. The BSE yield then depends on the atomic number Z of the material, which is the reason why the signal provides a so-called Z-contrast similar to HAADF-STEM, but for bulk samples. Additionally, the arrangement of the atomic lattice planes relative to the incidence angle of the primary electron beam plays a role due to channeling effects. However, the contrast contribution due to channeling is relatively weak compared to the topography and Z-contrast. In analogy to the SE yield δ, the BSE yield η is defined as the ratio between generated BSEs (N_{BSE}) and the primary electrons. For bulk samples and $E_0 > 5\,\mathrm{keV}$, an empirical expression for η is [Rei98, p 142]

$$\eta = \frac{N_{\mathrm{BSE}}}{N_{\mathrm{PE}}} = (1 + \cos\gamma)^{-\frac{9}{\sqrt{Z}}} \quad . \tag{2.38}$$

The angle γ in this formula again represents the angle between the surface normal and the incident beam. For a smooth specimen surface (e.g., prepared by grinding and polishing), the differences in γ are small and the contrast mainly depends on Z.

X-rays in an SEM. Besides BSEs and SEs, characteristic x-rays are produced by ionizing inelastic scattering events. These x-rays can be collected by a detector above the sample and used for chemical analysis using energy-dispersive x-ray spectroscopy, which is discussed in Section 2.2.5. In addition, a continuum of x-ray energies (bremsstrahlung) is produced when atomic nuclei deflect electrons.

Signal Detection in an SEM. The SE and BSE signals can be detected with different detectors. In conventional SEM imaging, the detectors are located above the sample. For example, the Everhart-Thornley detector (ETD) is placed next to the pole piece. It consists of a metal grid, a scintillator and a photomultiplier. A variable voltage can be applied to the grid. A small positive voltage is applied to accelerate the low energy SEs towards the detector for SE detection. For BSE detection, a slightly negative voltage ($< -50\,\mathrm{V}$) is applied. Then, only the more energetic BSEs can overcome the opposing electrical field on the grid and the SEs are repelled and excluded from the BSE-SEM image. In both cases, electrons entering the ETD are converted into photons in the scintillator material. An optical fiber guides these to a photocathode, which is typically located outside the sample chamber. The photons then again release electrons from a photocathode of a photomultiplier through the photoelectric effect. By using several dynodes the number of electrons is increased and a measurable current is generated at the end. An upgraded version of the conventional ETD is the in-chamber electron detector (ICE) [Ger+12]. In contrast to the ETD, the photomultiplier is located inside the sample chamber. Due to the shortened length of the light guide, signal losses can be reduced compared to an ETD. Due

to the geometrical arrangement of these detectors next to the pole piece, SEM images get a directional impression: SEs emitted from surfaces facing a detector with a clear line-of-sight reach the detector without further obstacles and the possibility of absorption in the sample. On the other hand, the sample may block SEs from averted surfaces. In an SE-SEM image, surfaces facing the detector, therefore, have a higher intensity. The contrast gives the impression that there is a light source in the position of the detector.

For the highest spatial resolution in SE-SEM imaging, the electron probe must be as small as possible and mainly SE1 must contribute to the image. The aberrations of the objective lens must be minimized to allow for a large convergence semi-angle (in the order of 5 mrad to 10 mrad) in the immersion mode to form a small electron probe. A small spherical aberration coefficient C_s is experimentally realized by minimizing the working distance (typically 1 mm to 2 mm) since C_s strongly depends on the focal length f as $C_\mathrm{s} \propto f^3$ [Rei98, p 24]. At small distances, the SE yield at the ETD/ICE is reduced due to the physical obstruction by the pole piece. Therefore, a special detector inside the OL is used, which works similar to the ETD/ICE. This detector is called thru-lens detector (TLD).

Because of their higher energy, most BSEs move on nearly straight trajectories after leaving the sample surface since they are not strongly attracted by the small positive voltage on the detector grid. As noted above, the ETD, ICE, and even the TLD can be used for BSE detection by applying a negative bias to the grid (to repel the SEs). However, since the ETD and ICE detectors typically only cover a narrow solid-angle range (around 1×10^{-2} sr [Rei98]), retractable annular solid-state detectors are used for efficient BSE-SEM imaging. A retractable annular BSE detector is inserted between the sample surface and the pole piece. It is called concentric backscatter detector (CBS) in the TFS Helios G4 FX instrument. Four different angular ranges can be selected (or combined) with the CBS detector (denoted as A–D in the microscope software). The innermost segment (A) collects BSEs close to the primary beam axis (small γ) and preferentially provides compositional Z-contrast. Electrons collected by the outer segment (D) are scattered far from the primary beam axis (large γ) and give more topographical information. The exact collection angles depend on the working distance and the objective-lens mode (field-free or immersion).

Focused-ion-beam system. A focused-ion-beam (FIB) instrument is typically used to structure materials on the (sub-)µm scale. The basic principle of scanning an ion beam over the sample surface is similar to an SEM. Due to their charge, ions are deflected by electric and magnetic fields. A difference to electrons is that ions have a larger mass. For this reason, electrostatic lenses are commonly used for focusing instead of magnetic lenses. The most commonly used ion source in FIB instruments is a Ga^+ liquid-metal ion source (LMIS), which has a low melting point of 29.8 °C [Sez16]. The Ga is melted in a crucible and diffuses to the tip of a W needle. Because of the low temperatures required for melting Ga, there are no undesired reactions between Ga and W. At the tip of the W needle, Ga^+ ions are extracted from a Ga droplet (Taylor cone [Tay64; Cox15]) by the field effect. The extracted Ga^+ ions are then accelerated by an electric field. In analogy to the SEM, the maximum accelerating voltage is 30 kV. The accelerated Ga^+ ions are focused into a small probe (few nm diameter) on the sample surface. As with the SEM, mechanical apertures control beam current and probe size. Typical beam currents range from 1 pA (for high-resolution imaging and fine-structure milling) to a few ten nA (for rough milling). The Ga^+-ion probe is systematically scanned over the surface. The ions hit the sample surface and are either directly backscattered (analogous to BSEs) or propagate into the sample. In the sample, an incident Ga^+ ion scatters at the sample atoms (nuclear

interaction) and the ion can interact with the electrons of the solid (electrical interaction). These elastic and inelastic scattering processes occur until an Ga^+ ion leaves the sample again or has deposited its entire kinetic energy. In the latter case, the Ga^+ ion is implanted in the sample. A FIB image can be generated by collecting various signals at each ion-probe position. A unique feature of a FIB system is that besides SEs also secondary ions (ejected sample atoms) can be used for imaging.

A FIB system is rarely used purely for imaging due to its surface-damaging properties. An example is the investigation of different grains in crystalline materials since FIB imaging provides strong channeling contrast. In addition, electrostatic lenses have more significant aberrations than magnetic lenses and, hence, an ion probe cannot be focused as small as an electron beam. The FIB systems used in this work, FEI Strata 400S and TFS Helios G4 FX, are so-called two-beam (or "DualBeam") systems, which means that the microscopes are equipped with an electron-beam column and a FIB column. The two columns are mounted at an angle of 52° with

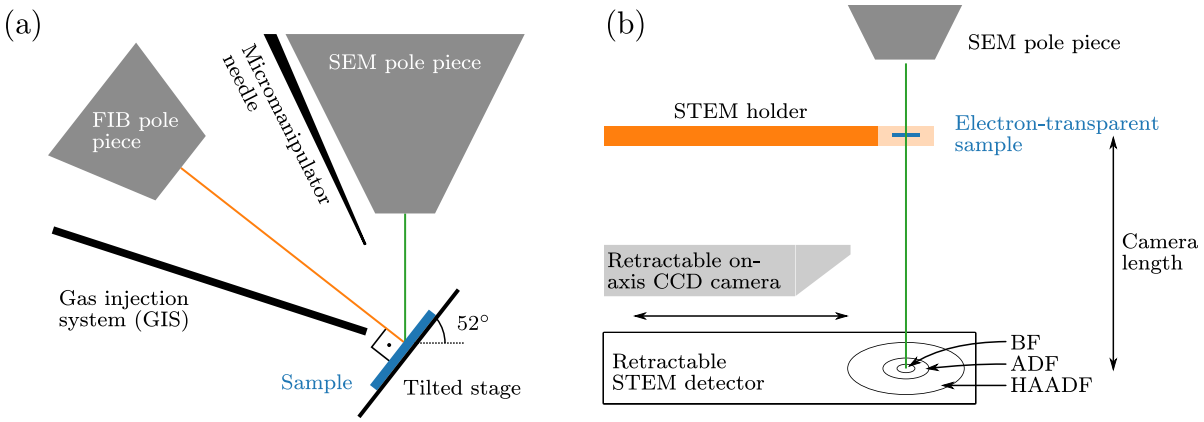

Figure 2.13: Schemes of a two-beam system and the STEM-in-SEM detectors. (a) Scheme of the geometrical setup of the pole pieces in a two-beam FIB/SEM system (not to scale). The FIB incidence is perpendicular to the sample surface for a 52° stage tilt. A GIS and a micromanipulator needle can be inserted for nanostructuring applications. (b) Additional detectors are available in the TFS Helios G4 FX instrument for STEM-in-SEM imaging. A STEM detector is used for STEM imaging with transmitted electrons. An on-axis CCD camera (here a Bruker Optimus TKD) can be used to acquire on-axis diffraction patterns.

respect to each other, as shown in Fig. 2.13a. The two-beam system combines the non-damaging SEM imaging capabilities with the nanostructuring capabilities of a FIB. The interaction between Ga^+ ions and the sample atoms causes a transfer of kinetic energy of the impinging ion to the sample since the masses of the scattering partners are in the same order of magnitude. This is different compared to the comparably light electrons in an SEM. With the transferred kinetic energy, a sample atom can be moved away from its lattice position or knocked out of the sample. This process is called sputtering and can be used to fabricate three-dimensional nanostructures, the main application for FIB instruments. The sputtering yield, which indicates how many sample atoms are sputtered per incident Ga^+ ion, depends on several factors, e.g. the Ga^+-ion energy or the FIB incidence angle. As a rule of thumb, materials with higher melting points have a lower sputtering yield. For example, MgO with a relatively high melting point $T_{m,MgO} = 2825\,°C$ is the material with the lowest sputter yield in this work. This results in longer FIB-milling durations or the use of higher FIB currents to speed up a milling process. A sputtered atom is either pumped away through the vacuum system or lands again on the

sample and can stick there (redeposition). Redeposition effects during sputtering depend on the adhesion coefficient of the surface and the milling geometry.

In addition to material removal by sputtering, a FIB can also be used to deposit materials on the sample surface. For this purpose, a gas-injection system (GIS) needle is inserted about 150 µm above the sample surface and a gaseous chemical precursor material is temporarily introduced into the vacuum chamber. For example, the precursor gas $C_5H_4CH_3Pt(CH_3)_3$ is used to deposit a mixed Pt/C layer. The gas first adsorbs on the surface of the sample. Then, bombardment with the electron or Ga^+-ion beam breaks the molecule bonds and atoms contained in the precursor remain on the surface. This method is denoted as "electron-/ion-beam-induced deposition" (EBID/IBID), depending on which beam is used. A film with the atomic constituents of the precursor is then formed in the scanned area. The by-products are pumped off via the vacuum system. With this technique, surface features below this protective Pt/C layer can be protected during further FIB processing. Typically, EBID deposition is slower but less damaging than IBID. Therefore, EBID is applied first on the bare sample surface for a few minutes to protect the sample surface and then IBID is used to deposit a $\sim$ 1 µm to 2 µm thick protection layer during TEM-sample preparation. In addition, nanostructures can be interconnected ("welded") by EBID/IBID. This capability is used to connect thin stripes of sample material to a micromanipulator needle. Such a needle is used to transport nanostructures within the sample chamber, e.g. an extracted TEM lamella. Figure 3.6h on Page 63 shows a top-view SEM image with the inserted GIS and the micromanipulator needle.

STEM-in-SEM. Modern SEMs can be used for STEM imaging of electron-transparent TEM samples similar to high-energy S/TEM instruments [Sun+20; HC20]. The term "STEM-in-SEM" distinguishes between the two instrument types. The highest available primary electron energy of $E_0 = 30\,\text{keV}$ in a SEM limits the usable TEM-sample thickness, which the electron beam can penetrate. However, advances in (FIB) sample preparation and optimization of the preparation process for a given material can often lead to high-quality TEM samples with a thickness of 50 nm and below. This makes most materials suitable for STEM-in-SEM imaging. Moreover, weakly scattering materials can benefit from higher scattering cross-sections at lower electron-beam energies. Furthermore, FIB preparation and STEM-in-SEM imaging can be combined in a two-beam instrument, reducing the cost and time requirements for materials analysis down to the nm scale. Another advantage of combined FIB preparation and STEM-in-SEM imaging is that TEM samples from reactive materials can be prepared and analyzed without exposure to ambient conditions.

Most of the fundamentals introduced for STEM imaging in section Section 2.2.3 on page 26 also apply to STEM-in-SEM. An important difference is that the attainable probe size (FWHM) for STEM-in-SEM is around $d_0 \approx 0.6\,\text{nm}$ (for the TFS Helios G4 FX), compared to $d_0 < 0.2\,\text{nm}$ for high-energy STEM. Direct HAADF-STEM imaging of atomic columns is therefore not possible (yet). However, bright-field (BF) STEM lattice-fringe imaging can reach a spatial resolution down to $\sim 0.3\,\text{nm}$ [Ngo+07]. STEM-in-SEM imaging uses the transmitted electrons to form an image (Fig. 2.13b). As already discussed for ADF-STEM imaging on Page 30, the scattering angles determine the image contrasts. For STEM-in-SEM imaging, a retractable STEM detector is inserted below a TEM sample. Modern detectors such as the "STEM 4" detector in the TFS Helios G4 FX are annularly segmented, which means that specific collection-angle ranges (e.g. ADF and HAADF) can be read out (simultaneously) to form STEM-in-SEM images. The physical sample-detector distance (or camera length) can be adjusted to change the collection angles on a STEM detector to a small degree. However, the range of accessible camera lengths is

much smaller than in S/TEM instruments because of the missing projection-lens system. Instead of a segmented STEM detector, a CCD camera can also be inserted below the TEM sample to record on-axis diffraction patterns. This can be used for diffraction analyses [Sun+20; Slo+21], to align the sample into a specific diffraction condition (e.g. for "two-beam" diffraction-contrast imaging [Sun+20]), or to align the sample into a low-index zone-axis orientation for BF-STEM lattice-fringe imaging. Like in a S/TEM instrument, chemical analyses with STEM-in-SEM are possible by energy-dispersive x-ray spectroscopy [Boo21] and recently also electron energy loss spectroscopy [Bro+19]. These analytical techniques are introduced in the next section.

2.2.5 Analytical Electron Microscopy (EDXS/EELS)

Analytical electron microscopy is concerned with the spatial distribution and concentration of elements within a sample. For this task, energy-dispersive x-ray spectroscopy (EDXS) and electron energy loss spectroscopy (EELS) were used in this work. In particular, the combination of STEM with these techniques enables (sub-)nanometer spatial resolution. This is because the detected chemical signals in EELS and EDXS mainly originate from the sample region directly sampled by the incident electron probe. In this section, the principles of EDXS and EELS are briefly explained.
In general, both techniques exploit inelastic scattering events which create element-specific signals for detection (Fig. 2.14). The incident electron beam inelastically scatters with the electrons of the sample atoms. In the shown example for O, a vacancy/hole is generated by excitation of an inner-shell electron (here the K shell). The incident electron undergoes an energy loss during a *primary* interaction process (red path). Inelastic scattering occurs mostly into small angles and the loss electron can be detected by an EELS detector. As a *secondary* process, the hole is filled by an electron from an outer shell (here from the L shell) to de-excite the atom. The binding-energy difference between the shells is released as a photon (blue path). The photon can (i) leave the sample without further interaction (radiative transition) or (ii) excite an electron of another outer shell of the same atom (Auger-Meitner effect). The x-ray is then absorbed and instead, an Auger-Meitner electron is emitted (radiationless transition). The ratio of radiative and radiationless transition is called fluorescence yield and depends on the atomic number Z [Gol+18, p 41] and used electron energy E_0. The effect of the latter is often described in terms of the "overvoltage" ratio E_0/E_c to excite a given atomic shell E_c. The overvoltage can be adjusted experimentally by selecting E_0 and should be at least 1.3 to effectively excite an atomic shell [Boy02]. Radiationless transitions are more probable for lower Z. The photon energies of radiative transitions are in the invisible range (x-ray), characteristic for a given element, and can be detected by an EDXS detector. In principle, both signals - the loss electrons by EELS and the characteristic x-rays by EDXS - can be detected simultaneously, which is technically realized in modern instruments.

Analytical electron microscopy is mainly done in combination with a strongly focused electron probe in S(T)EM to reveal the spatial distribution of elements on the (sub-)nm scale. This is because (in first approximation) the chemical signals only emerge from a local region around the probe position. Different types of signal-collection strategies exist:

- Point: The beam is parked on a selected region and the signal is collected for a given duration, typically a few (ten) seconds.
- Average-scan spectrum: The beam is continuously scanned over a sample region and an average spectrum is collected.

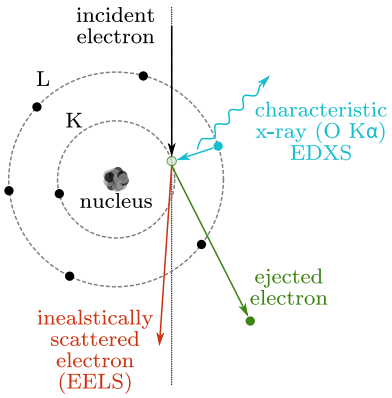

Figure 2.14: Scheme showing signal generation for analytical electron microscopy. The shown atomic model is O. In this example, the incident electron beam knocks out an electron in the K shell (green path) resulting in an inelastic scattering event with an energy loss (red path). The O-K core-loss edge starts at the K-shell binding energy of 532 eV. As a secondary process, a characteristic x-ray is generated when the ejected K-shell electron is replaced by, e.g., an L-shell electron (blue path). The energy of the x-ray is the difference between the binding energies of $L_{3,2}$- and K-shell, i.e. O K$\alpha_{1,2}$ = 525 eV (or $\lambda_{\mathrm{O\ K}\alpha} = hc/E$ = 2.4 nm).

- Line scan: The beam is scanned along a line and a spectrum is collected in specific spatial intervals for a given duration.
- Mapping/Spectrum imaging: The beam is scanned in a predefined two-dimensional raster (as for a regular S(T)EM image), and at each position a spectrum is collected (typical duration of a few (ten) ms per beam position). This creates a three-dimensional dataset (x, y, E), typically denoted as "spectrum image".

Typically, the signal-to-noise ratio per single-position spectrum decreases from point → line scan → spectrum image, but the "amount" of spatial information increases. The signal-to-noise ratio per pixel is relatively low for spectrum imaging as shown in the raw spectra Fig. 2.17c and d on Page 49. Spectrum imaging allows to retrieve a plethora of information from the multidimensional data set after the experimental acquisition.
Another important property for EDXS and EELS is related to the detection hardware. Read-out hardware has so-called "channels" (e.g., physical camera pixel elements for EELS) to store the events. The channels are related to the detected energy of an x-ray in EDXS and of an energy loss in EELS via the energy dispersion, i.e. energy per channel. A *higher* dispersion corresponds to a smaller energy-per-channel value. Typical values used in this work are 10 eV/channel (EDXS) and 0.5 eV/channel (EELS). The operator can change the dispersion: A higher dispersion leads to a better energy resolution but smaller (energetic) field of view and *vice versa*. In the following, EDXS and EELS are explained in more detail.

EDXS

The energy of x-rays is measured in EDXS. Silicon-drift detectors (SDD) are nowadays used for x-ray detection compared to older Li-drifted Si detectors (Si(Li)) because SDDs provide faster read-out ($> 1 \times 10^5$ counts per second) and only require Peltier-based cooling (instead of LN_2 as for Si(Li)). The detection principle is absorption of an incoming x-ray and the conversion of the x-ray energy into electron-hole pairs (3.62 eV per pair in Si at 300 K [Rit09]). The x-ray energy is measured on the basis of the number of counted electron-hole pairs in a specific time. For a more detailed discussion on x-ray detection with SDDs see Ritchie [Rit09].

Multiple electrons from different states can fill a hole generated by the primary beam (x-ray transitions). As a result, several peaks at different (known) energies appear for a single element in a typical EDXS spectrum. The x-ray transitions have different names to clearly identify them. Throughout this work, the standard Siegbahn nomenclature is used to denote the x-

ray transitions[8], which indicates the target shell by a roman letter (K, L, M, ...; quantum number $n = 1, 2, 3, \dots$) and the source shell by greek letters (α, β, γ, ...; quantum number $l = 0, 1, 2, \dots$). In addition, states with a different total angular momentum (quantum number j) are denoted by an additional index (1, 2, 3, ...). The latter is often omitted when peaks overlap due to the finite EDXS energy resolution so that two x-ray lines appear at the "same" energy. For example, O K$\alpha_{1,2}$ is combined to O Kα. Some example x-ray transitions for Fe are:

$$\mathrm{Fe\,K}\alpha \Leftrightarrow \mathrm{Fe\,K}\alpha_{1,2} \quad \rightarrow \quad \mathrm{Fe\,K} - \mathrm{Fe\,L_{3,2}} \tag{2.39}$$

$$\mathrm{Fe\,K}\beta_1 \quad \rightarrow \quad \mathrm{Fe\,K} - \mathrm{Fe\,M_3} \tag{2.40}$$

$$\mathrm{Fe\,L}\alpha \Leftrightarrow \mathrm{Fe\,L}\alpha_{1,2} \quad \rightarrow \quad \mathrm{Fe\,L_3} - \mathrm{Fe\,M_{5,4}} \tag{2.41}$$

The peaks are identified by their positions and (relative) intensities. The peak positions, i.e. the energies of the x-ray transitions, are well known and tabulated in literature and standard EDXS software[9]. For a given quantum number n (a "x-ray-line family"), the relative peak heights within such a family of x-ray transitions are mostly known with reasonable accuracy. These properties are used to separate overlapping peaks in EDXS spectra, as discussed in the methods section (Page 81). Compared to EELS, EDXS is relatively fast to set up experimentally, can measure all elemental signals at once (large energy window), and can also be carried out on bulk samples in an SEM (SEM-EDXS). However, EDXS also has some drawbacks. The energy resolution is in the range of 50 eV to 130 eV, whereas EELS is mainly limited by the energy spread of the electron source (about 0.7 eV for a non-monochromated Schottky FEG). Scattered electrons and high-energy x-rays can also produce unwanted, spurious x-rays from other sample regions, the TEM grid, and microscope hardware. In addition, the generation and detection of x-rays are hampered by the following aspects:

- The generation of x-rays competes against radiation-less de-excitation (secondary) processes by emission of Auger electrons (not shown in Fig. 2.14).
- X-rays are emitted isotropically in all directions, which means that an efficient EDXS detector must cover as much solid angle (4π sr total) as possible for high collection efficiency. This is typically limited by the available space in an SEM or S/TEM around the pole-pieces. Recent advances in instrumentation introduced multi-SDD detector setups which cover, e.g., 0.9 sr ("Super-X" detector [Sch+10]), 4.45 sr ("Ultra-X/XPAD" detector [Zal21]), 1.1 sr ("FlatQUAD" detector [Ter+17]), to collect as many x-rays as possible.
- X-rays are absorbed in matter (Lambert-Beer's law). Low-energy x-rays are more prone to absorption compared to high-energy x-rays. This can lead to self-absorption inside the sample or by a detector window. The latter aspect led to the development of "windowless" detectors, which offer higher collection efficiency for low-energy x-rays.

For the detection of low-energy x-rays (below 1 keV) the experimental parameters can be geometrically optimized during sample preparation and sample mounting, which is described in the methods section (Fig. 3.16 on page 80). This is especially important for beam-sensitive materials, which can only tolerate a limited total electron dose before destruction.

[8] Although the International Union of Pure and Applied Chemistry (IUPAC) recommends [Jen+91] to specify the x-ray transitions by their atomic-shell names rather than using the Siegbahn notation. The latter can be confusing for less common x-ray transitions and some transitions are not defined at all.

[9] For example, in *DTSA-II* the command `listTransitions('Ba')` can be used to list all x-ray transitions (and their weights) for Ba.

EDXS Signal Extraction. The background-corrected (net) x-ray peak intensities can be extracted by a simple integration method (for non-overlapping peaks) or a model-based fit of Gaussian functions for each x-ray peak (for overlapping peaks) [NR15a; NR15b]. The latter is discussed in the experimental methods section on Page 81. These net intensities are plotted in *qualitative* EDXS elemental maps shown throughout this work.

EDXS Quantification. The quantification of EDXS spectra aims to convert the intensities of x-ray peaks for (two or more) elements (I_x^A) into an elemental concentration (C_A). In general, both quantities are connected in a non-linear manner for different elements. For example, the O peak in SiO_2 is *not* twice as large as the peak for Si. Still, for the same element, a doubling of the elemental concentration C_A does lead to a doubling in the detected peak intensity I_x^A. For an accurate quantification, several experimental aspects have to be considered, which are briefly described in this paragraph. The intensity I_x of an x-ray peak of an element A depends on several factors and is given by [Fou+99]

$$I_x^A = \overbrace{C_\mathrm{A}}^{\text{Sample}} \cdot \underbrace{n_{\mathrm{e}^-}}_{\#\text{ electrons}} \cdot \overbrace{\frac{N_\mathrm{A}}{A_\mathrm{A}} Q_j(E_0)\omega_j p_{jl}\,(1+f)\,(1+g_\mathrm{ck})}^{\text{Atomic properties}} \cdot \overbrace{\frac{\Omega}{4\pi}\epsilon_\mathrm{d}(E_x)}^{\text{Detector properties}} \cdot \underbrace{\int_0^{R_\mathrm{max}} \varphi(\rho z) \exp\left(-\rho z \frac{\mu}{\rho}(E_x)\csc(\theta_\mathrm{d})\right) \mathrm{d}\rho z}_{\text{Depth distribution and self-absorption}} \quad (2.42)$$

with the number of incident electrons per second n_{e^-}, the Avogadro number N_A, the atomic mass A_A, the ionization cross-section Q_j, fluorescence yield ω_j, and p_{jl} transition probability/rate of a transition from shell j to a vacancy in shell l. The factor f/g_ck relates to extra x-ray production by secondary fluorescence/Coster-Kronig transitions. The detector properties are modeled by the solid angle Ω (including shadowing by a holder) and the total detector efficiency (detector window and active detector-layer thickness) $\epsilon_\mathrm{d}(E_x)$. The integral contains the ionization-depth distribution function $\varphi(\rho z)$ ("Phi-Rho-Z" function) with the mass depth (density ρ times depth z). The exponential term is related to absorption in the sample by Lambert-Beer's law, which depends on the take-off angle θ_d and the mass-absorption (or attenuation) coefficient (MAC) $\mu/\rho(E_x)$ of the sample. Even though in principle it is possible to quantify the sample composition from Eq. (2.42), in actual practice the required quantities are not all known or only within limited accuracy. Further developments are necessary to realize accurate "standardless" quantification based on Eq. (2.42). In the following the currently used methods for quantification approaches for bulk and TEM samples are described.

For quantifying bulk samples (SEM-EDXS), a flat sample surface and a homogeneous sample composition over the range of the interaction volume are typically assumed. Both conditions are not fulfilled for the superconducting films analyzed in this work (i) as the surface is uneven due to trenches and precipitates and (ii) the film thickness varies between 20 nm and 350 nm, which is typically smaller than the interaction volume. For these reasons, quantification in SEM-EDXS must be evaluated carefully. It is noteworthy that such stratified thin-film-substrate sample systems can be analyzed with a multi-E_0 measurement approach using the commercial *STRATAgem* [Küh+12; Ort+15; Sac+18] software or the open-source *BadgerFilm* [MF20] software.

For thin TEM samples, Eq. (2.42) can be simplified to [HS19, p 386]

$$I_x^A = C_\mathrm{A} \cdot n_\mathrm{e} \cdot \frac{N_\mathrm{A}}{A_\mathrm{A}} Q_j(E_0)\omega_j p_{jl} \cdot \frac{\Omega}{4\pi}\epsilon_\mathrm{d}(E_x) \cdot t \tag{2.43}$$

with the sample thickness t. In this approximation, the effects of x-ray self-absorption and secondary fluorescence are neglected ("thin-film criterion"). The atomic properties in Eq. (2.43) are not known for all materials and in addition, n_e, Ω, and t must be measured for an *absolute* quantification. However, often only the ratio between two or more elements (A, B, ...) is of interest, i.e. $C_\mathrm{A}/C_\mathrm{B}$, which leads to [HS19, p 387]

$$\frac{C_\mathrm{A}}{C_\mathrm{B}} = \left(\frac{\left(\frac{Q_j \omega_j p_{jl}}{A_\mathrm{B}}\right)_\mathrm{B}}{\left(\frac{Q_j \omega_j p_{jl}}{A_\mathrm{A}}\right)_\mathrm{A}} \cdot \frac{\epsilon_\mathrm{d}\left(E_x^\mathrm{B}\right)}{\epsilon_\mathrm{d}\left(E_x^\mathrm{A}\right)} \right) \frac{I_x^\mathrm{A}}{I_y^\mathrm{B}} \tag{2.44}$$

$$= k_\mathrm{AB}^{xy} \frac{I_x^\mathrm{A}}{I_y^\mathrm{B}} \tag{2.45}$$

$$\frac{C_\mathrm{A}}{C_\mathrm{B}} = k_\mathrm{AB} \frac{I^\mathrm{A}}{I^\mathrm{B}} \quad , \tag{2.46}$$

where in Eq. (2.45) the ratio of atomic properties and detector efficiency was combined in a proportionality factor k_AB^{xy}. The factor k can be determined/approximated for all combinations of x-ray transitions, so the superscript is omitted in Eq. (2.46) for brevity, leading to a general proportionality factor k_AB[10]. This proportionality factor in (S)TEM-EDXS is typically denoted as "Cliff-Lorimer factor" [CL75]. This approach is used in this work to approximate the (relative) sample composition. The concentrations are typically normalized to unity, i.e. $\sum_i C_i = 1$. A quantification example for simulated $GdBa_2Cu_3O_7$ EDXS spectra using the Cliff-Lorimer method is shown in Fig. 2.15b. The Monte Carlo simulation shows that the thin-film criterion for this material is only valid for sample thicknesses below $\sim 25\,\mathrm{nm}$ (vertical arrow). The O Kα x-rays are increasingly absorbed in the GdBCO sample (dashed horizontal arrow). This decreases the quantified O concentration. Due to the additional constraint $\sum_i C_i = 1$, the other element concentrations are falsely increased. This example shows that the thin-film criterion must be used carefully. However, an absorption-correction factor [HS19, p 389] can be applied in the Bruker *Esprit* software for a given material density and TEM-sample thickness. This enhances the elemental quantification with low-energy x-rays (even if the thickness and material density are only approximately known). The density and sample thickness are precisely known for the simulated EDXS spectra. Therefore, the absorption correction can be exemplified based on the simulated 200 nm thin GdBCO sample, as shown in Table 2.2. The quantification results with absorption correction are closer to the nominal, simulated concentrations than without absorption correction. Especially the O concentration is affected, due to the strong self-absorption of the low-energy O Kα x-rays in GdBCO.

The Cliff-Lorimer factors k_AB for each element can be measured experimentally for samples with known composition ("standards") or calculated from "first principles" from the atomic properties ("standardless"). The standardless approach is less accurate but does not require a reference standard (with ideally similar composition as the unknown material) for *each* element in the unknown material. A standards-based analysis is experimentally challenging, but rewards with significantly increased accuracy [NR13; NR15a]. Such inaccuracies are visible in the simulated

[10] Not to be confused with the "k-ratio" in standards-based EDXS-quantification, which relates the x-ray peak intensities between an unknown and a known standard material.

Table 2.2: Absorption correction for EDXS quantification. The simulated EDXS spectrum of a $GdBa_2Cu_3O_7$ sample with a TEM-sample thickness of 200 nm and a calculated material density of $7\,gcm^{-3}$ is quantified with and without absorption correction in the Bruker *Esprit* software (version 2.1).

	Gd / at. %	Ba / at. %	Cu / at. %	O / at. %
$GdBa_2Cu_3O_7$ (nominal, as simulated)	7.69	15.38	23.08	53.85
Without absorption correction	10.81	21.37	28.61	39.20
With absorption correction	8.08	15.85	20.95	55.12

spectra in Fig. 2.15b for sample thicknesses $< 25\,nm$, where, e.g., the Cu concentration is too low. This is also observed for the absorption-corrected quantification results in Table 2.2. In any case, the Cliff-Lorimer factors are related to a common element for tabulation (Si for the Bruker *Esprit* software):

$$k_{AB} = \frac{k_{ASi}}{k_{BSi}} \tag{2.47}$$

The values k_{ASi} for each element A (and the strongest x-ray transition for each x-ray family) are calculated and tabulated in *Esprit*. Another standards-based quantification approach with the possibility to use pure-element standards is the ζ-factor method [WW99b].

Monte Carlo modeling. Monte Carlo simulations [SZ92; Gol+18] are commonly used to model complex electron-solid interactions (cf. Eq. (2.42)) such as x-ray generation, absorption, and detection in EDXS. In this way, experiments can be planned out (e.g., which overvoltage to use for low-energy EDXS) and critical peak overlaps can be detected even before going to an SEM or TEM. The reader is referred to Shimizu and Ze-Jun [SZ92] for a detailed description of the Monte Carlo simulation method. Briefly, the electron-solid interactions are modeled as a random walk of single electrons consisting of (i) free movement in the solid related to the mean-free-path length and (ii) random elastic or inelastic scattering processes within the material. An electron continuously loses energy through these interactions and is eventually absorbed in a bulk sample or leaves the material at the sample surface (or the bottom side for a thin TEM sample). By repeating this random walk for many thousand electrons, insights into the electron-beam interactions are gained. For example, Fig. 3.1 on page 56 shows a few electron trajectories to approximate the size of the interaction volume for different sample geometries. The accuracy of the Monte Carlo method is limited by the accuracy of the interaction models and the used experimental values for atomic properties. Free software such as *CASINO* [Dro+07] and *DTSA-II* [Rit09] can be used for Monte Carlo simulations of EDXS spectra (Fig. 2.15). For example, Fig. 2.15a shows the difference in total detected x-rays for an increasing GdBCO sample thickness for a constant electron dose. A thicker sample (blue, 100 nm) generates more x-rays than the thinner TEM samples. Such simulations can show how much x-ray counts are needed in an EDXS spectrum to detected, e.g., a trace element.

EELS

The energy losses after beam-sample interactions contain information about the sample, e.g., composition, bonding states, or sample thickness. These signals are detected in EELS. A post-column GIF was used for EELS in this work. The GIF is a complicated arrangement of magnetic lenses, aberration correctors, bending magnets, and apertures and schematically shown in Fig. 2.5 on page 14. The following only describes the basic principle. For more information, the book by Egerton [Ege11] is recommended.
The incident beam enters the GIF through an entrance aperture, which defines the collection

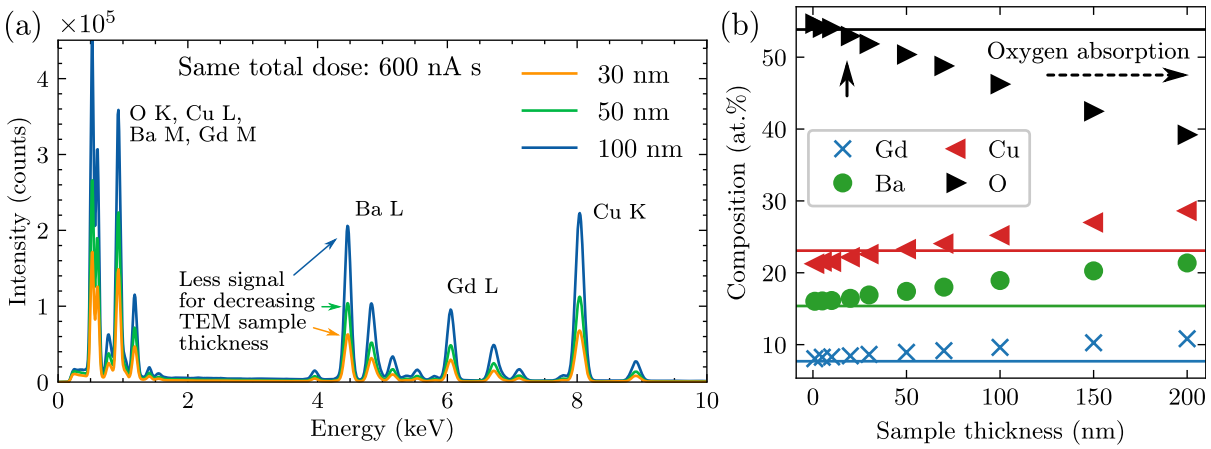

Figure 2.15: Monte Carlo EDXS-spectrum simulation for a GdBCO TEM sample. The simulation was done with *DTSA-II* for an electron energy of 200 keV, a constant total dose of 600 nA s, and varying TEM sample thicknesses. (a) Selected spectra for 30 nm, 50 nm, and 100 nm. The x-ray yield increases with increasing sample thickness for the same total dose. (b) Cliff-Lorimer standardless quantification results from the *Esprit* software for various sample thicknesses. The horizontal lines mark the simulated, nominal concentration values. For sample thicknesses below ∼ 25 nm (vertical arrow), the quantified concentrations agree well with the nominal values and the thin-film criterion is valid. However, the quantified O content decreases for increasing sample thickness due to increasing self-absorption of the low-energy O Kα x-rays (dashed horizontal arrow). The concentration of the other elements is falsely increased to satisfy the mathematical normalization to 100 %.

angle β in STEM-EELS experiments. A set of electron-optical elements aligns the beam. Then, a bending magnet is used to split the incoming beam into energy losses since the trajectory in the bending magnet depends on the electron energy. After the bending magnet, the beam is dispersed in an energy-selective plane. This is the EELS spectrum that is recorded in "spectroscopy mode". The EELS spectrum is (de-)magnified and stretched in the non-energy-dispersive direction by a set of lenses and finally detected by a CCD (or other) camera. By stretching the spectrum in one direction, the whole square- or rectangular-shaped camera area can be used and the total intensity of the EELS spectrum is distributed among many pixels, which prevents damage to the sensor. An "imaging mode" is also available (also called EFTEM), where an image of a specific energy loss selected by the slit is formed by the lenses and projected onto the CCD. This mode was not used in this work.

The energy-loss spectrum is – by convention – separated into the "low loss" ($\leq$ 50 eV) and "high loss" ($>$ 50 eV) regions. The latter contains most of the core-loss (ionization) edges, which were of main interest in this work. For example, the O K edge starts at an energy loss of 532 eV[11]. In general, the presence of a characteristic core-loss edge is used to identify an element in a sample. The intensity of a core-loss edge is related to the concentration of an element. In addition, the first ∼ 50 eV after an edge onset contains information about the bonding state and is called energy-loss near-edge structure (ELNES). A prominent ELNES feature are the so-called "white lines", which are intensive peaks for specific elements for the $L_{2,3}$- (transition metals) and $M_{4,5}$-edges (rare-earth elements). The white lines are visible even for low signal-to-noise ratio or small elemental concentrations (trace-element analysis) and elements with white-line ELNES are particularly favorable to be detected by EELS. As visible in Fig. 2.17 on page 49, the core-loss edges appear on top of a relatively intense, power-law-type background of the shape aE^{-r}, with the loss energy E and fitting constants a and r. In contrast, x-ray peaks in

[11] In *DTSA-II* the command `listEdges('O')` can be used to list all ionization edges for O or the "EELS Atlas" (`https://eels.info/atlas`, last accessed: 31.10.2021) can be used.

EDXS appear on a comparably small bremsstrahlung background. The rapidly falling signal in EELS with increasing E typically limits the usable energy range in EELS to 0 keV to 2 keV, although recent technological advances enable the analysis of larger energy-loss ranges. The experimental energetic field of view is restricted by the available energy dispersions of the GIF. For example, a maximum energy window of 1024 eV can be realized with the lowest dispersion of 0.5 eV/channel for the used 2048-channel CCD camera. The starting point of such an energy window can be shifted by using the "drift-tube" (used here), a temporary increase in electron energy E_0 ("offset"), or a "prism voltage offset" in the GIF. However, not all elements in a sample have a detectable core-loss edge in such a narrow energy window, which is a drawback compared to EDXS.

EELS Signal Extraction. Similar to EDXS, the background-corrected (net) core-loss intensities can be extracted by a simple integration method or a model-based fit of Hartree-Slater ionization cross-section (see below) for each core-loss edge [VV04; dlPeñ10]. The latter approach was generally used in this work, as it can effectively separate overlapping edges. The fit parameter for scaling the Hartree-Slater cross-sections is extracted as the edge's net-intensity value for the model-based approach. The net-intensities (from fitting or integration) at each probe position in a spectrum image are plotted in *qualitative* EELS elemental maps shown throughout this work.

EELS Quantification. Similar to EDXS, a quantification in EELS tries to convert the core-loss edge intensities I_x^{A} of a shell x to an elemental concentration C_{A} for an element A. Typically, the ratio between different elements is of interest and the same approach as for EDXS can be used: By using a concentration ratio, unknown or hard-to-measure quantities (e.g. the beam current) cancel. The relevant equation for two elements A and B with the core-loss edges x and y is again (see Eq. (2.46)) a connection of the intensities to the concentrations by a scaling factor κ_{AB}^{xy}:

$$\frac{C_{\mathrm{A}}}{C_{\mathrm{B}}} = \kappa_{\mathrm{AB}}^{xy} \frac{I_x^{\mathrm{A}}}{I_y^{\mathrm{B}}} \tag{2.48}$$

The scaling factor in EELS κ_{AB}^{xy} is given by the partial (i.e. integrated over an energy window Δ) ionization cross-sections σ [Ege11, p 271]

$$\kappa_{\mathrm{AB}}^{xy} = \frac{\sigma_y^{\mathrm{B}}(\Delta, \beta, \alpha)}{\sigma_x^{\mathrm{A}}(\Delta, \beta, \alpha)} \quad , \tag{2.49}$$

with the semi-convergence and semi-collection angles α and β. These angles are important experimental parameters and can be measured by taking a shadow image of the entrance aperture and the bright-field disc (see Fig. 3.11 on page 74 for an example).
The partial cross-sections can be calculated based on a hydrogenic or Hartree-Slater model. The latter was used throughout this work. The Hartree-Slater approach is based on tabulated values for the "generalized oscillator strength" (GOS) from [LRM80; AR85], which are included in the commercial EELS plugin for *DigitalMicrograph*. The influence of beam convergence α, which is essential in STEM, is included in an effective σ as proposed by Kohl [Koh85]. For more details on the correction of EELS intensities for beam convergence, see Egerton [Ege11, p 274]. Like EDXS, a theoretical calculation of σ (or standardless analysis) suffers from possible inaccuracies, which are given as a flat 10 % error for all edges in *DigitalMicrograph*. Standards-based analysis with samples of known composition under identical experimental parameters as the unknown material is also possible in EELS, but was not used in this work.

2.3 Multivariate Statistical Analysis

This section briefly introduces multivariate statistical analysis (MSA) which is used for data denoising and signal separation in this work. The following approaches are also often classified as "unsupervised machine learning" or "exploratory data analysis", because they seek patterns in a (large) dataset without being given any input labels by the user. The MSA algorithms are beneficial to extract information from multidimensional datasets, such as EDXS or EELS datacubes.

Dataset Denoising with Principal Component Analysis

Principal component analysis (PCA) [Pea01; Shl14; JC16] is probably the most well-known MSA method and can be used to remove noise (denoise) in a dataset by dimensionality reduction [Pot16] (Fig. 2.16a). In the following, the principle is briefly explained, similar to Keenan and Kotula [KK04]. Consider a two-dimensional feature space (for simplicity) as shown in Fig. 2.16a with N measurements (dots). From a geometrical point of view, the cloud of data points clearly shows a trend (or direction) when plotted in the basis of the two features. The PCA algorithm seeks a new set of basis vectors, which are linear combinations of the original feature basis vectors, in the following way:

1. Find a first direction which "explains" the highest amount of variance. This corresponds to a best-fit line through the data cloud. This is the first principal component (PC 1).
2. Find another principal component orthogonal to the first component and maximize the variance. This corresponds to the second principal component (PC 2).
3. This is repeated until the dimensionality of the principal components and the features are equal (2 in this example).

The original dataset can be expressed in the basis of the found PCs. An exact copy of the original dataset, including the noise, is retrieved if all found PCs are used in the process. However, often a few PCs already explain the majority of the variance/signal in a noisy dataset. In the example shown in Fig. 2.16a, the deviation of values along the direction of PC 2 might be just noise. The dataset can then be denoised by projecting it onto PC 1, thereby reducing the dimension by 1. Hence, the procedure is called *dimensionality reduction*.

This explanation is now transferred to a STEM-EELS dataset of shape (N_x, N_y, N_c) (Fig. 2.16b). Here, N_x and N_y are the measurement points (lateral beam positions) in a rectangular scan region and N_c is the number of energy channels that are read out at each position (typically $N_c = 2048$). The energy channels correspond to the measurement features in Fig. 2.16a, i.e. the plot would have 2048 feature axes.
Another way of thinking about MSA are matrices and linear algebra. The input dataset is described (or reshaped) as a two-dimensional matrix D with $N_\mathrm{m} = N_x \times N_y$ measurements (rows) and N_c features (columns). It is important to note that PCA does not consider any spatial relationships between the measurement points, i.e. if two measurement points were adjacent prior to reshaping the data into an input matrix D. Dimensionality reduction with PCA attempts to find an approximation of D which ideally preserves the signal by only keeping k principal components, with $k \ll N_c$:

$$D \approx TP^T \quad . \tag{2.50}$$

Here, T is called a $N_m \times k$ *score* matrix and P is called a $N_\mathrm{c} \times k$ *loading* matrix. The content of these two matrices is of particular interest for "blind source separation", which will be discussed

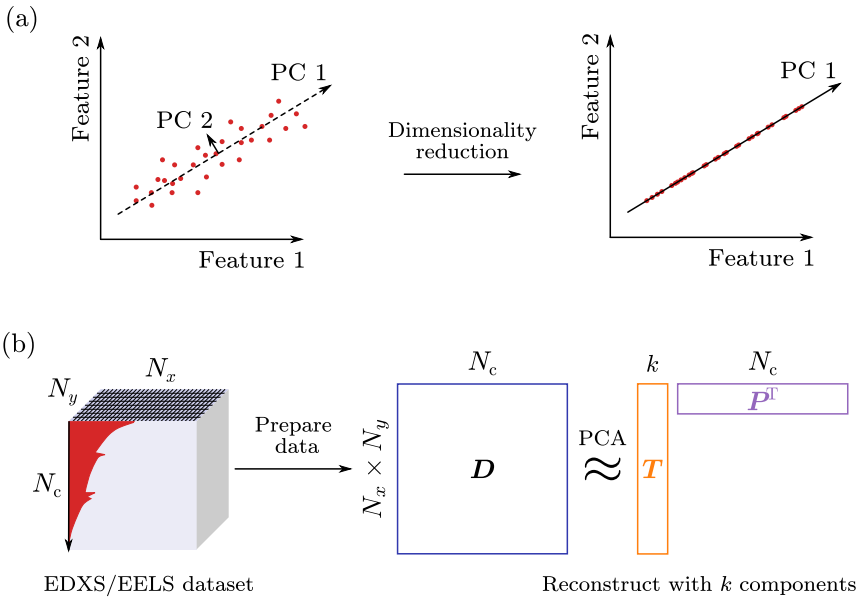

Figure 2.16: Principles of data denoising with PCA. (a) Scheme of dimensionality reduction of a two-dimensional dataset with one PC. (b) The PCA procedure (for STEM-EDXS/EELS datasets) described in matrix notation. The matrix D is decomposed and approximated by two smaller matrices T (scores) and P (loadings) after reconstruction with k PCs.

in the next section. For dimensionality reduction by PCA the original dataset is restored (with reduced noise) and the scores and loadings are not interpreted directly. Instead, the original dataset is reconstructed from k PCs. The so-called *scree plot* [Cat66] is commonly inspected to find an appropriate value for k. A scree plot is a plot of the ratio of explained variance of the dataset by each principal component sorted in descending order (see Fig. 2.17a and b). The difference in the ordinate scale (logarithmic vs. linear) is due to the use of different software packages for PCA: *HyperSpy* for Fig. 2.17a and *temDM MSA* for Fig. 2.17b. Ideally, a clear "elbow position" is observed, which separates principal components which describe signal (▲) or noise (●). The elbow position is visible for the EDXS example and marked by a vertical, dashed line. However, Fig. 2.17b shows an ambigous example for EELS, where selecting the cut-off point is not straightforward. In such a case, the scores and loadings can be inspected and used to determine a reasonable value for k. In doubt, a larger k should be used. More PCs just introduce some noise into the reconstructed dataset, whereas a too small k will throw away part of the actual signal and thereby seriously alter experimental results. In Fig. 2.17a and b, only the explained variances of the first 15 PCs (of in total 2048 PCs) are shown and the dimensionality was reduced from $N_c = 2048$ to (a) $k = 5$ (EDXS dataset) and (b) $k = 11$ (EELS dataset).

Examples of PCA denoising on noisy EDXS/EELS datasets are presented in Fig. 2.17c and d. The plots show typical raw and PCA-denoised signals from a single measurement position. The PCA-filtered signals are less noisy and resemble the original dataset. The denoised signals open up further data-processing steps. For example, peak-fitting of x-ray lines can be applied to separate the partially overlapping F Kα and Fe Lα lines (see inset in Fig. 2.17c), whereas the raw x-ray count signal would be too noisy for such a procedure. Likewise, the F K edge in Fig. 2.17d is visible in the denoised dataset and easily missed in the raw data. At this point, it is worth mentioning that the effect of PCA denoising on EDXS and EELS quantification is not fully understood and should be used carefully. Therefore, any quantification results shown in this work were derived from raw EDXS/EELS spectra instead.
A successful PCA denoise requires a clean-up of the data prior to PCA. This includes removal of outliers (e.g. x-ray peaks in EELS data when the CCD is hit by a cosmic x-ray during data collection), artificial signals (e.g. the zero-strobe EDXS peak at 0 keV as used by Bruker detectors,

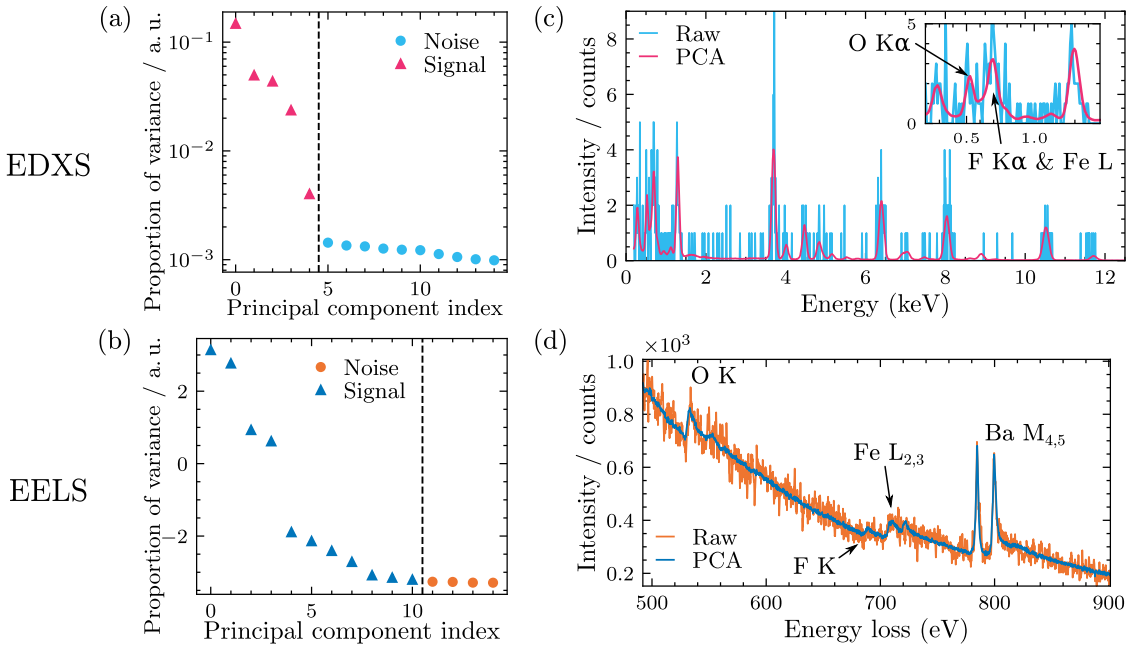

Figure 2.17: Application of principal component analysis to EDXS/EELS data set. The examples show EDXS (top row)/EELS (bottom row) data from a single spectrum-image position from $Ba(Fe_{0.92}Co_{0.08})_2As_2$ on CaF_2. PCA scree plots for (a) EDXS (using *HyperSpy*) and (b) EELS (using *temDM MSA*) show the relevant k components (▲) used for reconstruction. The corresponding denoised data sets in (c) and (d) show a clearly enhanced signal-to-noise ratio.

see Fig. 3.18 on page 83), and scaling the data to account for different types of noise. The latter is essential because PCA generally assumes Gaussian noise. Keenan and Kotula [KK04] proposed a weighting step of input data that follows Poisson noise, such as sparse EDXS spectra, prior to PCA. Their approach is directly implemented in *HyperSpy*. Finally, PCA is only successful for a high enough signal-to-noise ratio per measurement position, i.e. it cannot denoise a too noisy dataset [Pot16; Pot17]. Here, this aspect is only relevant for very sparse EDXS datasets (i.e. a few ten x-ray counts per position). In such a case, a binning operation (summation of adjacent spectra) or filtering with a Gaussian kernel can be useful to increase the signal-to-noise ratio per pixel (at the expense of spatial resolution).

Blind Source Separation

For denoising with PCA, the meaning of content of the score and loading matrices in Eq. (2.50) is irrelevant. This is because these matrices are only used to reconstruct the original dataset. However, the scores and loadings are directly related to any "trends" in a dataset, e.g. from varying chemical phases for EELS/EDXS analyses or crystalline phases for diffraction patterns. The aim of blind source separation (BSS) is to (i) extract physically interpretable scores and loadings and (ii) separate the underlying signals (also called *latent variables*) from a possible linear combination of such latent signals [DB12]. A popular BSS algorithm is *non-negative matrix factorization* (NMF) [LS99; MS20]. It is suited for non-negative datasets, typical in electron microscopy (i.e. counting data with only positive data entries). The NMF algorithm allows only non-negative values in the score and loading matrices, ideally resulting in physically interpretable score maps and loadings for a non-negative input matrix. In the case of EDXS/EELS, the loadings can be interpreted as spectra, whereas the corresponding score maps show the corresponding spatial distribution.

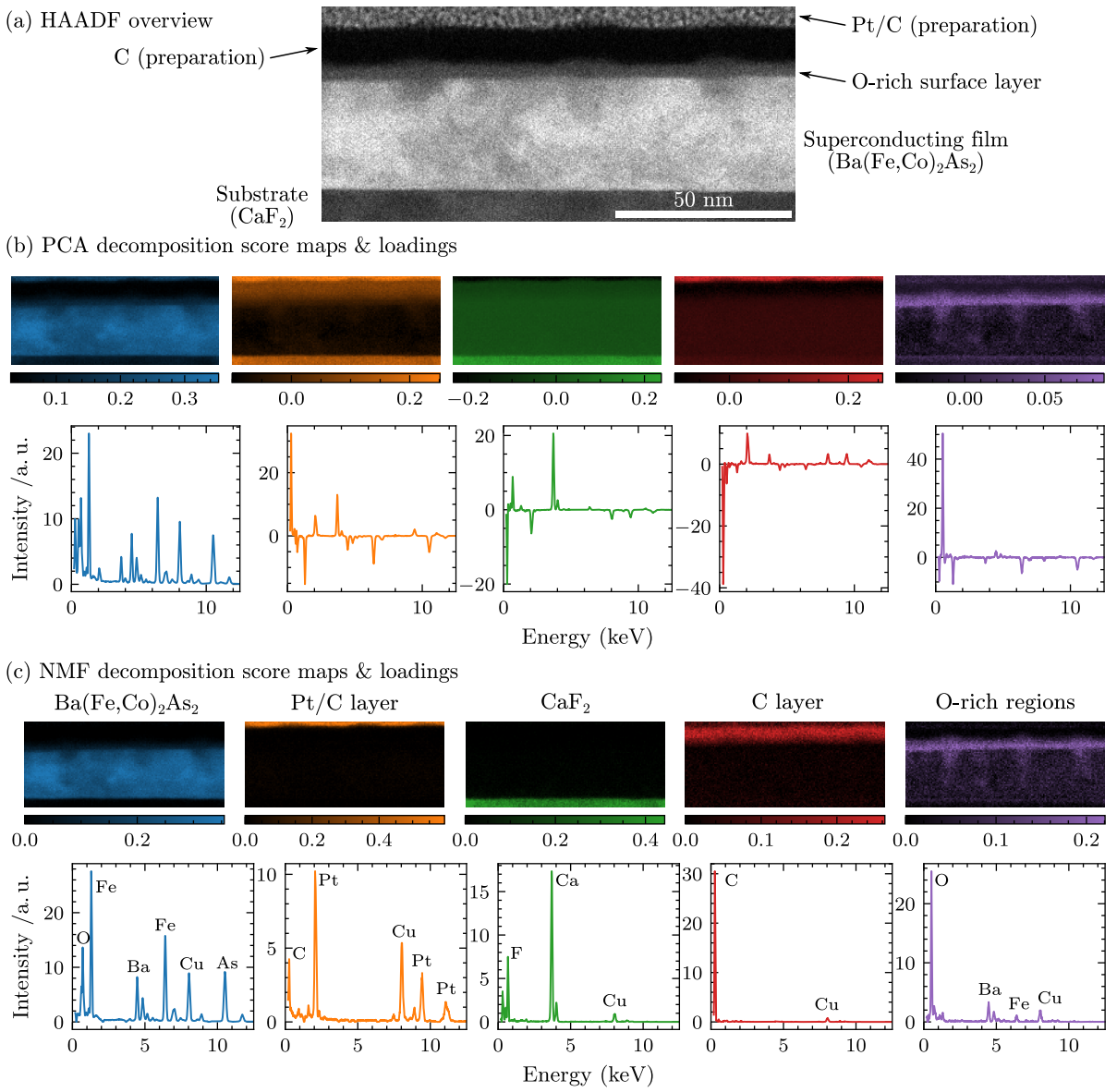

Figure 2.18: Comparison between PCA and NMF score maps and loadings. (a) HAADF-STEM overview image of $Ba(Fe_{0.92}Co_{0.08})_2As_2$ on CaF_2. (b) PCA loadings (top row) and score maps (bottom row). The first component corresponds to the mean spectrum with only positive values. However, all other loadings and maps contain negative entries, making physical interpretation impossible. (c) NMF loadings (top row) and score maps (bottom row). Note that all loadings and score maps are restricted to non-negative values. NMF enables chemical-phase separation. Some x-ray peaks are marked by their element abbreviations and the user-identified phases are denoted above the score maps.

Figure 2.18 shows PCA and NMF applied to an exemplary STEM-EDXS dataset of a Ba122 layer grown on a CaF_2 substrate (cf. HAADF-STEM image in Fig. 2.18a). Each score map shows the spatial distribution of the corresponding loading, and each pair is displayed with the same color. For PCA (Fig. 2.18b), the only constraint is the orthogonality of the PCs. Both the score maps and loadings show negative values. This makes an intuitive interpretation of PCA scores and loadings impossible for this dataset. The NMF score maps and loadings for the same dataset are shown for comparison in Fig. 2.18c. Due to the non-negativity constraint, the score maps and loadings now only contain non-negative values. The loadings after NMF show typical peaks similar to "normal" EDXS spectra and can therefore be *carefully* interpreted as such. However, the NMF loadings are purely mathematical. NMF separates the different chemical phases of the exemplary STEM-EDXS map. The layers consisting of different elements are visible in the NMF score maps, whereas complicated mixtures are observed in the PCA score maps. The interpretation of such NMF results is up to the user. NMF results are associated with chemical phases based on the spatial distribution in the score maps and the separated x-ray peaks in the loading spectra. The identified chemical phases are here denoted on top of the score maps.

Figure 2.19: Possible user bias introduced by choosing from several BSS methods. The comic ironically shows a potential problem, where the BSS algorithm may be adapted until the subjective user expectation from a data set is met. Image source: `https://xkcd.com/1838/` (last accessed: 18.10.2021).

Besides NMF, other algorithms with differing constraints can also be applied for BSS on electron microscopy datasets. Some examples are a *Varimax rotation* [Kai58; McA+20] of PCs in factor space to make them more interpretable, *independent component analysis* (ICA) [HO00; BN05; dlPeñ+11], *multivariate curve resolution* (MCR) [dJT06; KK06], *Bayesian linear unmixing* (BLU) [Dob+09], *vertex component analysis* (VCA) [PL21b], and probably even more. These methods are closely related to the field of chemometrics [Wol95] and are increasingly used in electron microscopy. Currently, there is no consensus on which technique is the "correct" one to choose for a given dataset. This "zoo" of BSS methods can lead to user bias, as some methods may extract components with the "expected" or "desired" features while others do not. An extreme situation is depicted in the cartoon in Fig. 2.19, where the BSS algorithms might be switched or the constraints adapted until the desired BSS is achieved. To prevent this bias, a careful cross-validation of experimental BSS results with other BSS algorithms is important. Here, NMF, Varimax and ICA were typically used on the same dataset for an initial exploration of the dataset. Still, mostly the (PCA-denoised) conventional elemental maps are shown for EELS and EDXS throughout this work instead of the BSS results. For these BSS methods,

openly available software (*HyperSpy*/*scikit-learn* [Ped+11] and *temDM MSA* [Pot16]) already exists for electron microscopy.

3. Experimental Methods

This chapter describes the methods used for the experiments, including thin-film deposition, sample preparation for SEM/FIB and TEM, (S)TEM imaging and spectroscopy, and various data-evaluation strategies. A few of the following analyses are performed with "Jupyter notebooks" [Klu+16], which are a mixture of executable (Python) code and comments. The latest versions of these notebooks are available in a data repository [Grü22], can be run with the provided exemplary datasets, and used (and improved) for other datasets in future studies. The electron microscopic analyses were performed at the Laboratory for Electron Microscopy (LEM) at the Karlsruhe Institute of Technology (KIT).

3.1 Thin-Film Deposition and Sample Preparation

Thin-Film Deposition. The investigated superconducting thin films were deposited by colleagues at the Institute for Technical Physics (ITEP) at KIT (Hermann-von-Helmholtz-Platz 1, 76344 Eggenstein-Leopoldshafen, Germany). Pulsed laser deposition and chemical solution deposition were used to fabricate the superconducting films.

PLD of IBS. The IBS films were fabricated by **Marco Langer**, **Sven Meyer**, and **Nico Beisig** (Bachelor student of Sven Meyer) using PLD. For exact details about the used experimental setup, the reader is referred to the thesis of Sven Meyer [Mey21, p 23]. $Ba(Fe_{0.92}Co_{0.08})_2As_2$ targets were prepared as described by Kurth et al. [Kur+13a]. Most important, the precursor materials are prepared in a glove box under an Ar atmosphere to prevent oxidation [Pak+20]. The deposition of IBS is done under ultra-high vacuum conditions (base pressure about 4×10^{-9} mbar [Lan+19a]) using a frequency-tripled Nd:YAG laser with $\lambda = 355\,\mathrm{nm}$ (Spectra-Physics Quanta-Ray INDI 40–10). The pulse frequency and energy can be adjusted to a maximum of $f_{\mathrm{PLD,max}} = 10\,\mathrm{Hz}$ and $E_{\mathrm{PLD,max}} = 100\,\mathrm{mJ}$ to modify the growth rate. Substrates were placed on a heated stage (T_{sub}) at a distance d_{PLD} from the target to facilitate epitaxial growth. Typical conditions for Ba122 growth on $CaF_2(0\,0\,1)$ $1\,\mathrm{cm}^2$ substrates (bought from CrysTec GmbH) were $T_{\mathrm{sub}} = 700\,^{\circ}\mathrm{C}$, $f_{\mathrm{PLD}} = 10\,\mathrm{Hz}$, $d_{\mathrm{PLD}} = 4\,\mathrm{cm}$ to $5\,\mathrm{cm}$, and $E_{\mathrm{PLD}} = 12\,\mathrm{mJ}$ to $48\,\mathrm{mJ}$. The substrates $LaAlO_3(0\,0\,1)$ and $MgO(0\,0\,1)$ were also tested for Ba122 growth besides $CaF_2(0\,0\,1)$. Typical Ba122 film thicknesses were 20 nm to 80 nm. **Sven Meyer** and **Nico Beisig** worked on multi-target PLD to introduce $BaZrO_3$ (bought from Kurt J. Lesker Company), $BaHfO_3$, or InAs (bought from Alineason Materials Technology GmbH) nanoparticles into the Ba122 matrix. For $BaHfO_3$, the "targets were prepared from $BaCO_3$ and HfO_2 powder. The powders are mixed, pressed and sintered up to 1150 °C. The result is ground and pressed again in an isostatic press and sintered

again up to 950 °C" [Mey21, p 24]. A carousel-type PLD stage enables intermittent switching of PLD targets during deposition.

PLD of GdBCO. Ruslan Popov fabricated pristine $GdBa_2Cu_3O_{7-\delta}$ films on MgO(0 0 1) substrates (T_{sub} = 800 °C) using the a similar PLD setup described in the previous paragraph [Pop+20]. Pristine $GdBa_2Cu_3O_{7-\delta}$ targets were used. The laser was set to a frequency of f = 10 Hz and a 2 mm spot with a laser energy density 2.5 J/cm^2. An O_2 partial pressure of p_{O_2} = 0.4 bar in the PLD chamber was applied. A film thickness of 250 nm to 270 nm resulted from 6000 laser pulses for each GdBCO sample. All samples were cooled down in p_{O_2} = 0.4 bar to room temperature at a rate of 15 °C/min.
Ex-situ oxygenation (or annealing) of the GdBCO films was performed afterward in a tubular furnace. O_2 and inert Ar atmospheres during heating can be produced with gas supplies. The heating rate was set to 1200 °C h^{-1} with an Ar flow of 2000 ml/min. Depending on the sample, 2000 ml/min Ar or 0.4 bar O_2 were used during cool-down to the annealing temperature T_{ann} = 450 °C. Oxygenation at this temperature was done at a pressure of p_{O_2} = 1 bar (2000 ml/min). This flow was kept during cool-down to room temperature.

CSD of REBCO. Manuela Erbe and **Pablo Cayado** grew $REBa_2Cu_3O_{7-\delta}$ films with different compositions on $SrTiO_3$(0 0 1) and $LaAlO_3$(0 0 1) substrates with CSD. The used procedure is described in detail by Erbe et al. [Erb+14]. The precursor salts (acetates, bought from Alfa Aesar) for the REs, Ba, and Cu are mixed in a stoichiometric ratio 1:2:3 in a mixture of deionized water and trifluoroacetic acid (bought from Alfa Aesar) [Cay+ed]. A precursor solution of Hf(IV) 2,4-pentanedionate ($C_{20}H_{32}HfO_8$, 97 % purity, bought from Alfa Aesar) with an equal amount of Ba was added to the REBCO solution to generate $BaHfO_3$ nanoparticles (12 mol % relative to RE) in the REBCO matrix for flux pinning [Erb+15]. The mixture is spin-coated (6000 rotations per minute, 30 s) onto 10 mm × 10 mm substrates. The previous steps are performed in a glove box (Ar atmosphere). A tubular furnace is used for pyrolysis, crystallization, and oxygenation using the temperature profiles by Erbe et al. [Erb+14]. The optimal crystallization and oxygenation temperatures depend on the RE or the mixture of REs and were optimized in each case to form a high-quality REBCO film [Erb+20]. In general, the processing windows are widest when the RE-ion size is close to that of Y^{3+}. The optimal processing windows become narrow for larger and smaller RE than Y^{3+}. Oxygen annealing was carried out after the crystallization step at 450 °C, 1 atm O pressure, for 120 min.

Sample Coating for SEM and FIB Sample Preparation

Preparation for SEM and FIB. The as-received superconducting thin films on different substrates are mostly grown on 1 cm^2 square-shaped substrates. The samples were fixed to conventional Al SEM-stub-holders with Ag glue (PLANO GmbH articles G302 and R1272) or conductive glue pads (PLANO GmbH article G3349C). Then, a small piece of household Al foil was cleaned with isopropyl alcohol, carefully laid on top of the film (to not damage the surface) and fixed to the SEM stub with scotch tape. The Al foil acts as a cover for the superconducting film during the evaporation of protective layers. Small parts of the Al foil cover were then removed by removing small parts of the Al foil with sharp tweezers near the foil edge so that only a fraction of the film is exposed. The method with the Al-foil cover was only used if the sample was used again for electrical measurements after SEM/TEM investigations. The (partially exposed) sample surface (i.e. thin film) was then covered with a layer of C (and sometimes sputtered Pt) to ensure conductivity for SEM investigations and TEM-sample preparation by FIB milling. A Leica ACE600 sputter coater was used for depositing C by adaptive carbon-thread

evaporation in vacuum (base pressure roughly 2×10^{-5} mbar or lower), where a C thread is heated rapidly by a high-current pulse. This method gives reasonable control of the thickness as each pulse generally yields ≈ 1 nm of C for the used experimental parameters: thread-sample distance of 50 mm, stage tilt $-20°$ (towards C source, thereby aligning the sample surface perpendicular to the C source), no rotation, and using a twisted C thread ("double-thread"). Thin-film analysis requires a careful evaluation of the required coating material and thickness. Even an EBID of a Pt-protection layer at an electron energy of typically 2 keV can already cause damage if the thin-film material is sensitive to electron-beam irradiation. Therefore different coating thicknesses were tested:

(1) 10 nm to 15 nm C: This thin C layer ensures electrical conductivity. It is the fastest method and is commonly used for SEM analysis.
Drawbacks: It does not protect the surface from electron-beam bombardment during high-electron-dose applications like EBID. As visible in Fig. 3.1a, most electrons at 2 keV can penetrate a 10 nm thin C coating (red) and reach the underlying film (blue, here $BaFe_2As_2$).

(2) 30 nm to 40 nm C: The larger C thickness than (1) gives better surface protection. In principle, the resulting $35 \times 35\,\text{nm}^2$ area of amorphous C of a cross-section sample can be used for alignment of an (image-side) C_s-corrector if no other amorphous sample regions are present. However, this is only applicable for very thin TEM samples < 30 nm because the amorphous ROI for corrector tuning should be as thin a possible (e.g. 10 nm thin C foils).
Drawbacks: A complete evaporation of all (four) C threads yields typically around 30 nm to 40 nm of C. Larger C thicknesses can be obtained by reloading the C threads. This method requires one (or more) fully loaded C threads. A few electrons still reach the underlying thin film for a coating thickness of 35 nm, as shown in Fig. 3.1b, although most energy is deposited in the C layer.

(3) Sputtered Pt: A 10 nm to 20 nm thick Pt layer ensures good conductivity and prevents most electrons from reaching the the sample surface in typical EBID-SEM beam conditions (e.g. 2 keV, Fig. 3.1c) and, therefore, gives good protection of the surface.
Drawbacks: The Pt forms an uneven, polycrystalline film which could worsen the milling behavior during low-energy FIB polishing. The Pt layer severely affects or makes low-energy EDXS measurements impossible due to strong scattering of the incident beam (reduced spatial resolution) and strong absorption of low-energy characteristic x-rays emitted from the sample.

In the end, most samples were coated with method (1) as no irradiation-induced damage could be observed for the Ba122 (cf. Fig. 4.12 on page 108) and REBCO films after EBID Pt-deposition at 2 keV. Furthermore, mostly STEM was used for characterization, which does not require an extended amorphous area for beam/corrector alignment.

SEM and SEM-EDXS

A FEI Strata 400S and a TFS Helios G4 FX were used for SEM imaging of the surface morphology. Primary electron energies between 1 keV to 5 keV were typically used for SEM imaging. The SE signal was detected either with the ETD, ICE, or in-lens (TLD) detector. BSE-SEM images were taken with a negative bias on the TLD detector or a dedicated solid-state detector in the Helios (CBS detector). The most inner segment (A) was used for the CBS detector to maximize

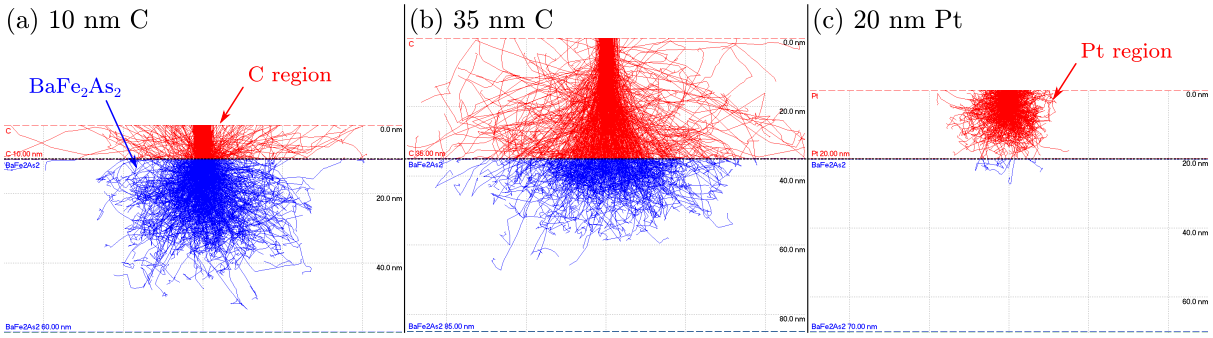

Figure 3.1: Monte Carlo simulations of electron-beam penetration depth for different sample coatings. The electron energy is set to 2 keV as generally used for EBID of a Pt/C protection layer. As an example, $BaFe_2As_2$ ($\rho = 6.5\,g/cm^3$) was used as film (blue) with different coating materials and thicknesses (red, C with $\rho = 2\,g/cm^3$ and Pt with $\rho = 21.45\,g/cm^3$). Less electrons reach the film for thicker coatings ((a)→(b)) and/or denser material ((a,b)→(c)).

the compositional BSE signal. Some noisy SEM images were filtered for display in this work using the *DenoisEM* [Roe+20] plugin for *Fiji* (e.g. a non-local means filter).
Chemical surface analyses by SEM-EDXS were done with a Bruker X-Flash 5010 and 6|60 series SDD EDXS-detector in the FEI Strata 400S and TFS Helios G4 FX microscopes, respectively. Both detectors have a MOXTEK AP 3.3 polymer window [Rob03]. Typical electron energies for SEM-EDXS ranged from 15 keV (conventional SEM-EDXS) to 2 keV (low-energy SEM-EDXS). The experimental parameters were tested with Monte Carlo simulations using *DTSA-II* [Rit09] also considering possible protection layers. The used beam currents ranged from 0.8 nA to 47 nA (nominal values), depending on the desired spatial resolution. For low-energy SEM-EDXS, a compromise between beam current and spatial resolution has to be found as the beam quality/resolution degrades stronger at higher currents when operating at lower beam energies (e.g. 2 keV). For example, spatial mapping of Fe precipitates with a size of ~ 50 nm on the Ba122 surface was done at 2 keV and a nominal current of 6.4 nA (Fig. 4.9 on page 105).

The TLD signal was typically used for sample-drift correction controlled by the Bruker *Esprit* 2.1 software. The SEM-EDXS spectrum images were saved as "Bruker container files" (bcf) and processed in the same way as STEM-EDXS datasets (see Page 81). In particular, NMF can be applied in SEM-EDXS to separate the chemical signals due to mixing because of the pronounced interaction volume in SEM-EDXS [JJK17].

TEM Sample Preparation with FIB

Cross-section sample preparation. Electron-transparent cross-section and plan-view samples for TEM were prepared with FIB/SEM systems (FEI Strata 400S/TFS Helios G4 FX). In this work, FIB preparation had some advantages compared to conventional TEM sample preparation (which involves cutting, grinding, dimpling, and Ar^+-ion milling):

- Sample regions for analysis can be targeted directly with a precision as good as 100 nm or less. This was useful for the preparation of TEM samples from films that were already processed for superconducting measurements by optical lithography and etching, which only leaves roughly 30 µm wide superconducting stripes (Fig. 3.2a and b).
- FIB preparation only requires a minimal amount of sample material. This was useful to extract TEM samples of superconducting films, which were not analyzed yet regarding their superconducting properties (Fig. 3.2c). Small, coated regions near the edge of a 1 cm^2

substrate are sufficient for FIB preparation, even for multiple TEM samples. In addition, multiple samples can be extracted to adapt to the milling behavior of new materials.

- FIB preparation can be combined with STEM-in-SEM to analyze films without exposure to air.

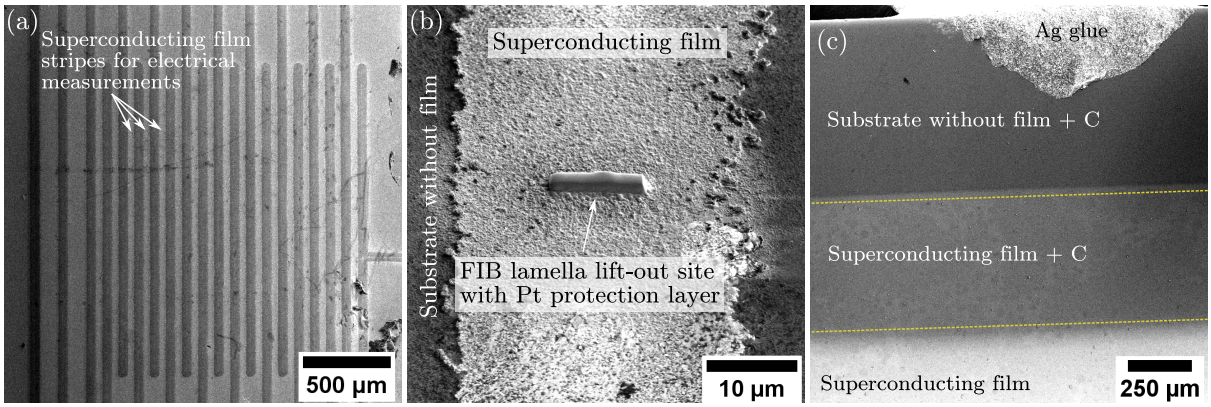

Figure 3.2: Advantages of site-specific FIB preparation. (a) Top-view SE-SEM image of a superconducting REBCO film sample that was prepared before by optical lithography for electrical measurements. The superconducting bands (bright) are approximately 30 µm wide. (b) Higher-magnification SE-SEM image of a lift-out site indicated by the EBID/IBID-deposited Pt stripe in the center. (c) Top-view SE-SEM image of a sample with multiple contacts for electrical measurements (not shown). A single contact near the substrate edge was partially covered with C (dark areas). This enables electrical measurements even after (multiple) TEM lamella lift-outs as most of the film is still in an as-deposited condition. The area in-between the dashed lines is suited for *in-situ* lift-outs.

Cross-section samples were prepared by the conventional *in-situ* lift-out technique [LC04]. The typical steps of this procedure are shown in Fig. 3.3 and briefly explained in the following:

1. Location of a ROI and setting of eucentric height.

2. Two-step deposition of a Pt/C-protection layer (Fig. 3.3a).
   First, EBID of a Pt/C stripe at 0° stage tilt (sample surface ⊥ electron beam) for about 3 min. Typical SEM conditions: 2 keV beam energy, 1 nA to 3 nA beam current, 1.3 µm by 10 µm to 20 µm ROI size. This creates a > 100 nm thin layer. This initial layer protects the sample from the 30 keV Ga^+ ions from the IBID of Pt.
   Second, IBID of Pt/C on top of the EBID stripe at 52° stage tilt (sample surface ⊥ ion beam). Typical FIB conditions: 30 keV beam energy, ~ 0.5 nA beam current, 1.5 µm × 20 µm, 1.5 µm by 10 µm to 20 µm ROI size, about 3 min deposition duration. The protective layer's final thickness/height should be about 1.5 µm.

3. Milling of trenches around the protection layer (Fig. 3.3b).
   Typical FIB conditions: 30 keV beam energy, 20 nA to 47 nA beam current, "Regular cross-section" pattern with "Multipass" set to 4. Stage tilted slightly $(52 \pm 3)°$ to create more parallel cross-section sides. Patterns were placed about 1 µm away from the Pt stripe to avoid accidental removal of the protection layer.
   After rough milling, a further thinning and cleaning of the cross-section sides is done at a lower current of (6.5 nA to 9 nA), "Cleaning cross-section" (CCS) pattern, and stage tilts $(52 \pm 3)°$. The final lamella thickness should be around 1 µm.

4. Partially cut the bottom of TEM lamella to free it from the bulk sample (termed J- or U-cut, Fig. 3.3c,d).

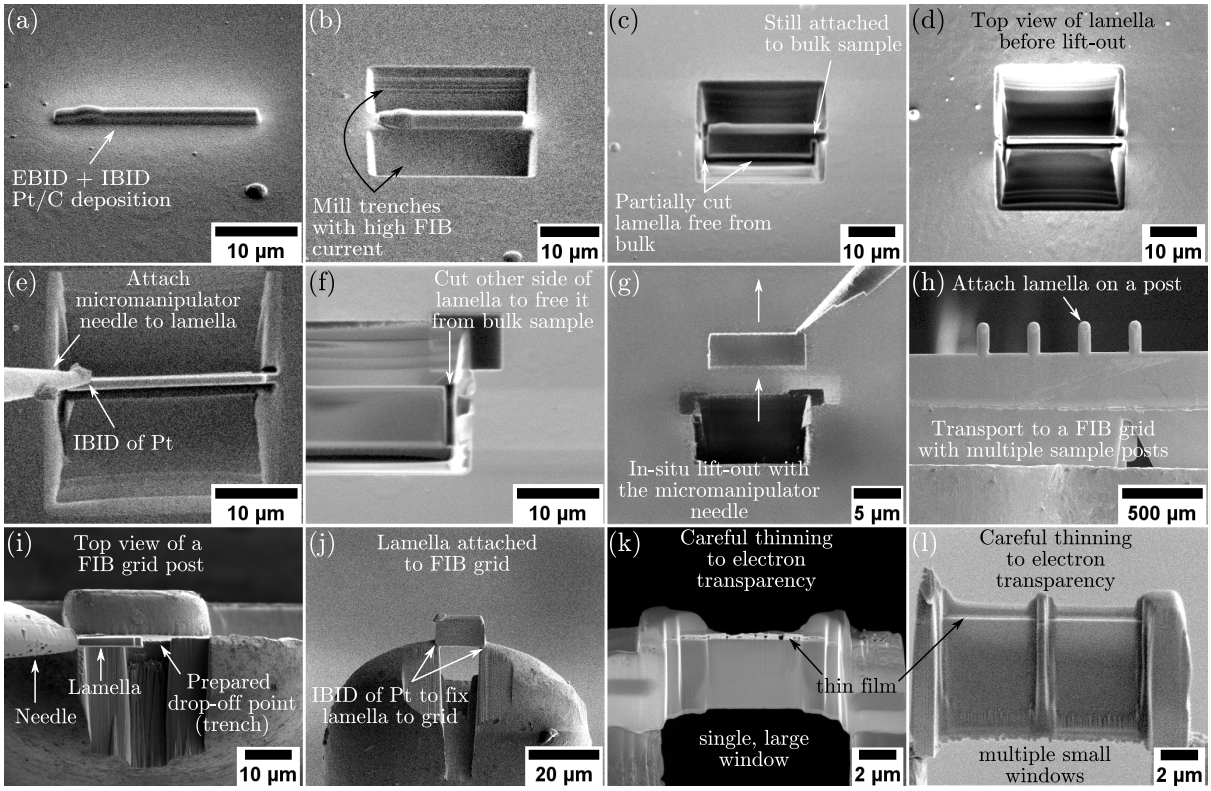

Figure 3.3: Basic steps of TEM cross-section sample preparation with a FIB/SEM. The images were taken from different sample preparations and the lamella dimensions can therefore vary between the images. Images were noise-filtered and contrast-adjusted for better visibility.

Typical FIB conditions: 30 keV beam energy, 2.7 nA to 9 nA beam current, stage tilt 0° (Strata) or −10° (Helios), overlapping "Rectangle" patterns with parallel milling enabled to avoid redeposition. Leave small bridge on the opposite side of the micromanipulator-attachment point.

5. Align and attach the micromanipulator needle (Fig. 3.3e). Typical FIB conditions: 30 keV beam energy, ∼ 10 pA beam current, stage tilt 0°, roughly $0.5\,\mu m^2 \times 0.5\,\mu m^2$ "Rectangle" pattern for welding the micromanipulator needle to the lamella (about 30 s deposition duration). A small FIB current (10 pA) is used to navigate the micromanipulator needle (in conjunction with the SEM top-view) with minimal FIB exposure to the TEM lamella.

6. Remove bridge to cut lamella free from bulk (Fig. 3.3f).
Typical FIB conditions: 30 keV beam energy, 2.7 nA to 9 nA beam current, stage tilt 0°, "Rectangle" pattern.

7. Lift-out of lamella (Fig. 3.3g), retracting of the needle with attached TEM lamella and GIS, stage movement to a desired drop-off point on FIB grid (Fig. 3.3h).

8. Optional: Preparation of an attachment point on the grid as shown in Fig. 3.4.
The goal is to attach the lamella on top of the grid post to fix *both* ends to the grid (as opposed to conventional mounting on the grid-post side, where the lamella is only attached on *one* end). This reduces the probability of sample bending for very thin (≤ 50 nm) regions.
Typical FIB parameters: 30 keV beam energy, 20 nA to 65 nA beam current, stage tilt 0°.
First, the rounded top of a grid post is flattened with a "Rectangle" pattern as shown in

Fig. 3.4a. Then, a 2 µm to 3 µm smaller trench than the lamella width is cut (Fig. 3.4b). The trench removes the grid material below the lamella and prevents a possible redeposition of grid material during the final thinning steps. The lamella is then attached with IBID Pt deposition on the edges of the trench (Fig. 3.4c).

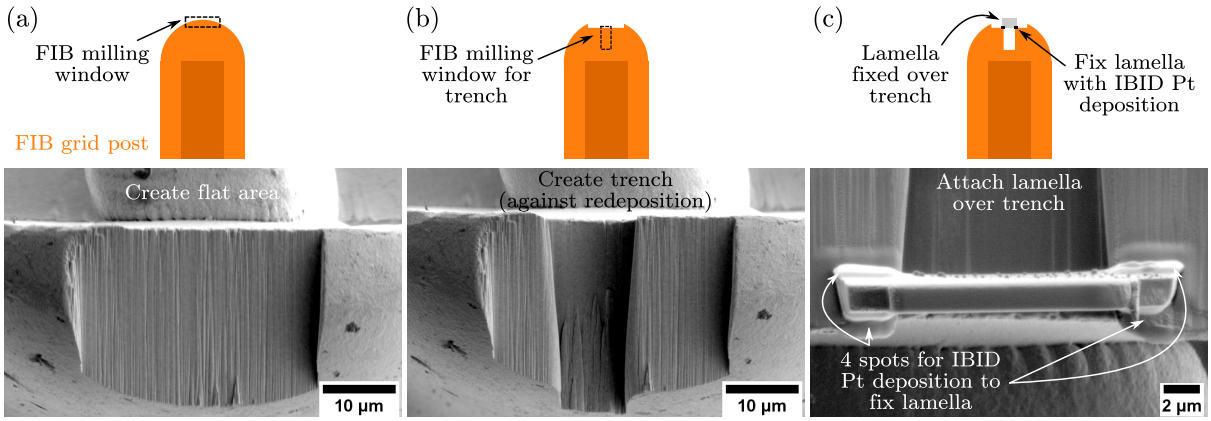

Figure 3.4: Attachment of TEM lamellas on top of grid posts. The top row shows schematics from the point-of-view of the FIB at 0° stage tilt with the milling patterns (dashed rectangles). The bottom row shows top-view SE-SEM images after the finished milling steps. (a) A flat area is milled at the top of a rounded grid post. (b) A trench with a slightly smaller width compared to the lamella is milled. This is done to minimize redeposition from the grid during lamella thinning. (c) The lamella is attached over the trench. Four patches of Pt depositions were used to fix the lamella to the grid.

9. Align and attach lamella on drop-off point (Fig. 3.3i).
   Typical FIB conditions: 30 keV beam energy, ∼ 10 pA beam current for navigation, stage tilt 0°, roughly 100 pA beam current for a $2\,\mu m^2 \times 2\,\mu m^2$ "Rectangle" pattern for welding lamella to Cu grid (about 30 s deposition duration). After welding the lamella to the grid, the needle is cut free (about 0.75 nA beam current, small "Rectangle" pattern). Needle and GIS can be retracted and the lamella is fixed to the grid (Fig. 3.3j).

10. Optional: Compucentric rotation of the stage by 180° and additional Pt welding of the lamella on the backside for better connection to the grid. This reduces the chance of losing a lamella during transport or grid handling with tweezers. An example is shown in Fig. 3.4c, where the two upper Pt pads were deposited after a stage rotation of 180°.

11. Optional: Storage of non-electron-transparent TEM samples.
    At this point, the TEM samples are attached to the grid but are still about 1 µm thick (Fig. 3.3j, Fig. 3.4c). TEM samples were mainly stored in this state and only thinned to electron transparency directly before a TEM session. This way, contamination and exposure to ambient air of an electron-transparent TEM sample is minimized.

12. Thinning of sample regions to electron transparency (examples are shown in Fig. 3.3k,l).
    The final thinning steps are a delicate process, which requires careful adjustments of beam current, beam voltage, and stage tilts. Details on the used procedures are described in the following.

In general, the aim of the final thinning steps is (i) to produce a homogeneously flat, thin region with a final TEM sample thickness below 100 nm and (ii) with minimal thickness of amorphous surface layers induced by the Ga^+ ions. The latter is achieved by (gradually) reducing the Ga^+-ion energy from 30 keV to 2 keV in the final step (see Fig. 2.10 on page 30). However, the

FIB quality worsens (larger beam diameter) at lower beam energies and control of the final shape of the TEM sample depends on the sample material, beam current, ion energy, stage tilts, pattern placements, and even possible unevenness of the protection layer. Often these parameters have to be adjusted during FIB preparation by the operator and it is not possible to give a general recipe for the final thinning steps. Still, some of the methods are explained in the following.
Two strategies for final thinning were tested in this work, termed *fast* and *slow* thinning:

1. **Fast thinning**. The FIB energy is kept at 30 keV for most of the steps. The sample is gradually thinned (normally in three to four steps) with decreasing beam currents (1000 pA to 100 pA) and stage tilts (1.5° to 0.8°). The steps at 30 keV are typically stopped when the protective Pt layer starts to vanish, occurring at sample thicknesses of around 100 nm to 150 nm. Final cleaning is then performed at lower energies (typically 5 keV followed by 2 keV) to further thin the sample to the desired final thickness and remove most of the damaged, amorphous surface layers from the steps at 30 keV. This method is commonly used in FIB preparation and relatively fast as the FIB energy is not changed often. However, the steps at 30 keV can, in principle, already introduce damage in the sample depending on the sample stability against Ga^+ ions. In addition, sample bending was more often observed for 30 keV, especially if large, homogeneous sample regions of constant thickness are desired.

2. **Slow thinning**. This method was introduced by Schaffer et al. [SSR12]. Compared to the fast-thinning method, the FIB voltages are gradually decreased when the TEM sample is still relatively thick, e.g. switching to 16 keV for a 1 µm thin-film solar cell sample [SSR12]. The aim is to prevent any FIB-induced damage to the sample and minimize the possibility of sample bending for thin ($\leq$ 50 nm) TEM samples. The full range of available steps for FEI/TFS instruments can be used, namely 30 keV, 16 keV, 8 keV, 5 keV, 2 keV, 1 keV, and 0.5 keV. However, 2 keV was typically used in this work for the final step for the FEI Strata 400S. In addition, a wedge-like sample shape is created ("wedge pre-milling", Fig. 3.5a) during the first thinning step to (i) keep the Pt protection layer intact as long as possible and (ii) to get a more uniform final sample thickness during the final milling steps at low FIB energies to minimize redeposition (Fig. 3.5b).

The fast-thinning method mostly yielded good results for Ba122 on CaF_2. The latter has a comparably high milling rate due to the lower melting point ($T_{m,CaF_2} = 1418\,°C$) compared to the oxide substrates investigated in this work ($T_{m,STO} = 2050\,°C$, $T_{m,LAO} = 2080\,°C$, $T_{m,MgO} = 2825\,°C$), which makes it easier to keep the lamella sides parallel. The typical thinning parameters are given in Table 3.1.
The slow-thinning method was adapted from Schaffer et al. [SSR12] so that only one current step is used per beam energy (as opposed to multiple steps with decreasing currents) to speed up the preparation process (Table 3.2). It was mainly used for samples with oxide substrates and for plan-view samples. For the latter, low voltages are helpful to prepare large field of views (few $µm^2$) with relatively constant thickness and without much sample bending. Both used FIB/SEM instruments provided good beam quality for lower voltages than 30 keV.

Samples were typically thinned as much as possible for STEM investigations. The final TEM sample thickness by FIB milling is ultimately limited by the complete removal of the Pt/C-protection layer. The thickness was judged qualitatively by observing contrast changes in the simultaneously acquired SE-SEM image. When the electrons can penetrate the TEM sample,

Table 3.1: Experimental conditions for the fast-milling method for FIB sample preparation. Values for (nominal) beam currents and residual thicknesses are rough guidelines. "Tilt" means relative tilt away from neutral milling position, i.e. from 52° if no bending is introduced to the lamella during mounting.

Step	Energy (keV)	Pattern	Current (pA)	Tilt ±(°)	Residual Thickness (nm)	Comment
1	30	CCS	440–1200	1.5	500–700	Cut through till bottom (substrate side) of lamella.
2	30	CCS	260–440	1.2	300	Reduce milling depth to create a window with thicker lower side[1].
3	30	CCS	90	0.8	100–150	Pt protection layer should just start vanishing at final step.
4	5	Rect.	26–64	5	–	Mill one side till IBID Pt reduces to half of starting width. Clean other side till none or only small amount of IBID Pt left. Increase tilt if Pt gets removed too fast.
5	2	Rect.	14–22	7	–	Final polish on both sides. Check[2] (i) that EBID Pt layer is still intact during milling and (ii) for possible damage[3] in film.

[1]Thicker lower side can enhance stability.
[2]Use periodic SEM snapshots or "intermittent switching between patterning and imaging (iSPI)" mode.
[3]E. g., amorphous, damaged REBCO appears dark compared to undamaged REBCO in SE-SEM imaging.

Table 3.2: Experimental conditions for the adapted slow-milling method for FIB sample preparation. Values for (nominal) beam currents and residual thicknesses are rough guidelines. CCS patterns are always cut through whole lamella depth. "Tilt" means relative tilt away from neutral milling position, i.e. from 52° if no bending is introduced to the lamella during mounting. Exact tilt angles depend strongly on the beam quality and were often adjusted based on the actual thinning behavior.

Step	Energy (keV)	Pattern	Current (pA)	Tilt ±(°)	Residual Thickness (nm)	Comment
1	30	CCS	440–900	3–4	600–800	Cut through till bottom (substrate side) of lamella.
2	16	CCS	240	3–4	150-200	-
3	8	CCS	110	2.5–3	100–150	Pt protection layer should start vanishing at final step.
4	5	CCS or Rect.	26–64	5	–	Same as in Table 3.1.
5	2	Rect.	14–22	7	–	Same as in Table 3.1.

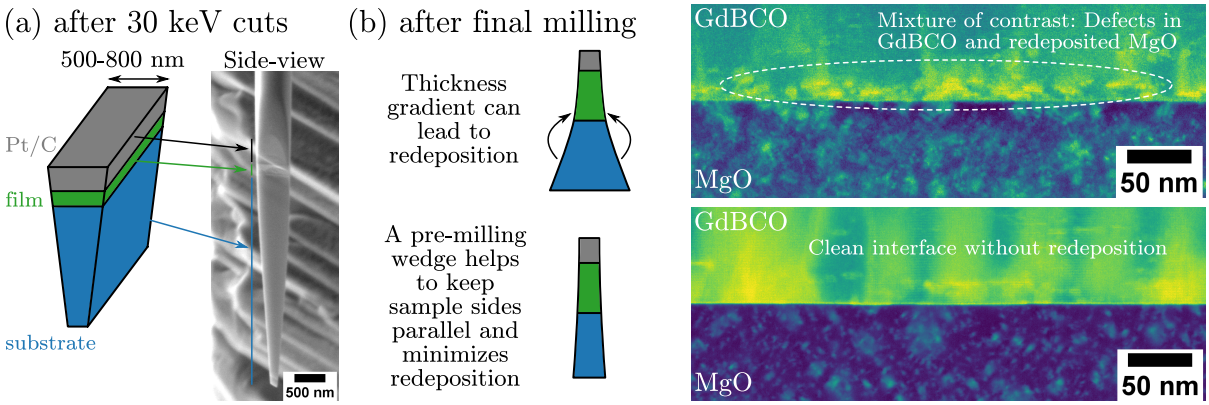

Figure 3.5: Wedge pre-milling for the slow-thinning FIB method. (a) Left: Scheme of the desired wedge shape of the targeted lamella region. The beam is slightly tilted into the sample at 30 keV to mill a wedge shape. Right: Exemplary side-view SE-SEM image of a lamella after wedge pre-milling. This is an example where the lamella was mounted to the side of a grid post. (b) Examples for possible redeposition effects during low-keV FIB milling. Exemplary LAADF-STEM images of GdBCO on MgO are shown. Top row: Possible redeposition artifacts can appear for fast increasing sample thickness after final milling. The redeposited material can prevent image interpretation, as seen on the right. Bottom row: Less redeposition appears for more parallel lamella sides.

additional SEs are generated on the backside and the TEM sample will appear brighter (ETD) or darker (TLD) depending on the selected SE detector. This was used in conjunction with Monte Carlo simulations (using *CASINO* version 2.5.1.0) to assess the lamella thickness during thinning for cross-section samples. The substrate contrast near the substrate-film interface was monitored for a given SEM beam energy (typically 2 keV to 5 keV) and compared with the size of simulated interaction volumes in bulk substrate samples at the same beam energy. Using the substrate as a reference has the benefit that the required properties for a Monte Carlo simulation (such as composition and material density) are well known compared to the film (with possible precipitates of unknown composition).

Plan-view sample preparation. Additional plan-view (i.e., viewing direction parallel to the [0 0 1]/growth direction) TEM samples were prepared for a few films by FIB milling (Fig. 3.6). The plan-view TEM-sample geometry is less common for FIB-based preparation compared to the cross-section geometry [JT14; Li+18; Mey+21], but is seeing increasing popularity due to advances in instrumentation (e.g. higher available FIB currents, more stable micromanipulators). The TFS Helios G4 FX instrument was used for this purpose because of the stable "Easylift" micromanipulator and the dedicated STEM holder with a high stage-tilt range. Some exemplary stage-tilt configurations for the latter are shown in (Fig. 3.6a). A special configuration not available on a conventional bulk stage is $\alpha = 142°$, where the FIB is perpendicular to the TEM grid.

The following steps for plan-view preparation were used:

1. Location of a region of interest (ROI) and setting of the eucentric height.

2. One-step deposition of a Pt/C protection layer (Fig. 3.6b).
   Compared to cross-section sample preparation, only EBID of a Pt/C pad was used. This makes it easier to see the transition between the protective Pt/C layer and the film (only one change in contrast). Using an additional IBID layer, two transitions are expected during thinning, i.e. EBID Pt → IBID Pt and IBID Pt → film, and in some cases this made it harder to decide if the film was already reached during thinning. The pad is

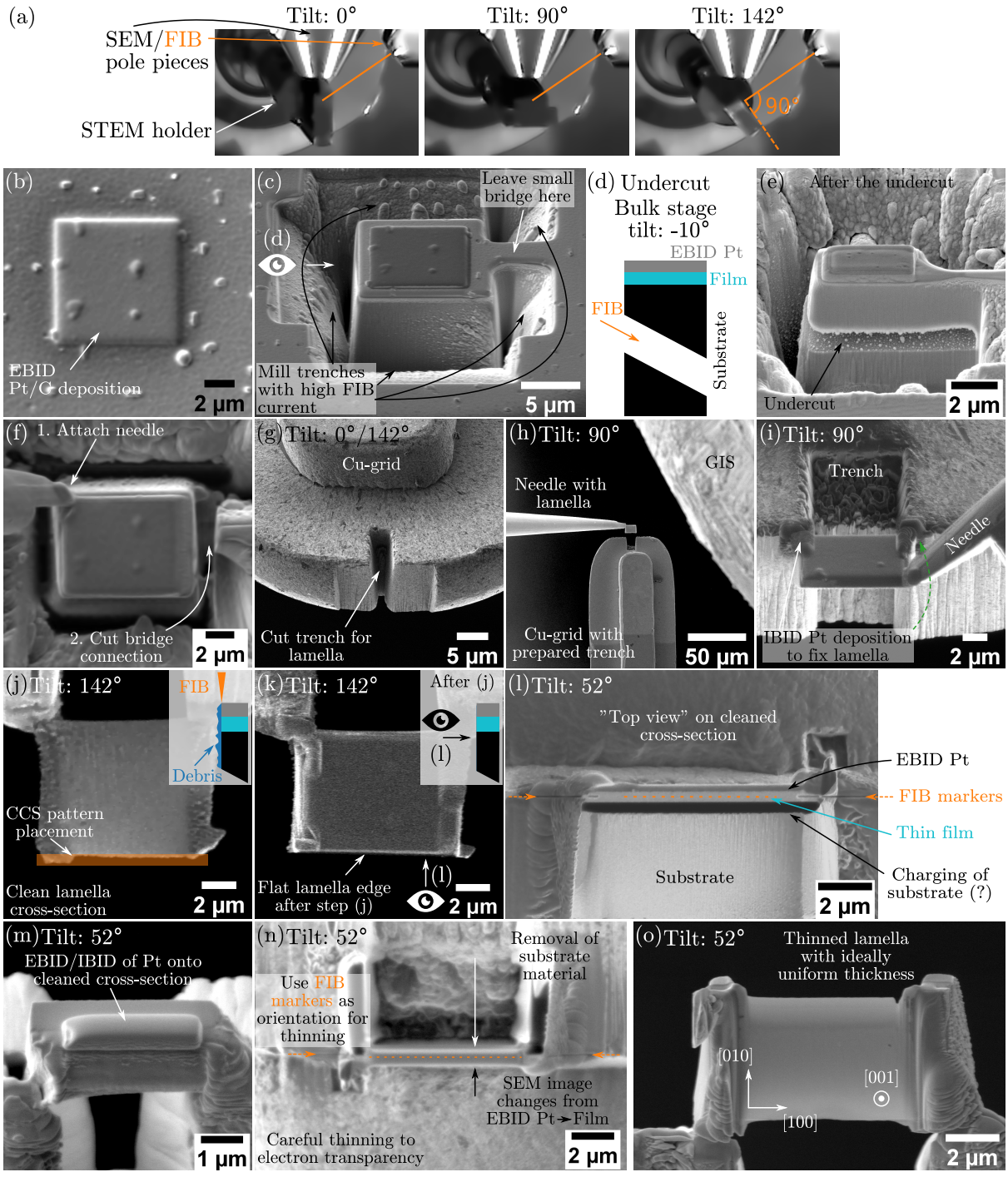

Figure 3.6: Plan-view TEM sample preparation steps with a TFS Helios G4 FX. The SE-SEM/FIB images were taken from different sample preparations and the lamella dimensions can therefore vary between the images. Images were noise-filtered and contrast-adjusted for better visibility. The indicated tilt values starting from (g) are a guidance for the used STEM-stage tilts during FIB milling. For the final thinning steps (n,o), deviations from these values should be made depending on the used FIB current/beam energy to keep the final sample thickness as uniform as possible.

deposited at 0° stage tilt (sample surface ⊥ electron beam) for about 4 min. Typical SEM conditions: 2 keV beam energy, about 6 nA beam current, 5 µm to 8 µm by 3 µm to 8 µm ROI size. This creates a roughly 200 nm thin EBID Pt/C layer (Fig. 3.6l).

3. Milling of trenches around the Pt/C protection pad (Fig. 3.6c).
   Narrow trenches are milled in sequence with regular cross-section patterns at high FIB currents (typically 20 nA). The sides can be cleaned with a CCS pattern (9 nA or 20 nA). A small bridge is kept on the side opposite to the manipulator needle.

4. An undercut is performed to partially release the ROI from the bulk sample (Fig. 3.6d and e).
   The eye/arrow in (c) depicts the viewing direction for the scheme in (d). The bulk stage is tilted to −10° (maximum for the Helios FIB/SEM), to cut as parallel as possible with respect to the film. Care must be taken that the bottom trench in (c) is cut deep enough to ensure a full release of the ROI as shown in (e). In addition, the top trench in (c) must be (vertically) wide enough to ensure that the FIB pattern can be placed a few µm below the film (see scheme in Fig. 3.6d). After this step, the ROI should only be connected to the bulk sample at the bridge.

5. Alignment and welding of the micromanipulator needle and release from the bulk sample (Fig. 3.6f).
   The needle should be welded to the top-left corner (with respect to the orientation shown in (c) and (e)), which is important in a later step when the sample is attached to the TEM grid (Fig. 3.6i). Fixation at the top-left corner creates a free line of sight of the FIB to the welding position on the grid (right welding spot marked by the green, dashed arrow in Fig. 3.6i). Another important aspect is that the needle should *not* touch the ROI during alignment because any pressure onto the (still-attached) ROI can cause sample bending. This impedes later thinning to electron transparency without losing the film during milling (since the milling is parallel to the film's *ab* plane). Instead, the needle should only be brought in the vicinity to the top-left corner (within 50 nm to 200 nm) and then welded to the sample.
   After fixation, the bridge connection to the bulk sample can be cut to release the ROI. Then the needle can be moved up and retracted.

6. The STEM holder with an empty TEM grid is inserted and the bulk stage retracted. The eucentric height of the drop-off point (a grid post) should be set up with stage movements.

7. Optional: Similar to the cross-section preparation, a drop-off point on a TEM-grid post can be prepared (Fig. 3.6g) while the sample is still safely attached to the retracted needle. Fixation on both sides reduces the chance of potential sample bending during thinning. This step can be done with α-tilt of 0° or 142°. However, the preparation also works by attaching the plan-view sample to the side of a grid post.

8. Alignment (Fig. 3.6h) and fixation (Fig. 3.6i) of the sample to the FIB grid.
   Care must be taken during alignment, as the FIB "view" is under an angle and the perspective must be considered. Careful needle movements at slow speeds should be employed to prevent a crash into the grid. The sample should not directly touch the grid to avoid any form of bending. When the sample is close to the grid (within 50 nm to 200 nm), IBID Pt deposition is used to fix the sample to it. By attaching the needle to the top-left corner (Fig. 3.6f) the FIB has clear line of sight to the right connection point (Fig. 3.6i, cf. dashed green arrow).

9. The connection to the needle can be cut and the needle is retracted.

10. Optional: A 180° α-tilt flip can be used to see the bottom side of the attached ROI and do additional IBID Pt depositions for a better fixation to the grid.

11. Cleaning of the cross-section (Fig. 3.6j) at $\alpha = 142°$.
    During milling/Pt deposition the cross-section is typically contaminated by debris. The latter is removed by FIB milling using a narrow CCS at $\approx 1\,\mathrm{nA}$ beam current, as shown schematically by the shaded region in Fig. 3.6j. After the cut, Fig. 3.6k, a view onto the clean cross-section is possible and the layers can be identified from the SEM/FIB image (Fig. 3.6l).

12. Locating the target region for thinning and generating FIB markers (Fig. 3.6l).
    The cleaned cross-section can be image first by SEM ($\alpha = 0°$) to locate the target (thin-film) region. In the shown case for a REBCO film, a clear difference in SE signal is visible between the sightly darker EBID Pt layer (top) and the film. In doubt, BSE imaging or even EDXS can be used at this stage to "find" the target region.
    When the target region is located, the FIB ($\alpha = 52°$) is used to mill lines at both ends of the sample aligned to the middle of the target region (dashed arrows in Fig. 3.6l). For this task, the smallest FIB current (1 pA, line pattern, few seconds milling duration) was used to maximize spatial resolution. These markers help during lamella thinning, as the location of the target region is always known with reasonable accuracy and not accidentally milled away.

13. Optional: EBID and IBID Pt patterns can be deposited (as for a conventional cross-section sample) onto the cleaned cross-section to protect the sample during the next thinning steps (Fig. 3.6m). Care should be taken not to cover the FIB markers from the previous step.

14. Final thinning to electron transparency (Fig. 3.6n and o).
    The following steps are the same as for thinning cross-section samples. Care should be taken to continuously observe the FIB markers during thinning to locate the target region. The following technique worked in the case of REBCO films:
    (i) Start at the EBID side (bottom side in n) and mill carefully at medium FIB current (below 1 nA, 16 keV, about 3° tilted away from 52°) while live-observing the SE signal with the SEM. A contrast change in the SE-SEM image indicates the transition between EBID Pt $\rightarrow$ thin film, meaning that the surface of the film is starting to be removed. The milling should be stopped when all of the EBID Pt layer is removed (i.e. a homogeneous contrast is observed with simultaneous SEM imaging). This "exposed" side should only be polished with low ion energies to remove FIB-induced amorphous surface layers.
    (ii) Stop at EBID (bottom) side and do milling from substrate (top) side. This should result in a situation similar to Fig. 3.6n. Now the "normal" milling steps for conventional cross-section samples can be used. However, the substrate side (top side in Fig. 3.6n) should be primarily milled until electron-transparency is reached since the sample surface is already exposed on the lower side. Usage of lower FIB energies and currents gives better control over the thinning while reducing the chance of sample bending (at the cost of longer milling duration), see also Table 3.2.

15. In the end, a uniform sample thickness of the target region is desired as shown in Fig. 3.6o. In this case, the central region is slightly thicker compared to the top and bottom sides as visible from the contrast changes in the image.

The final FIB-prepared TEM samples can be further polished with a low-energy (typically $\leq 500\,\text{eV}$) Ar^+ milling step [Wan+21]. This was done here in a Gatan "Precision Ion Polishing System" model II (PIPS-II) for a few selected samples. Still, most of the TEM samples were investigated directly after the final Ga^+-ion polishing step at 2 keV to minimize TEM-sample exposure to air.

3.2 High-resolution (S)TEM Imaging

STEM Imaging. HRSTEM imaging was carried out on an FEI Titan^3 80–300 at $E_0 = 300\,\text{keV}$ and an FEI Tecnai Osiris at $E_0 = 200\,\text{keV}$, both with $C_\text{s} = 1.2\,\text{mm}$ for the probe-forming lens. HRSTEM mainly was combined with the HAADF-STEM imaging mode to achieve directly interpretable Z-contrast. In addition, LAADF-STEM was used at low to medium magnifications to visualize crystalline defects, precipitates, and strain. Typical conditions for STEM imaging are listed in Table 3.3.
During the first months of training on the Titan, the C3 lens was switched off to ease STEM alignment, resulting in $\alpha \approx 8.2\,\text{mrad}$ (50 µm C2 aperture), which is smaller than $\alpha_{\text{opt},300} = 9\,\text{mrad}$. In addition, a smaller collection angle (33 mrad, camera length 185 mm) was partially used to increase the signal-to-noise ratio during STEM imaging of beam-sensitive Ba122 where the electron dose must be minimized. No appreciable difference in interpretability of atomic column positions was observed for $\beta = 33\,\text{mrad}$ and $\beta = 40\,\text{mrad}$, both fulfilling the rule-of-thumb criterion $\beta \geq 3\alpha$ for HAADF Z-contrast imaging [Mul09].
For the Osiris, a non-optimal $\alpha = 10.7\,\text{mrad}$ (70 µm C2 aperture) instead of $\alpha_{\text{opt},200} = 9.5\,\text{mrad}$ was normally used. Here, α is determined by the pre-aligned setting of the OL excitation for eucentric focus. In the experiments, the OL strength was not changed from this eucentric focus setting to ensure easier alignment and better reproducibility, even though adjusting the OL excitation and refocusing with the C2 lens can be used to tune α [WM05].

Table 3.3: Experimental conditions for STEM.

Microscope	Mode	Spot size	α	β	Comment
Titan	HAADF	9–10	9 mrad	40 mrad	Fischione ADF.
Titan	HAADF (MAADF)	9–10	8.2 mrad†	33 mrad	C3 lens off. Increased signal-to-noise ratio. Fischione ADF.
Titan	LAADF	6–8	9 mrad	11.5 mrad	Fischione ADF.
Osiris	HAADF	10–11	10.7 mrad†	53 mrad	Fischione ADF.
Titan	EELS	6–8	9 mrad	21 mrad	High-resolution setup. Gatan DF.
Titan	EELS	4–6	11.5 mrad	21 mrad	C3 off. High-current setup. Gatan DF.
Osiris	EDXS	3–8	10.7 mrad	53 mrad	For medium to high resolution and small ROIs.
Osiris	EDXS	2–4	15.3 mrad	≥ 53 mrad	For low to medium resolution and large ROIs and trace-element detection.

†Sub-optimal α. Determined by OL eucentric focus preset.

HRSTEM images were mainly recorded as single-frame acquisitions, i.e. long dwell times ($\geq$ 16 µs) per pixel and typical frame times of 15 s to 30 s (depending on sample drift and tolerable electron dose). However, single-frame acquisitions are prone to scanning distortions and sample drift [Jon+17]. Such distortions were analyzed for the FEI Titan^3 80–300 microscope (Fig. 3.7). HAADF-STEM imaging of a well-defined specimen such as $SrTiO_3$[1 0 0] (Fig. 3.7a) at different magnifications and quantitative analysis of the Sr-column positions (Fig. 3.7b) reveals the typical scan-direction-dependent scanning distortions (Fig. 3.7c, top).

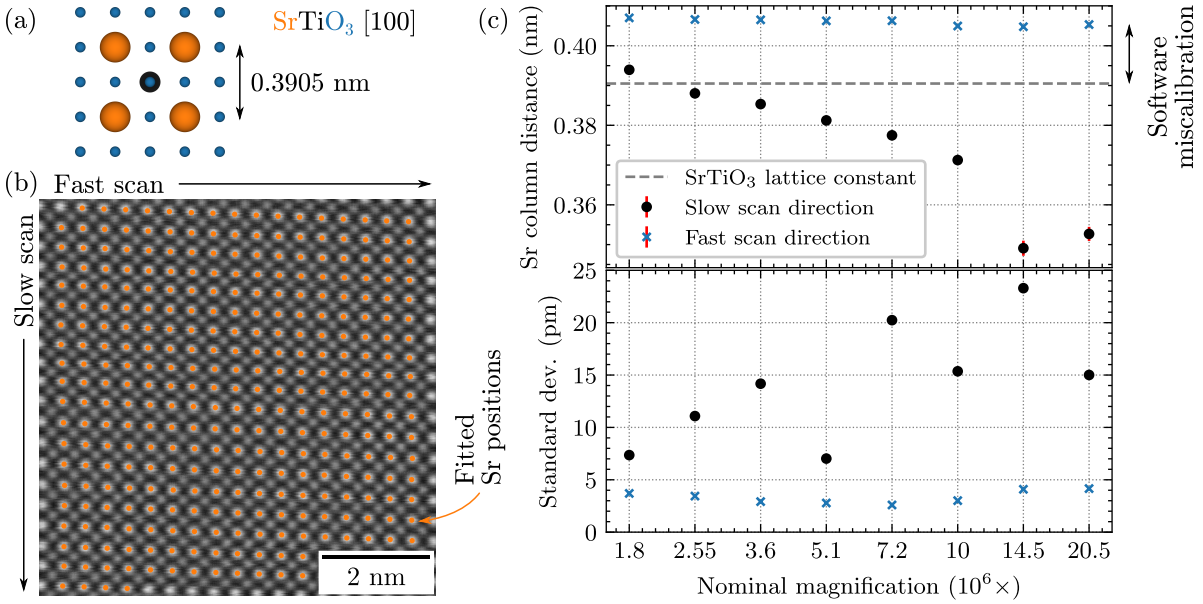

Figure 3.7: Analysis of STEM scanning distortions. (a) Scheme of STO in [1 0 0] zone-axis orientation. This sample and orientation were used to analyze the STEM scanning distortions. (b) Exemplary HAADF-STEM image acquired at a nominal magnification of 1×10^7 with fitted Sr atomic columns (highest Z-contrast) using *Atomap*. The Sr-plane distances determined from fast- (horizontal) versus slow-scan (vertical) directions are compared in (c). (c) Top: The determined Sr plane distances (which corresponds to the STO lattice constant) for different STEM magnifications show a larger spread for the slow-scan direction (•) compared to the fast-scan direction (×). The dashed line marks the bulk STO lattice constant of 0.3905 nm. The offset between the fast-scan values and the STO lattice constant is due to a faulty calibration of the TEM software and can be corrected. Bottom: A higher spread in Sr-plane-distance standard deviations is observed for the slow-scan direction, similar to the Sr-plane distances. The fast-scan direction is more suited for length calibrations and distance measurements in STEM images.

The slow-scan direction (•) shows significant variations in the measured Sr-column spacings compared to the expected value (lattice constant, dashed line) and between the different nominal STEM magnifications. This is probably due to an erroneous probe placement caused by the "flyback" at the end of each fast-scan line (horizontal). In contrast, the measured Sr-column spacings along the fast-scan direction (×) are similar for all magnifications, but are offset with respect to the expected value, which is due to a software miscalibration of the actual pixel size. The latter can be corrected, often even post-acquisition, if a reference region with a known lattice parameter is available in an image. The standard deviation of the two-dimensional Gaussian fits measure the precision in locating the atomic columns (Fig. 3.7c, bottom). The fast-scan direction shows higher precision ($<$ 5 pm) compared to the slow-scan direction (7 pm to 24 pm). From these observations, it can be concluded for single-frame acquisitions that (i) quantitative measurements of atom-column positions are more reliable along the fast-scan direction and (ii) re-calibration of pixel sizes of STEM images based on the FT should be done with lattice

reflections corresponding to the fast-scan direction.
Stage movements should be minimized to reduce distortions due to sample/stage drift. This can be achieved by using the beam-shift coils (trackball controller at the microscope) instead of stage movements to navigate to different sample regions at high magnification (Fig. 3.8). Often, 5 to 15 images were taken using the beam shift around a ROI before using the stage movements again. No noticeable degradation in image quality was observed for beam shifts up to around 500 nm to 1000 nm. It is essential to reset the beam shift prior to using stage movements.

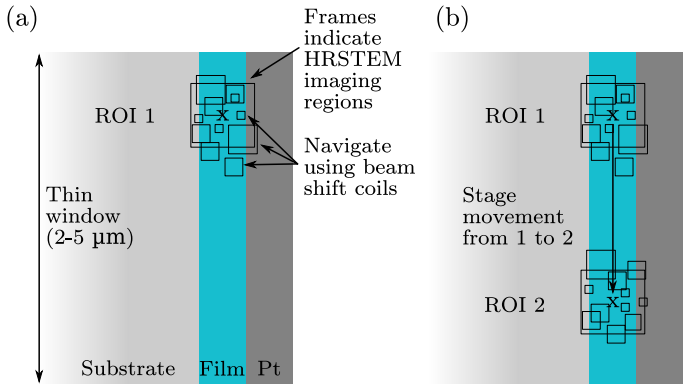

Figure 3.8: Minimizing stage-drift artefacts in S(T)EM. (a) Scheme showing a typical sample geometry (substrate, film, and Pt protection layer). After using stage movements to go to the first region of interest (ROI 1), multiple STEM images in its vicinity (up to $\approx 1\,\mu m$) are taken using the beam shift coils for navigation. (b) The stage shift is used for larger distances, i.e. to go to a distant ROI 2.

It should be noted that scanning distortions can be most effectively reduced by (non-)rigidly aligning multiple noisy images acquired with short dwell times [Ber+14; Jon+17; Fuj+20] or by taking and comparing multiple images with different scan directions [SL14; PL21a]. These techniques are necessary if both (fast and slow) scanning directions are to be analyzed quantitatively (e.g. for strain measurements) or if higher precision is desired (sub-pm precision is possible [Yan+14]). However, these techniques were only occasionally used in the present work because of the following reasons:

- Strain analysis was often not the priority.
- Sample quality can be more limiting than scanning distortions.
- The alignment of multiple, noisy HRSTEM images which contain strongly periodic images features (atomic columns) is often non-trivial. Even though (free) software solutions exist[1], software parameters have to be chosen/optimized carefully for each image series. The easy-to-apply *StackReg* [TRU98] plugin for *Fiji* was used in this work.
- Defects can form in beam-sensitive samples (e.g. Ba122) during multi-frame acquisitions, making the alignment of the frames impossible.

The fast-scan (horizontal) direction for single-frame acquisitions was aligned with the out-of-plane/growth direction of the film as indicated by the schemes in Fig. 3.8. This ensures the same conditions for each scan line at the substrate-film interface when the scan always starts inside the substrate and moves into the film area (or *vice versa*). The images were rotated by 90° for display in the rest of this work for more straightforward interpretation (substrate on bottom, film on top, c-direction vertical).

STEM sampling. The probe size d_0, Eq. (2.32) on page 27, determines the minimum required spatial sampling Δ (or scanning step size) for conventional STEM imaging according to Eq. (2.5) on page 20. With $k_{max} = 1/d_0$ follows $\Delta \leq d_0/2$ to avoid undersampling/aliasing artifacts.

[1] For example, *Match Series* [BL19], *Smart Align* [Jon+17], *StackReg* [TRU98] ....

However, the latter can also be used purposefully to detect defects or strain from the emerging Moiré fringes [SZ10; Pof+20; NOM18; Zha+21b]. For Moiré-fringe STEM imaging, Δ should be close to a crystalline spacing in the sample. This method was used to detect crystalline defects at lower magnification.

STEM-in-SEM imaging. STEM-in-SEM imaging was done on selected samples on the TFS Helios G4 FX. This technique was applied to combine sample preparation and high-resolution imaging without exposing a thin TEM sample to ambient air. This way, possible sample oxidation during TEM-sample transfer between preparation and (S)TEM imaging can be ruled out. The used instrument has a dedicated STEM holder (see also Fig. 3.17b on Page 82) and an insertable counter-pole piece for high-resolution BF phase-contrast imaging [Ngo+07]. In BF-STEM mode, one can ideally achieve a line resolution of around 0.3 nm, but this requires a thin, clean, and stable sample. High-resolution STEM-in-SEM imaging was possible directly after FIB preparation in the same instrument without exposing the sample to air. Still, even for freshly prepared FIB samples C-rich contamination patches were observed during and after high-resolution STEM imaging. These probably stem from residual gases in the microscope chamber. The "Drift-corrected frame integration" (DCFI) mode of the microscope software was used to compensate for sample drift. This mode averages multiple short frames (e.g. 16 to 32 with 0.5 s to 1 s frame time) by cross-correlation instead of taking a single, long exposure. The segmented STEM 4 detector was used for signal collection.

TEM Imaging. HRTEM imaging was occasionally used for phase contrast lattice-fringe imaging at (ideally) sub-Å resolution as the used FEI Titan^3 80–300 microscope is equipped with an image-side C_s-corrector. No objective aperture was used to maximize spatial resolution[2]. The corrector was tuned on an amorphous region on the sample if available. Else, corrector tuning was performed on a carbon-coated TEM grid (10 nm C thickness) prior to inserting the actual sample. The corrector mainly was tuned to $C_\mathrm{s} \approx -13\,\mu\mathrm{m}$, a typical setting [Len06; Spi+10; Yan+12; Gau+17] that maximizes phase contrast for a defocus of $\Delta f = 6\,\mathrm{nm}$, assuming an information limit of about 80 pm. The residual contrast delocalization under these conditions is about 50 pm [Len06]. However, typically experimental errors on $C_\mathrm{s}/\Delta f$ are in the range of $\pm 3\,\mu\mathrm{m}/\pm 5\,\mathrm{nm}$. For optimum HRTEM imaging, this necessitates the acquisition of multiple images under varying defocus (focal series), leading to a high total electron dose on the imaging area. Despite focal series, single-shot HRTEM images were taken at minimum contrast defocus. The latter was approximated to be around 2.5 nm using the formula $\Delta f_\mathrm{mc,NCSI} = +0.44\,(\lambda|C_\mathrm{s}|)^{0.5}$.

3.3 Image Processing and Analysis of High-Resolution Images

Atomic-resolution HRSTEM and HRTEM images were often processed to remove noise from the images while preserving crystalline detail. Even though many image filtering algorithms exist (for a recent review see Goyal et al. [Goy+20]), only a few methods were tested and applied. The main goal was to enhance image quality with the additional requirement for minimal parameter adjustment to minimize user bias during the filtering process. Here it is noteworthy that STEM images in the ser file format can be read into *DigitalMicrograph* (DM) using, e.g., the freely available *ImportImage* DM plugin[3] by Pavel Potapov.
The most used filter in this work is an "average-background-subtraction filter" (ABSF) [Kil98]

[2] The largest aperture (100 µm) was measured to correspond to 19 mrad or a maximum resolution of 105 pm at 300 keV.
[3] *ImportImage*, `http://temdm.com/web/plugins/` (last accessed: 21.09.2021)

combined with a Butterworth (BW) low-pass filter [DD20, p 475] from the *HRTEM-Filter* plugin[4] (v. 3.1) for DM by Mitchell [MS05]. An example image is shown in Fig. 3.9. The ABSF removes amorphous contributions from an image while trying to preserve crystalline details, i.e. sharp peaks in the corresponding FT (Fig. 3.9c). For the BW filter, the cut-off parameter `BW Ro` defines "the radius (relative distance from the center of the FFT to the edge) at which the filter function drops to half" (from the plugin code). The FT edge corresponds to the Nyquist frequency. To determine `BW Ro` for a given high-resolution image, the FT was calculated and the relative distance of the reflection of the highest resolved crystalline frequency from the center was roughly taken as `BW Ro` (e.g. 0.4 in Fig. 3.9 as the lattice reflection roughly reach out to 0.4 times the Nyquist frequency). The other parameters were left as default: `Step` 2, `Delta %` 5, `Cycles` 50, and an order `BW n` of 4 for the BW filter. The filtering enhances image fidelity (cf. Fig. 3.9a and b). Compared to the conventionally used Bragg-spot FT filtering, the ABSF does not introduce crystalline detail in amorphous regions.

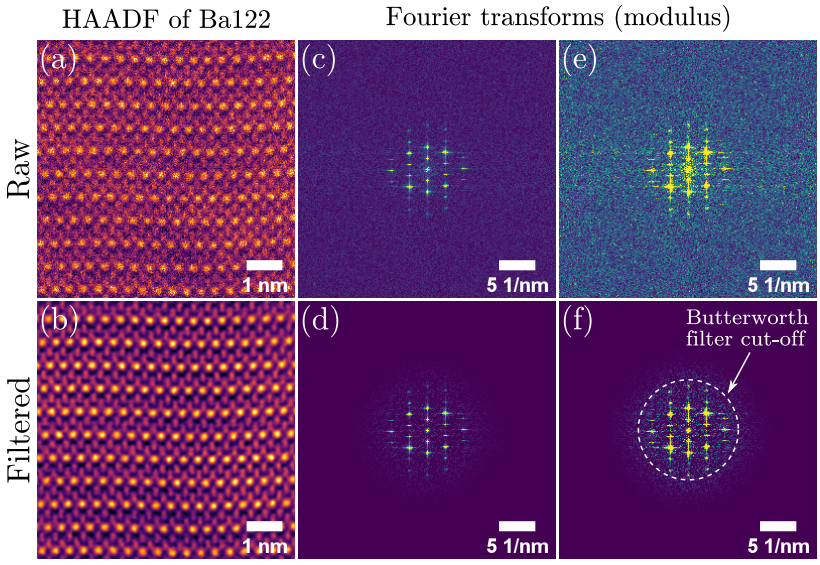

Figure 3.9: Application of average-background-subtraction and Butterworth filters for high-resolution image enhancement. (a) Raw and (b) filtered HAADF-STEM image of Ba122[1 0 0]. (c,d) Corresponding Fourier transforms with (e,f) gamma-adjusted intensity for better visibility of the Butterworth cut-off frequency (dashed circle). The latter was set to 0.4 (times Nyquist frequency) in this example to incorporate all crystalline reflections.

The shown filter is susceptible to low-frequency intensity modulations. A typical case for this is a substrate-film interface with considerable differences in mean atomic number $\overline{Z}$, such as $Ba(Fe_{0.92}Co_{0.08})_2As_2$ ($\overline{Z}$ = 34.83) on CaF_2 ($\overline{Z}$ = 12.67) (Fig. 3.10). The differences in $\overline{Z}$ cause differences in HAADF-STEM intensity. Filtering with ABSF/BW in such images introduces a sine-like low-frequency intensity modulation (Fig. 3.10b). A workaround for this is subtracting the low-frequency background while preserving the crystalline detail prior to applying the ABS/BW filter . The background can be, e.g., created by blurring the image with an anisotropic diffusion filter until the crystalline detail entirely vanishes. A *Fiji* plugin (`Anisotropic Diffusion 2D`) based on Tschumperle and Deriche [TD03] was used to create a background image. The `Number of Iterations` and `Smoothing per Iteration` parameters were increased until crystalline detail vanished from the image. The found background image was then subtracted from the original (using `Process → Image Calculator...` in *Fiji*). This creates a "flattened" image with ideally only crystalline detail (Fig. 3.10c), which can then be filtered in DM with ABSF/BW as described above (Fig. 3.10d). The crystalline structure can then by analyzed. However, Z-contrast is (mostly) removed from the image. Another example of this method can be found in Fig. A.1 in a related publication [Grü+21a].

[4] *HRTEM-Filter*, `http://www.dmscripting.com/hrtem_filter.html` (last accessed: 21.09.2021)

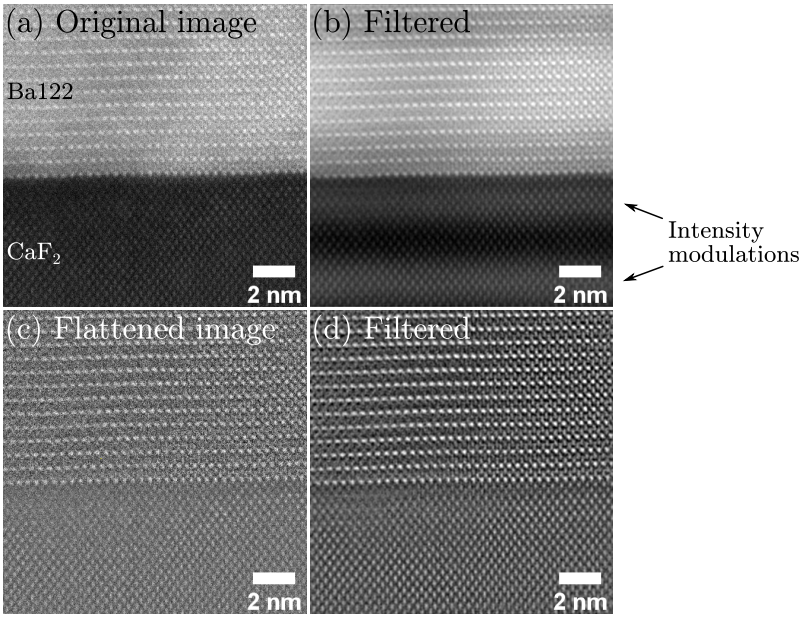

Figure 3.10: Removal of low-frequency background intensity followed by filtering. (a) Original HAADF-STEM image of an interface between Ba122 and CaF_2. (b) ABS/BW filtering introduces an unwanted coarse intensity modulation. (c) Background removal/"flattening" of the image prevents this artifact, as shown in (d).

Analysis of crystalline structures. Image filtering is typically the first step in analyzing the crystalline structure from high-resolution images. Here, aspects of interest are, e.g., (i) the identification of crystalline phases and orientations and (ii) possible strain in the films arising from lattice mismatch to the substrate or from precipitates. For (i), FT analysis was typically used.

Fourier-Transform analysis. The FT pattern reflects the periodicities of the sampled crystalline region similar to a diffraction pattern and can be applied to nm-sized regions. Another benefit is that processing can be done offline after acquiring high-resolution images. Often, small regions of crystalline phases were only detected after careful inspection of the acquired images. In contrast, NBED can reach a similar spatial resolution, but the NBED patterns must be acquired directly in the microscope. Conventional FT pattern analysis was primarily done in DM. For display of the complex numbers z in FTs, the magnitude (absolute) value $|z|$ or the power spectrum $|z|^2$ with

$$|z| = \sqrt{[\mathrm{Re}(z)]^2 + [\mathrm{Im}(z)]^2} \tag{3.1}$$

were typically calculated to obtain a real-valued image for display. The used menu option `Process → Diffractogram` first applies a Hann window to the image, which dampens the image intensity towards the edges and calculates the FT. The Hann window prevents horizontal and vertical streaks around the crystalline reflections. For non-square ROIs, the `Diffractogram` implementation of the *FRWRtools* plugin[5] by Christoph T. Koch was used.
For crystalline-phase analysis, the distance of the spots from the FT center and the angle between (at least) two non-collinear reflections have to be measured. For this task, the *Measure FT* plugin[6] by Ruben Bjorge was applied to reduce user bias from manual measurements. The obtained values for the angle and the distances can then be compared to simulated diffraction patterns. *JEMS*[7] [Sta87] was used for this task using the `Drawing → Diffraction` menu.

[5] `https://www.physics.hu-berlin.de/en/sem/software/software_frwrtools` (last accessed: 22.09.2021)
[6] `https://www.felmi-zfe.at/cms/wp-content/uploads/dm-scripts/5461/measure_FT.s` (last accessed: 22.09.2021)
[7] `https://www.jems-swiss.ch/` (last accessed: 22.09.2021)

Alternatively, the FT reflection positions can also be checked against a database of crystalline structures in *JEMS* using the `Indexing → Spot pattern` submenu. Here, a FT pattern can be loaded and the arrow markers placed on two non-collinear reflections. The FT image must be scaled correctly using the `Scale` menu, e.g. by specifying the pixel size. The marked reflection's order (1, 2, 3, ...) can also be specified. The highest available order from the experimental pattern was chosen to minimize measurement errors in setting up the reflection vectors. The final spot pattern can be visualized using `Options → Show mask` and should match with the experimental reflections. This then defines the angles and distances for searching a database. The default error ranges for angles (3 %) and distances (5 %) were used, which account for errors in specifying the reflection positions and miscalibration of the image scale. The database was built up of "Crystallographic Information File" (.cif) files obtained from the inorganic crystal structure database (ICSD) [Bel+02]. *Atomsk* [Hir15] was used for batch conversion of cif files to *JEMS*-specific text files to index spot patterns. Besides *JEMS*, the *ReciPro* software by Seto and Ohtsuka [SO22] was also used to calculate diffraction patterns. The software offers an intuitive user interface to create combined diffraction patterns of multiple phases and allows to save the diffraction patterns as "Enhanced Metafile" (emf), which can be imported and modified as vector graphics in a vector-graphic editor such as *Inkscape*.

Sliding-Window FFT. Another applied method for FT analysis is the "sliding-window FFT" [Vas+15; JJK20]. The Jupyter notebook by Jany [Jan19] was modified [Grü22]. Here, a (high-resolution) image is divided into patches of smaller sub-images. The sub-images are created by sliding a window with size s with a specified step size $x_{\text{step}}/y_{\text{step}}$ (all values in pixels) over the original image and extracting the sub-images at each step location. The parameters s and $x_{\text{step}}/y_{\text{step}}$ can be adjusted based on the desired resolution and computation speed. For example, a sub-image size of 128^2 pixels ($s = 128$) may be used for a 2048^2 pixel image with a step size of $x_{\text{step}} = y_{\text{step}} = 32$ pixels. The parameter s also determines the offset of size $s/2$ at the image edges because the used code does not interpolate/reflect the window at the image edge. For example, a row of 2048 pixels with $s = 128$ and $x_{\text{step}} = 32$ will be divided in $(2048 - 128)/32 = 60$ sub-images. Note that the offset $s/2$ is applied on both sides of the row. The dataset then has (60, 60) sub-images of size 128^2 pixels. In the next step, the FFT is calculated for each sub-image. Then, the modulus of each FFT is calculated to get a real-valued image. The high dynamic range in these images is compressed by taking the natural logarithm. This leads to real-valued images with values $\ln(|z|)$ and reciprocal dimensions (k_x, k_y). The final dataset is four-dimensional with two spatial and two reciprocal dimensions (of shape $(x, y, k_x, k_y) = (60, 60, 128, 128)$ in the example), similar to a 4D-STEM dataset. Compared to a full-frame FFT, the sliding-window FFT now contains information about the *local* crystalline spacings and orientations. In the next step, MSA can be applied to the dataset, whereby the 2D-FFTs are treated as the measurement signal (comparable to 1D EDXS/EELS spectra). PCA is used to find the number of trends in the dataset (i.e. phases with differing FFTs). BSS algorithms (ICA and NMF) were applied to cluster similar FFTs and to separate possibly overlapping phases.

2D Gaussian fitting. Quantitative evaluation of atom-column positions in HAADF-STEM images can provide valuable information of small shifts in a crystal structure., e.g. lattice strain. As already shown in Fig. 3.7 on page 67, *Atomap* [Nor+17] is a powerful Python package for this task. At the time of writing, the current package version is 0.3.1 and an example Jupyter notebook is available [Grü22]. The basic steps are described in the following. At first, the packages and a (filtered) HAADF-STEM image are loaded (as a signal `s`):

```
import hyperspy.api as hs
```

```
import atomap.api as am
s = hs.load('HAADF-STEM-image.dm3') #can also read emi/ser
```

The `get_feature_separation` method finds the rough positions of the bright atomic columns. An interactive figure shows the column positions for each separation value (in pixels) from the `separation_range` keyword. Here, one can find a value for the pixel separation which finds most of the desired atomic columns.

```
s_peaks = am.get_feature_separation(s, separation_range=(2, 15))
s_peaks.plot() #Interactively find good pixel separation value
```

With a separation value, e.g. 9, the raw column positions can be stored:

```
atom_positions = am.get_atom_positions(s, separation=9)
```

Often, some columns are missing or some wrong positions are found and this can be corrected interactively:

```
#Add/remove missing/false columns with mouse clicks
atom_positions_new = am.add_atoms_with_gui(s, atom_positions)
```

When all raw positions are found, a sublattice (`sl`) is generated from the column positions:

```
sl = am.Sublattice(atom_positions_new, s, fix_negative_values=True)
```

The raw column positions can be refined using the different methods center of mass or two-dimensional Gaussian fitting. Typically, both were run in sequence.

```
sl.find_nearest_neighbors()
sl.refine_atom_positions_using_center_of_mass()
sl.refine_atom_positions_using_2d_gaussian()
```

The results of position refinement can be inspected via `sl.get_position_history().plot()` and should ideally fit well to the experimental atomic column positions. A powerful feature of *Atomap* is the detection of symmetries from the positions of the atomic columns. This can be used to extract information from a specific set of atomic planes. The relevant functions are:

```
sl.construct_zone_axes() #Find symmetries
sl.plot_planes() #Inspect found planes
```

Atomap then provides different methods to extract information from the planes and column positions (not shown here, see the documentation[8] for details). A typical value measured here were the changes in spacing between different monolayers. An analysis is typically finished by saving the found column positions and planes to a file:

```
atom_lattice = am.Atom_Lattice(sublattice_list=[sl], image=s.data, name="My
                                        atomic columns", fix_negative_values=
                                        True)
atom_lattice.save("Atomap_atom_lattice.hdf5", overwrite=True)
```

Strain analysis in HAADF-STEM images was mostly prevented by scanning distortions and sample-drift artifacts. Typically, only the fast-scan-direction data were deemed as reasonably free from such artifacts.

[8]Examples: `https://atomap.org/analysing_atom_lattices.html` (last accessed: 21.09.2021)

3.4 STEM-EELS and STEM-EDXS Measurements and Analysis

STEM-EELS. Core-loss STEM-EELS was used for qualitatively mapping the spatial distribution of elements. STEM-EELS is especially powerful to locate light elements and map elements that can contain artifacts in EDXS spectra from spurious x-rays from microscope hardware (e.g. Cu, Ni, Zr). A FEI Titan^3 80–300 operated at 300 keV equipped with a GIF Tridiem 865 ER spectrometer was used. Two probe settings (termed "high-resolution" and "high-current" settings) were used in this work, which are listed in Table 3.3. The high-current setup (70 µm C2 aperture, C3 lens off, $\alpha = 11.5$ mrad) results in a probe current of 200 pA to 300 pA. The high-resolution setup (50 µm C2 aperture, $\alpha = 9$ mrad) results in a probe current of 50 pA to 100 pA and was used in some experiments to maximize spatial resolution (optimal α).
The images of the GIF entrance aperture plane for both settings are compared in Fig. 3.11. The images were taken with the GIF CCD camera with the Gatan DF detector inserted and the probe placed on a MgO substrate region. The Gatan DF detector acts as ADF detector and entrance aperture, defining the collection semi-angle β. The smallest available camera length of 29.5 mm for the regular (non-EFTEM) projection-lens series was used, resulting in $\beta \approx 21$ mrad as determined by the Bragg spots of a known material (e.g. a MgO substrate). The descan coils were activated to minimize movement of the transmitted beam in the GIF entrance/detector plane. Larger collection angles (smaller camera lengths) are available with the projection system set to EFTEM mode (14.85 demagnification compared to regular projection-lens series). Running the microscope in STEM mode with the projection lenses set to the EFTEM lens series leads to the EFSTEM mode. This EFSTEM setting was used for TEM-sample-thickness determination with the log-ratio method [Ege11, p 294] to realize $\beta \geq 20$ mrad as recommended by Zhang et al. [ZEM12].

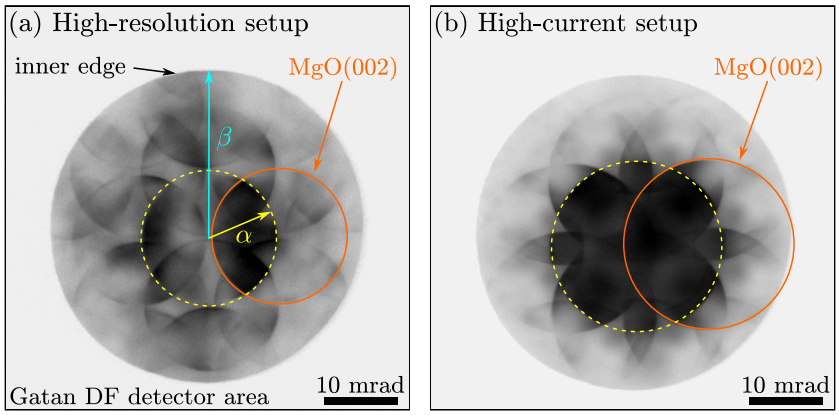

Figure 3.11: Typically used experimental STEM-EELS setups. Images of the GIF entrance plane for (a) a high-resolution setup with $\alpha_{\text{opt}} \approx 9$ mrad and (b) using the larger 70 µm C2 aperture for higher beam current, but larger probe size ($\alpha \approx 11.5$ mrad). The undiffracted central beam is marked by dashed lines. Image intensities were inverted for better visibility. (a) The collection semi-angle β is determined by the inner edge of the Gatan DF detector (black arrow). Both images were acquired for a nominal camera length of 29.5 mm, resulting in $\beta \approx 21$ mrad. The angles were calibrated by the visible diffraction discs of the MgO[1 0 0] zone axis.

The EFSTEM mode was also tested for core-loss STEM-EELS (Fig. 3.12). As a general trend, larger collection angles lead to a better signal-to-noise ratio but a worse signal-to-background ratio. The latter may obscure small core-loss edge onsets, e.g. for F. The normal STEM mode with $\beta = 21$ mrad was mainly chosen for STEM-EELS mappings for the following reasons:

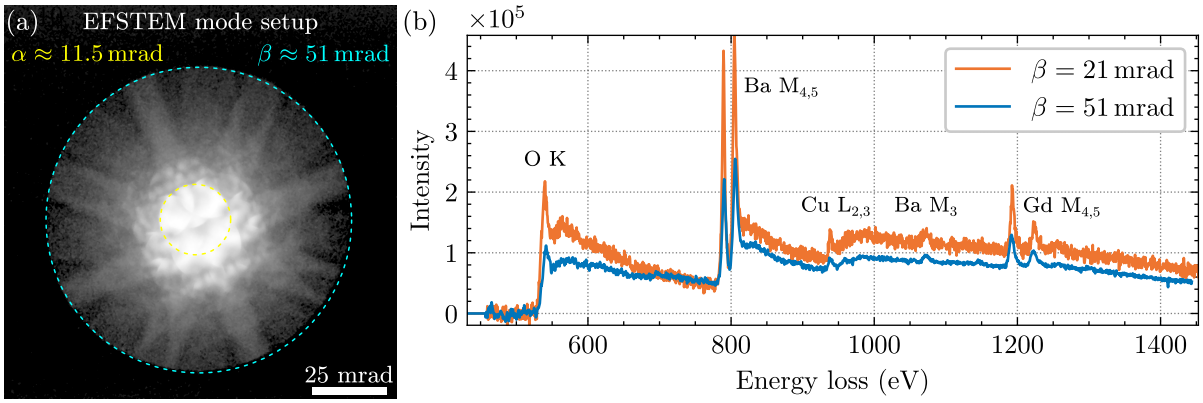

Figure 3.12: STEM-EELS in EFSTEM mode. (a) The EFSTEM mode enables large β for high collection efficiency in core-loss STEM-EELS. The image intensity is displayed on a logarithmic scale for better visibility. (b) Comparison of background-subtracted EELS spectra from GdBCO for the "high-current" setup (Fig. 3.11(b), $\beta = 21\,\text{mrad}$) and the exemplary EFSTEM setup ($\beta = 51\,\text{mrad}$) from (a). For the latter, a better signal-to-noise but a worse signal-to-background ratio is observed. Note that the spectra have a comparable total number of counts, which was achieved by having a smaller effective signal-collection duration for $\beta = 51\,\text{mrad}$.

- PCA-filtering can be used to deal with noise in spectrum images with a low signal-to-noise ratio.
- All investigated core-loss edges were below 2 keV and generally had a "high enough" collection efficiency for $\beta = 21\,\text{mrad}$.
- The minimum readout and processing speed of TIA seems to be limited to around 50 ms. Therefore, even shorter integration times than 50 ms per scan point combined with larger collection angles did not necessarily result in faster STEM-EELS acquisitions.

Regarding GIF parameters, energy dispersions of 0.2 eV per channel and 0.5 eV per channel were typically used for core-loss STEM-EELS. The used dispersions result in energy windows of 410 eV and 1024 eV, respectively, on the 2048 pixel^2 UltraScan 1000 CCD GIF camera. It is noteworthy that typically[9] 3 CCD channels in the horizontal (energy-dispersive) direction define the energy resolution at the GIF CCD due to broadening by the MTF. This means that for a non-monochromated Schottky FEG with $\Delta E \approx 0.7\,\text{eV}$ a dispersion of 0.2 eV per channel is sufficient to reflect the energy resolution of a Schottky FEG on the GIF CCD. A full GIF tuning was run in the morning before each STEM-EELS session to ensure a good GIF alignment. A fresh set of gain-reference images for the GIF CCD camera were taken when a structure or an uneven illumination (in a vacuum image) were visible on the GIF CCD camera. A vertical binning (i.e. along the non-energy-dispersive direction) of 128 was used to reduce read-out noise and speed up spectrum image acquisition. A drawback of such high binning is increased gain noise [Har+17]. Energy offsets (of the starting energy of EELS spectra) were applied with the drift-tube, which provides offsets up to 1 keV.
Synchronization of EELS spectrum acquisition and beam position, and drift correction is controlled by TIA (`Drift-corrected spectrum image` menu item). The acquisition positions were set to an integer multiple of the pixel size of the sampling of the survey image (see example in Fig. 3.13).

[9] See, e.g., recommendation by Gatan (`https://eels.info/how/spectroscopy/acquire-spectrum`, visited on 08/18/2021): "Generally choose the smallest dispersion (largest eV/ch value) that still gives the required energy resolution. Assume at least 3 channels are needed to define the energy resolution (e.g., 0.5 eV/ch will yield at best $0.5 \times 3 = 1.5$ eV resolution)."

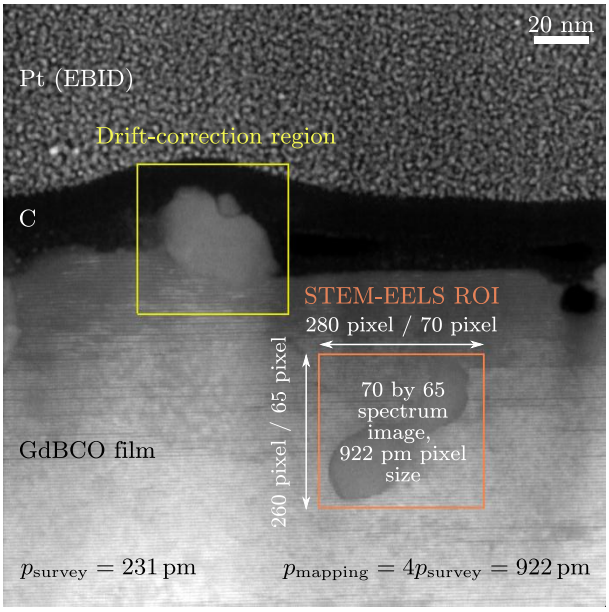

Figure 3.13: Example for a STEM-EELS spectrum image setup in TIA. Here, a precipitate in a GdBCO film is mapped. Rectangle markers for the spectrum image ROI (orange, 280×260 pixel^2) and drift-correction region (yellow, 256×256 pixel^2) are added to a 1024^2 pixel^2 survey image with a pixel size $p_{\text{survey}} = 231\,\text{pm}$. To reduce the total STEM-EELS spectrum image acquisition time, the ROI is sampled with $p_{\text{mapping}} = 4p_{\text{survey}} = 922\,\text{pm}$, leading to a 70×65 pixel^2 spectrum image. Integration time per pixel was 150 ms in this case. Total acquisition time including drift-correction was about 15 min.

In this example, an originally $280{\times}260$ pixel^2 ROI in a $1024{\times}1024$ pixel^2 survey image with a pixel size p_{survey} was sampled with $p_{\text{mapping}} = 4p_{\text{survey}}$ leading to a spectrum image size of $70{\times}65$ pixel^2. This approach ensures that the STEM-EELS beam positions nicely fit into the ROI, i.e. $(p_{\text{mapping}}) \mod (p_{\text{survey}}) = 0$, even though the scan steps are typically "uneven" (922 pm in this example). In contrast, directly specifying the scanning step in length units (e.g. setting $p_{\text{mapping}} = 1\,\text{nm}$) could lead to unwanted offsets at the edges of the STEM-EELS ROI as the software has to fit the given p_{mapping} into a fixed-size ROI.
The `Number of acquisitions in slice` parameter in TIA controls the frequency of drift correction and was set to an integer multiple of the total pixels (e.g. 70, 140, ... in Fig. 3.13) along the fast-scan direction (horizontal). This ensures that drift correction is done at the end (as opposed to somewhere in the middle) of a horizontal scan line in a STEM-EELS map. The EELS spectrum integration time per pixel is chosen to achieve a "high enough" signal-to-noise ratio and depends on the sample thickness and elemental edge energy-loss of interest. It was typically between 50 ms to 150 ms. As a rule of thumb for the signal-to-noise ratio, all core-loss edges of interest should be at least barely visible in a single, noisy EELS spectrum so that a noise reduction with PCA is successful (see, e.g., (d) in Fig. 2.17 on page 49). EELS spectra are acquired in sequence, meaning that each beam position is only visited once and the whole spectrum is collected for a given integration time of the CCD camera. The acquired EELS spectrum image was saved as an "Emispec (.emi)" file which also creates a .ser file with the actual data.

Data processing

EELS data was mainly processed in DM. As a first step, the emi/ser file was converted to the "ripple" file format (rpl/raw) using *HyperSpy* [Grü22]. The rpl file can then be imported to DM using the "ImportRPL" plugin by Luiz Fernando Zagonel[10]. After importing and specifying the data-set type using `Spectrum → Convert data to...→ EELS`, all options in DM for EELS processing become available.
Spurious x-ray peaks are typical artifacts in EELS spectrum images and appear as isolated "hot pixels" which can be removed using `Volume → Remove X-rays from Stack...` with a (default)

[10]Link: `https://github.com/hyperspy/ImportRPL/blob/main/ImportRPL.s` (last visited: 15/09/2021)

"Sigma deviation threshold" of 10. To quote the DM help menu, "the routine will check each image plane of the data-set for spikes that lie more than 10 standard deviations (default) above the local median. If an anomalous pixel is found, its value will be set to the local median."
Afterward, the dataset is denoised with PCA using the *temDM* plugin by P. Potapov [Pot16] (basic version 1.96). The signal-to-noise ratio was typically high enough so that no binning or Gaussian kernel filtering was required, even though this is possible using `temDM → MSA → filtering`. PCA was applied by first using `temDM → MSA → proceed PCA` and selecting `make matrix` with weighting set to "E & X,Y". The first 20 principal components (`number components: 20`) were calculated with the `center` option enabled. Extracting 20 components was always enough to reach the noise level in the scree plot, with k ranging from 6 to 13. For details on weighting and centering the dataset, see Potapov [Pot16]. The number of useful principal components k was determined by inspecting the scree plot, score maps, and loadings. Afterward, the denoised dataset is reconstructed with k components (`using components: k`) with the `Reconstruct DataCube` menu. The resulting denoised spectrum image was saved as a dm3 file before further processing.
The net intensity of the core-loss edges is extracted by (i) first subtracting a power-law background model and (ii) then integrating the signal in an energy window or fitting a theoretically calculated Hartree-Slater ionization cross-section based on tabulated values for the generalized oscillator strength (GOS) [LRM80; AR85] to the core-loss edges. The latter approach is helpful in separating overlapping edges but is currently only available in DM using the commercial EELS package by Gatan[11]. This commercial package was mainly used for extracting the core-loss signals using a combined fit of a power-law background and Hartree-Slater cross-section models (Fig. 3.14a). The relevant menu is found under `Technique Manager → Analytical → Elemental Quantification`.

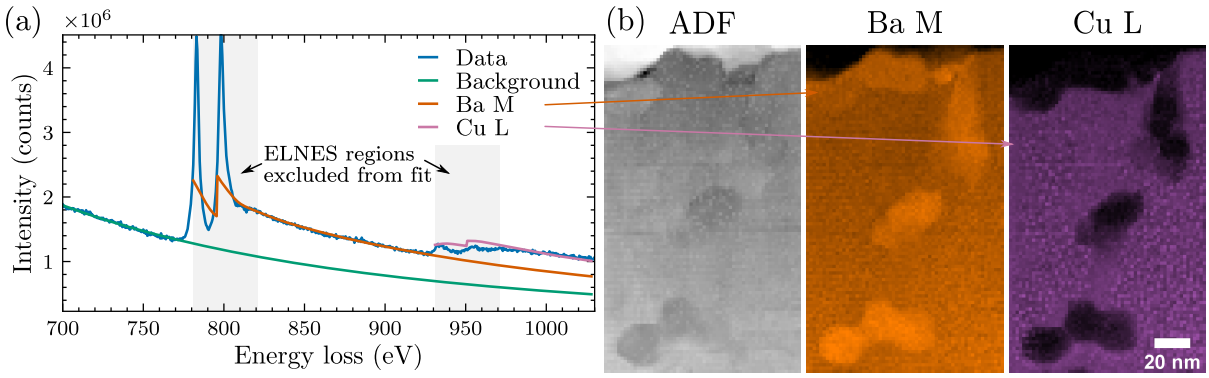

Figure 3.14: Signal extraction in STEM-EELS. The example shows a REBCO sample with BHO nanoparticles. (a) The plot shows a combined fit of a power-law background model and Hartree-Slater cross-sections for the Ba M and Cu L edges on the derived sum spectrum from the whole spectrum image. The ELNES regions (shaded areas) are excluded from the fit as they are not modeled well. Repeating the fit on each position and extracting the fitting coefficient yields (b) elemental maps. The ADF-STEM image is also shown.

A derived sum spectrum of the spectrum image is created using the `SI Picker` tool from the right-click menu in DM. All edges are typically visible in a summed-up spectrum and the element edges be added to the list in the `Elemental Quantification` menu. After adding

[11] Model fitting can also be done in *HyperSpy*, if the EELS package is not available. For a simple integration of the core-loss signal the freely available "EELSTools" plugin [MS05] from `http://www.dmscripting.com/` can be used.

all core-loss edges, the fit options were adjusted using the `Open Analysis setup` menu. The ELNES region was typically excluded (40 eV window starting from the edge onset, see shaded regions in Fig. 3.14a). The reason is that the Hartree-Slater cross-section models do not describe ELNES fine-structure features, as clearly visible, e.g., for the Ba $M_{4,5}$ edges in Fig. 3.14a. The experimental signal shows strong white-line peaks whereas the model only contains the edge onsets. The `Overlaps (PreceedingEdgeName)` option was enabled to fit the background and all edges simultaneously [VV04]. This approach corresponds to a multiple linear least-squares (MLLS) fit of scaling coefficients for the different core-loss-edge models. The fit can be checked for accuracy on a single-pixel level by selecting a few representative positions using the `SI Picker` tool. After validating the model setup, the fit is performed at each position using the `Map` button in the `Elemental Quantification` menu. The fitted core-loss-edge model coefficients are directly proportional to the elemental concentration and are extracted to generate (qualitative) elemental maps using the option `Signal integral` (Fig. 3.14b). The maps can then be saved to disc in different file formats.

NLLS fitting of ELNES. Fine-structure features of the ELNES can be fitted using different non-linear functions, i.e. non-linear least-squares (NLLS) fitting. A typical use-case is a Gaussian fit to $L_{2,3}$ or $M_{4,5}$ white lines. Possible changes in white-line intensities, ratio, position, and width can be caused by local chemistry/bonding-state changes. A good overview can be found by Yedra et al. [Yed+14] (and references therein), which focuses on ELNES analysis of oxides (using their *OxideWizard* plugin for DM). DM offers a NLLS fitting menu for this method, located under `Technique Manager → Data Fit → Least-Square Fitting`. With an EELS spectrum selected, different functions can be added for fitting (Fig. 3.15). White-lines were analyzed by first fitting a power-law background (`Power Law`), a calculated Hartree-Slater cross-section model from `EELS → Compute Cross-section...` as a `Reference`, and then a Gaussian (`Gaussian`) to each white-line peak (selecting the `Sequential` fit option in the `NLLS options` menu). Sometimes a combined (instead of sequential fit) yielded better results, so both fitting methods were typically tested (`Combined` fit option). Performing the fit at each pixel results in a map for each fit parameter, e.g. amplitude, position, and width for a Gaussian function. Basic scripting or the image calculator (`Process → Simple Math...`) in DM can be used for pixel-wise calculations on the parameter maps.

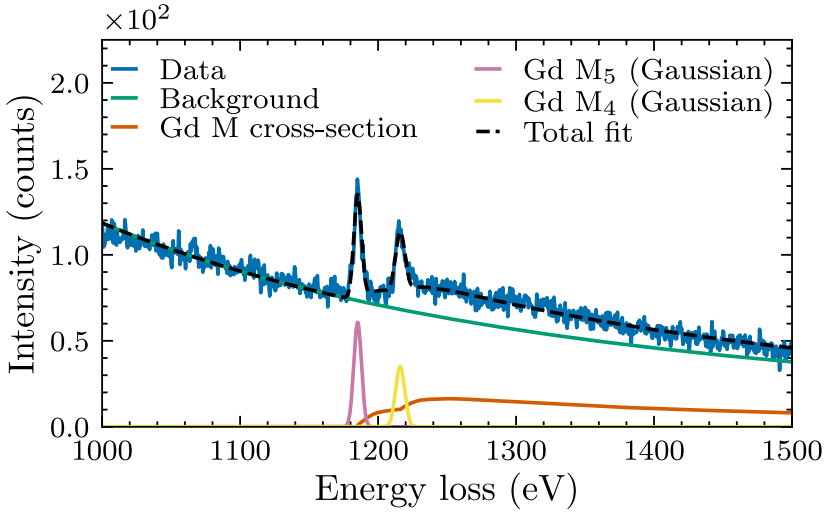

Figure 3.15: Non-linear least-squares fitting of ELNES features. The example shows a fit of the Gd $M_{4,5}$ ELNES in GdBCO. The model fit consist of a power-law background, a Hartree-Slater ionization cross-section for the Gd-M edge, and two Gaussian functions to model the $M_{4,5}$ white-line peaks. As an example, the white-line amplitude ratio M_4/M_5 is around 0.57 as expected for Gd^{3+} [FB96].

STEM-EDXS

STEM-EDXS is another technique used for qualitatively mapping spatial distributions of elements. An FEI Tecnai Osiris operated at 200 keV equipped with "ChemiSTEM" technology [Sch+10] was used which combines a high-brightness FEG ("X-FEG") and a "Super-X" multi-SDD detector system ($4 \times 30\,\mathrm{mm}^2$ detector area) for a high collection efficiency of x-rays. The latter stems from the relatively large solid angle of (0.64 ± 0.06) sr [Kra+17], resulting in a geometrical collection efficiency of $0.64/4\pi = 5\,\%$, which includes shadowing effects from the default double-tilt high-visibility ("HiVis") TEM holder for the Osiris [Kra+17]. The detector segments are located above the sample holder (see scheme in Fig. 3.16b). Care was taken to maximize collection efficiency:

- Mostly a commercial TEM grid with four grid posts was used (Fig. 3.16a) and the lamella was mounted on one of the two central posts. This gives mostly clear line-of-sight for emitted x-rays to the detectors without hitting the TEM sample holder (Fig. 3.16b).
- The grid is loaded into the TEM holder so that the thinner side (here about 9.5 µm) of the grid (relative to the lamella) points upwards, as shown in Fig. 3.16c. This minimizes the possible obstruction of x-rays from the grid and the TEM holder. In practice, the sample is loaded "upside down" compared to the scheme because the holder is rotated by 180° during loading into the TEM.
- The electron-transparent regions of the lamella should be as far "up" towards the EDXS detector side as possible to prevent x-ray shadowing from the thick lamella edges and any central pillars for multi-window samples (Fig. 3.16d). The schemes on the right in Fig. 3.16d show examples for cases where (upper scheme) an outgoing x-ray can leave the specimen and can be detected and (lower scheme) an outgoing x-ray is absorbed by the specimen. Low

The detector has a windowless design, enhancing collection efficiency for low-energy x-rays ($< 1\,\mathrm{keV}$) and enables spatial mapping of such x-ray transitions. However, the detector can be contaminated with ice and C-rich debris as the detector is cooled to around $-70\,°\mathrm{C}$ and can act as an unwanted cold trap for residual gas and water molecules introduced in the microscope [MN15]. Low-energy x-rays are also easily absorbed inside the specimen itself. These factors reduce the ratio of emitted versus detected x-rays, especially for low-energy x-rays, making STEM-EELS a more suitable technique for the latter.
The X-FEG has a higher brightness than a conventional FEG and provides more beam current for a given probe size. Typical probe settings were $\alpha = 10.7\,\mathrm{mrad}$ (70 µm beam-limiting C2 aperture), gun lens 5, and spot sizes between 3 to 8 depending on sample stability and desired setup of beam current vs. resolution/sampling. Low-magnification STEM-EDXS measurements on relatively irradiation-stable REBCO samples were performed with the 100 µm C2 aperture to increase the beam current. Typical nominal beam currents ranged from 80 pA to a few nA (the maximum indicated beam currents were about 1 nA to 2 nA/6 nA to 7 nA for 70 µm/100 µm C2 apertures and low spot-size values (2 to 4), respectively). Sampling for STEM-EDXS spectrum imaging was set up to approximately achieve a slight overlap between adjacent pixels (roughly at Nyquist frequency $d_0/2$ or slightly below for a given probe size d_0). The aim was to minimize irradiation damage while preserving details at interfaces, which could be lost for undersampling. However, the actual probe sizes for a given spot size value were not precisely measured and only

[12] Image link: `https://www.plano-em.de/media/image/a1/41/3b/10GC04_1.jpg` (last accessed: 02/09/2021)

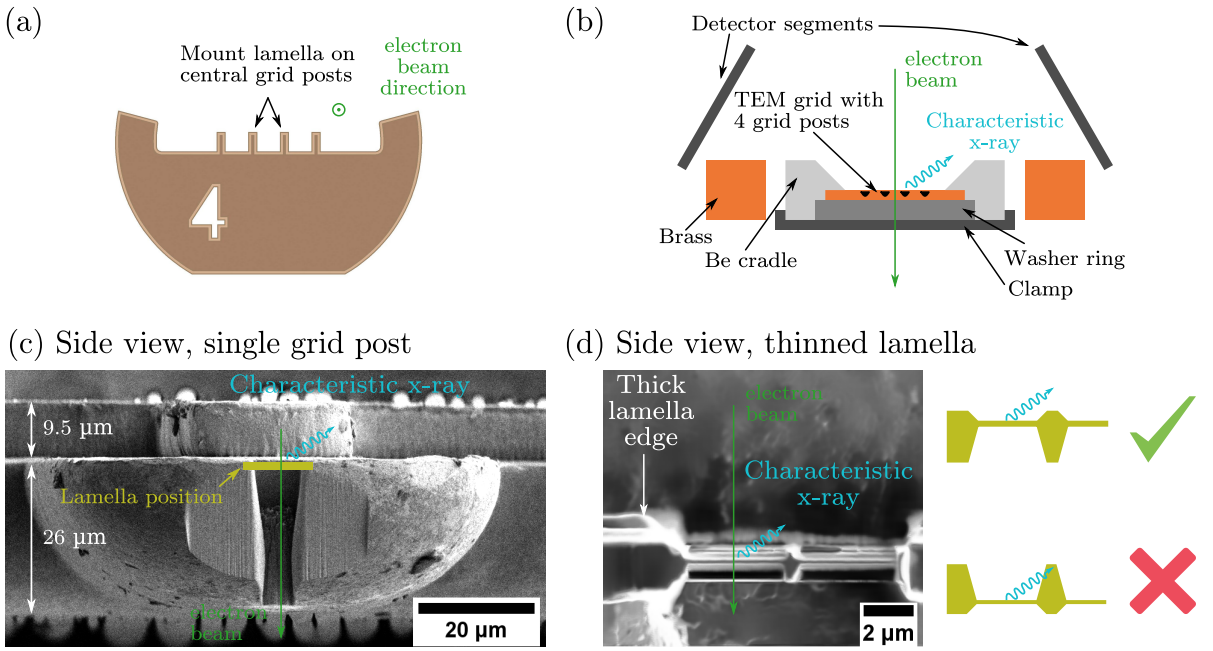

Figure 3.16: Mounting TEM samples for maximum collection efficiency for STEM-EDXS. (a) Scheme[12] of a TEM grid type with four grid posts commonly used in this work (PELCO 10GC04). The central two posts were mainly used for lamella mounting. (b) Cross-section scheme of a loaded TEM grid in the "HiVis" holder. A washer and a clamp fix the grid. A central and high up position in the holder is desired to maximize the unobstructed solid angle of the detector segments. Figure is adapted from fig. 5 in [Kra+17] and not to scale. (c) SE-SEM image of a grid post with indicated lamella position and measured thickness above (9.5 µm) and below (26 µm). The shown configuration with the indicated beam direction maximizes collection efficiency. (d) Electron-transparent windows should be milled as high up as possible to minimize obstruction by thicker sample regions (SE-FIB image). Schemes on the right show possible absorption for the lower milling configuration.

roughly approximated by the table measured by Mitchell for the same microscope type[13]. STEM-EDXS spectrum acquisition and sample-drift correction were controlled by the Bruker *Esprit* 1.9 software. The detector's shaping time was set to "Automatic". The maximum throughput of the detector is 200×10^3 x-ray counts per second. Energy dispersion was set to 10 eV per channel for almost all data sets. It it noteworthy that the *Esprit* 1.9 software does not change the energy dispersion between the "Maximum energy" settings 20 keV and 40 keV. Instead, the software adjusts the number of total channels (20 keV → 2048 and 40 keV → 4096 á 10 eV per channel, respectively). In contrast to STEM-EELS, EDXS spectra can be read out faster (µs instead of ms) because no comparably slow CCD camera is necessary to record the x-rays. Therefore, EDXS spectrum images can be recorded using "position-tagged spectrometry" [Fri96; MF99; FL06], where "the electron beam is continuously scanned while X-ray data are streamed to the computer and tagged with the position of their origin" [FL06]. Typical dwell times using this method were 20 µs to 50 µs in this work and EXDS spectrum images were collected for a few minutes to achieve a sufficient signal-to-noise ratio for offline processing with MSA. For thin TEM samples with a low amount of x-rays arising from bremsstrahlung, roughly $N_{\mathrm{tot/px}} = 200$ total x-ray counts per pixel often led to a satisfactory data treatment with PCA/NMF using *HyperSpy*. During EDXS data collection at the microscope, the minimum required mapping duration t_{EDXS} to achieve (at least) $N_{\mathrm{tot/px}}$ counts per pixel were approximated by the map size

[13] DM plugin "Osiris STEM Probe Selector", `http://www.dmscripting.com/osiris_stem_probe_selector.html` (last accessed: 02/09/2021)

in pixels (x, y), the input x-ray count rate k_{EDXS}, and an empirical correction factor $c_{\mathrm{EDXS}} \approx 1.3$:

$$t_{\mathrm{EDXS}} = \frac{x \cdot y \cdot N_{\mathrm{tot/px}} \cdot c_{\mathrm{EDXS}}}{k_{\mathrm{EDXS}}} \tag{3.2}$$

As an example, to achieve $N_{\mathrm{tot/px}} = 200$ for an input count rate of 30×10^3 and a map size of (256, 256) pixels, the mapping duration should be at least $t_{\mathrm{EDXS}} = 568\,\mathrm{s}$. The correction factor accounts for the difference between expected and experimental $N_{\mathrm{tot/px}}$ and was evaluated for a few spectrum images. This difference may arise because only x-rays up to a certain maximum energy are counted in a spectrum image, whereas the total x-ray flux given by *Esprit* may also account for x-rays with higher energies. The factor c_{EDXS} was not investigated in detail but may depend on the characteristic x-rays emitted by the sample, the set maximum energy, and the EDXS detector. Spatial dimensions were typically set up to allow for easy rebinning during post-processing, e.g. map dimensions of (180, 400) instead of (183, 398). The acquired EDXS spectrum image was saved as a "Bruker Container File" (.bcf).

STEM-EDXS in the Helios FIB/SEM. STEM-EDXS data sets were also acquired on the TFS Helios G4 FX. Samples were often directly analyzed with STEM-EDXS after FIB preparation in the same instrument. A dedicated STEM holder was combined with a Bruker X-Flash 6|60 EDXS detector (MOXTEK AP 3.3 window [Rob03]). Typically, a primary electron energy of 30 keV was used for STEM-EDXS to maximize spatial resolution.
A stable sample-drift correction is critical for STEM-EDXS mapping at high resolution. The experimental setup was optimized by using the signal of the Bruker "Argus" diodes for imaging instead of the standard, segmented STEM 4 detector. The latter is inserted about 40 mm below the pole piece and, therefore, a prominent source of spurious x-rays. In contrast, the Argus diodes are built into a retractable holder commonly used for on-axis diffraction measurements (Bruker Optimus TKD detector). By only partially inserting the Optimus detector, the space below the sample is free from back-scattering materials and the diodes acquire an ADF signal for sample-drift correction (Fig. 3.17b). In this way, spurious signals from the microscope hardware (mainly Cr, Fe, and Ni) could be minimized (Fig. 3.17a).
The Argus diodes only cover a small portion of the scattered electrons compared to a whole annular detector. Still, the signal yield is not a problem in practice due to the high currents typically used for STEM-EDXS in the range of a few nA. In fact, the detector had to be occasionally moved to higher scattering angles to reduce the collected electrons so that the diodes did not saturate (e.g. during mapping at about 25 nA). The diode bias and gain settings are controlled automatically within the *Esprit* software, which reports an error in the case of diode saturation.

Data processing

HyperSpy was mainly used for data processing of EDXS spectrum images. When writing this section, the current package version is 1.6.4. *HyperSpy* has a reader for bcf files and enables more advanced and reproducible data-analysis methods compared to the commercial *Esprit* software. A Jupyter notebook for EDXS analysis was constantly updated during the years of working on this thesis and the latest used version is available [Grü22].
The main goal is the extraction of qualitative elemental maps to analyze the spatial distribution of different elements. The typical steps are (1) pre-processing of the spectrum image, (2) application of MSA (PCA and NMF), (3) extraction of the net peak intensities of different x-ray peaks

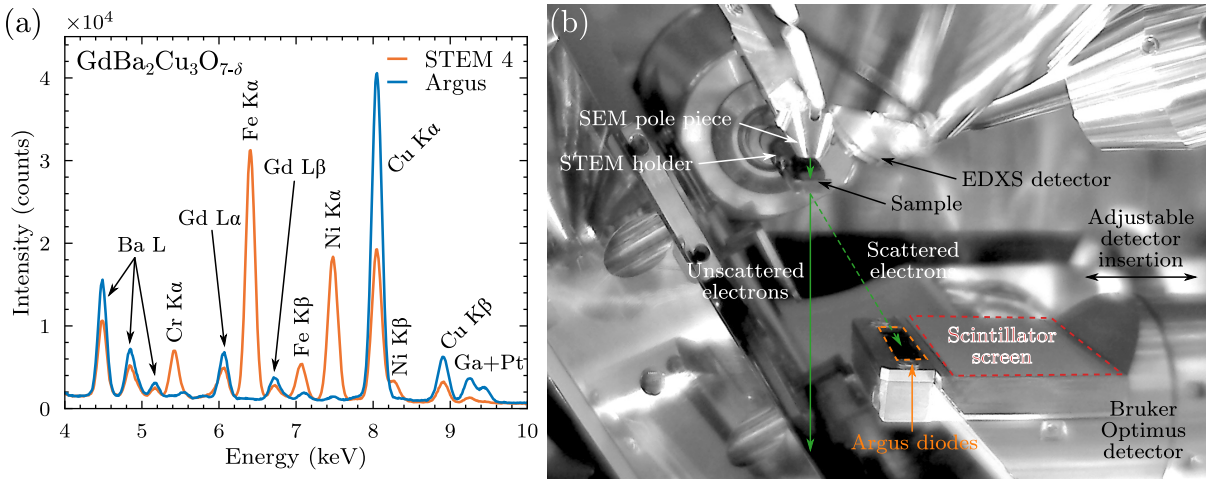

Figure 3.17: Optimized STEM-EDXS setup in the TFS Helios G4 FX. (a) Example EDXS spectra from GdBCO acquired with STEM 4/Argus diodes used for sample-drift correction. System x-ray peaks (sample x-ray peaks) are marked with the font aligned vertically (horizontally). Cu stems partially from the system and the sample. By removing the STEM 4 detector below the sample and instead using the Argus diodes for ADF imaging, the strong system peaks for Cr, Fe, and Ni are clearly reduced. (b) In-chamber CCD image acquired for the STEM-EDXS setup using the Argus diodes for ADF imaging. The Argus diodes collect elastically scattered electrons and the collection angle β can be freely adjusted by moving the whole Bruker Optimus detector.

(at least one for each element of interest) at each spatial position of a spectrum image to form elemental maps:

1. Pre-processing of EDXS spectrum images.
   As a fist step, the spectrum image is loaded into a variable `s`:

```
import hyperspy.api as hs
import numpy as np
s = hs.load('EDXS_dataset.bcf', select_type='spectrum_image')
```

   Then, the average total counts at each pixel $N_{\mathrm{tot/px}}$ of a spectrum image variable s with dimensions $(x, y \mid E)$ was calculated in *HyperSpy* via

```
np.mean(s.sum(-1).data[0])
```

   If $N_{\mathrm{tot/px}} < 200$, a $(2 \times 2, 4 \times 4, \dots)$ rebinning of adjacent pixels was typically applied to increase $N_{\mathrm{tot/px}}$ by a factor of $(4, 16, \dots)$, e.g.:

```
rebin_fac = [2, 2, 1] #x, y, energy
s = s.rebin(scale=rebin_fac)
```

   A drawback of binning is the reduction of spatial resolution by a factor of $(2, 4, \dots)$. Alternatively, the signal-to-noise ratio can be increased by a convolution of the dataset along the spatial (and optionally the energy dimensions) with a Gaussian kernel [PLO17]. Compared to simple binning, a Gaussian kernel retains the spatial resolution while still enhancing the signal-to-noise ratio. However, the "correct" shape of the kernel is hard to set objectively, as the physical signal mixing of adjacent pixels in a spectrum image depends on the probe size, beam broadening in the sample, and the x-ray interaction volumes at different x-ray energies. In addition, the sampling for the EDXS was already chosen at the lower limit to minimize beam damage/maximize the mapped area for a

given (approximated) probe size. For these reasons, simple binning was chosen over Gaussian-kernel filtering.

Another critical step is removing the zero-strobe peak at 0 eV (Fig. 3.18a), because its intensity changes locally in a spectrum image and appears as a periodic fluctuation (Fig. 3.18c–e).

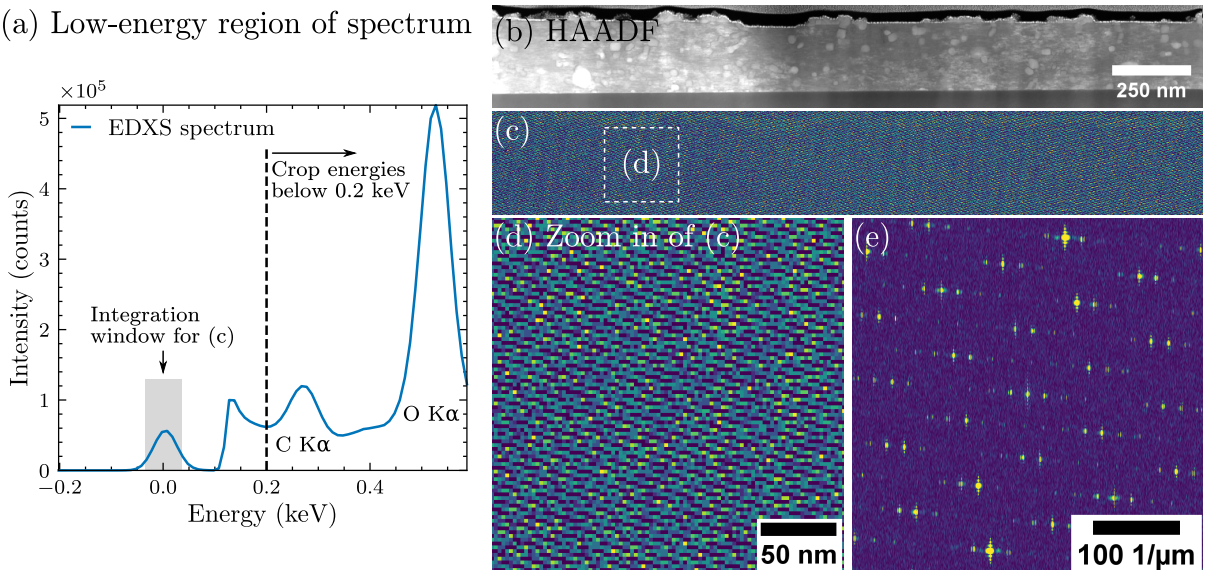

Figure 3.18: Analysis of the zero-strobe peak in EDXS spectra. An exemplary summed spectrum from an ErBCO map is shown. (a) Low-energy region for a typical EDXS spectrum with the zero-strobe peak centered at 0 eV. Energies below 0.2 keV (vertical, dashed line) contain no useful information and are cropped away. (b) HAADF-STEM and (c) zero-strobe-peak map from the integration window in (a) (−35 eV to 35 eV). (d) A periodic pattern in the zero-strobe-peak map is visible in the inset and (e) also as periodic spots in the FT of (c).

PCA/NMF detects the latter as an undesired feature. To remove the zero-strobe peak, the dataset `s` is cropped along the energy dimension via

```
startE = '0.2 keV'
endE = None
s = s.isig[startE:endE]
```

This step can be combined with a truncation of the energy axis above the highest x-ray peak of interest by also specifying an upper bound `endE` to reduce the size of the dataset to speed up any following computation. Finally, the data format of the x-ray counts (integer) are transformed to floating point numbers for the MSA calculations:

```
s.change_dtype('float')
```

2. Application of PCA and NMF.
   PCA is calculated first to inspect the scree plot and to determine the size of output dimensions for dimensionality reduction and NMF. The EDXS spectrum image is scaled to account for Poissonian noise [KK04] and PCA is calculated using the default "singular value decomposition" method:

```
s.decomposition(normalize_poissonian_noise=True)
```

Then, the scree plot, the score maps and the loadings are inspected simultaneously to find the number of principal components k containing most of the signal:

```
s.plot_decomposition_results() #Close windows after inspection
s.plot_explained_variance_ratio(vline=True) #Close windows after inspection
```

The denoised dataset is generated (and saved) by reconstructing with k principal components:

```
PCA_filtered = s.get_decomposition_model(k)
PCA_filtered.save(f'PCA_filtered_{k}.hdf5')
```

This file is used for signal extraction of x-ray-line intensities. With k output dimensions, the dataset can also be decomposed by NMF:

```
s.decomposition(normalize_poissonian_noise=True, algorithm='NMF',
                                        output_dimension=k, max_iter=2000)
```

Without any further specification, *HyperSpy* uses the default NMF algorithm of *scikit-learn* (version 0.24.2 at the time of writing), i.e. Frobenius norm as loss function and a coordinate descent solver. The maximum possible iterations `max_iter` were increased from the default 200 to 2000 to ensure the tolerance value (1×10^{-4}) is reached during calculations. After the calculation, the NMF results can be inspected using `s.plot_decomposition_results()` and saved in various formats. It is useful to save the loadings as "EMSA/MSA" (.msa) spectrum files for easy inspection and comparison in *DTSA-II* or *Esprit*.

3. Extraction of the net peak intensities.
   The background-corrected net x-ray-peak intensities are extracted at each (x, y) position to generate elemental maps. Typically, two situations can occur where (i) peaks are clearly separated and (ii) peaks are overlapping due to the finite energy resolution in EDXS. The latter is nearly always the case for x-ray transitions in the low-energy region below 2 keV. However, peak overlaps can also occur at higher energies depending on the sample composition.
   A simple energy integration-window and linear fit of the background underneath a peak is used for clearly separated peaks. The width of the integration window (`iw`) was set to $1.2 \times \mathrm{FWHM}(E)$ [WW99a; FL06], with the energy-dependent FWHM of the corresponding x-ray peak. The background is calculated by first specifying peak-free energy regions ("background windows", `bw`) on both sides of a peak. Then, the average background intensity values (I_{left}, I_{right}) are calculated for both background windows. Finally, a linear background is modeled by a line, which runs through (I_{left}, I_{right}) as vertical coordinates and the center of the background windows as the horizontal coordinates. The described steps are handled mostly automatically by *HyperSpy* methods:

```
bw = PCA_filtered.estimate_background_windows(line_width=[1.2, 1.2],
                                        windows_width=0.6)
iw =  PCA_filtered.estimate_integration_windows(windows_width=1.2) #1.2*
                                        FWHM
```

Afterward, the summed spectrum from all beam positions is plotted to check the window placements by using

```
PCA_filtered.sum().plot(True, background_windows=bw, integration_windows=iw
                                        )
```

Often, slight tuning of the `bw` values is necessary to place the background windows to peak-free regions. When all is set, the net peak intensities can be extracted using

```
PCA_filtered.get_lines_intensity(background_windows=bw, integration_windows
                                 =iw)
```

and the resulting elemental maps can be saved.
Gaussian-peak fitting was used for separation in combination with a background model for overlapping peaks. The latter was mainly modeled by a simple linear function $a_1 \cdot E + a_2$ with the fit parameters a_1 and a_2, which works well for (i) thin samples in STEM-EDXS and energies above 2 keV or (ii) narrow energy windows where the background is approximately linear over the whole fitting range. The first step is to crop the spectrum image along the energy direction to a peak-overlap region between `E1` and `E2`:

```
PCA_fit = PCA_filtered.deepcopy() #create a copy
PCA_fit = PCA_fit.isig[E1:E2] #crop to overlap region
```

This reduces the computation time compared to fitting the whole spectrum. If possible, the energy interval (`E1`, `E2`) should be wide enough to include multiple peaks of an x-ray line family to improve fitting.
In the next step, all expected/possible elements in a sample (as determined by experience or by inspection of the derived sum spectrum) are added to the variable `PCA_fit`. Spurious elements from the TEM holder, TEM grid, and microscope hardware should also be included:

```
PCA_fit.set_elements([]) #clear element list
PCA_fit.set_microscope_parameters(beam_energy = PCA_fit.axes_manager[-1].
                                  high_value) #same as E2
#Example for a GdBa2Cu3O7 sample with BaHfO3 nanoparticles
PCA_fit.add_elements(['Gd', 'Ba', 'Cu', 'O', 'Hf']) #sample x-rays
PCA_fit.add_elements(['Al', 'C', 'Cu', 'Si', 'Ni', 'Pt', 'Zn', 'Zr']) #
                                  spurious x-rays
```

The list of possible spurious x-rays is microscope dependent and can be checked e.g. with a (thick) reference sample that causes a lot of scattering and thereby spurious x-rays. Then a model `m` is created using

```
m = PCA_fit.create_model(auto_background=False)
m.add_polynomial_background(order=1) #for linearly falling/rising
                                  background
```

HyperSpy will automatically add a Gaussian peak for each possible x-ray transition in the energy interval (`E1`, `E2`) and the given element list. The peak-fitting method in EDXS can be applied to solve peak overlaps of only a few eV because some parameters are fixed or bounded because of physical knowledge about the x-ray peaks: (i) The energy positions are known and fixed[14], (ii) the energy-dependent width of the x-ray peaks is known from the detector energy resolution, and (iii) the emission-rate ratio (or line weights) in an x-ray family are known quite well for most transitions (K–L and L–M), especially at higher energies. To address aspect (ii), the following formula [Gol+18, p 210] is used to set (and

[14] Chemical shifts can be observed for low-energy transitions using EDXS.

fix) the FWHM of the Gaussian functions:

$$\mathrm{FWHM}(E) = \sqrt{2.5(E - E_{\mathrm{ref}}) + \mathrm{FWHM}_{\mathrm{ref}}^2} \quad , \tag{3.3}$$

with E being the energy of interest and E_{ref}/$\mathrm{FWHM}_{\mathrm{ref}}$ (all values in eV) the energy and FWHM of a reference peak (typically Mn Kα at around 5.9 keV). For example, FWHM(O Kα) $\approx$ 59 eV at E(O Kα) = 525 eV and a typically value of $\mathrm{FWHM}_{\mathrm{ref,Mn\ K}\alpha}$ = 130 eV. Aspect (iii) is exploited during fitting by fixing the amplitude ratio of the x-ray transitions within an x-ray family with the known line weights and fitting the whole x-ray-line family. The only free fit parameter is the amplitude of the Gaussian corresponding to the strongest line in an x-ray-line family. In this way, a Kβ peak can limit the height of the corresponding Kα peak and *vice versa*, because their amplitude ratio is fixed (e.g. Cu Kα_1/Cu Kβ_1 $\approx$ 1/0.14). Essentially, the intensities of a whole x-ray-line family are scaled simultaneously during fitting. *HyperSpy* uses the openly available tabulated x-ray energies and line weights from NIST's "Electron Probe Quantification" (EPQ) library [Rit07][15]. All x-ray-line families and the background are fitted simultaneously to the spectrum region by MLLS fitting.
In actual practice, the model is tested on a single (or a few) representative positions (`xr`, `yr`).

```
m.plot(True) #Plot the SI, model and initial Gaussians
m.axes_manager.indices = (xr, yr) #Move to representative position
m.fit(bounded=True, return_info=False) #Do test fit on current position
```

The fitted model should match the spectrum. If any peaks are not (well) described by the model, an x-ray transition is probably missing and should be added. When the fit at position (`xr`, `yr`) looks fine, the fitted values can be set as starting values for all other positions to speed up fitting and the fit can be performed on each position using `multifit`:

```
m.assign_current_values_to_all()
m.multifit(optimizer="lm", bounded=True, iterpath="serpentine",
                                        show_progressbar=True) # May take a
                                         long time.
```

After `multifit` is completed, the amplitude of the Gaussians for the desired x-ray transitions can be extracted:

```
#Example for Cu_Ka-Hf_La overlap
e = ['Cu_Ka', 'Hf_La'] #Specify x-ray transitions of interest
mI = m.get_lines_intensity(sorted(e)) #Get amplitude parameter of Gaussians
```

The elemental maps are stored in `mI` and can be saved in various formats for display.

Quantification in Bruker *Esprit*. Selected EDXS spectra were quantified using the Bruker *Esprit* 2.1 software to get insights into a sample's local composition in atomic percent (at. %). Standardless quantification using the Cliff-Lorimer approach was used in all cases, i.e. theoretically calculated Cliff-Lorimer factors from a single Cu standard. Absorption correction was applied in cases, where the sample thickness and density is roughly known. The concentration in standardless quantification was always normalized to 100 at. %. Elemental ratios between

[15] See, e.g., "LineWeights.csv" at `https://github.com/usnistgov/EPQ/tree/master/src/gov/nist/microanalysis/EPQLibrary` (last accessed: 15/09/2021)

different elements were calculated from the quantified concentrations. It should be noted that standardless quantification can be prone to significant errors compared to quantification with known standards. This means that *absolute* concentration values inherit these significant errors. Still, a *relative* comparison of different samples or sample regions is possible with standardless quantification.
Unprocessed EDXS spectrum images typically only contain few x-ray counts per beam position and the quantification on single (or even binned) pixel level has large quantification errors due to low count statistics. In a PCA-treated dataset, the signal-to-noise ratio is increased, which is tempting for quantification on a single-pixel level for a spectrum image. However, PCA denoising can affect quantification results and requires careful analysis [KKvH12; Mor+22]. Likewise, NMF loadings were also not used for quantitative chemical analysis because "quantification requires users to exercise the highest caution and they need to experiment with multiple methods to crosscheck the consistency and physical plausibility of the solution" [MS20]. Therefore, quantification was only performed on raw data in this work.
So-called "derived" spectra were quantified [NB06] to get sufficient signal for quantification. A derived spectrum is formed by, e.g., summing specific regions from a single chemical phase. *Esprit* offers the functionality of drawing geometric shapes onto the spectrum image, thereby selecting the desired regions to sum for a derived spectrum. However, for multi-phase samples, this approach is tedious and quickly introduces errors and bias by the user. Instead, derived spectra were calculated by first applying a threshold to an elemental or NMF score map. The resulting binary masks can be used for masking the desired regions in a spectrum image from which all x-ray counts are summed (so-called "masked sum spectra" [NB06]). The procedure is schematically shown in Fig. 3.19 and the following steps were used:

1. Thresholding of an elemental map/NMF score map reflecting the spatial distribution of the desired chemical phase (Fig. 3.19b,c).
   A saved map (typically in tiff file format) is loaded into *Fiji* and the "Graph Cut" plugin [BK04] is used to find a suitable threshold by adjusting the `Foreground bias` and `Smoothness` parameters. The thresholded binary image may need to be inverted (`Edit → Invert`), so that the regions corresponding to the chemical phase appear white with value 255 in an 8-bit image. The other regions have a value of 0. The binary 8-bit image was then saved as a tiff file.
   For some spectrum images, it was necessary to combine (add/subtract) different binary masks to isolate the desired region (using `Process → Image Calculator...`).

2. Application of the mask to the spectrum image and extraction of the derived spectrum (Fig. 3.19d).
   A Jupyter notebook [Grü22] based on *HyperSpy* was used to first load the original spectrum image (bcf file) and the prepared binary mask (tiff file):

   ```
   import hyperspy.api as hs
   import numpy as np
   s = hs.load('EDXS_dataset.bcf', select_type='spectrum_image')
   mask = hs.load('8-bit-mask.tif')
   ```

   The spatial dimension of the spectrum image and the binary image must match (by comparing `np.shape(s)` and `np.shape(mask)`), so binning may need to be applied to the spectrum image if this was used for extracting the elemental maps in a previous step. Then, the mask is normalized to the range $[0, 1]$ by dividing the mask by 255 (the maximum value):

```
mask = mask/np.max(mask.data)
```

The mask is then multiplied with `s` and the spectra from the masked regions are summed and saved as a EMSA/MAS spectrum file.

```
spec = (s * mask.T).sum() #transpose mask to navigation dimension
spec.save('DerivedSpectrum.msa')
```

3. Import in *Esprit* and parameter adjustment.
   The saved .msa file can be opened by *Esprit*. However, some metadata must be set to allow for quantification in the software. The relevant menu (`Spectrum Properties`) can be accessed by double-clicking the spectrum name. Some parameters (e.g. detector-window layers, take-off angle, ...) must be added to the `Detector`, `Parameters`, and `Spectrum` tabs. The parameters can be read from a single Bruker spectrum (spx file) obtained under the same experimental conditions. To get the spx file with the relevant information, the bcf-spectrum-image file is loaded into *Esprit* and a single (or derived) spectrum is directly saved from *Esprit* as an .spx file. The .spx file can be opened in *Esprit* together with the .msa file and the parameters in the `Spectrum Properties` menu can be matched. The detector info can be saved from the .spx file as a detector file (.det) and loaded for any other .msa files.
   As a side note, "artificial" spectra such as NMF loadings or simulated EDXS spectra from *DTSA-II* can be quantified in the same way in *Esprit*.

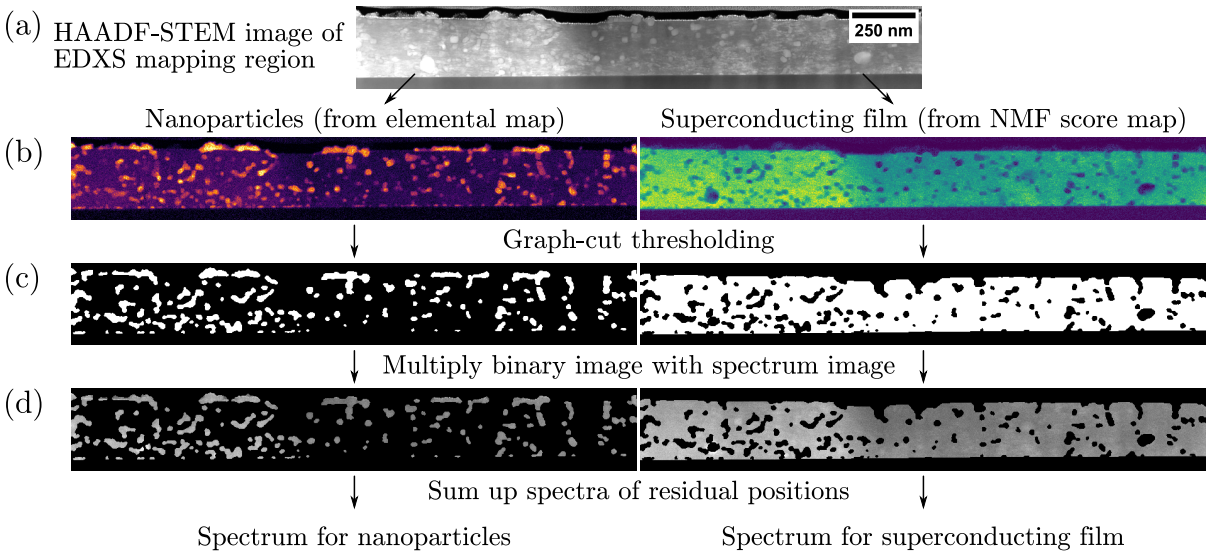

Figure 3.19: Extraction of derived spectra from different chemical phases from a raw EDXS spectrum image. The example shows a STEM-EDXS dataset for an ErBCO film with BHO nanoparticles. (a) HAADF-STEM image of the ROI. (b) The chosen signals for the chemical phases of nanoparticles (left) and the superconducting film (right) were an elemental map for Hf and a NMF score map, respectively. (c) Graph-cut thresholding leads to binary images which (d) are multiplied with the original spectrum image. The derived spectrum is then created by summing all residual positions.

3.5 Other Methods

This paragraph explains the additional methods used in this work.

General image processing. *Fiji* [Sch+12] and DM were used for general image processing and analysis. The images and elemental maps shown in this work were optimized regarding contrast/brightness for qualitative display. Care was taken to avoid any image modifications, which could alter experimental results or the interpretation of images [MN21]. For quantitative analysis of gray values, images were not filtered whenever possible or the effects of image filtering were thoroughly checked for possible introduced bias.

Particle-size analysis. Particle-size analysis was used to approximate the average size of precipitates and nanoparticles. Many manually or automatically labeled particles are desired for good statistics. The *Trainable WEKA Segmentation* (TWS) plugin for *Fiji* was used for supervised image segmentation of SEM images [Arg+17] by decision-tree-based pixel classification. The plugin is based on the "Waikato Environment for Knowledge Analysis" (WEKA) [Hal+09] suite and adapted for pixel classification. The general workflow is:

1. Loading of a training image.
2. Definition of the desired classes (e.g. "thin film" and "precipitate")
3. Labeling a few regions corresponding to the respective classes (ground-truth labels).
4. Choosing a set of ordinary image filters (e.g., Gaussian blur, Sobel filter, ...) and parameters to generate an image-feature stack.
5. Running the WEKA classification and inspecting the results. The standard "FastRandomForest" classifier was used with 200 trees with two random features per node. Typically, the results are tuned further by repeating step (3) and continue labeling a few falsely assigned regions. The segmentation improves with each iteration.
6. Once the classifiers are trained, they can be applied to other images acquired under the same conditions, resulting in robust, automatic segmentation.

The final outputs by TWS are "probability maps", which give each pixel a probability (between 0 and 1) for belonging to each of the pre-defined classes.
The choice of image filters, ground-truth labeling for training, and batch processing for the segmentation of surface precipitates in IBS were optimized by **Daniel Nerz** in his Bachelor thesis. Typically, an Otsu threshold [Ots79] was applied to the probability maps. A suitable automatic threshold such as the Otsu method is helpful for batch processing without user interaction. The resulting binary images after thresholding were cleaned up by morphological operations such as erosion and dilation and combinations of the two ("opening" and "closing" operations). The default watershed algorithm in *Fiji* was used to separate touching/overlapping objects. Then size analysis was run using the `Analyze → Analyze Particles...` menu in *Fiji*. Similar to the TWS plugin, the *LABKIT* plugin [Arz+22] was also used for a similar analysis. In addition, manual labeling was also done on selected images using *LABKIT*.
The measured particle or precipitate sizes were evaluated using Python via Jupyter notebooks [Grü22]. The area-equivalent diameter d_e was used as a size metric, which assumes a circle with the same area as the measured projected particle or precipitate areas A_p from SEM or STEM images, i.e. $d_e = \sqrt{4A_p/\pi}$. A Gaussian or log-normal distribution is typically fitted to a histogram of the extracted particle-size distribution as function of, e.g., the equivalent diameter

d_e. Following the suggestion by Limpert et al. [LSA01], the log-normal distribution is often more favorable for particle-size analysis than the Gaussian distribution. Therefore, it was primarily used throughout this work. A log-normal distribution of the form [LSA01]

$$f(x) = \frac{1}{\sqrt{2\pi}\sigma x} \exp\left(-\frac{(\ln(x)-\mu)^2}{2\sigma^2}\right) \quad \text{with} \quad x > 0 \tag{3.4}$$

with the mean μ and standard deviation σ of $\ln(x)$ used as the fit parameters was fitted to a normalized histogram. The arithmetic mean μ_x and arithmetic standard deviation σ_x of x can be calculated via

$$\mu_x = e^{\mu+\frac{\sigma^2}{2}} \tag{3.5}$$

$$\sigma_x = e^{\mu+\frac{\sigma^2}{2}} \sqrt{e^{\sigma^2}-1} \quad . \tag{3.6}$$

The values of μ_x and σ_x are used in this work to describe the particle size. The mode M is the maximum of the distribution (highest probability) and located at

$$M = e^{\mu-\sigma^2} \quad . \tag{3.7}$$

Error calculations. For the calculated mean value $\overline{x}$ of n values without errors, the arithmetic mean was calculated via

$$\overline{x} = \frac{\sum_{i=1}^{n} x_i}{n} \tag{3.8}$$

with the sample standard deviation

$$\sigma_x = \sqrt{\frac{1}{n-1}\sum_{i=1}^{n}(x_i-\overline{x})^2} \quad . \tag{3.9}$$

The latter is implemented in `numpy` as:

```
import numpy as np
sigma_x = np.std(value_array, ddof = 1) #ddof for Bessel's correction
```

The standard error on $\overline{x}$, $\sigma_{\overline{x}}$, is then given by $\sigma_{\overline{x}} \approx \sigma_x/\sqrt{n}$. If each value x_i has a known error, then the weighted mean $\overline{x}_w$ and the error on the weighted mean $\sigma_{\overline{x}_w}$ were calculated by

$$\overline{x}_w = \frac{\sum_{i=1}^{n} w_i x_i}{\sum_{i=1}^{n} w_i} \quad , \quad \sigma_{\overline{x}_w} = \left(\sum_{i=1}^{n} w_i\right)^{-\frac{1}{2}} \quad , \tag{3.10}$$

with the weights typically given by the standard deviation of each value, i.e. $w_i = \sigma_i^{-2}$. Error propagation was done using the *uncertainties* python package [Leb]. Errors are often reported as one standard deviation σ, e.g. by *Esprit* or *Atomap*.

Visualizations. Images and plots in this thesis were created with various software tools. The vector graphics program *Inkscape* (`https://inkscape.org/`, last accessed 12.09.2021) was used to create figure layouts for plots and images, and to add annotations. The *TexText* plugin (`https://github.com/textext/textext`, last accessed 12.09.2021) was used for LaTeX annotations.

Plots were created with the *matplotlib* [Hun07] and *scienceplots* [Gar21] Python packages. Most spectra were plotted in Python using *Hyperspy*. *DigitalMicrograph*, *scikit-image* [vdWal+14], and *Fiji* were used for general image processing. Scale-bar annotations were added with the *matplotlib-scalebar* Python package (`https://github.com/ppinard/matplotlib-scalebar`, last accessed 12.09.2021) or self-written *Fiji* macros (`https://github.com/lukmuk/em-scalebartools`, last accessed 12.09.2021). Atomic structures were visualized with *VESTA* [MI11]. Rasterized images were saved as png image files and compressed using *OPTIpng* (`http://optipng.sourceforge.net/`, last accessed 27.03.2022). All shown figures were prepared as pdf vector-graphic files and compressed with *ghostscript* (`https://www.ghostscript.com/`, last accessed 27.03.2022).

Computer hardware. All calculations in this work were run on a desktop computer running Windows 10 equipped with a Intel Core i3570K (4 cores/4 threads, 3.4 GHz to 3.8 GHz), 32 GB DDR3 RAM clocked at 1600 MHz, and a NVIDIA GeForce GTX 1650 graphics card (GPU) with 4 GB of memory. For MSA, 32 GB RAM are recommended to process typical dataset sizes in EDXS/EELS shown in this work.

4. Structural and Chemical Properties of $Ba(Fe,Co)_2As_2$ Thin Films

This chapter describes the microstructural and chemical properties of $Ba(Fe_{0.92}Co_{0.08})_2As_2$ (Ba122) thin films. The first section summarizes practical problems and commonly observed artifacts in the presented (S)TEM analyses. Section two (Page 101) shows the influence of the PLD growth rate on the Ba122 microstructure on CaF_2 substrates. The results of this section were published in an article [Grü+21a] and reproduced figures are mentioned in the figure captions. Next, the results of Ba122-nanoparticle nanocomposites grown by multilayer PLD are presented in the third section (Page 124). The last section shows results for Ba122 films grown on MgO and $LaAlO_3$ (Page 143). A brief literature overview is given in each section.

4.1 Experimental Problems and Solutions

This section presents practical problems and artifacts related to FIB preparation of TEM samples and (S)TEM investigations of Ba122 films. Most investigated Ba122 films were grown on CaF_2, for which reactions under electron-beam irradiation are known [CJW76; Jia12; Jia16]. Possible sources of electron-beam induced damage of Ba122 on CaF_2 are summarized in Fig. 4.1 [Grü+21a]. Artifacts can be introduced during FIB preparation of TEM samples (Fig. 4.1a), conventional (S)TEM imaging (Fig. 4.1b), and high-dose STEM-based spectroscopy (EDXS and EELS, Fig. 4.1c).

FIB preparation. FIB-irradiation-induced damage of the shown Ba122 film is observed for thin sample regions (Fig. 4.1a). The TEM-sample thickness here is probably below 50 nm. The cross-section LAADF-STEM images display two sample regions simultaneously milled under the same FIB conditions (2 keV, about 20 pA FIB current). The left image was taken near the center of the electron-transparent region with the smallest TEM-sample thickness. In contrast, the right image was taken near the edge of the same electron-transparent region, which is typically slightly thicker than the central region. The difference in TEM-sample thickness can also be qualitatively seen by comparing the protective EBID Pt/C layer thickness on top of the film. The thicker region (right) still has a thicker protective layer, indicating less FIB milling and, therefore, a thicker sample region than in the left image. The FIB-induced damage is located at the film-substrate interface (marked by red dashed lines in Fig. 4.1a) and shows a reduced LAADF-STEM intensity compared to the undamaged Ba122 film. This may be explained by the amorphization of Ba122 by FIB milling. The reduced Bragg scattering from amorphous regions leads to a decrease in signal on the LAADF-STEM detector. In contrast, the right

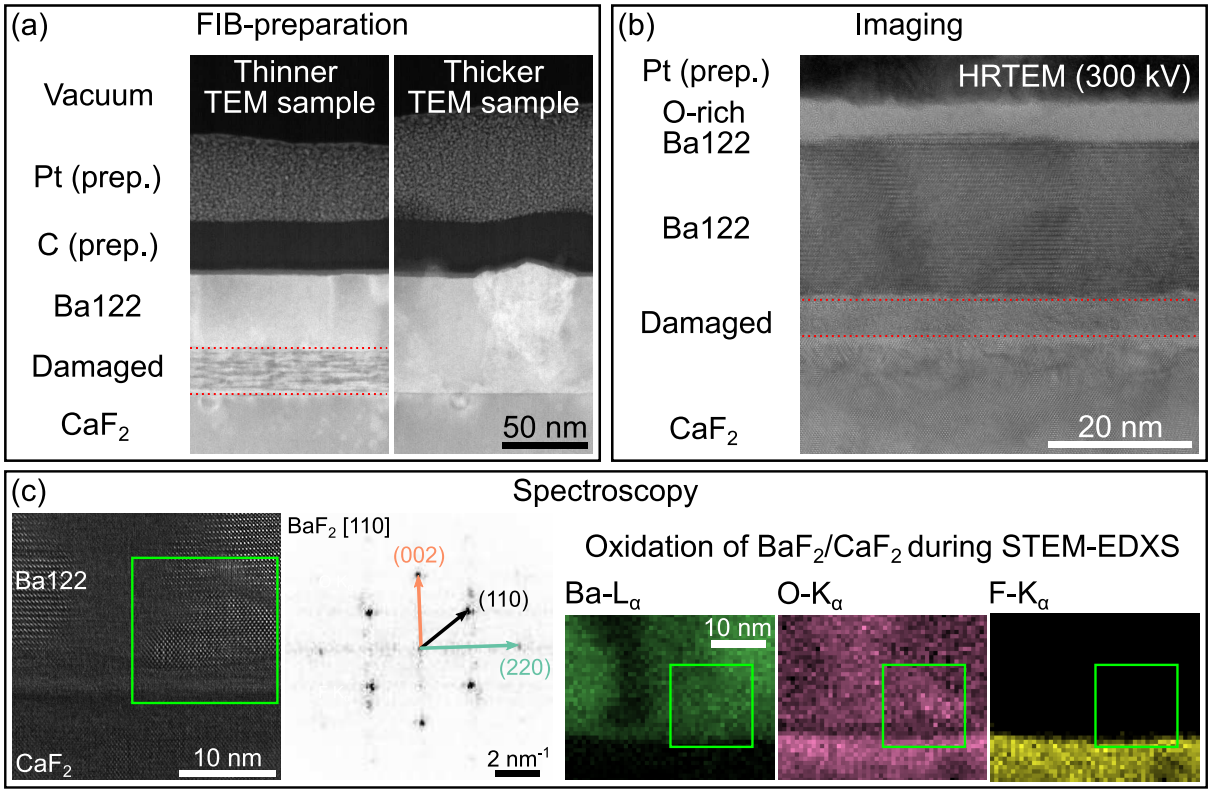

Figure 4.1: Overview of possible FIB- and electron-beam-induced irradiation damage in the Ba122-CaF_2 system. (a) Extensive FIB milling and (b) high-dose (S)TEM imaging can lead to destruction and amorphization of Ba122 close to the Ba122-CaF_2 interface (marked by red dashed lines). (c) CaF_2 and BaF_2 are oxidized during dose-intensive STEM-EDXS or STEM-EELS measurements. The secondary phase is identified as BaF_2 but no F signal but instead, an O signal is detected after a STEM-EDXS mapping. This figure is published [Grü+21a].

image does not show such an amorphous Ba122 region at the film-substrate interface. This result demonstrates that FIB milling can lead to an amorphization of Ba122 on CaF_2. The film-substrate interface is especially susceptible to FIB-induced amorphization, which is also observed during electron-beam irradiation (Fig. 4.1b). The final Ga^+ energies used here were 2 keV. Smaller Ga^+ energies or less damaging ion species such as Ar^+ may be needed to prepare artifact-free TEM samples with thicknesses below 50 nm. This was not investigated here. Still, TEM samples with thicknesses of roughly 50 nm to 120 nm could be prepared by FIB without obvious FIB-induced artifacts.

STEM-EDXS/EELS spectroscopy. *In-situ* oxidation of CaF_2 and BaF_2 (the latter forming as a secondary phase) was observed in dose-intensive STEM-EDXS and -EELS measurements (Fig. 4.1c). The HAADF-STEM cross-section image (left) of a precipitate near the Ba122-CaF_2 is identified as BaF_2 by Fourier-transform analysis. However, STEM-EDXS spectroscopy of the same precipitate does not show a F signal, but instead an enhanced O signal in the precipitate region (marked by a green square in all images in Fig. 4.1c). An oxidation of BaF_2 under electron-beam irradiation [Jia12; Nik+12] can explain this observation. The O may stem (i) from residual O-containing molecules in the microscope vacuum, (ii) from an O contamination of the PLD target material [Pak+20], or (iii) from the transport of the TEM sample between the FIB and TEM instruments (about 20 min exposure to air or transport in a slightly evacuated bag). Clearly, any STEM-EDXS and STEM-EELS results must be interpreted carefully for the Ba122-CaF_2 system regarding O and F. Tarantini et al. [Tar+14] show elemental maps

obtained from dose-intensive EFTEM measurements, where the Ba122-CaF_2 interface and the CaF_2 show a clear O signal. As noted by the same authors, "no fluorine was detected either in the film or in the top part of the substrate (the absence of fluorine in the substrate was verified down to at least 500 nm below the interface)" [Tar+14]. This shows that F can be fully removed from CaF_2 under intense electron-beam irradiation, resulting in CaO and metallic Ca [Jia12; Nik+12]. These findings may also be transferred to other IBS films than Ba122 or the 122 family. For example, Haindl et al. [Hai+19] reported similar electron-beam-induced artifacts in STEM-EDXS results for $SmO_{1-x}F_xFeAs$ films on CaF_2.

STEM and TEM imaging. Like FIB-induced damage, electron-beam irradiation also leads to the rapid amorphization of Ba122, preferentially at the film-substrate interface (Fig. 4.1b). The presented HRTEM image was acquired at 300 keV with a relatively high electron dose (not measured), which is typically used in materials science ($> 1000\,e/Å^2$). Electron-beam irradiation leads to the formation of an amorphous Ba122 layer at the film-substrate interface similar to FIB irradiation (marked by a red dashed line in Fig. 4.1b). Note that the amorphous, O-rich Ba122 surface layer is *not* induced by electron-beam irradiation or FIB milling but instead forms due to oxidation of Ba122 during sample storage. *In-situ* experiments using controlled STEM and TEM imaging of previously undamaged Ba122 regions (cf. the video "Irradiation-damage-Ba122-STEM" [Grü+20b]) verify that the amorphous Ba122 at the film-substrate interface forms under electron-beam irradiation in the investigated Ba122 films. Electron-beam irradiation of the Ba122-CaF_2 interface leads to the amorphization of Ba122 and an expansion of the Ba122 film in *c*-direction. The thickness of the amorphous surface layer can vary. For example, the video "Prolonged_Irradiation_200s_TEM_BrightField" [Grü+20b] shows a uniform thickness of the amorphous Ba122 layer under prolonged irradiation (200 s) in TEM mode (parallel beam). However, full destruction of the crystalline Ba122 was also observed for other TEM samples of Ba122 on CaF_2 (an example is shown in Fig. 4.3c-e). The formation of an amorphous Ba122 layer at the Ba122-CaF_2 interface can be mitigated mainly by minimizing the electron-beam exposure. Typical HAADF-STEM imaging conditions in this work used beam currents in the range of approximately 2 pA to 20 pA. However, this could not be measured accurately on the microscope screen's beam-current read-out[1] and was approximated by the values measured by Krause et al. [Kra+16] for the same microscope and STEM settings (spot size values 8 to 10). The exact beam current depends on the excitation of the monochromator focus (or gun lens). The amorphous Ba122 layer can already form during sample screening at lower magnifications without noticing by the TEM operator. In practice, all electron-beam alignments should be performed with care on adjacent sample regions and with minimal (or better no) exposure of the Ba122 layer. Another possibility may be sample cooling with liquid N_2 to reduce electron-beam-induced damage, which was not tested here.

The amorphous interface layer in the investigated Ba122 films on CaF_2 all resulted from FIB- or electron-beam-induced destruction of Ba122 at the film-substrate interface. In the literature, amorphous interface layers similar to the ones observed here were reported for the Ba122-CaF_2 system [Kur+13b; Ich+14b; Ric+17; Xu+19]. These were often interpreted as a reaction layer between Ba122 and CaF_2, which was assumed to have formed during (or after) film deposition. This is in contrast to the findings here, where the reaction layer is purely a measurement artifact. The shown damage mechanism for Ba122 on CaF_2 may be extended to other IBS-substrate combinations. Since other fluoride substrates such as BaF_2 and SrF_2 are similar

[1] The current meter on the *Fluscreen* directly dropped to 0 pA read out below an indicated beam current of about 50 pA.

to CaF_2 regarding electron-beam stability [Nik+12], amorphous interface layers of IBS-AF_2 combinations (A = Ba, Ca, Sr) may also be generated by FIB- or electron-beam-induced damage. For example, amorphous interface layers on CaF_2 were also reported for other IBS, such as Fe(Se, Te) [Bra+13; Ich+14a]. However, Fe(Se, Te) on CaF_2 can also form crystalline interface layers [Ich+13; Tsu+16], e.g. CaSe [Qiu+17]. The crystalline interface layers are probably present in the as-deposited Fe(Se, Te) films. If possible, dedicated experiments using low-dose (S)TEM imaging should be carried out for all IBS grown on fluoride substrates to rule out artifacts by (S)TEM imaging.

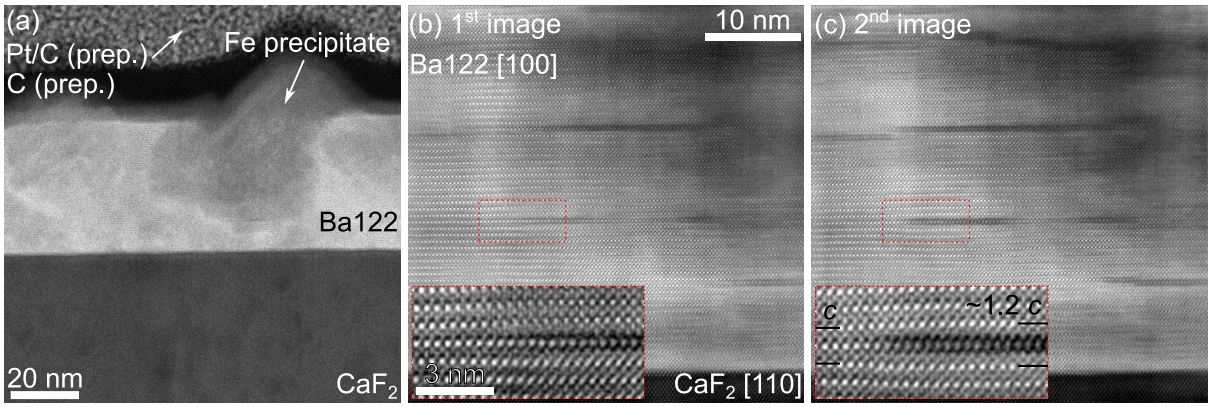

Figure 4.2: *In-situ* planar-defect generation in Ba122 by STEM imaging. (a) Overview HAADF-STEM image of an undamaged Ba122 film containing an Fe precipitate. (b) High-resolution HAADF-STEM image acquired at higher magnification. Planar defects appear with reduced HAADF-STEM intensity. The inset shows a magnified view of one of the defects. (c) Second exposure of the same sample region. The planar defects extend in the in-plane direction. This figure is published [Grü+21a].

Besides damage of the film-substrate interface, planar defects can be generated by electron-beam irradiation in Ba122 (Fig. 4.2). Figure 4.2a presents an overview HAADF-STEM cross-section image of a Ba122 layer on CaF_2. The formation of planar defects is observed after repeated STEM-image acquisition of the same region (cf. Fig. 4.2b and c). The defects appear as dark horizontal lines and grow in the *ab*-plane. The insets show a selected planar defect (marked with a red dashed rectangle) and the change in the Ba122 microstructure. The Ba122 unit cell at such a planar defect extends by about 20 % in *c*-direction and the Z-contrast of the brightest Ba atomic columns decreases significantly compared to the surrounding Ba columns in undamaged Ba122. The same effect was reported by Thersleff et al. [The+11][2] for Ba122 on Fe-buffered oxide substrates. This shows that these electron-beam-induced planar defects are intrinsic to Ba122 and do not depend on the substrate. However, these defects can also be present in the as-deposited films or in single-crystal bulk samples, as reported by Zheng et al. [Zhe+19].

So far, defect formation was only discussed for an electron energy of 300 keV. As a next step, defect formation was also evaluated for other electron energies (200 keV, Fig. 4.3, and 80 keV). The experiments at 200 keV were conducted in a Philips CM200 transmission electron microscope. Figure 4.3a shows a $\sim$ 20 nm thin Ba122 film grown on LAO with a large Fe-rich precipitate in the center. An amorphous film-substrate interface is visible with a bright appearance. The visible lattice fringes in this amorphous layer result from contrast delocalization (resulting from defocus and a finite C_s = 1.2 mm) from the surrounding crystalline Ba122 (upper) and LAO (lower) regions. The Ba122 is entirely destroyed and amorphous after a few seconds of exposure with the

[2]The poster is available at `http://urn.kb.se/resolve?urn=urn:nbn:se:uu:diva-165364` (last accessed: 21.03.2022).

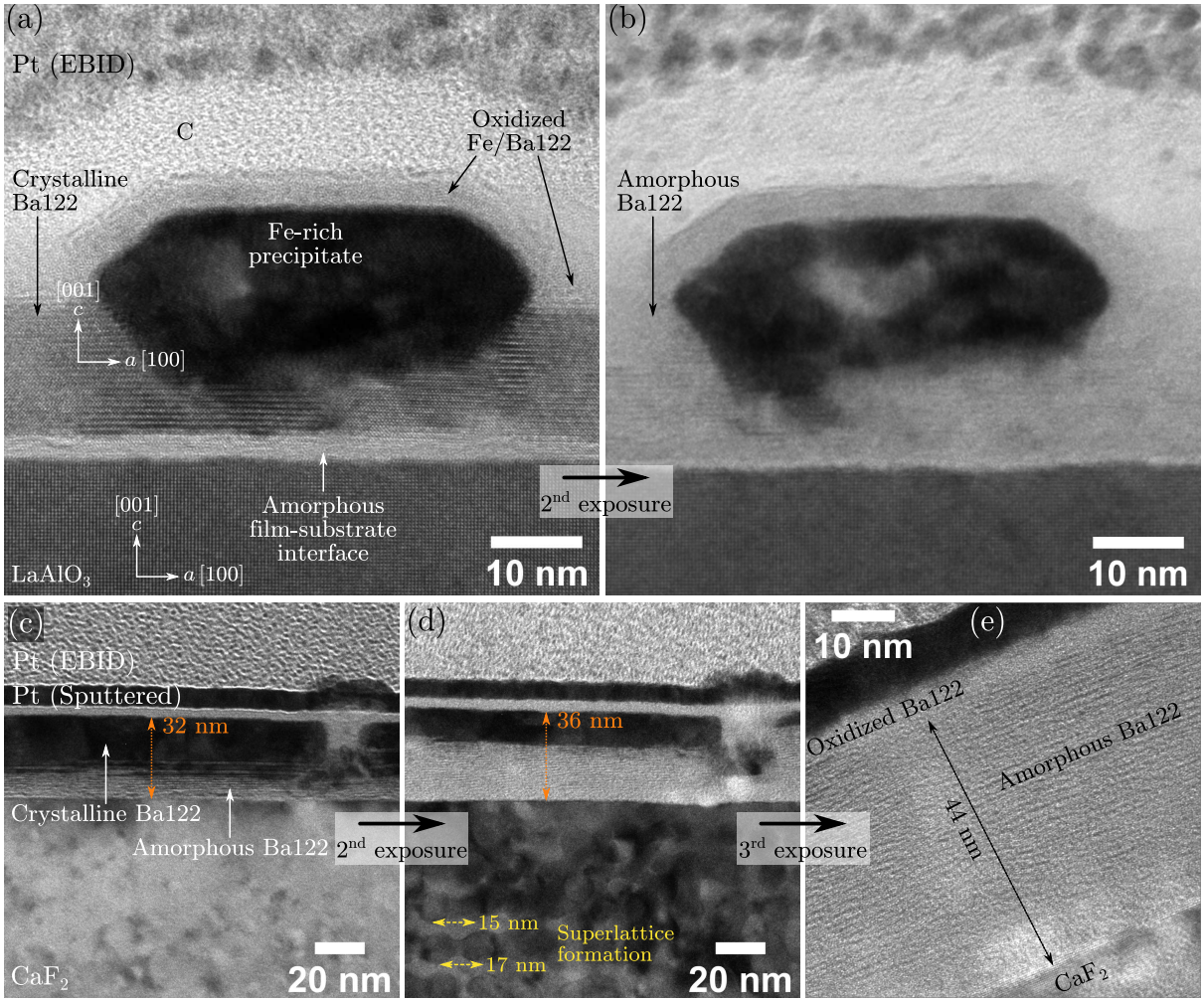

Figure 4.3: Electron-beam-irradiation damage at $E_0 = 200$ keV. The TEM images show the rapid degradation of Ba122 on LAO (top row) and CaF_2 (bottom row) for high electron doses. (a and b) Successive exposures (with some beam alignments in-between) of Ba122 on LAO with a large Fe-rich precipitate in the center. The Ba122 layer is completely amorphous after the second exposure. The film-substrate interface is already amorphous in (a). Lattice fringes are partly visible in this region due to contrast delocalization from the surrounding crystalline regions. (c–e) Successive exposures of the same sample regions of Ba122 on CaF_2. A rapid amorphization of the Ba122 layer starting from the film-substrate interface is visible. The Ba122-layer thickness increases slightly during this process from (c) 32 nm to (e) 44 nm (fully amorphous). (b) A superlattice of voids forms in CaF_2 during electron-beam irradiation.

200 keV electron beam (Fig. 4.3b). Note that the image in Fig. 4.3b is slightly astigmatic, which could as cause the disappearance of the Ba122 lattice fringes to the reduced spatial resolution. However, the Ba122 film here was genuinely amorphous after extended electron-beam exposure. A medium spot size of 5 and a medium-sized C2 aperture was used here, but the beam current was not measured. This shows that Ba122 itself is susceptible to electron-beam irradiation.

Ba122 grown on CaF_2 is rapidly destroyed by 200 keV electrons in a Philips CM200 microscope, as shown by consecutive images (Fig. 4.3c-e) of the same sample region with short pauses in-between the exposures for electron-beam alignments. Similar to the results presented in Fig. 4.1b, the amorphization starts at the film-substrate interface and continues here through the whole film. In the end, the Ba122 layer is completely amorphous (Fig. 4.3e). An expansion of the Ba122 layer in *c*-direction from about 32 nm (Fig. 4.3c) to 44 nm (Fig. 4.3e) is observed.

This effect is also observed at 300 keV. Figure 4.3d shows the formation of a superlattice in CaF_2 with a periodicity of about 15 nm. These structures were previously reported in the literature for CaF_2 [CJW76; Jia12; Nik+12]. These bubbles were identified as voids/gas bubbles, which result from the reaction products of CaF_2 disintegration (e.g. HF or F). The voids then form the observed rectangular superlattice structure. The formation of this superlattice can also be observed in the video file "Irradiation-damage-Ba122-STEM" [Grü+20b] for 300 keV. The observed electron-beam-induced damage of Ba122 at 200 keV was more severe than at 300 keV. However, the residual gas atmosphere in the microscope vacuum may influence the reaction and the Philips CM200 microscope presumably has a worse vacuum level near the sample than the FEI Titan^3 80–300 microscope. Therefore, the results for 300 keV and 200 keV may not be directly comparable.

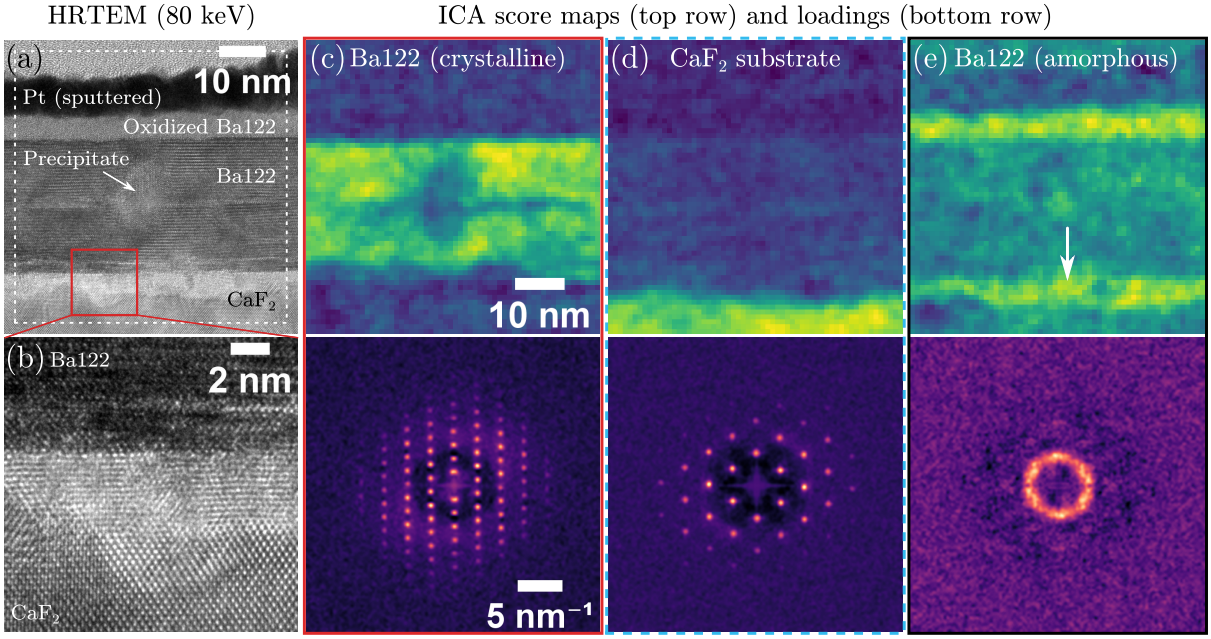

Figure 4.4: Electron-beam-irradiation damage at $E_0 = 80$ keV. (a) C_s-corrected HRTEM cross-section image of a Ba122 film grown on CaF_2. (b) Magnified view of the film-substrate interface from (a). The interface shows a higher image intensity than the substrate. (c–e) Sliding-window-FFT analysis with ICA. The score maps (top row) show the spatial distributions of the loadings (here FFTs, bottom row). Only three (of eight) selected ICA components are shown for brevity. The crystalline structure of (c) Ba122 layer and (d) CaF_2 leads to spot patterns in the loadings. (e) The film-substrate interface (marked with an arrow) shows a pronounced amorphous signal (ring pattern in the FFT) similar to the oxidized Ba122-surface layer.

Figure 4.4 presents a sliding-FFT-based analysis of a C_s-corrected HRTEM image of a Ba122 film on CaF_2 acquired at 80 keV in a FEI Titan^3 80–300 microscope. The original image is presented in Fig. 4.4a with a magnified inset of the film-substrate interface shown in Fig. 4.4b. The latter shows a region at the interface with a higher image intensity than the substrate below. Lattice fringes are visible in this region, indicating a crystalline structure. A sliding-window-FFT analysis is applied to separate the overlapping crystalline (and amorphous) regions in the HRTEM image. The local FFTs were analyzed with ICA to detect different patterns in the FFTs. Three selected components are shown in Fig. 4.4c-f. The top row shows the spatial distribution (or score maps) of the second row of FFT signals (or loadings). The signals of the crystalline phases of undamaged Ba122[1 0 0] (Fig. 4.4c) and CaF_2[1 1 0] (Fig. 4.4d) show distinct spots in the ICA loadings reflecting the periodicity of the corresponding crystal structures. An interesting

ICA component is displayed in Fig. 4.4e, where a round signal is visible in the loading. This corresponds to a uniform scattering in all directions associated with an amorphous phase. The radius is $(3.16 \pm 0.52)\,\mathrm{nm}^{-1}$ (the error is one standard deviation) as measured from a Gaussian fit to an azimuthally-integrated radial intensity profile (not shown). This value corresponds to a characteristic scattering vector of the amorphous phase. The amorphous phase is identified as amorphous Ba122 based on the corresponding spatial distribution above, where a high signal is observed for the oxidized Ba122 surface layer and the interface layer (marked by an arrow in Fig. 4.4e). The closest lattice spacing for Ba122 to the measured values is $3.07\,\mathrm{nm}^{-1}$ for the Ba122(0 0 4) planes. The stronger scattering intensity from the Ba122⟨1 0 3⟩ lattice planes ($3.42\,\mathrm{nm}^{-1}$) could also contribute to the measured signal. Note, however, that these lattice-plane reflections from these Ba122 planes would be present for a *polycrystalline* Ba122 structure but not for an *amorphous* Ba122 structure. The measured reciprocal distance observed in the FFT for an amorphous material is related to a medium-range order, as investigated by fluctuation electron microscopy [Tre+05]. This result indicates that the interface layer is a least partially amorphous. This amorphization was probably caused by electron-beam irradiation based on the previously shown results. It is noteworthy that similar crystalline layers with different contrast were also found in the literature [Ich+13; Tsu+16]. It can be speculated, that these (S)TEM images also show a partly destroyed IBS layer at the IBS-CaF_2 interface.
The damage mechanisms and preferential FIB milling at the film-substrate interface could be related to chemical reactions with the CaF_2 substrate, the abrupt change in composition, etching of Ba122 with reaction products (e.g. HF), and charging of CaF_2, which is an electric insulator. Electron-irradiation damage is typically distinguished into "knock-on damage" and "radiolysis" resulting from elastic and inelastic scattering processes, respectively. Jiang proposed another mechanism related to an electric field generated by electron-beam-induced excitation and ionization processes, which causes sample damage in insulating materials [Jia15; Jia16]. The same author also reported a detailed study for this damage type for CaF_2 [Jia12]. No further experiments were conducted in this work to study the damage mechanisms of Ba122 films on CaF_2 in more detail.

Electron-beam induced damage was also observed after dose-intensive SEM-EDXS surface analyses of Ba122 on CaF_2 (Fig. 4.5). This type of damage was analyzed by **Daniel Nerz** in his Bachelor thesis. Electron-beam irradiation can generate cracks in the Ba122 film (Fig. 4.5b-d),visible as dark lines in the SE-SEM images. The bright halos in the SE-SEM images are caused by electron-beam-induced C contamination. Crack formation is enhanced at higher electron energies, e.g. 8 keV in Fig. 4.5b and 10 keV in Fig. 4.5d. In contrast, some measurements do not show cracks at all, such as the EDXS spot/area measurements at 3 keV shown in Fig. 4.5a. In such measurements, the beam is parked or rapidly scanned over a sample region for a few ten seconds (here 60 s) during x-ray collection. In other samples, crack formation was also observed at 3 keV (Fig. 4.5c, here shown for an SEM-EDXS mapping).
Electron-beam-induced cracks impede dose-intensive SEM-EDXS analyses of Ba122 films on CaF_2. The crack formation may be related to an expansion effect along the *c*-direction, similar to the effect observed for cross-section TEM samples (cf. Fig. 4.3c-e on Page 97). The Ba122 layer expands away from the CaF_2 substrate under electron-beam irradiation. The expansion leads to stress and ultimately causes cracks. The energy dependence can be explained based on the penetration depth of electrons. Expansion of the Ba122 layer may only occur if electrons reach the film-substrate interface in SEM measurements, as illustrated by the Monte Carlo simulations in Fig. 4.6.

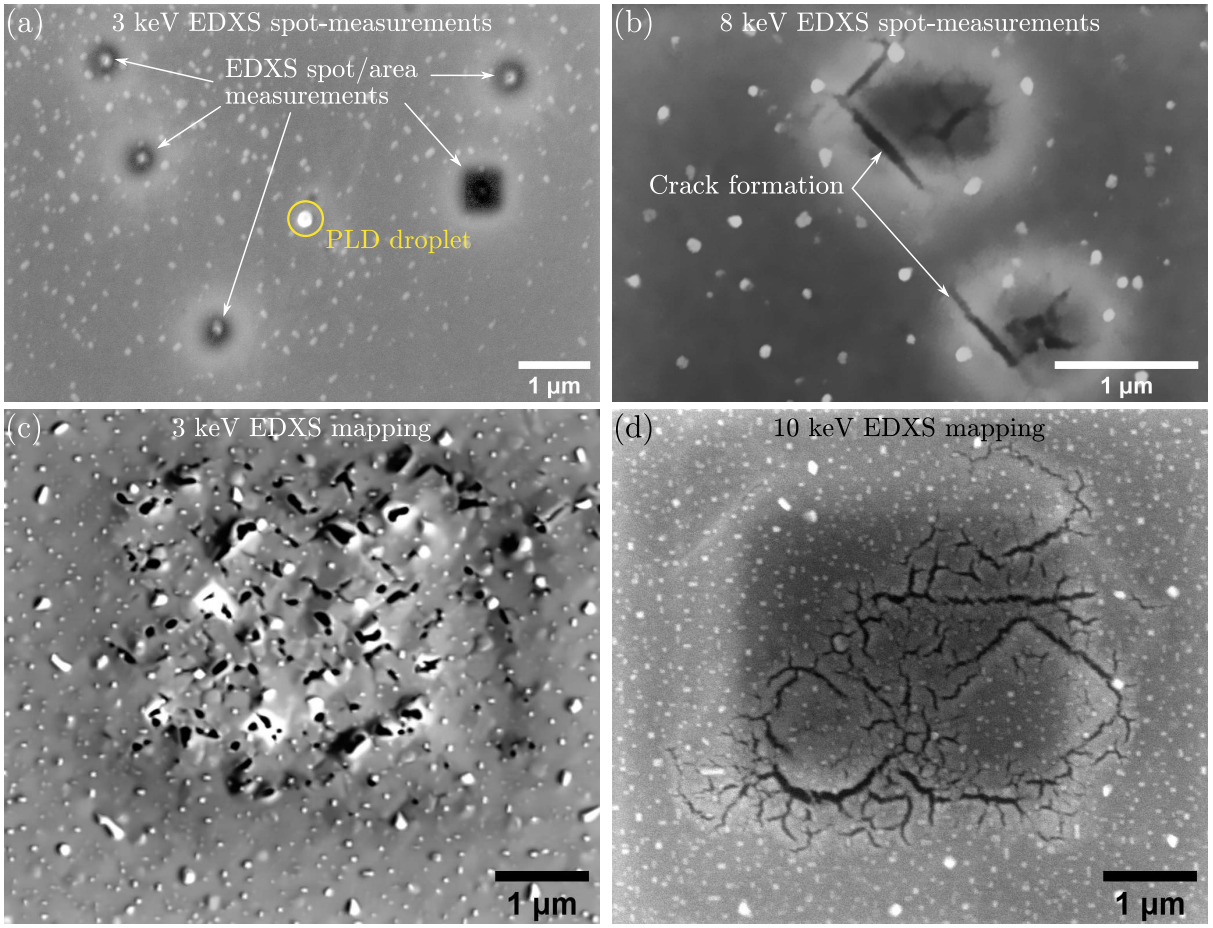

Figure 4.5: Electron-beam-irradiation damage in SEM of Ba122 on CaF_2. (a–b) Comparison of surface damage after EDXS spot measurements for (a) 3 keV and (b) 8 keV. No cracks are observed at (a) 3 keV in contrast to (b) 8 keV. C-contamination patches are visible as dark spots/areas with a bright halo. (c–d) Comparison of surface damage by EDXS mappings for (c) 3 keV and (d) 10 keV. Cracks are observed in both cases, but the crack formation is more severe for 10 keV. The SE-SEM images were acquired by Daniel Nerz.

Monte Carlo simulations of a 40 nm thin Ba122 film on CaF_2 at 3 keV using *CASINO* (Fig. 4.6a) show that electrons can reach the CaF_2 substrate (blue trajectories). At this electron energy E_0, however, most of the electron energy is deposited in the Ba122 layer as visible by the shown isocontours in Fig. 4.6c, which show the energy loss as fractions of the primary electron energy E_0. Electrons that reach the substrate contain only 5 % (150 eV) or less energy on average (cyan contour). The situation is different for 8 keV, where most electrons reach the CaF_2 substrate. The trajectories in Fig. 4.6b show an electron range of about 500 nm into the CaF_2 substrate. A significant portion of E_0 is deposited not only in the Ba122 film but also in CaF_2 and at the Ba122-CaF_2 interface (Fig. 4.6d). In this explanation, the threshold energy for crack formation is directly related to the thickness of the Ba122 film.

The formation of C-rich contamination patches impedes SEM imaging or SEM-EDXS spectroscopy. For the latter, low-energy x-rays may be absorbed in the contamination layer. The contamination layers are a typical problem in SEM imaging. Carbon-rich molecules (e.g. hydrocarbons) on the sample surface or from the residual gas atmosphere in the microscope vacuum are present on the sample surface and are polymerized by the electron beam leading to a solid carbon deposition. Sample-cleaning strategies can reduce contamination, e.g. sample heating or plasma cleaning. Here, only a mild sample heating was tested (80 °C for 1 h in air). However, no

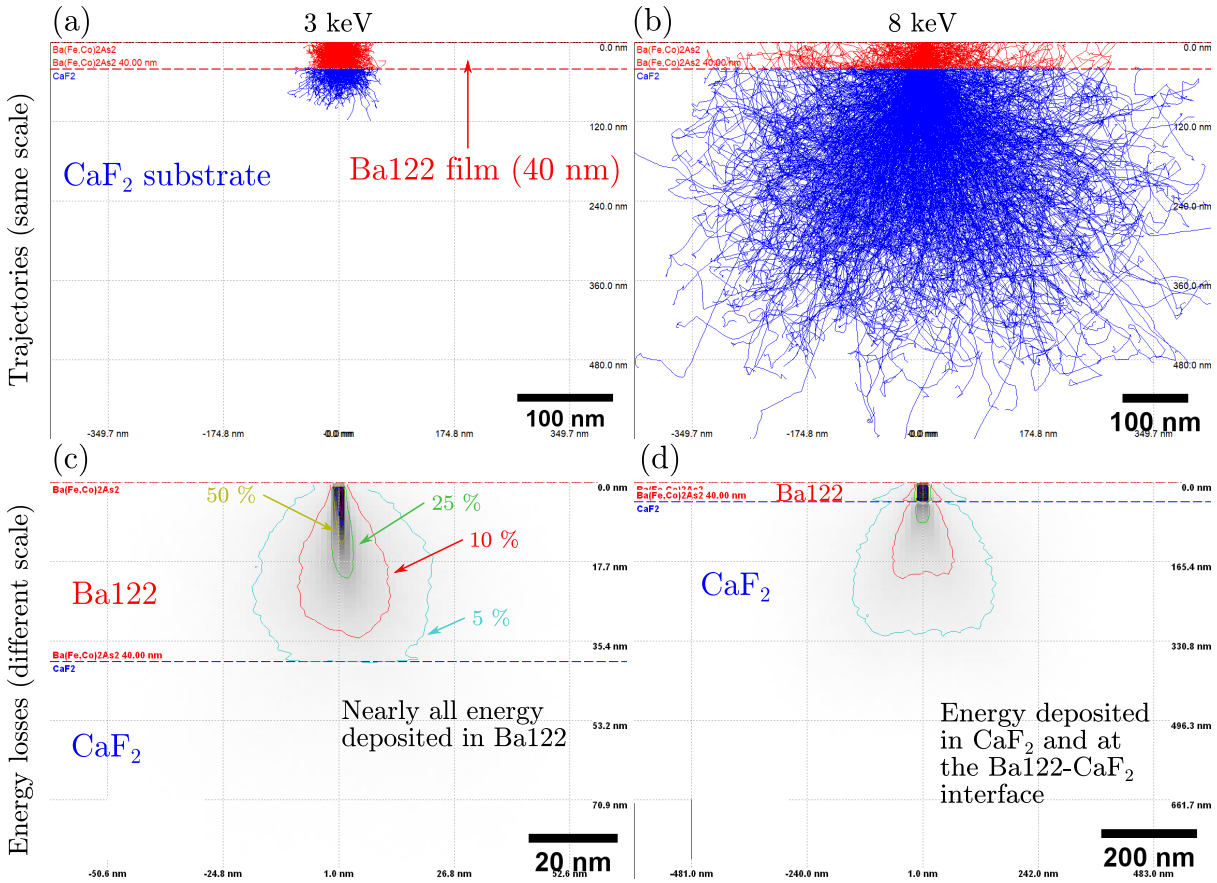

Figure 4.6: Simulated electron trajectories and energy losses of for a Ba122 film (40 nm) on CaF_2 for $E_0 = 3$ keV and $E_0 = 8$ keV. Left column: Monte Carlo simulation of (a) electron trajectories and (c) electron-energy losses of 3 keV electrons. Color-coded contours indicate the average energy of electrons in percent of the electron energy of the incident electrons. Only a few electrons with low energy (≤ 150 eV) reach CaF_2. Right side: Monte Carlo simulation for $E_0 = 8$ keV electrons for the same sample geometry. Most electrons reach the CaF_2 substrate and with higher residual energies. Note the same spatial scale for (a and b) but not for (c and d).

noticeable reduction in C-contamination was observed. Plasma cleaning was not tested, as it may modify the sample's surface. This is especially problematic for an O-containing plasma, as IBSs can oxidize. Ozone cleaning may be an alternative method in sample cleaning, which was unavailable. Samples were stored under a slight vacuum in a pumped-down desiccator before and after investigation in the microscope.

4.2 $Ba(Fe,Co)_2As_2$ Films on CaF_2: Influence of Growth Rate

Previous work. This section presents results on the influence of the growth rate on the Ba122-film microstructure grown on $CaF_2(0\,0\,1)$ substrates. CaF_2 is a popular substrate material for Ba122 films [Kur+13b; Tar+14; Hän+15; Iid+16; Lee+17; Yua+17; Qin+21] but also other IBS materials [Tsu+11; Tak+12; Bra+13; Ich+13; Qiu+17; Hai+19; Tho+21] resulting in high quality films with good superconducting properties. However, a more detailed understanding of the growth process of Ba122 (and other IBSs) is desired.

The investigated Ba122 films were grown by **Marco Langer** on $CaF_2(0\,0\,1)$ substrates. A preliminary study [Lan+19b] by SEM, atomic-force microscopy, and x-ray diffraction analyses showed the formation of secondary phases (Fe and BaF_2) in addition to Ba122. The formation and density of these phases depends on the growth rate. This publication also reports more

details regarding the PLD setup [Lan+19b]. Here, supplementary SEM and STEM analyses were performed to get further insights into the microstructure. Two films were chosen from the samples series:

- **Ba122/fast.** This sample was grown at a rate of $0.9\,\text{Å s}^{-1}$ (laser energy of 48 mJ, laser fluence $4.8\,\text{J cm}^{-2}$).
- **Ba122/slow.** This sample was grown at a rate of $0.4\,\text{Å s}^{-1}$ (laser energy of 12 mJ, laser fluence $1.2\,\text{J cm}^{-2}$).

Most of the results were published in an article [Grü+21a] and the reproduced figures are marked in the respective figure captions. The investigated aspects can be summarized:

- **Fe-rich precipitates.** Fe-rich precipitates can grow in Ba122 as reported earlier [Lee+10; Hän+11; Kat+12; Kat+13; Yoo+16; Dai+19]. These were also observed in all investigated Ba122 films. A higher number density of Fe-precipitates is observed with increasing growth rate.
- **BaF_2 precipitates.** BaF_2 was reported [Kur+13b; Lan+19b] as a possible secondary phase for Ba122 on CaF_2. The formation of BaF_2 at the Ba122-CaF_2 interface is confirmed here, which is probably related to F diffusion [Sum+14; Hai+16; Hai+19]. Regarding the growth rate, BaF_2 forms more easily at lower growth rate and is suppressed at higher growth rates [Lan+19b]. These were also observed in all investigated Ba122 films. A higher number density of Fe-precipitates is observed with increasing growth rate.
- **Ba122-CaF_2 interface.** A first complication arises from the observation that CaF_2 can react with the IBS film during PLD. The formation of a reaction layer at the IBS-CaF_2 interface is reported [Kur+13b; Tar+14; Lee+17] (for Ba122) [Tsu+11; Bra+13; Ich+13; Tsu+16; Hai+19; Tho+21] (for other IBSs). These could be caused by electron- or ion-beam irradiation during (S)TEM investigations, as already discussed in the previous section (Section 4.1 on page 93).
- **Antiphase boundaries.** Atomic substrate steps at the CaF_2 substrate with a step height $a_{CaF_2}/2$ can induce antiphase boundaries (APBs) in Ba122. The APBs were more extended for Ba122/fast since less planar defects were present, which could annihilate the APBs.
- **Planar defects.** Two types of planar defects were observed in this work. The first type is a stacking fault at the Ba planes, which is accompanied by an in-plane $\langle 1\,0\,0\rangle/2$ shift and was reported in earlier studies [Lee12; Hän+15; Yua+17; Shi+19]. Another planar-defect type without an in-plane shift was reported by Zheng et al. [Zhe+19] in single crystal Ba122. The c-lattice parameter around a Ba plane is locally enlarged. The defect can also be generated under electron-beam irradiation (Fig. 4.2 on page 96, also reported by Thersleff et al. [The+11]) but most likely exists also as a genuine planar defect in Ba122.

Theses microstructural aspects are discussed in detail for Ba122/slow and Ba122/fast in the following.

4.2.1 Fe Precipitates and Surface Analysis

The surface of both films was analyzed by SEM. All investigated Ba122 films show PLD droplets and smaller precipitates growing on the film surface, as shown in Fig. 4.35 on page 144. However, different precipitate densities are observed for Ba122/fast and Ba122/slow (Fig. 4.7). Figure 4.7a

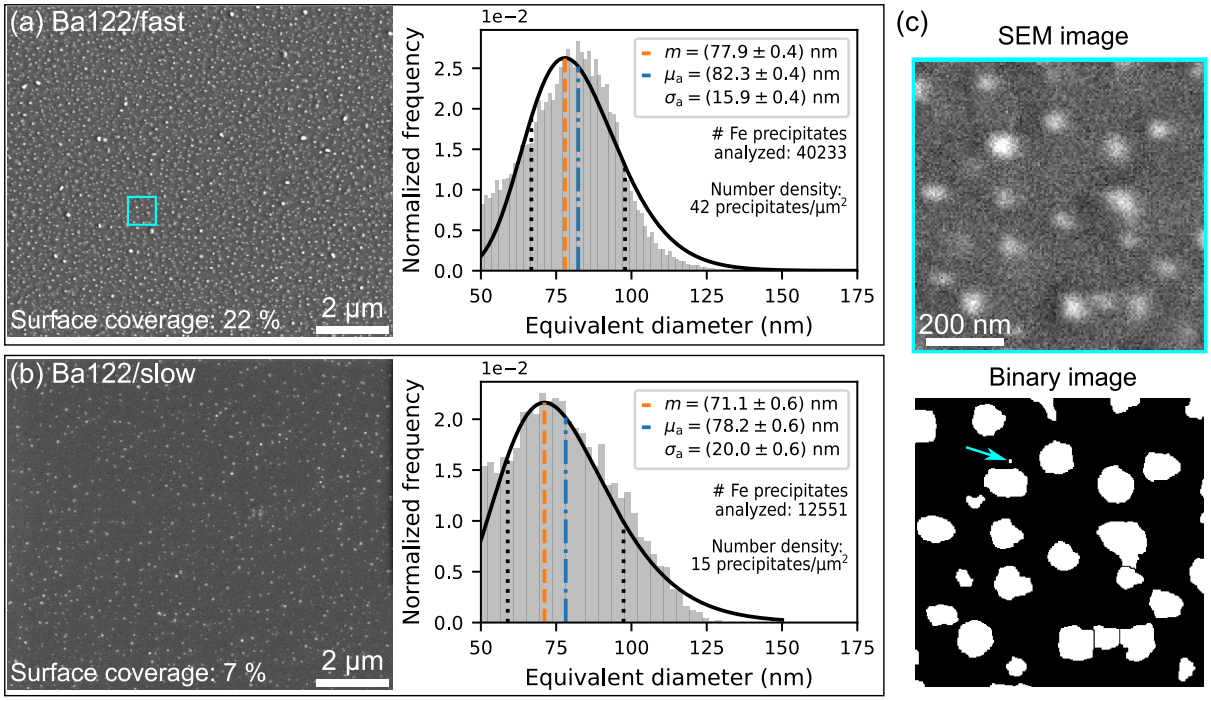

Figure 4.7: Growth-rate dependence of precipitate size and density in Ba122 films. SE-SEM images at $E_0 = 5\,\text{keV}$ and fitted particle-size distributions for (a) Ba122/fast and (b) Ba122/slow. A higher density of precipitates is visible for Ba122/fast. The equivalent diameter of the precipitates is similar. (c) Magnified image (top) of (a) and fully processed binary image (bottom) after segmentation. An arrow marks a falsely assigned pixel. This figure is adapted from a publication [Grü+21a].

and b show SE-SEM images for Ba122/fast and Ba122/slow and corresponding size analysis to obtain the equivalent diameters of the precipitates. The observed precipitate areas were determined with the *Trainable WEKA segmentation* plugin for *Fiji* as described on Page 89. This method enables segmentation and evaluation of a large number of precipitates from typically ten SE-SEM images similar to the ones shown in Fig. 4.7a and b.

A higher surface coverage with precipitates is observed for Ba122/fast (22 %) than Ba122/slow (7 %). The number density of precipitates was measured as 42 precipitates per µm^2 for Ba122/fast and 15 precipitates per µm^2 for Ba122/slow. Size analysis by fitting a log-normal distribution (solid black line in the normalized histograms Fig. 4.7a and b) yields similar equivalent diameters of $(82.3 \pm 15.9)\,\text{nm}$ (Ba122/fast) and $(78.2 \pm 20.0)\,\text{nm}$ (Ba122/slow). The values correspond to the arithmetic averages μ_a (dashed orange lines) and standard deviations σ_a of the size distribution. The black-dotted lines show the range containing 68.3 % of all values ("1σ" interval). The mode m (dashed orange line) shows the maximum of the log-normal distribution. Similar diameters are found if Gaussian distributions are fitted to the size distributions [Grü+21a].

The absolute values of the equivalent diameters should be interpreted carefully for several reasons. First, only precipitates with equivalent diameters $> 50\,\text{nm}$ were chosen for the fitting range since an increase of particles with smaller sizes were observed for $< 50\,\text{nm}$ (not shown here). This effect is mainly caused by faulty segmentation of precipitates, as shown in Fig. 4.7c. Here, a region from Fig. 4.7a is shown at higher magnification with the fully segmented binary image shown below. The surface precipitates appear bright on a dark Ba122-film surface. An arrow in the binary image marks a single, isolated pixel, which was falsely assigned as a precipitate. Such pixels (or regions) are potential sources of errors. Second, the used electron energy of 5 keV provides only a limited spatial resolution. Therefore, precipitate sizes may not be accurately

measured. Here, 5 keV was chosen instead of a lower electron energy (with higher surface sensitivity and SE-SEM resolution) to facilitate an easier segmentation of the precipitates. This

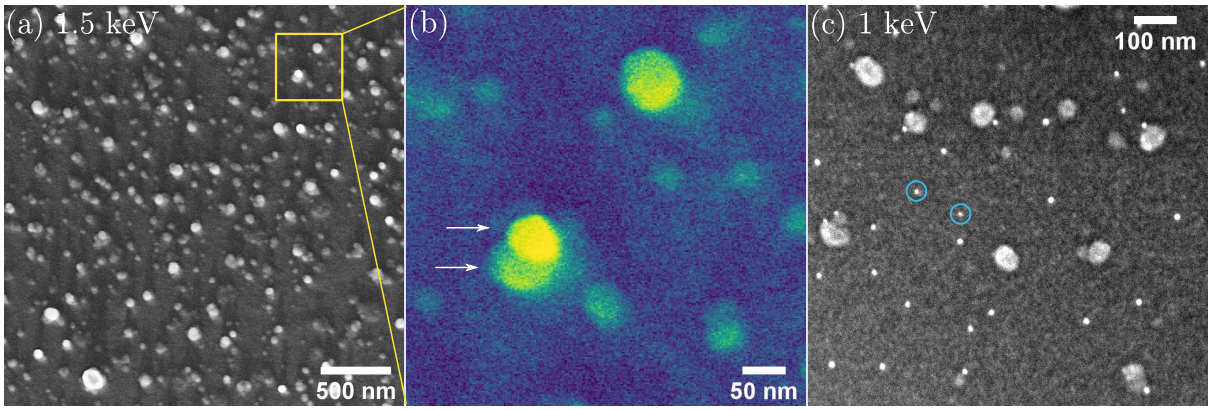

Figure 4.8: High-resolution SE-SEM surface images of Ba122/slow. (a) SE-SEM image at 1.5 keV showing contrast variations of the precipitates. (b) Magnified region of (a). The arrows mark different image intensity levels for the selected precipitate. (c) SE-SEM image at 1 keV from another sample region showing bright precipitates with ~ 10 nm diameter (marked by blue circles).

is because the precipitates show a mostly homogeneous SE signal at 5 keV making an automated segmentation possible. In contrast, Fig. 4.8 shows SE-SEM images of Ba122/slow at lower electron energies (≤ 1.5 keV) and at higher magnification. The precipitates are resolved more clearly than in Fig. 4.7c showing a round shape. However, more complex contrasts are visible, e.g. in the magnified image in Fig. 4.8b, where the arrows point at two different intensity levels at a precipitate. Presumably, such contrast differences vanish at 5 keV. At 1 keV, even smaller precipitates (~ 10 nm) become visible with high SE-SEM image intensity (Fig. 4.8c, two examples are marked with blue circles). These precipitates are not visible at 5 keV due to the limited spatial resolution. The high-resolution SE-SEM images show that the precipitate-size analyses (Fig. 4.7) only serve as a relative comparison between Ba122/fast and Ba122/slow.

Furthermore, SEM-EDXS was applied to study the chemical composition of the observed precipitates. The electron energy must be minimized to maximize the spatial resolution of this technique [Boy02] because the precipitate diameter is in the order of 80 nm. Here, an electron energy of 2 keV was chosen resulting in an overvoltage of about 1.3 for the As L_1 shell at 1.527 keV (1.527 keV $\times$ 1.3 = 1.99 keV). Boyes [Boy02] suggests a minimum overvoltage of 1.3 to excite x-rays for low-energy SEM-EDXS effectively. Similarly, Goldstein et al. [Gol+18] recommend a minimum overvoltage of 1.25 and provide useful periodic tables for low-energy SEM-EDXS analyses [Gol+18, pp 362 sq.]. Besides the As Lα transition (1.282 keV), all other elements in Ba122 have x-ray transitions below 2 keV, namely O Kα (0.525 keV), Fe Lα (0.705 keV), and Ba Mζ_1 (0.601 keV). In addition, NMF was applied to the SEM-EDXS dataset to separate the overlapping chemical phases (i.e. precipitates and surrounding Ba122 film) based on the approach by Jany et al. [JJK17]. Figure 4.9a shows an SE-SEM overview image taken at 2 keV with the SEM-EDXS mapping region marked with a yellow square (also shown in Fig. 4.9c). The dataset was acquired by **Daniel Nerz** from another Ba122 film on CaF_2, i.e. the sample denoted as "highIA" in Section 4.3.2 on page 136. However, the Fe precipitates were observed for all Ba122 films so that the following SEM-EDXS results are equally valid for Ba122/fast and Ba122/slow. A beam current of 6.4 nA was chosen to maximize the x-ray signal. Higher beam-current settings led to a drastic loss in spatial resolution at 2 keV and the precipitates could not longer be resolved. A spatial sampling of about 10 nm was used for mapping and the

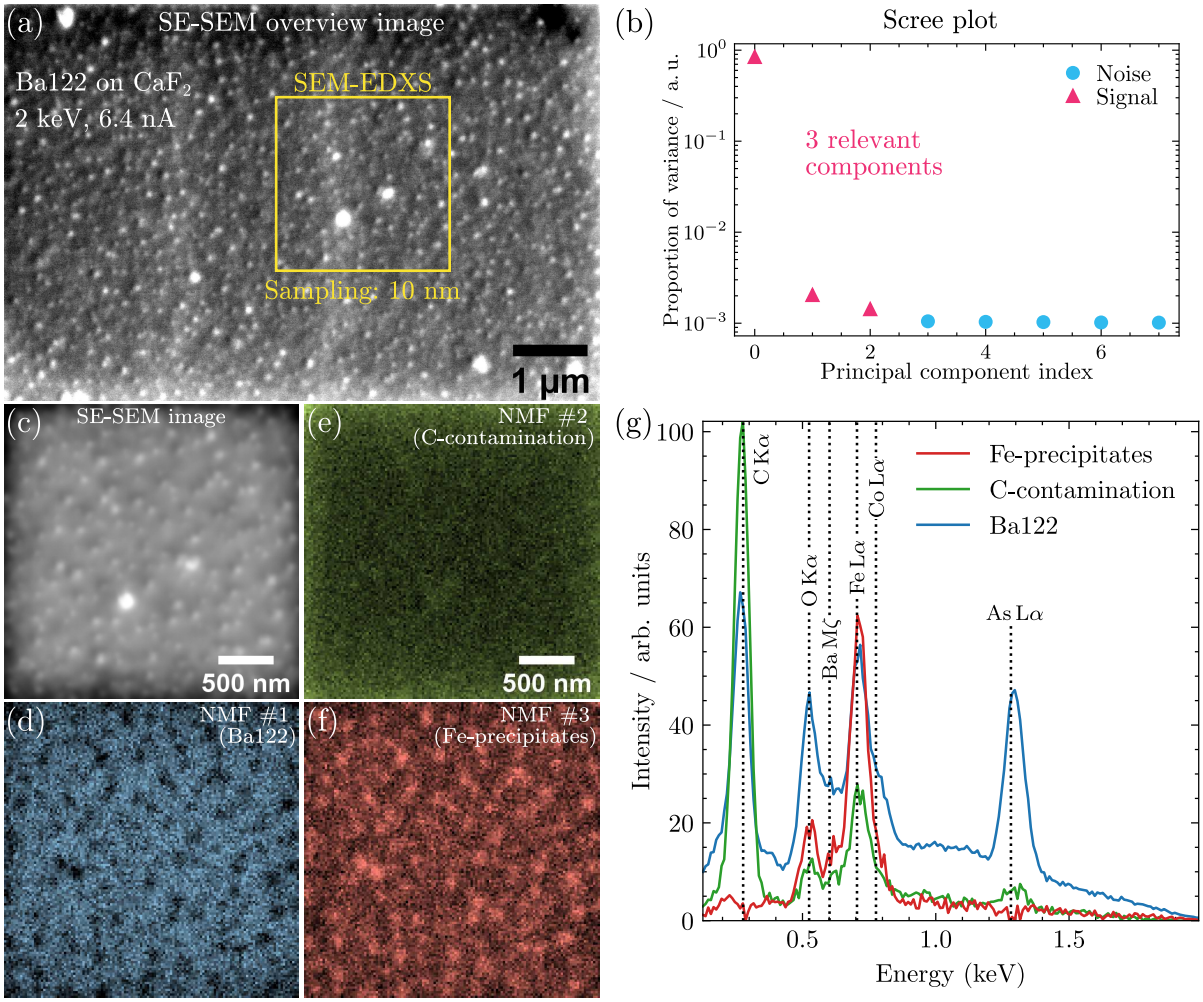

Figure 4.9: Low-energy SEM-EDXS analysis of $Ba(Fe_{0.92}Co_{0.08})_2As_2$ on CaF_2. (a) Overview SE-SEM image taken at 2 keV. A yellow square marks the SEM-EDXS mapping region. (b) PCA scree plot showing three relevant components in the SEM-EDXS dataset. (c) SE-SEM image and (d–f) corresponding NMF score maps for the NMF loadings shown in (g). The chemical phases are identified and denoted in the images. The precipitates show an enhanced Fe signal. The dataset was acquired by Daniel Nerz.

total mapping duration was 18 min.

Post-processing of the SEM-EDXS dataset with PCA reveals three relevant components in the scree plot (Fig. 4.9b, ▲) above the noise level (●). Therefore, three dimensions were chosen as output dimensions for the NMF algorithm. The NMF score maps in Fig. 4.9d–f show the spatial distribution of the corresponding NMF loadings in Fig. 4.9g. The three NMF components can be identified as Ba122 (blue, d), C-rich contamination (green, e), and (Fe) precipitates (red, f) based on the score maps and the x-ray peak positions in the NMF loadings. For example, the precipitate signal shows a strong Fe Lα and no As Lα peak. The Ba signal is not clearly resolved in all spectra. However, the Fe-precipitate signal (red curve) shows a lower Ba Mζ intensity relative to the Fe Lα peak than the Ba122 phase (blue curve). From this analysis, the precipitates are identified as being rich in Fe (and possibly also Co). The precipitates are denoted as Fe precipitates. An O Kα peak is also present in the Fe-precipitate signal, probably due to surface oxidation. Similarly, Ba122-surface oxidation causes the O signal in the Ba122-NMF component. Fe is a typical impurity phase reported for Ba122 [Lee+10; Hän+11; Kat+12; Kat+13; Yoo+16; Dai+19].

These results show that low-energy SEM-EDXS is a valuable technique for preliminary surface analysis for Ba122 (or other superconducting) films. The main challenges are C-rich contamination and achieving a high enough signal-to-noise ratio in the SEM-EDXS dataset for further processing. C contamination impedes low-energy SEM-EDXS analyses by (i) absorbing low-energy x-rays and (ii) reducing SE-SEM-image quality for sample-drift correction. The latter was often the limiting factor for long SEM-EDXS acquisitions in this work, where the acquisition software (Bruker *Esprit*) terminated the acquisition due to its inability for sample-drift correction. Another problem regarding the analysis are the Ba M x-ray transitions. Here, the relative intensity distribution between the Ba M x-ray transitions was notably different from the one tabulated in, e.g., *DTSA-II*. This difference may be due to a complicated dependence of these x-ray transitions probabilities from the bonding environment of Ba in a sample and x-ray absorption [FB67; AW03]. This means, that the x-ray-peak intensity ratios for the Ba M x-ray family is likely different between different samples and cannot be easily compared to tabulated data. This makes peak fitting challenging (or even impossible without reference spectra).

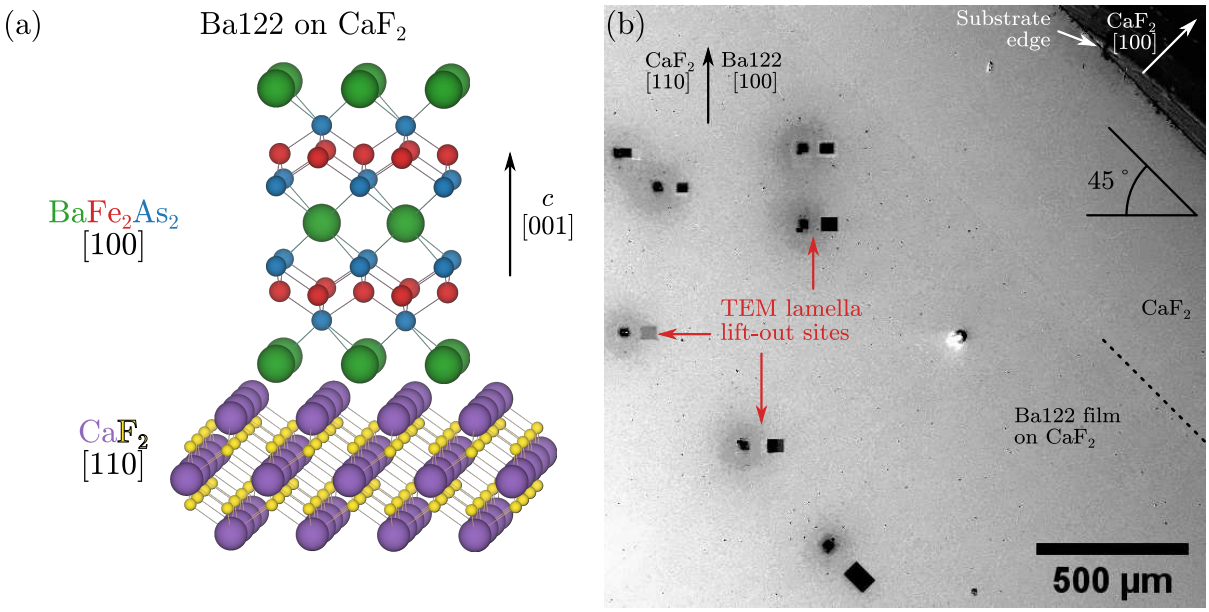

Figure 4.10: Crystallographic orientation of Ba122 on CaF_2. (a) Scheme showing the crystalline relationship $[1\,0\,0](0\,0\,1)\mathrm{Ba122}\|[1\,1\,0](0\,0\,1)\mathrm{CaF_2}$. The room-temperature in-plane lattice parameters are $a = b = 0.396\,\mathrm{nm}$ for Ba122 and $a/\sqrt{2} = 0.387\,\mathrm{nm}$ for the $(1\,1\,0)$-type interplanar spacing of cubic CaF_2 (lattice constant $a = 0.547\,\mathrm{nm}$). (b) Top-view SE-SEM image of a Ba122 film grown on a CaF_2 substrate. A $\{1\,0\,0\}$-oriented substrate edge is visible at the top right. The sample is rotated by 45° with respect to the substrate edge to prepare cross-section TEM lamellas that are oriented along the Ba122$\langle 1\,0\,0\rangle$ direction.

TEM analysis was performed for Ba122/fast and Ba122/slow. The TEM samples were prepared by FIB milling. To align the Ba122$\langle 1\,0\,0\rangle$ direction parallel to the electron beam, the expected epitaxial relationship $\mathrm{Ba122}[1\,0\,0](0\,0\,1)\|\mathrm{CaF_2}[1\,1\,0](0\,0\,1)$ (cf. structure model in Fig. 4.10a) was considered by rotating the Ba122-CaF_2 samples by 45° with respect to the CaF_2 substrate edges (Fig. 4.10b). Several TEM lift-out sites are visible as dark rectangles in the SE-SEM surface image in Fig. 4.10b since only freshly prepared samples were investigated. This approach was used since Ba122 oxidizes when not stored under an inert gas atmosphere. The freshly prepared TEM samples were transferred from the FIB instrument to the S/TEM instrument within an evacuated bag using a CASO VC10 vacuum sealer.

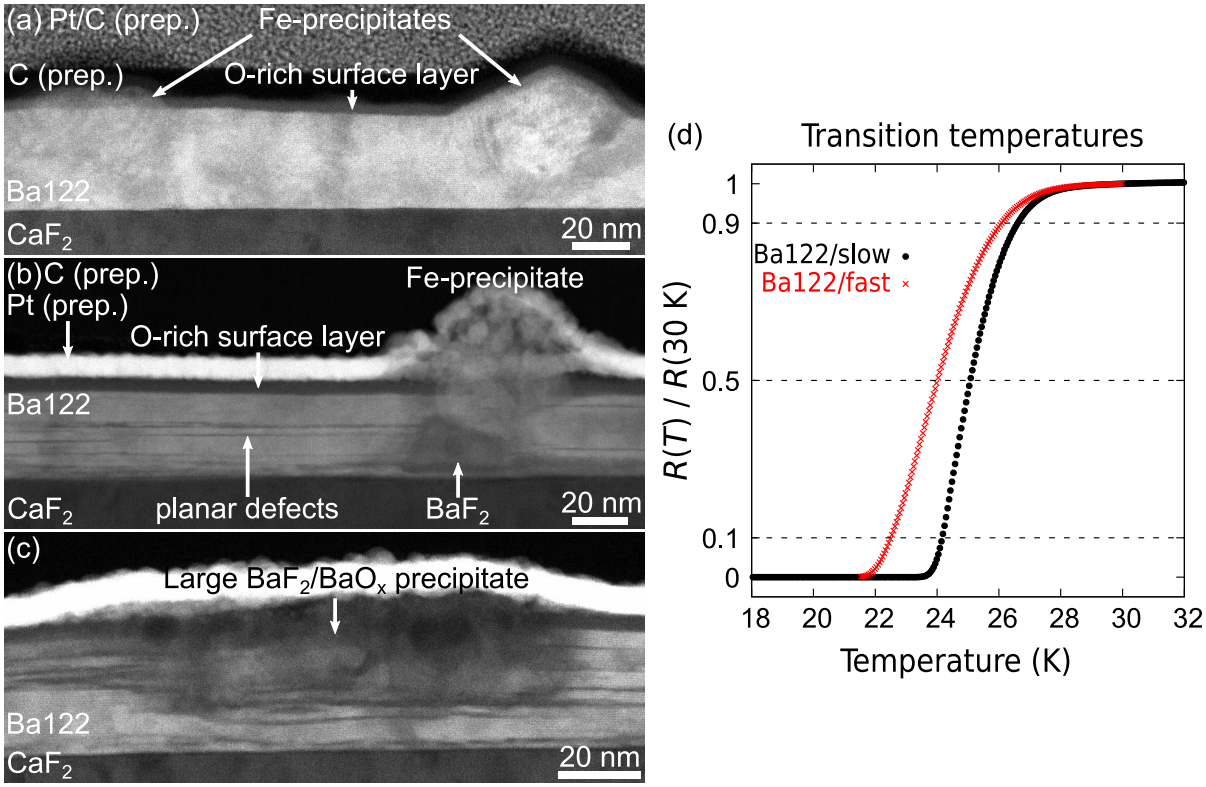

Figure 4.11: Representative cross-section HAADF-STEM images of Ba122/fast and Ba122/slow and transition temperatures T_c. Representative HAADF-STEM cross-section images of (a) Ba122/fast and (b,c) Ba122/slow showing different defects. (d) $R(T)$ resistance measurement showing the superconducting transitions for both samples. These figures are adapted from two published figures [Grü+21a].

Figure 4.11a–c present cross-section HAADF-STEM images of Ba122/fast (Fig. 4.11a) and Ba122/slow (Fig. 4.11b and c). Different types of defects are visible, which are discussed based on structural and chemical analyses in the following. In addition, the resistance curve (Fig. 4.11d) shows the superconducting transitions for both samples. Ba122/slow shows a slightly higher $T_{c,50} \approx 25\,\mathrm{K}$ than Ba122/fast with $T_{c,50} \approx 24\,\mathrm{K}$. Here $T_{c,50}$ denotes the temperature, where 50 % of the normal-state resistance is observed.
Both samples show comparable sample thicknesses of about 40 nm (Ba122/fast) and 37 nm (Ba122/slow). An O-rich surface layer with a thickness of about 5 nm is visible with lower intensity. This surface layer results from surface oxidation of Ba122 due to sample storage [Ple+13; GR15], which can be considered as sample aging or degradation.

Besides oxidation, an alternative possibility for the amorphous surface layer can also be SEM-induced amorphization of Ba122 by EBID of Pt during TEM-sample preparation by FIB. This possibility was ruled out by an extra experiment (Fig. 4.12). By depositing a dense Pt protection layer ($\sim 10\,\mathrm{nm}$, by sputtering) on Ba122/slow, a more effective protection layer than only amorphous C ($\sim 35\,\mathrm{nm}$, by adaptive C thread evaporation) is generated. Note that the *ex-situ* sputtered Pt layer is different (i.e. more dense and deposited without electron-beam bombardment) from the *in-situ* deposited EBID Pt layer. Figure 4.12a shows a HAADF-STEM cross-section image of Ba122/slow with the surface layer visible below the bright Pt protection layer. Similarly, the dense, high-Z Pt protection layer appears bright in Fig. 4.11b and c. Electron-beam-induced deposition of the Pt/C layer during FIB preparation was always performed at an electron energy of 2 keV. Therefore, the electron-beam range at 2 keV for the

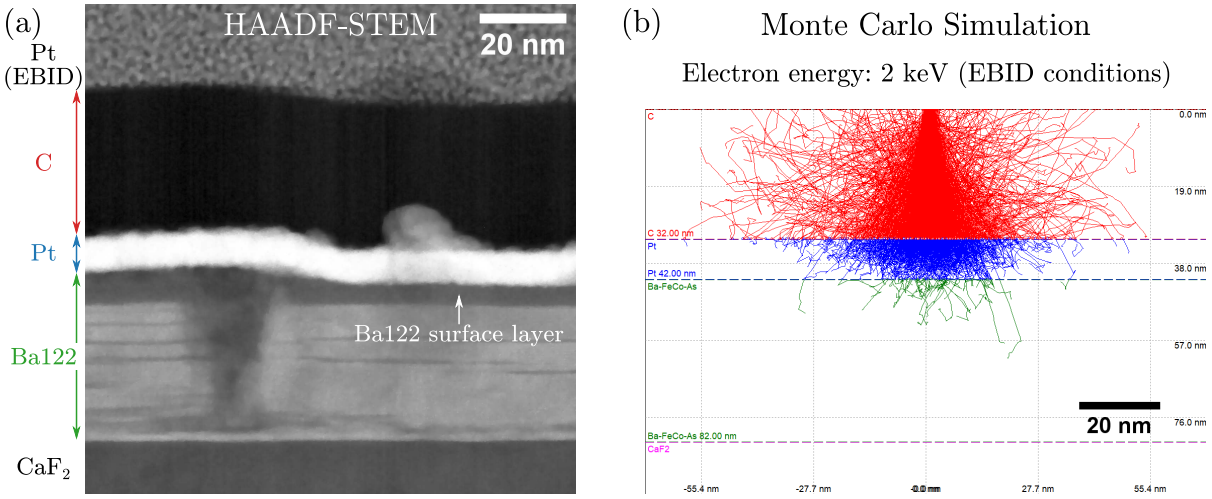

Figure 4.12: Surface oxidation of Ba122 films. Layers of dense sputtered Pt (cf. brightest layer in a, blue trajectories in b) and amorphous C (dark layer in a, red trajectories) are deposited *ex-situ* on Ba122/slow. These layers protect the Ba122 film during electron-dose-intensive EBID of Pt (top most layer in a) during FIB preparation. (b) Corresponding Monte Carlo simulation of electron trajectories for $E_0 = 2\,\mathrm{keV}$. Only a few electrons reach the Ba122 film (green trajectories).

sample configuration in Fig. 4.12a was simulated using *CASINO* (Fig. 4.12b). Note the same scale as for the HAADF-STEM image. The electron trajectories are color-coded and only a few electrons reach the Ba122 film (green). In contrast, most electrons are absorbed in the pre-deposited C (red) and Pt (blue) layers. This provides evidence that the amorphous surface layer on Ba122/slow is unlikely to result from electron-beam-induced damage during EBID. Since the amorphous surface layer also appears independent of the additional Pt-protection layer on Ba122/slow (cf. Fig. 4.11a and b) and the layer thickness is constant, an electron-beam induced amorphous Ba122 layer can finally be ruled out. Indeed, this surface layer was observed in all investigated Ba122 films. This further provides evidence for surface oxidation of Ba122. To mitigate this oxidation, it may be possible to deposit a protection layer *in-situ* directly after PLD of Ba122 without breaking vacuum by using a different target, e.g. Cr [Iid+10]. Considering Ba122 oxidation is essential for very small film thicknesses (e.g. below $< 20\,\mathrm{nm}$), where a 5 nm oxidation layer affects a significant portion of the total film thickness.

The oxidized surface layer is visible in the qualitative elemental map for O Kα obtained from STEM-EDXS measurements of Ba122/fast (Fig. 4.13). Here, two precipitates were mapped with STEM-EDXS and the enhanced Fe/Co and reduced Ba/As signals at the precipitates confirm the results obtained from SEM-EDXS measurements (Fig. 4.9). The precipitates are rich in Fe and Co, which partly substitutes Fe. In all analyses, an increased Fe signal is accompanied by Co. Therefore, only Fe is evaluated in the following for brevity and the term Fe precipitates is used for the Fe/Co-rich precipitates. The Fe precipitates were observed in all investigated Ba122 films. The visible differences in signal intensity for the two observed precipitates in Fig. 4.13 is caused by the different sample geometries as shown in Fig. 4.13c. Since the precipitate diameters are in the range of the typical TEM-sample thickness ($\sim 80\,\mathrm{nm}$), a precipitate may be entirely (upper scheme) or only partly (lower scheme) embedded in a TEM sample. In STEM, the projected structure then results in a lower Fe/Co signal for the partially-contained Fe precipitate than for the largely-contained Fe precipitate. Regarding the substrate elements, F and Ca, no visible diffusion into the Ba122 film is observed in the elemental maps.

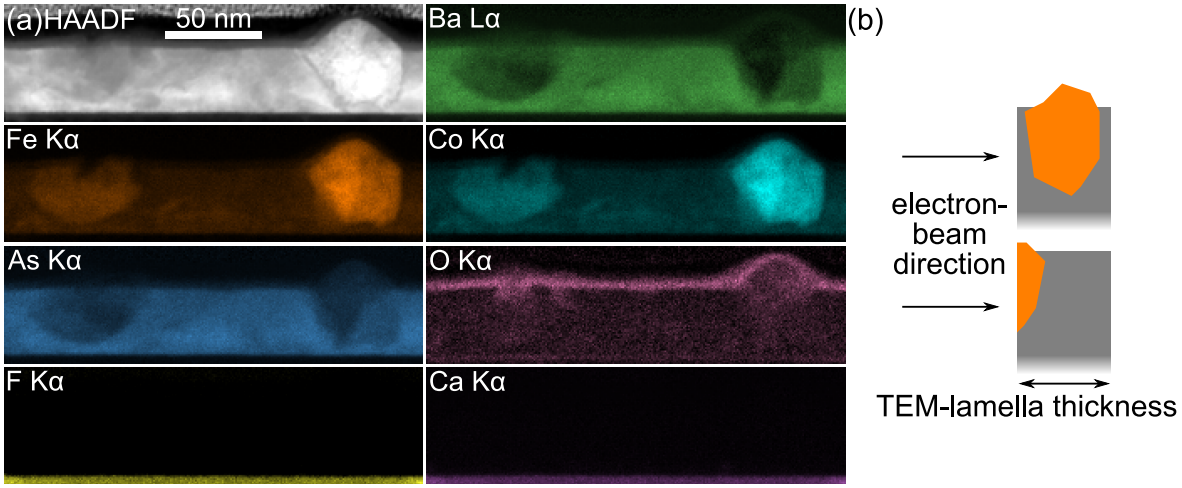

Figure 4.13: Elemental maps of two precipitates in the Ba122/fast film obtained by STEM-EDXS. (a) HAADF-STEM cross-section image and corresponding elemental maps for Ba122/fast. Two precipitates are observed, which show enhanced Fe and Co signals. (b) Scheme showing a possible positions for the two precipitates in (a) in a TEM sample. Different chemical signals are observed for the precipitates depending on how a precipitate is contained in a TEM sample. This figure is published in an article [Grü+21a].

Next, the microstructures of two different Fe precipitates were analyzed by NBED (top row) and HRTEM analyses (bottom row, Fig. 4.14). For NBED, the µP-STEM mode was used with a convergence angle $\alpha \approx 1.6\,\text{mrad}$ to avoid overlap of the Bragg reflections for the Ba122$\langle 1\,0\,0\rangle$ at $E_0 = 300\,\text{keV}$ (Fig. 4.14b). The STEM probe size in this configuration is about $0.61 \cdot \lambda/\alpha \approx 0.75\,\text{nm}$ (FWHM). Figure 4.14a shows an overview HAADF-STEM image with the marked acquisition regions for the PACBED patterns shown in Fig. 4.14b (Ba122 film) and c (Fe precipitate). The PACBED patterns are displayed on a logarithmic intensity scale to visualize the Bragg-disc positions. The latter were compared with calculated diffraction patterns of Ba and Fe using the appropriate structure files. A good agreement with the α-Fe structure ("ferrite", ICSD entry 631 736) viewed along the [1 1 0] zone axis is found for the Fe precipitates (Fig. 4.14c). The measured values agree within experimental error with the simulated values given in parentheses. The in-plane Fe($\bar{1}\,1\,0$) (0.203 nm) reflection nearly aligns with the in-plane Ba122($0\,\bar{2}\,0$) reflection (0.198 nm) as shown in the simulated pattern in Fig. 4.14f (cf. small arrows, 2.2 % mismatch). The open, red circles correspond to the Fe reflections. The small difference between the lattice planes enables syntaxial[3] growth of Fe (partly substituted by Co) in the Ba122 film. The same crystalline orientations were reported for Ba122 grown on Fe buffer layers [The+10; Iid+11]. A larger mismatch is found for the lattice planes in c-direction as visible by the non-matching Ba122(0 0 8) (or (0 0 10)) and Fe(0 0 2) reflections in Fig. 4.14f. This leads to inclined boundaries between Ba122 and Fe precipitates, as schematically shown by dotted lines Fig. 4.14a.

The latter can also be seen in HRTEM images of a part of a Fe precipitates in Ba122/slow (Fig. 4.14d). The inset shows a magnified view of the Fe lattice fringes. The crystal structure is analyzed by Fourier transformation and the corresponding power spectra of the Fe precipitate shows the same crystalline orientations as the PACBED pattern in Fig. 4.14c. Note that two different Fe precipitates are analyzed in Fig. 4.14a and d. This shows that the crystalline orientation Fe[1 1 0](0 0 1)‖Ba122[1 0 0](0 0 1) is common in Ba122 films. The Fe precipitates can

[3]Syntaxial growth is meant here for (semi-)coherent growth of a secondary crystalline phase *inside* another crystalline phase and not on its *surface* (epitaxy) [Bon72].

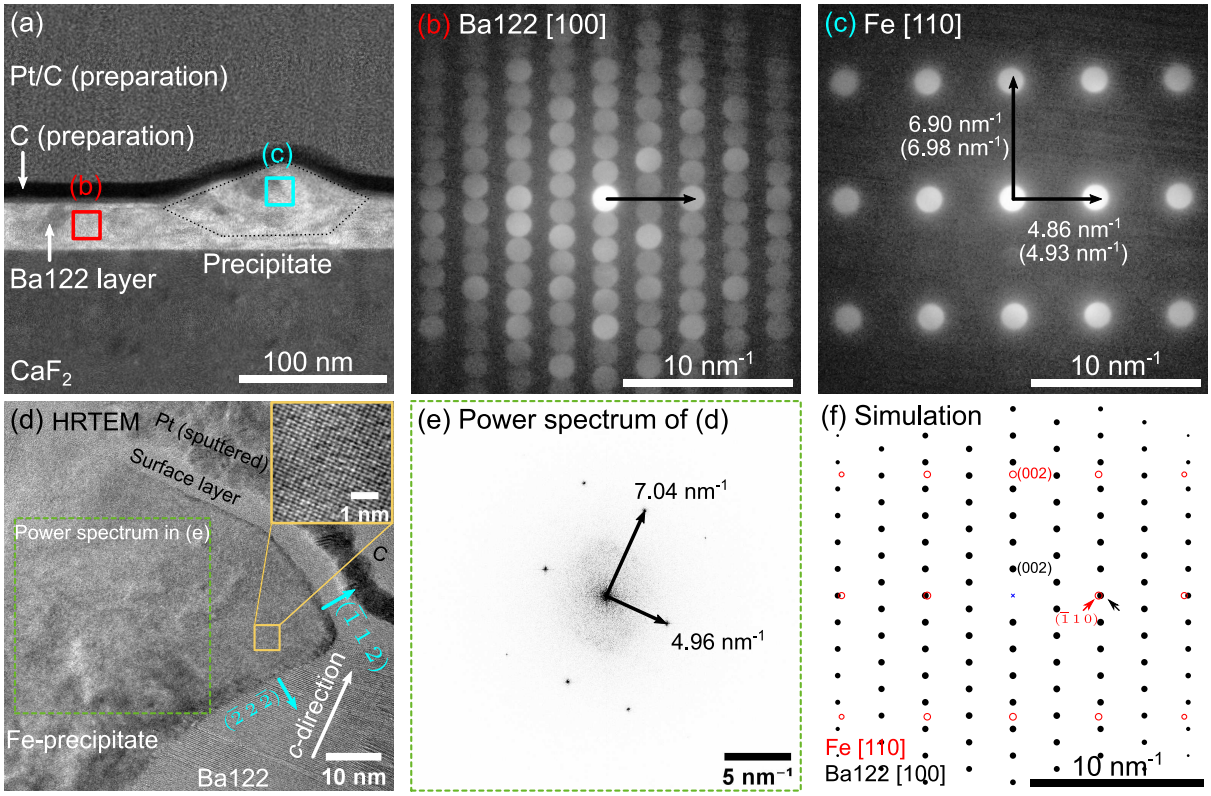

Figure 4.14: Structural analysis of Fe-rich precipitates. (a) HAADF-STEM image of Ba122/fast and (b,c) PACBED patterns from the regions marked in (a). Image intensities in (b,c) are displayed on a logarithmic scale for better visibility. The crystalline phases and orientations are identified as (b) Ba122[1 0 0] and (c) Fe[1 1 0]. The shown values (in parentheses) correspond to experimental (simulated) values for the reciprocal distances. (f) A simulation of the combined diffraction patterns of both phases shows the slight in-plane lattice mismatch (arrows). (d) HRTEM image (300 keV) of another Fe precipitate from a Ba122 film grown on $LaAlO_3$ (cf. Fig. 4.36 on Page 145). The inset shows the Fe lattice fringes. Two crystal facets of Fe are marked with blue arrows. (e) The power spectrum from the region in (d) shows the same reflections as the PACBED pattern in (c). Both precipitates show the same orientation in Ba122. The images in the top row are published in an article [Grü+21a].

grow out of the Ba122 film's surface. The facets of the Fe phase can be observed in cross-section view (Fig. 4.14d and f, Fig. 4.11, Fig. 4.3a) or SEM/atomic-force microscopy imaging [Lan+19b]. Two facet directions are marked in Fig. 4.14d with blue arrows. For example, the Fe($\bar{1}$ 1 2) facet normal is tilted by $\gamma = 35.3°$ away from the film's surface normal (or Fe(0 0 2)-facet direction) based on the following equation for cubic crystal structures [TG14, p 100]:

$$\cos\gamma = \frac{h_1 \cdot h_2 + k_1 \cdot k_2 + l_1 \cdot l_2}{\sqrt{(h_1^2 + k_1^2 + l_1^2) \cdot (h_2^2 + k_2^2 + l_2^2)}} \tag{4.1}$$

The formation of Fe precipitates from stoichiometric $Ba(Fe_{0.92}Co_{0.08})_2As_2$ PLD targets suggests a loss of Ba and As during PLD. Ba-rich or As-rich phases were *not* observed besides Fe precipitates in Ba122/fast. This suggests that Ba and As may partially evaporate or are sputtered during PLD. These processes affect the stoichiometric transfer of the PLD target material to the thin film [Sch09; Kla+16]. For a discussion for IBSs, see also the book by Haindl [Hai21, p 32]. Here, Fe has a comparably lower vapor pressure compared to Ba and As at a deposition temperature of $T_{sub} = 700\,°C$ [Hon69]. This leads to possible evaporation of Ba and As, especially for increasing substrate temperatures. However, the deposition rate (controlled by the laser fluence) also

affects film growth [Kla+16]. For example, Klamt et al. [Kla+16] showed that nearly pure W (low relative vapor pressure) or pure Cu (high relative vapor pressure) films can be grown from a single (80 wt. % W, 20 wt. % Cu) target by PLD by only adjusting the laser fluence. They observed a higher W content for higher deposition rates. A similar effect may be seen here for Ba122/slow and Ba122/fast, where a higher deposition rate for Ba122/fast leads to a preferential formation of phases of the high-vapor-pressure element, here in the form of Fe precipitates. This shows that the PLD target composition (e.g., a reduction of Fe or increase of Ba/As) or the deposition parameters (e.g. laser fluence) may be further optimized to avoid the formation of Fe precipitates.

4.2.2 BaF_2 Precipitates

The Ba122 films were grown on CaF_2 at a substrate temperature $T_{sub} = 700\,°C$. Diffusion of elements from Ba122 into CaF_2 or *vice versa* is possible during PLD. Indeed, Haindl et al. [Hai+19] found and purposefully used F diffusion from a CaF_2 substrate into $SmO_{1-x}F_xFeAs$ films ($T_{sub} = 840\,°C$). The superconducting properties of this material are enhanced by F substitution for O. Sumiya et al. [Sum+14] grew a CaF_2 layer on top of NdFeAsO films by molecular-beam epitaxy and reported F diffusion already at $T_{sub} = 600\,°C$ (for the CaF_2 deposition). For completeness, significant diffusion and reactions at the film-substrate interface were also reported for YBCO films on CaF_2 ($T_{sub} = 800\,°C$) [Vas+93]. This shows that the film-substrate interface and diffusion processes are of interest for thin-film growth on CaF_2.

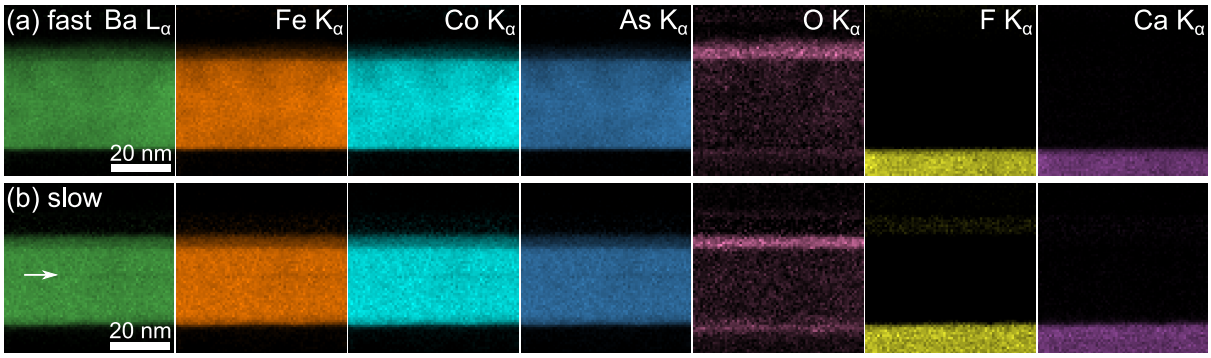

Figure 4.15: Elemental maps for Ba122/fast (top row) and Ba122/slow (bottom row) obtained from STEM-EDXS. A faint O signal is observed at the film-substrate interface for Ba122/slow. The arrow marks a planar defect in Ba122/slow. This figure is published [Grü+21a].

STEM-EDXS was used to study (mostly) defect-free regions of Ba122/fast and Ba122/slow (Fig. 4.15). The spatial distribution of Ba, Fe, Co, and As shows the Ba122-film region, whereas F and Ca show the substrate region. The arrow in the Ba Lα map in Fig. 4.15b marks a planar defect in Ba122/slow (cf. dark horizontal lines in Fig. 4.11b), which is barely visible here. Both films show the expected spatial distribution of the respective elements without visible signs of F diffusion. A summed-up EDXS spectrum of the Ba122-film region was quantified to obtain the chemical composition (Table 4.1). Here, spurious signals (e.g. C, O) were excluded from the quantification. Especially the O content is hard to measure without artifacts since the TEM sample may already oxidize during transport between FIB and the S/TEM instruments. Precise measurement of the O concentration in Ba122 samples requires transport under a vacuum or an inert gas atmosphere, requiring specialized hardware. Both layers show the same chemical composition. The composition agrees well with the nominal composition of Ba122 within the margin of error of standardless quantification. Erroneous Cliff-Lorimer factors may explain the

increased Co and decreased As contents. However, the possibility of As loss during deposition cannot be ruled out. The oxidized Ba122-surface layer is again found for both films and visible in the O Kα maps. A difference between the films is observed in the O maps, where a faint O signal at the film-substrate interface is only visible for Ba122/slow. This indicates a possible film-substrate interface reaction for Ba122/slow.

Table 4.1: Chemical composition of Ba122/fast and Ba122/slow. Given errors correspond to one standard deviation reported by the *Esprit* software.

	Ba / at. %	Fe / at. %	Co / at. %	As / at. %
$Ba\,(Fe_{0.92}Co_{0.08})_2\,As_2$	20	36.8	3.2	40
Ba122/fast	21.5 ± 3.7	37.5 ± 0.8	3.6 ± 0.1	37.4 ± 1.1
Ba122/slow	21.0 ± 3.6	37.4 ± 0.8	3.7 ± 0.1	37.9 ± 1.1

Additional STEM-EELS analyses were performed on both Ba122 films to confirm the presence of this interface layer at the Ba122-CaF_2 interface. STEM-EELS is better suited for light-element detection since low-energy x-rays may be absorbed in the sample or in possible contamination layers on the used windowless EDXS detector [MN15]. Figure 4.16 presents elemental maps obtained by STEM-EELS. A large sample area was covered using a spatial sampling with 2.58 nm pixel size. Large Fe precipitates were in the field of view for Ba122/fast (Fig. 4.16a). The O-rich surface layer is visible for both samples (cf. O maps for Fig. 4.16a and b). A comparison of the O maps shows an pronounced O-rich film-substrate interface for Ba122/slow (Fig. 4.16a and b), which was also observed by STEM-EDXS (Fig. 4.15b). However, a close inspection of the STEM-EELS O map for Ba122/fast also reveals a faint O signal at the film-substrate interface (cf. arrow in Fig. 4.16a). This was not observed by STEM-EDXS, probably due to the lower sensitivity for light-element detection compared with STEM-EELS and a too low signal-to-noise ratio in the STEM-EDXS dataset for detecting the small O concentration.
In addition, vertical structures are visible for Ba122/slow (Fig. 4.16b), which show enhanced O and Ba signals. This secondary phase is most likely BaF_2 which is oxidized during the STEM-EELS measurement. The BaF_2 phase was detected in preliminary XRD measurements [Lan+19b]. EELS spectra from four selected regions (1–4) (marked in the ADF-STEM image in Fig. 4.16b) are plotted in Fig. 4.16c. The core-loss edges for the different elements are marked with dashed vertical lines. The power-law background was removed, spectra (1) and (2)/(3) and (4) were normalized with the same integrated loss intensity in the energy interval (460 eV to 525 eV) and vertically shifted for easier comparison.
First, spectra (1) and (2) from the Ba122 and Ba/O-rich regions are compared. A F signal is observed for both spectra (marked by a dashed arrow) confirming the presence of F in the Ba122 layer for Ba122/slow. Region (2) shows a strong O signal that is already visible in the O map in Fig. 4.16b. Regarding the ELNES, a shift of the Fe L_3 white line of about 1 eV towards higher energies was measured at the O-rich region (2) compared to region (1). This is probably caused by a change of the oxidation state for Fe in region (2). The Fe white lines shift towards higher energies for increasing oxidation state [Tan+12]. The Fe^{2+} in Ba122 may change to Fe^{3+} during oxidation, e.g. in the form of Fe_2O_3 or $Ba_2Fe_2O_5$.
Next, spectra (3) and (4) are discussed. Spectrum (3) was chosen because it shows a pronounced O signal in the CaF_2 substrate region (Fig. 4.16b). Spectrum (4) acts as a horizontally offset reference region for spectrum (3) without this O enhancement. Note that both spectra are located at the same distance away from the Ba122 film. Both spectra show the expected F

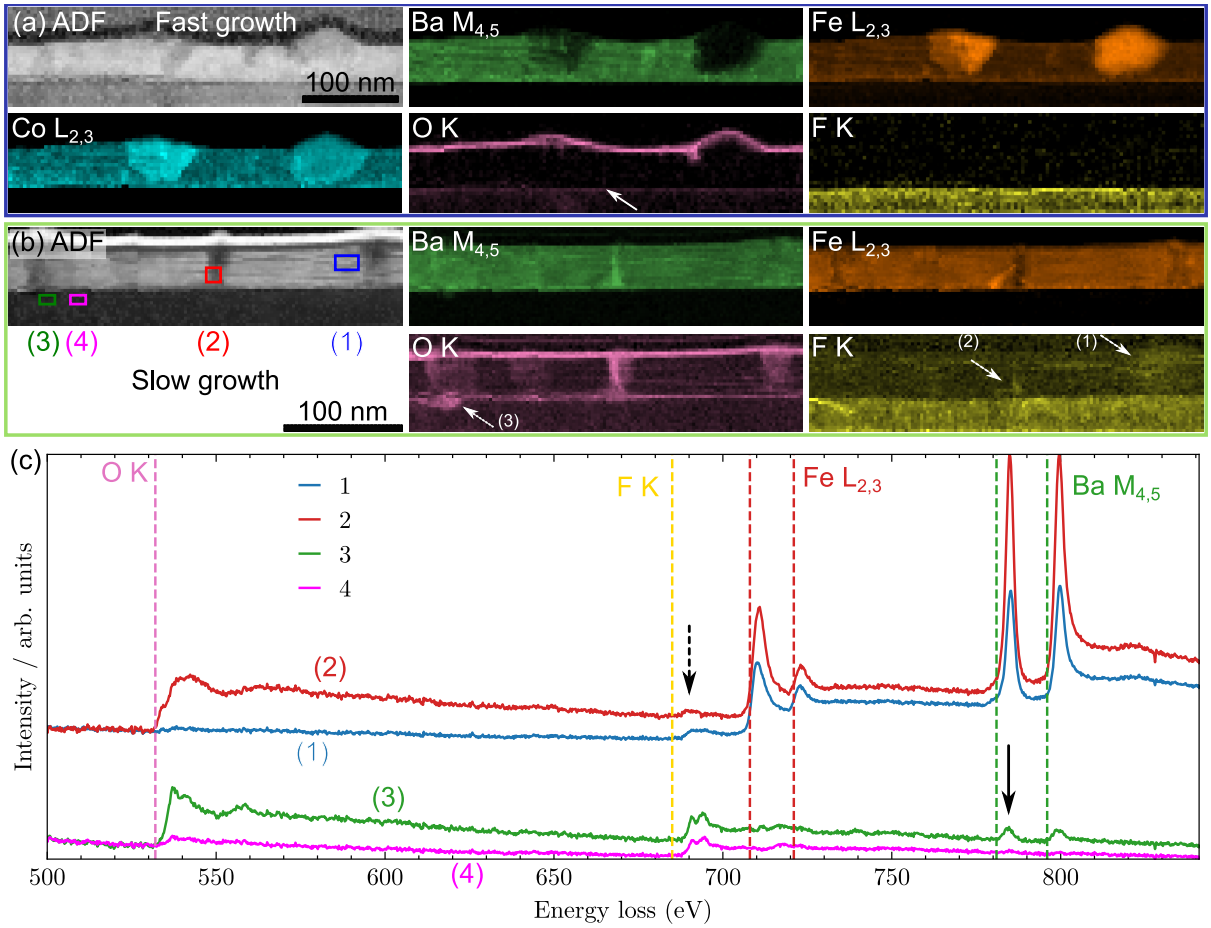

Figure 4.16: Elemental maps for (a) Ba122/fast and (b) Ba122/slow obtained from STEM-EELS. (b) An enhanced O signal is observed at the film-substrate interface for Ba122/slow. The latter also shows vertical defect structures with increased Ba/O signals. (c) Extracted EELS spectra from the regions marked in the ADF-STEM image in (b). Spectra (1) and (2) show F in the Ba122 film and at a vertical defect (dashed arrow). Spectrum (3) shows a Ba signal in the CaF_2-substrate region (solid arrow). Spectrum (4) acts as a reference for spectrum (3), confirming that the Ba signal is not an artificial signal from the nearby Ba122 film. This figure is adapted from a published figure [Grü+21a].

signal for CaF_2. However, spectrum (3) shows a slight Ba signal as Ba $M_{4,5}$ white lines (marked by a solid arrow in Fig. 4.16c). This observation confirms the diffusion of Ba into the CaF_2 substrate for Ba122/slow. Since spectrum (4) does not show a Ba signal, the observed Ba signal for spectrum (3) is not generated by an artifact from the Ba122 layer, e.g. by beam broadening in the TEM sample. Finally, the slight O signal for spectrum (4) may be caused by *in-situ* oxidation of CaF_2 during STEM-EELS acquisition.

So far, chemical analyses by STEM-EDXS and STEM-EELS revealed an O-rich film-substrate interface layer and a Ba/O-rich secondary phase. These were observed only for Ba122/slow and not for Ba122/fast.

Next, the Ba/O-rich phase is compared with structural information from HAADF-STEM imaging. Figure 4.17 shows HAADF-STEM images (upper row) of different secondary phases observed in Ba122/slow and corresponding analyses of the crystalline phases based on Fourier transforms (lower row). In all cases, a good agreement is found for BaF_2 (cf. measured and simulated values in parentheses in the power spectra), which grows syntaxially in different orientations in Ba122 (or epitaxially on CaF_2). Figure 4.17a shows a BaF_2 precipitate, which partly grows into the Ba122/slow film and into the CaF_2 substrate. Analysis of the power spectrum reveals the same

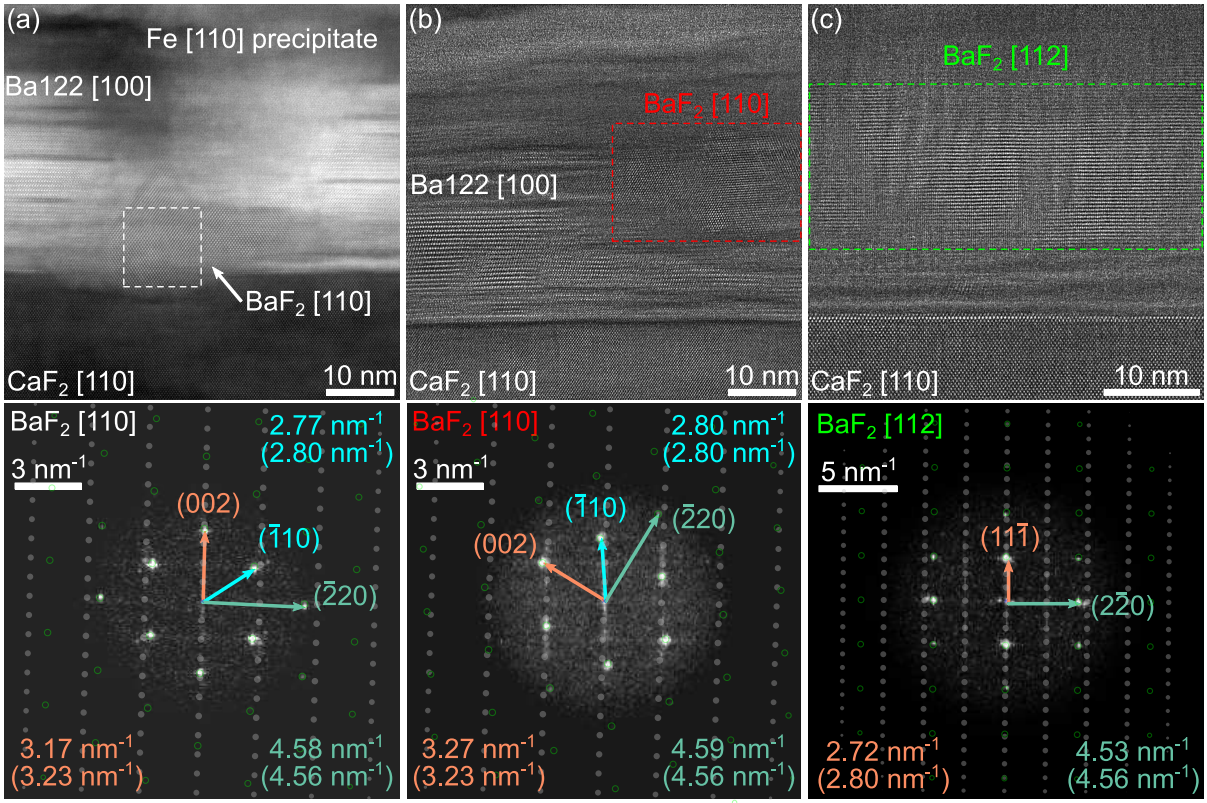

Figure 4.17: Fourier-transform analysis of BaF_2 in Ba122/slow. HAADF-STEM cross-section images (top row) and corresponding power spectra (bottom row) from the marked regions. A comparison with simulated reflections (green circles) shows a good agreement for BaF_2 in all three cases. Different orientations of BaF_2 are observed in (a–c). The gray circles in the power spectra are simulated reflections for Ba122[1 0 0], showing a small in-plane mismatch between all BaF_2 orientations and Ba122[1 0 0]. The values. This figure is adapted from a published figure [Grü+21a].

orientation of BaF_2 as the substrate, i.e. $BaF_2[1\,1\,0](001)\|CaF_2[1\,1\,0](001)$. Both materials have the same crystal structure but BaF_2 has a 13.2 % larger lattice parameter (6.1964 Å for BaF_2 vs. 5.4712 Å for CaF_2). The simulated reflections for BaF_2 are shown in the power spectra as green circles, whereas faint gray spots mark simulated reflections for Ba122[1 0 0]. Note that the latter are not visible in the power spectra because the power spectra were extracted from BaF_2 regions.

In addition, an Fe precipitate (in [1 1 0] zone-axis orientation) is observed above the BaF_2 phase in Fig. 4.17a. Such a configuration is also seen in Fig. 4.11b on Page 107, suggesting that BaF_2 formation can result in the formation of Fe precipitates. The latter may be explained by the local depletion of Ba due to BaF_2 formation. However, no As-rich phases were observed, which would also be expected besides Fe precipitates. It may be possible that the volatility of As during PLD results in a general loss of As during deposition. For example, Lee et al. [Lee+10] used a 10 % higher As content (i.e. elemental ratios Ba/Fe/Co/As = 1 : 1.84 : 0.16 : 2.2 instead of Ba/Fe/Co/As = 1 : 1.84 : 0.16 : 2) for their Ba122 target to compensate for As loss during PLD.

Figure 4.17b and c show that BaF_2 can also grow in different crystalline orientations on CaF_2 or in Ba122. The BaF_2 phase in Fig. 4.17b is rotated by 60° around the $BaF_2[1\,1\,0]$ (i.e. viewing direction). In Fig. 4.17c, a $BaF_2[1\,1\,2]$ orientation is observed. Figure 4.17b and c also show larger BaF_2 precipitates which are also partially amorphous, probably due to oxidation. These larger precipitates are rarer than the Fe precipitates but can grow from the film-substrate interface up

to the Ba122-film surface (cf. also Fig. 4.11c on Page 107 for another example). It is noteworthy that all observed orientations of BaF_2 show a small in-plane lattice mismatch of the reflections in the power spectra with the simulated Ba122[1 0 0] reflections (cf. small offset between the simulated reflections in the horizontal direction for both phases in the power spectra in Fig. 4.17). This confirms that BaF_2 can grow syntaxially inside of Ba122 in various orientations.

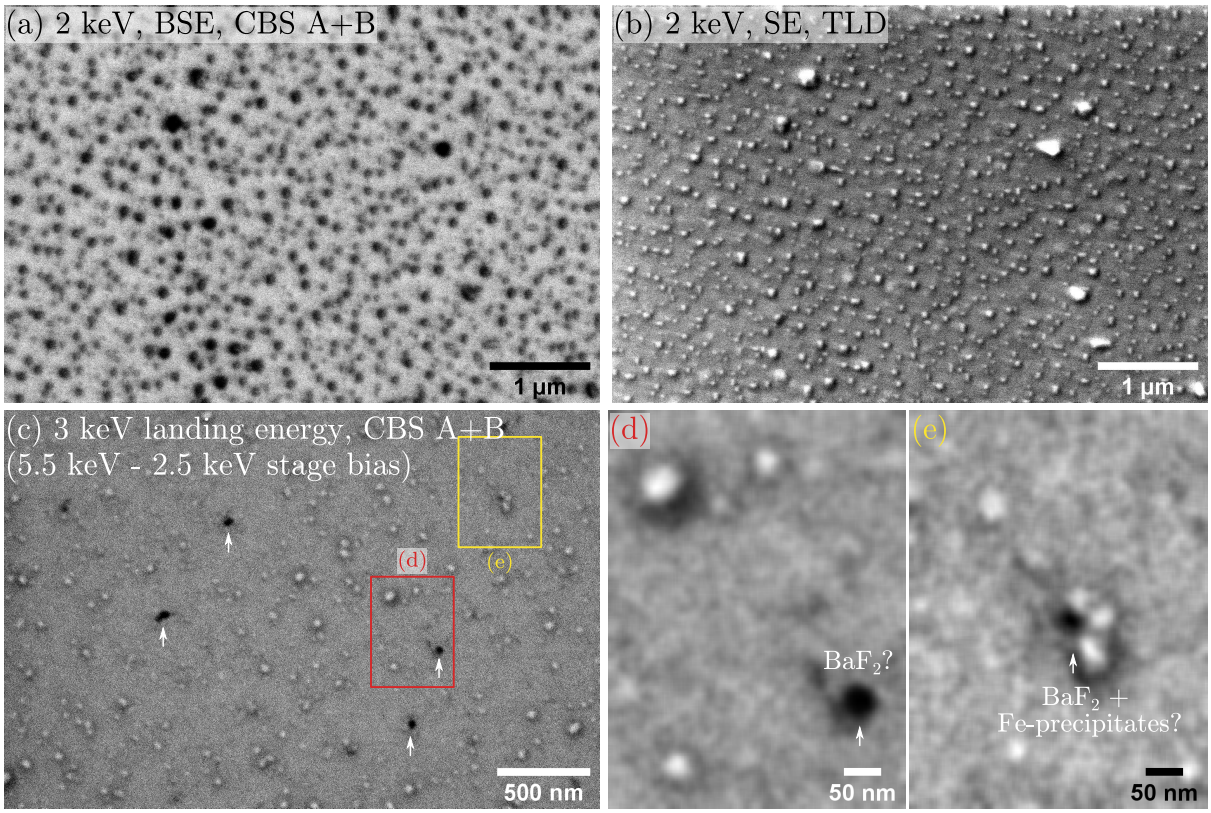

Figure 4.18: Possible observation of BaF_2 in SEM imaging. Top row: Simultaneously acquired (a) BSE- and (b) SE-SEM images of Ba122/slow at 2 keV. Fe precipitates (and possibly BaF_2 precipitates) appear dark in the BSE-SEM image. (c) SEM image with a landing energy of 3 keV of another sample region. Here, the Fe precipitates appear bright with a dark halo. The arrows mark precipitates with a distinct dark appearance compared to the Fe precipitates. These may be BaF_2 precipitates. (d and e) Higher magnification images of the region in (c). All images were acquired at a working distance of 4.1 mm.

Additional SEM imaging of Ba122/slow was performed to visualize the BaF_2 precipitates by SEM imaging (Fig. 4.18). The top row in Fig. 4.18 presents simultaneously acquired (a) BSE-SEM and (b) SE-SEM images of Ba122/slow. Fe precipitates appear bright in the SE-SEM image due to their topography, resulting in an increased SE yield (Eq. (2.37) on page 34). In contrast, a lower BSE signal is observed in compositional BSE imaging (Fig. 4.18a). This is because Fe has a lower atomic number $Z_{Fe} = 26$ than Ba122 with $\overline{Z}_{Ba122} = 34.83$[4]. BaF_2 has an average atomic number $\overline{Z}_{BaF_2} = 24.67$, slightly lower than Fe. Therefore, Fe and BaF_2 cannot be easily distinguished in the BSE-SEM image in Fig. 4.18a.

Modern SEM instruments can apply a negative bias to the sample stage to improve performance of low-energy SEM imaging. This is because the electron beam can be focused at higher beam energies by the electron optics with less aberrations and then brought to a lower landing energy

[4]Calculated by averaging using the atomic fraction of the elements in the compound. Other formulas can be used to estimate the average Z for compounds [HDB98]. A Python command-line tool (*Manuca*) was written for the calculations (`https://github.com/lukmuk/manuca`).

with a stage bias ("beam deceleration"). For example, in Fig. 4.18c, $E_0 = 5.5\,\text{keV}$ was used with a stage bias of $-2.5\,\text{kV}$ resulting in a landing energy of 3 keV. A consequence of applying a stage bias is the acceleration of generated SEs and BSEs away from the negatively biased sample surface. The BSE and SE electron trajectories depend on the working distance, detector geometry, and stage bias. This can be used to alter the effective BSE collection angles on the CBS-detector segments to optimize compositional BSE contrast for a specific sample material (see, e.g., Wan et al. [Wan+16] or Bouwer et al. [Bou+16]). Here, only a qualitative test using beam deceleration was used to investigate the changes of the BSE image contrast. This led to an interesting observation shown in Fig. 4.18c. Note that a different sample region than in Fig. 4.18a is shown. The same working distance of 4.1 mm was used for Fig. 4.18a and c. In the latter image, the Fe precipitates show a slightly higher intensity than the Ba122 film but with a dark halo. The latter may be an artifact of the imaging conditions, but could also stem from increased oxidation around Fe precipitates, leading to a reduction in atomic number compared to Fe/Ba122. Interestingly, a few dark regions are also visible (Fig. 4.18c, marked by arrows) with lower concentration than the Fe precipitates. These precipitates may be BaF_2 precipitates. Figure 4.18d and e show two regions from c at higher magnification, again with possible BaF_2 precipitates marked with arrows. The isolated, larger BaF_2 precipitate in Fig. 4.18d could be similar to the one shown in Fig. 4.11c on Page 107, i.e. without an associated Fe precipitate and growing through a large portion or the whole Ba122 film. Similarly, the BaF_2 precipitate in Fig. 4.18d is surrounded by Fe precipitates, similar to the situation shown in Fig. 4.11b on Page 107. However, the chemical composition of the dark regions in Fig. 4.18c was not further investigated and the BaF_2 phase was not explicitly confirmed. Still, based on the lower concentration and the sudden change in contrast compared to the other (Fe) precipitates shown in the same SEM image, BaF_2 seems quite likely. These SEM analyses show that contrast in BSE-SEM imaging can be optimized using the stage bias as an additional parameter (together with electron energy, landing energy, working distance, and CBS-detector segments). This enables the investigation of the size and distribution of BaF_2 precipitates on larger samples areas (not done here).

To summarize until here, BaF_2 forms in Ba122/slow and not in Ba122/fast. This is in agreement with XRD measurements [Lan+19b]. BaF_2 is found at the film-substrate interface and can grow into the CaF_2 substrate. BaF_2 at the film-substrate interface can lead to the formation of Fe precipitates on top of BaF_2. In addition, BaF_2 can also form in the Ba122 film as large precipitates. Chemical analyses using high electron doses show an O signal instead of F for BaF_2 due to *in-situ* oxidation (Fig. 4.1 on page 94). Possible other Ba/O-rich phases such as BaO or BaO_2 were also checked but disagree (not shown) with the atomic structures observed by HAADF-STEM analyses. Finally, it was shown that BaF_2 precipitates can be imaged by altering the BSE contrast with stage bias in SEM imaging.

4.2.3 Ba122-CaF_2 Interface

Next, the crystalline structure of Ba122/fast (a,d,e) and Ba122/slow (b,f,g) are compared in Fig. 4.19. The images are background-subtracted and ABS-filtered for better visibility of the crystal structure (cf. Fig. 3.9 on page 70). A high-quality Ba122-film structure is visible for Ba122/fast (Fig. 4.19a). In contrast, Ba122/slow shows horizontal lines with reduced HAADF-STEM intensity. These may be caused by the presence of BaF_2, where the mismatch between Ba122 and BaF_2 along the *c*-direction result in stacking faults. This is similar to nanoparticles in REBCO films and the formation of extra CuO planes as stacking faults (cf. Fig. 5.31 on

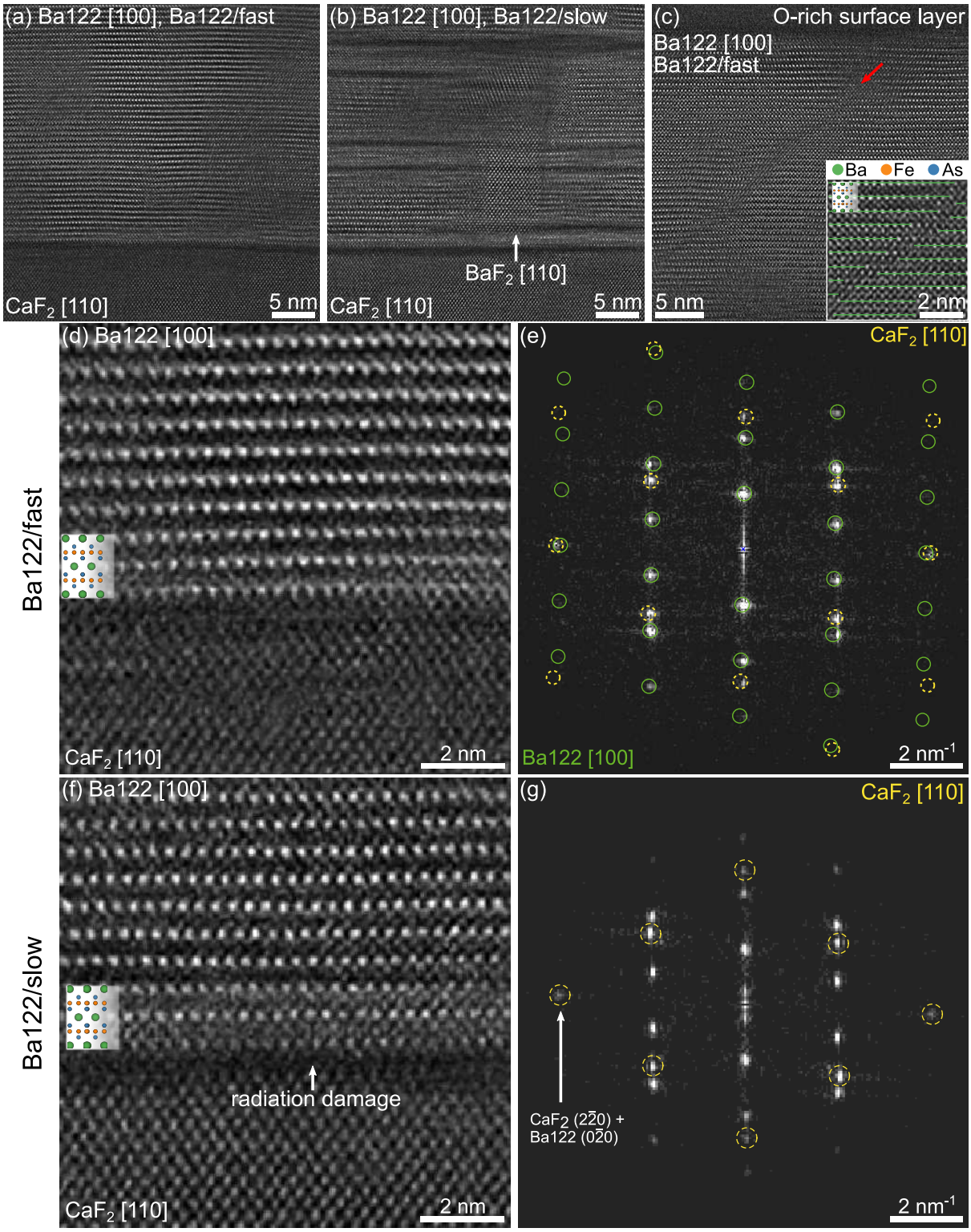

Figure 4.19: High-resolution HAADF-STEM cross-section images and Fourier-transform analysis of Ba122/fast and Ba122/slow. Background-subtracted and ABS-filtered HAADF-STEM images of (a) Ba122/fast and (b) Ba122/slow. BaF_2 and planar defects (dark horizontal lines) are visible for Ba122/slow. Epitaxial growth without an amorphous interface layer is visible in the magnified images of the film-substrate interfaces for (d) Ba122/fast and (f) Ba122/slow and the corresponding power spectra (e,g). Simulated positions of Bragg reflections for Ba122[1 0 0] (green, solid circles) and CaF_2[1 1 0] (dashed, yellow circles) are overlaid in the power spectra. (c) An extended antiphase boundary in Ba122/fast (red arrow). The inset shows the offset of the Ba122 structure in *c*-direction with the Ba planes marked with green lines. This figure is adapted from a published figure [Grü+21a].

page 198). These planar defects will be discussed further below.
Both films show a sharp, crystalline film-substrate interface without any amorphous interaction layer (cf. Fig. 4.19d for Ba122/fast and f for Ba122/fast). As shown in Fig. 4.1 on page 94, such an amorphous layer can result from electron-beam irradiation. The dark region at the interface in Fig. 4.19f may be caused by electron-beam irradiation. The epitaxial relationship $Ba122[1\,0\,0](0\,0\,1)\|CaF_2[1\,1\,0](0\,0\,1)$ is confirmed by the power spectra in Fig. 4.19e and g of the corresponding HAADF-STEM images in d and f. In Fig. 4.19e, the simulated reflections of both phases are overlaid as circles (dashed yellow circles for CaF_2, green solid circles for Ba122). Only the CaF_2 reflections are marked in Fig. 4.19g for better visibility. Ba122 growth starts with the Ba plane (brightest atomic columns in the HAADF-STEM images of Ba122), which was also observed by Lee [Lee12, p 70]. The epitaxial growth of Ba122 starting with a Ba plane can also be observed in the (less noisy) HAADF-STEM images in Fig. 3.10 on page 71.

4.2.4 Antiphase Boundaries

An antiphase boundary (APB) in Ba122/fast is identified in Fig. 4.19c (marked by a red arrow). As shown in the inset, the Ba122 structure is shifted in c-direction between the two Ba122 grains. Here, the Ba planes are highlighted with green solid lines as a guide for the eye. The shift along the c-direction between the two Ba122 grains in Fig. 4.19c was measured as (0.272 ± 0.025) nm. The error corresponds to a statistical error from the determination of the Ba-column positions using *Atomap*. However, systematic experimental errors due to an erroneous length calibration in the STEM image may result in a larger error. The measured value corresponds roughly to the Ca-plane spacing of 0.274 nm (i.e. half the CaF_2-lattice constant) in CaF_2 along the c-direction. This suggests that the APBs may be caused by atomic steps with step height of 0.274 nm (i.e. a $a_{CaF_2}/2[0\,0\,1]$ shift) at the CaF_2 surface. This agrees with the findings of Haindl et al. [Hai+19] for $SmO_{1-x}F_xFeAs$ on CaF_2.
Indeed, such atomic steps are occasionally observed at the Ba122-CaF_2 interface (Fig. 4.20a,b). The steps are visible by the vertical shift of the first Ba planes, which appear brightest in the shown HAADF-STEM Z-contrast images. The APB in Fig. 4.20a is marked by a red square and magnified in Fig. 4.20b (red dashed line). The green lines again mark the Ba planes and show the offset of the first few unit cells of Ba122. Here, the APB is annihilated by another planar defect (marked by a solid arrow), which could not be identified in this image. Up to here, APBs were only shown for Ba122/fast. This is because the APB density was higher and the APBs more extended for Ba122/fast than for Ba122/slow. However, APBs can also form in Ba122/slow (Fig. 4.20d). In this example, the APB is present in the lower half of the HAADF-STEM image and annihilated by a stacking fault (marked by an arrow in Fig. 4.20d). The Ba planes align in the upper part of the image (see solid green lines as a guide).
This observation provides an explanation for the difference in APB density between Ba122/fast and Ba122/slow. In Ba122/slow, more planar defects are present, which annihilate APBs. Additionally, the formation of BaF_2 at the film-substrate interface for Ba122/slow may act as a competing process to APB formation, since the substrate steps could also act as nucleation sites for BaF_2. The effect of APBs on the superconducting properties was not measured here. However, APBs are also observed in other IBSs [Hai+19] and clearly interrupt the superconducting FeAs planes.
Another interesting observation at the Ba122-CaF_2 interface is shown in Fig. 4.20c. Here the first unit cell shows a stacking fault, where the first two Ba planes grow in a "cube-on-cube" instead of a "zigzag" configuration. The Ba-plane spacing is also increased from ~ 0.65 nm to

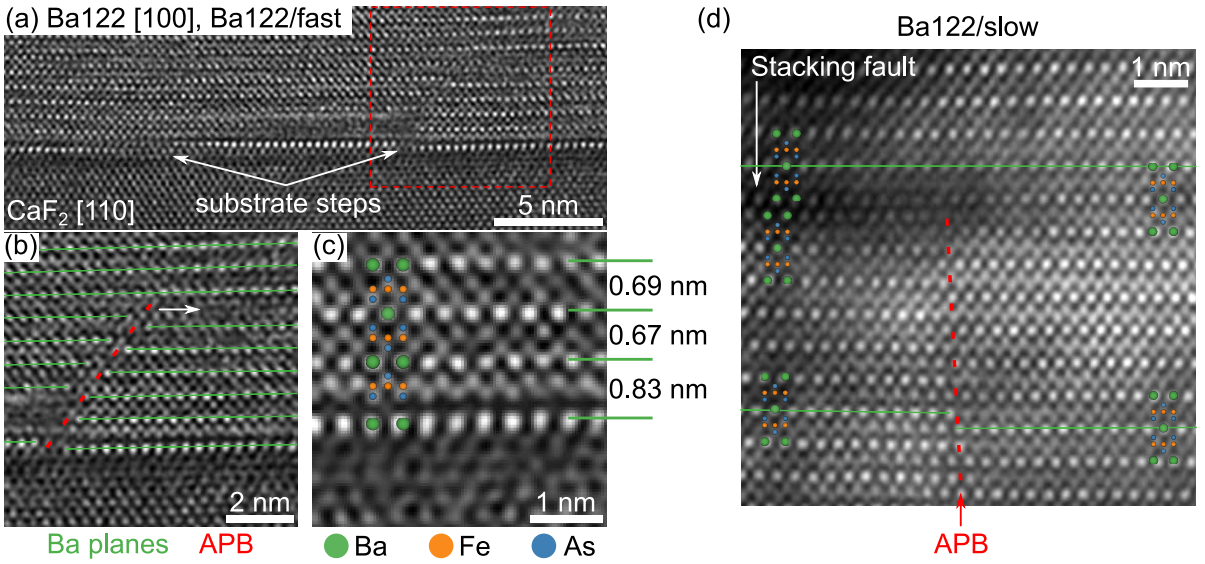

Figure 4.20: Antiphase boundaries in Ba122 films on CaF_2. Background-subtracted and ABS-filtered HAADF-STEM images of the Ba122-CaF_2 interface for Ba122/fast with two atomic substrate steps (marked with arrows). (b) An antiphase boundary (APB, red dashed line) in Ba122 resulting from the substrate step. The APB is annihilated at another planar defect (marked by an arrow), visible by the vertically aligned Ba planes (green lines) above the planar defect. (c) Alternate Ba122 stacking (i.e. cube-on-cube alignment of Ba columns in the first Ba122 unit cell) is observed for the region in (a). (d) Example for an APB in Ba122/slow. A stacking fault annihilates the APB in the top-left region (marked by an arrow). This figure is adapted from a published figure [Grü+21a].

about 0.83 nm. The distance between the first Ba plane and the first FeAs plane is larger than the expected Ba-As distance (cf. overlaid structure models in Fig. 4.20c). The reduced intensity between the first Ba and As planes suggests the presence of a light element, possibly an atomic plane of O or F. This could not be clarified in this work. STEM imaging techniques which are more sensitive to light elements such as annular bright-field (ABF) [Fin+10] or integrated differential phase-contrast (iDPC) [LBL16] STEM imaging may be able to clarify the exact atomic structure.

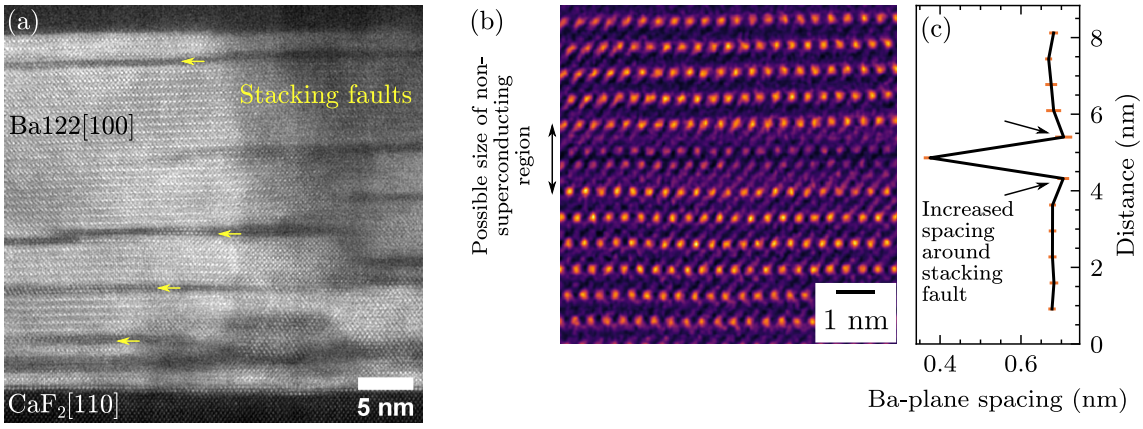

Figure 4.21: Strain analysis of stacking faults in Ba122/slow. (a) Representative HAADF-STEM cross-section image of a region in Ba122/slow with several stacking faults (marked by arrows). Image filtering: Non-linear filter [Du15] with (Power 2, Ro 0.6, Cycles 5, Step 2, Delta 5, Wp 0.65). (b) Color-coded HAADF-STEM image and (c) corresponding quantitative STEM analysis of out-of-plane strain around the stacking fault, which shows a $\sim 4\,\%$ increase in Ba-plane spacing of adjacent Ba planes (marked by arrows). Error bars correspond to one standard deviation. Figures (b) and (c) are adapted from a related publication [Grü+21a].

4.2.5 Planar Defects

The observed planar defects in Ba122 films are discussed in the following. In general, planar defects appear as dark, horizontal lines in HAADF-STEM Z-contrast imaging (cf. Fig. 4.19b, Fig. 4.17a and b on Page 114, Fig. 4.11b and c on Page 107). Figure 4.21a presents an overview image of Ba122/slow showing a few stacking faults (marked by yellow arrows). Stacking faults appear at the Ba planes and shift the Ba122 structure by $\langle 1\,0\,0\rangle/2$ (Fig. 4.21b). The positions of the Ba-atomic columns in Fig. 4.21b were quantitatively analyzed with two-dimensional peak fitting using *Atomap*. The Ba-plane spacing along the c-direction at the analyzed stacking fault was evaluated and is plotted in Fig. 4.21c. The nominal Ba-plane spacing is about 0.65 nm for Ba122, corresponding to $c/2$ with $c = 1.3022\,\text{nm}$. The Ba-plane spacing reduces to $(0.375 \pm 0.016)\,\text{nm}$ at the stacking fault due to the missing FeAs planes. In addition, a slight increase in Ba-plane spacing to $(0.705 \pm 0.012)\,\text{nm}$ compared to the (average) Ba122 matrix $(0.677 \pm 0.003)\,\text{nm}$ is visible for the Ba planes adjacent to the stacking faults (marked by arrows in Fig. 4.21c). This corresponds to a 4.1 % strain for the Ba planes surrounding a stacking fault. The bond angles in the $FeAs_4$ tetrahedrons have a strong influence on the superconducting properties [Uch15, p 64]. The optimal T_c is achieved for an angle of 109.5°, i.e. an undistorted tetrahedron. Therefore, the distortions caused by the increase in Ba-plane spacing around a stacking fault may increase the vertical extension of the non-superconducting region to about $2 \times 0.7\,\text{nm} + 0.4\,\text{nm} = 1.8\,\text{nm}$ (marked with a double-headed arrow in Fig. 4.21b). The increase of the measured $c/2$ values for Ba122 films on CaF_2 compared to literature data for bulk Ba122 is also observed in XRD measurements [Lan+19b]. This is explained by a compressive biaxial in-plane strain of Ba122 on CaF_2, which is compensated by an enlargement of the Ba122 unit cell in c-direction for these films (Poisson effect [Hän+19; Sat+20]). However, STEM distortions and sample drift during image acquisition can introduce systematic errors in the absolute length values measured in single-frame HAADF-STEM images.

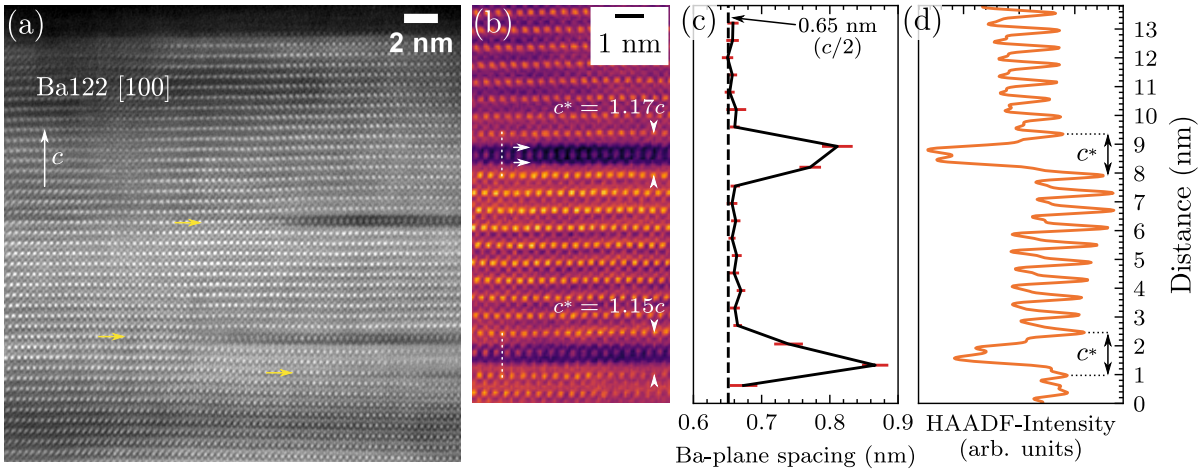

Figure 4.22: Strain analysis of Ba planes with reduced HAADF-STEM intensity. (a) ABS-filtered HAADF-STEM image of Ba122/slow showing a few planar defects (marked by arrows) with reduced intensity. Low-frequency HAADF-STEM intensity modulations are caused by image filtering. (b) Magnified image of the two upper defects in (a) and corresponding line profiles in c-direction of (c) the Ba-plane spacing and (d) the horizontally summed-up HAADF-STEM intensities. The local lattice parameter c^* at the planar defects is 15 %/17 % larger than the c-lattice parameter in Ba122. The local decrease in intensity hints at possible intercalation of light elements (O, F) at the defects. Figure a–c are adapted from a published figure [Grü+21a].

Another type of planar defect was observed in Ba122 (mostly in Ba122/slow), showing a reduced image intensity compared to the surrounding Ba122 matrix (Fig. 4.22a, marked with yellow arrows). However, no double Ba planes are visible at the planar defect compared to the previously discussed stacking faults. Instead, a single Ba plane shows reduced Z-contrast and the local c-lattice parameter is increased by about 15 % to 20 % (Fig. 4.22b) to c^*. Note that no $\langle 1\,0\,0 \rangle/2$ shift is observed in contrast to the previously shown stacking faults (cf. Fig. 4.21b). This can be more easily observed by following the dashed lines in Fig. 4.22b. These defects were also reported by Zheng et al. [Zhe+19] for Ba122 bulk samples. Because of their appearance, these planar defects are denoted as "isolated Ba planes" in the following. It is important to note that these isolated Ba planes can also be generated *in-situ* by electron-beam irradiation (Fig. 4.2 on Page 96). However, careful HAADF-STEM imaging at lower magnification often shows these defects in Ba122 films, indicating that these planar defects can also form in the as-deposited Ba122 films. In addition, the appearance of these planar defects in different Ba122 samples was reproducible (not shown). For example, TEM samples of Ba122/fast often did not show planar defects, whereas TEM samples of Ba122/slow were rich in planar defects. This consistency between different TEM samples of the same Ba122 sample provides evidence that the planar defects are not (only) caused by FIB preparation or electron-beam irradiation. The TEM samples of Ba122 single crystals containing these planar defects investigated by Zheng et al. [Zhe+19] were prepared by low-energy Ar^+ milling.
The Ba-plane spacings for the two isolated Ba planes were evaluated analogous to the stacking fault in Fig. 4.21, i.e. by fitting the bright atomic-column positions of Ba. Figure 4.22c and d show the Ba-plane spacing and horizontally-summed HAADF-STEM intensities of Fig. 4.22b, respectively. Here, the lattice parameter c^* is increased by (15.6 ± 1.7) % (lower defect) and (17.2 ± 1.5) % (upper defect) compared to the averaged c-lattice parameter of the surrounding Ba122 matrix. The decrease in intensity at the defects (Fig. 4.22d) hints at possible incorporation of light elements at the isolated Ba planes. However, these cannot be resolved together with high-Z elements in HAADF-STEM Z-contrast imaging and other imaging techniques (ABF- or iDPC-STEM) are required. Alternatively, the Ba plane might be partially substituted by an FeAs plane, since Zheng et al. [Zhe+19] reported a slightly enhanced Fe signal at these planar defects. An extra FeAs plane, however, should lead to a similar HAADF-STEM intensity as the surrounding FeAs planes in the undisturbed Ba122 film instead of the observed reduction in Z-contrast. It is therefore concluded that light elements (O/F) are also located at the isolated-Ba-plane defects, similar to stacking faults.

STEM-EELS mapping was used to get insights into the chemical composition of the planar defects with a dark appearance in HAADF-STEM imaging, i.e. (i) stacking faults and (ii) isolated Ba planes. Figure 4.23a shows an overview ADF-STEM image of Ba122/slow with the marked STEM-EELS acquisition region. After the acquisition, the EELS spectra were summed up along the horizontal (in-plane) direction and the core-loss-signal line profiles along the vertical (out-of-plane/c-) direction were extracted and plotted as an overlay on the ADF-STEM signal (Fig. 4.23b). Due to the limited spatial resolution of the used STEM-EELS probe settings, the planar-defect type (stacking fault or isolated Ba plane) cannot be identified based on the ADF-STEM images. However, the increase of the Ba signal at the planar defect identifies the planar defect as a stacking fault. The double Ba planes at the stacking fault are probed simultaneously with the used STEM-EELS settings (probe size probably around 0.5 nm). This increases the Ba signal at the stacking fault compared to the surrounding Ba122 matrix. Regarding the other elements, a depletion of Fe, As, and Co is visible as expected for a stacking fault with a double

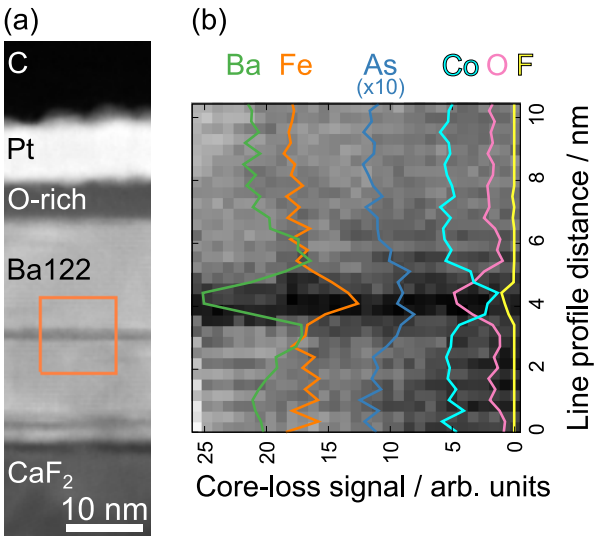

Figure 4.23: EELS analysis of a stacking fault in Ba122/slow. (a) ADF-STEM image of Ba122/slow with the marked acquisition region (orange square). (b) ADF-STEM image and overlaid vertical line profiles of the core-loss intensities for different elements. Enhanced O and F signals are observed at the stacking fault. The increased signals for Ba and the decreased signals for Fe, As, and Co agree with the atomic structure shown in Fig. 4.21b. This figure is published in an article [Grü+21a].

Ba plane (cf. atomic structure in Fig. 4.21b). The As signal is multiplied by a factor 10 since the As $L_{2,3}$ edges are weak at their onset energies of 1323 eV (L_3)/1359 eV (L_2). A clear O and a faint F signal is visible at the stacking fault, as expected from the reduced HAADF-STEM Z-contrast. The non-vanishing O signal in the Ba122 film may result from TEM-sample-surface oxidation during TEM-sample transfer in air between the FIB and S/TEM instruments (about 20 min exposure).

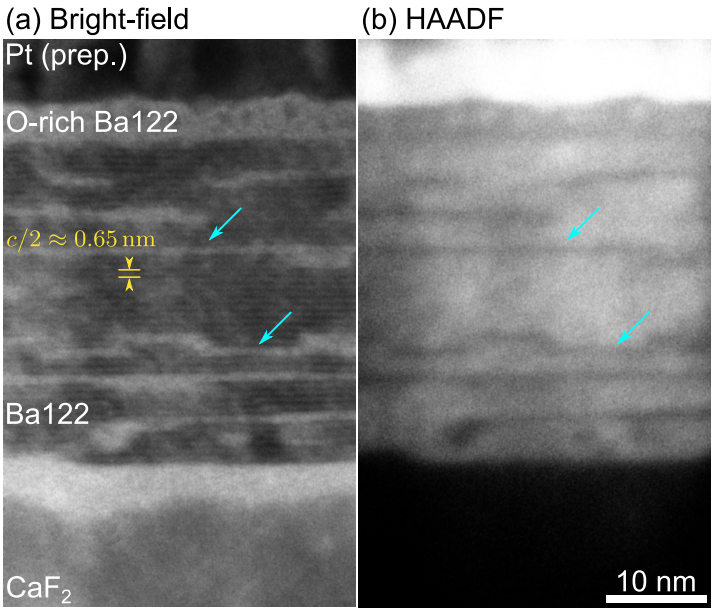

Figure 4.24: STEM-in-SEM imaging of planar defects in Ba122/slow. Exposure of the TEM sample to ambient air was avoided by *in-situ* FIB preparation and subsequent STEM imaging. Simultaneously acquired (a) bright-field and (b) HAADF-STEM-in-SEM images at $E_0 = 30$ keV of Ba122/slow. The diagonal arrows mark two exemplary planar defects showing reduced intensity. The Ba122(0 0 2) lattice fringes are resolved in (a) (marked by the yellow lines/arrows). This figure is adapted from a published figure [Grü+21a].

Additional STEM-in-SEM imaging was used to rule out possible oxidation of planar defects during sample transfer. The TEM sample is prepared by FIB milling and imaged by STEM-in-SEM without breaking the microscope vacuum. Figure 4.24a and b show simultaneously acquired bright-field- and HAADF-STEM-in-SEM cross-section images of Ba122/slow at $E_0 = 30$ keV. The diagonal, blue arrows mark two exemplary planar defects. The latter show a reduced intensity in the HAADF-STEM-in-SEM image, similar to the other conventional HAADF-STEM images shown earlier. This confirms that light elements (O or F) are present at the planar defects in the as-deposited Ba122/slow film. A close inspection of the bright-field STEM-in-SEM image reveals the lattice fringes of the Ba122(0 0 2) lattice planes with a separation of $c/2 = 0.65$ nm

(Fig. 4.24a, yellow arrows). The bright layer at the Ba122-CaF_2 interface is probably caused by electron-beam irradiation or amorphization by FIB milling.

To conclude, this section showed experimental results for two types of planar defects in the investigated Ba122 films. Both types appear with reduced Z-contrast in HAADF-STEM images. One planar defect is a stacking fault consisting of a double Ba plane (or described as a missing FeAs plane) and an $\langle 1\,0\,0\rangle/2$ shift of the Ba122 structure. In addition, the adjacent lattice planes around a stacking fault are strained along the c-direction. STEM-EELS analysis reveals the presence of O and F at the stacking faults. FIB preparation and subsequent *in-situ* STEM-in-SEM imaging confirm that these light elements are most likely present at stacking faults in the as-deposited film. However, dose-intensive analysis by electron microscopy in the Ba122-CaF_2 material systems are often destructive and should be evaluated carefully. This is also true for the shown STEM-EELS and STEM-EDXS results.
The second type of planar defects are "isolated Ba planes" where the Ba122 unit cell is about 15 % to 20 % enlarged in c-direction and the HAADF-STEM intensity is reduced. This type of defect is present in the as-deposited films, as confirmed by lower-magnification imaging with reduced electron dose. However, the isolated Ba planes can *also* be generated *in-situ* under electron-beam irradiation, requiring careful STEM imaging with minimal electron dose. The susceptibility of a particular investigated TEM sample of Ba122 can be tested by a repeated acquisition of STEM images at the same region. Monitoring the (possible) formation of the isolated Ba planes upon imaging can give the operator a feel for the TEM-sample stability. The latter may depend, e.g., on the TEM-sample thickness and duration of exposure to ambient air. Ba122/slow showed a higher concentration of both planar-defect types than Ba122/fast. A reason for this could be the oxidation of Ba122 during PLD with residual gases in the PLD chamber. A slower deposition of Ba122 may result in oxidation during PLD, which in turn promotes the formation of planar defects. Another source of O might be the PLD target itself. However, the same PLD targets were used for Ba122/slow and Ba122/fast, and the latter showed only a small concentration of planar defects. This may rule out the Ba122 target material as the primary source of O.
The formation of BaF_2 in Ba122/slow is another possible explanation for the formation of planar defects (mainly) in Ba122/slow. Planar defects may form to compensate for the out-of-plane lattice mismatch between the BaF_2 and Ba122 crystal structures. Additionally, F might diffuse into the planar defects, leading to a reduction in Z-contrast. F could be exchanged for O during the exposure of the TEM sample to air and during TEM analysis.
A better understanding of planar-defect formation is essential for the growth of high-performance Ba122 films for technical applications. The defects have an extension in the c-direction of about 1.6 nm (isolated Ba planes) and 1.8 nm (stacking faults, assuming the adjacent, strained FeAs are non-superconducting). This is in the range of the out-of-plane coherence length of Ba122 $\xi(0\,\mathrm{K})_{\mathrm{Ba122},c} \approx 1.2\,\mathrm{nm}$ (cf. Table 2.1 on page 7), meaning that these defects act as efficient, two-dimensional, plate-like pinning centers for $H \parallel ab$. Only the T_c values were measured for Ba122/slow and Ba122/fast, and not $J_c(H)$. As a result, the effectiveness of the planar defects on J_c could not be clarified here. However, Yuan et al. [Yua+17] measured an increase in J_c for $H \parallel ab$ for their Ba122 films on CaF_2 showing a high density of stacking faults. They attributed the increased $J_c(H \parallel ab)$ to vortex pinning at planar defects. This shows, that a detailed understanding of planar-defect formation could lead to purposeful planar-defect engineering and increased $J_c(H \parallel ab)$ in Ba122 films.

4.3 $Ba(Fe,Co)_2As_2$ with Artificial Pinning Centers

Previous work. This section covers the microstructural characterization of Ba122 films with embedded nanoparticles (so-called nanocomposite films). Nanoparticles (NPs) can act as artificial pinning centers if they have a favorable size – in the range of the coherence length ξ – and shape [FKM17]. Associated crystalline defects such as dislocations or stacking faults may be introduced by the NPs in the Ba122 matrix, thereby providing further pinning centers. Still, a high-quality superconducting Ba122 film with good crystalline quality (or texture) is desired. The combination of (i) a high-quality superconducting film and (ii) homogeneously distributed NPs requires precise knowledge about the relation between the fabrication parameters and the resulting film. The NP concentration is given as $x\,\mathrm{mol}\,\%$ for a composition of $(Ba(Fe_{0.92}Co_{0.08})_2As_2)_{1-x}(NP)_x$.
Here, a quasi-multilayer PLD approach is used, where the pristine Ba122 and nanoparticle targets are repeatedly swapped during PLD between a given number of laser pulses. This process is more common for REBCO films [Cai+05b; Gap+05; Kie+11; Aye+21] and is investigated here for IBSs. In principle, this method offers a high degree of flexibility as the NP concentration can be freely tuned during PLD. This is in contrast to pre-mixing the Ba122 and NP contents directly in a single, sintered PLD target. In the latter, the mixed Ba122-NP targets have to be fabricated before PLD and the NP concentration is fixed during target fabrication. A complication for quasi-multilayer PLD is the possible interaction of Ba122 and the NP materials to form other secondary phases.
For Ba122, the multilayer approach was not employed yet for nanoparticles. However, it was used to fabricate superlattices of Ba122 and another material to control the strain in the films [Lee+13], but not with the aim of introducing nanoparticles. However, Lee et al. [Lee+13] used a O-rich $BaFe_2As_2$ target (besides $SrTiO_3$) and observed nanoparticle formation in the resulting film, which is similar to the results found here for $BaHfO_3$ and $BaZrO_3$. $BaZrO_3$ was successfully incorporated into Ba122 films by other groups with premixed Ba122-$BaZrO_3$ targets [Miu+13; Miu+19; Lee+17], leading to higher J_c values due to improved flux pinning. Xu et al. [Xu+19] used Y_2O_3 nanoparticles instead of $BaZrO_3$ and observed the formation of amorphous c-aligned nanocolumns. These O-containing nanoparticle materials are chosen due to their chemical stability and popularity in REBCO nanocomposites. However, in contrast to REBCO, Ba122 is not an oxide material and the Ba122 matrix (and other IBSs) can easily oxidize. Therefore, novel nanoparticle materials should be explored for the IBSs. Here, InAs is tested as a NP material since it is an arsenide similar to Ba122. The investigated Ba122-NP samples were fabricated by **Sven Meyer** and **Nico Beisig**. The reader is referred to the thesis of Sven Meyer [Mey21] on details of the growth of the materials and their superconducting properties.

4.3.1 $BaHfO_3$ and $BaZrO_3$ Nanoparticles

The barium oxide perovskites $BaHfO_3$ (BHO) and $BaZrO_3$ (BZO) are commonly used as NPs in REBCO films and BZO was already employed for IBSs [Miu+13; Lee+17; Miu+19] using premixed Ba122-BZO PLD targets. Therefore, BHO and BZO were chosen first for testing the quasi-multilayer PLD method. The results of this chapter are partially published in an article [Mey+20]. $CaF_2(0\,0\,1)$ was used as substrate since it resulted in reproducibly well-grown Ba122 films for the used PLD setup. The substrate temperature during PLD was between 700 °C to 750 °C. Preliminary XRD measurements for the BHO/BZO-Ba122 nanocomposites showed a clear trend towards a reduced Ba122 film quality with increasing NP content. The Bragg

reflections in XRD for BHO/BZO became only visible at such high NP concentrations that the Ba122 reflections nearly vanished [Mey21, p 48]. In addition, the T_c values also decrease with increasing NP concentration. This indicates an increased disturbance of the Ba122 film with NP concentration and is expected. The BHO/BZO concentration must be well balanced in Ba122, which is possible with the quasi-multilayer PLD method.

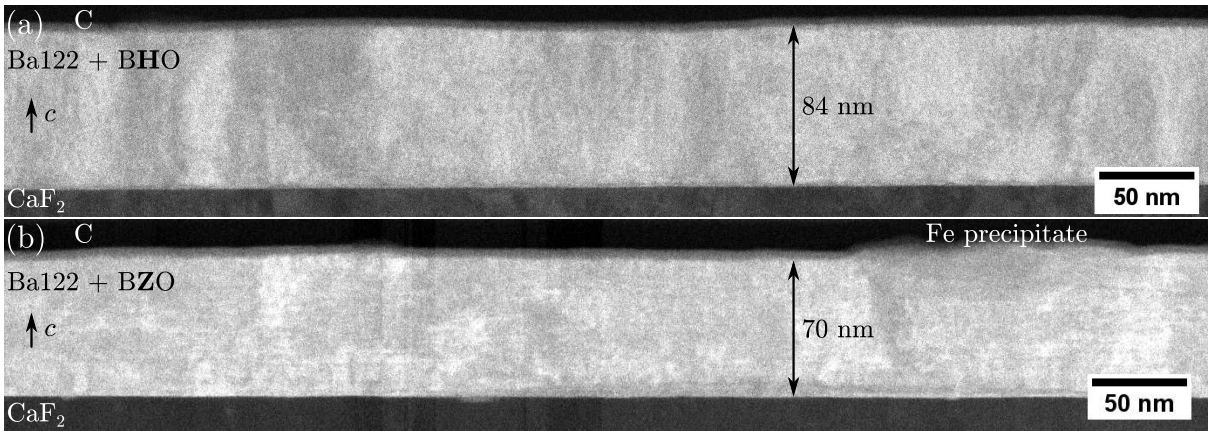

Figure 4.25: Low-magnification HAADF-STEM cross-section images of (a) Ba122-BHO and (b) Ba122-BZO nanocomposite films. A homogeneous film thickness of about (a) 84 nm for the Ba122-BHO film and (b) 70 nm for the Ba122-BZO film is observed. (b) On the right side, an Fe precipitate is observed, which grows slightly out of the film's surface.

Figure 4.25 shows low-magnification HAADF-STEM cross-section images of (a) Ba122-BHO (upper row) and (b) Ba122-BZO nanocomposite films (lower row). The low-magnification images reveal a homogeneous film thickness of about 80 nm for the Ba122-BHO film and 74 nm for the Ba122-BZO film. The homogeneous film thickness indicates a high-quality Ba122 film growth. An Fe precipitate is visible on the right side in Fig. 4.25b. The precipitate is identified by the slight change in image intensity and the fact that Fe precipitates can grow out of the film surface (here only a few nm). The nominal NP concentration in these films is about 2 mol %, as determined by inductively coupled plasma mass spectroscopy (ICP-MS). However, STEM-EDXS analyses suggests a higher concentration of about 20 mol % of BHO/BZO for the films. This will be discussed further below.

Figure 4.26 presents representative HAADF-STEM cross-section images of Ba122-BHO- (upper row) and Ba122-BZO-nanocomposite films (lower row). In both cases, a layered structure in the *c*-direction is observed (marked by horizontal arrows in Fig. 4.26a and Fig. 4.26d), indicating an aggregation of NPs. The NP layers are interrupted by Ba122 and do not form a complete NP layer Hence, the name "quasi-layer" is used for such microstructures. The layer spacing in *c*-direction is about 5 nm to 10 nm. In a layer, cloud-like contrast variations along the in-plane direction are observed with a spacing of a few nm (e.g. 6 nm, marked with vertical dashed arrows in Fig. 4.26a). Here, the cloud-like contrast variations are interpreted as embedded NPs with a diameter of about 5 nm.
The HAADF-STEM intensities at the NPs are different for BHO and BZO, where BHO appears brighter than Ba122 (marked by arrows with filled heads in Fig. 4.26a) and BZO appears darker than Ba122 (Fig. 4.26d). At first glance, the bright structures are associated with the NP positions since they appear with a more roundish shape. However, the dark structures (marked with white-headed arrows in Fig. 4.26a) could be the actual positions of BHO NPs. The latter

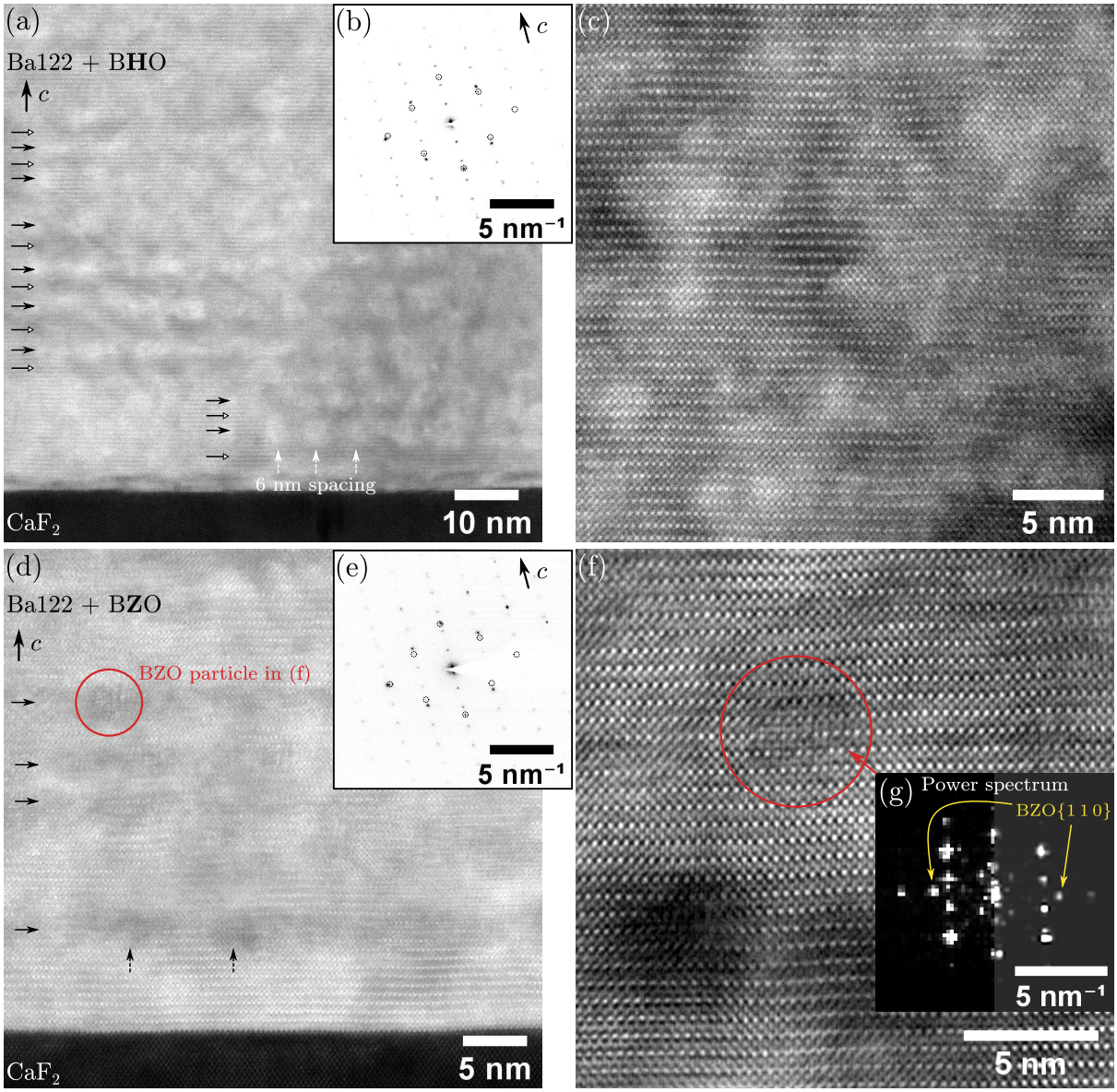

Figure 4.26: HAADF-STEM images of Ba122 nanocomposite films with added $BaHfO_3$ (upper row) and $BaZrO_3$ (lower row) nanoparticles. HAADF-STEM images at medium (a and d) and high (c and f) magnification reveal Ba122 films with a layered aggregation of NPs. The latter appears with a cloud-like contrast variation. Note that the BHO NPs are associated with the dark regions in (a) and (c). (f) A single NP shows lattice fringes, which are in good agreement with the BHO{1 1 0} lattice-plane distances in the power spectrum (g) of the image in (f). (b and e) SAED patterns of the film and CaF_2 substrate region. The circles mark the inner Bragg reflections of CaF_2. Only Ba122 and CaF_2 reflections are visible and no NP reflections.

interpretation of the HAADF-STEM image contrast is more likely because of the following observations:

1. BHO nanocolumns with a reduced HAADF-STEM intensity with respect to Ba122 are observed in another Ba122-BHO nanocomposite (Fig. 4.29h on Page 132).

2. A bright BHO contrast in Ba122 cannot be explained by the average atomic numbers (using the atomic fractions a_i as weights for the individual atomic numbers Z_i) of these

compounds, i.e.

$$\overline{Z} = \sum_i a_i Z_i \quad . \tag{4.2}$$

Using this formula, Ba122 ($\overline{Z} = 34.83$) appears brighter than BHO ($\overline{Z} = 30.4$) and BZO ($\overline{Z} = 24$), assuming pure Z-contrast. However, average atomic numbers for compounds may be calculated with different formulas, e.g. as shown by Howell et al. [HDB98] for BSE-SEM imaging. For example, Müller [Mül54] proposed a weighting of the individual atomic numbers Z_i with the atomic weights c_i (instead of atomic fractions) [HDB98]

$$\overline{Z} = \sum_i c_i Z_i \quad . \tag{4.3}$$

Then, the average atomic numbers are $\overline{Z}_{\mathrm{Ba122}} = 38.97$, $\overline{Z}_{\mathrm{BHO}} = 57.52$, and $\overline{Z}_{\mathrm{BZO}} = 42.39$. These average Z values would indicate a higher HAADF-STEM intensity for both NP materials in Ba122. A bright BZO contrast in Ba122, however, can be ruled out by comparison with literature data for Ba122-BZO nanocomposites [Lee+17; Miu+19]. As a result, the aforementioned average atomic numbers calculated by Eq. (4.2) are used for image interpretation. The dark regions in the HAADF-STEM images of Ba122-BHO nanocomposites are therefore associated with the BHO nanoparticles.
Still, there is the possibility of residual Bragg diffraction contrast in the shown HAADF-STEM images, which could complicate image interpretation. The shown HAADF-STEM images in Fig. 4.26 were acquired with $\alpha = 8.2\,\mathrm{mrad}$ and a HAADF detector collection angles of about $\beta_{\mathrm{inner}} = 33\,\mathrm{mrad}$ and $\beta_{\mathrm{outer}} = 200\,\mathrm{mrad}$.

Selected-area electron-diffraction patterns were acquired for both films covering part of the nanocomposite and the CaF_2 substrate (Fig. 4.26b and e). The innermost Bragg reflections from CaF_2 are marked with black circles. The other reflections stem from Ba122. The alignment of the CaF_2 and Ba122 reflections confirms a high-quality epitaxial film growth. The latter is also observed in high-resolution HAADF-STEM images for both samples (Fig. 4.26c and f). The crystalline Ba122 matrix is visibly overlaid with cloud-like contrast variations from the NPs. In most cases, no atomic-structure detail is visible in the NPs. Since the NPs are probably randomly oriented in the film and only of a size of $\sim 5\,\mathrm{nm}$ embedded in a 50 nm to 100 nm TEM sample, the atomic structure may not be resolved here. One exception is shown in the inset in Fig. 4.26f, which shows a power spectrum from the region marked with a red circle. The right half of the power spectrum was upscaled and interpolated with a bicubic spline to better visualize the reflections. Here, an additional reflection (at $3.41\,\mathrm{nm}^{-1}$) compared to the surrounding Ba122 matrix is observed (marked by yellow arrows in the power spectrum), which may correspond to the BHO$\{1\,1\,0\}$ lattice planes ($3.37\,\mathrm{nm}^{-1}$). The FT-analyzed NP was the only NP from many acquired HAADF-STEM images, which showed crystalline detail. In addition, a ring pattern for BHO or BZO was not observed in the SAED patterns, which would be expected for a random alignment of crystalline NPs. The abscence of the BHO/BZO reflections can be a result of (i) the low nominal concentration of NPs (2 mol %) or (ii) amorphous NP phases instead of crystalline BHO/BZO NPs. Since a higher NP concentration was measured by EDXS than the nominal value (shown in context of Table 4.2), the second assumption may be more probable.

STEM-EDXS analyses for both samples were conducted to get additional insights into the microstructure. Starting with the BHO-Ba122 nanocomposite in Fig. 4.27, the elemental maps reveal Fe precipitates (cf. Fe map) and the oxidized Ba122 surface layer (cf. O map). The As

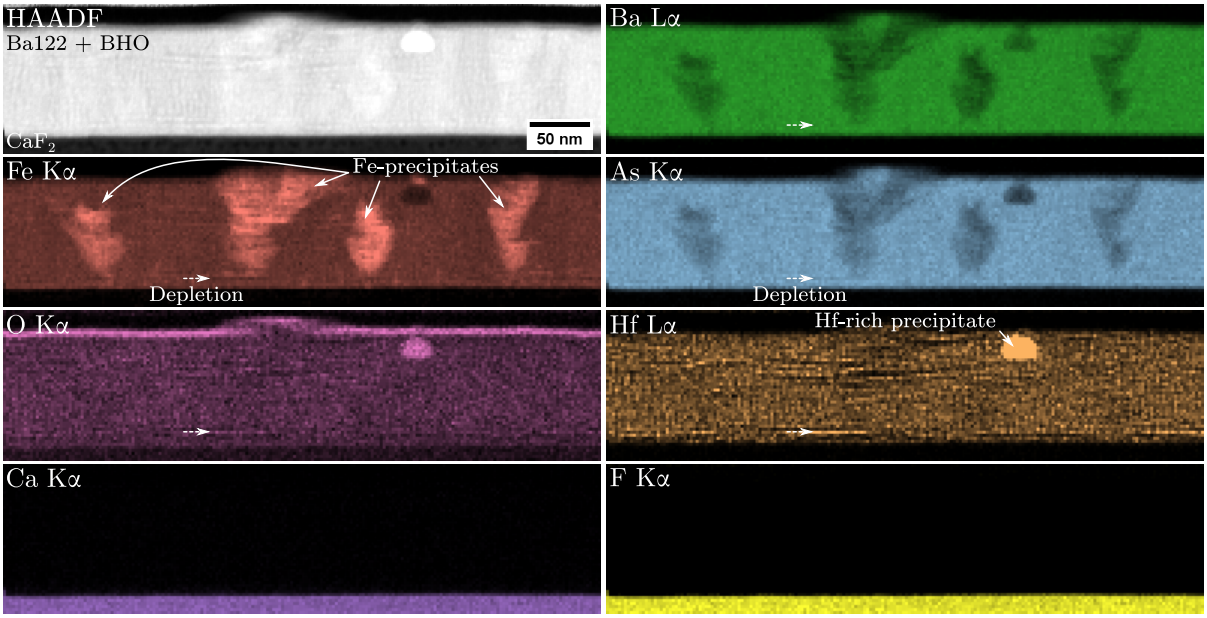

Figure 4.27: STEM-EDXS elemental maps of a Ba122-BHO nanocomposite film grown on CaF_2. Fe precipitates and an O-rich Ba122 surface layer are visible. The Hf map identifies the BHO regions. A layered structure is observed, e.g. in the region marked by the dashed arrows. An As and Fe depletion at the BHO regions is observed as expected for $BaHfO_3$ in $Ba(Fe_{0.92}Co_{0.08})_2As_2$.

and Ba maps (Ca and F maps) reveal the position of the nanocomposite film (substrate). No diffusion of F or Ca into Ba122 is visible in the elemental maps. The Hf map reveals the position of the NPs, since Ba and O (by oxidation of the TEM sample) are also present in the Ba122 film. A larger Hf-rich precipitate (about 25 nm diameter) is observed, which is probably HfO_2 as determined by a Cliff-Lorimer-based quantification of the Hf-rich region (not shown). Such an Hf-rich precipitate was only observed once. The image contrast in the shown Hf map was non-linearly gamma-adjusted[5] so that the Hf-rich precipitates and the layered structure are both visible. The horizontal dashed arrows in Fig. 4.27 mark an exemplary layer containing BHO NPs. An As and Fe depletion is observed in this region. In contrast, Ba is unchanged and an enhanced O signal is visible in the marked region. Note that a general O signal in the Ba122 region results from oxidation of the TEM sample. The unchanged Ba signal matches the expectation for BHO in Ba122 since both materials contain the same Ba concentration of 20 at. %.

Figure 4.28 presents the elemental maps for the BZO-Ba122 nanocomposite obtained from STEM-EDXS. Similar features as for BHO are observed, i.e. Fe precipitates and the layered BZO structure. The latter is visible in the Zr Lα x-ray map. An example is marked with a horizontal dashed arrow in some elemental maps. In addition, a single BZO NP is marked with a vertical arrow. Similar to the BHO-Ba122 nanocomposite, a depletion of As and Fe is observed at the BZO regions. This is again expected for $BaZrO_3$ in $Ba(Fe_{0.92}Co_{0.08})_2As_2$. Zr measurements by STEM-EDXS are slightly impeded by spurious Zr signal stemming from the microscope hardware (FEI Tecnai Osiris). The high-energy Zr Kα x-rays (~ 15.7 keV) generated below the TEM sample penetrate the latter (mean free path of 24.5 µm in Ba122[6]) and thinner parts of the Cu TEM grid (mean free path of 17.6 µm in Cu) and are registered by the EDXS

[5] See, e.g., `https://imagej.net/imagej-wiki-static/Image_Intensity_Processing.html#Gamma` (last accessed: 18.02.2022) for details.

[6] Calculated in *DTSA-II* using the `mac(Ba122, 'Zr')` function with pre-defined `Ba122` material with a density $\rho = 6.48\,\mathrm{g/cm^3}$.

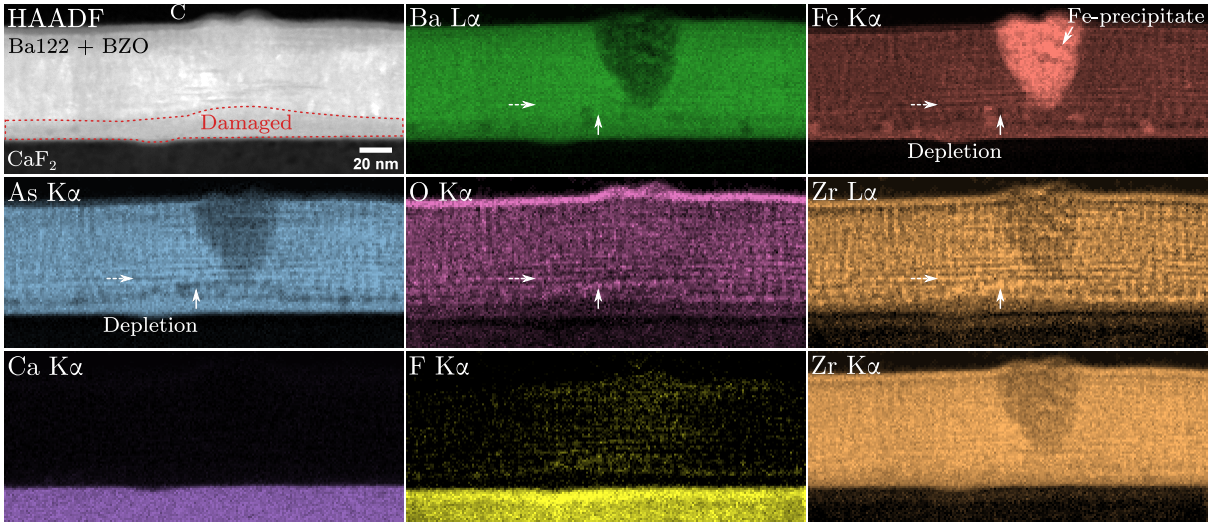

Figure 4.28: STEM-EDXS elemental maps of a Ba122-BZO nanocomposite film grown on CaF_2. The marked region in the HAADF-STEM image shows a damaged Ba122 region close to the substrate interface, resulting from an electron-dose intensive STEM-EDXS acquisition. A heart-shaped Fe precipitate is observed in the analyzed region. A few Fe-rich regions are visible close to the film-substrate interface. The horizontal dashed arrows mark a Zr-rich BZO layer in the film. A depletion in As and Fe is observed. The vertical arrows mark a single BZO nanoparticle. The Zr Lα and Zr Kα maps are shown for comparison since Zr is also present as a spurious signal stemming from microscope hardware.

Table 4.2: Chemical composition of the analyzed BMO-Ba122 nanocomposites (M = Hf, Zr) and calculated nominal compositions. Elemental concentrations for each element are reported in at. %. Given errors correspond to one standard deviation reported by the *Esprit* software.

	Ba	Fe	Co	As	O	M	NP (mol %)
Ba122-BHO	24.4 ± 3.9	34.3 ± 0.7	3.2 ± 0.1	34.6 ± 0.9	–	3.6 ± 0.8	16 ± 3
Ba122-BZO	25.3 ± 4.1	33.5 ± 0.7	3.1 ± 0.1	34.0 ± 0.9	–	4.2 ± 0.5	19 ± 2
$Ba122_{0.98}(BMO)_{0.02}$	20	36.06	3.14	39.2	1.2	0.4	2
(without O)	20.24	36.50	3.18	39.68	–	0.41	2
$Ba122_{0.8}(BMO)_{0.2}$	20	29.44	2.56	32	12	4	20
(without O)	22.73	33.45	2.91	36.36	–	4.55	20

detector. Therefore, the Zr Kα signal is a mixture of actual Zr in the TEM sample and spurious Zr signal resulting from strongly scattering sample regions. The latter leads to more electron scattering into microscope hardware, hence more spurious x-rays. The Ba122 film scatters more strongly than the protective C region or the CaF_2 substrate, leading to a general Zr Kα signal in the Ba122 film region. In contrast, the low-energy Zr Lα x-rays (~ 2.04 keV) generated below the sample are more strongly absorbed in the TEM sample (mean free path of 721 nm in Ba122) and Cu TEM grid (mean free path of 569 nm). The Zr Kα signal, therefore, contains more signal from the actual Zr-rich regions in the analyzed TEM sample.
An increased F signal is visible at the Ba122-CaF_2 interface, probably induced by electron bombardment, as discussed earlier (Fig. 4.1 on page 94). A faint F signal is observed in the Ba122 region, but this again is probably just a measurement artifact.

The elemental concentration for the Ba122-BHO/BZO nanocomposite films was approximately measured by STEM-EDXS (Table 4.2). All EDXS spectra from the Ba122 film region without Fe precipitates were summed. This was performed for multiple datasets (not shown here) and all spectra from the Ba122 regions were summed to maximize count statistics for the standardless

Cliff-Lorimer quantification. O was excluded from the quantified elements as TEM-sample oxidation falsifies the actual O concentration. The first two rows in Table 4.2 present the experimental values for the Ba122-BZO/BHO nanocomposites. The rows below serve as a comparison with calculated values assuming nanocomposites with 2 mol % and 20 mol % BMO (M = Hf, Zr). The NP concentration in the nanocomposites can be calculated by the ratio

$$r = \frac{C_{\mathrm{M}}}{(C_{\mathrm{M}} + C_{\mathrm{x}} \cdot a_x)} \tag{4.4}$$

where C_{M} and C_{x} are the quantified elemental concentrations for $M = \mathrm{Hf}, \mathrm{Zr}$ and an element in Ba122, which is not present in the NP material. The factor a_x is used to achieve the same concentrations of C_{x} in Ba122 and C_{M} in BMO (or another nanoparticle material). For the Ba122-BMO nanocomposites, the ratios of

$$r_1 = \frac{C_{\mathrm{M}}}{(C_{\mathrm{M}} + C_{\mathrm{As}}/2)} \tag{4.5}$$

$$r_2 = \frac{C_{\mathrm{M}}}{(C_{\mathrm{M}} + (C_{\mathrm{Fe}} + C_{\mathrm{Co}})/2)} \tag{4.6}$$

are averaged to calculate the NP concentrations. Here, Ba cannot be used since it is present in Ba122 and BHO/BZO. The elemental ratios do not change when O is removed from the measured or calculated concentrations because the other compounds are scaled to fulfill

$$\sum_i C_i = 100\,\% \quad . \tag{4.7}$$

The NP concentration for both investigated nanocomposites is (16±3) mol % (BHO) (19±2) mol % (BZO). The errors result primarily from the uncertainties associated with the quantified elemental concentrations. The NP concentrations measured by EDXS are significantly higher than the nominal (and ICP-MS-reported) values of about 2 mol % [Mey21, p 50]. The reason for this large discrepancy is unclear. The EDXS quantification procedure was thoroughly checked for possible artifacts. For example, the used Hf Lα peak overlaps partly with a Cu Kα peak, but this overlap can, in principle, be separated with MLLS fitting. However, it is worth noting that even a slight misalignment of the EDXS detector's energy calibration can affect the Hf concentrations because the MLLS fitting assumes the correct position for the Gaussian functions at the tabulated x-ray energies. Here, the zero-strobe peak (0 keV) and the As Kα peak (10.54 keV) were used as two references to scale all investigated spectra after the acquisition. This ensures comparability between the different measurements.

Regarding Zr, the Zr Lα x-ray peak was used for quantification, which overlaps with Pt and partly contains spurious x-rays. This may explain the higher Zr concentration in BZO compared with Hf in BHO, which ultimately leads to a higher calculated BZO concentration compared to BHO using EDXS. The standardless Cliff-Lorimer factors certainly induce a systematic error but cannot explain the significant difference between nominal ($\sim$ 2 mol %) and measured ($\sim$ 19 mol % using EDXS) NP concentrations. A more considerable difference between the measured elemental concentrations and, e.g., the calculated 20 mol % BMO nanocomposites would be measured if the Cliff-Lorimer factors were significantly wrong (cf. Table 4.2). In addition, both nanocomposites show a similar NP concentration, independent of the B-site element of the barium oxides (Hf or Zr). This can be expected from two samples fabricated with nearly identical PLD conditions

(assuming that BHO and BZO behave similar in PLD). Therefore, the increased NP concentration compared to the nominal values is assumed to be correct and not a measurement artifact.

Sample series with increasing $BaHfO_3$ concentration. In the following, a sample series of four Ba122-BHO nanocomposites with increasing BHO content was investigated. One sample was prepared without BHO as a reference (denoted as "noBHO"). The other three samples with BHO are denoted as "lowBHO", "medBHO", and "highBHO" respectively, standing for low, medium, and high concentrations of BHO in the Ba122-BHO nanocomposite films. The BHO concentration was measured using EDXS and will be discussed further below.
The microstructures are compared using STEM imaging of cross-section TEM samples (Fig. 4.29). The LAADF-STEM images show varying Ba122 film thicknesses between 53 nm for highBHO (Fig. 4.29d) and 81 nm for lowBHO (Fig. 4.29b). All films contain the typical Fe precipitates (marked with orange arrows) discussed earlier (see Fig. 4.13 on page 109 and Fig. 4.14 on page 110). The TEM sample of medBHO (Fig. 4.29c) shows a dark region close to the film-substrate interface, probably caused by FIB milling during TEM-sample preparation. An interesting contrast variation is observed in the LAADF-STEM image of highBHO (Fig. 4.29d), where vertical columnar structures are visible. This suggests the formation of vertical defects in the Ba122-BHO nanocomposites, which were later identified as BHO nanocolumns by STEM-EDXS (Fig. 4.30). No evidence for a crystalline BHO structure is visible at the nanocolumns in the HAADF-STEM images, similar to most of the nanoparticles in Fig. 4.26 on page 126. This agrees with the findings by Xu et al. [Xu+19] for Ba122-Y_2O_3 nanocomposites, where similar nanocolumns with an amorphous structure were observed. Still, crystalline BZO nanoparticles were reported in Ba122 as round precipitates [Miu+13] or nanocolumns [Lee+17] (using premixed PLD targets).
No signs of the BaF_2 phase was observed in this sample series. This may result from the high deposition rate of $0.9\,\text{Å}\,\text{s}^{-1}$ used for these films (see Section 4.2 on page 101 for microstructural differences in Ba122 regarding the deposition rate). Overall, all the samples show successful growth of an epitaxial film with constant thickness.
This is also confirmed in the high-resolution HAADF-STEM images in Fig. 4.29e to h. In all cases, the crystalline structure of Ba122 is visible. Note the 45°-rotated zone-axis orientation (viewing direction) of the Ba122 structure from Ba122[1 0 0] (Fig. 4.29e,f) to Ba122[1 1 0] (Fig. 4.29g,h). The Ba122[1 1 0] zone-axis orientation results from a shortfall during TEM-sample preparation, where the CaF_2 samples were *not* rotated by 45° with respect to the substrate edges (cf. Fig. 4.10 on page 106). A few dark patches are observed for noBHO and lowBHO (marked by horizontal arrows in Fig. 4.29e and f) showing small planar defects. These are most likely caused by FIB preparation or STEM imaging. However, it cannot be ruled out that these small planar defects are present in the as-deposited films. The columns are again observed at high magnification for highBHO (Fig. 4.29h, marked by yellow dashed arrows).

Next, STEM-EDXS was performed to analyze the chemical compositions of the films (Fig. 4.30). Here, only the elemental maps for the BHO-containing samples are shown and the pure film is omitted. The latter did not show any remarkable features compared to the already shown STEM-EDXS analyses of pure Ba122 films on CaF_2 (see, e.g., Fig. 4.13 on page 109). The HAADF-STEM overview images show a dark layer at the film-substrate interface (marked by dotted lines). This layer is amorphous Ba122 caused by electron-beam irradiation during the dose-intensive STEM-EDXS mapping. A long STEM-EDXS acquisition was used here to resolve the Hf distribution and to map the position of possible BHO NPs. This was successful for highBHO (Fig. 4.30c), because the columnar structure of the BHO nanocolumns could be

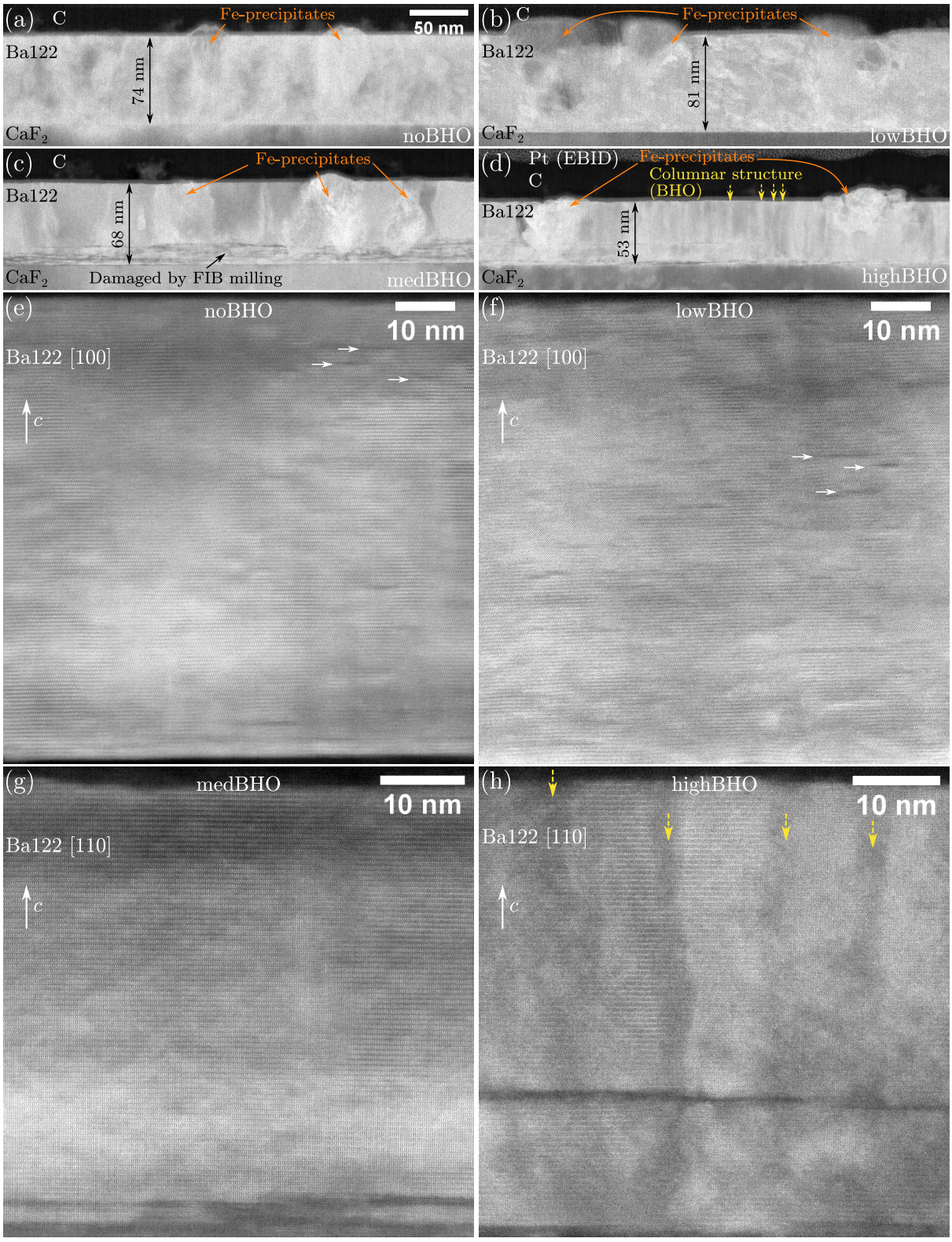

Figure 4.29: STEM cross-section images of Ba122-BHO nanocomposites with varying BHO concentrations. (a–d) Low-magnification LAADF-STEM and (e–h) high-magnification HAADF-STEM cross-section images of (a,e) pure Ba122 and Ba122 with (b,f) low, (c,g) medium, and (d,h) high BHO concentration. Note the difference in Ba122 zone-axis orientations between (e,f) [1 0 0] and (g,h) [1 1 0]. All films show Fe precipitates (orange arrows). The dark region close to the film-substrate interface in (c) is caused by FIB preparation. Horizontal arrows in (e) and (f) indicate planar defects. (d and h) A columnar structure is visible for highBHO (marked by dashed yellow arrows), indicating the formation of BHO nanocolumns.

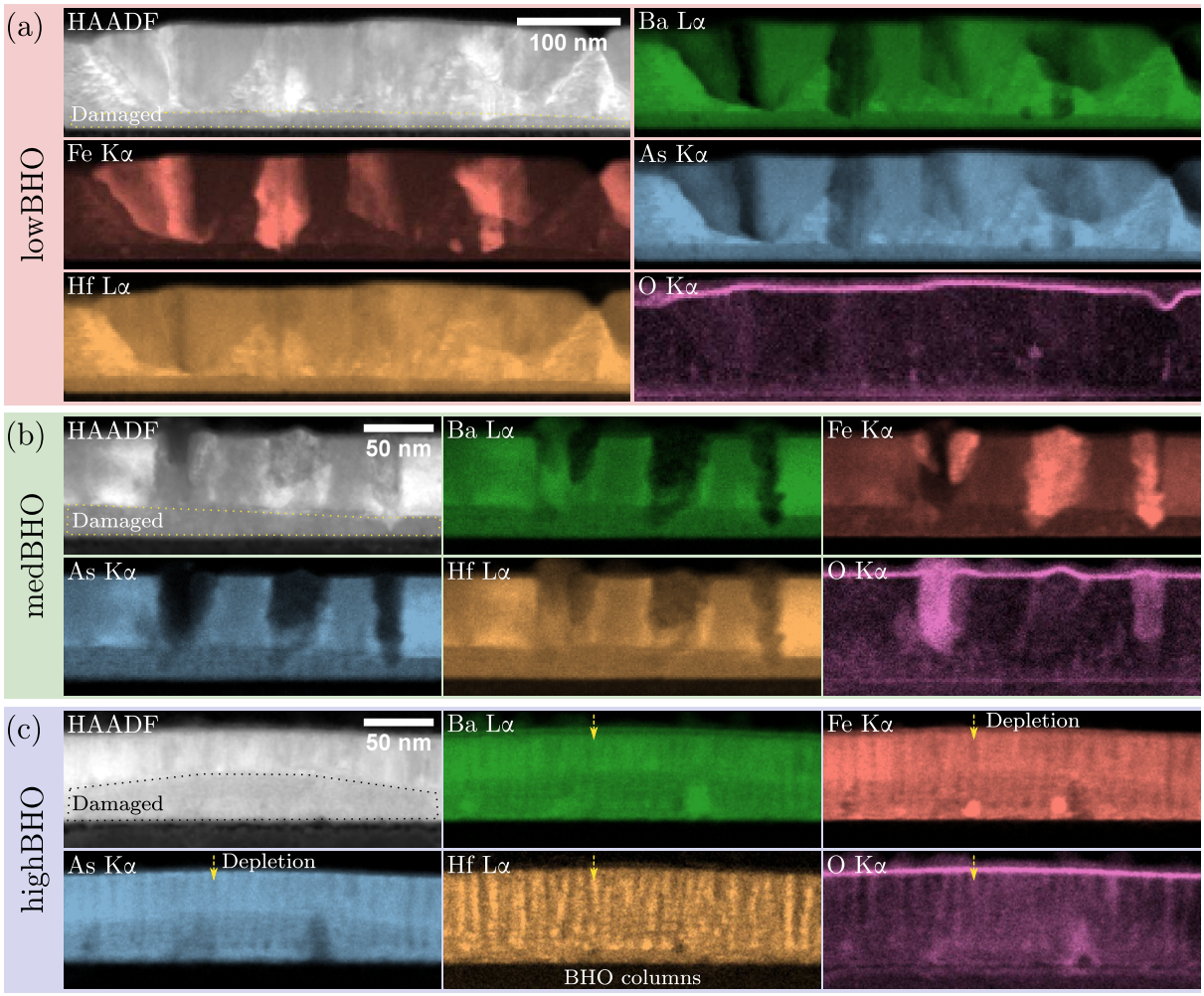

Figure 4.30: STEM-EDXS elemental maps of Ba122-BHO nanocomposites with varying BHO concentrations. HAADF-STEM image and corresponding elemental maps for (a, red) low, (b, green) medium, and (c, blue) high concentrations of BHO in the Ba122-BHO nanocomposites. The vertical arrows in (c) mark a BHO nanocolumn. The dotted regions mark damaged Ba122 regions generated by electron-beam irradiation.

resolved. The other two samples show a homogeneous Hf distribution throughout the Ba122-BHO film. The latter may be partially caused by the overlap of Hf Lα with the Cu Kα x-ray peak from spurious Cu x-rays.
The NP concentration was evaluated with the same method as shown in the context with the Ba122-BHO/BZO nanocomposites. The procedure is as follows:

1. Sum up the EDXS spectra from the film regions (neglecting the Fe precipitates) from all STEM-EDXS acquisitions for a given sample.
2. Calibrate the energy axis between the zero-strobe peak and the As Kα peak.
3. Quantify the elemental concentrations with the standardless Cliff-Lorimer approach.
4. Calculate the BHO concentration (in mol %) using Eq. (4.4).

The results are presented in Table 4.3. No Hf was detected for noBHO (as expected) and lowBHO, which is unexpected since BHO was introduced in the Ba122 film. However, the BHO concentration may be below the detection limit. The "Counts" column in Table 4.3 reports the total counts of the summed-up EDXS spectra used here for quantification. Less STEM-EDXS

Table 4.3: Chemical composition of the BHO-Ba122 nanocomposites with varying BHO concentration. Elemental concentrations for each element are reported in at. %. Given errors correspond to one standard deviation reported by the *Esprit* software. The total counts for the quantified spectra are given in the last column.

	Ba	Fe	Co	As	Hf	NP (mol %)	Counts
noBHO	22.0 ± 3.8	36.5 ± 0.8	3.4 ± 0.1	38.1 ± 1.1	–	–	24.5×10^6
lowBHO	21.6 ± 3.7	36.9 ± 0.8	3.7 ± 0.1	37.9 ± 1.1	–	–	26.9×10^6
medBHO	21.0 ± 3.6	39.2 ± 0.8	3.7 ± 0.1	36.0 ± 1.0	0.12 ± 0.05	0.6 ± 0.3	51.9×10^6
highBHO	21.4 ± 3.7	38.3 ± 0.8	3.7 ± 0.1	36.3 ± 1.0	0.4 ± 0.1	2.0 ± 0.5	67.6×10^6

Table 4.4: Simulated EDXS spectrum to test the detection limits of Hf. The simulated sample (100 nm thickness, density 6.5 g/cm^3) has the composition $Ba122_{0.7984}BHO_{0.0016}Cu_{0.2}$. The same total counts were used for the simulation and experiment (26.9×10^6). Elemental concentrations for each element are reported in at. %. Given errors correspond to one standard deviation reported by the *Esprit* software.

	Ba	Fe	Co	As	Hf	NP (mol %)
lowBHO	21.6 ± 3.7	36.9 ± 0.8	3.7 ± 0.1	37.9 ± 1.1	–	–
Simulation (0.2 mol % BHO)	21.9 ± 3.7	34.8 ± 0.7	2.95 ± 0.09	40.3 ± 1.1	0.11 ± 0.05	0.6 ± 0.3

datasets were acquired for lowBHO and noBHO, leading to fewer total counts in the summed up spectra than in the medBHO and highBHO spectra.
A simulation was performed using *DTSA-II* to test if the count statistics limits the detectability of Hf (down to 0.2 mol % BHO). An EDXS spectrum with the same total counts as for lowBHO was simulated with a composition $Ba122_{0.7984}BHO_{0.0016}Cu_{0.2}$. This results in a BHO/Ba122 ratio of 0.2 mol %, i.e. the simulated BHO concentration. The latter was chosen arbitrarily based on the measured highBHO and medBHO NP concentrations, where highBHO shows a three times higher NP concentration than medBHO (Table 4.3). Consequently, the medBHO content was arbitrarily assumed to be three times higher than lowBHO, resulting in 0.2 mol %. To simulate spurious Cu x-rays, 20 % Cu is added to the simulated sample. This is important to test the quantification procedure since the Hf and Cu peaks overlap. A TEM sample with a thickness of 100 nm and a density of 6.5 g/cm^3 was assumed in the simulation. The electron dose was adjusted to achieve 26.9×10^6 total counts in the simulation, the same as the experimental lowBHO spectrum.

Table 4.4 presents the quantification for the experimental spectrum for lowBHO, where no Hf was detected, and the simulated spectrum for a Ba122-BHO nanocomposite with 0.2 mol % BHO. Cu was not quantified. A Hf signal is detected in the simulated spectrum for the given total counts and Hf concentration. From this result it can be concluded that the count statistics in the experimental lowBHO spectrum should be good enough to detect concentrations down to at least 0.2 mol % BHO. Therefore, it can be concluded that the BHO concentration in the lowBHO sample is probably below this value. Another interesting observation is that the quantified value of the BHO content from the simulated spectrum is (0.6 ± 0.3) mol %, which is about three times larger than the nominal value of 0.2 mol %. Also, the quantified Ba content in the simulation increases compared to the nominal value of 20 at. %. This is caused by a systematical error of the Cliff-Lorimer factors. The possible errors associated with standardless quantification are the reason that the quantified and reported absolute elemental concentrations should be interpreted carefully.

Conclusions for Ba122-BHO/BZO nanocomposites. This section showed results for Ba122-BHO/BZO nanocomposites fabricated by quasi-multilayer PLD. In this approach, the Ba122 and BHO/BZO targets are changed multiple times during deposition for a given number of laser pulses, thereby adjusting the BHO/BZO concentration. The introduced NPs appear with a cloud-like contrast in HAADF-STEM images. The crystalline structure was only resolved for one observed BZO NP (cf. Fig. 4.26f). This may be attributed to the (i) small NP size of about 5 nm (embedded in a 50 nm to 100 nm TEM sample) or (ii) a partly amorphous NP structure. SAED patterns also did not show visible signs in form of a ring pattern of polycrystalline BHO or BZO nanoparticles. The NP concentration for the Ba122-BHO/BZO samples shown in Fig. 4.26 were calculated as (16 ± 3) mol % (Ba122-BHO) and (19 ± 2) mol % (Ba122-BZO) using STEM-EDXS. These values are significantly higher than the nominal values of about 2 mol %, which was measured by ICP-MS [Mey21, p 50]. The reason for this difference is unclear. Remarkably, the Ba122 films showed high-quality epitaxial growth despite the high concentration of NPs. This is an important observation since the barium oxides may introduce O into the Ba122 film. Section 4.2 on page 101 shows that O can be found at planar defects. However, nearly no planar defects (i.e. stacking faults, cf. Fig. 4.21, or isolated Ba planes, cf. Fig. 4.22 on page 120) were observed in the nanocomposite samples. The latter were grown with a relatively high deposition rate of about $0.9\,\text{Å}\,\text{s}^{-1}$. The absence of planar defects agrees with the results of the pristine Ba122 samples grown with the same rate (Ba122/fast in Section 4.2 on page 101). Furthermore, no BaF_2 phases were detected for the nanocomposite samples shown so far. This provides further evidence that BaF_2 formation may form associated planar defects for a low growth rate.

The BHO/BZO NPs self-assemble as (i) a layered structure for high NP concentrations ($\sim$ 20 mol %, cf. Fig. 4.27 on page 128 and Fig. 4.28) or (ii) as nanocolumns for lower concentrations ($\sim$ 2 mol %, cf. Fig. 4.29h). The formation of nanocolumns (or nanorods) is a typical phenomenon in REBCO nanocomposites (see, e.g., the references [Can+11; IY17; Gau+18; Maj+21]) and in IBS nanocomposites [Tar+12; Hor+21; Lee+17]. The nanorod diameter, distribution, and density depend on the fabrication parameters [IY17]. The *c*-oriented nanocolumns are efficient pinning centers for $H \parallel c$. Electrical measurements confirmed this for the investigated samples series with increasing BHO concentrations [Mey21, p 52]. The $J_c(H \parallel c)$ values increase with increasing BHO concentration because more pinning centers (and vertical nanocolumns) are present in the films. For the highest doping level, i.e. sample highBHO, a $J_c(H \parallel c, T = 0\,\text{K}) \approx 10 \times 10^6\,\text{A/cm}^2$ was calculated. For a more detailed discussion, the reader is referred to the thesis of Sven Meyer [Mey21, pp 51 sq.].

Interestingly, *c*-oriented nanocolumns were reported in the literature even for NP concentrations of about 20 mol % or higher [Sel+15; Xu+17] in REBCO films, which is in contrast to the *ab*-oriented quasi-multilayers in Ba122 observed here. The observed aggregation of BZO/BHO nanoparticles in the *ab*-plane is in good agreement with a publication by Lee et al. [Lee+13], who also observed *ab*-aligned quasi-multilayers in a Ba122 sample with added O-rich $BaFe_2As_2$ (instead of BHO/BZO here). This indicates that O plays an important role in the formation of these defects. As mentioned above, the crystallinity of the BZO/BHO NPs could *not* be verified in most cases. O (and the other elements in the nanoparticle materials) may be locally diluted into the Ba122 matrix as O-rich Ba122 NPs.

The NP concentrations were calculated based on quantified elemental concentrations from several STEM-EDXS measurements. A few complications specific to BHO and BZO were observed besides general uncertainties associated with standardless quantification. For BZO, the elemental concentrations of Zr may be artificially increased by spurious Zr x-rays stemming from the

microscope hardware. Here, a FEI Tecnai Osiris with a Super-X EDXS detector [Sch+10] was used. A spectrum from a Zr-free, strongly scattering TEM sample can serve as a test specimen for different microscopes to test the level of spurious x-rays from Zr. Regarding BHO, the quantification of Hf – especially in low concentrations – using the Hf Lα peak requires careful evaluation of the energy calibration. Here, the Hf Lα line overlaps with Cu Kα. Slight offsets of a few eV or a non-linearity of the energy scale can change the Hf concentration for the peak fitting routine. For the used EDXS detector (first-generation Super-X) and *Esprit* software, a zero-strobe peak is recorded as a reference for 0 eV. This peak can be used with an isolated x-ray peak (here As Kα) to calibrate the energy axis. Possible ways to reduce this problem may be (i) the use of Cu-free TEM grids and specimen holders, (ii) STEM-EELS (no spurious x-rays), or (iii) using the isolated Hf Kα_1 x-ray transition at 55.79 keV. The latter, however, has a low collection efficiency in the used Super-X EDXS detector since such high-energy x-rays penetrate the thin Si-detection layer of silicon-drift detectors (450 µm thickness) instead of being absorbed. Only around 2 % of Hf Kα_1 x-rays reaching the detector are registered, as determined using the detector-efficiency curve from Schlossmacher et al. [Sch+10]. Despite these challenges, a relative comparison of the NP concentrations for the different Ba122-BHO/BZO nanocomposite samples is possible.

4.3.2 InAs Nanoparticles

This section presents the microstructural analysis of quasi-multilayer PLD-grown Ba122-InAs nanocomposite films deposited on CaF_2. So far, results for $BaHfO_3$ (BHO) and $BaZrO_3$ (BZO) nanoparticles were shown. These materials are commonly used for REBCO and IBS nanocomposites. However, BHO and BZO are oxides and may partly lead to oxidation of the surrounding Ba122 matrix during film fabrication. Alternatively, arsenide nanoparticles may be interesting for Ba122 nanocomposites. Here, commercially available InAs was chosen as a non-oxide nanoparticle material for Ba122. InAs has a relatively low melting point of $T_m = 942\,°C$ close to the used PLD substrate temperature $T_{sub} = 700\,°C$. The volatility of InAs during PLD is an important aspect of Ba122-InAs fabrication.
Two Ba122-InAs nanocomposites were chosen for TEM analyses, i.e. one with low (0.35 mol %) and one with high (1 mol %) InAs concentration. These samples are denoted as "lowIA" and "highIA". The nominal InAs concentrations were deduced from a calibration of laser pulses vs. InAs concentration and ICP-MS measurements. The T_c values for the Ba122-InAs nanocomposites decreases linearly with increasing InAs concentration [Mey21, p 72], i.e. $T_c \approx 25\,K$ (pristine Ba122), $T_c \approx 19\,K$ (lowIA), and $T_c \approx 16\,K$ (highIA). This is similar to the Ba122-BHO/BZO nanocomposites. Also, the J_c values reduced with increasing InAs content. The electrical measurements suggest that no pinning centers (e.g. in the form of InAs nanoparticles) have formed in the Ba122 films. This is confirmed by the microstructural characterizations shown in the following.
The samples were prepared by **Nico Beisig** and **Sven Meyer**. The best conditions for the PLD were 39 Ba122/InAs-target exchanges and a variation of 10 to 30 laser pulses on the InAs target per exchange to adjust the InAs concentration. The investigated samples were grown with

- 468 total laser pulses on the InAs target (lowIA, 468/39 = 12 pulses per exchange → 0.35 mol %), and
- 1170 total laser pulses on the InAs target (highIA, 1170/39 = 30 pulses per exchange → 1 mol %).

The total laser-pulse number for the Ba122 target was constant (18 000) to achieve a similar film thickness for the nanocomposites. See also Meyer [Mey21, pp 70 sqq.] for more details.

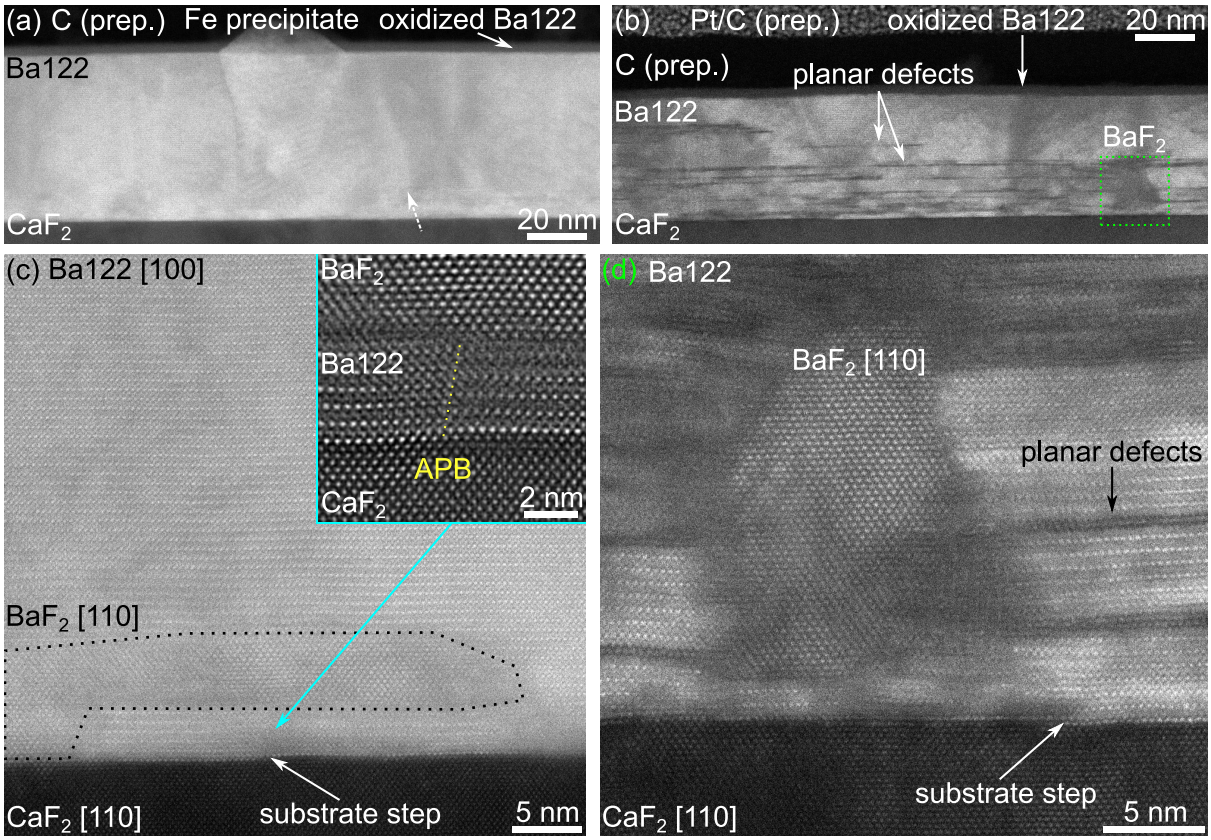

Figure 4.31: HAADF-STEM images of Ba122-InAs nanocomposites with high (left column) and low (right column) InAs concentrations. (a and b) Both samples show the typical oxidized Ba122 surface layer and Fe precipitates, although none is present in the particular region in (b). (a and c) A high-quality epitaxial film without any visible planar defects is observed for highIA. Vertical defects are visible, marked by a dashed arrow in (a). (b and d) Planar defects in the form of stacking faults and isolated Ba planes are observed for lowIA as dark horizontal stripes. The formation of BaF_2 and antiphase boundaries due to substrate steps is observed for both samples. The inset in (c) shows a short antiphase boundary (dotted yellow line) interrupted by BaF_2 formation.

Figure 4.31 presents an overview over the microstructures for highIA (left) and lowIA (right). The microstructure differs significantly, as observed at low magnification (cf. Fig. 4.31a and b). Fe precipitates are observed in both films but none were in the particular field of view for lowIA in Fig. 4.31b. The sample highIA shows a mostly clean Ba122 layer without visible planar defects and a film thickness of 59 nm. Vertical defects structures are visible (e.g. at the dashed arrow in Fig. 4.31a), similar to the defects shown by Hiramatsu et al. [Hir+14]. These may be dislocations or grain boundaries. In contrast, the lowIA film is disturbed by planar defects (dark horizontal lines in Fig. 4.31b). The film thickness for lowIA is also smaller with 45 nm. The formation of BaF_2 is observed for both samples (Fig. 4.31c and d). Note that the image in Fig. 4.31d shows a comparably large BaF_2 marked in Fig. 4.31b. The BaF_2 phase was determined by Fourier-transform analysis (not shown here), in analogy to Fig. 4.17 on Page 114. In addition, substrate steps can introduce antiphase boundaries (APBs), visible in the ABS-filtered inset in Fig. 4.31c.

The vertical defect structures in highIA (cf. dashed arrow in Fig. 4.31a) were investigated in more detail. The latter mainly showed clean epitaxial growth (Fig. 4.32a), which reveals the

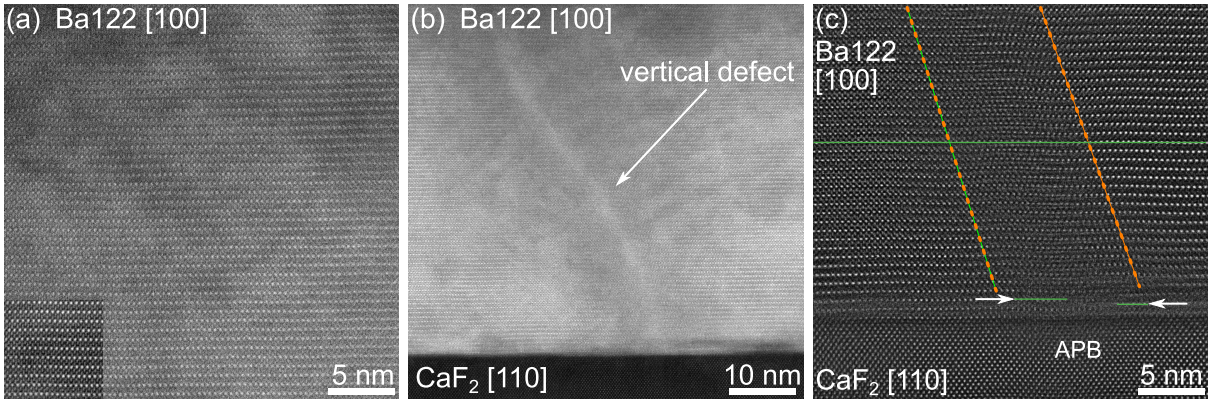

Figure 4.32: High-resolution HAADF-STEM images of a Ba122-InAs nanocomposite with a high nominal InAs concentration. (a) Cross-section image showing the undisturbed Ba122 structure. The inset in the bottom left is ABS-filtered for better visibility. (b) Overview and (c) high-magnification, ABS-filtered images of a vertical defect. (c) The dashed orange lines mark the vertical-defect region. The Ba-plane spacing is slightly disturbed at the defect (cf. horizontal green line). An antiphase boundary is observed at the film-substrate interface (cf. misaligned Ba planes marked by the arrows).

vertical defects more easily than in lowIA with an overall high defect content. Slight contrast variations are visible in the unfiltered HAADF-STEM image. At first glance, these appear similar to the cloud-like contrast variations for BHO/BZO (cf. Fig. 4.26c and f on Page 126). However, the contrast variations observed for highIA are more subtle and are attributed to TEM-sample-preparation artifacts, i.e. slight thickness variations and TEM-sample contamination. Figure 4.32b presents a HAADF-STEM image of a slightly tilted vertical defect, which shows a distinct dark-bright-dark contrast variation along the horizontal direction. Another HAADF-STEM image of the same defect is shown in Fig. 4.32c. Removal of the background intensity and ABS-filtering reveals the crystalline structure of the defect (Fig. 4.32c). The defect region is marked with a dashed orange line. The horizontal alignment of the Ba planes is uninterrupted, as shown by the horizontal green line in the center. However, slight bending of the lattice planes in *c*-direction is observed. This may be caused by the stress field introduced by the vertical defect, probably a dislocation. An APB is observed for the first 2 to 3 unit cells of Ba122 (cf. arrows and small green lines in Fig. 4.32c).
No signs of In-rich nanoparticles were found by HAADF-STEM imaging. Only BaF_2 and Fe precipitates were observed for both Ba122-InAs nanocomposites, which are also present in pristine Ba122 films. One reason may be that the InAs content is too low in the films. Therefore, additional EDXS measurements were performed to detect InAs. Because As is also present in Ba122, InAs may be detected by the In signal. First, conventional STEM-EDXS mappings were acquired to resolve the spatial distribution of In (not shown). This was unsuccessful since no In could be detected. It was suspected that the actual In concentrations might be lower than the nominal values of 0.35 mol % for lowIA and 1 mol % for highIA. Therefore, dedicated EDXS measurements were performed to detect trace amounts of In in the two samples (Fig. 4.33).

A fresh set of TEM cross-section samples was prepared and the layer was continuously scanned during EDXS spectrum acquisition to get an average spectrum of the Ba122-InAs films. The scanned regions are marked with red rectangles in the HAADF-STEM images in Fig. 4.33a. The TEM sample for highIA (marked in blue in Fig. 4.33) was deliberately prepared with a thickness of around 120 nm (i.e. thicker than normally used) to maximize the EDXS signal. The beam current was adjusted to around 1.6 nA (as measured on the TEM screen), resulting

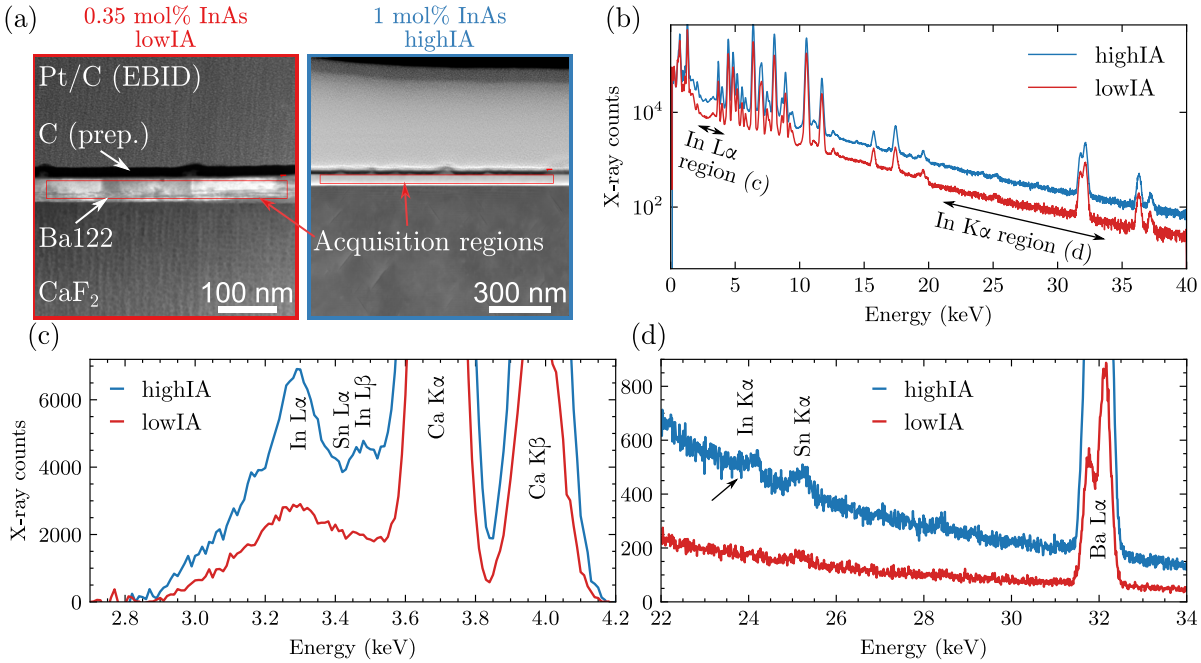

Figure 4.33: Qualitative STEM-EDXS analysis of small In concentrations in Ba122-InAs nanocomposites. (a) Overview HAADF-STEM images of lowIA (red frame) and highIA (blue frame) with the acquisition regions marked with red rectangles. The beam was continuously scanned during EDXS acquisition resulting in an average spectrum. (b) Full EDXS spectra for lowIA (red) and highIA (blue) on a logarithmic intensity scale. The regions for (c) and (d) are marked. (c) Magnified view on the In Lα region. A broad In Lα signal is visible for both samples. Possible overlaps with other x-ray peaks impede the qualitative analysis. (d) Magnified view on the In Kα region. An In Kα peak is visible for highIA but not for lowIA. The Sn peaks result from spurious x-rays.

in a input count rate of 1.3×10^5 counts per second[7]. The energy range was set from 0 keV to 40 keV (10 eV/channel energy dispersion) to capture the In K$\alpha_{1,2}$ x-ray transitions at about 24.2 keV. The total counts in the spectra were 76.4×10^6 (highIA) and 38.4×10^6 (lowIA). All relevant spectra from all acquired EDXS datasets were summed up to maximize the total x-ray counts prior to quantification. STEM-EDXS analysis at 30 keV in the TFS Helios G4 FX was also considered since more x-rays are generated at 30 keV compared to 200 keV (FEI Tecnai Osiris). However, the In K shell (27.94 keV) is not sufficiently excited due to a low overvoltage of 30 keV/27.94 keV = 1.07. Therefore, STEM-EDXS measurements were performed in the FEI Tecnai Osiris at 200 keV.

The acquired EDXS spectra for lowIA (red) and highIA (blue) are qualitatively evaluated and compared in Fig. 4.33b–d. The overview of the total energy range up to 40 keV is presented in Fig. 4.33b. A logarithmic intensity scale is applied to highlight the small x-ray peaks at high energies together with the low-energy range. The double-headed arrows mark the magnified energy regions around the In Lα (Fig. 4.33c) and In Kα (Fig. 4.33d) x-ray transitions.

The In Lα region is discussed first (Fig. 4.33c). An In Lα signal is visible for highIA superimposed on a broad peak from about 3 keV to 3.5 keV. The broadening towards the right side of the In Lα peak is attributed to the In Lβ (3.49 keV) and Sn Lα (3.44 keV) peaks. The latter results from spurious x-rays resulting from Sn-containing microscope components. The source of Sn is probably the Cu_xSn_y (bronze) clamp of the low-background double-tilt high-visibility TEM holder [Kra+17]. However, it is not clear which spurious signal/element (Cd being a possible

[7]The used Super-X (G1) EDXS detector on the FEI Tecnai Osiris has a maximum throughput rate of 2×10^5 counts per second.

Table 4.5: Quantification of the In concentration for the highIA sample. The first row presents the nominal composition for an 1 mol % InAs concentration. Elemental concentrations for each element are reported in at. %. Given errors correspond to one standard deviation reported by the *Esprit* software.

	Ba	Fe	Co	As	In	NP (mol %)
highIA (nominal)	19.92	36.65	3.19	40.04	0.2	1
highIA (STEM)	18.9 ± 3.4	41.5 ± 0.9	4.2 ± 0.1	35.2 ± 1.0	0.11 ± 0.03	0.5 ± 0.2
highIA (SEM) (SEM-EDXS, cf. Fig. 4.34)	10.4 ± 1.1	39.4 ± 1.6	4.9 ± 0.2	45.2 ± 1.2	0.13 ± 0.03	0.9 ± 0.2

candidate) or detector artifact causes the broadening on the left side of the In Lα peak. Only a broad peak is visible for lowIA, centered at the In Lα position. Therefore, it is concluded that In is also present and detected in the lowIA sample. The Ca signals from the substrate stem from scattering and beam broadening. Here, Ca x-rays are generated even though the beam is only scanned over the Ba122 film region. The EDXS bremsstrahlung background is subtracted in Fig. 4.33c for better visibility of the x-ray lines.
Regarding the high-energy x-ray region, Fig. 4.33d, a small In Kα peak is visible (marked by an arrow), which confirms the presence of In in highIA. As mentioned in context with Fig. 4.33c, spurious Sn x-rays are detected, which cause a small peak at the Sn Kα energy (25.27 keV for Sn Kα_1). The prominent peak at around 32 keV belongs to Ba. The Ba Lα_1 (32.19 keV) and Ba Lα_2 (31.82 keV) peaks are split, as seen in the red lowIA spectrum. No In Kα peak is visible for lowIA above the noise level. This can be explained by the overall lower amount of In in the lowIA sample compared to highIA sample (where an In Kα signal is barely visible) in combination with fewer total counts collected in the corresponding EDXS spectrum.

A Cliff-Lorimer quantification for highIA was performed to get an approximate value for the In concentration. The results are tabulated in Table 4.5, but should be interpreted carefully due to the high noise level for the In Kα peak. The latter was used for quantifying the In concentration since it does not overlap with other peaks. An In concentration of (0.11 ± 0.03) at. % is found, corresponding to a NP concentration of (0.5 ± 0.2) mol % in highIA. The NP concentration was calculated using Eq. (4.4),

$$r_1 = \frac{C_{\mathrm{In}}}{(C_{\mathrm{In}} + C_{\mathrm{Ba}})} \tag{4.8}$$

$$r_2 = \frac{C_{\mathrm{In}}}{(C_{\mathrm{In}} + (C_{\mathrm{Fe}} + C_{\mathrm{Co}})/2)} \quad , \tag{4.9}$$

and averaging r_1 and r_2. The value (0.5 ± 0.2) mol % is only half the nominal value of 1 mol %. The reason for the deviation between EDXS and ICP-MS measurements is not clear, similar to the results obtained for the Ba122-BHO/BZO nanocomposites (Table 4.2 on Page 129). The increased Fe/Co (and decreased As) concentrations compared to the nominal composition partly result from the fact that the Fe precipitates were also sampled by scanning the sample areas shown in Fig. 4.33a.

A possible reason for the measured discrepancies between STEM-EDXS and ICP-MS measurements might be the formation of In-rich phases at the film surface, which are not probed in the STEM-EDXS measurements of TEM cross-section samples. In addition, STEM-EDXS analyses only cover a comparably small volume, especially in cross-section TEM samples. Due to these two reasons, In-rich phases might be missed in STEM-EDXS measurements. To address this issue, additional SEM-EDXS trace analysis of In was performed by **Daniel Nerz**. A relatively

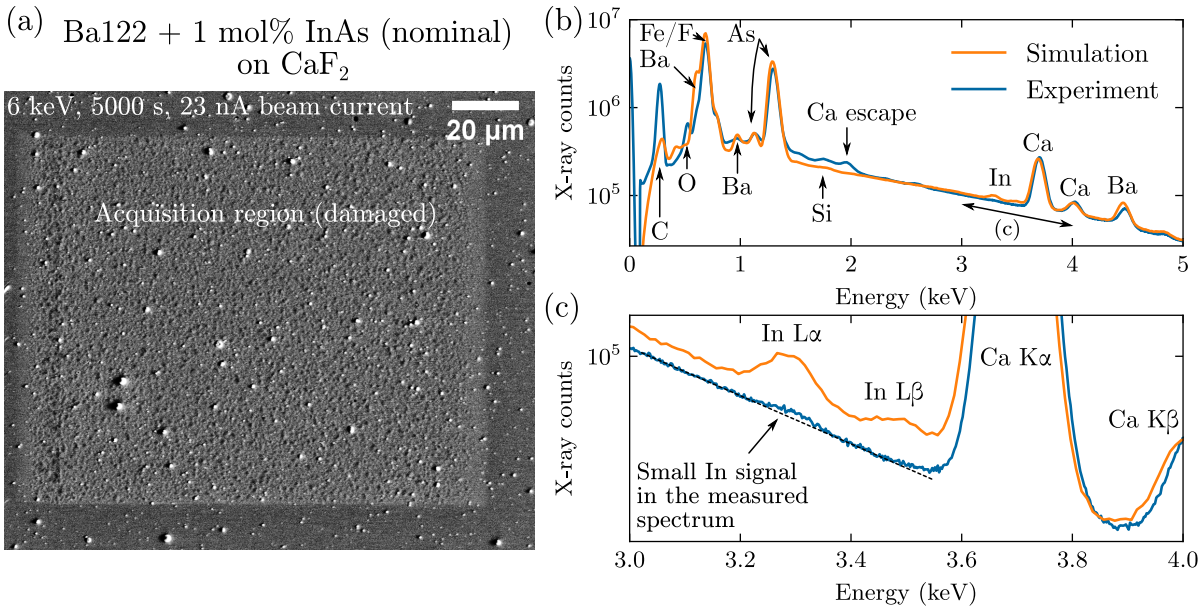

Figure 4.34: SEM-EDXS trace-element analysis of In in the highIA sample. (a) SE-SEM image showing the acquisition region, which appears slightly brighter compared to the surrounding Ba122 film. The scanned region was damaged during the dose-intensive acquisition. Image contrasts were enhanced using contrast-limited adaptive histogram equalization (CLAHE) in *Fiji*. (b) Experimental (blue) and simulated (orange) EDXS spectra, assuming a composition $Ba122_{0.99}(InAs)_{0.01}$. (c) Magnified energy region of (b) containing the In x-ray peaks. A small In signal in the experimental spectrum is visible. The In Lα is larger in the simulated spectrum.

large sample area (about 135 µm × 110 µm) was continuously scanned (cf. Fig. 4.34a) during EDXS spectrum collection. However, only the In Lα x-ray transition is available in a scanning electron microscope since (i) the high-energy In K shell is barely excited in SEM due to a low overvoltage of 1.07 at 30 keV and (ii) measurements at 30 keV would lead to a rapid destruction of Ba122 on CaF_2 (cf. crack formation in Ba122 in Fig. 4.5 on Page 100). An electron energy of 6 keV was used, resulting in an overvoltage of 1.6 for the In L_3 shell (to efficiently excite In Lα x-rays). Note that the highIA sample is already damaged at 6 keV, which is visible in Fig. 4.34a as a change of contrast in the scanned area. The beam current was set to 23 nA and the spectrum was collected for 5000 s, resulting in 713×10^6 counts in the spectrum. A Monte Carlo simulation for the same experimental conditions and a sample composition $Ba122_{0.99}(InAs)_{0.01}$ (i.e. nominal 1 mol % InAs concentration) was run for comparison with the experiment.

The experimental (blue) and simulated (orange) EDXS spectra are plotted in Fig. 4.34b and c. Figure 4.34b presents the energy range between 0 keV and 5 keV with element markers for the different x-ray peaks. In general, a good match is found for both spectra regarding the elements in the Ba122-InAs sample. A few more minor peaks are visible in the experimental spectrum, which stem from typical measurement artifacts not included in the Monte Carlo simulation. For example, a Ca escape peak is visible. This peak results from the generation of Si Kα x-rays (1.74 keV) in the Si detector by Ca Kα x-rays. The Si Kα x-rays can escape the detection layer, resulting in an associated peak to Ca Kα, which is shifted by 1.74 keV towards lower energies (i.e. at 3.69 keV − 1.74 keV = 1.95 keV). Other examples are the O and C peaks arising from Ba122 oxidation and C contamination of the sampled area. The apparent C (and O) peak in the simulated spectrum results from the C-containing detector window (MOXTEK AP 3.3 polymer), where x-rays are partly absorbed by C atoms. This leads to an abrupt decrease in x-ray-detection efficiency above the C K edge at 284 eV, giving the impression of a peak.

The region shown in Fig. 4.34c contains the relevant In x-ray transitions. Here, an In signal for the simulated spectrum (orange) is observed, whereas the experimental spectrum (blue) shows a small bump at the In Lα peak position. A straight line is drawn as a guide for the eye to see this small peak. The small bump in the experimental spectrum confirms the presence of In in the highIA sample using SEM-EDXS. However, the In concentration is most likely lower than the nominal value of 1 mol % based on the larger In peaks in the simulated spectrum. A quantification[8] was performed for the SEM-EDXS dataset (cf. bottom row in Table 4.5). The In concentration of (0.13 ± 0.03) at. % is similar to the quantified value obtained from the STEM-EDXS measurement, suggesting an InAs NP concentration of about (0.9 ± 0.2) mol %. However, the Ba concentration is significantly lower than the nominal value, probably due to a systematic error in the quantification. The latter might be due to uncertainties regarding the physical properties of the Ba M x-ray peaks used here for quantification[9]. The uncertainties regarding the physical properties of the Ba M x-ray transitions also result in the differences between the simulated and experimental spectra in Fig. 4.34b, e.g. for the Ba Mζ_1 (Ba M5-N3 transition) peak at 0.601 keV. Therefore, the quantification results should be interpreted carefully. The errors then also influence the calculated NP concentration.
The possibility mentioned above for a surface decoration with In-rich phases cannot be completely ruled out from the SEM-EDXS measurement. The In concentration is different compared to the STEM-EDXS measurements. However, this could be explained by the uncertainties regarding the quantification using the Ba M lines. The In concentration is also close to the detection limit of the SEM-EDXS technique since the bremsstrahlung background nearly obscures the In Lα peak in the experimental spectrum. The vertical offset between the two spectra results from a difference in total counts. This is caused by a slightly different detector geometry (i.e. effective solid angle) set in the simulation compared to the experiment. A more precise calibration of the simulation regarding the collected counts is possible, but was not done here.

Conclusions for Ba122-InAs nanocomposites. This section presented the microstructural analysis of two Ba122-InAs nanocomposites grown on CaF_2 using quasi-multilayer PLD. In general, high-quality films similar to BHO/BZO nanoparticles were fabricated with this technique. BaF_2 and Fe were detected as secondary phases in both investigated samples, similar to pristine Ba122 films. The sample with lower InAs concentration (sample "lowIA") showed a high density of planar defects. In contrast, planar defects are absent for higher InAs concentrations (sample "highIA"). It is not clear, if these different microstructures can be solely attributed to the InAs content. Slight (unwanted) changes in deposition condition, e.g. the growth rate, may have also caused the pronounced differences between the two films. For example, a lower growth rate for lowIA would explain the formation of BaF_2 and the smaller film thickness compared to highIA (for the same nominal deposition duration). However, the reason for a possible difference in growth rate is unclear.
EDXS analyses were performed to search for traces of In in the samples because no NPs could be observed in the acquired HAADF-STEM images. Low concentrations of In could be unambiguously detected for highIA. However, the quantified InAs concentration was lower than the nominal value ((0.5 ± 0.2) mol % using STEM-EDXS vs. 1 mol % nominal). A value of (0.9 ± 0.2) mol % for SEM-EDXS quantification is close to the nominal value, but must be

[8] Using the peak-to-background method with a ZAF acorrection in Bruker *Esprit*. This method is less sensitive to changes in surface morphology, which are present here as precipitates and PLD droplets. See Goldstein et al. [Gol+18, pp 408 sq.] for a detailed discussion.
[9] The Ba Lα could not be selected in the Bruker *Esprit* software for quantification for this spectrum, even though the Ba Lα peak is contained in the spectrum.

interpreted carefully due to uncertainties concerning the Ba M x-ray transitions. Indium could not be detected for lowIA, probably because of the low InAs concentration. In addition, the large-area SEM-EDXS measurement rules out possible segregation of In-rich phases to the film surface, which would not be detected by STEM-EDXS measurements.
The volatility of InAs due to its low melting point may be the main reason for the absence of InAs NPs in the investigated films. Ba122 requires a CaF_2 substrate temperature of 700 °C, where In and As may partly evaporate during PLD (probably at different rates). The residual In and As may be dissolved in the Ba122 structure. The striking differences in the film microstructures (cf. Fig. 4.31) for the two investigated samples complicated the analysis of the structure-property relationship and the exact influence of InAs.
Regarding the methodology, SEM-EDXS analyses combined with Monte Carlo simulations provide a valuable tool to estimate the InAs (and other NP) concentrations for superconducting nanocomposite films. Larger sample areas can be analyzed quickly compared to a dedicated TEM analysis. However, the detection limits are worse in SEM-EDXS due to the higher bremsstrahlung background than for thin TEM samples. In addition, some x-ray transitions at low energies may have unfortunate overlaps with other elements. Here, the In Lα line was used to detect In in Ba122.

4.4 Growth of $Ba(Fe,Co)_2As_2$ on MgO and $LaAlO_3$ Substrates

This section covers results for Ba122 films grown on other substrates than CaF_2. PLD of Ba122 on the other substrates ($LaAlO_3$ and MgO) was less reproducible than for CaF_2, maybe due to the limited growth rate of about 1 $Å s^{-1}$ of the PLD setup [Mey21, p 41]. Therefore, the following section presents selected results for preliminary Ba122 samples, which have no relation to each other and are not part of a systematic study of a fabrication parameter. Still, the Ba122 showed some remarkable structural features and film-substrate interfaces. In addition, so-called "PLD droplets" are briefly discussed, which are observed for all investigated Ba122 films. PLD droplets appear as µm-sized spheres on the surface of all investigated Ba122-film (Fig. 4.35a). These structures appear in PLD films, and their size and concentration depend on the fabrication parameters and target material [Hol+92; vdRND93].
As shown in Fig. 4.35b, the PLD droplets can be distinguished from other precipitates (e.g. Fe precipitates) if the size difference is significant. This was the case for all investigated Ba122 films, where Fe precipitates are significantly smaller than most PLD droplets (Fig. 4.35b). A random PLD droplet was cut in half and prepared as a TEM sample (Fig. 4.35c and d). A PLD droplet from a Ba122 film grown on CaF_2 was arbitrarily chosen. The HAADF-STEM-in-SEM images in Fig. 4.35c and d show the random distribution of phases in a PLD droplet, as determined by the random intensity variations in the images. The actual Ba122 film is barely visible compared to the large PLD droplet and magnified in the inset image (dashed blue region in Fig. 4.35c). Besides this analysis, the PLD droplet size, density, and chemical structure were not further evaluated as their density was quite low in the investigated films. This suggests that the PLD process was already optimized for the investigated films regarding PLD-droplet mitigation. Therefore, the PLD droplets were not further investigated here.

Ba122 growth on MgO and $LaAlO_3$ Ba122 films grown on CaF_2 showed the best reproducibility and film quality among CaF_2(001), MgO(001), and $LaAlO_3$(0 0 1) (LAO) substrates. A few Ba122 films were also investigated for the latter two substrates and the results regarding film growth are described in the following. The lattice mismatch between the substrates and

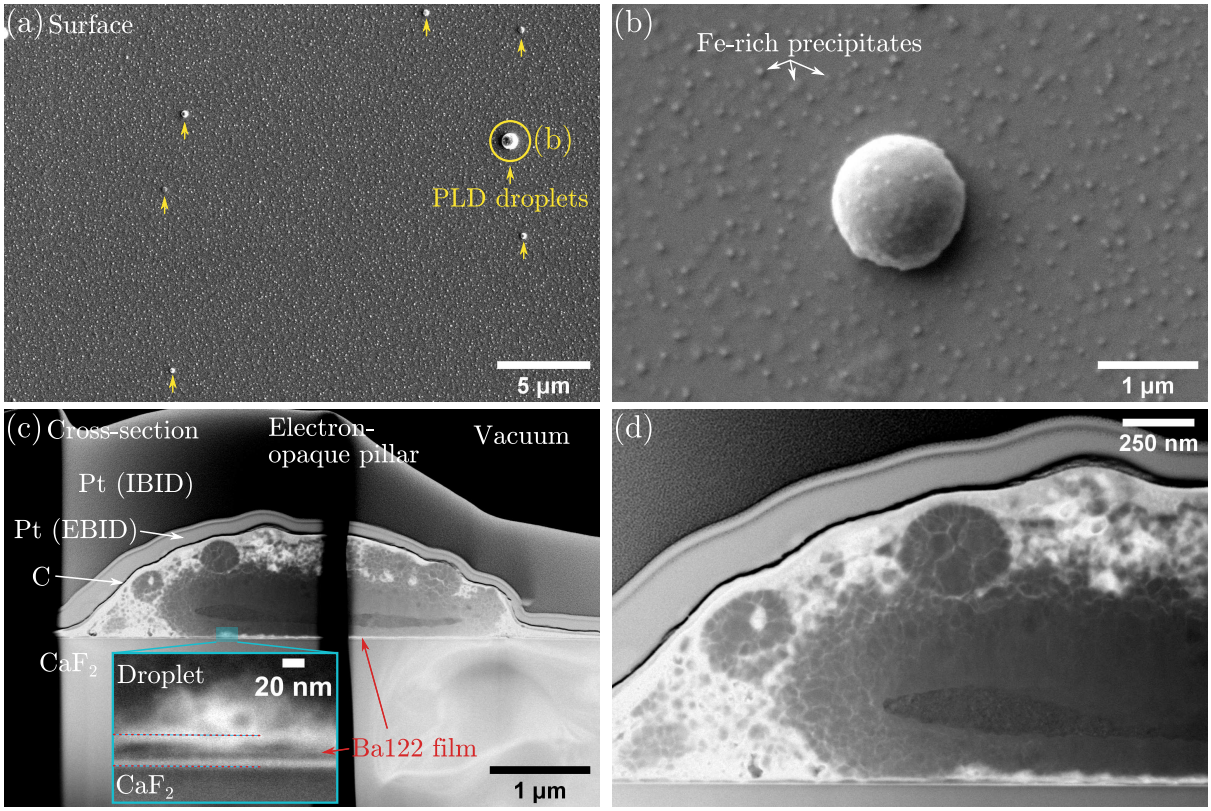

Figure 4.35: PLD droplets on Ba122 films. (a) SE-SEM surface image of a Ba122 film with PLD droplets marked with arrows. A large droplet is shown at higher magnification in (b). (b) Fe precipitates in the investigated Ba122 are smaller than a typical PLD droplet. (c and d) HAADF-STEM-in-SEM cross-section image of a randomly chosen PLD droplet from a Ba122 film grown on CaF_2. The inset shows the film-substrate interface with the Ba122 film marked with a dashed line. The droplet extends over two electron-transparent windows of the TEM sample separated by a thicker electron-opaque region.

Ba122 are calculated using the formula

$$\epsilon = 1 - a_\mathrm{f}/a_\mathrm{s} \tag{4.10}$$

with the in-plane lattice parameters for the (Ba122) film a_f and substrate a_s (Table 4.6). The typically higher T_c of Ba122 on CaF_2 is attributed to compressive strain, which is induced during sample cool-down from deposition to room temperature [Hän+19; Sat+20]. This is discussed in detail by Iida et al. [Iid+16] in their supplementary information. For the Ba122-CaF_2 system, the lattice parameters of Ba122 on CaF_2 at the deposition temperature (700 °C) are relatively close to the lattice parameters for Ba122 single crystals. Then, compressive strain is introduced in Ba122 on CaF_2 upon cooling. This effect is caused by the large difference in thermal expansion coefficient (cf. Table 4.6) for Ba122 and CaF_2. The substrate temperatures for PLD are also given in Table 4.6 and the preparation of the substrates for PLD is described by Meyer [Mey21, p 35]. For a literature overview of IBSs growth on various substrates, the reader is referred to the review by Hänisch et al. [Hän+19].

Figure 4.36 presents representative elemental maps obtained by STEM-EDXS analyses for Ba122 films on (a) MgO (left column), (b) LAO (middle column), and (c) CaF_2 (right column). The latter is shown for completeness but contains an additional interesting microstructural feature compared to the previous sections in the form of O-rich pillars (cf. dotted arrows in the O map in Fig. 4.36c). These may have formed by oxidation of vertical defects, e.g. grain

Table 4.6: Lattice mismatch ϵ, room-temperature thermal expansion coefficients α_t (from references [Hän+19; Sie+90]), and deposition temperatures T_{sub} of Ba122 and selected substrates.

Material	a_s (Å)	ϵ (%)	α_t ($10^{-6}\,K^{-1}$)	T_{sub} (°C)
$Ba(Fe_{0.92}Co_{0.08})_2As_2$	3.963	—	8.5 ($\langle 1\,0\,0\rangle$) 25 ([0 0 1])	—
CaF_2(0 0 1)	3.869†	−2.44	18.5	700
MgO(0 0 1)	4.214	5.95	10.5	700
$LaAlO_3$(0 0 1)	3.787	−4.66	12.5	750

†$a/\sqrt{2}$ with $a = 5.471$ Å.

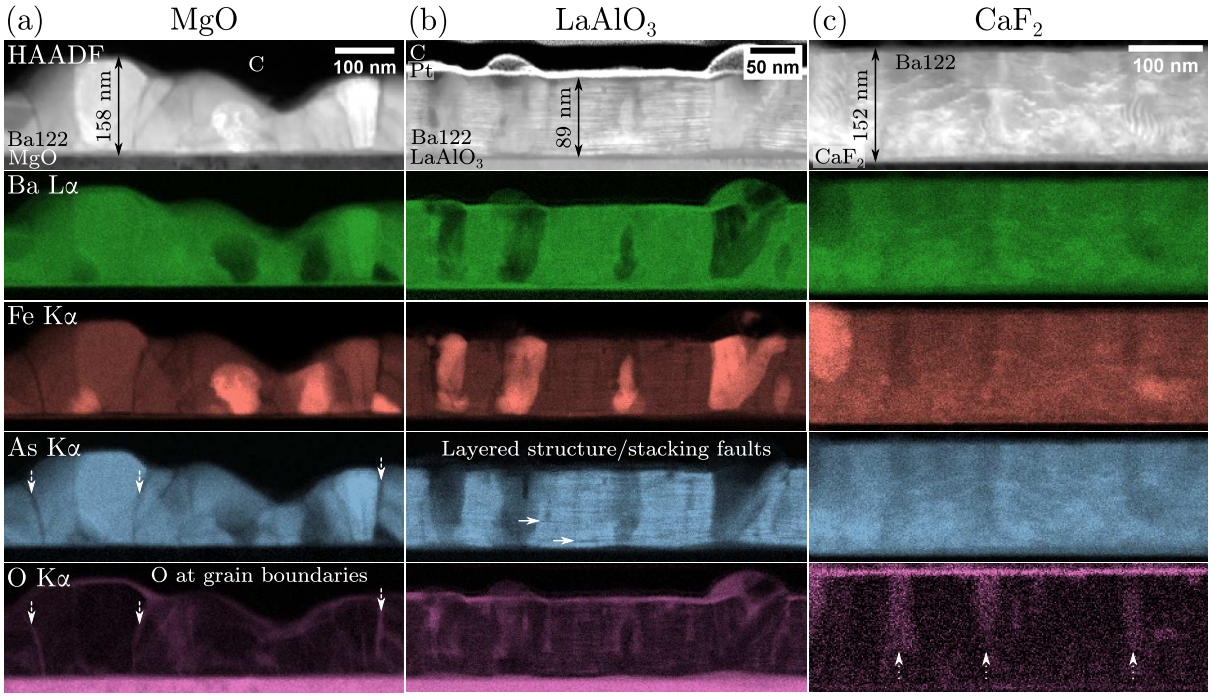

Figure 4.36: STEM-EDXS elemental maps of Ba122 films on (a) MgO, (b) $LaAlO_3$, and (c) CaF_2. The elemental maps for each element are displayed side by side for easier comparison. Substrate elements are omitted for brevity. Note the different thicknesses of the Ba122 films. (a) Polycrystalline growth of Ba122 is observed on MgO. The grain boundaries are Ba/O-rich and Fe/As-depleted (see examples marked with dashed arrows). (b) Ba122 growth on $LaAlO_3$ shows epitaxial growth with a layered structure resulting from planar defects (stacking faults, see solid arrows). (c) Ba122 grows epitaxially on CaF_2 with the best film quality for the three substrates and used PLD setup. A few O-rich columns are visible (dotted arrows). A striped contrast is visible in the HAADF-STEM image in (c) near the right Fe precipitate, which is probably caused by a Moiré effect between the Ba122 and Fe crystal lattices. All Ba122 films contain Fe-rich precipitates. Figure in (a) and (b) are adapted from a poster publication [Grü+19a].

boundaries [Pak+20; HI20]. The Ba122 film on CaF_2 shows a constant layer thickness resulting from high-quality epitaxial growth. A similar situation is visible for LAO, but MgO shows large thickness variations and grain boundaries, which are already visible in the HAADF-STEM images (Fig. 4.36a). Mostly polycrystalline films were produced because the parameter window for epitaxial growth on MgO seems relatively narrow for the used PLD setup [Mey21, p 41]. With more optimal conditions, Ba122 can be grown with high quality on MgO [Iid+16]. The grain boundaries in the polycrystalline film on MgO are rich in O and Ba and Fe-/As-depleted (cf. dashed arrows in Fig. 4.36a). Oxygen at grain boundaries was also observed for bulk

samples of polycrystalline IBSs of the 122-type family [Wan+11; Kim+14; Pak+20]. Pak et al. [Pak+20] improved the superconducting properties of their Ba122 bulk samples by using a high-performance glove box to reduce O and H_2O contamination of the starting materials. From the presented measurements it is unclear if O segregation occurs during film deposition or as a form of sample aging during storage. However, polycrystalline films may provide additional insights into the grain-boundary chemistry in IBSs.

A layered structure is observed for the film grown on LAO, which is visible in the HAADF-STEM image and the As map in Fig. 4.36b (cf. arrows). This layered structure results from a high density of planar defects, as discussed further below in context with Fig. 4.39. Fe precipitates are visible for all samples. However, the Fe precipitates reach the film-substrate interface for MgO and LAO. This suggests that Fe precipitates may grow directly on LAO and MgO, whereas Fe growth starts in Ba122 on CaF_2. Indeed, Fe buffer layers were deposited on MgO to enhance Ba122 growth [The+10].

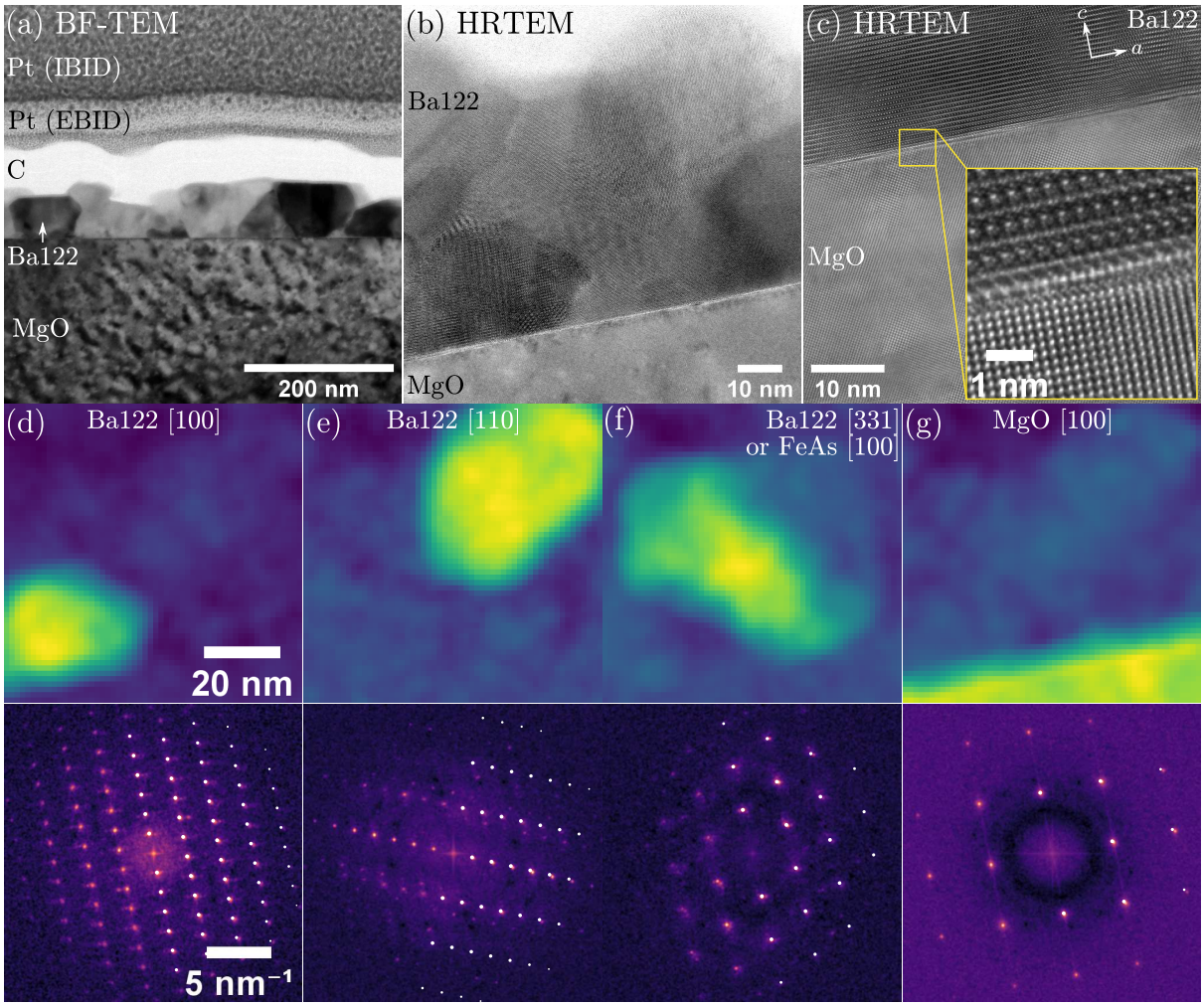

Figure 4.37: HRTEM analysis of the Ba122 film grown on MgO. (a) BF-TEM overview image showing polycrystalline Ba122 with several grains. HRTEM images of (b) several grains and (c) the film-substrate interface. The inset shows a magnified view of the yellow-marked region. (d–g) Sliding-window-FFT analysis combined with ICA. The score maps (top row) show the spatial distribution of the corresponding ICA loadings (bottom row). The latter are similar to diffractograms and show the local periodicities of the HRTEM lattice fringes. The grains are identified as (d–f) Ba122 and (g) MgO based on a comparison with simulated positions (white dots). (f) FeAs is another possible phase, which agrees with the ICA loading.

The polycrystalline structure of the investigated Ba122 films on MgO is confirmed by HRTEM imaging (Fig. 4.37). Figure 4.37a presents a low-magnification BF-TEM image of a Ba122 film grown on MgO. The individual grains appear with different diffraction contrast based on their orientation. The HRTEM image shown in Fig. 4.37b was analyzed using the sliding-window-FFT method in combination with ICA. The ICA score maps (middle row) and corresponding loadings (bottom row) show the spatial distribution and FFT-like signals of different grains. Here, four ICA components were selected as examples. The crystalline orientations were identified by comparison with simulations and the simulated positions of the reflections are shown as white dots in the ICA loadings. Three grains of Ba122 are identified from the HRTEM image in Fig. 4.37b and shown in Fig. 4.37d–f. One grain, Fig. 4.37d, grew in the desired epitaxial orientation Ba122[1 0 0](0 0 1)‖MgO[1 0 0](0 0 1). Figure 4.37e and f show Ba122 in the ⟨1 1 0⟩- and ⟨3 3 1⟩-type zone-axis orientations. In principle, the FFT-like signal in Fig. 4.37f could correspond to FeAs in a ⟨1 0 0⟩-type zone-axis orientation. The ICA component for MgO is shown for completeness (Fig. 4.37g) and its location in the substrate in the score map.
Some parts of the Ba122 films on MgO grow in the expected epitaxial orientation. This is also exemplarily shown in the HRTEM image in Fig. 4.37c, where the inset shows the lattice fringes at the film-substrate interface. Note that this image was taken from another region than the Ba122 grain in Fig. 4.37d, but it shows the same crystalline orientation. Ba122 grains were often found in this orientation but did not cover the whole substrate surface to form a complete epitaxial layer. An increased Ba122 growth rate may be required, but the used PLD setup is limited to about $1\,\text{Å}\,\text{s}^{-1}$ for Ba122 growth [Mey21, p 38].

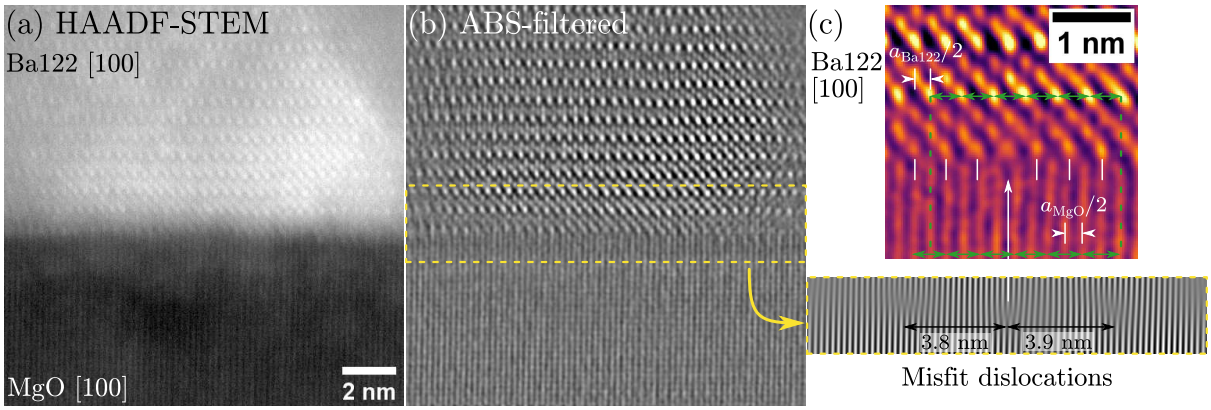

Figure 4.38: HAADF-STEM analysis of the Ba122-MgO interface. (a) Unfiltered HAADF-STEM image of the Ba122-MgO substrate interface for a grain with an epitaxial Ba122-MgO orientation according to Ba122[1 0 0](0 0 1)‖MgO[1 0 0](0 0 1). The low image quality results from non-optimized sample preparation. (b) Background-subtracted and ABS-filtered image of (a) revealing the crystal structure. The dashed yellow lines mark the position of the MgO{2 0 0} Bragg-filtered image in (c). (c) Bottom: Bragg-filtered image of (b). Top: ABS-filtered image of the central misfit dislocation. The vertical lines are a guide for the eye to show the position of the Ba atomic columns with respect to the MgO lattice planes. The green arrows and dashed lines indicate the Burgers circuit.

HAADF-STEM imaging was used to study the Ba122-MgO interface for Ba122[1 0 0]‖MgO[1 0 0] grains (Fig. 4.38). The image quality in the HAADF-STEM image in Fig. 4.38a is not optimal since FIB preparation was not optimized for the Ba122-MgO samples[10]. The crystalline detail in the image was optimized by removal of the background intensity and ABS-filtering (Fig. 4.38b).

[10]MgO has a low milling rate due to its high melting point and ideally requires the pre-wedge milling technique to reduce redeposition of milled sample material. This was not used here due to a lack of experience at the time of sample preparation.

The interface could then be analyzed. The periodicity of the MgO(2 0 0) lattice planes was isolated using a Bragg-filtering mask for the MgO(2 0 0) reflection in the Fourier-transformed image. The lower image in Fig. 4.38c shows the Bragg-filtered image of the film-substrate interface region (marked with a dashed yellow rectangle). Here, dislocations are observed with a separation of about 3.9 nm. These are probably misfit dislocations, which form due to the relatively large lattice mismatch of Ba122 on MgO of about 6 % (cf. Table 4.6). The misfit-dislocation spacing D can be calculated (see, e.g., Haindl [Hai21, p 206]) with the length of the Burgers vector $\vec{b}$ and the lattice mismatch

$$D = \frac{|\vec{b}|}{\epsilon} \quad . \tag{4.11}$$

Alternatively, the formula for the Moiré-fringe spacing is also used in literature to report the dislocation spacing, given by [ZTW13]

$$D_\mathrm{m} = \frac{d_1 d_2}{|d_1 - d_2|} \tag{4.12}$$

for two lattice-plane distances d_1 and d_2 (corresponding to $|\vec{b}|$). Both formulas yield similar values and only D is used in the following for brevity. Figure 4.38c presents a color-coded HAADF-STEM image of a misfit dislocation (inserted lattice plane) in the center of the image. The vertical white lines mark the positions of the first plane of Ba atomic columns of the Ba122 film. The central Ba column is located between two MgO{2 0 0} planes, whereas the other Ba planes line up directly above a MgO{2 0 0} plane. A Burgers vector $\vec{b} = a_\mathrm{Ba122}/2[0\,1\,0]$ (projected onto the viewing direction) is found around the dislocation, as indicated by the green double-headed arrows. Note that the atomic steps in the c-direction could not be counted here for the Burgers circuit because of the unresolved MgO(0 0 2) planes. However, the Ba122 structure appears flat on the MgO surface, and a Burgers vector component in c-direction can be most likely excluded.

A value $D = 3.3$ nm is found using the bulk lattice parameters for both materials ($a_\mathrm{Ba122} = 3.9633$ Å, ICSD entry 169 555, and $a_\mathrm{MgO} = 4.214$ Å, ICSD entry 52 026). This value is smaller than the observed value of 3.9 nm, probably due to the following reasons. First, only a few misfit dislocations were analyzed from the few available HRTEM images and the shown HAADF-STEM image, yielding poor statistics. Second, the calculated D value assumes a fully relaxed Ba122 film. However, residual tensile strain is most likely present in the Ba122 film.

The Ba122 film grown on LAO is discussed in the following. Figure 4.39a shows a higher-magnification HAADF-STEM image of the Ba122 film analyzed with STEM-EDXS. The film thickness here is about 95 nm. A high density of planar defects is visible as dark horizontal lines (marked by arrows in Fig. 4.39a) similar to the planar defects shown for Ba122 films on CaF_2 (cf. Fig. 4.31b on Page 137 or Fig. 4.21a on Page 119). Qualitative STEM-EELS analysis of the region in Fig. 4.39b reveals the same trends at the planar defects regarding the chemical composition as for the Ba122-CaF_2 samples (cf. Fig. 4.23 on page 122), i.e. an O increase and a Fe depletion. Ba is increased due to the double Ba plane at stacking faults, which are simultaneously sampled by the electron probe (see discussion for Fig. 4.23 on page 122). Note that the same stacking fault is marked by a dashed arrow in Figure 4.39a and b.
The oxidized Ba122 surface layer was also mapped here. Enhanced O and Ba signals are observed, whereas Fe is depleted. This effect can also be seen in all previously shown STEM-EDXS datasets of Ba122 films by carefully comparing the elemental signals of the surface layer (e.g. in Fig. 4.36).

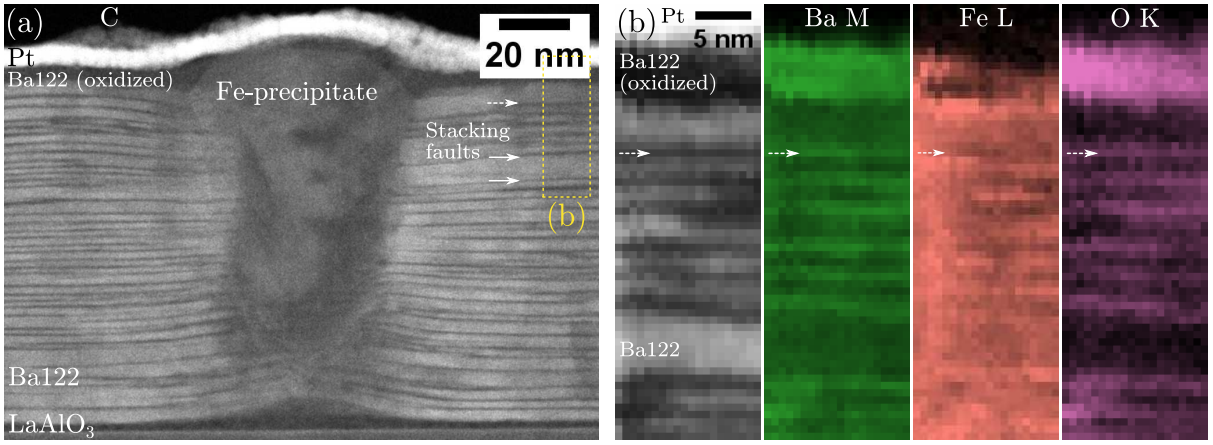

Figure 4.39: STEM-EELS analysis of planar defects in the Ba122 film grown on $LaAlO_3$. (a) HAADF-STEM cross-section overview image with the STEM-EELS acquisition region marked with a yellow dashed rectangle. A high density of planar defects (dark horizontal lines) is observed (marked by arrows). A large Fe precipitate bends the surrounding Ba122 lattice planes. (b) ADF-STEM image and elemental maps for Ba, Fe, and O. The planar defects and the oxidized surface layer show increased Ba and O signals and a reduced Fe signal. The same planar defect is marked with a dashed arrow in (a) and (b). Figure (b) is adapted from a poster publication [Grü+19a]

Arsenic shows a similar depletion as Fe in the STEM-EDXS maps. The chemical signals of the surface layer are similar to the aforementioned grain boundaries, e.g. seen for the Ba122-MgO samples (Fig. 4.36a).

A large Fe precipitate is visible in the center of Fig. 4.36a, which bends the surrounding Ba122 lattice planes. Interestingly, this is different from the Fe precipitates in Ba122 films on CaF_2 where such a bending was not observed for any of the investigated films (see, e.g., Fig. 4.31b on Page 137a). Since the film on LAO is thicker than all investigated films on CaF_2, it cannot be fully ruled out that the strong bending partly results from the increased layer thickness. However, the pristine Ba122 film on CaF_2 shown in Fig. 4.29a is only $\sim 20\,\text{nm}$ thinner than the here shown Ba122 film on LAO and does not show such a strong bending of Ba122 lattice planes around Fe precipitates. Another aspect is that the Fe signal reaches down to the Ba122-LAO interface, whereas this was not observed for Ba122-CaF_2 samples. This may provide evidence that the direct growth of Fe precipitates on LAO is related to the strong disturbance of the surrounding Ba122 film.

The film-substrate interface shows a low HAADF-STEM intensity (Fig. 4.39), which results from an amorphous interface structure. The dark amorphous region is larger below the Fe precipitates (only one is shown here). Figure 4.40 presents HRTEM and HAADF-STEM images of different TEM samples of various Ba122 films grown on LAO. Note that these Ba122-LAO samples are not from the same samples series and grown with different thickness. Still, the same deposition temperature (750 °C) was used in all cases with maximum deposition rates around $1\,\text{Å s}^{-1}$. An amorphous Ba122-LAO interface was observed for all investigated TEM samples. However, the thickness of the amorphous layer even varied between different TEM samples of the *same* Ba122 film. For example, Fig. 4.40b shows an amorphous layer thickness of about 2.2 nm, whereas Figure 4.40c – from the same Ba122 film – only has a $\sim 1\,\text{nm}$ thin amorphous interface layer. This indicates a possible amorphization caused by TEM-sample preparation, where FIB milling may destroy the highly strained film-substrate interface. Similarly, TEM samples from other Ba122-LAO films also showed an amorphous interface layer (Fig. 4.40d and e). Nevertheless, the findings for the Ba122-LAO interface are summarized here.

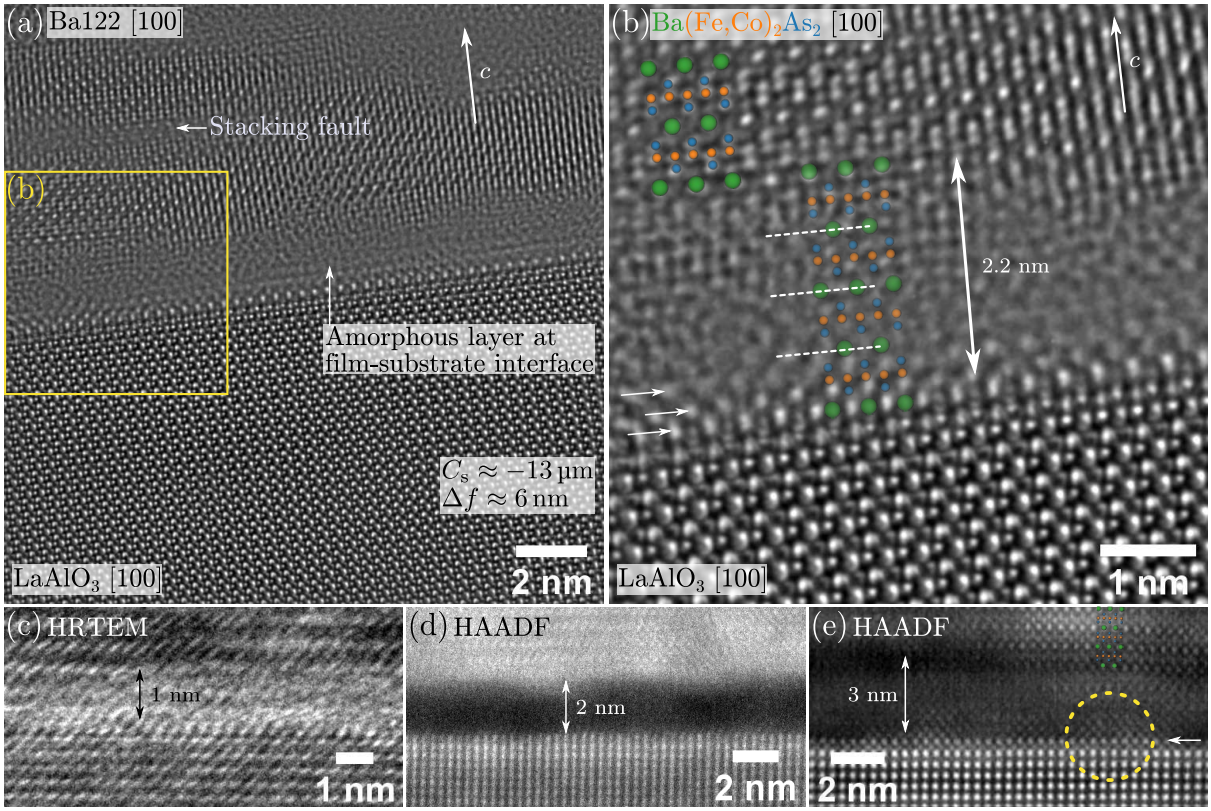

Figure 4.40: Analysis of the Ba122-$LaAlO_3$ interface. (a) NCSI-HRTEM image of the Ba122-LAO interface. Atomic columns appear bright. An amorphous interface layer is observed. (b) Magnified image of the region in (a). A structure model of Ba122[1 0 0] is overlaid in the top-left corner. A continuation of the structure (faint overlaid model) does not fit with the atomic positions at the film-substrate interface (marked with arrows). The dashed lines mark the positions of the Ba planes as a guide for the eye. (c–e) HRTEM and HAADF-STEM images of TEM samples from the (c) same and (d,e) other Ba122-LAO films. An amorphous interface is observed in all cases, although with varying thicknesses. (e) The region marked with a dashed circle shows a similar stacking of atomic columns as in (b) (cf. arrows).

An overview HRTEM image of the Ba122-LAO interface is shown in Fig. 4.40a. The image was taken from a defocus series under NCSI conditions (Eq. (2.27) on page 25), i.e. for $C_s \approx -13\,\mu m$ and $\Delta f = 6\,nm$. This results in bright atomic columns on a dark background and good interpretability of the HRTEM image contrast. The amorphous Ba122-LAO substrate interface is marked by a vertical arrow. The Ba122 film is partly amorphous (cf. top region in Fig. 4.40a), possibly an artifact of TEM-sample preparation. A stacking fault is also observed. These appeared with high density in this Ba122-LAO sample. The region marked with a yellow rectangle is magnified in Fig. 4.40b and displays the film-substrate interface. A structure model is overlaid in the top-left region of the image to indicate the possible positions of the atomic columns.

The continuation of the Ba122 stacking is indicated by the faint transparent structure model in the amorphous interface layer. The dashed lines indicate the positions of the Ba planes in *c*-direction. Interestingly, the positions of the first Ba plane on LAO does not agree with the bright HRTEM image contrast. The overlaid structure model is shifted by $[0\,1\,0]/2$. Therefore, a simple continuation of the Ba122 structure down to the LAO substrate is not consistent with the HRTEM image. In addition, the first atomic planes (marked by solid horizontal arrows) show a different contrast than the Ba122 structure above the amorphous interface. Stacking of multiple Ba planes at the Ba122-film substrate interface may be present, based on the similar

size and image intensity of the first atomic planes compared with the Ba122 structure in the top part of the image. A similar stacking of atomic columns is visible in the HAADF-STEM image in Fig. 4.40e (marked with a dashed yellow circle).

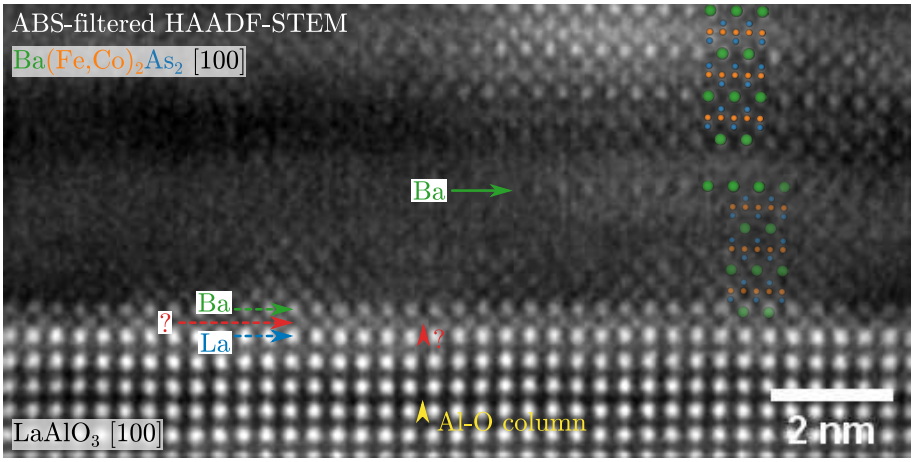

Figure 4.41: HAADF-STEM image of the Ba122-LAO interface. Magnified image from Fig. 4.40e. See text for a discussion.

The HAADF-STEM image in Fig. 4.40e is magnified in Fig. 4.41. The top-right region shows the Ba122 layer as indicated by the overlaid structure model for Ba122[1 0 0]. A faint row of atomic columns is still visible in the disordered layer (marked by a solid green arrow). This atomic layer is identified as a Ba plane because of the size and (residual) Z-contrast of the atomic columns. A continuation of the Ba122 structure down to the Ba122-LAO interface is again overlaid as a possible structure model. In this image, the Ba positions end close to the expected position based on the observed atomic columns at the interface. This is in contrast to the sample region shown in Fig. 4.40b, where the structure model did not fit with the observed atomic-column positions at the Ba122-LAO interface. The terminating layer of LAO in Fig. 4.41 seems to be La (blue dashed arrow) and the first Ba plane of Ba122 grows in a "cube-on-cube" configuration on the La atomic columns. The atomic plane between the terminating La and the first Ba could not be identified (red dashed arrow). It has a visible Z-contrast as opposed to the invisible Al-O atomic columns in LAO (cf. vertical arrowheads). However, the exact atomic structure cannot be clarified with confidence due to the disorder and possible artifacts introduced by the applied ABS-filtering.

It is unclear whether the amorphization occurs during TEM-sample preparation or during PLD. An explanation for the latter case may be (i) epitaxial growth of Ba122 on LAO (with or without a special atomic configuration of the first few lattice planes) and (ii) subsequent oxidation after or during PLD due to O diffusion from LAO into Ba122. In this explanation, the interface layer is similar to the oxidized Ba122 surface layer. The latter acts as a passivation layer after reaching a certain thickness, thereby preventing further oxidation. However, a reduction of LAO (i.e. oxygen diffusion into Ba122) is reported to be less likely compared to, e.g., $SrTiO_3$ since "LAO does not get reduced due to the invariant Al^{3+} state as opposed to the mixed valence Ti^{3+} and Ti^{4+} states in STO" [Yu+08]. The faint signature of a partly "intact" Ba plane in the amorphous layer region shown in Fig. 4.41 also provides evidence that the interface is only partly amorphous. In addition, the "TEM Interface Atlas" for IBS films by Haindl [Hai21, pp 215 sq.] shows a great variety of clean epitaxial or amorphous film-substrate interfaces for IBSs grown on oxide substrates. The structural variability for the interface layers may be caused by different FIB-milling conditions used for TEM-sample preparation. FIB milling during TEM-sample preparation could also promote oxidation from oxide substrates, thereby oxidizing

the film-substrate interface. Therefore, it is concluded that the observed disordered interface layers are caused by FIB milling during TEM-sample preparation.

4.5 Summary

This chapter presented experimental results for pure and nanoparticle-doped $Ba(Fe_{0.92}Co_{0.08})_2As_2$ (Ba122) films grown by PLD on CaF_2, MgO, and $LaAlO_3$. The first section (Page 93) showed practical problems encountered during the electron-microscopic analyses. Especially Ba122 grown on CaF_2 is susceptible to electron- or ion-beam irradiation, which leads to a rapid amorphization of the Ba122 film starting from the Ba122-CaF_2 interface. In addition, CaF_2 and BaF_2 (a possible secondary phase in Ba122-CaF_2 samples) oxidize during TEM measurements. The highest available electron energies for TEM measurements and the lowest possible electron dose for atomic-resolution imaging are possible remedies to mitigate Ba122-film destruction. Dose-intensive analyses of the chemical composition by STEM-EDXS or STEM-EELS must be interpreted carefully due to the aforementioned oxidation of CaF_2/BaF_2 and Ba122 itself.
Cracks in the film can form during SEM surface imaging, especially for primary electron-beam energies above 5 keV. Here, the primary electron energy should be chosen according to the Ba122-film thickness such that most electrons do not penetrate the Ba122 film. The maximum electron energy, which can be used without causing significant damage, can be determined by Monte Carlo simulations prior to a measurement session given that the film thickness is (roughly) known. The observations for Ba122-CaF_2 samples are important since CaF_2 is a popular substrate material for Ba122 and other IBS films.

The growth rate dependence of the Ba122 microstructure was studied (Page 101) by investigating two films grown on CaF_2 with different growth rates of $0.9\,Å\,s^{-1}$ (Ba122/fast) and $0.4\,Å\,s^{-1}$ (Ba122/slow). Both films grew epitaxially on CaF_2 with the expected crystalline orientation relationship Ba122[1 0 0](0 0 1)‖CaF_2[1 1 0](0 0 1). Larger Fe precipitates (diameter ~ 80 nm at the film surface) are observed in both samples, forming in the film and growing out of the surface. The Fe precipitates grow with the crystalline orientation relationship Fe[1 1 0](0 0 1)‖Ba122[1 0 0](0 0 1) with respect to Ba122. A higher density of Fe precipitates is observed for Ba122/fast. The formation of Fe precipitates may be related to (i) As loss during PLD or (ii) a deposition-rate dependence (higher → more Fe precipitates). Therefore, the Fe-precipitate density may be controlled by adjusting (probably reducing) the deposition rate or the PLD target stoichiometry. In contrast, the formation of BaF_2 as a secondary phase was only observed in Ba122/slow. BaF_2 grows at the film-substrate interface (sometimes even into the CaF_2 substrate) as isolated grains or in combination with Fe precipitates. The most commonly observed orientation is BaF_2[1 1 0](0 0 1)‖CaF_2[1 1 0](0 0 1)‖Ba122[1 0 0](0 0 1). Antiphase boundaries were observed, which are induced by atomic steps at the CaF_2-substrate surface. These grain boundaries cause an offset of about 0.274 nm, i.e. half the CaF_2 lattice parameter, of adjacent Ba122 grains in c-direction. These structures may be relevant for $H \parallel c$ pinning. Two types of planar defects were observed:

1. Stacking faults appear at the Ba planes and shift the Ba122 structure by $\langle 1\,0\,0\rangle/2$.
2. The c-lattice parameter increases by about 15 % at "isolated Ba planes" without any other structural changes.

Both types of defects were reported in the literature and appear with reduced intensity in HAADF-STEM images. STEM-EELS analysis showed evidence for O (and F) at stacking faults.

An *ex-situ* oxidation was ruled out by *in-situ* HAADF-STEM-in-SEM imaging of the planar defects, where the same reduced HAADF-STEM intensity was observed as in TEM samples, which were exposed to air. A better understanding of planar-defect formation is desired to mitigate them or purposefully introduce them into Ba122 for $H \parallel ab$ pinning.

Artificial pinning centers are desired in superconducting films for enhanced vortex pinning, leading to increased J_c values. For this purpose, Ba122 films with added nanoparticles were prepared by quasi-multilayer PLD, where the Ba122 and nanoparticle-material targets are exchanged multiple times during film deposition. $BaHfO_3$ and $BaZrO_3$ were used first as nanoparticles, since these materials are already commonly used for REBCO and IBS films. The nanoparticles aggregate in a *ab*-aligned, layered structure for both materials with a high nanoparticle content of about 20 mol % (as measured by EDXS). Note that the EDXS-determined nanoparticle concentrations were noticeably higher than the nominal value of 2 mol % measured by ICP-MS. Nanocolumns (or "nanorods") were observed in Ba122-$BaHfO_3$ films for a $BaHfO_3$ concentration of about (1.8 ± 0.6) mol %. These nanocolumns are desired since they act as efficient pinning centers for $H \parallel c$, which was also observed in electrical measurements of these samples. In all cases, a high-quality Ba122 crystal structure was observed (grown on CaF_2 substrates), even for a relatively high nanoparticle concentration of about 20 mol %.
InAs was tested as another nanoparticle material since Ba122 is also an arsenide. However, InAs nanoparticles were not detected by HAADF-STEM imaging even for the sample prepared with the highest nominal InAs concentration. No defects other than the typical Fe and BaF_2 precipitates were found for the two investigated Ba122 films grown on CaF_2. Indium was only detected in trace concentrations of about ~ 0.1 at. % in one of the samples. A possible problem is the low melting point (942 °C) and high partial vapor pressure of As at the typical substrate temperatures (700 °C) for PLD of Ba122 films. The residual trace concentrations of In may be homogeneously distributed in the Ba122 structure. Other arsenide materials could be tested in future studies, e.g. GaAs.

Finally, TEM results for Ba122 films grown on MgO and $LaAlO_3$ are summarized in the last section (Page 143). Overall, epitaxial Ba122 film growth was not reproducible for MgO for the used PLD setup. This resulted in polycrystalline Ba122 films on MgO. Here, the grain boundaries showed enrichment in O and Ba, similar to grain boundaries in polycrystalline bulk samples. Polycrystalline films deposited under various conditions may be used to get a better understanding of the grain-boundary structure and chemistry. A film-substrate interface with periodic misfit dislocations was observed for a few MgO grains that showed the desired epitaxial Ba122[1 0 0](0 0 1)‖MgO[1 0 0](0 0 1) orientation. For $LaAlO_3$, a high density of planar defects was observed. Additionally, the Fe precipitates caused significantly more strain in the surrounding Ba122 matrix compared to Fe precipitates in Ba122-CaF_2 samples. The Ba122-$LaAlO_3$ showed a disordered interface layer for all investigated TEM samples. However, these are probably caused by TEM-sample preparation using FIB milling.

To conclude, this chapter presented experimental problems and solutions associated with SEM and (S)TEM analyses of $Ba(Fe_{0.92}Co_{0.08})_2As_2$ thin films. The findings here could lead to a better understanding of Ba122 film growth, ultimately resulting in (i) improved quality and reproducibility of the Ba122 film quality or (ii) a precise fabrication of pinning centers in Ba122 to increase J_c for technical applications. Whenever possible, relevant SEM results and methods were shown. SEM instruments are more commonly available, easier accessible, and faster to apply for thin-film analyses compared to time-consuming TEM-sample preparation and dedicated

TEM analyses. The shown SEM methods may be useful to increase sample throughput, e.g., to test more fabrication parameters.

5. Structural and Chemical Properties of $REBa_2Cu_3O_{7-\delta}$ Thin Films

This chapter shows and discusses the results for the microstructural investigations of rare-earth barium copper oxide ($REBa_2Cu_3O_{7-\delta}$, REBCO) thin films. The first part introduces common structural defects in REBCO films and their appearance in (S)TEM imaging. The next section is dedicated to experimental problems and observed artifacts during sample preparation by FIB and TEM investigations. In particular, the formation of nanoscale planar defects as an artifact of TEM-sample degradation in air are discussed in detail. Then, TEM results for PLD-grown *ex-situ* oxygenated $GdBa_2Cu_3O_{7-\delta}$ are presented (Page 178). Finally, the results for CSD-grown REBCO nanocomposites with embedded $BaHfO_3$ (BHO) nanoparticles are shown (Page 196).

The rare-earth barium copper oxides are a family of similar structures (Fig. 5.1) but with largely different superconducting properties [YF89]:

- $REBa_2Cu_3O_{7-\delta}$ with $\delta \approx 0$ (here abbreviated as REBCO or RE123, Fig. 5.1a) is the most famous compound in this family due to its high $T_c \approx 93\,\mathrm{K}$. The unit cell is slightly orthorhombic since the $a \approx 0.382\,\mathrm{nm}$ and $b \approx 0.388\,\mathrm{nm}$ parameters are slightly different ($(0.382/0.388) - 1 = -1.5\,\%$ relative difference). The c-lattice parameter is about 1.17 nm (depending on the O content [BBR04]), which is $c \approx 3a \approx 3b$. Here, only rare-earth elements (REs) with an atomic number $\overline{Z}_{RE}$ greater than $Z_{Ba} = 56$ were investigated. Hence, the RE atomic columns appear brightest in HAADF-STEM Z-contrast imaging, followed by Ba and Cu (bottom row of images in Fig. 5.1a, Cu columns marked by red dots). O is not visible due to its low atomic number $Z_O = 8$.

- $REBa_2Cu_4O_8$ (RE124) [Mar+88; Kar+88] contains double CuO chains between two Ba planes instead of a single CuO chain for REBCO (Fig. 5.1b and c). RE124 has $T_c = 80\,\mathrm{K}$. The extra CuO chains are implemented with an in-plane offset of $b/2$ [Zan+88]. This results in a different projected structure for the [1 0 0] (Fig. 5.1b) and [0 1 0] (Fig. 5.1c) zone-axis orientations, where a glide symmetry (zigzag alignment of the Cu columns) or mirror symmetry (parallel alignment of the Cu columns) is observed for the double CuO chains. The symmetry is directly visible in HAADF-STEM Z-contrast imaging of the Cu columns of a double CuO chain (bottom row). Note that only one extra CuO chain (instead of two as necessary for the RE124 phase) is present in the shown HAADF-STEM images. The extra CuO chain is a stacking fault (SF) in RE123. Such a stacking fault is often denoted as a "RE124 intergrowth" in RE123 in the literature.
  The RE124 phase was first observed in TEM samples [Zan+88] and later synthesized as a

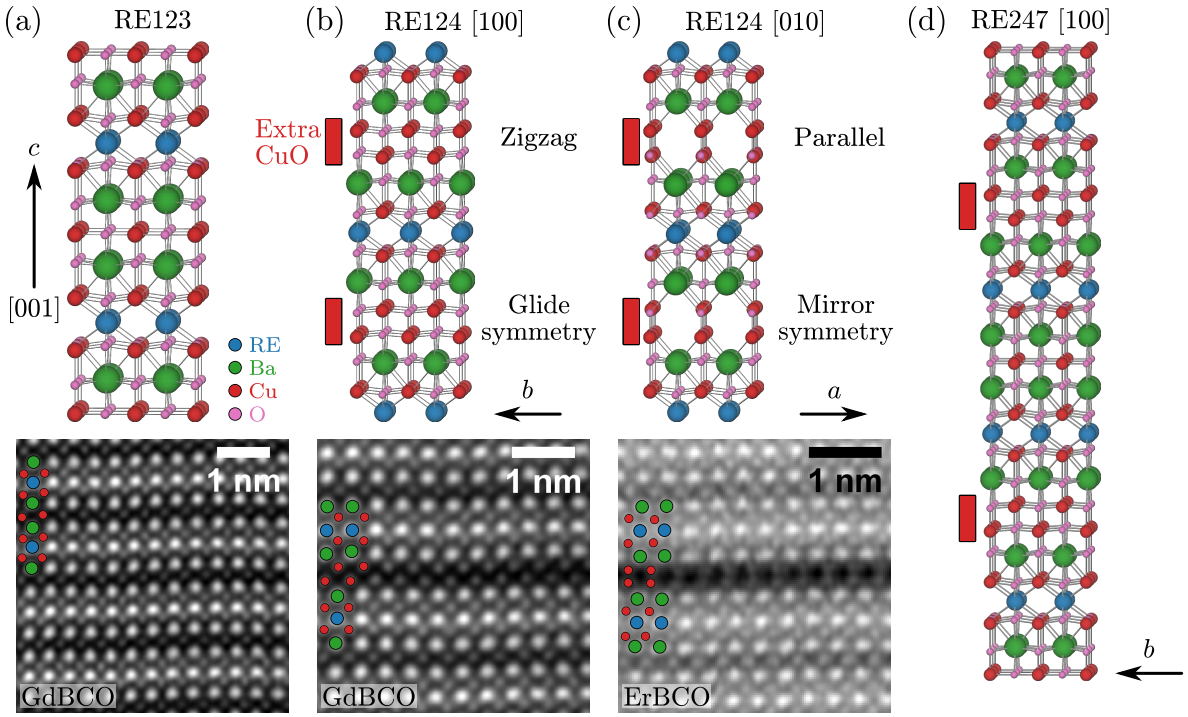

Figure 5.1: Overview of different rare-earth barium copper oxide unit-cell structures. The difference arises from the addition of extra CuO chains. The color coding for the different atoms is displayed in (a). (a) $(1 \times 2 \times 2)$ unit cells of $REBa_2Cu_3O_{7-\delta}$ (RE123). (b) and (c) Unit cells of $REBa_2Cu_4O_8$ (RE124), viewed along two orthogonal directions $[1\,0\,0]/a$ and $[0\,1\,0]/b$. The $b/2$-shift at an extra CuO chain appears with glide or mirror symmetry (zigzag or parallel alignment). The bottom row shows corresponding HAADF-STEM images of the extra CuO chains. Note the different alignment of the Cu atomic columns for (b) and (c). (d) Unit cell of $RE_2Ba_4Cu_7O_{15-\delta}$ (RE247), which is a mixture of RE123 and RE124.

bulk material. Similarly, stacking sequences of more than two CuO chains were observed by TEM [Zha+18], such as RE125 (three stacked CuO chains) [Guz+13; Guz13] or RE126 (four stacked CuO chains) [Señ+91].

- $RE_2Ba_4Cu_7O_{15-\delta}$ (RE247) [Bor+88] is a mixture of RE123 and RE124 (Fig. 5.1d) with a relatively large unit-cell size in c-direction ($c \approx 5\,\mathrm{nm}$) and $T_c = 40\,\mathrm{K}$.
- $REBa_2Cu_3O_6$ is a non-superconducting, O-deficient variant of RE123 with a tetragonal unit cell (similar to RE123 in Fig. 5.1a, but with a high O-vacancy concentration).

During REBCO fabrication, The O content is increased by an oxygenation step to form the superconducting $REBa_2Cu_3O_{7-\delta}$ phase with $\delta \approx 0$ from the non-superconducting $REBa_2Cu_3O_6$ phase. The exact O stoichiometry influences the superconducting properties in REBCO films [Con01], e.g. the highest $T_c = 93\,\mathrm{K}$ is achieved for $YBa_2Cu_3O_{6.92}$ for YBCO [Con01]. During oxygenation from tetragonal $REBa_2Cu_3O_6$ to orthorhombic $REBa_2Cu_3O_{7-\delta}$, a tetragonal-to-orthorhombic transition of the REBCO structure results in the formation of twin boundaries. The a- and b-orientations switch at a twin boundary (i.e. a 90° rotation around the c- (or $[0\,0\,1]$) direction) and the twin boundaries are oriented along the $\langle 1\,1\,0\rangle$-directions (Fig. 5.2). Due to the orthorhombic REBCO strucutre, the rotation is actually slightly off from 90° (about 1.5°, depending on the orthorhombicity) and given by [Guz13, p 93]

$$\theta_{TB} = 90° - 2\arctan\left(\frac{b}{a}\right) \quad . \tag{5.1}$$

Still, $\theta_{TB} \approx 90°$ is used in the following to describe this rotation for simplicity.

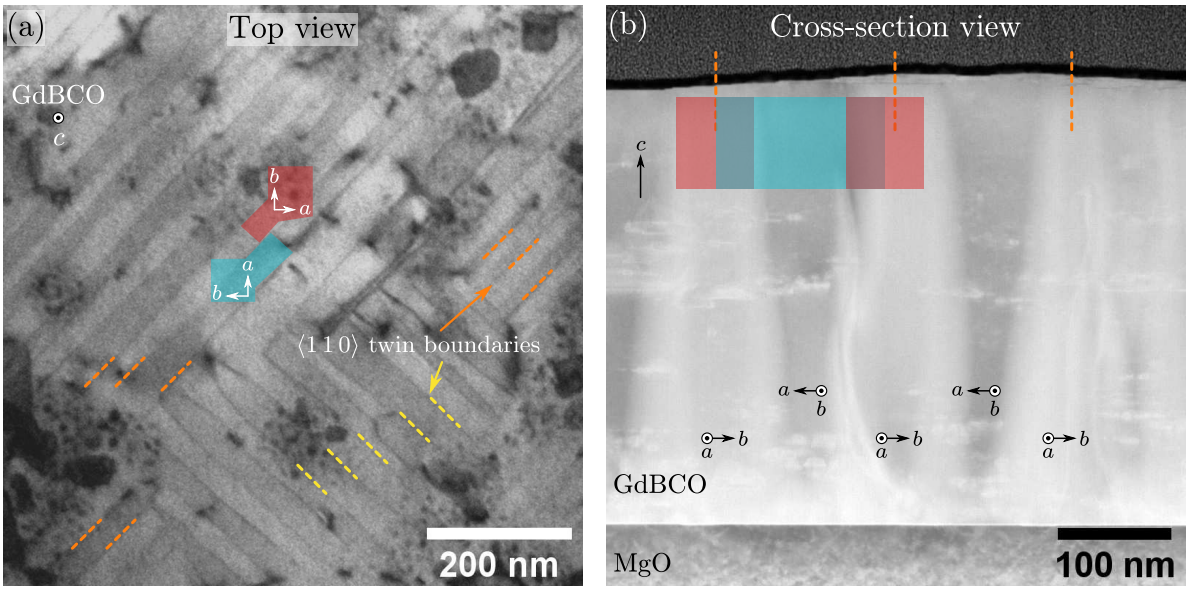

Figure 5.2: Twin boundaries in REBCO films. (a) Top-view BF-STEM-in-SEM image of a GdBCO film showing alternating *a*- and *b*-orientations (cyan and red regions). These 90° [0 0 1]-tilt twin boundaries run along the ⟨1 1 0⟩-directions and form two orthogonal domains of parallel aligned twin boundaries (orange/yellow dashed lines). (b) Side-view LAADF-STEM image along the *a*- or *b*-directions. The twin boundaries are not viewed edge-on in *a*- or *b*-directions, leading to an overlap region of *a*- and *b*-oriented grains in the projected structure.

The twin boundaries are viewed edge-on in the shown top-view BF-STEM-in-SEM image in Fig. 5.2a. The sample was FIB-prepared in a plan-view geometry as described in Fig. 3.6 on page 63. The alternating, 90°-flipped grain orientations appear with different image intensities in diffraction-contrast imaging. A large number of precipitates is also observed, which will be discussed in Section 5.3 on page 178. Twin-boundary domains with a lateral size of a few hundred nm form (marked by orange and yellow dashed lines), where the orientation of the twin boundaries are rotated by about 90° [Her+87]. Most of the TEM samples were prepared in cross-section geometry and imaged along the [1 0 0] and [0 1 0] zone-axes, where the twin boundaries are *not* viewed edge-on but at an angle of 45° (Fig. 5.2b). Due to this viewing angle, a complicated diffraction contrast appears as vertical structures in the shown LAADF-STEM image. The *a*- and *b*-oriented grains overlap at the twin boundary regions, as shown schematically by the overlapping cyan and red rectangles in Fig. 5.2b. The extent of the overlap region depends not only on the grain sizes but also on the TEM-sample thickness.
Three different substrates were used for REBCO films in this work, i.e. $SrTiO_3$(0 0 1), $LaAlO_3$(0 0 1), and MgO(0 0 1). The lattice mismatches are listed in Table 5.1 for an overview. Note that the lattice parameters of YBCO were used. However, the actual lattice parameters depend on the RE [Erb+20] and the O content [BBR04], so that the values only serve as a rough guideline.

Table 5.1: Lattice mismatch of YBCO on $SrTiO_3$, $LaAlO_3$, and MgO substrates. The YBCO phase with the lattice parameters $a = 3.821$ Å and $b = 3.884$ Å (ICSD number 56 507) was used to calculate the lattice mismatches ϵ_a and ϵ_b using Eq. (4.10) on page 144. A positive/negative value of ϵ means tensile/compressive strain.

Substrate	a_s (Å)	ϵ_a (%)	ϵ_b (%)
$SrTiO_3$(0 0 1)	3.905	2.2	0.5
$LaAlO_3$(0 0 1)	3.787	−0.9	−2.6
MgO(0 0 1)	4.214	9.3	7.3

5.1 Experimental Problems and Solutions

FIB preparation. All (but one) shown TEM samples were prepared by FIB milling. The preparation process had to be changed compared to the FIB preparation for IBS on CaF_2, since the substrates for the REBCO samples ($SrTiO_3$, $LaAlO_3$, and MgO) have a lower milling rate for Ga^+ ions compared to REBCO thin film. This resulted in preferential milling of the REBCO film, especially during final milling steps at FIB energies of 5 keV and 2 keV. The problem is exemplified for GdBCO on MgO (Fig. 5.3).

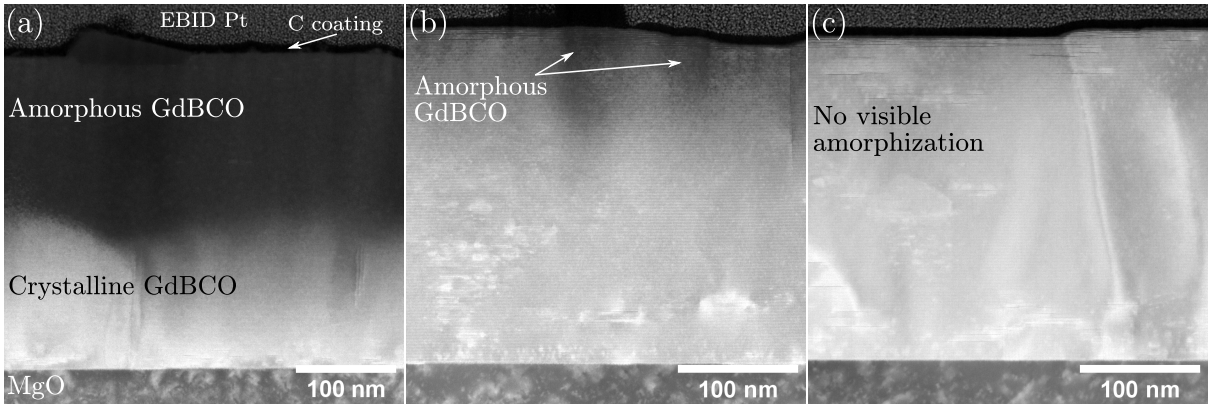

Figure 5.3: Optimization of sample preparation by FIB for GdBCO. LAADF-STEM images for (a) strongly damaged GdBCO, (b) slightly damaged GdBCO, (c) mostly undamaged GdBCO after FIB preparation. The dark areas in GdBCO are amorphous and stem from FIB-induced damage.

Preferential milling of the film can destroy it before the desired TEM sample thickness is reached (Fig. 5.3a). Amorphous REBCO shows a lower intensity in the displayed LAADF-STEM images than crystalline REBCO. Such unwanted FIB damage was observed more often if the conventional FIB preparation routine (Table 3.1 on page 61) or if a too low wedge angle (about 2° from perpendicular FIB incidence) for the slow FIB preparation approach (Table 3.2 on page 61) during the 30 keV steps was used. Better results and control over the milling process were obtained by increasing the wedge angle to 3° to 4° for the FIB cuts at 30 keV (Fig. 5.3b and c). This problem was most prominent for MgO, which showed the slowest milling rate. In addition, the MgO region always shows a cloud-like contrast, which may stem from redeposited material, as already discussed in Fig. 3.5 on page 62. However, the bright areas in the crystalline GdBCO regions stem from strain fields arising from actual grown-in defects and precipitates in the film.

Moiré Fringes in STEM EELS. Another experimental problem can arise from spatial undersampling in STEM-EELS (or STEM-EDXS) spectroscopy. This can lead to a periodic change in the measured chemical signals, which can be falsely interpreted as real changes in

sample composition. For example, Fig. 5.4 shows an overview HAADF-STEM image of a GdBCO cross-section sample (Fig. 5.4a) and the extracted chemical signals for different elements obtained by a STEM-EELS mapping of the marked ROI. Interestingly, a $\sim 25\,\mathrm{nm}$ periodicity of Gd, Ba, and (slightly) O signals is observed. This composition change was not observed by Z-contrast imaging at higher magnification and is therefore unexpected. In addition, the Gd and Ba signals are complementary. This aspect is visible by comparing the regions on the central left side in the images, where two arrows mark the same position in the Gd and Ba map.

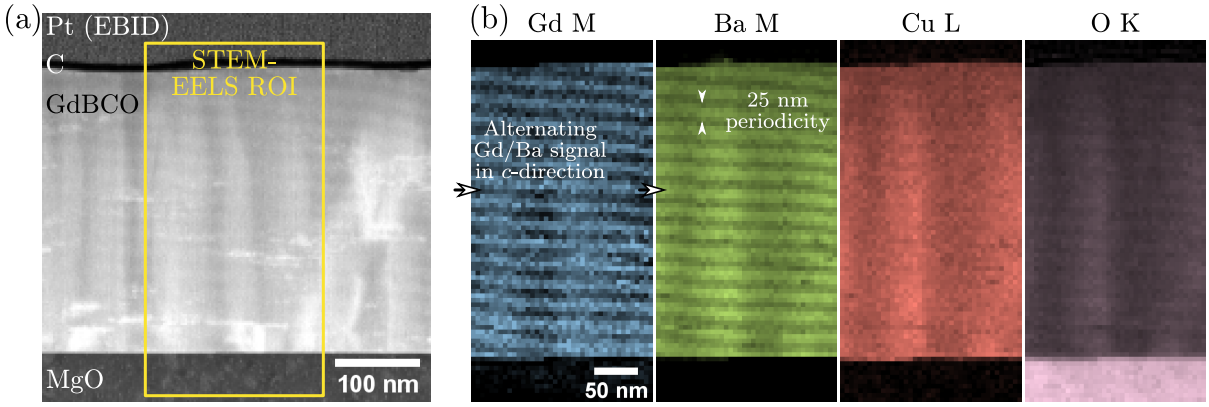

Figure 5.4: STEM-EELS Moiré artifact. (a) ADF-STEM overview image with the marked STEM-EELS acquisition region. The slightly visible bright-dark periodicity in c-direction is an artifact of undersampling (STEM-probe sampling of 2.58 nm). Vertical structures are twin boundaries. (b) Elemental distributions for Gd, Ba, Cu, and O extracted from the STEM-EELS dataset. Moiré fringes with a periodicity of about 25 nm appear in the elemental maps due to undersampling (STEM-probe sampling of 5.16 nm).

The observed changes in composition are an artifact. The observed fringes arise from an undersampling condition of the electron probe during STEM-EELS mapping, which was accidentally used here. A relatively large electron-probe sampling interval of 5.16 nm was used to map a large sample region (40×80 pixels spectrum image). Periodically, the Ba or Gd planes of GdBCO align with the sampling interval (Moiré effect), which causes an increase in the recorded EELS elemental signal. Therefore, the visible structure corresponds to a magnified view of the GdBCO unit-cell structure. This explains the alternating Gd and Ba signals. The effect only occurs if the electron probe can resolve the lattice-plane spacing, i.e. if the probe size (here probably around 0.4 nm) is smaller than (or in the order of) the Gd-Ba spacing (about 0.37 nm). Consequently, the even smaller Cu spacing is not resolved by the used electron-probe size, which results in a homogeneous Cu map. A slight defocusing of the electron probe to reduce the spatial resolution can be used to mitigate the appearance of unwanted Moiré effect in STEM-EELS (or EDXS) spectroscopy. Alternatively, the spatial-sampling frequency must be increased (i.e. smaller step size). It is noteworthy that this undersampling method can – if used intentionally – be useful to perform low-dose spectroscopy [KO14; Kon+17].

5.2 Nanoscale Planar Defects in REBCO

Previous work. This section presents experimental results for the formation of *nanoscale planar defects* in thin TEM samples. These nanoscale planar defects are (often) structurally similar to stacking faults but are smaller in the *ab*-direction. The nanoscale planar defects were observed in varying concentrations in all REBCO samples and similar defects were reported in the literature, especially for nanoparticle-containing REBCO films [Guz+13; Guz+17]. However,

it was also shown that a structural degradation of TEM samples can lead to similar nanoscale defects [Fen+90; Ram+90; Zan92]. The nanoscale defects often have sizes in the order of the coherence length ξ, making them relevant for possible flux pinning. Therefore, it is important to validate if the here-observed nanoscale planar defects are artifacts or actual defect structures in the as-deposited films. A discussion and comparison with literature follow after the experimental results. It will be shown that the nanoscale planar defects in this work are most likely an artifact of rapid TEM-sample degradation.

Samples. The following results show images from differently fabricated REBCO samples to investigate the defect formation in dependence of the fabrication parameters and the influence of embedded $BaHfO_3$ nanoparticles. The samples can be classified into three groups:

1. CSD-grown REBCO films (with a single RE or several REs) *with* BHO nanoparticles (cf. also Table 5.3 on page 197)
2. A CSD-grown ErBCO film *without* nanoparticles (cf. also Table 5.3 on page 197)
3. PLD-grown GdBCO films *without* nanoparticles

Besides the following analysis of nanoscale planar defects, the reults for Items 1 and 2 are presented in Section 5.4.1 on page 196 and Section 5.4.2 on page 216, whereas the results for Item 3 are discussed in Section 5.3 on page 178.

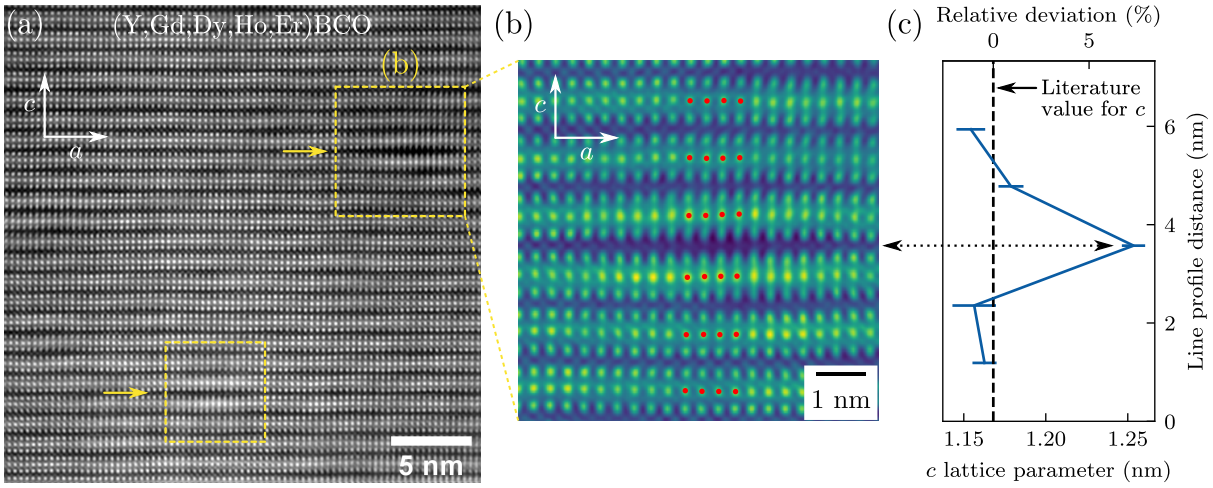

Figure 5.5: Nanoscale defects observed in (Y,Gd,Dy,Ho,Er)BCO. (a) ABS-filtered HAADF-STEM image showing a mostly defect-free REBCO structure. Nanoscale defects are marked with dashed yellow lines and arrows. (b) Magnified region from (a) and fitted RE atomic columns (marked by red circles). (c) Evaluated strain along c-direction from (b). The dashed line marks the literature value for $c \approx 1.17\,\text{nm}$. A 7 % strain is visible at the defect (dotted double-headed arrow). This figure is adapted from a publication [Grü+21d].

Experimental Results. Nanoscale defects in the REBCO films were observed at higher magnification (Fig. 5.5). The shown example is taken from one of the first investigated TEM samples of REBCO, here CSD-grown (Y,Gd,Dy,Ho,Er)BCO. Even though most of the REBCO structure is free from defects, a slight buckling of the REBCO structure is observed in a few regions in Fig. 5.5a (cf. arrows). A closer look (Fig. 5.5b) at the right-marked region in Fig. 5.5a reveals an enlargement of the REBCO c-spacing by about 7 % (Fig. 5.5c) for this particular defect (cf. dotted double-headed arrow). The strain was measured by fitting the RE atomic-column positions (red circles) and evaluating the plane spacing along the c-direction. A similar defect is observed in the bottom-left part in Fig. 5.5a. In addition to the strain, a slightly

increased HAADF-STEM intensity is observed for the adjacent RE planes. The latter also appear elongated or "stretched" in *c*-direction. These observations could lead to the conclusion that the RE concentration is locally enhanced which could cause local strain in the REBCO matrix. In addition, these defects have a size in the range of the coherence length ξ for REBCO and seem ideal regarding vortex pinning [Fen+90]. However, the same defects could not be observed in another TEM sample of the same REBCO film, which already hinted at a possible artifact. With the results shown in the following, we suspect that the nanoscale defects in Fig. 5.5 are the first signs of either FIB-preparation-induced damage or sample degradation in air.

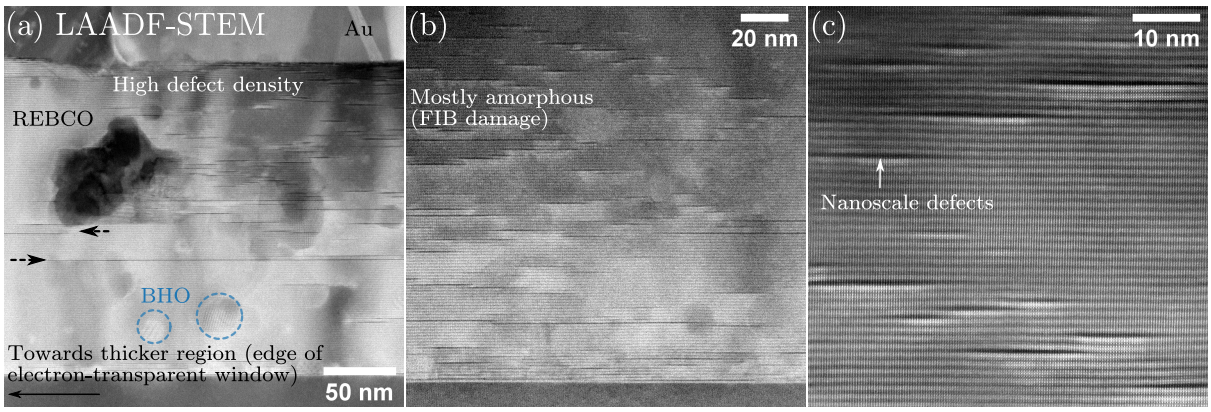

Figure 5.6: TEM-sample thickness and nanoscale-defect density in (Y,Gd,Dy,Ho,Er)BCO. (a) LAADF-STEM image near the edge of the electron-transparent region. The TEM-sample thickness increases towards the left and towards the bottom (substrate). Nanoscale planar defects are only observed in the thin, dark region in the upper right. Only a few extended stacking faults are visible in the left part of the image (dark horizontal lines marked with dashed arrows). (b-c) HAADF-STEM images of a strongly damaged region with a high defect density. Note the striped appearance of the REBCO structure parallel to the *c*-direction in (c) for a nearly amorphous REBCO structure.

Another TEM sample of the (Y,Gd,Dy,Ho,Er)BCO film was prepared by FIB to validate the presence of these defects (Fig. 5.6). However, the FIB preparation was worse. Most of the sample was damaged through FIB preparation (cf. darker areas in Fig. 5.6b and c). Smaller planar defects with a lateral extent of a few ten nm are observed in all STEM images in Fig. 5.6, especially in the thinnest (and most damaged) regions. These defects are more extended in lateral and in *c*-direction ($\approx 1.5\,\mathrm{nm}$) compared to Fig. 5.5b. We suspect that both types of defects are the same, but that they are more evolved/developed in Fig. 5.6 compared to Fig. 5.5.

Another observation from the LAADF-STEM image in Fig. 5.6a is that the density of the nanoscale defects also depends on the TEM-sample thickness. The image was taken at the edge of the electron-transparent sample region. No nanoscale defects are observed in the left, thicker part of the image where the sample is probably $> 100\,\mathrm{nm}$ thick. Still, extended planar defects appear as long, dark, horizontal lines (cf. dashed arrows Fig. 5.6a). In contrast, a high density of nanoscale defects is observed in the top-right, thinner region. The results so far could indicate that the nanoscale defects

1. could be actual defect structures in the as-deposited (Y,Gd,Dy,Ho,Er)BCO (or other REBCO) film and are only visible in thin TEM samples due to their small size,
2. could be an artifact of FIB preparation,
3. could be an artifact of TEM sample degradation,

4. or only be present in the (Y,Gd,Dy,Ho,Er)BCO film and not in other REBCO films.

To rule out Item 4, nanoscale defects were searched in other REBCO samples. Figure 5.7 shows HAADF-STEM cross-section images for CSD-grown (Y,Ho,Er)BCO (Fig. 5.7a) and ErBCO (Fig. 5.7d) films in the top row. The TEM samples were prepared by FIB milling. The bottom row of images presents color-coded insets at higher magnification.

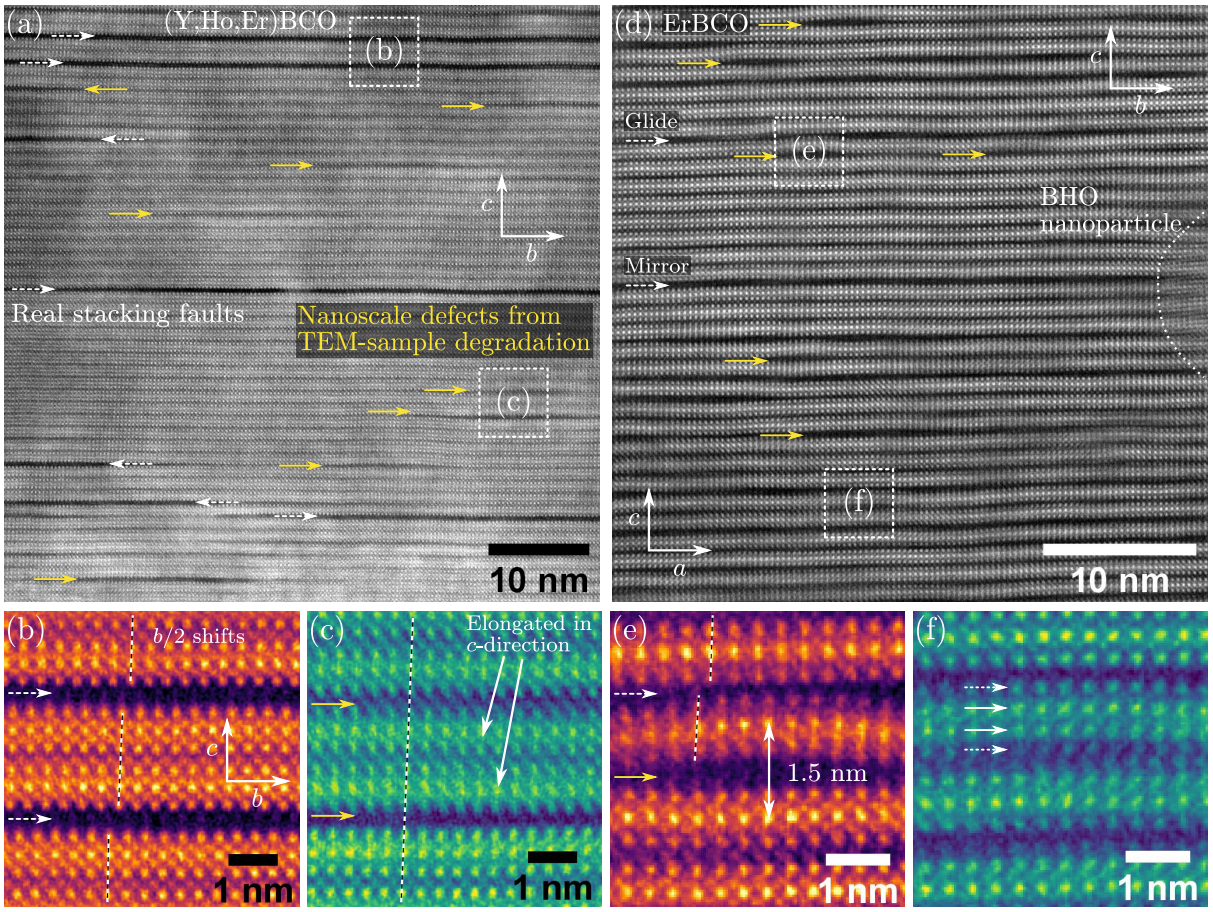

Figure 5.7: Planar nanoscale defects in CSD-grown (Y,Ho,Er)BCO and ErBCO. HAADF-STEM images of (a) (Y,Ho,Er)BCO and (d) ErBCO films. The color-coded images (b-f) are ABS-filtered. Solid yellow arrows indicate artificial nanoscale defects, whereas dashed white arrows mark real stacking faults. See the text for a full description.

Focusing first on Fig. 5.7a, one can observe horizontal defects with a lateral extent of about 10 nm to 30 nm (solid yellow arrows) and extended planar defects across the whole image width (dashed white arrows). The latter are interpreted as "real" SFs already present in the as-deposited REBCO film. These are the same defects as the long-extended planar defects in Fig. 5.6a (cf. dashed arrows). In Fig. 5.7a, all these real SFs show glide symmetries, which indicates that the REBCO structure is here viewed along the [1 0 0] zone axis. The glide symmetry is visible in the magnified image (dashed vertical lines in *c*-direction in Fig. 5.7b). At the less-extended nanoscale defects (Fig. 5.7c) an elongation in the *c*-direction similar to Fig. 5.5 is observed in combination with a mirror symmetry (cf. connected dashed line Fig. 5.7c). The mirror symmetry *could* be interpreted as a change in viewing direction compared to Fig. 5.7b, i.e. the REBCO structure viewed along the [0 1 0] zone axis. However, here this is interpreted as an artificial nanoscale defect.

A high concentration of nanoscale defects is also observed for ErBCO (Fig. 5.7d, solid yellow arrows). Here, the defects are smaller (about 5 nm to 30 nm lateral extension), but more extended in *c*-direction. The *c*-lattice parameter is enlarged from $c \approx 1.17$ nm to ≈ 1.5 nm for some defects (Fig. 5.7e), similar to the defects in Fig. 5.6c. A similar defect type with a 1.5 nm spacing along the *c*-direction was reported by Zandbergen [Zan92]. In the example in Fig. 5.7e, the upper REBCO unit cell is directly connected to a real, extended SF with glide symmetry, indicating that the *b*-direction is parallel to the horizontal direction in the top part of the image. Conversely, the SF in the center of Fig. 5.7d shows a mirror symmetry. The bottom part of the HAADF-STEM image in Fig. 5.7d may therefore show the REBCO structure along the [0 1 0] zone axis (and the *a*-direction is parallel to the horizontal). On the right, the faint lattice fringes of a randomly oriented BHO nanoparticle are visible in Fig. 5.7d. The inset in Fig. 5.7f shows a slightly elongated REBCO structure along the *c*-direction. In this case, a stack of four brighter atomic planes is visible, whereby each plane is marked by an arrow. This is different compared to the expected REBCO stacking in the order Cu^{29}-Ba^{56}-$RE^{60.8}$-Ba^{56}-Cu^{29} (the superscript denotes *Z*), i.e. only three heavy planes from the Ba-RE-Ba sequence. The slightly less intense outer planes in Fig. 5.7f (marked with dotted lines) may result from the projected structure of a mixed Ba/RE column, which will be discussed later in context with Fig. 5.16 on page 174.

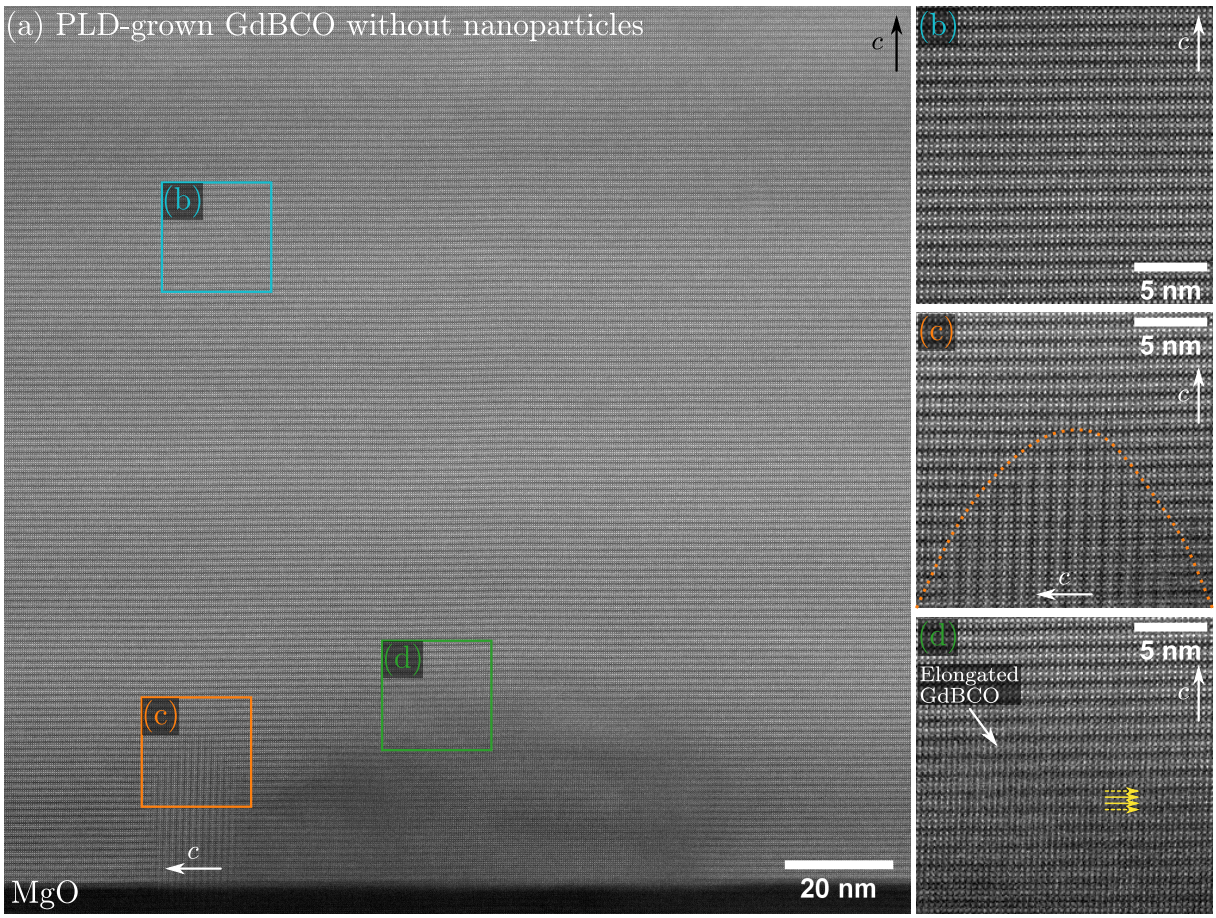

Figure 5.8: Large-area HAADF-STEM image of PLD-grown GdBCO on MgO. (a) ABS-filtered overview HAADF-STEM image showing a mostly homogeneous GdBCO-film structure without (nanoscale) planar defects over the entire sample region. (b-d) show magnified insets of (a). (b) Randomly-chosen film region showing undisturbed GdBCO without any nanoscale defects. (c) Misoriented GdBCO grain growing at the film/substrate interface. (d) Slightly disturbed region showing a *c*-elongated GdBCO structure and a similar change in *Z*-contrast stacking as for CSD-grown REBCO films.

Since these nanoscale defects were observed in several CSD-grown REBCO films, one can rule out Item 4 on page 162. In contrast, fewer nanoscale defects were found in the five investigated PLD-grown GdBCO films grown on MgO. Figure 5.8a exemplifies this with a representative, large-area high-resolution HAADF-STEM image of one of the GdBCO films. A high-quality film is observed (cf. Fig. 5.8b) with a few misoriented grains (denoted as "*ab*-grains" further below) close to the substrate interface (cf. *ab*-oriented grain in Fig. 5.8c). No planar defects (nanoscale or extended stacking faults) are observed in this HAADF-STEM image. However, a few sample regions show similar structural features as the CSD-grown samples (Fig. 5.8d), i.e. an elongated appearance of the GdBCO structure in the *c*-direction and the apparent change in stacking sequence based on HAADF-STEM *Z*-contrast similar to Fig. 5.7f. Another example for an *c*-elongated GdBCO structure is shown in Fig. 5.9b.

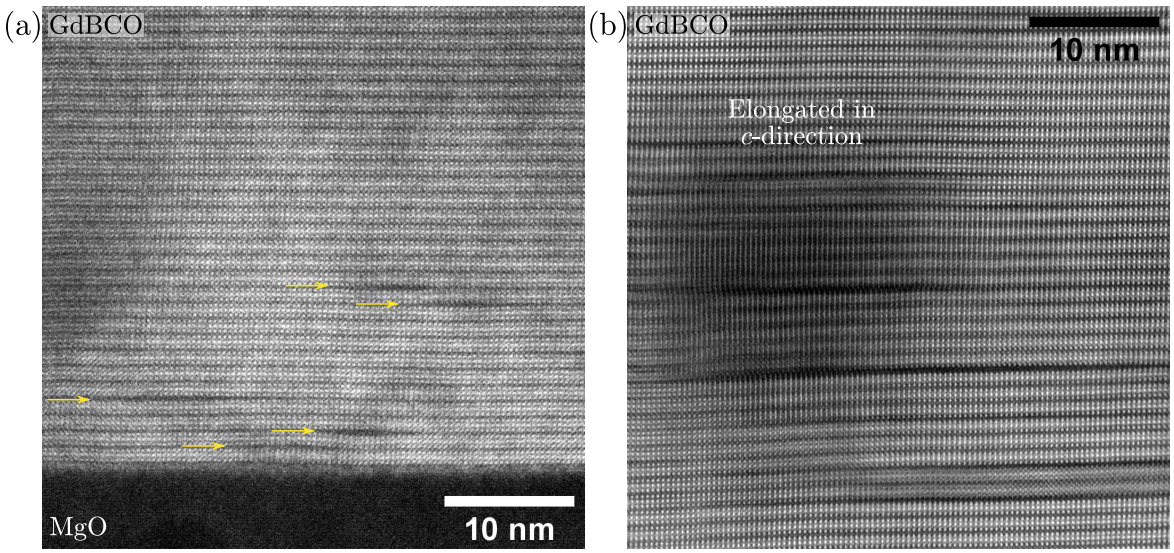

Figure 5.9: Rare nanoscale defects in PLD-grown GdBCO on MgO. (a) Gaussian-filtered HAADF-STEM cross-section image showing the preferential formation of nanoscale planar defects (marked with solid arrows) close to the film-substrate interface. (b) ABS-filtered HAADF-STEM image of a film region with a larger disturbed region with a *c*-elongated GdBCO structure.

Nanoscale planar defects were only observed in a few TEM samples of PLD-grown GdBCO. The defects were often close to the film-substrate interface (Fig. 5.9a). This shows that the nanoscale defects are not only present in CSD-grown REBCO films. However, the CSD-grown REBCO films with BHO nanoparticles have a higher nanoscale-defect density than PLD-grown GdBCO films without nanoparticles. Both sample types – PLD- or CSD-grown – were prepared for TEM by FIB milling with a final polish with a Ga^+ energy of 2 keV. The reduced number of nanoscale defects in GdBCO indicates that FIB preparation may not be (solely) responsible for nanoscale-defect formation.

As a next step, an attempt was made to test hypothesis of Item 1 by preparing a sample with a thickness < 50 nm without using Ga^+-FIB milling (to also rule out Item 2). The latter aspect is essential since thin TEM samples are especially prone to FIB-induced sample damage, even at a Ga^+ energies of only 2 keV as applied for all samples shown so far. The preparation process of such a TEM sample of (Y,Gd,Dy,Ho,Er)BCO is presented in Fig. 5.10. The procedure is similar to the standard *in-situ* lift-out process for cross-section sample preparation by FIB. First, a lamella is milled from the bulk material (Fig. 5.10a) and mounted on the side of a grid post ("flag" position) (Fig. 5.10b). The grid post is prepared by removing part of the Cu near the

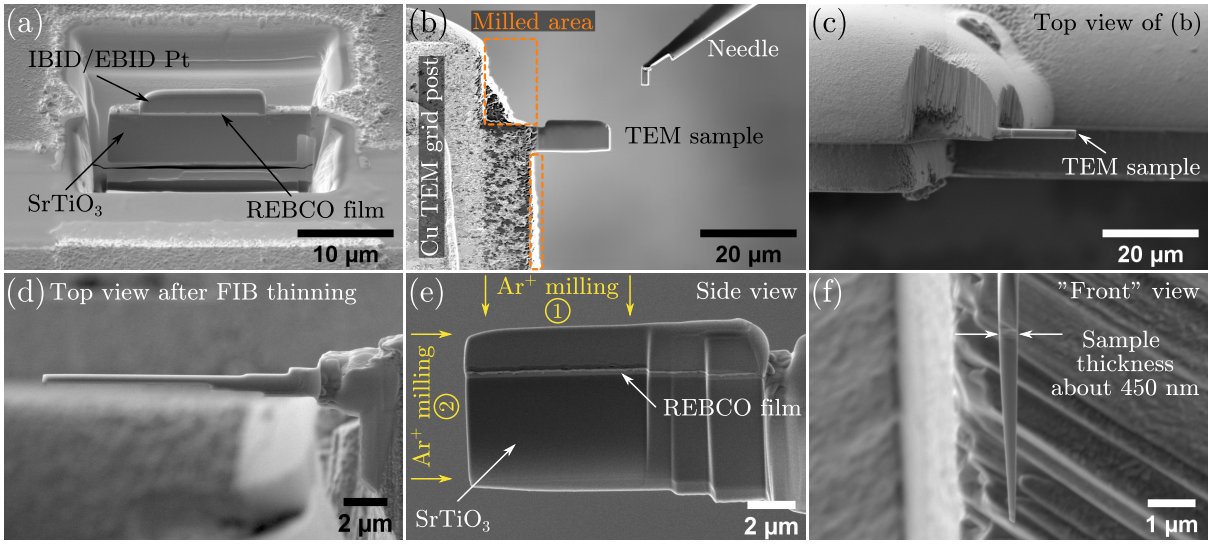

Figure 5.10: Steps of a combined FIB-PIPS TEM-sample preparation. (a) FIB lamella, which is still attached to the bulk sample. (b) Lamella fixed to a Cu TEM grid. Part of the grid was removed by FIB to reduce the chance of redeposition from the TEM grid (dashed orange regions). (c) Top view of the attached lamella. (d) Top view, (e) side view, and (d) front view after the FIB thinning steps. (d) The sample thickness in the film region is $\approx 450\,\mathrm{nm}$ after FIB preparation. (e) The side view schematically shows the Ar^+-milling directions during thinning in the PIPS-II. The sample was investigated by TEM after milling from directions ① and ②. (f) Front-view SE-SEM image showing the wedge-shaped TEM sample after FIB milling and prior to Ar^+ milling. The REBCO films is located at the region marked by the two arrows.

lamella prior to mounting it (the dashed orange rectangles roughly mark the milling areas). This is done to reduce possible redeposition from the grid during Ar^+ milling in a Gatan PIPS-II. Figure 5.10c shows the mounted lamella in the top view. Next, the sample is pre-thinned to about 500 nm thickness at the film region (Fig. 5.10d-f). The milling is performed at a Ga^+-ion energy of 30 keV. A stepwise reduction of the thickness is milled to enhance the stability of the TEM sample [SSR12] (cf. top view in Fig. 5.10d). A wedge-shaped pre-thinned lamella is prepared, as shown from the front in Fig. 5.10f. The film is located near the top (marked by arrows in Fig. 5.10f), below the protective layer of IBID/EBID Pt. Figure 5.10e displays a side-view SE-SEM image ($E_0 = 5\,\mathrm{keV}$) of the lamella after FIB preparation and prior to Ar^+ milling in a Gatan PIPS-II. The thinner bottom part of the STO substrate is already thin enough for 5 keV electrons to penetrate the sample, which results in a bright appearance in the SE-SEM image. The Ar^+-milling directions for the first and second set of TEM investigations are marked with ① and ②. These will be discussed further below. The parameters for Ar^+ milling were as follows: Ar^+-energies between 1 keV to 0.2 keV, Ar^+-gun-tilt angles between 8° to 10°, no stage rotation, and varying milling durations (typically 30 s to 60 s for each step). The integrity of the Pt protection layer was checked after each milling step in an optical microscope (Leica DMRX) to ensure that the REBCO film is not milled away.

Figure 5.11 presents STEM images after Ar^+ milling from the top direction, i.e. from the Pt side as shown as ① in Fig. 5.10. The low-magnification LAADF-STEM image in Fig. 5.10a shows that most of the protective Pt/C layer was milled away during Ar^+ milling, while the REBCO film beneath is mostly preserved. However, the top-left sample region is already milled away to a small degree (cf. Fig. 5.10a and b). Undesired intensity modulations become visible at medium magnification (Fig. 5.10b). These are probably caused by different milling rates for the protective layers, the REBCO film, and the STO substrate, typically observed for FIB-prepared

samples (so-called "curtaining" artifact[1] [Sch+03]). These artifacts are possibly removed by optimizing the combined FIB-PIPS sample preparation process, which was not done here.

Figure 5.11c shows an (contrast-inverted) HAADF-STEM image of a thicker TEM sample region, where the curtaining artifacts are visible as vertical stripes in the image. Long-extended stacking faults are observed as bright horizontal lines (marked by dashed arrows). No other nanoscale planar defects are observed, in contrast to the purely FIB-prepared TEM samples Fig. 5.5 on page 160 and Fig. 5.6 on page 161. However, these nm-sized nanoscale defects could also be "buried" in a comparably thick TEM sample. Therefore, there is a possibility that such defects are not visible in (S)TEM images of thicker regions such as in Fig. 5.11c. Indeed, a HAADF-STEM image of a sample region with smaller TEM-sample thickness contains a few of these nanoscale defects (marked with solid black arrows in Fig. 5.11d). This HAADF-STEM image was taken near the sample edge (marked by a blue square in Fig. 5.11b), where presumably the TEM sample is thinnest. Extended stacking faults are also visible (a few examples are marked with dashed white arrows). Since these nanoscale defects are observed in Ar^+-milled samples, one can rule out Item 2 on page 161. This means that these nanoscale planar defects are not (purely) created during FIB milling with Ga^+ ions (which are typically more damaging to TEM samples compared to lighter Ar^+ ions).

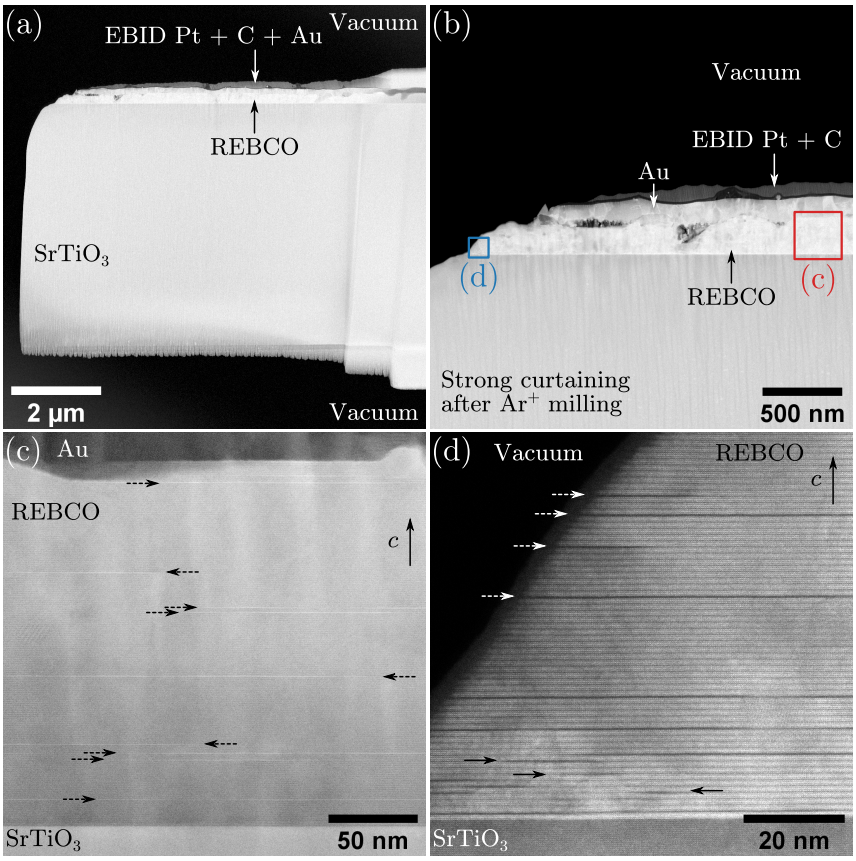

Figure 5.11: STEM images of a FIB-PIPS prepared REBCO sample after top-down Ar^+ milling. LAADF-STEM overview cross-section images at (a) low and (b) medium magnification showing a nearly complete removal of the protection layers (Pt, C, and Au) but a mostly preserved REBCO film region. Curtaining after Ar^+-ion milling is observed in (b) and (c) as vertical stripes. (c) Contrast-inverted HAADF-STEM of a ticker region only showing extended stacking faults (dashed arrows). (d) A thinner sample region additionally contains a few nanoscale planar defects (solid arrows).

The TEM sample thickness for the thin TEM-sample region (about 20 nm away from the vacuum edge in Fig. 5.11d) is about 70 nm as approximated by the EELS log-ratio method [Ege11, p 294] (cf. spectrum "Low-Loss 1" in Fig. 5.12c). The high-intensity zero-loss peak at 0 eV ("Zero-Loss 1", dashed line) was modeled by the "reflected tail" method in *DigitalMicrograph*.

[1] It is noted that more subtle intensity variations, such as curtaining, are only visible in the digital version of this thesis.

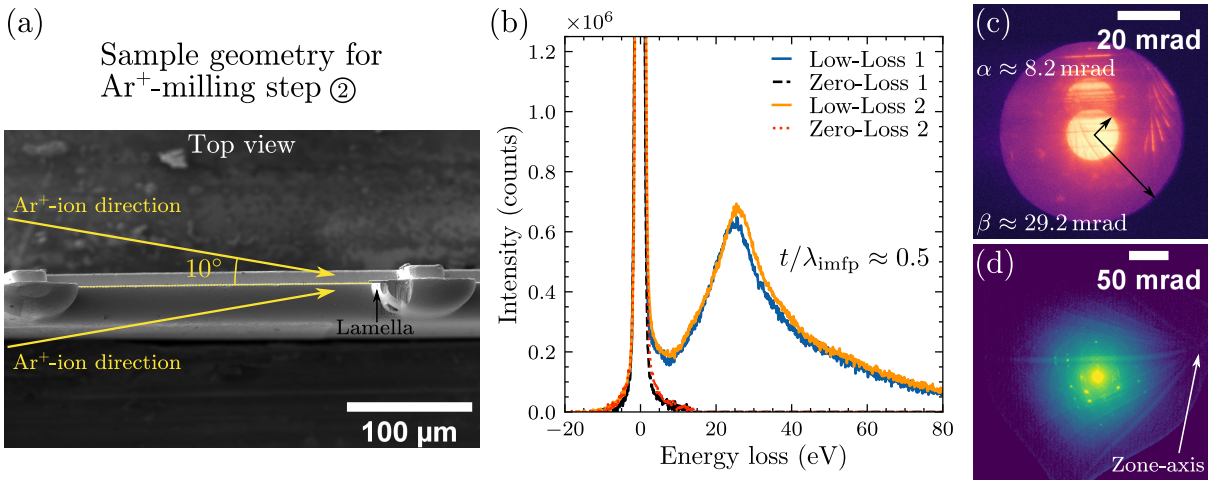

Figure 5.12: Experimental setups for Ar^+ milling and sample-thickness measurement with EELS. (a) Ar^+-milling geometry for an Ar^+-ion incidence parallel to the film. A high gun-tilt angle of 10° avoids a shadowing of the Ar^+ ions by the left grid post. (b) Sample-thickness measurements by the EELS log-ratio method after Ar^+ milling ① and ②. No noticeable change in sample thickness is observed. (c) Shadow image of the GIF entrance aperture and (d) diffraction-space image showing experimental parameters for the EELS experiments.

Bulk-plasmon excitations mainly cause the second pronounced peak at ≈ 25 eV in the low-loss spectrum [HRT93; GS98]. Note, that the "Intensity" axis was adjusted for better visibility of the small plasmon peak compared to the (here cropped) zero-loss peak at 0 eV. The relative sample thickness t/λ_{imfp} in multiples of the inelastic mean free path λ_{imfp} can be calculated from the zero-loss-peak intensity I_{ZLP} and the total (low-loss) spectrum intensity I_{total} using $t/\lambda_{\text{imfp}} = \ln(I_{\text{total}}/I_{\text{ZLP}})$ [Ege11, p 294]. An inelastic mean free path for (Y,Gd,Dy,Ho,Er)BCO $\lambda_{\text{imfp}} \approx 141$ nm is estimated with the formula given by Iakoubovskii et al. [Iak+08] ($\alpha = 8.2$ mrad, $\beta = 29.2$ mrad, and a calculated REBCO density $\rho = 6.9\,\text{g/cm}^3$). This method is recommended for large collection angles $\beta > 20$ mrad [ZEM12], which was set up using the EFSTEM mode (Fig. 5.12c). The sample was tilted away from zone-axis orientation to reduce the influence of diffraction effects (Fig. 5.12d).

The measured sample thickness of 70 nm close to the sample edge (Fig. 5.11d) suggests a strong thickness gradient of the TEM sample. For ≈ 70 nm TEM sample thickness, only a few nanoscale defects are observed (Fig. 5.11d). Purely FIB-prepared TEM samples are also in the range of 40 nm to 100 nm. This shows that the nanoscale defects are observable for typical TEM-sample thicknesses and not only for samples, which were prepared to a thickness below about 40 nm. In thicker TEM samples, only extended stacking faults and no nanoscale defects are observed (Fig. 5.11c).

A second Ar^+ milling step was applied to reduce the TEM sample thickness below 40 nm. The aim was to study the density of the nanoscale defects for decreasing TEM sample thickness. It is important to note that the TEM sample was stored for 14 days in a pumped-down desiccator before the second round of Ar^+ milling and the subsequent TEM investigation. Since the protection layers were already too thin for another top-down Ar^+ milling, the Ar^+-ion incidence was rotated by 90°. This is, with the Ar^+-ion incidence parallel to the REBCO film, schematically drawn as ② in Fig. 5.10e on Page 165. A 10° gun tilt of the Ar^+ sources in the PIPS-II was used to ensure that the Ar^+ ions are not blocked by another grid post on the used TEM grid (cf. Fig. 5.12a). The sample was milled for an additional 90 s at an Ar^+ energy of 300 eV.

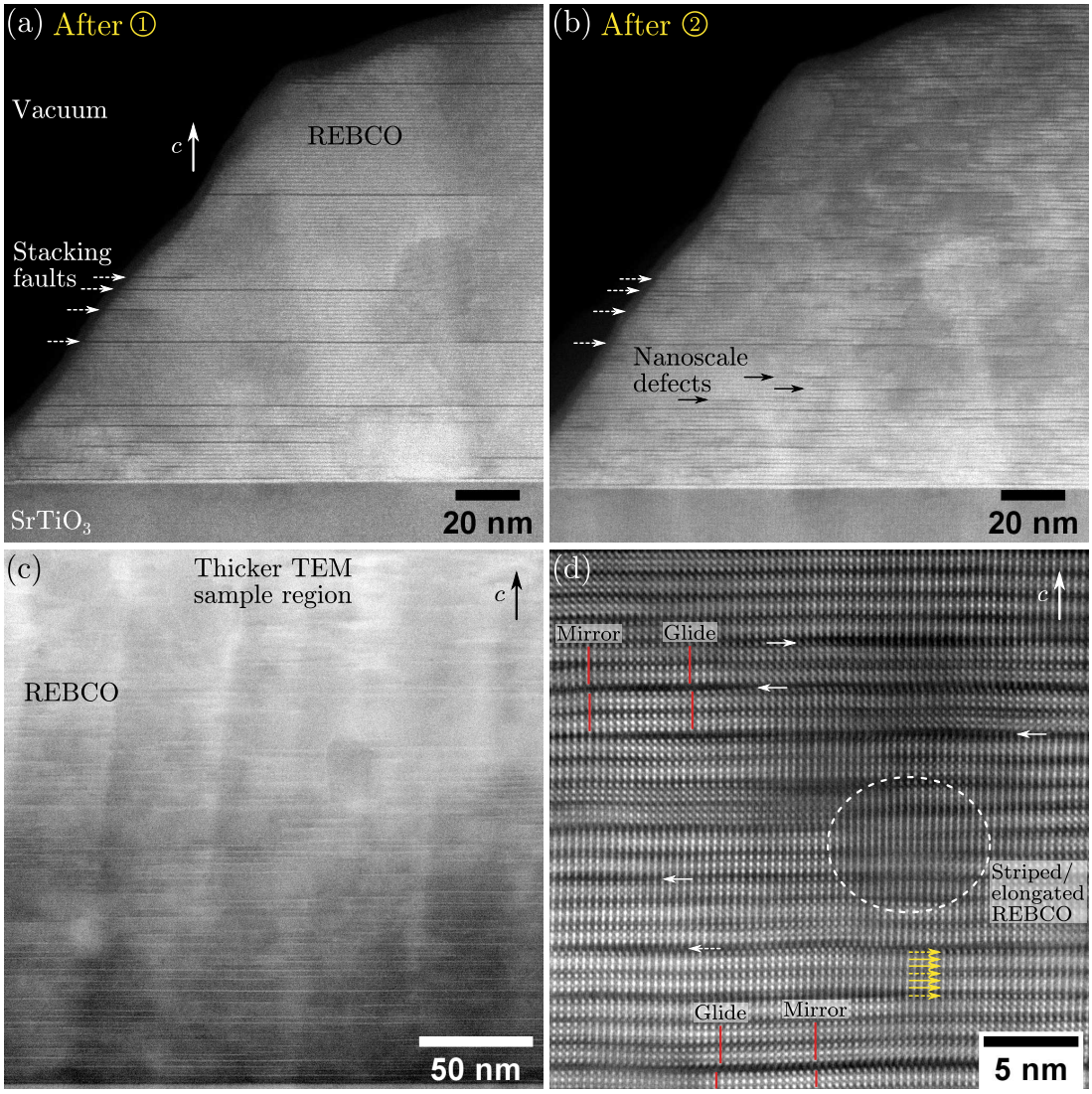

Figure 5.13: Comparison of REBCO microstructure between two different TEM measurement sessions. HAADF-STEM cross-section images close the TEM-sample edge after (a) top-down Ar^+ milling (①) and (b) 14 days of storage of the TEM sample in a desiccator and Ar^+ milling from the left side (②). (c) Thicker and (d) thinner sample regions from the sample shown in (b). The formation of nanoscale planar defects is observed in (b-d).

Afterward, the sample was again investigated by STEM (Fig. 5.13) and EELS (Fig. 5.12b) to measure the sample thickness after Ar^+-milling step ②. The sample thickness was nearly unchanged, as visible by comparing the spectra (Fig. 5.12b) "Low-Loss 2" and "Low-Loss 1". Probably only a few nm of surface contamination and sample material was removed during the second round of Ar^+ milling. The removal of such amorphous surface layers leads to higher-quality HAADF-STEM images.

Figure 5.13a and b compare the same sample region after the first (①) and second (②) round of Ar^+ milling. A completely different microstructure is observed in both cases, where a high density of nanoscale defects (few examples marked by solid black arrows in Fig. 5.13b) is observed after step ②. Clearly, the interpretation of the defect landscape and the associated pinning properties would be entirely different for the two shown HAADF-STEM images in Fig. 5.13a and b. A higher nanoscale-defect density (bright horizontal lines) is also observed in thicker sample regions (Fig. 5.13c) compared to Fig. 5.11c. The HAADF-STEM images for the thicker

sample regions were not taken at the same sample region. Since the sample thickness between the two TEM sessions (i.e. after the Ar^+-milling steps ① and ②) is nearly the same and low-energy Ar^+ milling is assumed not to introduce structural changes in REBCO, one may assume at this point that most of the observed structural changes between Fig. 5.13a and b are caused by the 14 days of storage of the TEM sample in the desiccator. This would correspond to sample degradation in air or vacuum being (primarily) responsible for the formation of nanoscale planar defects in TEM samples of REBCO (Item 3 on page 161).

High-resolution HAADF-STEM imaging (Fig. 5.13d) reveals a strongly disrupted REBCO structure mainly along the *c*-direction. A buckling of the REBCO structure is observed with the same structural features already observed for the FIB-prepared TEM samples, namely (i) an elongated REBCO structure along the *c*-direction (cf. dashed region in Fig. 5.13d with Fig. 5.7c on Page 162) and (ii) a change in REBCO-plane stacking from the expected "3×-bright structure" from the Ba^{56}-$RE^{60.8}$-Ba^{56} sequence for REBCO[1 0 0] to a "4×-bright structure" (cf. yellow solid/dashed arrows in Fig. 5.13d with Fig. 5.7f on Page 162). Solid arrows in Fig. 5.13d mark nanoscale defects, whereas the dashed arrow marks an extended stacking fault. The *a*-/*b*-orientation switches along the lateral direction (i.e. a 90° [0 0 1] rotation) in two regions in the image with nanoscale defects (red vertical lines), leading to a switching from a mirror symmetry to a glide symmetry (or *vice versa*) of the adjacent REBCO unit cells. This configuration is associated with a Frank type (sessile) partial dislocation [VKA91; ZTW13; Guz+17], that is characterized by a $\frac{1}{2}[1\,1\,0]$ Burgers vector with a (0 0 1) glide plane.

The four extended stacking faults marked in Fig. 5.13a and b with dashed white arrows are compared in Fig. 5.14. The same planar defects in Fig. 5.14a and b after the Ar^+-milling steps ① and ② can be related by their position within the TEM sample and the number of REBCO unit-cells between the stacking faults (e.g. 3 unit cells along the *c*-direction between the stacking faults marked with 1 and 2). The structure is more clearly resolved in Fig. 5.14b, probably due to a removal of amorphous surface layers after Ar^+ milling step ②, thereby enhancing STEM resolution. Higher-magnification images of Fig. 5.14a and b are presented in the color-coded images in Fig. 5.14c and d, respectively. The image in Fig. 5.14c was ABS-filtered for better visibility of the atomic structure. The REBCO structure surrounding planar defect 1 and 2 shows a transformation from glide symmetry (Fig. 5.14c, zigzag-configuration of the double CuO planes) to mirror symmetry (Fig. 5.14d, stacked-configuration of the double CuO planes). This observation indicates a switch of the *a*-/*b*-orientations of the orthorhombic REBCO structure (orientations are marked by horizontal arrows in the images) between the two TEM sessions. The vertically aligned white lines indicate the presence (or absence) of a lateral shift of the REBCO unit cells adjacent to the stacking faults. Planar defect 3 shows glide symmetry in both images. Elongated REBCO unit-cells along the *c*-direction are visible in Fig. 5.14d, as already shown in Fig. 5.13d. Cu vacancies at a stacking fault are visible as a reduction in *Z*-contrast at the double CuO chain when viewed along the [0 1 0] zone axis (vertical arrows in Fig. 5.14d).

So far, the shown CSD-grown films all contain BHO nanoparticles. The growth kinetics of the PLD-grown GdBCO samples are likely to be different compared to CSD and, therefore, hardly comparable. Therefore, a pristine CSD-grown ErBCO film without BHO nanoparticles was investigated to study the influence of BHO nanoparticles on the density of nanoscale planar defect in TEM samples of CSD-grown REBCO films (Fig. 5.15). A cross-section HAADF-STEM image of the ErBCO film reveals a high density of extended planar defects, identified as stacking faults with an extra CuO plane. A few are marked with dashed arrows in the central region in Fig. 5.15a. These typically have lateral extends $> 50\,\text{nm}$, in contrast to the nanoscale planar

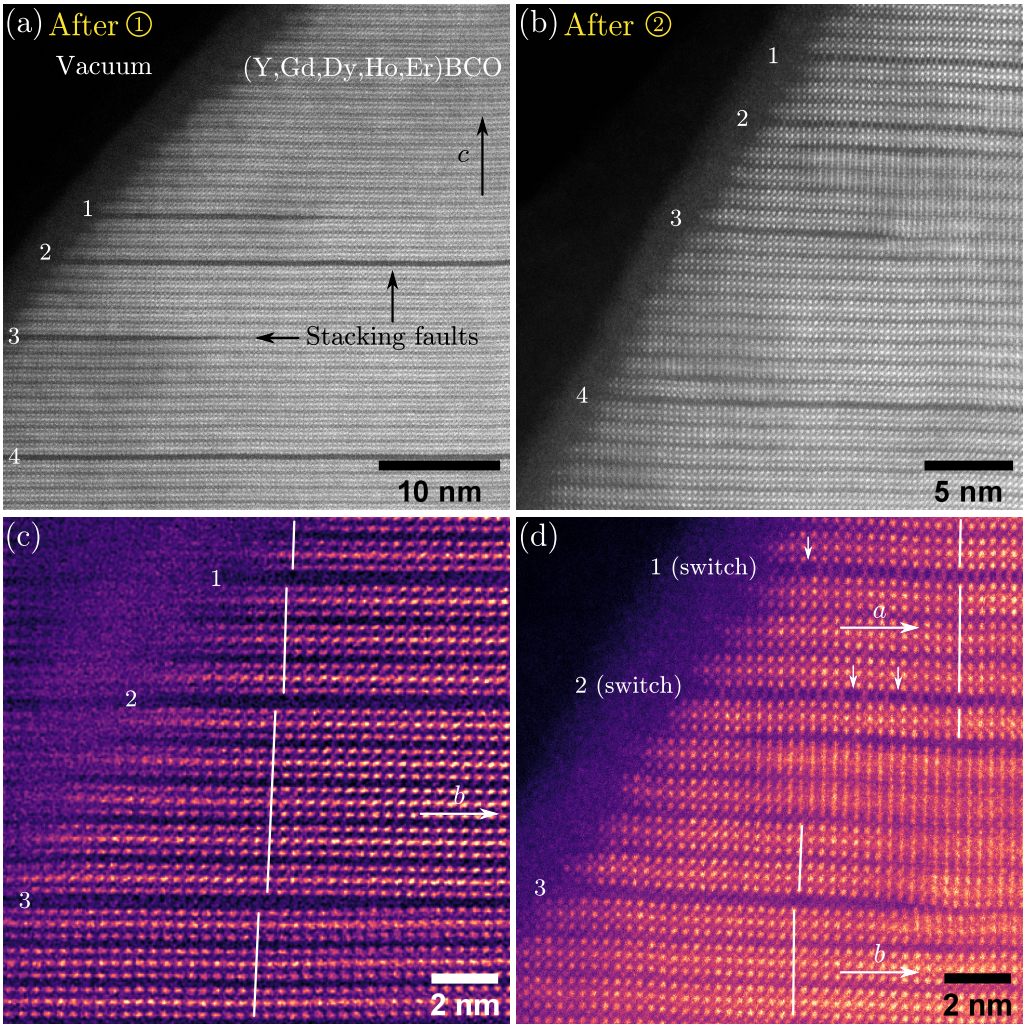

Figure 5.14: Direct observation of switching between *a*- and *b*-orientations of REBCO between different TEM measurement sessions. HAADF-STEM images of the REBCO structure near the sample edge showing 4 planar defects (denoted as 1 to 4) after (a) top-down Ar^+ milling (①) and (b) 14 days of storage of the TEM sample in a desiccator and Ar^+ milling from the left side (②). Corresponding magnified images of (a) and (b) are presented in (c) and (d). Image (c) was ABS-filtered. A structural transition from an *a*- to *b*-aligned REBCO is observed for the upper sample region containing planar defects 1 and 2. This is visible from a switch of a zigzag configuration (glide symmetry) of the CuO-plane alignment in (c) to a stacked CuO-plane alignment (mirror symmetry) in (d). The REBCO orientation is determined from the known $b/2$-shift at planar defects. Cu vacancies can be observed in (d) by a local reduction in HAADF-STEM Z-contrast for some CuO columns (vertical arrows), when REBCO is viewed along the [0 1 0] zone axis.

defects. Close to the film's surface, the density of stacking faults is high so that every unit cell of REBCO contains an extra CuO plane (cf. the top-right region in Fig. 5.15a). This corresponds to the Er124 phase. A few nanoscale planar defects are visible close to the substrate-film interface (marked with solid arrows in Fig. 5.15a). This is more clearly visible at higher magnification (Fig. 5.15b). The preferred formation of nanoscale defects in close to the interface was similarly observed for the CSD-grown (Y,Gd,Dy,Ho,Er)BCO-BHO sample (Fig. 5.11d on Page 166).

Discussion. Now follows a discussion of the experimental findings for the shown nanoscale planar defects and a comparison with literature for TEM samples of REBCO. REBCO is generally susceptible to structural degradation under ambient conditions, also denoted as "aging" or "corrosion". A typical phenomenon is the loss of O due to continuous out-diffusion from

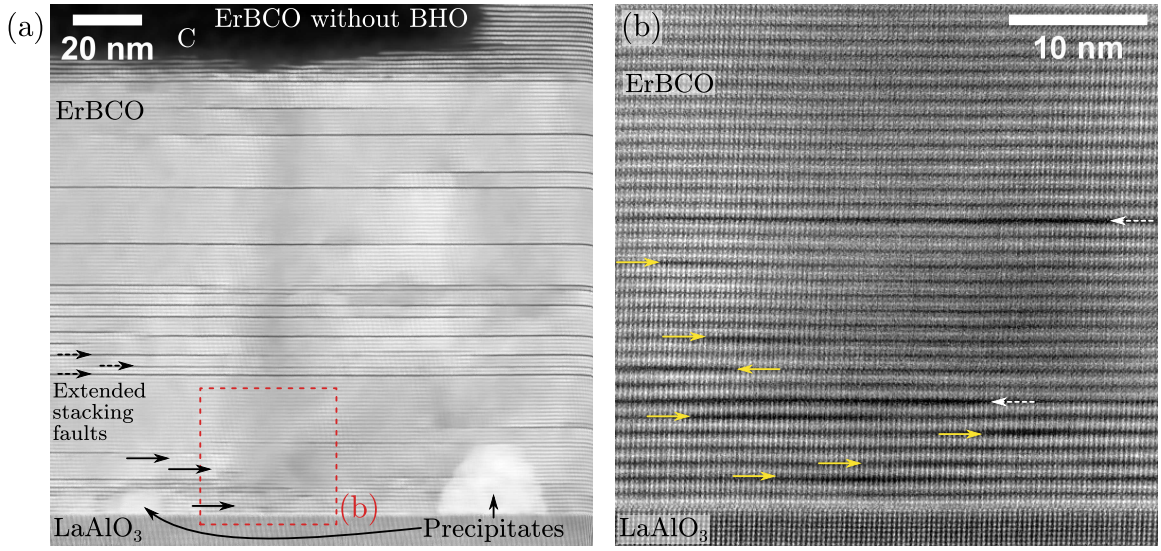

Figure 5.15: Reduced nanoscale-planar-defect density in pristine CSD-grown ErBCO on LAO. (a) Overview cross-section HAADF-STEM image of ErBCO showing a low/high concentration of nanoscale (solid arrows)/extended (dashed arrows) planar defects. Nanoscale planar defects preferentially form close to the film-substrate interface. Two precipitates at the film-substrate interface are visible. The image is non-local-means-filtered for better visibility. (b) Magnified and ABS-filtered image from the interface region marked in (a).

the REBCO structure [ST91; HS92; Lu+21]. REBCO-degradation speed depends on the microstructure [Kum+94], as defects act as diffusion paths. The fully oxidized, orthorhombic $REBa_2Cu_3O_{7-\delta}$ phase with $\delta \approx 0$ (denoted as RE123 in the following discussion) is not stable regarding its O content [YF89] and prone to O loss. Diffusion of O (and probably other intercalated molecules) along single CuO chains is faster in RE123 than in double CuO chains in RE124 or RE247. The extra CuO plane in the latter two phases is structurally related to stacking-fault formation in $REBa_2Cu_3O_{7-\delta}$ (extra CuO plane). These stacking faults appear as dark horizontal lines in the shown ADF-STEM images of REBCO. Shi and Tu [ST91] argued that O out-diffusion from Y123 leads to the formation of a passivating shell of Y124 at the YBCO surface, preventing further degradation. In contrast, Müller et al. [Mül+92] and Zandbergen [Zan92] proposed an amorphous YBCO passivation layer. The reaction of REBCO with gases in the surrounding atmosphere is another reason for degradation besides O out-diffusion. Water (H_2O) [Bör+95; GS96; Gün+96; Gün+99] and CO_2 [EFH89; RKH99] were shown to react with REBCO, forming secondary phases such as $BaCO_3$ or $Ba(OH)_2$ [RKH99].

Most of the cited studies were conducted on bulk samples. The aging effects are likely more pronounced (or occur faster) in thin cross-section samples for TEM with a typical thickness of 50 nm to 100 nm. For cross-section samples, most of the exposed area is parallel to the(1 0 0) and (0 1 0) surfaces. This contrasts with as-deposited (unprepared) REBCO films where the film's (0 0 1) surface is exposed.Therefore, the diffusion paths are entirely different for the two sample geometries (thin film or TEM sample). Different exposed surfaces have a strong impact on the O diffusion. Rothman et al. [Rot+91] showed that O diffusion is fastest along the *b*-direction $D_b > D_a \gg D_c$. Most important, the diffusion along the *c*-direction D_c is $\sim 1 \times 10^{-6}$ slower compared to the in-plane diffusion D_{ab}. This means that degradation by O out-diffusion from the "open" *ab*-sides of a cross-section TEM sample must be considered. For example, a structural transformation of orthorhombic $REBa_2Cu_3O_7$ to tetragonal $REBa_2Cu_3O_6$ may appear for O loss [HS92].

The observed nanoscale planar defects appear as dark horizontal lines similar to a typical CuO stacking fault but with reduced length along the *ab*-directions (approximately 3 nm to 30 nm). Two types were identified based on the local elongation of the *c*-lattice parameter around such defects:

1. Most nanoscale defects increase the *c*-lattice parameter of REBCO from $c_{123} = 1.17\,\text{nm}$ by about 0.2 nm to approximately $c_{124\text{-type}} \approx 1.37\,\text{nm}$ (cf. Fig. 5.7b). This fits well with one additional CuO plane in the RE123 structure to form a similar structure as RE124. For this reason, this defect type is denoted as "124-type defect" in the following, in accordance with Zandbergen [Zan92].

2. A few nanoscale defects increase the *c*-lattice parameter to about 1.5 nm (cf. Fig. 5.7e). This agrees well with similar defects observed by Zandbergen [Zan92], who proposed that these defects are of composition $REBa_2Cu_{5-x}C_xO_{10}$ and "are formed by intercalation of Cu, O and small amounts of CO_3, whereby Cu is replaced to a small degree by C" [Zan92]. The structure is structurally similar to two additional CuO planes in RE123. This defect type is denoted as "125-type defect".

At first glance, the 124-type defects are structurally equal to an extra CuO plane. However, the 124-type defects are shorter in the *ab*-plane than extended stacking faults consisting of an extra CuO plane (e.g., cf. extended stacking faults and short nanoscale planar defects in Fig. 5.13a and b). The formation of 124-type defects consisting of an extra CuO plane would require a source of Cu and O, or the precipitation of Ba- and RE-rich phases if the REBCO structure is decomposed into 124-type defects. The latter is not observed experimentally (at least for thin TEM samples). Two possibilities for 124-type-defect formation were proposed in the literature. A first possibility is that an amorphous REBCO surface layer on a TEM sample acts as a supply for Cu and O [Zan92]. A second possibility is the formation of Cu vacancies with the possibility of intercalation of molecules from air or the residual microscope vacuum such as $(OH)^-$ [Rup+92; Bör+95; Zak+96] or CO_3 [Zan+91]. The stoichiometry is similar to RE123, but the *c*-spacing is the same as RE124 ("pseudo-RE124" phase). Zakharov et al. [Zak+96] showed evidence for the pseudo-RE124 phase by HRTEM observing Cu vacancies formed at every second lattice site in the *ab*-plane (effectively doubling the *a* lattice parameter [Zan+91; Zan92]). In the latter model, no extra Cu or O has to be provided for 124-type-defect formation.
The structure of the extra CuO planes is not clearly resolved in the HAADF-STEM images shown here. As a result, the exact composition (e.g. if Cu vacancies are present) or formation mechanism could not be clarified from the shown experimental results. The loss of STEM resolution may result from a generally too low signal-to-noise ratio or caused by the local disorder at a nanoscale planar defect. Defect formation may start at the TEM sample's surface and – at the beginning – may be limited to the TEM-sample surface [Zan92]. In contrast, the structure of the RE123 phase in the middle of a TEM sample may still be fully preserved. The resulting structural changes in the atomic structure may reduce the electron-probe channeling at defects, ultimately resulting in a loss in HAADF-STEM resolution.An important takeaway from the discussion is that these nanoscale planar defects probably have formed after TEM-sample preparation, independent of whether the defect is 124- or 125-type. The clearest evidence of this result is the comparison of Fig. 5.13a and b on Page 168 with 14 days of sample storage between the two TEM measurements (and a short Ar^+ milling).

The observed striped appearance (or elongation) of the REBCO structure (cf. Fig. 5.7c, Fig. 5.8d, Fig. 5.13d, Fig. 5.14d) and also the appearance of the "4×-bright structure" (cf. Fig. 5.7f,

Fig. 5.8d, Fig. 5.13d) in HAADF-STEM imaging may be directly related to 124- and 125-type defect formation (Fig. 5.16). Both defects cause a structural deformation of the RE123 structure by locally increasing the c-lattice parameter, effectively inducing antiphase boundaries (APBs) along the c-direction. The result is a buckling of the REBCO unit cells in c-direction [Fen+90; Zan92].

- **Striped/elongated REBCO structure in c-direction.** Figure 5.16a-c (top row) show a possible atomic model that could lead to the observed striped appearance of the REBCO structure in HAADF-STEM images. The formation of a 124-type planar defect shifts part of the REBCO structure in a TEM sample by about $c/6$ ($\sim 0.2\,\mathrm{nm}$) in addition to a $b/2$-shift. This is visualized in the side-view scheme in [1 0 0] projection in Fig. 5.16a and front view (here meant as being parallel to the incident [0 1 0] electron-beam direction) in Fig. 5.16b. The $c/6$ shift results in a local region (here between the two dashed horizontal lines) with strongly reduced atomic distances in the c-direction, but preserves the periodicity in the a-direction. The model shows an abrupt step where the extra CuO plane is inserted (Fig. 5.16a). However, this change may be more gradual (along the b-direction), which would further "wash out" the alignment of REBCO planes along the c-direction. The combination of this gradual shift of unit cells along the c-direction in combination with a limited spatial resolution (here about 150 pm) in the used HAADF-STEM setup leads to the striped appearance of the REBCO structure in c-direction as exemplarily shown in Fig. 5.16c.
- **4×-bright structure.** A possible atomic model for the observed 4×-bright structure is shown in Fig. 5.16d-f with the same orientations as in Fig. 5.16a. The addition of two CuO planes forms a 125-type defect, here shown in the central region of Fig. 5.16d. This corresponds to a $c/3$ shift of the adjacent REBCO unit cells (here shifted down) and leads to a peculiar stacking of the Ba and RE planes. Specific atomic columns along the b-direction are then a mixture of Ba and RE columns (marked with solid blue-green arrows with white arrowheads). Two of such mixed Ba-RE columns are separated by a single Ba column (marked with dashed green arrows). Figure 5.16e. The average atomic number in the mixed Ba/RE column is higher than Ba ($Z_{\mathrm{Ba}} = 56$) as the average RE atomic number for $(Gd_{0.2}Dy_{0.2}Y_{0.2}Ho_{0.2}Er_{0.2})Ba_2Cu_3O_{7-\delta}$ is $\overline{Z} = 60.8$ (calculated from the atomic ratios). This leads to a higher HAADF-STEM intensity at the mixed Ba/RE column compared to the pure Ba column and the experimentally observed structure shown in Fig. 5.16f. The average atomic number of the mixed Ba/RE column depends on the extent of the 125-type defect at the TEM-sample surface [Zan92] parallel to the beam direction relative to the undisturbed RE123 phase. In this model, a mixed Ba/RE column should appear with lower HAADF-STEM intensity than a pure Ba column for YBCO with $Z_{\mathrm{Y}} = 39$. However, no YBCO samples were investigated in this work to validate this.

Both proposed atomic models work only for a mixture of c-shifted and undisturbed RE123 structure throughout the thickness of a TEM sample. HAADF-STEM imaging shows the projected structure along the [0 1 0] electron-beam direction. This agrees with the explanation of defect formation mainly occurring at a TEM sample's surface. The subtle increases in REBCO c-spacing observed in Fig. 5.5 on page 160 are probably the first signs of 124-/125-type defect formation.

So far, mainly the c-direction shift was discussed. A nanoscale defect can also inhibit a translation in the a- or b-direction, e.g. as shown in Fig. 5.16a with displacements vectors $\vec{R} = 1/6[0\,3\,\overline{1}]$ and $\vec{R} = 1/6[0\,3\,1]$ for the upper and lower CuO plane, respectively. The work by Yan et al. [YBW91]

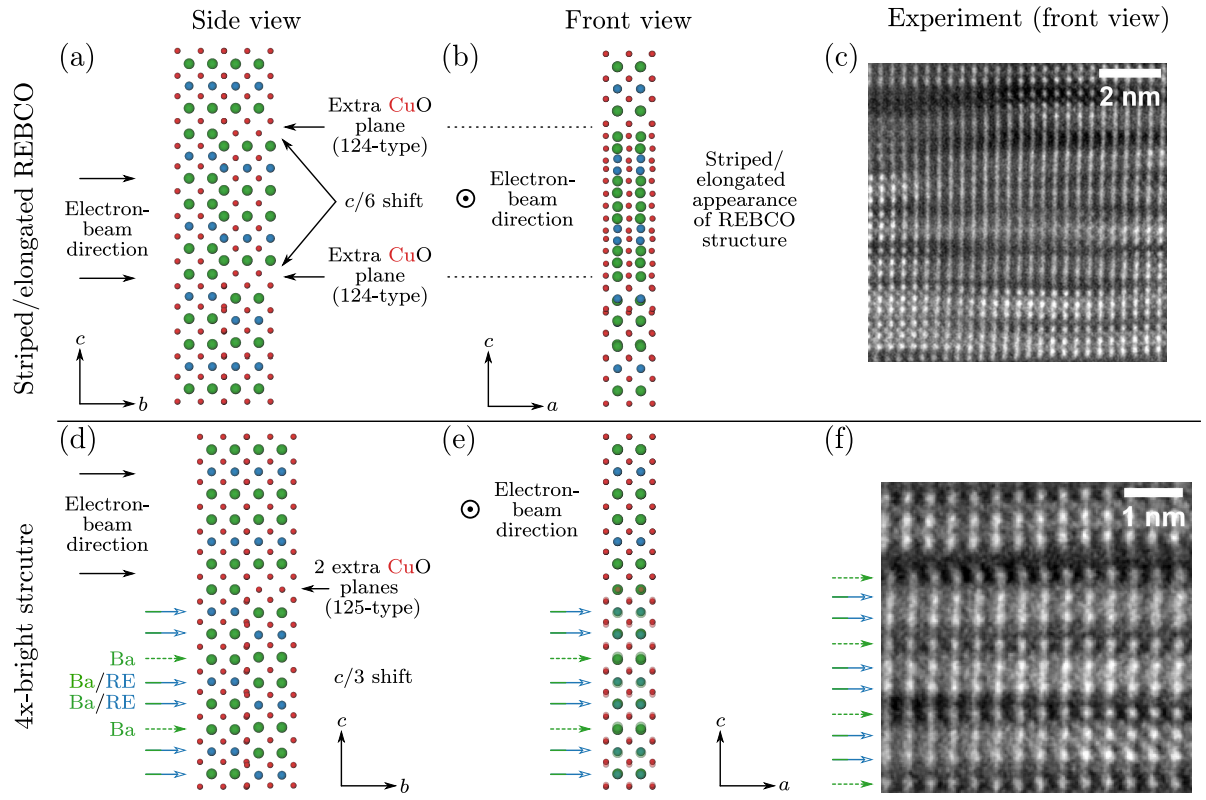

Figure 5.16: Possible atomic models for 124- and 125-type defects in TEM samples of REBCO. The top (bottom) row shows the model for the striped/elongated appearance (4×-bright structure) of the REBCO structure in HAADF-STEM images. The first column displays a side view of the atomic model in [1 0 0] projection. Defects in the form of extra CuO plane are introduced with displacement vectors 1/6[0, 3, ±1] are added. The middle column shows the structure along the [0 1 0] zone-axis direction, which corresponds to the experimental orientation shown in the right column. The structures were generated by overlaying atomic structures from ICSD numbers 400 090 (Y247) and 56 507 (Y123). O is omitted for clarity. See the text for a detailed explanation.

lists other possibilities for nanoscale defects with a pure displacement along the *c*-direction. They investigated such planar defects in HoBCO, and the reader is referred to their paper for a detailed explanation of planar defect configurations in REBCO. A planar defect must be imaged from multiple directions (i.e. [1 0 0], [0 1 0], and [1 1 0]) to identify its displacement vector, which was not done here. A consequence of some of the discussed defect configurations by Yan et al. [YBW91] is the appearance of $a/2$- or $b/2$-shifts at (nanoscale) planar defects at 90° [0 0 1]-tilt twin boundaries, where the *a*- and *b*-directions switch. This changes the symmetry of a defect from a glide to a mirror symmetry or *vice versa*, which is also observed in this work (Fig. 5.13d). The reason for the observed change between *a*- and *b*-direction in the REBCO orientation shown in Fig. 5.14d is not apparent. However, strain induced by the buckling unit cells below theses planar defects or a transition to the tetragonal $REBaCuO_6$ structure may induce this orientation change.

An interesting REBCO structure can be obtained by combining the atomic model shown in Fig. 5.16d with other $c/3$-shifted grains along the *b*-direction (Fig. 5.17a). A high concentration of such $c/3$ APBs leads to an average concentration of 2/3 Ba and 1/3 RE atoms along the mixed Ba/RE columns, the same as the ordered RE123 structure viewed parallel to the [0 0 1] zone axis (Fig. 5.17b). The latter can appear in *c*-oriented REBCO films (i.e. *c*-direction parallel to the growth direction) as a misoriented grain, also called *ab*-oriented REBCO or *ab*-grain (i.e.

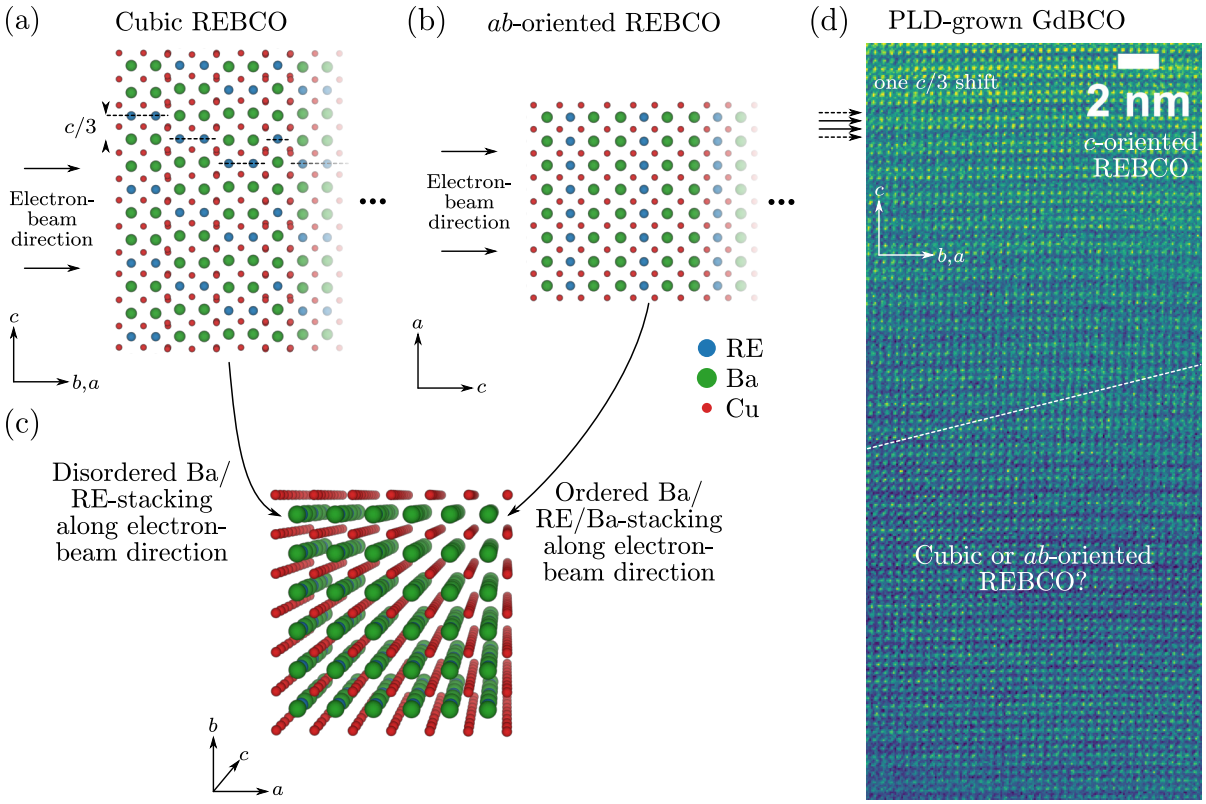

Figure 5.17: Formation of cubic REBCO by a stacking of $c/3$-antiphase boundaries. (a and b) Structural models for (a) cubic and (b) *ab*-oriented REBCO. Note the (a) disordered and (b) ordered stacking of the Ba and RE planes. A similar average HAADF-STEM Z-contrast is visible for both configurations for the shown electron-beam incidence direction. (c) View on the structure from (b) in electron-beam direction. (d) Experimental HAADF-STEM image of GdBCO. The lower-right area could be cubic, non-superconducting or *ab*-oriented, superconducting GdBCO.

ab-direction parallel to the growth direction). The disordered REBCO structure is denoted as (pseudo) "cubic REBCO" or "REBCO*" and is non-superconducting [ACB91; Köh+97; Köh+04]. The cubic structure has a lattice constant of 0.39 nm [ACB91], which corresponds to $c/3$ with $c = 1.17$ nm for REBCO. The structure is a perovskite ABO_3 with Ba and REs occupying the A site and Cu occupying the B site, i.e. $(REs,Ba)CuO_{3-\delta}$ [Haa+98]. Cubic REBCO and *ab*-oriented REBCO are structurally similar (the difference being the disordered or ordered Ba/RE stacking), which means they cannot be distinguished easily, e.g. by EDXS [Köh+97] or by HAADF-STEM as the average Ba/RE-column intensity is the same (Fig. 5.17c). An example of this is shown in (Fig. 5.17d) for a PLD-grown GdBCO film. A *c*-oriented GdBCO film with a 4×-bright structure is visible in the top part of the HAADF-STEM image. This HAADF-STEM-intensity pattern arises from the projected structure of two GdBCO grains with a $c/3$-shift as discussed in Fig. 5.16d-f. The structure gradually transforms into a cubic structure towards the lower-right region of the HAADF-STEM image (Fig. 5.17d). The here-observed cubic GdBCO structure (non-superconducting cubic GdBCO or superconducting *ab*-oriented GdBCO) cannot be distinguished from this image alone and is therefore not clearly identified here[2]. A tilting of the sample around the [0 0 1] axis may be used to clarify the structure [ACB91]. Imaging from another direction (i.e. along the viewing direction in Fig. 5.17d) may reveal the (absence of) *c*-periodicity for *ab*-oriented REBCO (cubic REBCO). For example, an *ab*-oriented

[2]However, a misoriented *ab*-grain of GdBCO is more likely here since these grains were detected in the shown GdBCO film (cf. Fig. 5.8c on Page 163).

grain is clearly identified in Fig. 5.8a and c on Page 163 by the expected *c*-periodicity for GdBCO in the horizontal direction.

Influence of electron- and Ga^+-ion-beam on defect formation. No changes in the undisturbed REBCO and nanoscale-defect structures were observed during HAADF-STEM (and occasionally HRTEM) image acquisition. However, Midgley et al. [MVC92] showed by large-angle CBED that electron irradiation at room temperature can lead to a loss of orthorhombicity of $REBa_2Cu_3O_{7-\delta}$, i.e. a transformation to the non-superconducting tetragonal $REBa_2Cu_3O_6$ structure. This change is subtle and may be missed by the microscope operator in direct HAADF-STEM imaging. Still, no nanoscale planar defects were introduced by electron-beam irradiation with the used imaging parameters (cf. Table 3.3 on page 66).
The influence of Ga^+-ion milling during FIB preparation on nanoscale-planar-defect formation was investigated by comparison with a Ar^+-ion-milled TEM sample. In both cases, nanoscale defects were observed in varying concentration (cf. Fig. 5.6 and Fig. 5.11d). A higher concentration of nanoscale planar defects is observed for (i) thinner TEM samples (cf. Fig. 5.6a) and (ii) samples stored in air or a desiccator (cf. Fig. 5.13a and b for a difference of 14 days). Both observations agree with the formation of 124- and 125-type defects in REBCO as discussed above. High-energy ion bombardment (e.g. 1.4 GeV ^{208}Pb ions [Kwo+18]) of REBCO films is ordinarily used to introduce structural defects for vortex pinning. Although this high-energy ion bombardment cannot be directly compared to comparably low-energy Ga^+ ions in a FIB, an amorphization of the REBCO structure results from both ion species. The ions create amorphous columns (or tracks) in the REBCO structure, where a formation of short planar defects (similar to the nanoscale planar defects here) is observed [Kwo+18]. The amorphous columns may act as Cu and O reservoirs to form the extra CuO planes. This may be similar to an amorphous REBCO surface layer on a TEM sample [Zan92].

Defect formation in CSD- and PLD-grown REBCO films. The highest concentration of nanoscale planar defects was observed in CSD-grown films with BHO nanoparticles (e.g., cf. Fig. 5.7 on page 162 (with BHO) and Fig. 5.15 on page 171 (no BHO)). An exception to this is the $(Gd_{0.2}Dy_{0.2}Y_{0.2}Ho_{0.2}Er_{0.2})Ba_2Cu_3O_{7-\delta}$ sample prepared with Ar^+ milling shown in Fig. 5.11c and d. Here, only a few nanoscale planar defects are observed close to the substrate-film interface. However, the relatively large TEM-sample thickness of 70 nm may partially disguise a possible degradation of the TEM-sample surface for this TEM sample. As shown in Fig. 5.6a, thinner TEM-sample regions are more susceptible to defect formation. The degradation for the 70 nm thick Ar^+-milled TEM sample is apparent from the results of a second TEM session after 14 days (cf. Fig. 5.13a and b). Similarly, the CSD-grown ErBCO film on LAO (Fig. 5.15) and the PLD-grown GdBCO films (Fig. 5.9) – both without BHO nanoparticles – only showed nanoscale planar defects close to the substrate-film interface.
The BHO particles introduce strain in the surrounding REBCO film. Similarly, strain is present close to a film-substrate interface due to the lattice mismatch between the substrate and the REBCO film. The appearance of nanoscale planar defects (i) close to the film-substrate interface and (ii) in films with BHO particles may be related to strain in the REBCO films. In this explanation, the *ab*-strain is partly relieved by an elongation along the *c*-direction. This elongation might be easier to realize by the strained RE123 structure in thin TEM samples than in bulk samples. For the latter, part of this strain is relieved by stacking-fault formation during deposition and film growth.

Conclusions. This section is concerned with planar defects in REBCO films. The following observations and conclusions are drawn from the experimental results:

- Planar defects with a lateral extension in the *ab*-plane of around 3 nm to 30 nm are observed in varying concentrations in nearly all TEM samples of REBCO. These nanoscale planar defects are structurally similar to the more extended stacking faults. Both defect types (extended stacking faults and nanoscale planar defects) appear as dark, horizontal lines in HAADF-STEM imaging due to a decreased local atomic number Z.
- The defect concentration varied between different TEM samples (even of the same REBCO film) and was not reproducible. This is attributed to TEM-sample thickness variations, where thinner TEM samples show a higher concentration (and faster formation) of defects. All shown TEM samples were directly observed by STEM after sample preparation with a transfer time of 30 min in air between the FIB and the S/TEM instruments.
- The concentration of nanoscale planar defects increases with time. The formation of nanoscale planar defects is, therefore, an artifact of thin TEM-samples and the defects are not present in the as-deposited REBCO film.
- Nanoscale defects were observed in TEM samples thinned with 2 keV Ga^+ ions. Using 300 eV Ar^+ ions does not prevent nanoscale defect formation.
- Nanoscale defects locally increase the *c*-lattice parameter, probably to relieve lattice strain in the REBCO structure. This conclusion arises from a higher density of nanoscale defects in strained regions, i.e. close to the film-substrate interface and generally in BHO-containing REBCO films.
- Two nanoscale-defect types were observed and compared with the literature. A "124-type" defect is structurally similar to one additional CuO plane in *c*-direction. Similarly, a "125-type" defect contains two additional CuO planes. In both cases, the local composition may differ from CuO by incorporating residual gas molecules from ambient air and microscope vacuum. However, the exact chemical structure of the nanoscale defects could not be clarified here.
- The 124- and 125-type defect can create particular projected atomic structures in HAADF-STEM imaging, such as an elongation of the REBCO unit cell in *c*-direction or an apparent change in the stacking order of the bright Ba and RE planes along the *c*-direction.
- Genuine stacking faults consisting of an extra CuO chain in the REBCO matrix are typically more extended (>30 nm) in the *ab*-plane and can be observed in thicker TEM-sample regions. These stacking faults – in contrast to the nanoscale planar defects – are most likely present in the as-deposited films and contribute to the electronic properties (e.g. $H \parallel ab$ pinning).

The influence of different RE species on nanoscale-defect formation cannot be discussed based on the investigated REBCO films. Similarly, no PLD-grown and CSD-grown films with the same composition were directly compared here. The influence of the fabrication method – CSD or PLD – can therefore not be evaluated. For example, CSD-grown films might contain residual elements from the precursor solutions (such as F) after pyrolysis, which could influence the formation of 124- or 125-type nanoscale defects. In addition, CSD is a non-vacuum process and other residual molecules may act as impurities and promote REBCO degradation, e.g. CO_2 [Del+90]. A TEM-sample transfer under an inert gas atmosphere between FIB and S/TEM instruments should be used for REBCO (if available).

5.3 *Ex-Situ* Oxygenated PLD-grown $GdBa_2Cu_3O_{7-\delta}$ Films on MgO

Previous work. This section presents results on microstructural changes during an *ex-situ* oxygenation of PLD-grown GdBCO films. The oxygenation process is used to increase the O content close to $GdBa_2Cu_3O_7$, i.e. an O-deficit $\delta \approx 0$ [Cav+90], to achieve the best superconducting properties. The oxygenation process is essential and requires optimization similar to other fabrication parameters, e.g. substrate temperature, deposition rate, or oxygen-partial pressure [Ros+10]. Optimized oxygenation requires knowledge about the O diffusion in REBCO. Many studies are available investigating the oxygen diffusion for YBCO [TO90; LP92; LP93; Mic+98] or the effect of O stoichiometry on the critical temperature [Cav+87; Cav+90]. However, the microstructure of REBCO also changes during the oxygenation process. This aspect depends on the oxygenation parameters and is not fully understood yet. Recent studies for GdBCO [Oh+20; Oh+18; Par+18a; Par+18b; Lee+16] showed microstructural changes after *ex-situ* oxygenation. For example, Oh et al. [Oh+20] observed a change in stacking-fault density in dependence of the annealing temperatures. This shows that the stacking-fault density can be tuned during the oxygenation process. Park et al. [Par+18a] noticed the formation of Gd_2CuO_4 in their GdBCO samples.
An *ex-situ* oxygenation is performed in a tubular furnace by annealing the PLD-grown samples in a pure O-atmosphere. Hence, the oxygenated samples are also denoted as "annealed" REBCO samples. In contrast, *in-situ* oxygenation can also be performed in an O atmosphere in the PLD chamber after PLD [Pop+20]. However, the oxygenation step is also performed *ex-situ* in a tubular furnace for industrial production using the reel-to-reel method [Pru+06]. Therefore, a better understanding of the *ex-situ* oxygenation process is desired.

Sample fabrication. The GdBCO films were grown with PLD as described on Page 54. Six GdBCO films were investigated here, where five films were *ex-situ* annealed and one reference sample was not annealed, i.e. has a "as-deposited" microstructure after PLD. The annealing conditions in the tubular furnace (450 °C, O flow 1 bar, 30 min holding time) were based on previous work [Pop+20]. The annealed samples had different heating routes to the final set point 450 °C for O annealing, e.g. heating in Ar to 450 °C, or heating in Ar to 800 °C followed by cooling in Ar (or Ar/O mixture) to 450 °C. However, the microstructural differences between the different annealing routes were small and some parameters are unfortunately unknown. Therefore, the following discussion is mostly concerned with a more general comparison between annealed and unannealed GdBCO films. The T_c of the unannealed film is 32.7 K, whereas all oxygenated films have $T_c \approx 92$ K (with a self-field $J_c(0\,\mathrm{T}, 77\,\mathrm{K})$ in the range of 1.8 $\mathrm{MAcm^{-2}}$ to 4.2 $\mathrm{MAcm^{-2}}$). The films were prepared by **Ruslan Popov**.

Experimental results. In general, all annealed films showed similar sample features with minute differences in, e.g., twin-boundary spacing. Therefore, not all films are compared, but instead only a comparison between annealed and unannealed GdBCO films is presented. This section is subdivided in subsections and discusses various structural features:

- An **SEM surface analysis** shows the formation of flat GdBCO film with various precipitates at the surface. Some precipitate phases could not be identified from the experimental results, e.g. C-rich precipitates for the unannealed sample. Rectangle-shaped, µm-sized Cu_xO_y precipitates are observed for all GdBCO films.

- **Twin-boundary formation** is only observed for the annealed films. This is expected since the twin boundaries are formed during the tetragonal-to-orthorhombic transition during O-annealing.
- **Large precipitates** are observed in all GdBCO films, which extend parallel *a*- and *b*-directions (similar to the Cu_xO_y precipitates). These are identified as misoriented GdBCO grains, i.e. *c*-direction *not* aligned with the substrate-surface normal. These precipitates may form preferentially at substrate steps of the MgO substrate.
- **Small precipitates** are observed in all films, but are more agglomerated after annealing. These precipitates are identified as Gd_2CuO_4 with a lateral $\sim$ 5 nm to 30 nm and the crystalline orientation $Gd_2CuO_4[1\,0\,0](0\,0\,1)\|GdBCO[1\,0\,0](0\,0\,1)$.
- Finally, **other observations** for the GdBCO are collected in a final subsection. Here, vertical defects in the unannealed film are analyzed. A [0 0 1]-tilt low-angle grain boundary and an antiphase boundary are shown. In addition, the GdBCO-MgO interface shows a periodic arrangement of misfit dislocations to compensate for the relatively large mismatch between GdBCO and MgO.

SEM surface analysis. The surface topography of the investigated GdBCO films is discussed first. Figure 5.18a and b compare the film's surface from (a) an as-deposited, unannealed and (b) an *ex-situ* annealed GdBCO film. All films generally show a mostly flat GdBCO topography with few large surface precipitates. The unannealed film shows a high density of small, round precipitates (Fig. 5.18c), whereas the size of the small precipitates is significantly reduced after annealing (cf. Fig. 5.18d). The small precipitates (bright structures Fig. 5.18c) consist mainly of C as measured by EELS and EDXS (not shown). In addition, small amounts of O, Cu, and traces of N (using EELS) were measured. The source of these elements is not clear. Sample contamination with C-rich debris after PLD cannot be ruled out.
Some structural features are observed in both images, e.g. *a*-/*b*-oriented rectangular precipitates (solid yellow arrows in Fig. 5.18a and b) or large roundish precipitates (dashed white/black arrows). The latter might be PLD droplets. The rectangular precipitates are rich in Cu and O as measured by SEM-EDXS (cf. Fig. 5.19), indicating a Cu_xO_y phase. It could not be clarified if these Cu_xO_y precipitates preferentially align with the *a*- or *b*-directions or with equal probability for both directions. It is also worth mentioning that similar *a*- and *b*-aligned "needle-shaped" precipitates can also result from *ab*-oriented GdBCO grains [AH03; Ruf+06; Wan+13]. Indeed, such *ab*-oriented GdBCO grains were observed in plan-view TEM samples and are discussed further below (in context with Fig. 5.21 on page 183).
For the annealed film, Fig. 5.18b, a few small "pinholes" [Low+97; Wan+13] (marked with red arrowheads) and small roundish precipitates (cyan arrowheads) are observed. The latter are rich in Gd/Ba, as measured by SEM-EDXS (Fig. 5.19). The exact composition could not be clarified. All investigated annealed GdBCO film showed similar topography and features as the film shown in Fig. 5.18b. However, some annealed films showed precipitates of another phase with a triangular shape at high magnification (Fig. 5.18e). Low-energy SEM-EDXS analysis similar to Ba122 precipitates (cf. Fig. 4.9 on page 105) was applied to study these precipitates, but without success.

Low-magnification SEM-EDXS analysis was used to get insights into the composition of larger precipitates in the µm range (cf. SE-SEM overview image in Fig. 5.19a). Here, a primary electron energy of 8 keV was chosen to efficiently excite the Ba L shell (5.247 keV) while still preserving the required spatial resolution. Starting with the rectangular, *a*-/*b*-aligned precipitates (dashed

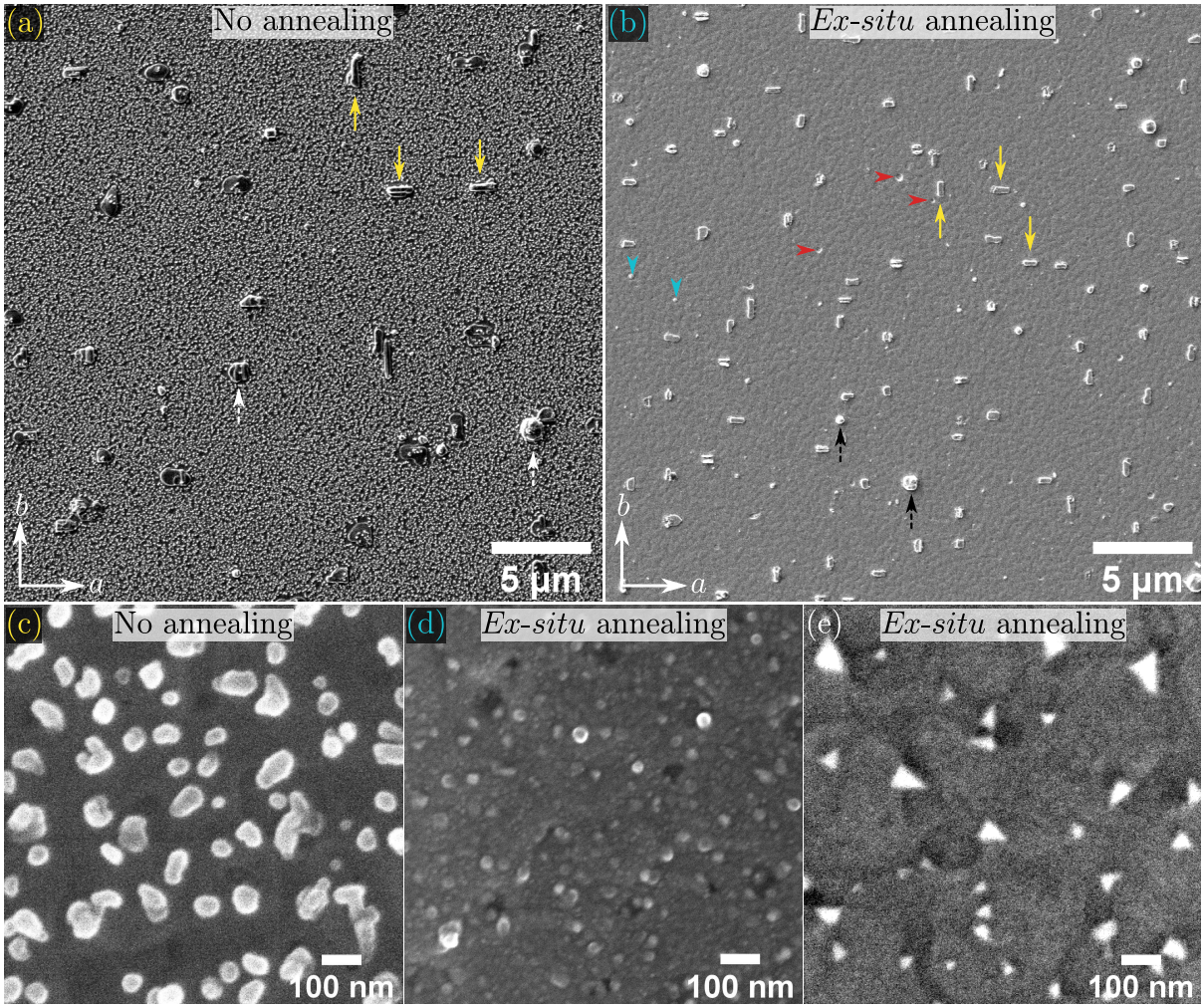

Figure 5.18: SE-SEM surface imaging of (a,c) as-deposited and (b,d,e) annealed GdBCO films. (a,b) 30 µm × 30 µm surface image of an (a) as-deposited PLD-grown GdBCO film and (b) another GdBCO film after *ex-situ* annealing in O. Solid yellow arrows mark *a*-/*b*-oriented surface precipitates (here probably Cu_xO_y). Dashed arrows mark round precipitates, possibly PLD droplets. (b) Small pinholes (marked by red arrowheads) and small roundish precipitates (marked by cyan arrowheads) are observed for the annealed film. (c,d) 1 µm × 1 µm surface image of of the same films as in (a) and (b). Roundish precipitates are rich in C. (e) Another annealed GdBCO film showed the formation of an unidentified precipitate phase with a triangular shape.

arrows), increased Cu/O signals and decreased Ba/Gd signals are observed. This indicates a Cu_xO_y phase. In contrast, the small roundish precipitates (solid arrow) show increased Ba/Gd signals and a Cu depletion. The O signal is nearly unchanged compared to the GdBCO matrix. The Gd-/Ba-rich phase could not be identified from the shown results.

To summarize the surface analysis by SEM, a complicated mixture of various surface precipitates is observed. Rectangular Cu_xO_y seemingly show a preferential alignment along the *a*- and *b*-axes of GdBCO. The composition and crystalline phase of some of the observed precipitates could not be clarified. For example, a C-rich phase was observed for the unannealed film (Fig. 5.18c) and a triangular phase for some annealed GdBCO films (Fig. 5.18e).

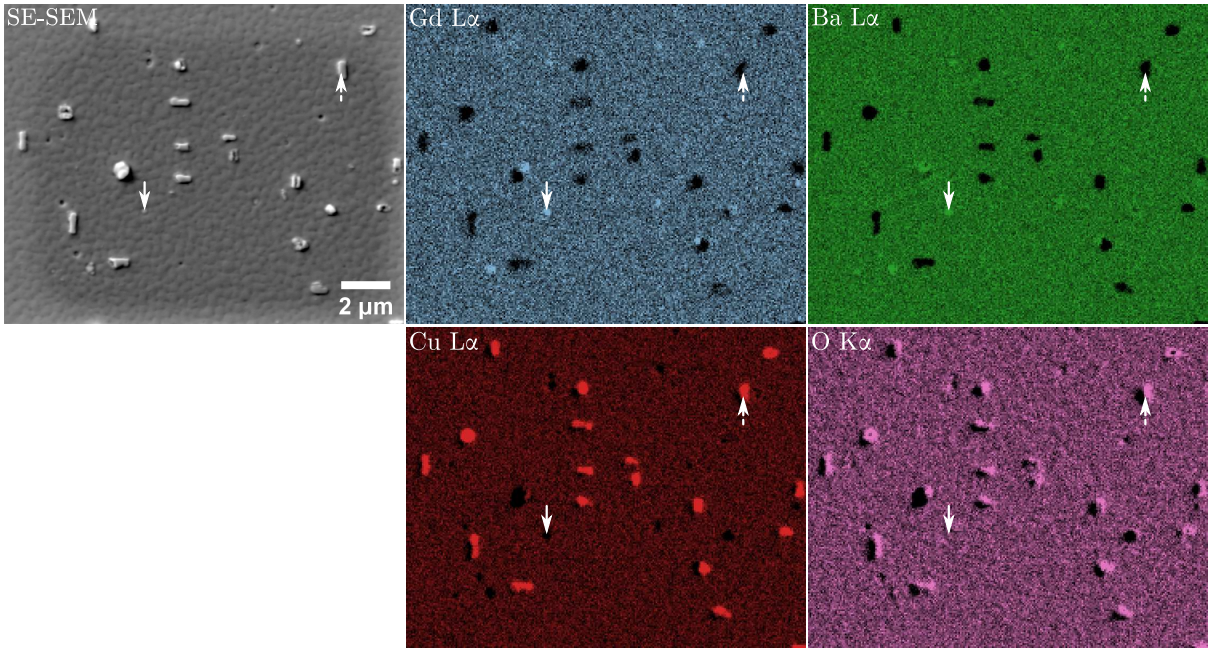

Figure 5.19: SEM-EDXS mapping of an *ex-situ* annealed GdBCO film. SE-SEM overview image and elemental maps of a GdBCO film with precipitates. Cu-/O-rich precipitates (cf. example marked with a dashed arrow) show an elongation along the *a*- or *b*-direction, indicating preferential growth in these directions. Smaller precipitates with a round shape (solid arrow) with an increase in Gd and Ba signal are also visible. Note that the EDXS detector is located towards the top-right corner, which causes a shadowing effect on the opposite side (i.e. lower-left region) of the precipitates in the Cu Lα and O Kα maps due to x-ray absorption.

Twin-boundary formation after annealing. The formation of twin boundaries oriented along the $\langle 1\,1\,0 \rangle$ directions is a typical phenomenon in REBCO related to the tetragonal-to-orthorhombic phase transition. Therefore, twin boundaries were only observed for the oxygenated samples (Fig. 5.20).

Figure 5.20a and b compare GdBCO films (a) without and (b) after *ex-situ* annealing in an O atmosphere. Twin boundaries (TBs) are visible as dark horizontal lines in the BF-STEM-in-SEM images (Fig. 5.20b, marked by orange arrows). Twin-boundary formation is only observed for the annealed film. The TBs are oriented along the $\langle 1\,1\,0 \rangle$ directions and adjacent GdBCO grains show an alternating image intensity. Representative LAADF-STEM cross-section images of the same two GdBCO sample are shown in Fig. 5.20c (unannealed) and d (annealed). The TBs appear as vertical, columnar structures (orange arrows in Fig. 5.20d). However, most TEM samples were prepared and imaged so that the electron-beam (or viewing) direction is along the [1 0 0] or [0 1 0] zone axis, whereas the TBs are oriented along $\langle 1\,1\,0 \rangle$. Therefore, the TBs are not viewed "edge-on" in Fig. 5.20d but instead at an angle of about 45°. This washes out the diffraction contrast at the TBs and impedes image interpretation. Some vertical defects are also visible for the unannealed film (cf. dashed arrows in Fig. 5.20c), which are not identified here. Maybe these are low-angle grain boundaries or threading dislocations.
Besides TBs, the formation of large (blue arrows in Fig. 5.20a and b) and small precipitates (green arrows) is observed in both films. The large precipitates are probably misoriented GdBCO grains, where the GdBCO *c*-direction is not parallel to the growth direction. This is discussed further below. In addition, agglomerations of small precipitates were observed for the annealed GdBCO film (dark spots in the dashed green circle in Fig. 5.20b). The same small precipitates are also visible for the unannealed film as dark spots in Fig. 5.20a, but with a more homogeneous

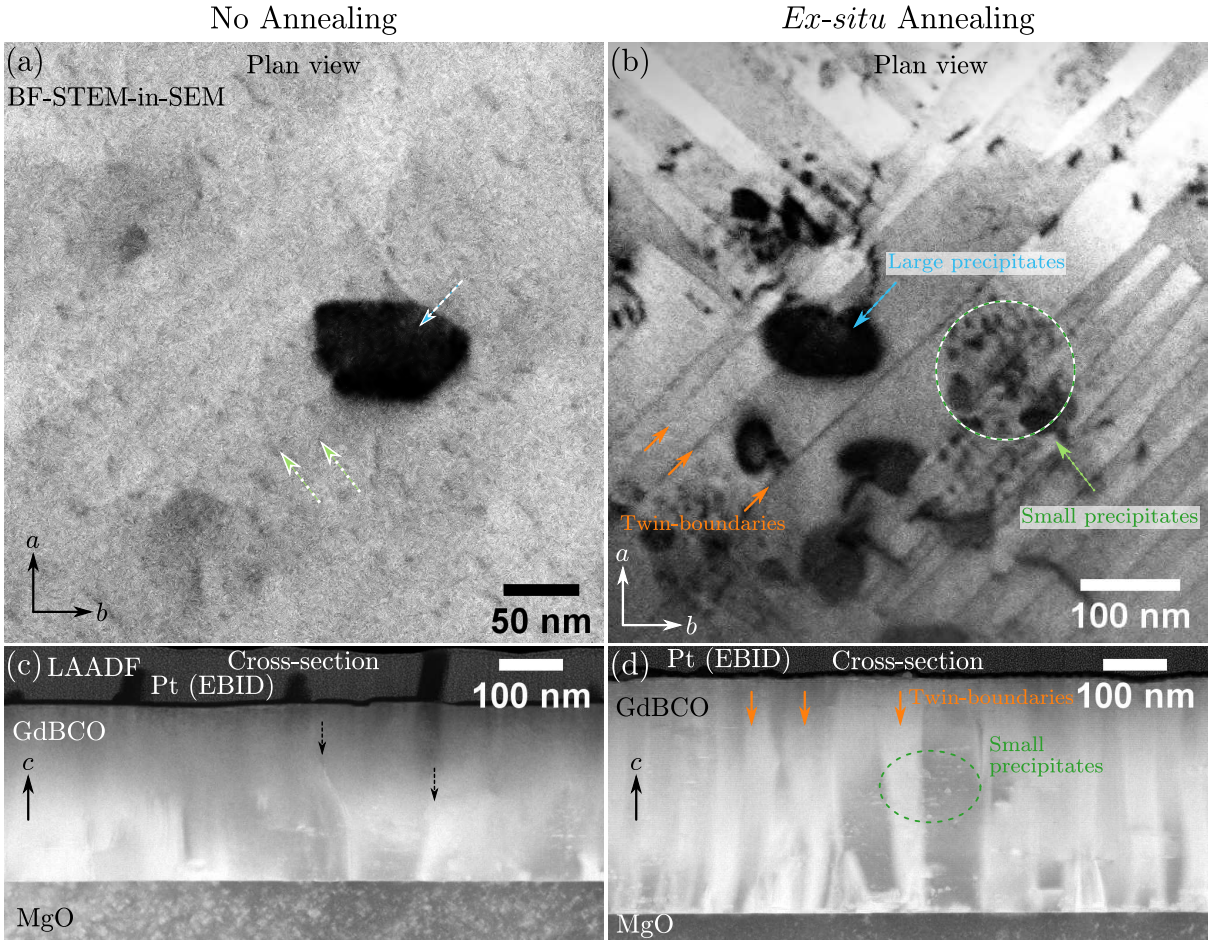

Figure 5.20: Comparison of GdBCO-film microstructures without oxygenation and after O annealing. 30 keV plan-view BF-STEM-in-SEM images of the films (a) without and (b) with *ex-situ* annealing. Large precipitates (blue arrows) with dark contrast are observed in both images, probably *ab*-aligned GdBCO grains. (b) Twin boundaries along the $\langle 1\,1\,0 \rangle$ directions (orange arrows) are visible only for the oxygenated film. Agglomerations of small precipitates are observed in the (b) oxygenated film (cf. green arrow and circle). The films were prepared in plan-view geometry as described in Fig. 3.6 on page 63. (c, d) 300 keV LAADF-STEM cross-section images of the films (c) without and (d) with *ex-situ* annealing. Twin boundaries appear as vertical structures in (d) and are marked with orange arrows. The small precipitates are also marked in (d). A few vertical defects are observed in (c) and marked by arrows.

spatial distribution. The small precipitates are likely to consist of the Gd_2CuO_4 phase. They show a bright cloud-like contrast in the cross-section LAADF-STEM image (cf. dashed green circle in Fig. 5.20d).

Plan-view FIB preparation enables large-area REBCO film analyses. This is exemplified with the BF-STEM-in-SEM plan-view image shown in Fig. 5.21a. A large number of precipitates and TBs are observed in the image. A few large precipitates are aligned parallel to the *a*- or *b*-directions of GdBCO instead of having a roundish shape as in Fig. 5.20a and b (examples marked with dashed double-headed arrows). These precipitates were subsequently analyzed by STEM-EDXS and did not show a change in composition compared to the surrounding GdBCO films (Fig. 5.23b on Page 186). Therefore, these precipitates are also identified as misoriented GdBCO grains.

A close inspection of the TBs (dark horizontal lines) reveals the presence TB domains, i.e. regions where the TBs are aligned in the same orientation. The orientation of the TBs can rotate by 90°, thereby forming a new domain. Such a boundary between two TB domains is

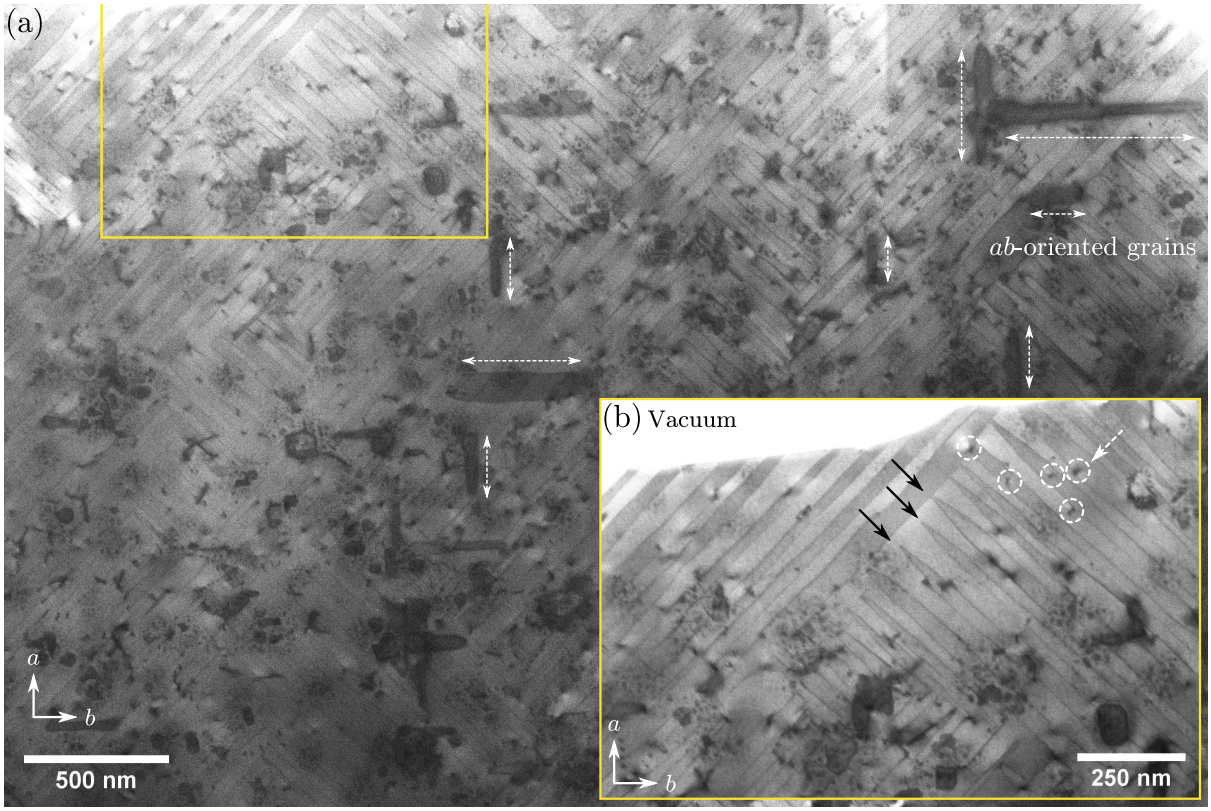

Figure 5.21: 30 keV plan-view STEM-in-SEM imaging of an oxygenated GdBCO film. (a) Large-area BF-STEM-in-SEM plan-view image an oxygenated GdBCO film acquired at $E_0 = 30\,\text{keV}$. A few precipitates are aligned parallel to the GdBCO *a*- and *b*-directions (see examples marked with dashed double-headed arrows). (b) Magnified image of the marked region in (a) showing adjacent twin-boundary domains. The arrows point to a region where every second twin boundary merges towards a point to minimize the strain energy [ZvT90; BCC01]. Some of the intensity variations (marked with dashed white circles) might be caused by other defects, e.g. threading dislocations.

visible in the magnified image shown in the inset image in Fig. 5.21b, close to the three arrows. This TB-domain boundary additionally shows an interesting phenomenon, where every second TB merges towards a point (cf. arrows in Fig. 5.21b). This merging of TBs is reported in the literature [ZvT90; BCC01] and leads "to a minimization of the strain energy as is commonly observed in ferroelectric domains" [ZvT90]. Twin boundaries can affect the pinning properties. Therefore, the TB spacing, which is related to the TB density, is an interesting property of REBCO films. Plan-view imaging is useful to estimate the TB spacing. The latter was measured by manual tracing of TBs using *Fiji* for two differently annealed GdBCO films and resulted in similar values of $(43.4 \pm 20.0)\,\text{nm}$ (for the shown film in Fig. 5.21) and $(39.5 \pm 20.4)\,\text{nm}$ (another film, cf. Fig. 5.23a). The values correspond the arithmetic means and standard deviations and around 300 TB distances were analyzed for each sample. The similarity in TB spacing indicates a good reproducibility of the *ex-situ* annealing (at least regarding the TB density). A few isolated defects (or precipitates) are also observed with a similar size as the clustered small precipitates (marked with dashed white circles in Fig. 5.21b). These could be threading dislocations instead of secondary-phase precipitates, which was not clarified here.

The TBs can be unambiguously identified in plan-view TEM samples. However, the conventional FIB preparation results in cross-section samples. Indeed, most of the investigated TEM samples were prepared in a cross-section geometry (i.e. viewed along the GdBCO [1 0 0] or [0 1 0] zone axis) instead of the plan-view geometry (i.e. viewed along the GdBCO *c*-direction). Therefore, a few

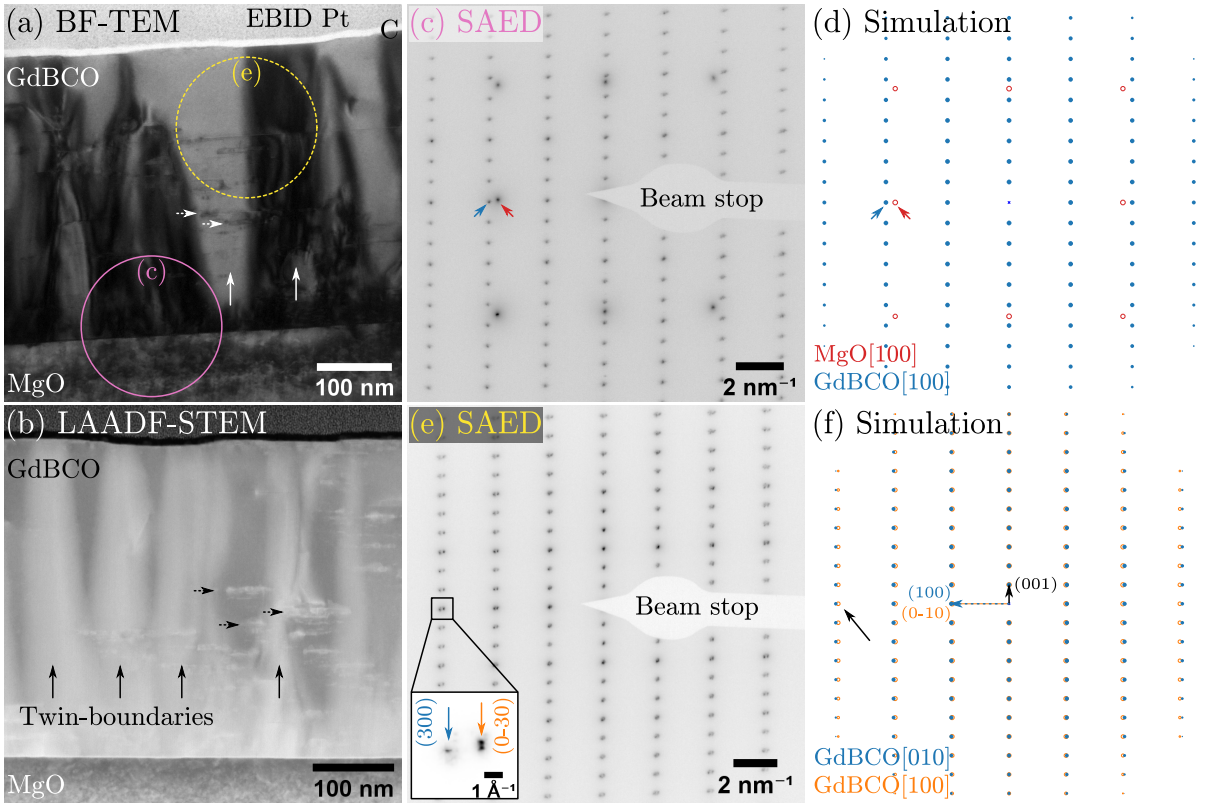

Figure 5.22: Selected-area electron diffraction analyses of PLD-grown GdBCO on MgO. (a) BF-TEM cross-section overview image. The approximate position of the selected-area aperture for the diffraction patterns in (c)/(e) is marked with a solid circle/dashed circle from the GdBCO-MgO interface/a twin-boundary region. Twin boundaries are marked with vertical arrows and small precipitates are marked with dashed arrows. (b) LAADF-STEM image showing twin boundaries (solid arrows) and small precipitates (dashed arrows), similar to (a). Note that two different sample regions are shown in (a) and (b). (c) Experimental and (d) simulated diffraction patterns of the GdBCO-MgO substrate region with the alignment GdBCO[1 0 0](0 0 1)‖MgO[1 0 0](0 0 1). (e) Experimental and (f) simulated diffraction patterns of two adjacent GdBCO grains. Note the splitting of the outer Bragg reflections due to the small difference of the *a*- and *b*-lattice parameters of orthorhombic GdBCO.

TEM analyses were performed on the cross-section TEM samples to identify the TB structures. Figure 5.22 shows an SAED analysis of an annealed GdBCO film on MgO. Diffraction-contrast imaging with (a) BF-TEM or (b) LAADF-STEM reveals the TBs with clear contrast variations (a few examples are marked with vertical arrows). Note that two different sample regions are displayed in Fig. 5.22a and b. Small precipitates are also visible in both imaging modes (marked with dashed arrows). Next, SAED patterns were acquired from the regions marked with circles in Fig. 5.22a, i.e. from the GdBCO-MgO interface (solid pink circle) and a TB (dashed yellow circle). The size of the circles corresponds roughly to the size of the used SAED aperture. The corresponding diffraction patterns are displayed together with simulated diffraction patterns (using the *ReciPro* software [SO22]) for the GdBCO-MgO interface region (Fig. 5.22c and d) and the TB region (Fig. 5.22e and f). A beam stop was used for the experimental diffraction patterns to prevent the undiffracted central beam from damaging the camera sensor. The expected epitaxial relationship GdBCO[1 0 0](0 0 1)‖MgO[1 0 0](0 0 1) is confirmed since the experimental SAED pattern in Fig. 5.22c agrees well with the simulation in Fig. 5.22d. The blue/red arrows mark a ⟨1 0 0⟩-type Bragg reflection of GdBCO/MgO. The significant horizontal offset between the ⟨1 0 0⟩-type Bragg spots is related to the relatively large lattice mismatch (about 7 % to 9 %) between MgO and GdBCO (Table 5.1 on page 158). The SAED pattern acquired at the

TB region (Fig. 5.22e) shows a splitting of the Bragg reflections. The effect is more clearly visible for higher-order Bragg reflections, e.g. GdBCO(3 0 0) (blue) and GdBCO(0 $\overline{3}$ 0) (orange), as shown in the magnified inset. The difference in the horizontal direction is a result of the slightly different lattice parameters a and b. The simulation shows a similar splitting of Bragg reflections (cf. black arrow in Fig. 5.22f). Close inspection of the inset in Fig. 5.22e reveals also splitting of the GdBCO(0 $\overline{3}$ 0) reflection along the vertical [0 0 1] direction. The reason for this is not clear and could (i) result from another structural feature but also (ii) from misalignment of the diffraction-lens focus/stigmator or another microscope parameter. Therefore, this vertical splitting was not further investigated.

To summarize, twin boundaries are an important defect type in REBCO films and are generated during the tetragonal-to-orthorhombic phase transition. The latter aspect was confirmed since the unannealed GdBCO film (mostly tetragonal) did *not* contain TBs, whereas all annealed GdBCO samples (with orthorhombic structure) have TBs. Plan-view TEM-sample preparation gives a good overview over the TB density of a REBCO film and the TB domains. A TB spacing of around (40 ± 20) nm was measured for the *ex-situ* annealed samples.

Analysis of large precipitates (misoriented GdBCO). Different types of precipitates were observed in the GdBCO films besides twin boundaries. This section is dedicated to the large precipitates (cf. blue arrows in Fig. 5.20a and b). The large precipitates grow preferentially along the a- or b-directions of GdBCO (cf. double-headed dashed arrows in Fig. 5.21 on page 183), indicating a syntaxial growth inside the GdBCO film. Most large precipitates are identified as misoriented GdBCO grains, meaning that the c-direction is *not* parallel to the growth direction (or substrate-surface normal). The following shows experimental evidence supporting this conclusion.

STEM-EDXS was applied to the plan-view TEM sample shown in Fig. 5.21 on page 183 to map the elemental distributions of the elements present in GdBCO (Fig. 5.23). The STEM-EDXS datasets were acquired with a TFS Helios G4 FX at 30 keV. The first dataset presented in Fig. 5.23a shows two large precipitates appearing with a higher HAADF-STEM intensity with respect to the surrounding GdBCO matrix (cf. arrows in the HAADF-STEM image and Gd Lα map). The HAADF-STEM overview image also shows smaller, dark precipitates. The TBs are only vaguely visible, running along the diagonal GdBCO$\langle 1\,1\,0 \rangle$ directions. The two bright precipitates marked with the arrows show an increased Gd signal, a Ba/Cu depletion and a nearly unchanged O signal. These two Gd-rich precipitates were the only Gd-rich precipitates in the analyzed STEM-EDXS regions of the TEM sample. This indicates that the Gd-rich precipitates are only sparsely present in the GdBCO films. Their concentration is lower than the large, *ab*-aligned precipitates, as shown in Fig. 5.23b. The Gd-rich precipitates might be Gd_2CuO_4 or Gd_2O_3 [Lee+16]. The Gd_2O_3 phase was detected by XRD but could not be found by TEM in any of the analyzed TEM samples. However, the Gd_2CuO_4 phase cannot be ruled out since it is present as small precipitates (discussed on Page 189). Note that the Cu Lα and O Kα x-rays have energies below 1 keV and are more strongly absorbed in the sample compared to the Ba Lα and Gd Lα x-ray transitions. Cu x-rays are also generated as spurious x-rays stemming from the used Cu TEM grid. The x-ray absorption also causes the elemental-signal gradient along the vertical direction. The TEM sample gets thicker towards the lower parts of the elemental images, causing a depletion of Gd, Ba, O. Cu is less affected because more spurious Cu x-rays are generated from the higher electron scattering into the Cu TEM grid from thicker TEM-sample regions.
STEM-EDXS was also applied to investigate the large, *ab*-aligned precipitates (Fig. 5.23b, see

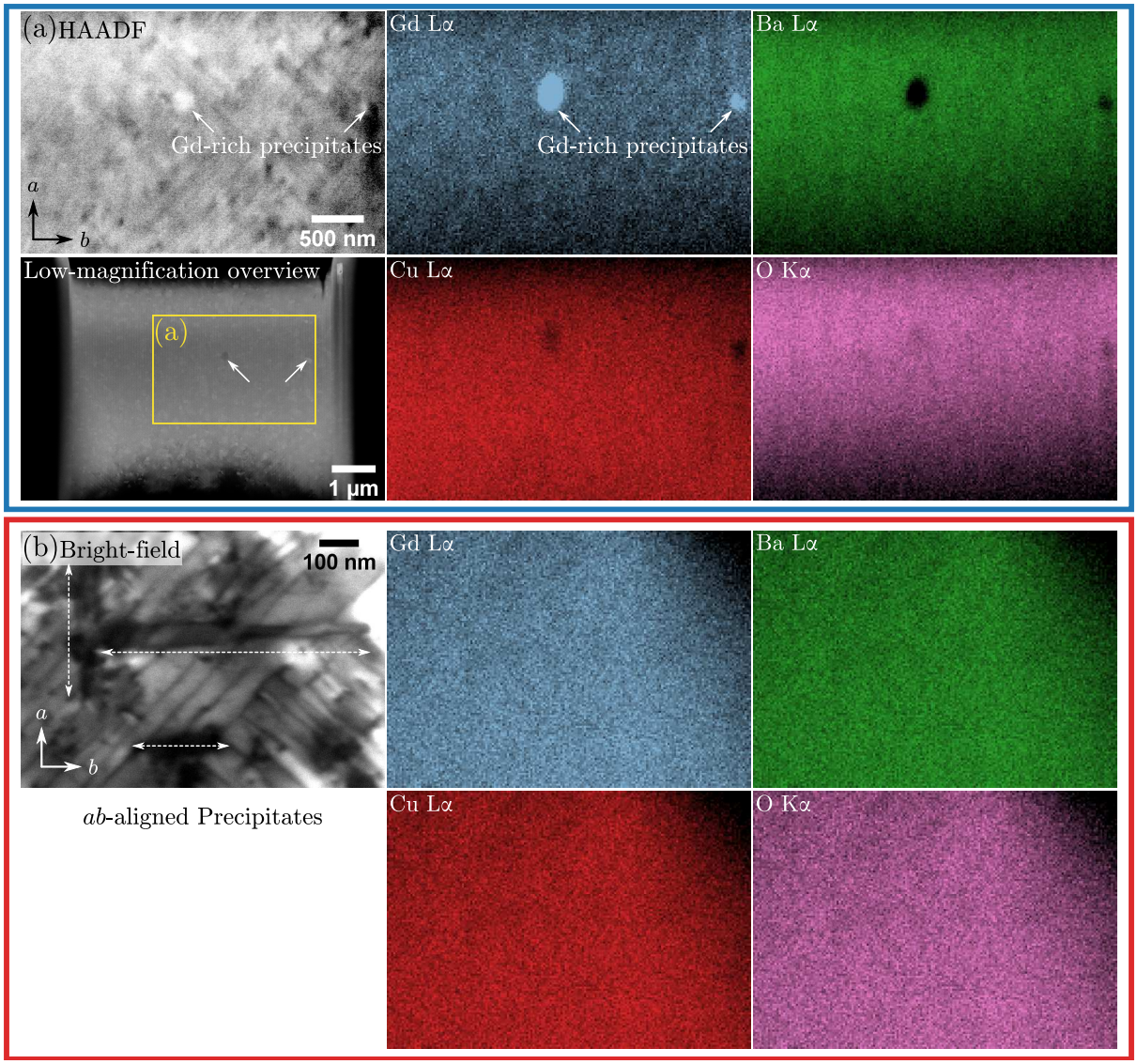

Figure 5.23: STEM-EDXS analysis of precipitates in annealed GdBCO films. (a) 30 keV HAADF-STEM-in-SEM images and corresponding elemental maps. Two large Gd-rich precipitates are observed. The signal gradients along the vertical direction in the elemental maps are caused by TEM-sample thickness variations and the associated x-ray absorption. (b) 30 keV BF-STEM-in-SEM image and elemental maps for a sample region with extended *ab*-aligned precipitates with a dark appearance (marked with dashed double-headed arrows). No change in elemental composition is observed compared to the GdBCO matrix.

dashed double-headed arrows). Note that the same precipitates were already shown in the top-right region in Fig. 5.21a on Page 183. All elemental maps show no visible changes between the large precipitates and the surrounding GdBCO film. This observation indicates the same chemical composition of the large, *ab*-aligned precipitates and the GdBCO film. The difference in the diffraction contrast in the BF-STEM-in-SEM images may arise from a different crystalline orientation of the large precipitates. The top-right region in the elemental maps in Fig. 5.23b shows a vacuum region without any elemental signals.

The results from the STEM-EDXS mapping shown in Fig. 5.23 are now compared to HAADF-STEM cross-section images. In cross-section TEM samples, misoriented GdBCO grains were detected with a similar size and concentration as in plan-view STEM-in-SEM images. A few examples for such misoriented GdBCO grains are presented in Fig. 5.24. Note the indicated

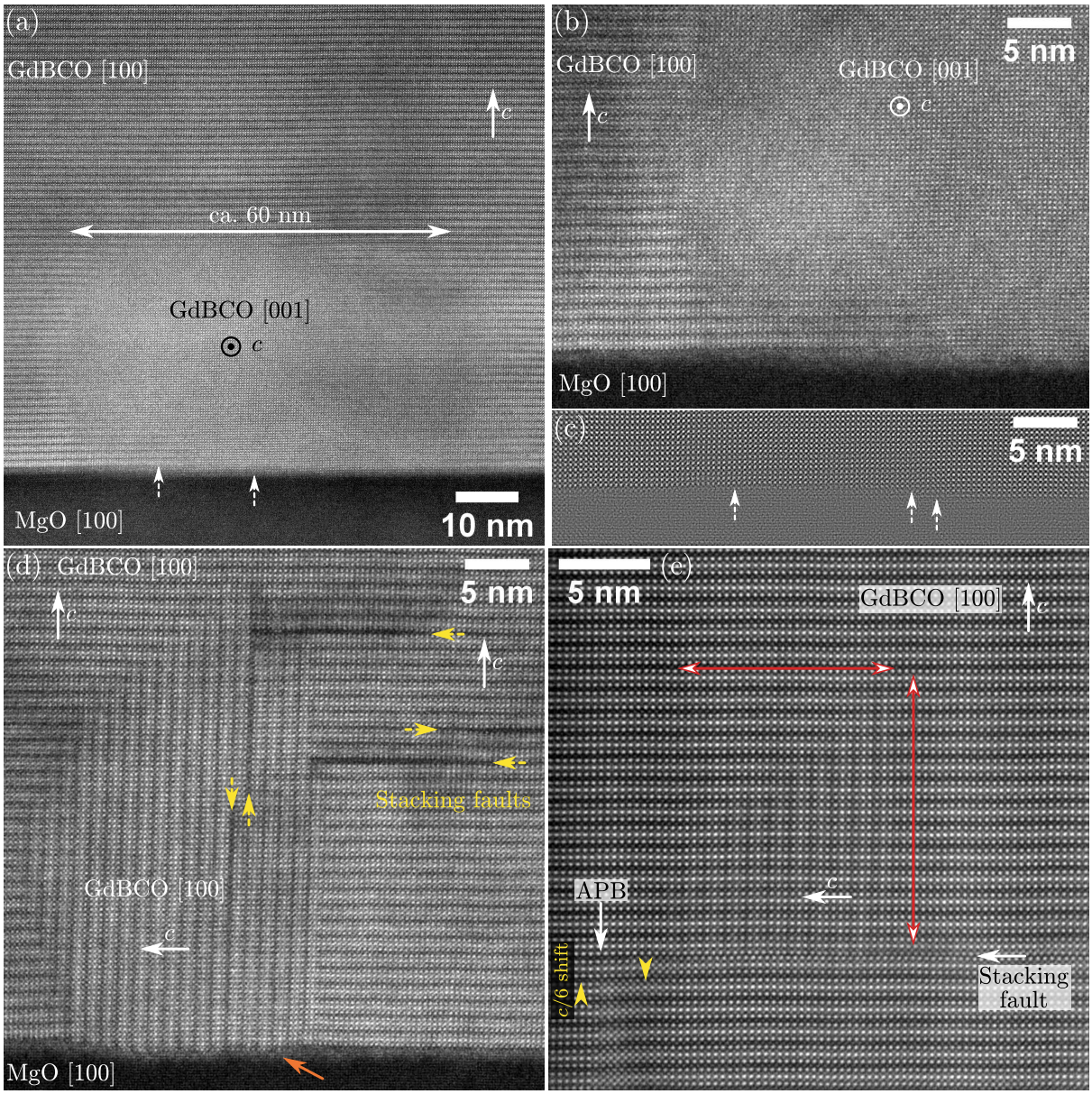

Figure 5.24: HAADF-STEM cross-section images of misoriented GdBCO grains. Note the indicated GdBCO *c*-directions in the images. (a) Overview and (b) higher-magnification images of a $\sim 60\,\text{nm}$ wide misoriented GdBCO grain. The GdBCO-MgO interface of the misoriented grain starts deeper into the MgO region, indicated by dashed arrows in (a). The atomic steps are more clearly visible in the Butterworth-filtered image of the GdBCO-MgO interface in (b) shown in (c). (c) The atomic substrate steps are marked with dashed arrows. (d) Another example for a misoriented GdBCO grain causing associated stacking faults (dashed yellow arrows). The orange arrow highlights GdBCO growth into MgO. (e) A misoriented grain in the GdBCO-layer region. The red double-headed arrows are a guide to see the grain more easily. An antiphase boundary is observed in the lower-left corner, which is annihilated by a stacking fault at the Ba planes.

c-directions in all HAADF-STEM images. The misoriented GdBCO grains have a differing *c*-direction alignment with respect to the biaxially aligned GdBCO film ($c \parallel$ growth direction). These misoriented REBCO regions are also denoted as "*ab*-grains" in the literature, which is also used in the following. Figure 5.24a shows an *ab*-grain with a lateral size of about 60 nm. The growth starts at the GdBCO-MgO interface. Interestingly, the *ab*-grains penetrate deeper into the MgO substrate compared to the GdBCO film (cf. dashed arrows in Fig. 5.24a). For better visualization of this aspect, the lower-left region from the same *ab*-grain is displayed in Fig. 5.24b. High-pass image filtering removes the background signal and reveals the atomic substrate steps between the GdBCO film and *ab*-grains (cf. dashed arrows in Fig. 5.24c). The same effect is also observed for another *ab*-grain shown in Fig. 5.24d. Here, the (0 0 1) plane is parallel to the (1 0 0) or (0 1 0) plane of the film. A few associated stacking faults with an extension of about 10 nm are observed in the surrounding GdBCO film (horizontal dashed arrows) and also in the *ab*-grain (vertical dashed arrows). Again, the *ab*-grain extends further into the MgO substrate region than the surrounding GdBCO film (cf. solid orange arrow in Fig. 5.24d). This effect was also observed in a TEM investigation of YBCO on MgO by Træholt et al. [Træ+94]. They proposed that the *ab*-grains preferentially nucleate at relatively large MgO substrate steps, i.e. "larger steps of a height of 3 MgO unit cells up to several YBCO unit cells" [Træ+94]. The *ab*-growth mode seems to be preferred for such heavily faulted MgO-substrate-surface regions. This effect was also reported by Savvides and Katsaros [SK94], who showed SEM images of *ab*-grains, with similar size and the preferential *a*- or *b*-orientation as observed in the plan-view STEM-in-SEM images (Fig. 5.21 on page 183). The authors also note that "prolonged exposure of polished MgO substrates to the laboratory atmosphere causes a slight surface degradation due to attack by water vapour, i.e. MgO reacts with water to form $Mg(OH)_2$" [SK94]. Substrate-surface degradation leads to more *ab*-grains. The lattice mismatch of the GdBCO *ab*-grains ($\epsilon_{ab} = 7.5\,\%$, using $a_\mathrm{f} = c/3$) is similar to the *a*- and *b*-directions of *c*-oriented GdBCO ($\epsilon_a = 8.9\,\%$, $\epsilon_b = 7.6\,\%$). Here, Eq. (4.10) on page 144 was used with the lattice parameters for GdBCO from the ICSD entry 56 514 (cf. Table 5.2 on page 191) for a_f and $a_\mathrm{s} = 4.214\,\text{Å}$ for MgO.

The *ab*-grains can grow syntaxially inside the GdBCO matrix since the out-of-plane lattice parameter *c* is (in good approximation) an integer multiple of the in-plane lattice parameters $a \approx b \approx c/3$. As a result, the misoriented *ab*-grains can be nicely incorporated into the GdBCO matrix, mostly without forming other defects in GdBCO. An exception to this are the few stacking faults shown in Fig. 5.24d.

Large *ab*-grains were only observed close to the GdBCO-MgO interface. However, smaller *ab*-grains can also form within the GdBCO matrix (Fig. 5.24e). These precipitates are not easily detectable by HAADF-STEM imaging since the small *ab*-grains are embedded in a $\sim 50\,\text{nm}$ thick (or thicker) GdBCO film. Therefore, the *ab*-grain region in Fig. 5.24e is indicated with red double-headed arrows. The small *ab*-grain has the same orientation as the *ab*-grain in Fig. 5.24d, i.e. with the *c*-direction parallel to the in-plane direction of the surrounding GdBCO matrix. A close inspection reveals a "stair-case-like" diagonal shape at the left side of the the *ab*-grain. In the shown example, the *ab*-grain might have nucleated because of a stacking fault (marked by a solid horizontal arrow), which itself resulted from an APB (marked by a solid vertical arrow). Note that the stacking fault here appears at the Ba planes. This stacking-fault type was only observed a few times compared to the commonly observed SFs at the Cu planes. At the APB, a $c/6$ shift along the *c*-direction is observed between the neighboring GdBCO grains (indicated by yellow arrows). The *ab*-grain in Fig. 5.24e demonstrates again that the *ab*-grains can grow syntaxially inside the GdBCO matrix without the formation of associated defects. In addition, it also shows that the *ab*-grains do not only nucleate at substrate steps.

Overall, large precipitates with preferential alignment along the *a*- and *b*-directions were observed for the unannealed and annealed GdBCO films. The precipitates were identified as misoriented GdBCO grains ("*ab*-grains") based on a STEM-EDXS analysis (Fig. 5.23b) and a correlation with HAADF-STEM cross-section images (Fig. 5.24). Most *ab*-grains are located at the GdBCO-MgO interface since they might nucleate at significant substrate steps [Træ+94]. However, small *ab*-grains were also observed in conjunction with other defects in the GdBCO layer. In both cases, the misoriented *ab*-grains grow syntaxially inside the GdBCO matrix without forming many (if any) associated defects.

Analysis of small Gd-rich precipitates. The *large* precipitates shown in Fig. 5.20a and b on Page 182 are identified as misoriented GdBCO grains. However, *small* precipitates are also observed for unannealed and annealed GdBCO films, forming clusters in the annealed films (cf. dashed green circle in Fig. 5.20b). The following shows experimental results related to these small precipitates, which are identified as the Gd_2CuO_4 phase. However, it cannot be ruled out that some these small Gd-rich precipitates are Gd_2O_3 since not all precipitates were investigated with chemical analyses *and* high-resolution HAADF-STEM imaging.

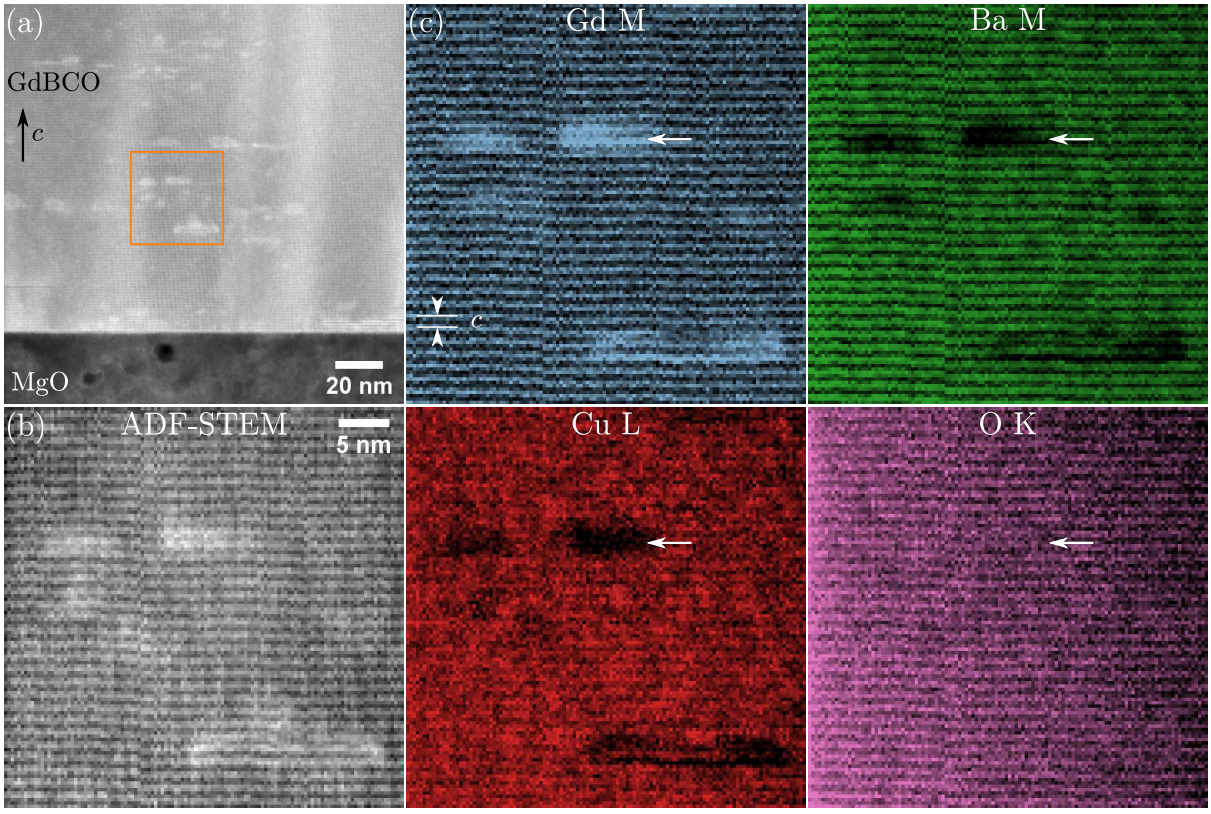

Figure 5.25: STEM-EELS analysis of small Gd-rich precipitates in GdBCO. (a) ADF-STEM cross-section overview image of a GdBCO film on MgO. The STEM-EELS acquisition region is marked with an orange rectangle and displayed in (b). (b) ADF-STEM signal and corresponding (c) elemental maps of the Gd M, Ba M, Cu L, and O K core-loss signals. The Gd-rich precipitates show a Gd enrichment and Ba/Cu depletion compared to the GdBCO matrix.

The small precipitates can be recognized by a cloud-like contrast in cross-section TEM samples (Fig. 5.25a). STEM-EELS was applied to map the spatial distribution of elements in the marked region (orange rectangle). The ADF-STEM signal and the corresponding net-intensity core-loss signals for different elements are shown in Fig. 5.25b and c. The small precipitates show an increased ADF-STEM and Gd signal, and a Ba/Cu depletion. The O signal is nearly unchanged

compared to the surrounding GdBCO matrix. In addition, the small, Gd-rich precipitates show an elongation along the *a*- and *b*-directions, i.e. have a plate-like structure. No stacking faults or other visible defects are introduced into GdBCO by the presence of the small, Gd-rich precipitates. Overall, the STEM-EELS elemental maps in Fig. 5.25 show similar signals trends relative to the GdBCO matrix as the STEM-EDXS mapping in Fig. 5.23a. Therefore, Gd_2CuO_4 and Gd_2O_3 are possible candidates for the small-precipitate phase. Again, the presence of Gd_2O_3 was suspected from preliminary XRD measurements. Indeed, the precipitate marked with an arrow in Fig. 5.25 shows a full Cu depletion, which favors the Cu-free Gd_2O_3 phase in contrast to the Cu-containing Gd_2CuO_4 phase. Still, the latter also has a lower nominal Cu content (14.3 at. %) than the surrounding GdBCO matrix (23.1 at. % for $\delta = 0$), so a Cu depletion relative to GdBCO is also expected for Gd_2CuO_4.

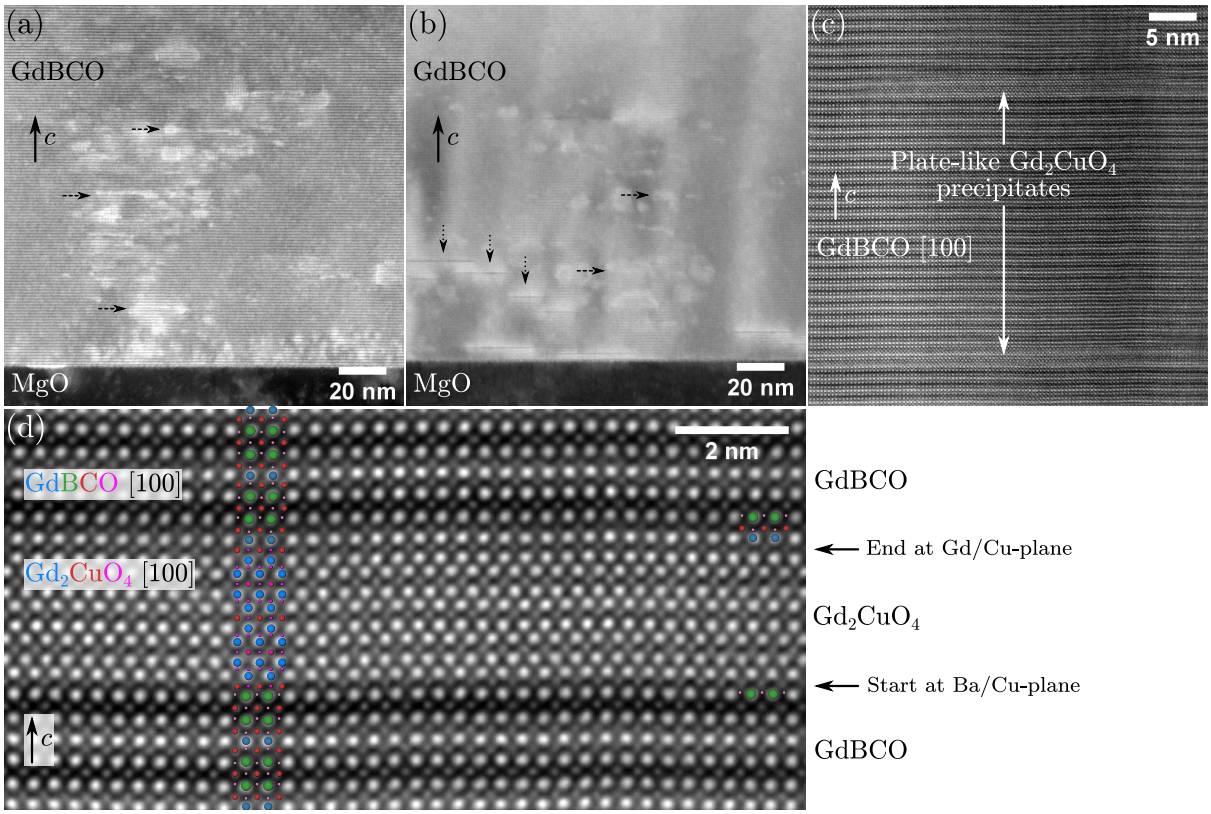

Figure 5.26: Microstructure of Gd_2CuO_4 precipitates in GdBCO films on MgO. Comparison of LAADF-STEM cross-section overview images of GdBCO (a) without oxygenation and (b) after *ex-situ* oxygenation. Cloud-like contrast variations (cf. dashed arrows) are caused by local strain and a higher average atomic number of Gd_2CuO_4 ($\overline{Z} = 27$) than GdBCO ($\overline{Z} = 24.5$, for $\delta = 0$). (b) Stacking faults cause strain in the surrounding GdBCO matrix as visible by the higher LAADF-STEM intensity (marked by dotted vertical lines). (c) Higher-magnification HAADF-STEM image of the annealed sample from (b) showing plate-like Gd_2CuO_4 precipitates growing syntaxially in GdBCO. (d) HAADF-STEM image of the upper precipitate in (c). A structure model is overlaid. Note the different starting (or terminating) atomic planes of Gd_2CuO_4, marked with arrows at the right. The image was denoised and upscaled with *AtomSegNet* [Lin+21].

HAADF-STEM imaging was used to investigate the atomic structure of the small precipitates, ultimately identifying some of them as Gd_2CuO_4 (Fig. 5.26). Figure 5.26a and b compare cross-section LAADF-STEM images for (a) unannealed and (b) annealed GdBCO samples. In both samples, cloud-like contrast variations indicated the presence of small precipitates (cf. horizontal dashed arrows). However, some of the contrast variations may also be caused by other defects, e.g. the strain fields around the SFs in Fig. 5.26b (cf. vertical dotted arrows). Higher-magnification

Table 5.2: Lattice parameters for GdBCO and Gd_2CuO_4.

	$GdBa_2Cu_3O_7$	Gd_2CuO_4	Lattice mismatch
Crystal structure	Orthorhombic	Tetragonal	—
a (Å)	3.8405	3.892	−1.3 %
b (Å)	3.8959	3.892	0.1 %
c (Å)	11.6959	11.878	−1.5 %
$\alpha = \beta = \gamma$	90°	90°	—
ICSD number	56 514	65 015	—

imaging reveals the plate-like shape of the small precipitates, which grow syntaxially and without other defects inside the GdBCO matrix (Fig. 5.26c). The atomic structure in the center of the upper precipitate in Fig. 5.26c is shown in the ABS- and *AtomSegNet*-filtered HAADF-STEM image in Fig. 5.26d. The observed structure agrees well with Gd_2CuO_4 oriented as $Gd_2CuO_4[1\,0\,0](0\,0\,1) \| GdBCO[1\,0\,0](0\,0\,1)$ inside the GdBCO matrix. A structure model is overlaid. The increased HAADF-STEM intensity of the precipitates in Fig. 5.26c can be explained by the higher average atomic number of Gd_2CuO_4 ($\overline{Z} = 27$) than GdBCO ($\overline{Z} = 24.5$, for $\delta = 0$). In LAADF-STEM imaging, the contrast variations are partly caused by the strain field around Gd_2CuO_4. Coming back to Fig. 5.26d, Gd_2CuO_4 growth at the lower side seems to start at the Ba/Cu plane of GdBCO. In contrast, the Gd_2CuO_4 structure ends at a Gd/Cu plane. Gd_2CuO_4 seems to have a vertical extent of two Gd_2CuO_4 unit-cells, as shown by the zigzag stacking of the Gd columns (blue).

The growth of Gd_2CuO_4 was also observed in similar annealing experiments of GdBCO films by Park et al. [Par+18a; Par+18b] and Lee et al. [Lee+16]. In particular, Park et al. [Par+18a] note that the Gd_2CuO_4 phase was not detected by XRD but only by STEM-EDXS. The same effect was observed here since the Gd_2CuO_4 concentration is relatively low compared to the GdBCO phase. As shown by Lee et al. [Lee+16], Gd_2CuO_4 in GdBCO causes a peak close to the GdBCO peaks in XRD, which can be missed for low Gd_2CuO_4 concentrations. This is because the crystal structures of GdBCO and Gd_2CuO_4 are similar (Table 5.2). This similarity may also be the reason that Gd_2CuO_4 precipitates can grow in the GdBCO matrix without causing additional defects such as stacking faults. The mismatch causes elastic strain in GdBCO and Gd_2CuO_4.

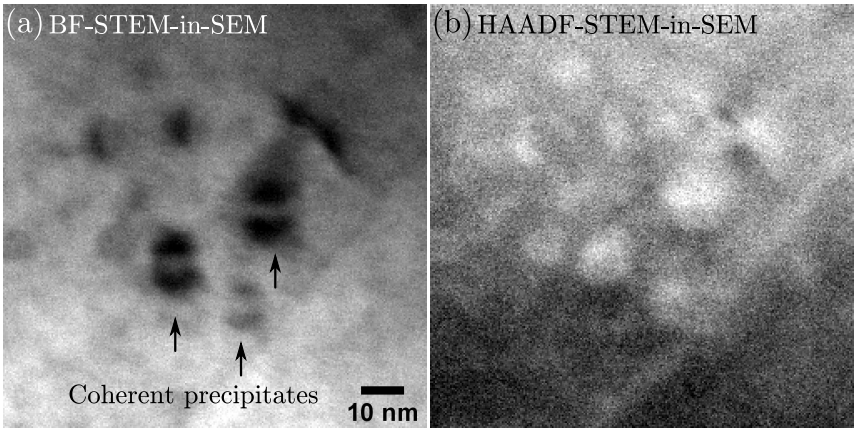

Figure 5.27: 30 keV STEM-in-SEM imaging of Gd_2CuO_4 precipitates. (a) BF- and (b) HAADF-STEM-in-SEM images of precipitates in GdBCO, probably Gd_2CuO_4. (b) The latter show an increased Z-contrast. (a) The precipitates are in a two-beam condition causing a "coffee-bean"-like diffraction contrast as described by Ashby and Brown [AB63b; AB63a].

The associated strain caused by the coherent Gd_2CuO_4 precipitates can be seen in BF-STEM-in-SEM imaging (Fig. 5.27a). Coherent precipitates can show a characteristic contrast change if a TEM sample is oriented in a two-beam condition (marked with arrows in Fig. 5.27a). This causes a "coffee-bean" or "Ashby-Brown" contrast. The latter is named after the authors who described this diffraction contrast in detail [AB63b; AB63a]. The Ashby-Brown contrast is typically assumed for coherent precipitates with a spherical shape and not the plate-like shape as for the Gd_2CuO_4 precipitates. Still, the Ashby-Brown contrast can most likely also arise from such non-spherical coherent precipitates with slightly modified diffraction contrast. Another example of coherent Y_2O_3 particles in YBCO with the same Ashby-Brown contrast was reported by Feldmann et al. [Fel+10] in BF-TEM images under a $\vec{g} = (0, 0, 6)$ two-beam condition. The similarities between BF-TEM and the shown BF-STEM-in-SEM images can be explained by the reciprocity theorem [RK08, p 208]. A parallel illumination in BF-TEM (small convergence angle) corresponds to a small collection angle in STEM (small BF detector, here about $\beta = 9\,\text{mrad}$). Similarly, a the use of a small collection angle with an objective aperture in BF-TEM (more contrast, reduced spatial resolution) corresponds to a small convergence angle in STEM (larger probe size, reduced spatial resolution). In Fig. 5.27, a relatively large convergence angle was used (probably around $\alpha = 10\,\text{mrad}$, not measured) since the immersion mode of the TFS Helios G4 FX was used. Still, the Ashby-Brown contrast is visible, probably due to the relatively small collection angle of the BF detector of the instrument[3].
The BF- and HAADF-STEM-in-SEM images in Fig. 5.27 were acquired near the edge of the TEM sample. The coherent Gd_2CuO_4 precipitates were then accidentally aligned in a favorable imaging condition (near a two-beam condition) so that the Ashby-Brown contrast was observed. However, modern SEMs can be equipped with dedicated cameras, which can be used for sample alignment and subsequent two-beam imaging [Sun+19]. The HAADF-STEM-in-SEM image shows a higher image intensity than the surrounding GdBCO due to a larger average atomic number of Gd_2CuO_4. This aspect further supports evidence that the small precipitates observed in STEM-in-SEM images (Fig. 5.20b on Page 182) are Gd_2CuO_4 precipitates embedded in the GdBCO matrix. However, coherent Gd_2O_3 precipitates cannot be completely ruled out and could also be present in the GdBCO film.
To recapitulate, small, plate-like Gd_2CuO_4 precipitates (and possibly Gd_2O_3 precipitates) with a lateral size of about 5 nm to 30 nm were observed in all GdBCO samples. Gd_2CuO_4 grows coherently inside the GdBCO films and no associated planar defects were observed. This is explained by the structural similarities of GdBCO and Gd_2CuO_4. A discussion of Gd_2CuO_4 in context with the phase diagram of annealed GdBCO can be found in the literature [Par+18a; Par+18b; Lee+16].

Other observations for GdBCO films on MgO. In the following, a few noteworthy observations for the GdBCO films are shown. First, Fig. 5.28a presents an interesting grain boundary observed in the unannealed GdBCO film. Here, the grain on the left side of the image is nicely aligned "on-axis" along GdBCO[1 0 0], which leads to the resolved atomic structure in the HAADF-STEM image. In contrast, the right grain shows a reduced spatial resolution and less image detail. However, the GdBCO plane stacking along the *c*-direction (i.e. the bright Ba-Gd-Ba-Ba-Gd-Ba planes) is still observed. This indicates that the right grain is rotated slightly around the [0 0 1] direction, as indicated by the yellow arrow in Fig. 5.28a. The right grain is then not aligned parallel to the incident electron beam ("off-axis") and the STEM probe cannot channel along the misoriented atomic columns. This ultimately causes the observed loss

[3]The small BF detector is required for BF-STEM-in-SEM lattice-fringe imaging [Ngo+07].

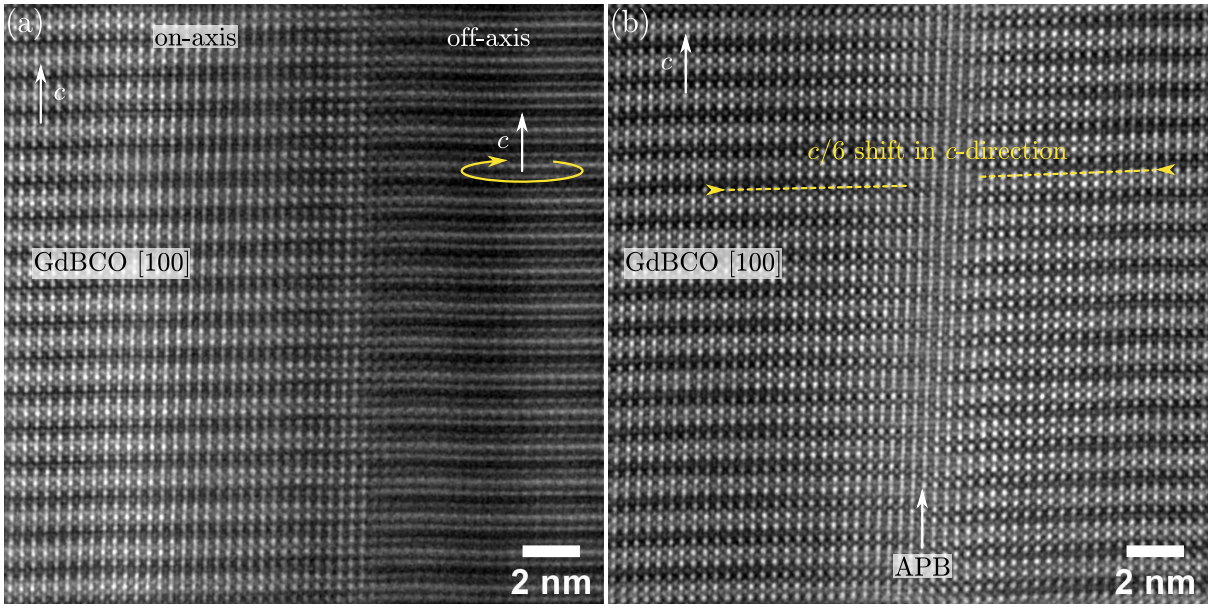

Figure 5.28: HAADF-STEM cross-section images of vertical defects in PLD-grown GdBCO films. (a) Grain boundary between two GdBCO grains, where the left side is parallel to the incident electron-beam (on-axis) and the right side is slightly rotated around the [0 0 1]-axis (off-axis). The latter causes a loss of spatial resolution along the [1 0 0] (or /[0 1 0]) zone-axis. (b) Antiphase boundary (marked by a vertical arrow) causing a $c/6$ shift along the c-direction between the left and right GdBCO grains.

of spatial resolution. Therefore, the grain boundary is probably a [0 0 1]-tilt low-angle grain boundary. Such [0 0 1]-rotated c-oriented grains may be introduced as a result of the relatively large lattice mismatch between GdBCO and MgO [NC92].

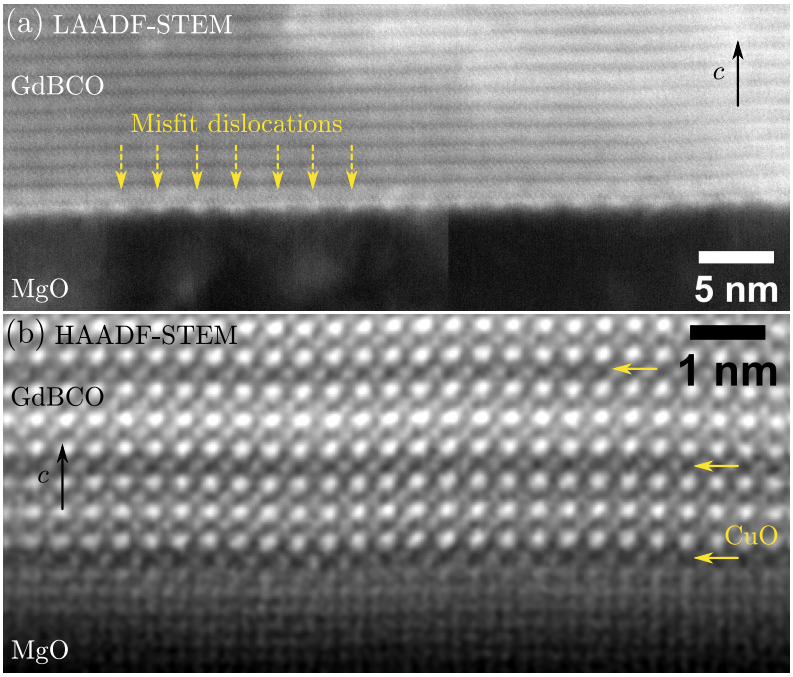

Figure 5.29: Analysis GdBCO-MgO interface. (a) LAADF-STEM diffraction-contrast image showing a periodic intensity modulation (dashed arrows, ∼ 2.4 nm lateral spacing) at the GdBCO-MgO interface resulting from misfit dislocations. (b) HAADF-STEM image showing GdBCO growth starting with a CuO plane (marked by yellow arrows).

The GdBCO-MgO interface is described next. Figure 5.29a shows a LAADF-STEM image with periodic contrast variations along the GdBCO-MgO interface (marked with dashed yellow arrows). This is caused by periodic misfit dislocations, similar to Ba122 growth on MgO (cf. Fig. 4.38 on page 147). HAADF-STEM imaging of the GdBCO-MgO interface reveals

the start of GdBCO growth on MgO with a CuO plane (Fig. 5.29b). This observation is also reported in the literature [Træ+94; ZTW13]. Pennycook et al. [Pen+92] point out that, for YBCO on MgO, the thermodynamically preferred growth mode on MgO(0 0 1) is the observed *c*-oriented REBCO film. However, *ab*-oriented growth is kinematically preferred, e.g. for high supersaturation and substrate-surface roughening. The latter aspect was discussed earlier in context with the large, misoriented *ab*-grains (Fig. 5.24 on page 187).

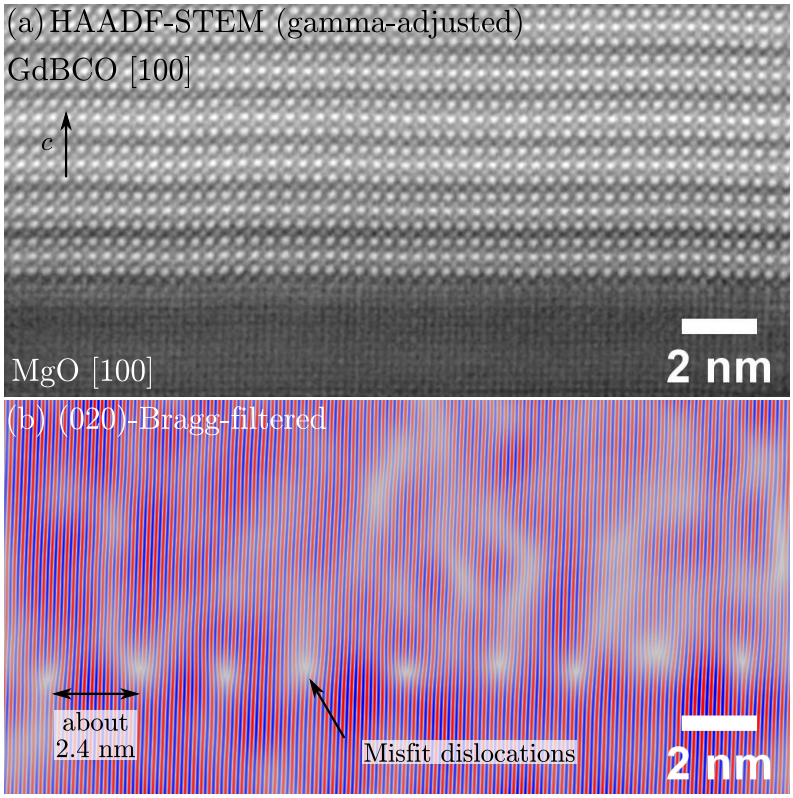

Figure 5.30: Misfit dislocations at the GdBCO-MgO interface. (a) ABS-filtered and gamma-adjusted high-resolution HAADF-STEM image showing the GdBCO-MgO interface. (b) Bragg-filtered image using the GdBCO and MgO(0 2 0) reflections. The misfit dislocations appear white in the color-coded image (here the "phase" lookup table for the image values in *Fiji*).

Figure 5.30a presents another ABS-filtered HAADF-STEM image of the GdBCO-MgO interface. Note that the image intensity was gamma-adjusted for better visibility. Bragg filtering of the (0 2 0)-reflections in the FFT reveals the periodic misfit dislocations at the interface (cf. white regions at the GdBCO-MgO interface in Fig. 5.30b). The misfit dislocations are formed to compensate for the relatively large lattice mismatch between GdBCO and MgO of $\epsilon_a = 8.9\,\%$ and $\epsilon_b = 7.6\,\%$ for the *a*- and *b*-orientations of GdBCO. The measured lateral spacing is about $(2.4 \pm 0.2)\,\mathrm{nm}$, which agrees well with the value observed in the literature [ZTW13; NC92] and the calculated dislocation spacings D based on Eq. (4.11) on page 148 and the observed (projected) Burgers vectors

$$D_a = 2.17\,\mathrm{nm} \quad \text{with} \quad |\vec{b}_a| = a_{\mathrm{GdBCO}}/2 \tag{5.2}$$

$$D_b = 2.58\,\mathrm{nm} \quad \text{with} \quad |\vec{b}_b| = b_{\mathrm{GdBCO}}/2 \quad , \tag{5.3}$$

especially for D_b. Since the D_b value is closer to the experimental value, the GdBCO[1 0 0] zone axis is parallel to the viewing direction and the GdBCO[0 1 0] direction lies in the horizontal direction in the shown LAADF-STEM image in Fig. 5.29a. However, the orientation was not verified with other experimental techniques and the measured values for D might be affected by experimental uncertainties (e.g. length calibration) and residual strain.

Conclusions. In this section, the microstructural changes in PLD-grown GdBCO by an *ex-situ* oxygenation in a tubular furnace were investigated. The annealed GdBCO films have improved superconducting properties compared to the unannealed (and only slightly oxygenated) GdBCO film since the O content after annealing is close to $GdBa_2Cu_3O_7$. As a result of this, the oxygenation process is another crucial step during film fabrication, which influences the film microstructure [Par+18a; Par+18b; Lee+16].
All investigated films show a high-quality, (mostly) *c*-oriented GdBCO film. Almost no stacking faults (i.e. extra CuO planes) are present in the GdBCO films, probably because of the absence of large nanoparticles or (incoherently grown) secondary phases. Therefore, the oxygenation effect on the stacking-fault density cannot be evaluated and compared to the literature [Oh+18; Oh+20]. Extended twin boundaries are only observed for the annealed films, where the tetragonal-to-orthorhombic transitions are fully completed. The effect of the twin boundaries has to be considered regarding the superconducting properties (e.g. for $H \parallel c$ pinning). The TB spacing was evaluated for two different annealed films and somewhat similar, i.e. about (40 ± 20) nm.
A few misoriented *ab*-grains were observed in all films. These may preferentially form on uneven regions of the MgO substrate. These grains may form directly during PLD since the *ab*-grains are observed in annealed and unannealed films. Additional surface treatments of the substrate may enhance the MgO-surface quality prior to PLD, thereby reducing *ab*-GdBCO-grain formation.
In addition, the formation of small Gd-rich precipitates was also observed for all films. Only Gd_2CuO_4 grains could be verified but the presence of Gd_2O_3 precipitates cannot be excluded. In annealed films, a few Gd_2CuO_4 precipitates (about 5 to 15) seem to agglomerate to small clusters locally. The Gd_2CuO_4 precipitates have a good size for flux pinning for high-T (e.g. at 77 K). At low temperatures, Gd_2CuO_4 also becomes superconducting at around 20 K [Mat+08].
Preliminary XRD measurements indicated the formation of Gd_2O_3. However, this phase could not be detected in the TEM samples. There might be the possibility (i) for the formation of rare and relatively large Gd_2O_3 precipitates (Fig. 5.23 on Page 186), (ii) that some of the small precipitates are Gd_2O_3 (full Cu depletion for the marked precipitate inFig. 5.25 on page 189), or (iii) for small Gd_2O_3 surface precipitates (e.g. the triangle-shaped phase in Fig. 5.18e on Page 180). Indeed, the phases of some of the surface precipitates could not be identified here. Low-energy SEM-EDXS was applied without success and the surface precipitates often did not show a difference in signal relative to the underlying GdBCO film. However, further optimization of the SEM-EDXS acquisition parameters may be possible. A test of different sample-cleaning methods would also be beneficial since most of the SEM-EDXS acquisitions were terminated due to excessive C-contamination during the electron-beam bombardment.
Regarding the five annealed GdBCO samples, no significant differences between the microstructures were observed, i.e. large/small precipitates, and TB spacings. However, better statistics in the form of many measured particles or TBs may be necessary to reveal differences between the films. Plan-view TEM-sample preparation enables imaging of large sample areas to achieve good statistics. Additional large-area SEM measurements or a close inspection of the XRD patterns (e.g. regarding peak shapes) may also reveal more differences between the films.

5.4 Characterization of CSD-grown $REBa_2Cu_3O_{7-\delta}$ with $BaHfO_3$ Nanoparticles

This section presents REBCO nanocomposite films grown by chemical solution deposition (CSD). $BaHfO_3$ (BHO) is used as a nanoparticle (NP) material and the NP concentration for all REBCO-BHO nanocomposites is 12 mol %. Section 5.4.1 will present the fabrication of REBCO-BHO films with a mixture of different rare-earth elements (REs) and compares them with single-RE REBCO-BHO films, which are more commonly used. The second subsection (Page 216) presents experimental evidence for a RE-dependent intermixing of REs with the embedded BHO NPs.

5.4.1 Fabrication of Single- and Mixed-Rare-Earth REBCO-$BaHfO_3$ Nanocomposite Films

Previous work. A mixture of different REs in a REBCO film can introduce atomic-scale defects. The latter are commonly seen as the cause for the enhanced pinning capability at low operating temperatures T (and low magnetic fields H) since the coherence length decreases with decreasing T [Mac+06]. A high-quality REBCO film with a mixture of different REs requires a thorough optimization of the fabrication parameters. The mixing of multiple REs was already investigated for REBCO, but mostly for two to three REs [Mac+94; Cay+19; MM00; Cay+18; Jia+13; Cai+05a; Mac+05]. Here, the aim is to create "high-entropy"-type REBCO thin films with at least five different REs [Sar+19]. This concept of high-entropy REBCO compounds was recently applied to bulk REBCO samples [Shu+20; YSM21]. However, no studies are present for epitaxial REBCO films. The formation of a high-entropy-type REBCO film is not easy to achieve experimentally since (i) REs with *larger* ionic radii than Y have an increasing possibility to substitute for Ba in REBCO [Mur+96; Mac+05] and (ii) REs with *smaller* ionic radii than Y leads to increased instability of the REBCO phase due to RE vacancies [Mac+94]. The optimal crystallization temperature for a single-RE REBCO film varies with the RE species for *single* REBCO films [Erb+20]. Therefore, the growth of a REBCO film with several REs requires careful optimization of the fabrication parameters. In addition, the REs might self-assemble in single-RE REBCO clusters instead of forming a homogeneous mixture [Ara+18]. Here, a homogeneous distribution of the REs in the REBCO matrix is desired to create point defects. The optimized fabrication parameters can be used as a starting point by using the *average* fabrication-parameter windows for each RE in the multi-RE mixture. This approach was used to create a high-entropy REBCO film, i.e. (Dy, Gd, Y, Er, Ho)BCO. Three single-RE films and a multi-RE film with only three REs (medium-entropy REBCO) are used as a reference to compare the microstructures. The results in this section are partially found in publications [Cay+ed; Hän+ed], where the superconducting properties are also shown.

Sample fabrication. Different single-RE and multi-RE REBCO films were prepared with CSD as described on Page 54. Two mixed-RE REBCO films (fabricated by **Pablo Cayado**) are analyzed and structurally compared to single-RE REBCO films (fabricated by **Manuela Erbe**). The samples are listed in Table 5.3 with some basic microstructural parameters (substrate, film thickness, and NP size). The sample "5BCO" contains an equal amount of Gd, Dy, Y, Ho, and Er on the RE site and is a high-entropy REBCO film. Two REs with larger (Gd and Dy) and lower (Ho and Er) ionic radius than Y were chosen to get an average RE size around Y. The latter is the RE for the relatively stable YBCO phase. The crystallization for 5BCO was performed at 810 °C for 60 min in oxygen ($p_{O_2} = 50$ ppm). Similarly, three different REs are mixed with equal concentration as sample "3BCO", but with two REs with smaller

Table 5.3: Properties and acronyms of CSD-grown samples shown in this section. The nominal composition of $REBa_2Cu_3O_7$ is 7.7 at. % RE, 15.4 at. % Ba, 23.1 at. % Cu, and 53.8 at. % O. All substrates are (0 0 1)-oriented. The $BaHfO_3$ (BHO) nanoparticle size is given as the average and the standard deviation of the equivalent diameter of the projected particle areas. A pristine ErBCO sample was investigated for comparison with the ErBCO-$BaHfO_3$ nanocomposite film.

Acronym	RE-site composition	Substrate	Thickness (nm)	BHO Size[1] (nm)
5BCO	$(Gd_{0.2}Dy_{0.2}Y_{0.2}Ho_{0.2}Er_{0.2})$[2]	STO	220	24.6 ± 6.9
3BCO	$(Y_{1/3}Ho_{1/3}Er_{1/3})$[3]	STO	350	28.2 ± 9.8
SmBCO	Sm	LAO	220	20.5 ± 7.3
GdBCO	Gd	LAO	190	25.1 ± 9.3
ErBCO	Er	STO	240	21.9 ± 8.2
ErBCO (no BHO)	Er	LAO	160	—

[1] Arithmetic mean and standard deviation.
[2] Corresponding to 1.54 at. % per RE.
[3] Corresponding to 2.57 at. % per RE.

ionic radii (Ho and Er). This sample can be classified as a medium-entropy REBCO film. The crystallization temperature for 3BCO was 790 °C (60 min, $p_{O_2} = 200$ ppm). The other samples are "conventional" CSD-grown REBCO films with a single RE. The crystallization temperatures and oxygen pressures were (830 °C, $p_{O_2} = 150$ ppm) for SmBCO, (810 °C, $p_{O_2} = 50$ ppm) for GdBCO, and (780 °C, $p_{O_2} = 150$ ppm) for ErBCO. A BHO concentration of 12 mol % is added to most REBCO film, i.e. a mixed composition $(REBCO)_{0.88}(BHO)_{0.12}$ [Cay+17; Erb+15]. A pristine ErBCO sample without BHO was also investigated. The substrates $LaAlO_3$(0 0 1) (LAO) and $SrTiO_3$(0 0 1) (STO) were used.

Experimental Results. A general overview of the representative microstructure for all five samples containing BHO nanoparticles is shown in Fig. 5.31. The cross-section LAADF-STEM images show the successful growth of high-quality REBCO films in all cases. The left column shows a low-magnification overview, whereas the right column shows a randomly selected 80 nm × 80 nm region (marked by red squares in the overview images). The TEM sample of 3BCO showed some pores (Fig. 5.31b). The presence of pores might result from sample fabrication (e.g. a problem during spin coating). The pores can explain the increased film thickness of 3BCO compared to the other films. However, the performance of 3BCO was not significantly affected by the pores since it showed the highest J_c from all films at low temperatures (30 K) and medium magnetic fields (3 T), i.e. $J_c = 5.7\,\mathrm{MAcm^{-2}}$ (3BCO) vs. $J_c = 4.1\,\mathrm{MAcm^{-2}}$ (5BCO) vs. $J_c = 3.7\,\mathrm{MAcm^{-2}}$ (GdBCO). The GdBCO sample, Fig. 5.31c, was slightly damaged during FIB-milling, resulting in a dark (amorphous) REBCO film close to the film's surface.
The BHO nanoparticles have a diameter of about 20 nm to 28 nm and appear primarily dark in the shown images. The NPs are mostly randomly oriented in the REBCO matrix. Sometimes, crystalline facets are visible. These random crystalline alignments cause contrast variations of BHO nanoparticles in the LAADF-STEM images. An important observation is that BHO NPs that nucleated directly at the film-substrate interface often appear bright instead of dark in LAADF-STEM images (cf. right image in Fig. 5.31e). This is caused by the syntaxial alignment of BHO with the substrate, e.g. here BHO[1 0 0](0 0 1)‖STO[1 0 0](0 0 1). The low-index zone-axis alignment of BHO causes enhanced Bragg scattering. The signal of these Bragg-scattered electrons is mainly collected by the LAADF-STEM detector, resulting in a high LAADF-STEM

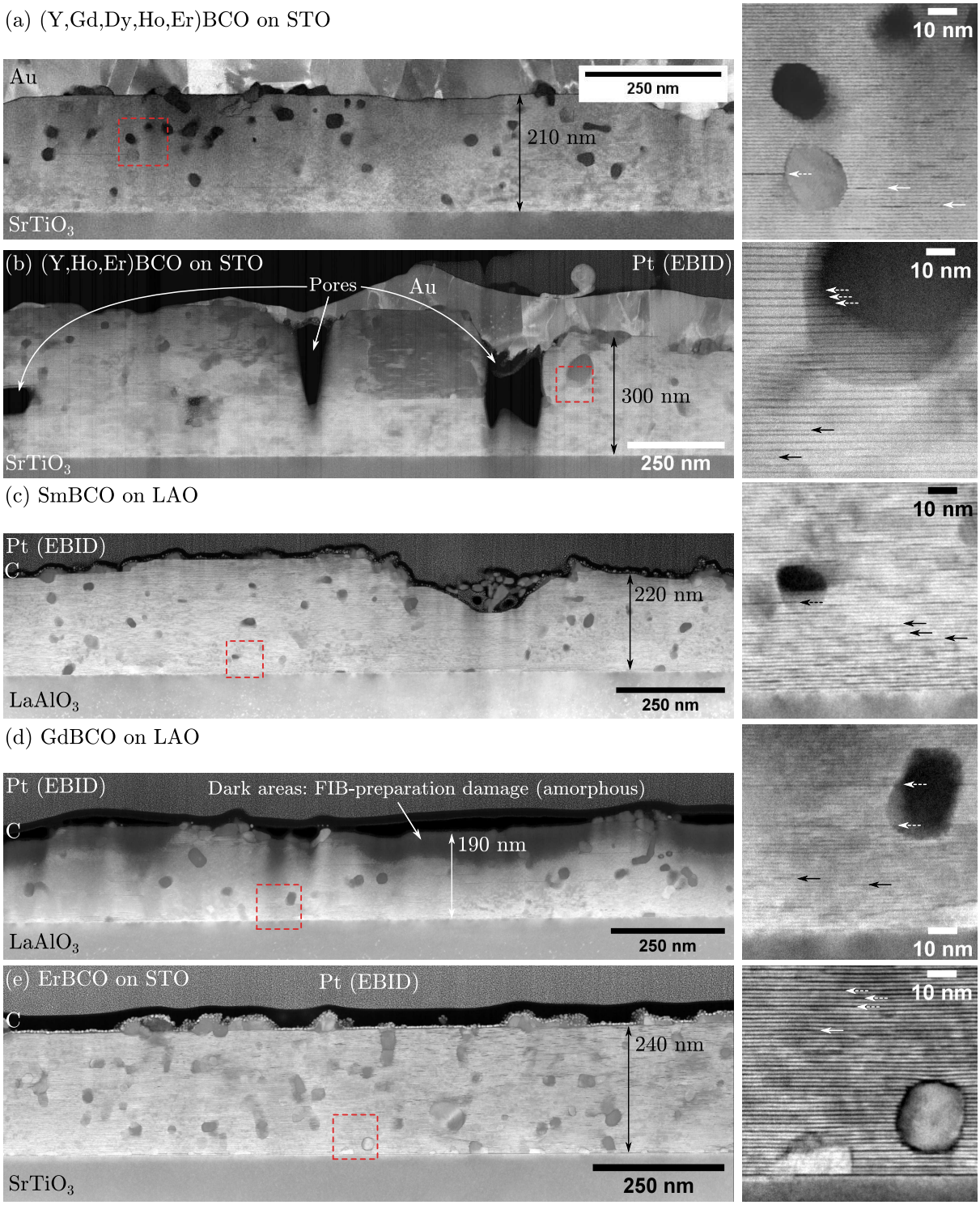

Figure 5.31: LAADF-STEM cross-section overview images of CSD-grown REBCO films. Left column: Low-magnification overview images. $BaHfO_3$ nanoparticles appear primarily dark in the films and bright at the film-substrate interface. (b) Pores are visible for 3BCO, and (d) the TEM sample of GdBCO is partly damaged by FIB-sample preparation (dark regions). Right column: Magnified regions from the marked areas in the left column. Short (solid arrows) and extended planar defects (dashed arrows) are observed in varying concentrations.

intensity of syntaxially aligned BHO[4]. The Au layers on top of the 5BCO and 3BCO films are deposited with PLD and ensure good electrical conductivity for electrical measurements.
The magnified views on the microstructures (right column inFig. 5.31) reveal apparent differences between the films. Two types of planar defects are observed, i.e. short (solid arrows) and extended planar defects (dashed arrows). Both planar-defect types were discussed in Section 5.2 on page 159. The BHO particles generate extended SFs in the REBCO films. Here, BHO NPs cause strain in the surrounding REBCO lattice planes and SFs relieve this strain. The SFs can then mainly act as pinning centers for $H \parallel ab$. The short planar defects are probably caused by TEM-sample degradation in air, even though all shown TEM samples were directly investigated by TEM after FIB preparation. The films with high Er concentrations (3BCO and ErBCO) show a significantly higher density of extended planar defects (or stacking faults, SFs). This suggests the presence of RE124 and RE247 phases in these samples (cf. Fig. 5.1 on page 156). A reason might be the incorporation of Er into BHO, as discussed in Section 5.4.2 on page 216. However, the pores in 3BCO might also lead to the formation of SFs. In contrast, 5BCO and GdBCO show a low concentration of SFs and a few short planar defects. SmBCO lies in-between and shows a relatively high density of short planar defects.
The REBCO-LAO interface shows significant LAADF-STEM contrast variations, whereas the REBCO-STO interface is relatively homogeneous. This is probably caused by strain fields arising from crystalline defects at the REBCO-LAO interface. Interestingly, LAO ($\epsilon_a = -0.9\,\%$ and $\epsilon_b = -2.6\,\%$) has similar absolute values as STO ($\epsilon_a = 2.2\,\%$ and $\epsilon_b = 0.5\,\%$) regarding the lattice mismatch to the a- and b-lattice parameters. However, LAO introduces tensile strain (a negative sign of ϵ), whereas STO leads to compressive strain. Furthermore, the a- and b-directions in REBCO are not equal regarding defect formation. For example, SFs introduce a $b/2$-shift. As a result, the lattice mismatch for a and b are important for REBCO films.

STEM-EDXS was used to map the chemical composition of the films and the elemental maps for SmBCO are displayed in Fig. 5.32. The Sm and Cu signals reveal the SmBCO layer. Ba is present in similar elemental concentrations in BHO (20 at. %) and SmBCO (15.4 at. %) and shows a nearly homogeneous signal for both phases. The Hf signal reveals the location of the BHO NPs in the SmBCO film. Note that the Hf Lα x-ray transitions can also be used but must be separated from Cu Lα with MLLS fitting (this peak overlap and the fitting method are presented in Fig. 5.46d on Page 218). The elemental maps for the other REBCO films showed similar features and are omitted here for brevity. In all cases, a homogeneous distribution of BHO nanoparticles was observed in the REBCO matrix, confirming the initial observation by LAADF-STEM imaging (Fig. 5.31).
The NP concentration was approximated using Eq. (4.4) on page 130. Ba is present in both materials, the Cu signal may be falsely increased by spurious x-rays, and the O concentration is prone to errors due to x-ray absorption. Therefore, the NP concentration is calculated as

$$r = \frac{C_{\mathrm{Hf}}}{C_{\mathrm{Hf}} + \sum_{\mathrm{RE}} C_{\mathrm{RE}}} \quad , \tag{5.4}$$

and yields values close to the nominal value (12 mol %) for all REBCO films. The measured NP concentrations are displayed in Fig. 5.33 in the top-right corner of the Hf maps, i.e. (12.5 ± 1.5) mol % for the 5BCO-, (14.1 ± 1.8) mol % for the 3BCO-, (11.8 ± 1.6) mol % for the SmBCO-, (11.8 ± 1.6) mol % for the GdBCO-, and (12.3 ± 1.6) mol % for the ErBCO-BHO nanocomposites.

[4]Another way to image the NPs with more uniform contrast is to tilt the TEM sample away from a low-index zone-axis orientation and to use the chemical sensitivity of the HAADF-STEM signal.

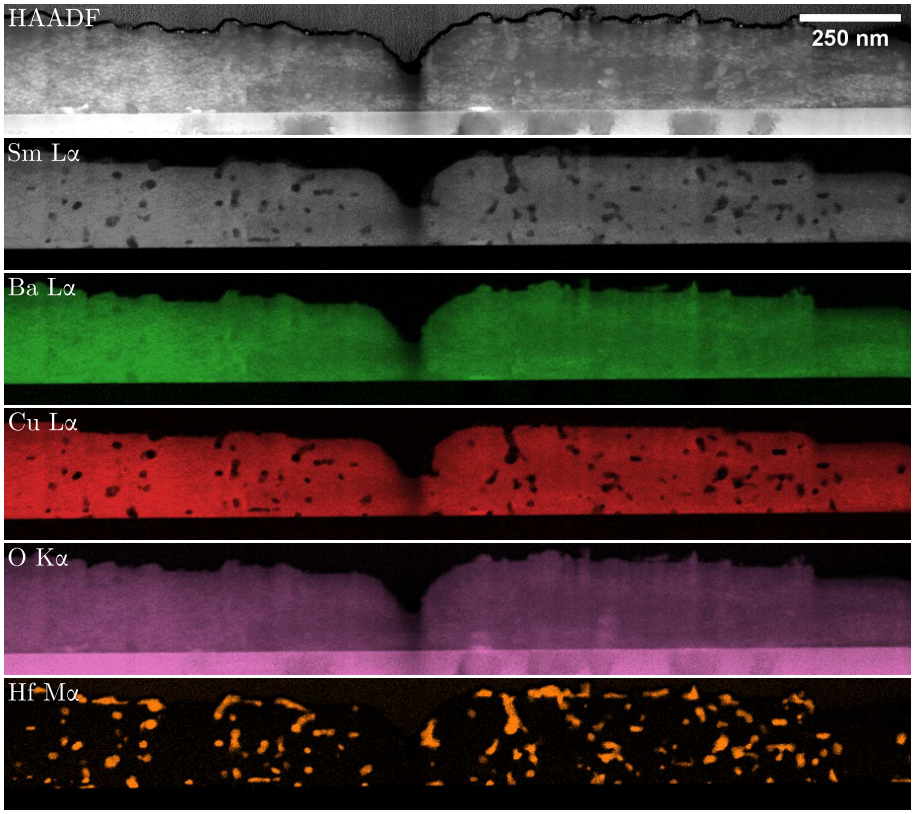

Figure 5.32: Qualitative STEM-EDXS elemental maps for SmBCO with 12 mol % $BaHfO_3$ nanoparticles. The Sm and Cu signals indicate the SmBCO film and Hf identifies the $BaHfO_3$ nanoparticles. The latter are homogeneously distributed in the SmBCO matrix. Ba is present in SmBCO and $BaHfO_3$.

The error values for r are propagated from the errors on the quantified elemental concentrations C_x (one standard deviation) resulting from the Cliff-Lorimer quantification in the Bruker *Esprit* software. The 3BCO-BHO film shows a slightly increased BHO concentration, for which the reason is not clear.

Besides the NP concentration, Fig. 5.33 presents RE and Hf elemental maps for the mixed-RE (a) 5BCO, (b) 3BCO, and single-RE REBCO films (c) SmBCO, (d) GdBCO, and (e) ErBCO. The maps were chosen to visualize the distribution and shape of the BHO NPs in the films. Note that the left half of the ErBCO map was acquired at a slightly thicker TEM sample region and, therefore, shows a significantly higher BHO concentration than SmBCO and GdBCO. This is an artifact since more BHO NP are viewed in projection in a thicker TEM sample. The morphology of the BHO NPs is different in the three samples (cf. right half in the Hf map in Fig. 5.33). Smaller BHO NPs are observed for ErBCO and SmBCO compared to GdBCO. This may be caused by different growth conditions since each single-RE REBCO film was fabricated with an optimized crystallization temperature for the specific RE [Erb+20]. The differences in these temperatures might affect the growth kinetics and coarsening of the BHO NPs. A single temperature cannot guarantee a high-quality REBCO film for different REs, therefore the NP size and shape are mostly fixed by the growth conditions of the REBCO matrix. The BHO NPs are partly located at the film surfaces, where they do not influence the film microstructure.
The formation of Er-rich precipitates is observed in the Er map for ErBCO (cf. arrows in Fig. 5.33e). The EDXS spectra from Er-rich areas were summed and a quantification of the elemental concentrations (not shown) suggest the Er_2O_3 phase for these precipitates[5]. In addition, no Er depletion is observed in the BHO regions in the Er map. Er is partly incorporated into the

[5]The quantified concentrations were (32±8) at. % Er, (1.4±0.3) at. % Ba, (2.4±0.3) at. % Cu, and (64.3±0.5) at. % O. Er_2O_3 contains 40 at. % Er and 60 at. % O and lies within the experimental error of standardless EDXS quantification.

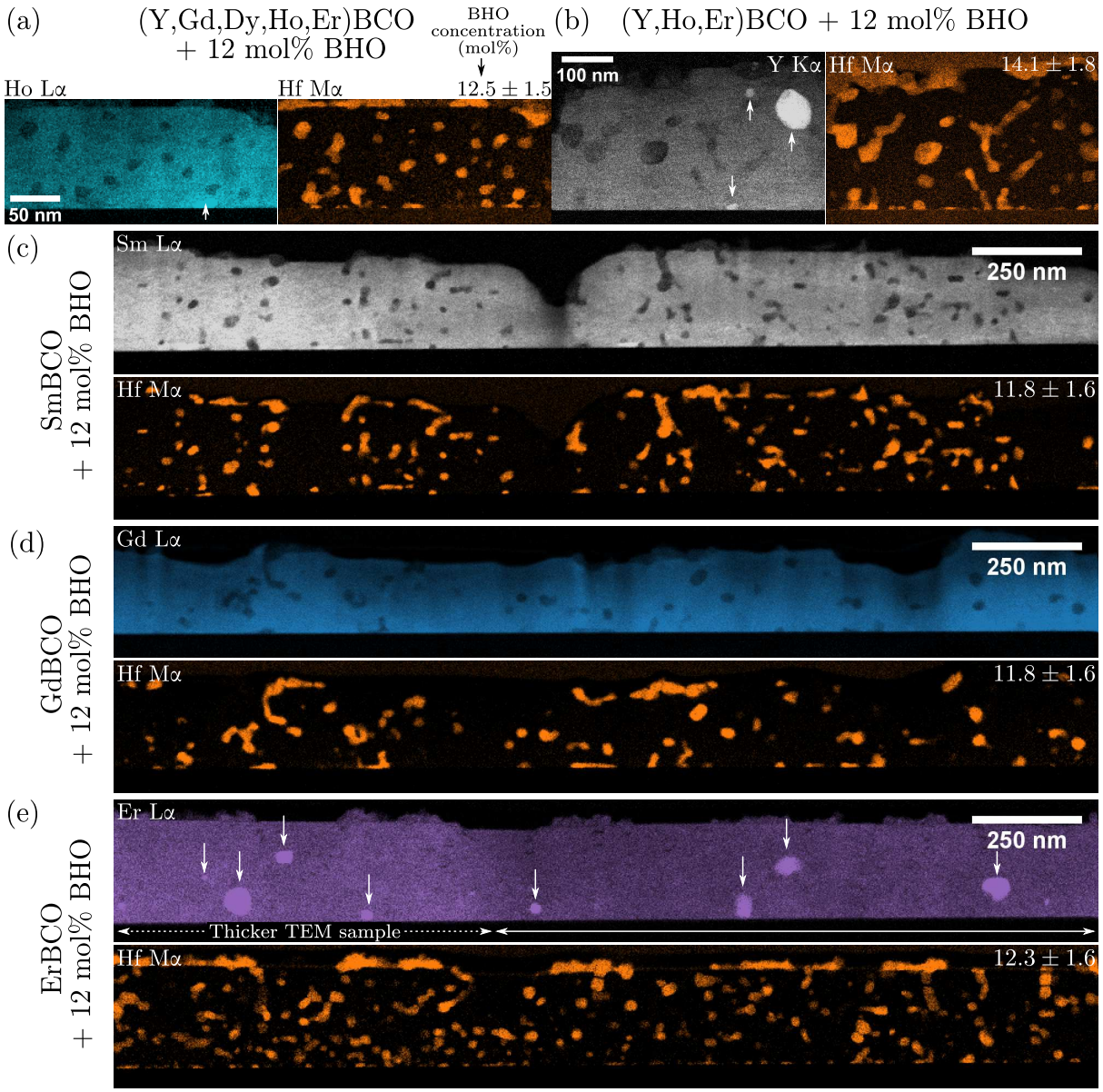

Figure 5.33: $BaHfO_3$ distribution in single-rare-earth REBCO films. STEM-EDXS elemental maps of the REs and Hf for (a) 5BCO, (b) 3BCO, (c) SmBCO, (d) GdBCO, and (e) ErBCO. The Ho Lα and Y Kα signals were arbitrarily chosen for 5BCO and 3BCO to visualize the RE distribution. The right side for the three single-RE TEM samples had a similar TEM-sample thickness and are comparable. The formation of RE_2O_3 (cf. arrows) is observed for 5BCO, 3BCO, and ErBCO. In addition, the Er signal near BHO is nearly unchanged for ErBCO compared to the RE maps for SmBCO and GdBCO.

BHO (more so than, e.g., Sm or Gd), which will be investigated in more detail in Section 5.4.2 on page 216. The representative LAADF-STEM images (Fig. 5.31) and STEM-EDXS mappings show the successful growth of high-quality REBCO films with different REs.

Another ErBCO film without BHO NPs (a "pristine" ErBCO film) was analyzed to directly compare it with the ErBCO-BHO nanocomposite film. The main microstructural differences are shown in Fig. 5.34. Low-magnification LAADF-STEM images of (a) a pristine ErBCO and (b) an ErBCO-BHO film show distinct differences in twin-boundary formation. Extended twin boundaries appear as vertical structures in LAADF-STEM images along the ErBCO[1 0 0] (or [0 1 0]) zone-axis orientation (marked by arrows in Fig. 5.34a). Two larger Er_2O_3 precipitates are also visible in this TEM sample (dashed arrows). These precipitates disrupt the "coherence" of

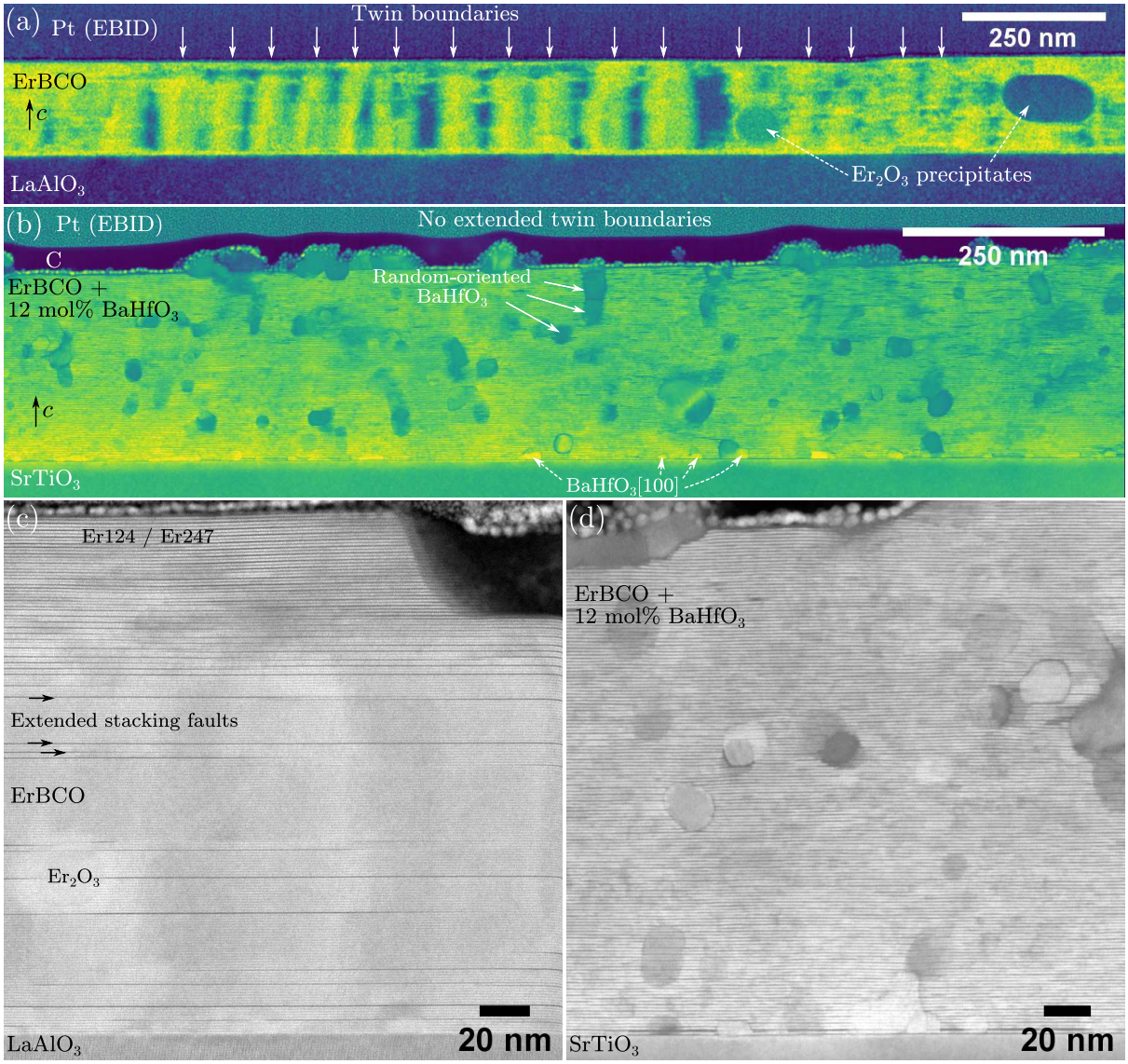

Figure 5.34: Comparison of pristine (a,c) ErBCO and (b,d) ErBCO-$BaHfO_3$ films. (a and b) Representative color-coded LAADF-STEM cross-section image of (a) a pristine ErBCO and (b) an ErBCO-BHO films. The presence of nanoparticles (Er_2O_3 and BHO) disrupts the ordered twin-boundary arrangement. (c and d) HAADF-STEM image of the microstructure revealing a significantly higher stacking-fault density for the ErBCO-BHO film. (d) Some of the short stacking faults may result from TEM-sample degradation in air. (c) A high density of extended stacking faults (marked with arrows) close to the pristine ErBCO film's surface leads to the formation of Er124 and Er247.

the twin boundaries, i.e. the ordered and uninterrupted of twin boundaries along the *c*-direction, so that the columnar shape of the adjacent twin boundaries is not as clearly resolved in the right part of the image compared with the left part. This phenomenon can be extended to the ErBCO-BHO nanocomposite. Here, the density of nanoparticles (BHO or Er_2O_3) is high and the twin-boundary coherence is fully disrupted (Fig. 5.34b) so that no vertical-defect structures are visible in the LAADF-STEM images. These results are in agreement with the literature [Guz+13; Rou+14; De +16; Díe+20]. As discussed before, the BHO NPs in BHO[1 0 0](0 0 1)‖STO[1 0 0](0 0 1) orientation at the film-substrate interface (marked by dashed arrows) appear bright in LAADF-STEM image compared to the random-oriented BHO NPs (solid arrows) in the rest of the ErBCO film.

Higher-magnification HAADF-STEM images (Fig. 5.34c and d) show an increased density of

stacking faults for the ErBCO-BHO nanocomposite. This is partly caused by the presence of BHO. Regarding pristine ErBCO (Fig. 5.34c), mainly extended SFs are observed, especially close to the substrate surface. Here, the SF density is high, leading to the formation of the Er124 and Er247 phases (cf. Fig. 5.1 on page 156).
The SF density in the TEM sample of the ErBCO-BHO film is remarkably higher than in the GdBCO- and SmBCO-BHO nanocomposites (cf. Fig. 5.31 on page 198). The extra SFs in ErBCO might be caused by the increased formation of Er_2O_3 and possibly also a loss of Er into BHO. The latter aspect is discussed in Section 5.4.2 on page 216. A loss of Er into BHO should result in a precipitation of the residual elements Cu, O, and Ba (assuming a stoichiometric ErBCO mixture). Cu and O might form the observed extended SFs. However, no accompanying Ba-rich phases were detected.
The high density of short SFs could also result from a rapid TEM-sample degradation. Zandbergen [Zan92] note that the formation of 124- and 125-type defects depend on the RE and the value of δ in $REBa_2Cu_3O_{7-\delta}$ compounds. It is noteworthy that – regarding the short SFs – they found "hardly any of the $ErBa_2Cu_3O_7$ compound" [Zan92], which is in stark contrast to the observed microstructures here. The CSD-grown films might be contaminated by residual chemicals, even after pyrolysis. All CSD-grown films showed a F signal in STEM-EDXS (not shown) and approximately a 1:1 ratio of F:REs was quantified for the CSD-grown films. However, if and how the residual F contamination affects the formation of SF was not investigated in more detail.

RE distribution in multi-RE REBCO films. Next, the distribution of REs in the multi-RE REBCO films 5BCO and 3BCO is discussed. A homogeneous mixture is desired here for the 5BCO and 3BCO samples (instead of clustered single-RE REBCO regions [Ara+18]) to create atomic-scale disturbances in the REBCO film for efficient low-T pinning. This formation of high- (5BCO) and medium-entropy (3BCO) REBCO-BHO nanocomposite films was achieved with the CSD method, as shown in the following.

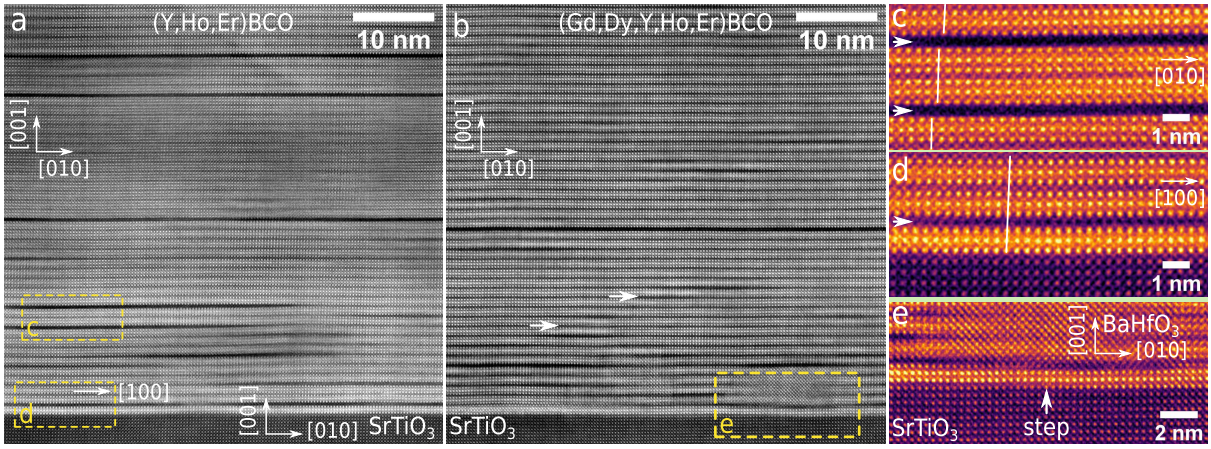

Figure 5.35: HAADF-STEM images of (a) (Y,Ho,Er)BCO and (b) (Gd,Dy,Y,Ho,Er)BCO. Extended stacking faults are visible as dark horizontal lines. Some short nanoscale planar defects are marked by arrows in (b). The right column shows magnified, color-coded images from the region marked in (a) and (b). (c and d) The switch of symmetries from (c) glide to (d) mirror symmetry indicates a change in REBCO orientation along the growth direction (i.e. c-direction). (e) A $BaHfO_3$ precipitate close to the REBCO-$SrTiO_3$ interface and a substrate step. This figure is published [Cay+ed].

Figure 5.35a and b show ABS-filtered HAADF-STEM images of 3BCO and 5BCO viewed along the REBCO$\langle 1\,0\,0\rangle$ orientations. High-quality REBCO films are observed for both samples. The dark lines are extended SFs, introduced mainly by the embedded BHO NPs. A few areas show

the formation of short SFs (marked by arrows in Fig. 5.35b), probably resulting from the short exposure of the TEM sample to air during TEM-sample transfer. The right column displays color-coded, magnified images of the regions marked in Figure 5.35a and b. The orientation of the REBCO unit cell can switch between [1 0 0] and [0 1 0] as shown by comparing the SF symmetries, i.e. zigzag or cube-on-cube alignment (cf. Fig. 5.35c and d, the vertical lines are a guide for the eye). The REBCO orientations are marked in the images. This switching of [1 0 0]- and [0 1 0]-directions along the [0 0 1]-direction (growth direction) agrees with the literature [Rou+14; Gaz+16; Zha+13; Pal+18; Pin+20].
A BHO NP is observed at the 5BCO-STO interface (Fig. 5.35e, magnified from the marked region in b). In addition, an atomic step of the STO substrate with a step height a_{STO} is located below the BHO precipitate (marked by an arrow). Such substrate steps do not lead to extended antiphase boundaries in the REBCO film and are quickly annihilated by a stacking fault. The "resistance" of REBCO to STO-substrate steps might be related to a possible formation of cubic REBCO (with a perovskite structure) directly at the REBCO-STO interface. Haage et al. [Haa+98] showed evidence for nucleation of the cubic YBCO phase on STO. The growth switches to the superconducting YBCO phase after one monolayer or full coverage of the STO surface. The possibility for REBCO to form a cubic structure with $a = c/3 \approx 0.3987\,\mathrm{nm}$ [ACB91] can account for the step height of $a_{\mathrm{STO}} = 0.3905\,\mathrm{nm}$ of STO.

The distribution of REs in the mixed-RE films 3BCO and 5BCO was analyzed qualitatively by HAADF-STEM (Fig. 5.36) and high-resolution STEM-EDXS (Fig. 5.37). Both methods show a homogeneous distribution of REs in 3BCO and 5BCO without forming RE clusters. The HAADF-STEM analysis is discussed first. The chemical sensitivity of HAADF-STEM Z-contrast imaging enables the comparison of the RE atomic-column intensity for different REBCO films. Figure 5.36 is split into three columns, which show the analysis for GdBCO (left, used as a reference), 3BCO (center), and 5BCO (right). The first row presents the as-acquired HAADF-STEM images with the analyzed region marked with yellow dashed squares. Background-intensity modulations resulting from TEM-sample contamination and residual TEM-sample imperfections from FIB milling are mostly removed in the extracted region (middle row in Fig. 5.36). The background model for subtraction was generated with an anisotropic-diffusion filter in *Fiji*, i.e. the same procedure used as for the background-subtracted ABS-filtering (cf. Fig. 3.9 on page 70). The HAADF-STEM intensity is then integrated along the [0 0 1] direction to calculate HAADF-STEM-intensity line profiles (bottom row). The line-profile width (i.e. perpendicular to the c-direction) was chosen nearly as the total image width (see dashed areas in Fig. 5.36d–f) of the extracted regions to maximize the signal-to-noise ratio. In contrast, only the left half of the image was used for GdBCO due to a significant shift of the REBCO structure in the [0 0 1] direction caused by sample drift during STEM-image acquisition (Fig. 5.36d).
The extracted HAADF-STEM-intensity line profiles along the [0 0 1] direction were normalized with the maximum intensity value in each line profile for easier comparison and are shown in Fig. 5.36g–i. Note that the plotted line-profile directions are 90° rotated with respect to the directions shown in the middle row. The line profiles show three major intensity levels resulting from the atomic columns of REs (blue), Ba (green), and Cu (red). O with its low atomic number $Z = 8$ is not visible in HAADF-STEM imaging in combination with heavier elements since the dynamic range of the HAADF-STEM detector does not cover such a significant intensity difference. The contributions of O to the laterally-averaged line profiles are neglected in the following discussion. The peak positions and intensities for each line profile were extracted and the horizontal lines mark the average peak-intensity values. The standard error (cf. Page 90) is

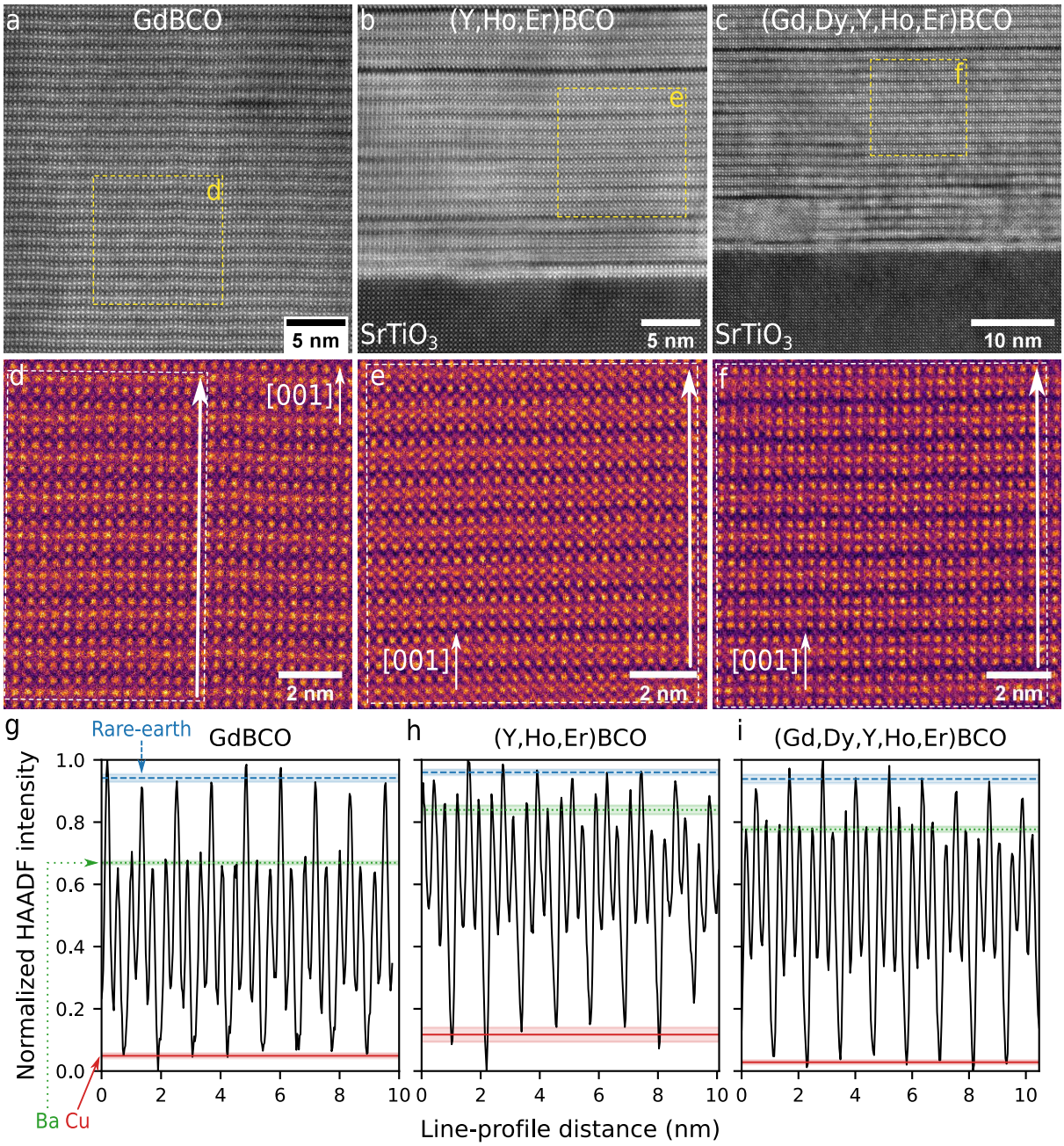

Figure 5.36: Qualitative comparison of the average atomic number of the rare-earth elements by HAADF-STEM. The panel is divided in GdBCO (left column), 3BCO (middle column), and 5BCO (right column). Top row: As-acquired HAADF-STEM images with the extracted region marked with yellow dashed squares. Center row: Color-coded background-subtracted HAADF-STEM images from the marked regions. The arrows mark the direction of the line profiles. The dashed region shows the width of summed intensities for the line profiles. Bottom row: Extracted, normalized HAADF-STEM-intensity line profiles. The horizontal arrows/lines mark the average intensity levels for REs (blue), Ba (green), and Cu (red). This figure is published [Cay+ed].

displayed by the shaded areas around the horizontal lines.
Next, the differences between the HAADF-STEM intensities of the RE and Ba columns are analyzed. This difference can be used to compare the average atomic number of the RE columns between different REBCO films. The ratio

$$P = \frac{I_{\mathrm{RE}} - I_{\mathrm{Ba}}}{I_{\mathrm{RE}} - I_{\mathrm{Cu}}} \tag{5.5}$$

is calculated for each line profile from the average intensity values. The normalization with the intensity difference $I_{\mathrm{RE}} - I_{\mathrm{Cu}}$ accounts for differences in HAADF-STEM detector settings (bias and gain) since the images were acquired during different TEM sessions.

Table 5.4: Extracted intensity value I_x and calculated P values. Experimental values for the HAADF-STEM intensities I_x (with x = RE, Ba, or Cu) and the ratio $P = (I_{\mathrm{RE}} - I_{\mathrm{Ba}})/(I_{\mathrm{RE}} - I_{\mathrm{Cu}})$. The latter decreases for decreasing average atomic number Z_{RE} ($Z_{\mathrm{Gd}} = 64$, $\overline{Z}_{5\mathrm{BCO}} = 60.8$, and $\overline{Z}_{3\mathrm{BCO}} = 58$). The $P_{1.7}$ values are calculated assuming a simple $I_x \propto Z_x^{1.7}$ dependence of the HAADF-STEM intensities.

Intensity	GdBCO	(Y,Ho,Er)BCO	(Gd,Dy,Y,Ho,Er)BCO
I_{RE}	0.942 ± 0.012	0.960 ± 0.009	0.939 ± 0.014
I_{Ba}	0.669 ± 0.006	0.839 ± 0.014	0.777 ± 0.009
I_{Cu}	0.049 ± 0.008	0.117 ± 0.023	0.028 ± 0.006
P	$\mathbf{0.31 \pm 0.01}$	$\mathbf{0.14 \pm 0.02}$	$\mathbf{0.18 \pm 0.02}$
$P_{1.7}$	0.27	0.08	0.18

The values for P are tabulated in Table 5.4 together with the extracted intensities I. The value P decreases with increasing Y concentration in the RE mixture. This is in accordance with the expectation since Ba with $Z_{\mathrm{Ba}} = 56$ has a smaller atomic number than all investigated REs with the exception of Y ($Z_{\mathrm{Y}} = 39$). The Z-contrast difference between Ba and REs becomes smaller with increasing Y concentration. The shown qualitative analysis of HAADF-STEM intensities can be used to compare the average atomic number Z_{RE} between different REBCO films. The P values for an assumed and simplified $I \propto Z^{1.7}$ HAADF-STEM-intensity dependence [HS19, p 61] are given as $P_{1.7}$ for completeness. However, it should be noted that the HAADF-STEM intensities do not only depend on Z but are also affected by electron-probe channeling for typical TEM-sample thicknesses. Therefore, the shown analyses should be interpreted carefully and only used for qualitative analysis. Quantitative analysis requires dedicated image simulations, which were not done here. Another drawback of the shown method is that information in the lateral direction is lost by summing the HAADF-STEM intensities in this direction. This can be avoided if enough signal is present in the as-acquired HAADF-STEM images (i.e. by using longer dwell times or higher beam currents).

Additional STEM-EDXS analyses were performed to analyze the lateral RE distribution in 3BCO (Fig. 5.37a) and 5BCO (Fig. 5.37b). A high numerical spot-size value of 8 and a medium gun-lens setting of 5 were used on the FEI Tecnai Osiris to achieve a small probe size ($\sim 0.4\,\mathrm{nm}$ FWHM) with about 100 pA of beam current (70 µm C2 aperture). The acquisition duration was a few minutes and limited mainly by sample drift. The microscope stage was not moved for a few minutes before acquisition to reduce stage drift.
Starting with 3BCO (Fig. 5.37a), the elemental maps for all three REs show a homogeneous intensity level. The vertical spacing corresponds to the c-lattice parameter of REBCO (about 1.17 nm). The Ba signal is slightly depleted at the RE planes as expected. The O signal is slightly higher at the RE planes since the CuO_2 planes are located at the REs compared to the CuO chains near the Ba planes. The arrow in the Ti Kα map shows a slight Ti signal at the

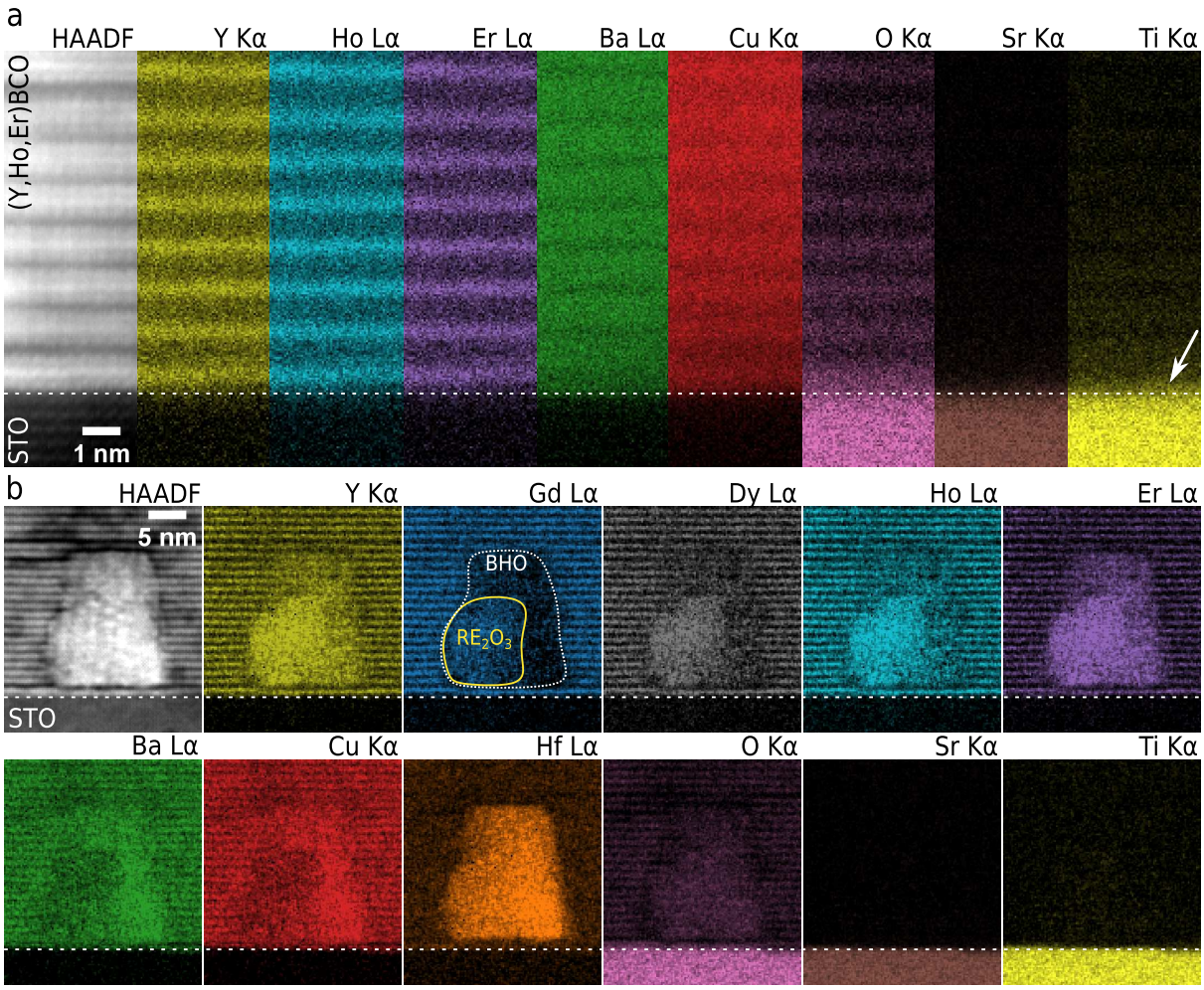

Figure 5.37: High-resolution STEM-EDXS elemental maps of the (a) 3BCO and (b) 5BCO samples. A homogeneous RE distribution is observed in the elemental maps. The vertical spacing of the RE planes is $c = 1.17\,\text{nm}$. (a) The arrow in the Ti Kα map indicates a possible Ti diffusion into the 3BCO film. (b) A mixed BHO/RE_2O_3 precipitate close to the 5BCO-STO interface is mapped. The RE signals in BHO vary with RE species. This figure is adapted from a publication [Cay+ed].

REBCO-STO interface, which slowly fades into the REBCO region. This might be an artifact of electron-beam broadening into the STO region near the interface but could also result from Ti diffusion into REBCO [NI95; Mol+15; Erb+15].
A homogeneous distribution of elements in the REBCO film is also observed for 5BCO (Fig. 5.37b). This is visible from the continuous horizontal lines in all five RE signals, again corresponding to the RE planes with a vertical spacing $c = 1.17\,\text{nm}$. Note that a precipitate at the 5BCO-STO interface was mapped here, which is a mixture of a BHO and a $(Gd,Dy,Y,Ho,Er)_2O_3$ precipitate (indicated by dotted lines in the Gd Lα map). Note that the RE signals vary in the BHO NP, which hints at a RE-dependent intermixing of REs into BHO (see also Section 5.4.2).

BHO and RE_2O_3 nanoparticles at the REBCO-STO interface. The crystalline structure and alignment of the BHO and RE_2O_3 precipitates is discussed in the following. The REBCO-STO interface mostly shows clean cube-on-cube growth. Still, BHO and RE_2O_3 nanoparticles can from at the REBCO-STO interface (cf. Fig. 5.38b). The upper row in Fig. 5.38 shows a (a) raw and (b) background-subtracted and ABS-filtered HAADF-STEM image of the same RE_2O_3 precipitate as in Fig. 5.45 on page 217. The direction of the 5BCO film is determined by the mirror alignment across the SF, as shown in the color-coded inset in Fig. 5.38a. Note that a

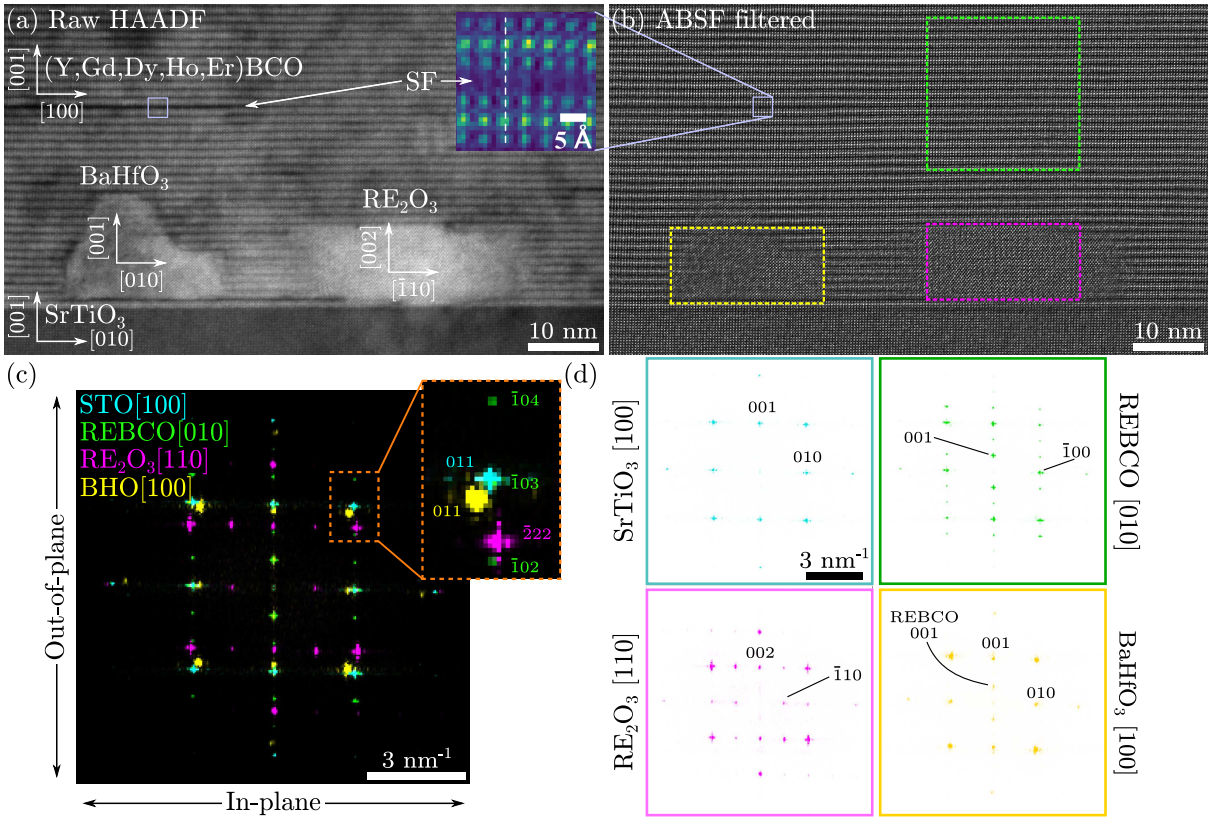

Figure 5.38: Crystalline orientation of RE_2O_3 in REBCO grown on $SrTiO_3$. (a) Raw and (b) background-subtracted and ABS-filtered HAADF-STEM images of $BaHfO_3$ and RE_2O_3 nanoparticles in REBCO. The orientations are shown in (a). (c) Overlaid and (d) individual power spectra from the regions marked in (b). The Bragg reflections reveal the crystalline orientations of the different phases. The zone-axis orientations are given in the legend. A small in-plane mismatch between the phases is observed, enabling syntaxial growth of the phases.

BHO particle is also visible, growing after one completed REBCO unit cell and not directly on STO [Mol+15]. The power spectra from the marked regions in Fig. 5.38b are extracted and overlaid in Fig. 5.38c. Here, a small in-plane mismatch between the different crystalline phases is observed by the small differences between the Bragg reflections in the horizontal in-plane direction. The inset shows a selected set of spots. The zone-axis orientations of the different phases are listed in the legend. The crystalline orientation of the RE_2O_3 precipitate in/on REBCO/STO is $RE_2O_3[1\,1\,0](0\,0\,1)\|REBCO/STO[1\,0\,0](0\,0\,1)$. The separated Bragg reflections are also displayed separately in Fig. 5.38d with a few indexed Bragg reflections for completeness.

A higher-magnification view at the precipitate-substrate region demonstrates differences in the growth mode between BHO (Fig. 5.39a) and RE_2O_3 (Fig. 5.39b). The REBCO-STO interface is marked with a dashed orange line. The left column of HAADF-STEM images is ABS-filtered, whereas the right side was upscaled and denoised with *AtomSegNet* [Lin+21]. The latter was useful for the shown images since a relatively low spatial sampling was used for these images. The growth of BHO starts after the second CuO plane (marked with an arrow in the right image in Fig. 5.39a after one unit cell of REBCO. The latter is marked with a left-open yellow square bracket in Fig. 5.39b. This was also observed in the literature [Mol+15]. Another observation is that BHO grows slightly tilted around the $[1\,0\,0]$ (or $[0\,1\,0]$) directions (not shown here), which was also reported by Maeda et al. [Mae+17]. It seems that the direct growth of BHO on STO is

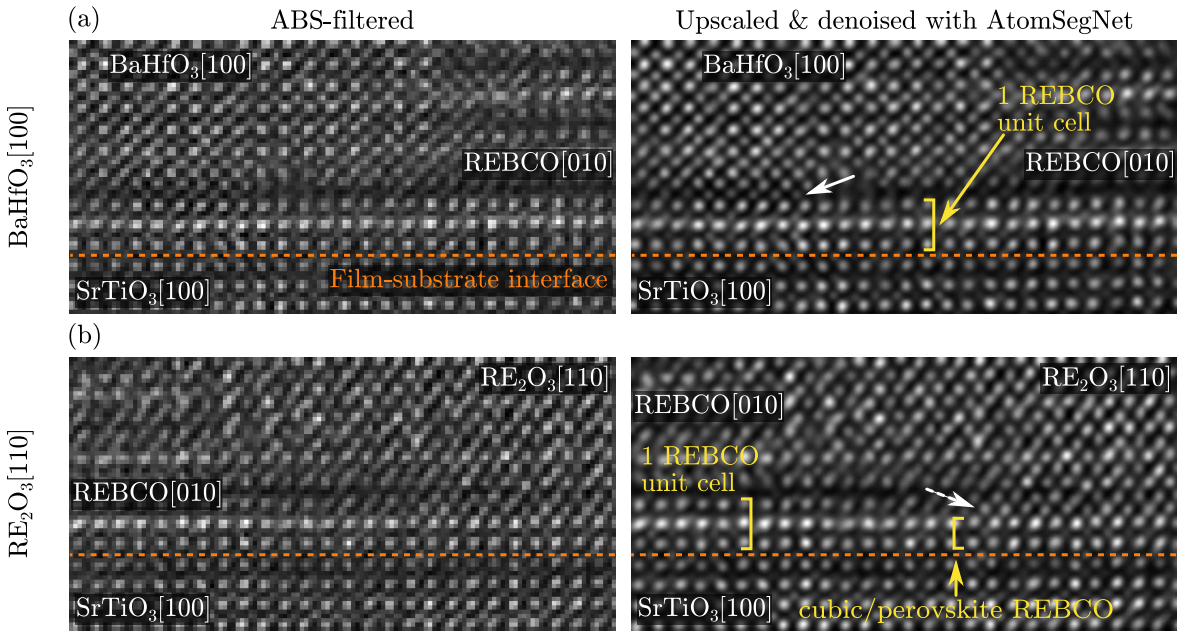

Figure 5.39: HAADF-STEM analysis of the (a) REBCO-$BaHfO_3$ and (b) -RE_2O_3 interfaces. A dashed orange line marks the film-substrate interface. Left column: ABS-filtered HAADF-STEM images. Right column: Upscaled and *AtomSegNet*-denoised [Lin+21] images. The arrows indicate the start of (a) BHO growth after one unit cell of REBCO (marked by a left-open yellow square bracket) and (b) RE_2O_3 growth after the first RE plane of the first REBCO unit cell. The two atomic planes (right-open yellow square bracket) at the film-substrate interface might correspond to cubic REBCO.

energetically less favorable compared to the shown growth mode, i.e. starting with REBCO on STO.

In contrast, the RE_2O_3 precipitate starts growing after the first RE plane of REBCO (marked with an arrow in the right image in Fig. 5.39b). The two atomic layers (marked with an right-open yellow square bracket in Fig. 5.39b) below the RE_2O_3 precipitate of the cubic (perovskite) REBCO phase may form initially on STO [Haa+98], which is then located below the RE_2O_3 phase, as observed here.

The REBCO-LAO interface. The following paragraphs are dedicated to the analysis of the REBCO-LAO interface, which significantly differs from the REBCO-STO interface. For the latter, only the expected cube-on-cube growth with a limited number of substrate steps was observed. The LAO substrates shown here were thermally treated by annealing at 900 °C in an O_2 atmosphere for 5 h, a typical procedure to clean and homogenize the substrate surface [NSC90]. As described by Norton and Carter [NC92], "high-temperature annealing produces a surface consisting of a series of well-defined terraces and steps". Note that substrate steps are still present on annealed substrate surfaces. Jones et al. [Jon+19] reported better YBCO-growth reproducibility and 10 % to 15 % higher J_c values after a 1000 °C LAO treatment for 2 h in air. LAO is a perovskite with a rhombohedral (pseudo-cubic) structure $a = b = c = 0.3788$ nm and $\alpha = 90.066°$ at room temperature [Kaw+02]. The structure is cubic above 708 K [Kaw+02] (or 436 °C). Twin formation occurs at the cubic-to-rhombohedral phase transitions, similar to REBCO twinning during the tetragonal-to-orthorhombic transition.

Figure 5.40a shows a HAADF-STEM image of a pristine CSD-grown ErBCO film on LAO. The REBCO structure close to the right border of the image is distorted due to scan distortions during STEM-image acquisition. Multiple regions are marked and magnified in Fig. 5.40b–e. Three growth configurations at the ErBCO-LAO interface are observed for this ErBCO film:

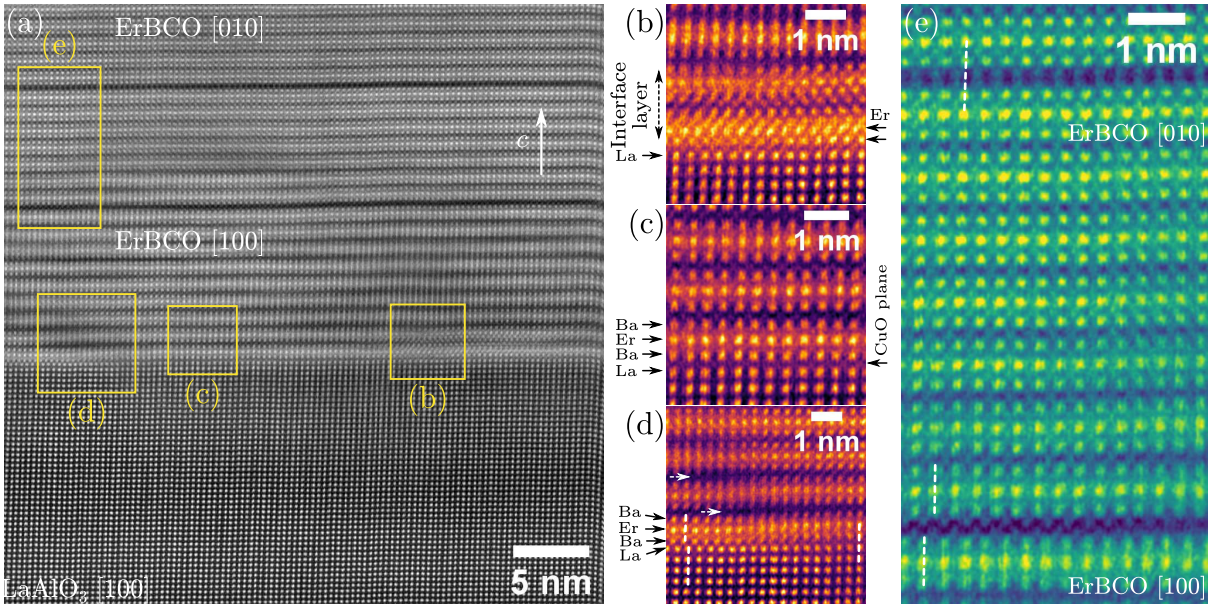

Figure 5.40: HAADF-STEM images of the ErBCO-$LaAlO_3$ interface. Stacking faults are visible as dark horizontal lines. (a) High-resolution HAADF-STEM image of the REBCO-LAO interface. Three growth modes at the ErBCO-LAO substrate interface are observed, i.e. (b) secondary phase formation (probably Er_2CuO_4), (c) cube-on-cube growth with a CuO starting plane, and (d) growth with a displacement vector $\vec{R} = (a/2, 0, c/6)$ or $\vec{R} = (0, b/2, c/6)$. The growth modes of (b) and (c) can swap by introducing additional defects, i.e. dislocations and antiphase boundaries (marked by dashed arrows in d). (e) Magnified image of the stacking faults showing the switch in REBCO orientation.

- A secondary phase (probably Er_2CuO_4) can form at the film-substrate interface (Fig. 5.40b). This is deduced from the change in Er- and Ba-plane stacking, i.e. formation of double Er planes. The formation of the RE_2CuO_4 phase at the film-substrate interface is also observed for GdBCO- and SmBCO-BHO nanocomposite films (Fig. 5.41).
- The (expected) simple cube-on-cube growth, which is similar to the REBCO-STO interface (Fig. 5.40c). The first atomic plane might be CuO (located between the La and first Ba plane), as suggested by Zhu et al. [ZTW13]. An LAO termination with Al-O_2 is ruled out here since a faint Z-contrast is observed for the interface plane compared to the invisible AlO planes in the LAO substrate region.
- ErBCO can grow with a lateral $\langle 1\,0\,0\rangle/2$-shift relative to the LAO and a vertical offset. This corresponds to a displacement vector $\vec{R} = (a/2, 0, c/6)$ or $\vec{R} = (0, b/2, c/6)$ for REBCO. The lateral shift is indicated by an interrupted dashed line in the left region of Fig. 5.40d. The growth mode between cube-on-cube (right side) and $\langle 1\,0\,0\rangle/2$-shifted ErBCO (left side) can swap along the lateral direction (cf. also Fig. 5.44 on Page 215). Additional defects (marked by horizontal arrows) are introduced to accommodate the structural changes.

Despite these structural differences at the REBCO-LAO interface, the growth of an ErBCO film without extended antiphase-boundaries or other structural defects is observed. The investigated REBCO films compensate for structural disorder in the first few nm of film growth.
The two extended SFs in Fig. 5.40a show again the possibility for a switch between the ErBCO[1 0 0] and ErBCO[0 1 0] directions in the growth direction (cf. symmetry at the SFs in the magnified image in Fig. 5.40e).

The formation of RE_2CuO_4 is observed for GdBCO and SmBCO (Fig. 5.41a and b). Note that these samples contain BHO NPs, which are not present in the ErBCO film in Fig. 5.40. This

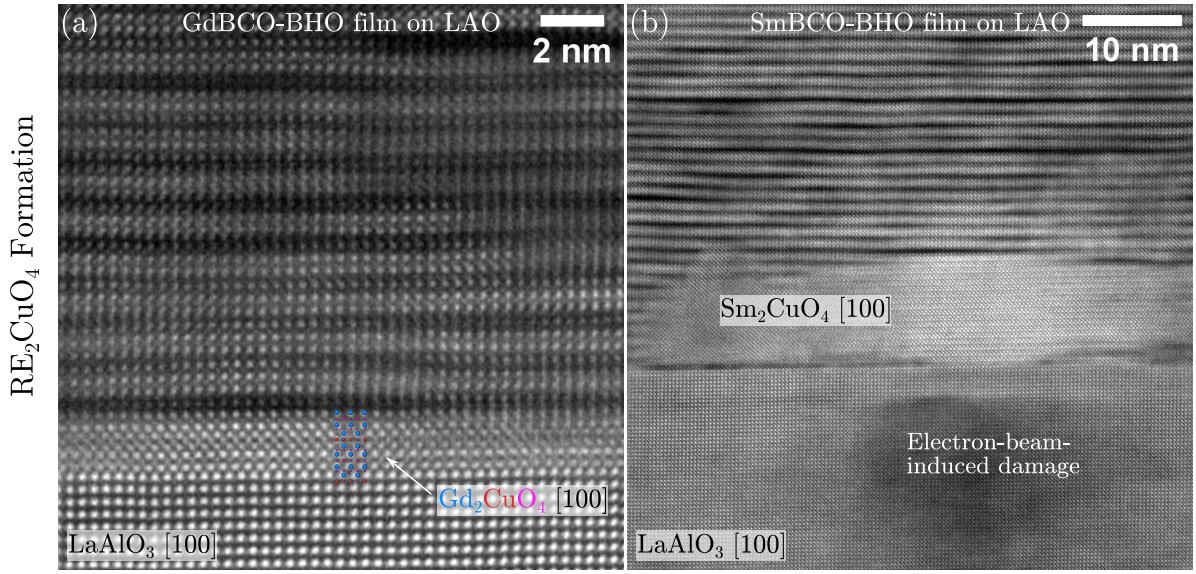

Figure 5.41: RE_2CuO_4 formation in CSD-grown (a) GdBCO and (b) SmBCO films. (a) A $\sim 2\,\text{nm}$ thin $Gd_2CuO_4[1\,0\,0]$ layer is observed at the LAO surface. An overlaid structure model shows the position of the atomic columns. The GdBCO layer is disturbed by short stacking faults, which are probably nanoscale planar defects from TEM-sample degradation. (b) A relatively large Sm_2CuO_4 precipitate has formed at the SmBCO-LAO interface. The SmBCO layer contains short stacking faults, similar to (a). The dark region in LAO is caused by electron-beam irradiation induced by electron-beam alignments on this area. The image in (b) is adapted from a publication [Hän+ed].

suggests that RE_2CuO_4 formation does not depend on BHO addition in CSD-grown REBCO films on LAO. The extent of the RE_2CuO_4 precipitates can vary significantly. The sizes in c-direction in increasing order are (roughly) 1 nm, 2 nm, and 10 nm for the shown examples for ErBCO (Fig. 5.40b), GdBCO (Fig. 5.41a), and SmBCO (Fig. 5.41b), respectively. A structure model of $Gd_2CuO_4[1\,0\,0]$ is overlaid in Fig. 5.41a. The GdBCO and SmBCO films are disturbed by short SFs, which are probably nanoscale planar defects introduced by rapid TEM-sample degradation. In addition, the "4× bright structure" (cf. Fig. 5.16 on page 174) arising from $c/3$ shifts of the GdBCO structure is visible in Fig. 5.41a.

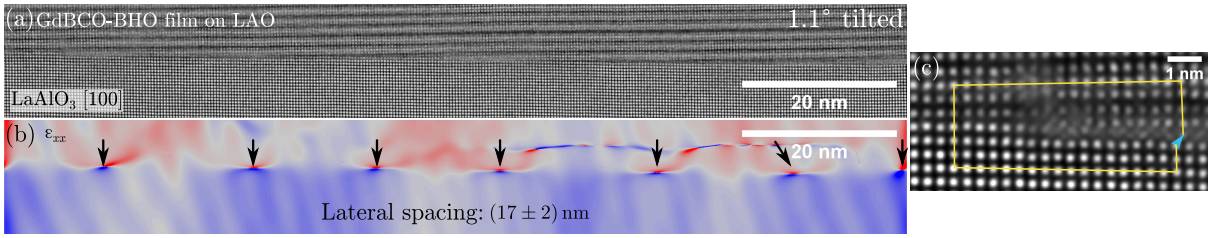

Figure 5.42: Tilted growth of GdBCO on $LaAlO_3$. (a) HAADF-STEM image of the GdBCO-LAO interface. The shown image is background-corrected, ABS-filtered and contrast-adjusted for better visibility of the crystal structure. (b) GPA-obtained ϵ_{xx}-strain map (depicting strain along the horizontal direction) derived from the HAADF-STEM image in (a). The dislocations cause an abrupt change in the geometric phase (marked with arrows). The periodic spacing between the dislocations is $(17 \pm 2)\,\text{nm}$. (c) Magnified region of a dislocation with the Burgers circuit (solid yellow line) and the projected Burgers vector $\vec{b} = (a/2, 0, c/6)$ (blue arrow).

The possibility of a slightly $\langle 1\,0\,0 \rangle$-tilted REBCO growth was observed on LAO in addition to the shown REBCO-LAO interface structures. A tilt of 1.1° is measured between LAO and GdBCO in Fig. 5.42a. Rows of the GdBCO unit cells periodically "merge" with LAO at the GdBCO-interface. The structure is comparable to a low-angle grain boundary. Geometrical

phase analysis[6] (GPA) [HSK98] was used to visualize these discontinuities. The extract ϵ_{xx} strain map in the lateral direction, Fig. 5.42b, shows a lateral spacing of about (17 ± 2) nm (cf. arrows). This dislocation spacing d can be compared with Frank's formula [Tsu+98; Kun+99]

$$d = \frac{|\vec{b}|}{2\sin\left(\frac{\theta}{2}\right)} \approx \frac{|\vec{b}|}{\theta} \tag{5.6}$$

with the Burgers vector $\vec{b}$ and the grain-boundary angle θ. The Burgers vector is measured as $\vec{b} = (a/2, 0, c/6)$ (or $\vec{b} = (0, b/2, c/6)$) from one of the dislocations (cf. blue arrow in Fig. 5.42c). The average value of $a = 3.8405$ Å and $b = 3.8959$ Å of GdBCO is used for the calculation since both configurations are possible in $\vec{b}$. With $c = 11.6959$ Å and $\theta = 1.1° = 19.2$ mrad, a calculated value $d = 14.3$ nm is found. The differences between the experimental value (17 ± 2) nm and the calculated value might be explained by limited statistics, uncertainties in the lattice parameters of GdBCO on LAO (possible strain), or Burgers vector components, which are not visible in the projections along the [1 0 0] or [0 1 0] zone axes.
Besides this low-angle grain-boundary explanation, the dislocations could be LAO surface steps with the measured periodicity d. However, periodic substrate steps do not necessarily lead to a tilted REBCO growth. The exact atomic configuration of the GdBCO-LAO interface could not be clarified since the HAADF-STEM Z-contrast between the terminating La atomic columns of LAO and the first Ba (or mixed Ba/Gd) columns for REBCO (cubic REBCO) are similar in the shown images. GdBCO might form a cubic GdBCO perovskite structure at the interface to compensate for the steps similar to REBCO films on STO [Haa+98]. To conclude, the tilted REBCO growth might result (i) as a way to reduce the interfacial strain by forming a low-angle grain-boundary configuration with periodic dislocations or (ii) as a result of periodic substrate steps on the LAO interface.

STEM-EDXS was applied to study the REBCO-LAO interface to detect possible LAO substrate steps using the La signal. However, this was unsuccessful due to the limited signal-to-noise ratio in the STEM-EDXS data sets. The latter resulted from the limited possible STEM-EDXS acquisition duration due to TEM-sample drift. Two representative STEM-EDXS mappings are shown in Fig. 5.43, i.e. for (a) ErBCO on LAO and (b) GdBCO on LAO. Note that the c-direction in these images is parallel to the horizontal direction. Line profiles along the c-direction were extracted from the elemental signals because the signal-to-noise ratio was not sufficient to generate two-dimensional elemental maps with the required spatial resolution. The total x-ray counts along the vertical (i.e. in-plane direction) were summed to obtain a high signal-to-noise ratio for the line profiles. The dataset was also denoised with PCA and a Savitzky-Golay smoothing[7] was applied to the line profiles. Note that the elemental signals may be affected by electron-beam channeling, which can affect the elemental signals from neighboring atomic columns in a complicated fashion [Kot+14].
The ErBCO-LAO interface is discussed first (Fig. 5.43a). A cube-on-cube alignment of ErBCO on LAO in this region is observed, similar to Fig. 5.40c. The Er, Ba, and O signals mostly follow the expected atomic-plane configuration of GdBCO. The Cu signal increases near the heavy Er plane, probably partly caused by spurious Cu x-rays. The similarity of the La and Al signals (purple and blue lines) across the GdBCO-LAO interface indicates the spatial resolution of

[6] Using the freely available *Strain++* software by Jonathan Peters (`https://github.com/JJPPeters/Strainpp`, last accessed 28.02.2022).
[7] The implementation in *HyperSpy* was used, i.e. `line_profile.smooth_savitzky_golay(polynomial_order=2, window_length=9, differential_order=0)`.

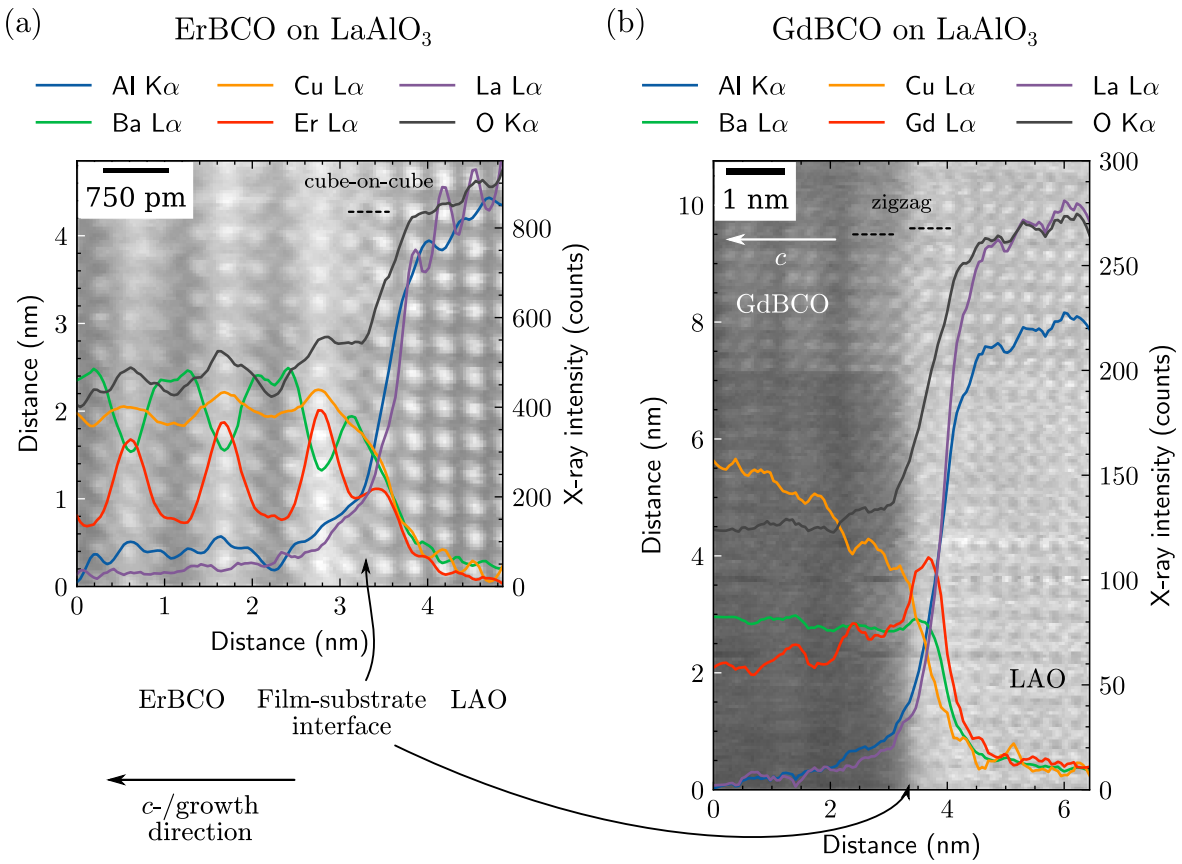

Figure 5.43: High-resolution STEM-EDXS analyses of the (a) ErBCO- and (b) GdBCO-$LaAlO_3$ interfaces. The c-direction is horizontal. The STEM-EDXS x-rays signal were summed along the vertical direction prior to further data treatment and signal extraction. (a) The Er signal (red line) increases towards LAO and an Er peak is visible at the terminating La atomic plane of LAO. The continuous elemental signals across the interface (e.g. Al and La) are caused by electron-beam broadening due to a finite TEM-sample thickness and cannot be interpreted as elemental interdiffusion processes. The Cu signal (orange line) is affected by spurious Cu x-rays, thereby increasing the Cu signal at heavier atomic columns such as Er. (b) The Gd signal (red line) increases towards LAO, similar to Er in (a). The STEM-EDXS was severely affected by TEM-sample drift, which reduces the line profiles' spatial resolution and probably shifted the HAADF-STEM signal slightly to the left with respect to the line profiles.

STEM-EDXS across this interface. The electron probe near the GdBCO-LAO interface broadens into the other material and washes out the sharp transition between GdBCO and LAO in the elemental signals. Therefore, the La and Al signals are *not* interpreted as diffusion of La and Al into GdBCO. The Er signal slightly increases towards LAO and a pronounced Er peak at the terminating La plane is observed. This might be the result of an Er-La intermixing at the ErBCO-LAO interface or possible substrate steps at the LAO surface along the TEM-sample thickness (i.e. along the viewing direction).

Figure 5.43b shows the elemental signals across a GdBCO-LAO interface. Here, a "zigzag" alignment similar to Fig. 5.40b is visible at the film-substrate interface. Note that significant sample drift caused a horizontal shift of the HAADF-STEM signal to the left compared to the overlaid elemental signals. This also washes out and reduces the spatial resolution compared to Fig. 5.43a. In addition, scan distortions are visible as horizontal streaks in the HAADF-STEM signal. The spatial distribution of elements in Fig. 5.43b should be more carefully interpreted than in (a). Nevertheless, a few similarities to (a) are visible, e.g. an increase of the Gd signal

(red) towards the LAO substrate. The Gd-signal increase is enhanced with respect to the Er signal in Fig. 5.43a. A possible explanation might be the presence of the Gd_2CuO_4 phase at the GdBCO-LAO interface in this region, which significantly increases the measured Gd signal compared to GdBCO.

Moiré-STEM for REBCO analyses. So far, the microstructure of REBCO films was observed with conventional high-resolution HAADF-STEM imaging, where the spatial sampling of the electron probe (i.e. the scan step Δ) was set up to prevent undersampling artifacts (aliasing) in the HAADF-STEM images. This means that the scan step Δ is related to the attainable resolution of the STEM probe, i.e. given by the FWHM of the electron probe d_0 in HAADF-STEM imaging. Conventional HAADF-STEM imaging requires $\Delta \leq d_0/2$ to prevent aliasing artifacts in the images. For example, the FEI Tecnai Osiris has $d_0 \approx 180\,\mathrm{pm}$ at 200 keV, which requires $\Delta \leq 90\,\mathrm{pm}$. The scan generator on the same microscope is limited to 2048^2 pixel. The maximum image width (or height) for high-resolution HAADF-STEM imaging without aliasing artifacts is limited to $2048 \cdot 90\,\mathrm{pm} = 184\,\mathrm{nm}$. Typically, even smaller sample regions were imaged with HAADF-STEM in this work. This impedes the analysis of larger sample areas, especially regarding the REBCO orientations by the observed symmetries of the atomic REBCO structure at interfaces and SFs. These aspects are important to get a better understanding of REBCO growth.
Moiré-STEM is an alternative method to map out the REBCO symmetries at SFs (and the REBCO-substrate interface) for larger sample areas. The spatial sampling Δ in Moiré-STEM is chosen close to a lattice-plane spacing d_{hkl} in the sample material. This causes periodic Moiré fringes in the Moiré-STEM images, which depend on the periodicity of the corresponding lattice planes. The observed Moiré-fringe spacing depends on the difference between Δ and d_{hkl} and the angle between the crystalline lattice and the square-shaped STEM scan grid. For detailed information, see the literature [SZ10; Pof+20; NOM18; Zha+21b].

Table 5.5: Scanning parameters used for Moiré-STEM and HRSTEM imaging of REBCO films. The HAADF-detector signal was used in both cases. A FEI Tecnai Osiris was used with spot size 10, gun lens 5, and 10.7 mrad convergence semi-angle.

	Moiré-STEM	HRSTEM
Sampling	433 pm	27 pm
Scan window	512^2 pixel	2048^2 pixel
Magnification	450 000	1 800 000

The feasibility of the Moiré-STEM method applied to REBCO films was tested for a pristine ErBCO sample grown on LAO. The scan step Δ was varied with the STEM magnification (fixed by microscope manufacturer) and the scan grid (e.g. 128 pixel, ..., 2048 pixel, in powers of two). The used sampling for Moiré-STEM and HAADF-STEM are tabulated in Table 5.5. Note that the electron-probe parameters and the detector signal (HAADF) are the same for both STEM modes and tuned for HRSTEM, i.e. 10, gun lens 5, and a 10.7 mrad convergence semi-angle (70 µm C2 aperture) for the FEI Tecnai Osiris. This emphasizes that Moiré-STEM can be rapidly applied during conventional high-resolution HAADF-STEM imaging by simply adjusting $\Delta \approx d_{hkl}$ (and possibly the scan rotation). Here, $\Delta = 433\,\mathrm{pm}$ is close to the (1 0 0) and (0 1 0) lattice planes with a spacing corresponding to the a- and b-lattice parameters of REBCO (about $a \approx 382\,\mathrm{pm}$ and $b \approx 388\,\mathrm{pm}$).

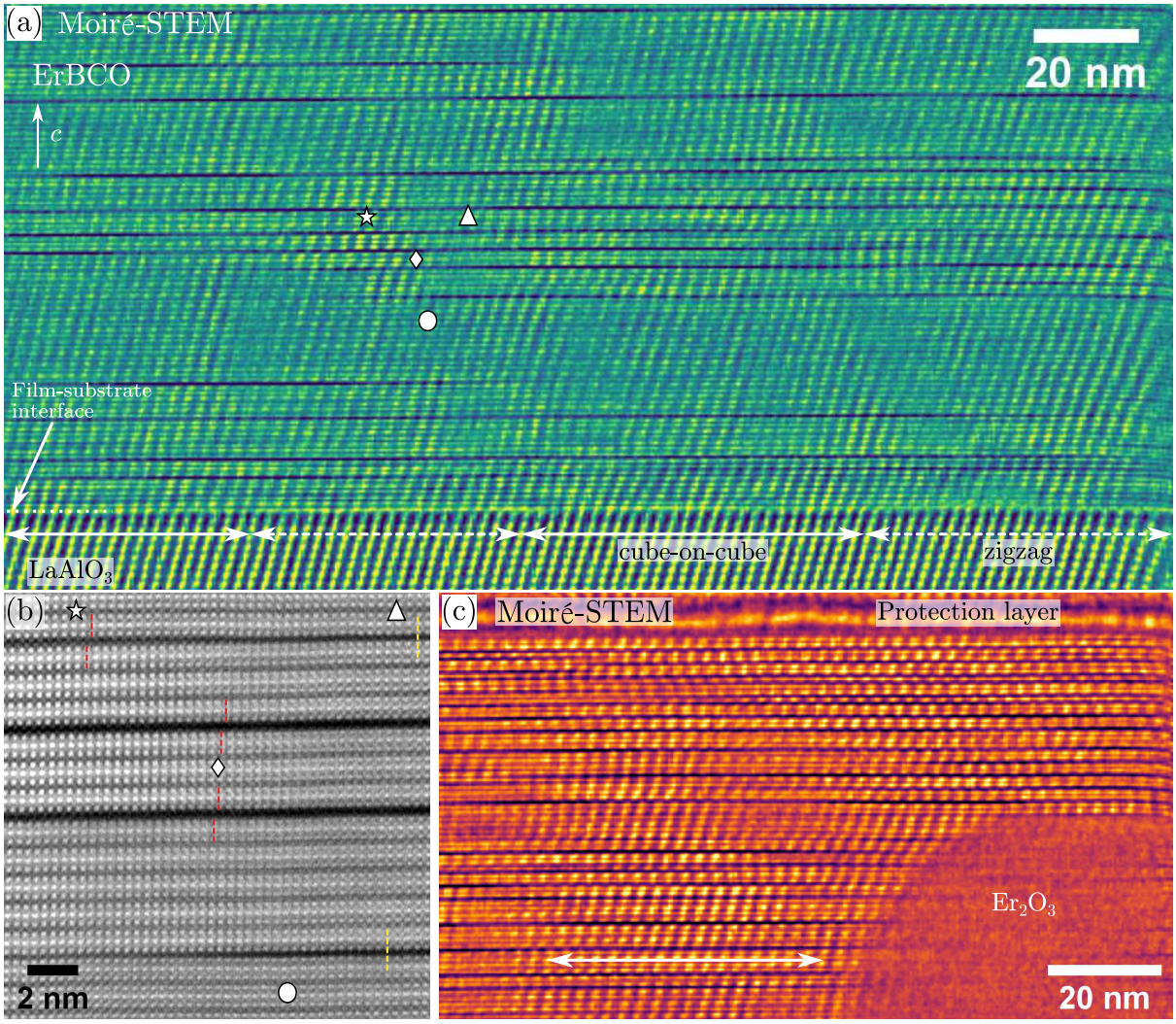

Figure 5.44: Moiré-STEM imaging of an ErBCO film on $LaAlO_3$. (a) Moiré-STEM image with a spatial sampling of 433 pm. Moiré fringes arising from the (1 0 0) and (0 1 0) lattice planes reveal the symmetries (mirror/cube-on-cube vs. glide/zigzag) at stacking faults and the ErBCO-LAO interface. The markers can be compared with the region in the HAADF-STEM image in (b). The double-headed arrows show the periodic switching of cube-on-cube (solid) and zigzag (dashed) growth mode of ErBCO on LAO. (b) The dashed lines indicate glide (red) and mirror symmetries (yellow) across the stacking faults. (c) Moiré-STEM image of ErBCO with a high density of stacking faults caused by an Er_2O_3 precipitate. The double-headed arrow indicates a transition between glide and mirror symmetry.

A first example of applying the Moiré-STEM method for a CSD-grown ErBCO film on LAO is shown in Fig. 5.44a. The image was processed by removing the low-frequency background and ABS-filtering (without Butterworth-filtering). This highlights the Moiré fringes. The Moiré fringes are visibly tilted from the vertical direction, caused by a slight angle between the STEM-scan grid and the ErBCO structure. This tilt [NOM18] and the Moiré-fringe spacing [SZ10] are not of interest here. Stacking faults in the ErBCO film appear as dark horizontal lines. The ErBCO-LAO interface is marked with an arrow in the bottom-left corner in Fig. 5.44a. Even though the atomic detail is lost, the periodicity of the Moiré fringes resulting from the (1 0 0)/(0 1 0) lattice planes reveals the symmetries (glide or mirror) at the stacking faults and the ErBCO-LAO interface. The regions marked with symbols (☆, ◊, ○, △) can be directly compared to a conventional HAADF-STEM image from the same region (Fig. 5.44b). The latter shows a glide symmetry (zigzag alignment, dashed red lines) near the ☆ and ◊ markers. In contrast, a

mirror symmetry (cube-on-cube alignment, dashed yellow lines in Fig. 5.44b) is observed near the ○ and △ markers. Note the transition of the symmetries in the lateral direction from △ to ✰ (a partial Frank type (sessile) dislocation [VKA91; ZTW13; Guz+17]). The same symmetries are visible for the Moiré fringes in Fig. 5.44a as an offset (for glide symmetry) or no offset (for mirror symmetry) across a stacking fault. The symmetries can be tracked for a large number of stacking faults and the local alignment, i.e. [1 0 0] or [0 1 0], of REBCO is revealed over a large sample area.

The ErBCO-LAO interface can be analyzed similarly since cube-on-cube (mirror symmetry) and shifted (glide symmetry) growth modes were observed for the investigated REBCO films on LAO (Fig. 5.40 on page 210). The Moiré fringes again show the same symmetries and reveal a periodic switching of both growth configurations (cf. solid → mirror and dashed → glide double-headed arrows in Fig. 5.44a).

Figure 5.44c presents another Moiré-STEM image acquired near a relatively large Er_2O_3 precipitate (the same large precipitate as in the right part of Fig. 5.34a on Page 202). The latter introduces a plethora of SFs, again visible as dark horizontal lines. The stacking-fault density close to the film's surface is high so that SFs appear for every 1 or 2 REBCO unit cells, effectively forming the Er124 and Er247 phases. The SF symmetries can be tracked even for a single unit-cell spacing in the *c*-direction, for example, visible below the "Protection layer" label. The double-headed arrow in the lower part of Fig. 5.44c again depicts are transition from a mirror (right end) to a glide symmetry (left end) along the in-plane direction.

These examples show that Moiré-STEM imaging enables the fast analysis of the REBCO [1 0 0] and [0 1 0] orientations over large sample areas (compared to HRSTEM). In addition, Moiré-STEM can be used to find crystal defects or other "interesting" sample regions at lower magnification for a subsequent study at high magnification. Finally, it should be noted that BF-TEM diffraction-contrast imaging could also reveal the REBCO orientations (see, e.g., Rouco et al. [Rou+14]). However, Moiré-STEM can be conveniently combined with *Z*-contrast HAADF-STEM imaging since no re-alignment of the microscope is necessary.

5.4.2 Chemical Intermixing of Rare-Earth Elements and $BaHfO_3$ Nanoparticles

Previous work. This section presents results on the intermixing of rare-earth elements (REs) and $BaHfO_3$ nanoparticles (BHO NPs). A few studies already observed such an intermixing [Mac+04], primarily by STEM-EDXS measurements. Kai et al. [Kai+07] and Yamada et al. [Yam+08] investigated ErBCO with $BaNb_2O_6$ NPs and found the formation of $Ba(Nb,Er)_2O_6$ nanorods. In addition, they quote a possible formation of $BaEr_{0.67}W_{0.33}O_3$ pervoskites in ErBCO with $BaWO_4$ (unpublished) [Yam+08]. In these publications, Er was partially incorporated into the NPs. More recently, Díez-Sierra et al. [Díe+21] showed experimental evidence of Y diffusion from YBCO into $BaZrO_3$ (BZO) nanoparticles by STEM-EDXS. A similar effect was reported by Majkic et al. [Maj+21], who showed evidence for incorporation of Y and Gd in $BaZrO_3$ (BZO) nanorods in a (Y,Gd)BCO film. They showed direct evidence for a RE substitution to the Zr-site (B-site) of BZO with the perovskite structure ABO_3 by atomic-resolution STEM-EDXS. Therefore, they concluded the formation of a $Ba^{2+}(Zr^{4+}_{1-x}RE^{3+}_x)O^{2-}_{3-\delta}$ NP compound. These studies show that RE intermixing into barium oxide nanoparticles is possible. A better understanding of this phenomenon could help to better control the RE concentration in the REBCO film, e.g., by adjustments to the used REs, RE concentrations, and nanoparticle materials. Here, the RE intermixing is investigated for BHO nanoparticles. The high- and medium-entropy REBCO films 5BCO and 3BCO from the previous section are ideal test samples since several

REs are present in a single film and can be investigated simultaneously. The comparison of single- and multi-RE samples enables the comparison of the RE-BHO intermixing for multi-RE and single-RE REBCO-BHO films.

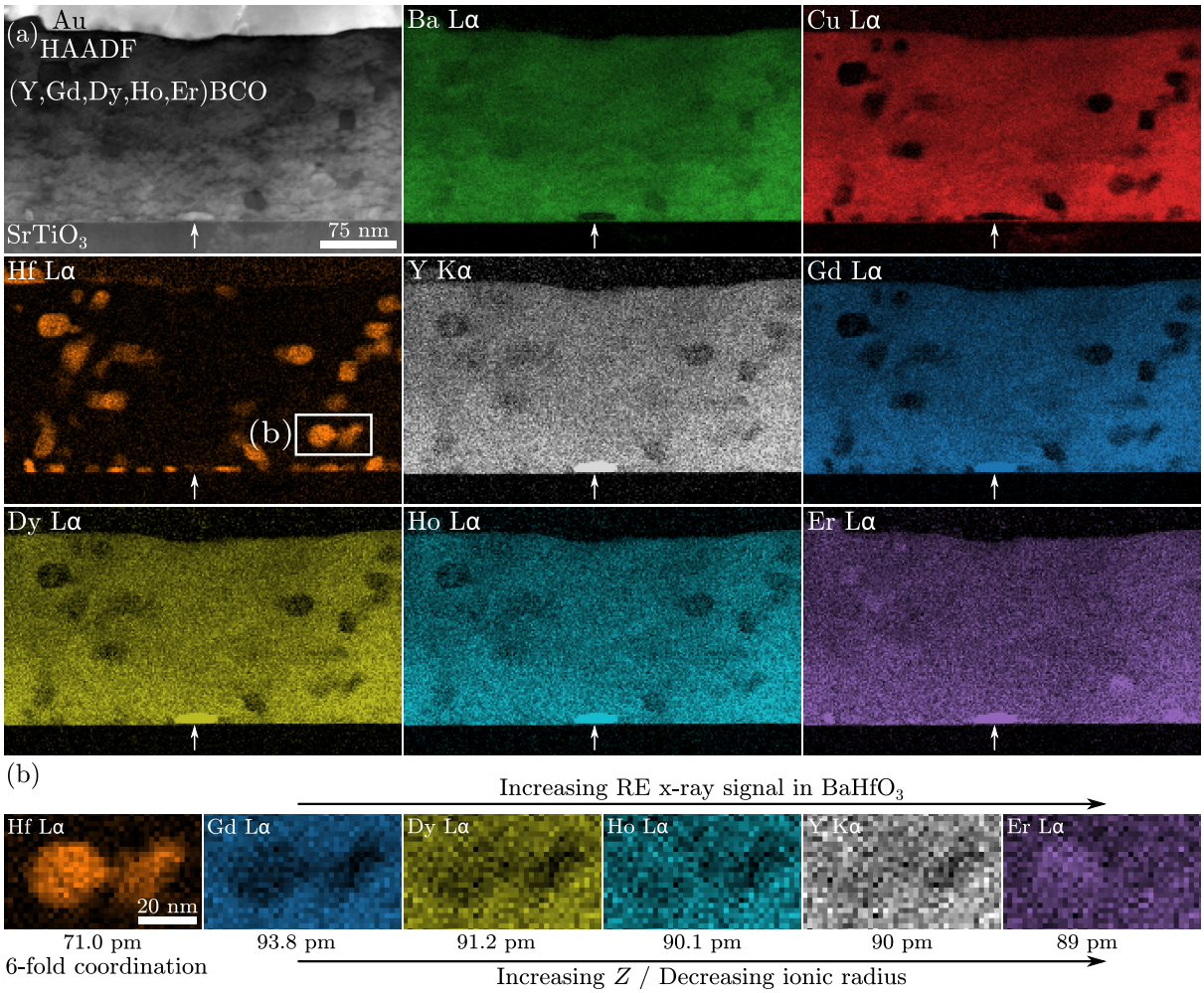

Figure 5.45: STEM-EDXS elemental maps of a (Y,Gd,Dy,Ho,Er)BCO-$BaHfO_3$ nanocomposites film. (a) HAADF-STEM overview image and corresponding qualitative net-intensity elemental maps. The Hf signal (orange) shows the BHO-nanoparticle positions. The arrow marks a RE_2O_3 precipitate at the REBCO-$SrTiO_3$ interface. (b) Magnified region of (a) from two BHO precipitates. The RE signals in BHO increase with decreasing ionic radius (here given for RE^{3+} and coordination number 6).

Experimental results. First, the experimental results and used methods are shown for the multi-RE REBCO-BHO nanocomposite film 5BCO. Then the RE-BHO intermixing is compared to the other REBCO films. Figure 5.45a shows an HAADF-STEM cross-section image and the corresponding elemental maps for 5BCO. Note that five different REs (Y, Gd, Dy, Ho, and Er) are present in 5BCO. The RE signals were extracted using MLLS peak fitting (for example, see Fig. 5.46c and d). The position of the BHO NPs is related to the Hf signal (orange in Fig. 5.45a). The arrow marks a RE-rich precipitate at the 5BCO-$SrTiO_3$ interface, which is identified as RE_2O_3 with a homogeneous RE mixture, i.e. $(Y, Gd, Ho, Er, Dy)_2O_3$. As expected, a depletion of Ba, Cu, and Hf signal is visible for this precipitate.

A close inspection of the RE elemental maps reveals slight signal differences in the BHO region, exemplified in the region marked in the Hf map in Fig. 5.45, which is magnified in (b). The RE signals are sorted in the order of decreasing ionic radius, which is given below the elemental maps for a 6-fold coordination number (CN) of RE^{3+}. The latter corresponds to the CN of the

Hf^{4+} atom in BHO. Gd with the largest ionic radius shows the most substantial signal depletion of the REs, whereas Er even shows a slightly increased signal in BHO compared to the 5BCO matrix. The other three elements lie in-between. A gradual change from Gd to Er is observed in the x-ray maps.

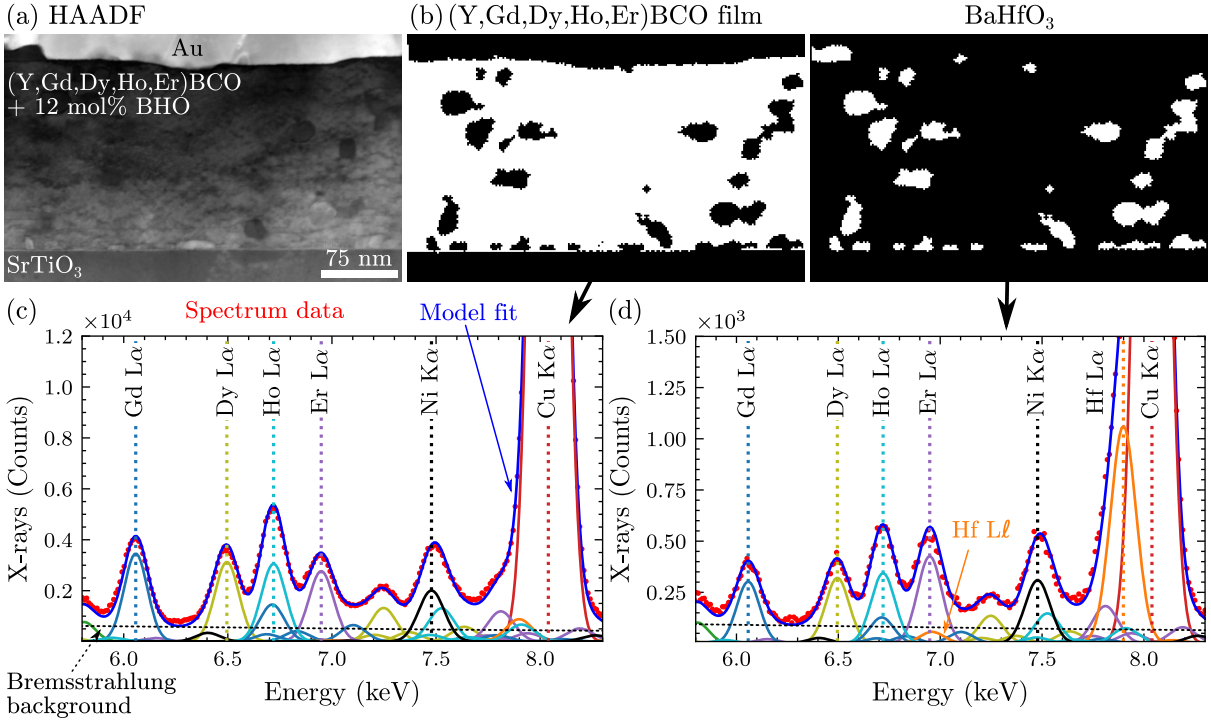

Figure 5.46: Model fitting for EDXS-peak separation in (Y,Gd,Dy,Ho,Er)BCO. (a) HAADF-STEM overview image and (b) segmented binary masks to extract summed-up EDXS spectra for the (c) (Y,Gd,Dy,Ho,Er)BCO film and (d) $BaHfO_3$ nanoparticles. (c,d) The model fit (solid blue line) shows a good agreement with the experimental spectrum (red dotted line). The individual contributions of the different x-ray transitions are displayed with a color-coding. The strongest peaks are labeled. (d) The Hf Lα peak overlaps with Cu Kα and Hf Lℓ overlaps with Er Lα (marked by an orange arrow).

The STEM-EDXS dataset shown in Fig. 5.45 was (i) denoised with PCA and (ii) is prone to peak overlaps due to the large number of different elements in 5BCO. The peak overlaps can introduce errors in the elemental analyses. The mentioned error sources were carefully evaluated to rule out possible artifacts that could cause the observed differences in RE signals in BHO.
Regarding the peak overlaps for 5BCO, Fig. 5.46 shows the peak-fitting procedure used to extract the elemental signals and Hf applied to the raw x-ray data. The summed-up spectra from the raw data are analyzed to prevent possible artifacts from PCA denoising. The upper row presents the (a) HAADF-STEM image and the binary masks for (b) the 5BCO layer region (left) and the BHO NPs (right). Only the white regions in (b) were considered to form the summed-up EDXS spectra for the (c) 5BCO film and (d) the BHP NPs. A selected energy region is shown, which contains the RE Lα x-ray transitions (with the exception of Y). In both summed spectra, the solid blue line shows the total model fit to the data (dotted red line). The individual x-ray peaks are modeled as Gaussian functions and are color-coded for each element. The strongest peak of each x-ray family is marked with a dotted vertical line and the name of the x-ray transition. The pronounced Cu Kα peak partly results from spurious x-rays from the Cu TEM grid. Similarly, the Ni signal is caused by spurious x-rays. Peak fitting was done in *HyperSpy*.
The MLLS peak fitting generally shows a good agreement with the experimental spectra. This

indicates that all relevant (spurious and sample) elements are present in the model. A qualitative comparison of the RE signals in Fig. 5.46c and d shows a (c) decreasing and (d) increasing trend in RE Lα intensities for the (c) 5BCO matrix and (d) BHO NPs. Even though these intensities cannot be directly interpreted in terms of elemental concentrations, this qualitative comparison already shows that the RE distribution in 5BCO is different from BHO. Figure 5.46d clearly shows the overlap between the Hf Lα and Cu Kα peaks, resolved by the MLLS fit. Another important aspect is that the Hf Lℓ x-ray transition (IUPAC notation: Hf L3-M1) at 6.96 keV overlaps with the Er Lα transition at 6.95 keV (marked with an orange arrow in Fig. 5.46d). At first glance, this could explain the increased Er signal in BHO since the Hf Lℓ peak will increase with increasing Hf concentration. However, the MLLS fitting also considers the relative peak intensities within an x-ray-line family. The peak-intensity ratio of Hf Lα to Hf Lℓ is about 1:0.05 (as tabulated in *DTSA-II*). With this constraint, the MLLS fitting separates the Er Lα and Hf Lℓ contributions from the combined peak. The separated Er Lα peak in Fig. 5.46d shows the highest intensity compared to the other REs, the same results as observed in the PCA-filtered elemental maps in Fig. 5.45 on page 217.

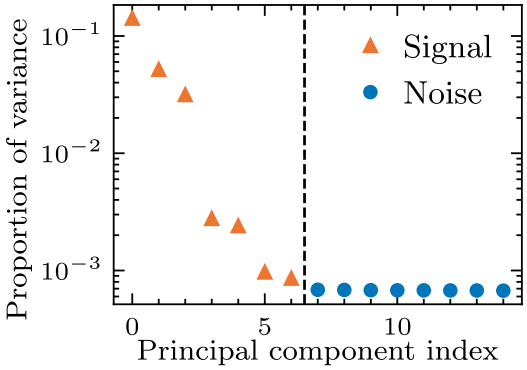

Figure 5.47: Scree plot for the STEM-EDXS dataset of (Y,Gd,Dy,Ho,Er)BCO. Seven signal components (▲) are clearly identified and separable from the noise components (●). The vertical line indicates the cut-off point.

The PCA filtering was also checked for possible artifacts, i.e. if a sufficient number of principal components were used to reconstruct the denoised dataset. The analyzed dataset showed a clear elbow position in the scree plot (Fig. 5.47), so that the $k = 7$ signal components (▲) are nicely separable from the noise components (●).

As a next step, STEM-EELS analysis of the BHO NPs was performed for 5BCO. Here, no spurious x-rays can impede the measurements as in STEM-EDXS. Therefore, STEM-EELS is applied to confirm the observed trends for the RE signals in BHO. Figure 5.48 presents the STEM-EELS analysis of (c,d) raw summed-up data and (e) PCA-filtered elemental maps of a few BHO NPs in 5BCO. The methodology is similar to the STEM-EDXS measurements, where the inspection of the summed up EELS spectra from the raw dataset is analyzed first to rule out possible PCA-induced artifacts in the elemental maps. An overview cross-section ADF-STEM image (Fig. 5.48a) shows the typical features of 5BCO in the form of stacking faults and BHO NPs in the film. The STEM-EELS acquisition region is marked with a red rectangle. A few BHO NPs are visible in the ADF-STEM image as round precipitates with a reduced ADF-STEM intensity.

The summed-up EELS spectrum from all measurement positions in the STEM-EELS mapping is displayed in Fig. 5.48b. The smallest available energy dispersion of 0.5 eV channel^{-1} was used here to maximize the energy window of the spectrometer. The energy window contains a core-loss edge for nearly every element in the 5BCO-BHO film, the exceptions being O (O K at 532 eV) and Y (e.g. Y L_3 starts at 2080 eV, Y $M_{4,5}$ are at around 160 eV). The onset energies

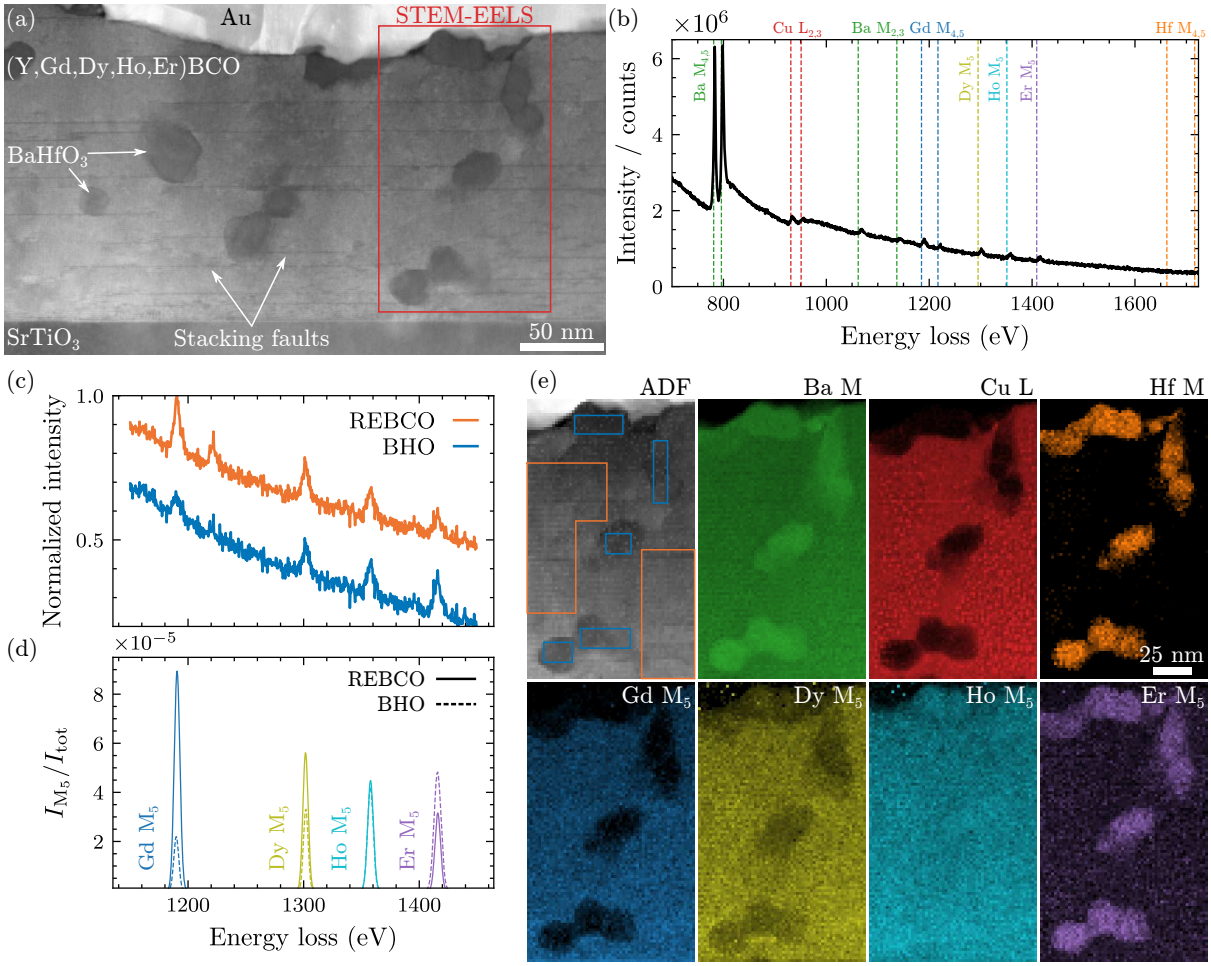

Figure 5.48: STEM-EELS analysis of the rare-earth distribution in the (Y,Gd,Dy,Ho,Er)BCO-$BaHfO_3$ nanocomposite. (a) ADF-STEM cross-section image of the REBCO film with BHO nanoparticles (dark). A red rectangle marks the STEM-EELS acquisition region. (b) Summed-up EELS spectra showing the different elemental core-loss signals (marked with dashed vertical lines). The REs (Gd, Dy, Ho, Er) show small M_5 white-line peaks. (c) Summed-up EELS spectra from the regions shown in the ADF-STEM signal in (e) for REBCO (orange) and BHO (blue). Only the energy interval containing the RE signals is shown. (d) Extracted and normalized RE M_5 white-line intensities from (c) for REBCO (solid line) and BHO (dashed line). Note the increased Er signal in BHO relative to REBCO. (e) Upper row: ADF-STEM signal and elemental maps for Ba, Cu, and Hf. The latter shows the BHO positions. Lower row: RE M_5 white-line intensities maps showing the RE distributions.

for the present element edges in Fig. 5.48b are marked with vertical lines. The Ba $M_{4,5}$ edges show pronounced white lines and the weaker Ba $M_{2,3}$ edges are also slightly visible. Similarly, the RE M_5 white lines are recognized for Gd (blue), Dy (yellow), Ho (cyan), and Er (purple). Note that the RE M_4 white line is only visible for Gd due to (i) the limited signal-to-noise ratio, (ii) the relatively small concentration of each RE (~ 1.5 at. % per RE in 5BCO), and (iii) the decreasing RE M_4 white-line intensity relative to RE M_5 for increasing Z [FB96] (i.e. here towards Er). The Cu $L_{2,3}$ also show a white-line peak due to the local bonding environment with O. In contrast, metallic Cu does not show $L_{2,3}$ white lines [TS89]. Here, Hf from BHO has comparably weak $M_{4,5}$ edge onsets without white lines at 1662 eV and 1716 eV, which is not clearly visible in Fig. 5.48b.

The RE M_5-white-line intensities were extracted to get insights into the local RE concentration. First, summed spectra from the rectangular regions marked in the ADF-STEM image in Fig. 5.48e were extracted, i.e. for 5BCO film (orange) and the BHO NPs (blue). The energy interval around

the four REs from the summed-up spectra is shown in Fig. 5.48c. Here, the extracted spectra were (i) normalized with the maximum value of the shown energy interval and (ii) vertically offset by 0.3 for easier comparison. The white lines appear as peaks above the power-law-type EELS background. As a next step, a combined fit consisting of a power-law background and a Gaussian function for each RE M_5 white line was used to extract the M_5 white-line intensities for the 5BCO film (solid line in Fig. 5.48d) and BHO (dashed line in Fig. 5.48d). The extracted M_5 white-line intensities in Fig. 5.48d were normalized with the total counts in the summed-up spectra to qualitatively compare the RE concentration in 5BCO (solid line) and BHO (dashed line). A higher Gd concentration in 5BCO than in BHO is observed. In contrast, Er shows a higher signal in the BHO NPs. Dy and Ho lie in-between. Remarkably, the Ho is nearly unchanged in the 5BCO film and the BHO NPs. These trends are the same that were already observed in the STEM-EDXS analyses (cf. Fig. 5.45 on page 217 and Fig. 5.46 on page 218).
The STEM-EELS dataset was subsequently denoised with PCA and the NLLS procedure above was applied to extract the RE M_5 white-line intensities on a single-pixel level to obtain elemental maps for the REs (lower row in Fig. 5.48e). The other elements Ba, Cu, and Hf were extracted by a combined fit of a power-law background and Hartree-Slater cross-section models using the commercial EELS package by Gatan for *DigitalMicrograph*. The Hf M signal shows the position of the BHO NPs. The Er signal in the BHO NPs is increased compared to the surrounding 5BCO matrix, whereas Gd shows a significant depletion. The trend for the RE signals can be directly compared to the EDXS-obtained elemental maps in Fig. 5.45b on Page 217. The slightly increased Ba signal in BHO agrees with the expectation since the Ba concentration is slightly higher in BHO (20 at. %) than in REBCO ($\sim$ 15.4 at. %). No Cu is present in BHO and the EELS signal shows the expected lack of Cu. In addition, the Cu L signal in EELS is *not* convoluted with spurious Cu signal such as for the EDXS signal.
It is worth noting that the observed changes in RE M_5 white-line intensities could result from a change in the local bonding environment of the REs. This is because the ELNES is sensitive to such changes in the local bonding. However, the same trends are observed in EDXS, which is (mostly) insensitive to these effects. Therefore, the changes in RE M_5 white-line intensities directly relate to the local RE concentration in the REBCO-BHO material system.

Up to here, mostly STEM-EDXS and STEM-EELS analyses for the 5BCO sample were shown. Figure 5.49 shows and compares elemental maps for BHO NP regions for (a) 3BCO, (b) SmBCO, (c) GdBCO, and (d) ErBCO, obtained from STEM-EELS measurements. An ADF-STEM overview image with the marked acquisition region is shown for each sample. STEM-EELS was chosen here since the small differences in RE signals between REBCO and BHO were more pronounced in the EELS signal for 5BCO (cf. Fig. 5.45b on Page 217 for EDXS and Fig. 5.48e for EELS). The RE signals in the elemental maps are highlighted with a dashed yellow line. Starting with 3BCO (Fig. 5.49a), a higher Er signal in BHO than in the 3BCO film is observed, similar to 5BCO. However, the difference between the Er concentration in REBCO and 3BCO seems smaller than for the 5BCO film. This is also observed for ErBCO (Fig. 5.49d), where the Er signal is nearly identical in BHO and ErBCO. This indicates that the RE-BHO mixing not only depends on the RE but also if a single- or multi-RE REBCO-BHO nanocomposite is considered. This will be discussed further below.
Figure 5.49c shows a significant Gd depletion in BHO. This is again similar to the Gd signal in 5BCO. Similarly, the Sm signal also shows a substantial depletion in BHO. The latter was expected since Sm has an even larger ionic radius (or smaller Z) than Gd. Still, the expected trend that REs with larger ionic radii show a reduced RE-BHO intermixing is confirmed here.

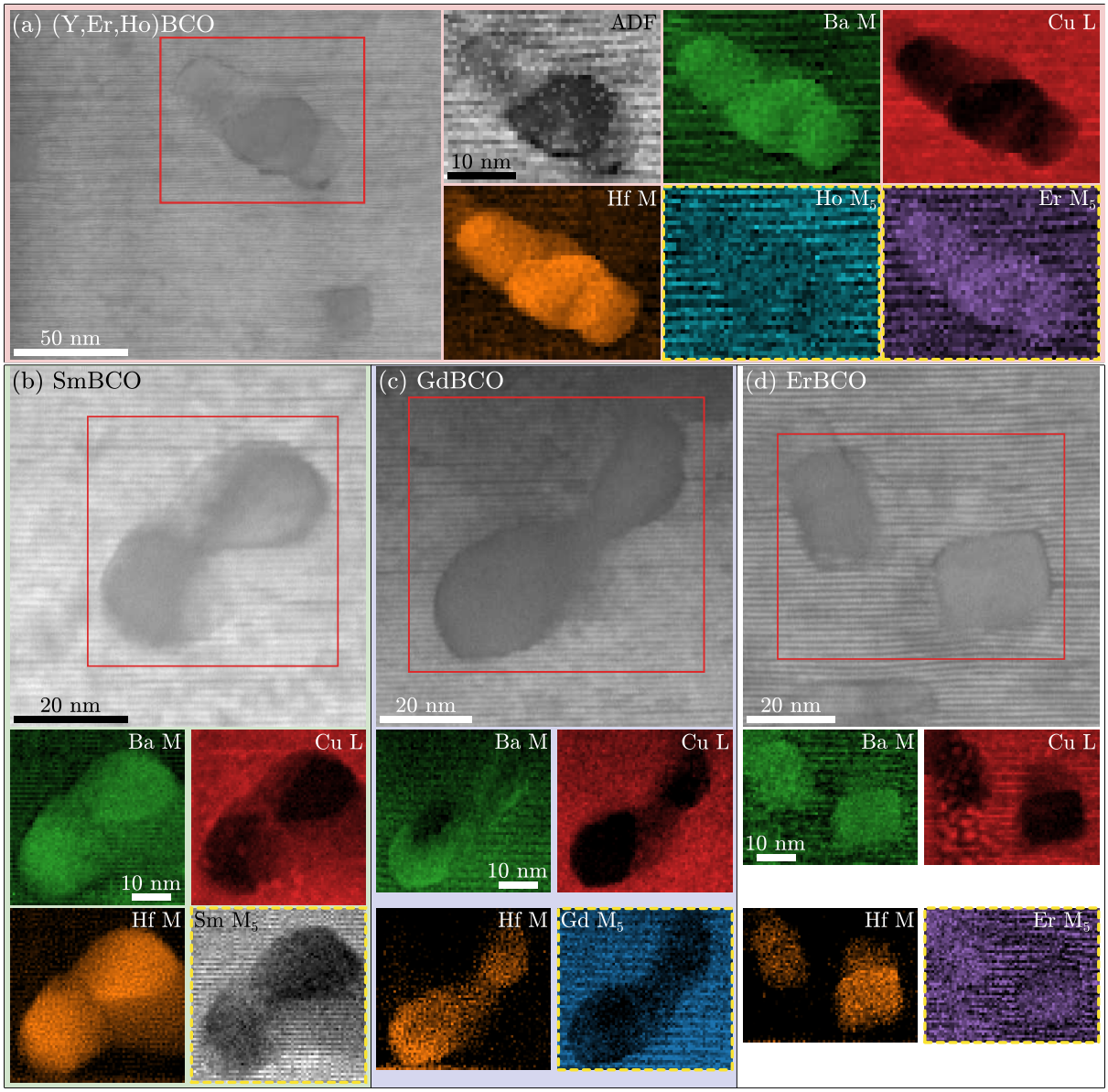

Figure 5.49: STEM-EELS elemental maps for $BaHfO_3$ particles in different REBCO films. The ADF-STEM images show the acquisition regions with a red rectangle. The RE elemental maps are highlighted with a dashed yellow line.

Elemental analysis with STEM-EDXS was used to get insights into the relative differences in RE concentrations in the single- and multi-RE REBCO-BHO nanocomposite films. A mixture of BHO and REBCO signals is measured in STEM-EDXS and STEM-EELS since the BHO NPs with an average diameter of around 20 nm to 28 nm are embedded in a surrounding REBCO matrix in a TEM sample (about 50 nm to 100 nm thickness). As a result, the measured BHO composition depends on the size of a NP and how it is contained in a TEM sample, i.e. if and how the BHO NPs are intersected by the TEM-sample surface after TEM-sample preparation. To overcome this problem, the data from as many NPs as possible was averaged. However, this procedure assumes the same NP size for each REBCO-BHO nanocomposite, which is not strictly valid due to differences in fabrication parameters, which affect the NP size and shape. Therefore, the following analyses should be interpreted carefully. STEM-EDXS was used rather than STEM-EELS since larger sample areas could be analyzed with the required spatial sampling for the given microscope hardware.

Masked-sum spectra from the (i) REBCO matrix and (ii) BHO NPs were extracted from the raw STEM-EDXS datasets (cf. Fig. 3.19 on page 88). Then, the elemental concentrations were quantified with the standardless Cliff-Lorimer approach. The relative deviations ΔC of the RE concentrations in REBCO $C_{\mathrm{RE,REBCO}}$ and BHO $C_{\mathrm{RE,BHO}}$ were calculated for each nanocomposite, i.e.

$$\Delta C = \frac{C_{\mathrm{RE,BHO}}}{C_{\mathrm{RE,REBCO}}} - 1 \quad . \tag{5.7}$$

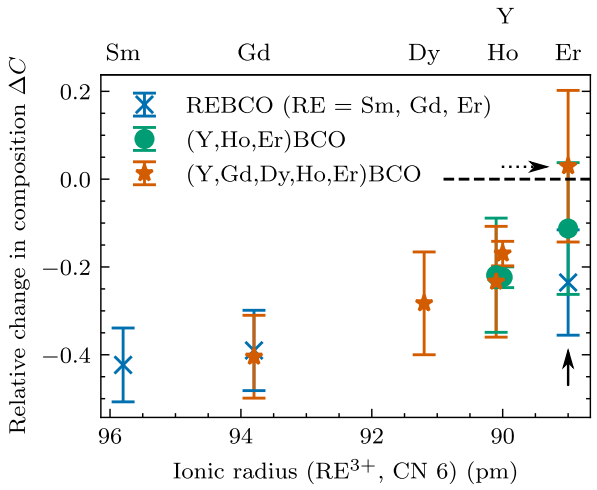

Figure 5.50: Comparison of rare-earth concentrations in REBCO and $BaHfO_3$ nanoparticles. The values $\Delta C = C_{\mathrm{RE,BHO}}/C_{\mathrm{RE,REBCO}} - 1$ are plotted against the ionic radii of the different REs.

The ΔC values are plotted against the ionic radii (for oxidation state 3+ and a CN 6[8]) in Fig. 5.50. The corresponding RE symbols are listed on top of the plot. The dashed horizontal line marks $\Delta C = 0$, which can be interpreted as the same RE concentration in REBCO and BHO. A higher (lower) RE concentration in BHO compared to REBCO is found for $\Delta C > 0$ ($\Delta C < 0$). Two key points can be observed from Fig. 5.50:

1. A higher tendency for RE-BHO intermixing is observed for decreasing ionic radius because ΔC increases.
2. The RE-BHO intermixing shows a stronger RE dependence for multi-RE samples. This corresponds to a higher "slope" for ΔC towards smaller ionic radii for multi-RE samples than for single-RE samples.

The second aspect can be seen by comparing the Er signal for 5BCO, 3BCO, and ErBCO (solid arrow in Fig. 5.50). Single-RE ErBCO shows the least pronounced Er-BHO intermixing, followed by multi-RE 3BCO and 5BCO. The latter even shows an increased Er concentration in BHO relative to the 5BCO matrix ($\Delta C > 0$, marked by a dotted arrow).
These observations should be considered in REBCO-BHO nanocomposite fabrication by a RE-dependent adjustment in the precursor solutions. For example, a higher Er content may be used in 5BCO to force more Er into the REBCO matrix. The RE-dependent RE-BHO mixing is still important even for single-RE REBCO films and must be considered during fabrication and also regarding the microstructural results. For ErBCO, most of the Er still occupies the expected RE site in ErBCO and only a minor part is contained in BHO. The films with a high

[8] CN 6 was chosen in the assumption that RE^{3+} substitutes Hf^{4+} in BHO. In REBCO, the REs are coordinated with CN 8. Both could be used, as this only changes the offset of the abscissa.

Er concentration (ErBCO and 3BCO) also showed the highest SF density (cf. Fig. 5.31e and b on Page 198), which might be related to the Er-BHO intermixing. The RE-BHO intermixing is less pronounced for SmBCO and GdBCO, which is in line with the expectation that BHO does *not* chemically (or in negligible amounts) interact with the REBCO matrix.

ELNES analysis of REs. This subsection shows analyses of the ELNES of the REs to get insights into the bonding configuration in REBCO and BHO. This is important since the bonding configuration influences the ionic radii of the REs, which are essential to understand the RE-BHO intermixing. The ionic radii depend on the oxidation state and CN. Figure 5.51 summarizes these properties for (a) REBCO and (b) BHO. For example, Ba^{2+} is present in REBCO with CN 10 and in BHO with CN 12. The values for the ionic radii were taken from the *mendeleev* Python package [Men21] (`https://github.com/lmmentel/mendeleev`, last accessed 03.03.2022).

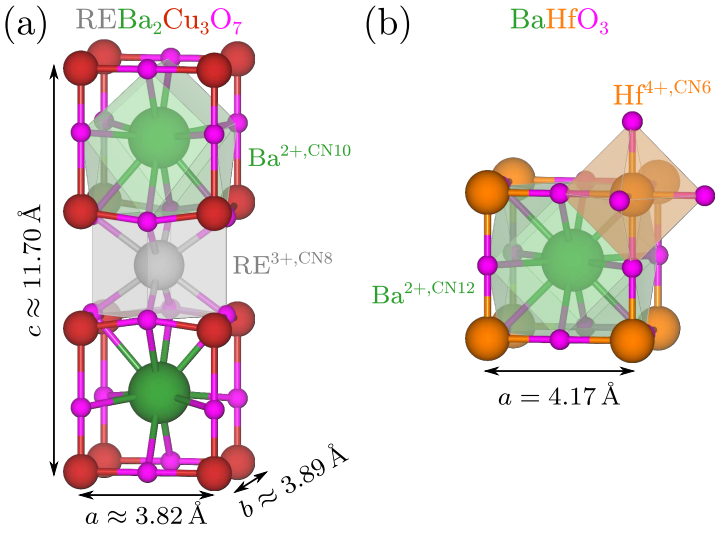

Figure 5.51: Bonding configuration of various elements in (a) REBCO and (b) $BaHfO_3$. The shaded polyhedra show the O coordination of selected elements.

Most REs have an oxidation state RE^{3+}, e.g. in REBCO or in RE_2O_3. An exception is Sm, which was also reported as Sm^{2+} [Oka+00]. The difference of Sm^{3+} and Sm^{2+} can be measured by EELS. Okazaki et al. [Oka+00] measured an onset shift of 2 eV to 3 eV of the Sm $M_{4,5}$ white lines between the two oxidation states. Therefore, the ELNES of the Sm M edge was compared for the SmBCO matrix and the embedded BHO NPs (Fig. 5.52).

Figure 5.52a shows an ADF-STEM cross-section image of the SmBCO sample with the marked acquisition positions for the EELS point spectra (denoted as P1–P5). Point spectra were collected instead of spectrum images to collect spectra from multiple BHO NPs with a good signal-to-noise ratio. The point spectra can also be acquired faster, which reduces the chance of spectrometer energy-drift during acquisition (compared to spectrum images). Point P1 was taken in SmBCO, whereas P2 to P5 were taken from BHO NPs. The five EELS spectra are compared in Fig. 5.52b and the elemental edges are marked with the chemical symbols and the edge name. The spectra were normalized to the same energy interval (gray shaded region before the Ba M edges). The inset shows a magnified view on the Hf $M_{4,5}$ edges, only visible for the BHO spectra P2 to P5. In contrast, Cu $L_{2,3}$ is only observed in SmBCO (P1, magnified in Fig. 5.52c). The absence of the Cu signal for P2 to P5 indicates that the signal mostly originates from the Cu-free BHO nanoparticles and has nearly no contributions from the surrounding Cu-containing SmBCO matrix.
Most importantly, no white-line shift is observed for Sm $M_{4,5}$ between SmBCO and the BHO

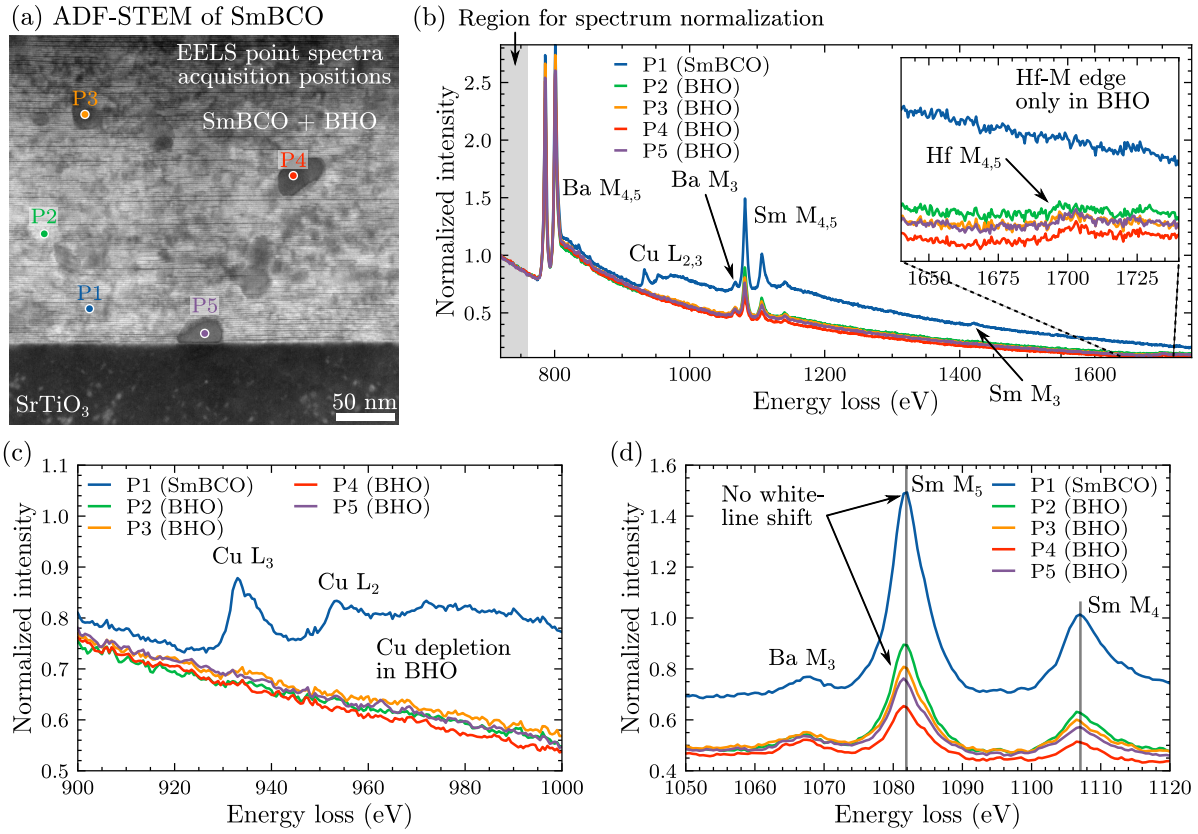

Figure 5.52: Oxidation-state analysis of Sm in a SmBCO-$BaHfO_3$ nanocomposite. (a) ADF-STEM overview image of a SmBCO film with BHO nanoparticles. The acquisition points for EELS spectra from SmBCO (P1) and BHO (P2–P5) are overlaid. (b) Normalized EELS spectra for an overview. The core-loss edges are marked and denoted by the chemical symbols and edge types. The inset shows the weak Hf $M_{4,5}$ edges. (c and d) Magnified view at the (c) Cu $L_{2,3}$ and (d) Sm $M_{4,5}$ edges. (d) No Sm $M_{4,5}$ white-line shifts are observed between SmBCO and BHO.

spectra, as indicated by the vertical line in Fig. 5.52d. This indicates the same oxidation state Sm^{3+} for SmBCO and BHO.

A similar analysis was performed for GdBCO and ErBCO. Note that only the single-RE films were evaluated. This is because the multi-RE films only have a reduced elemental concentration per RE, which significantly reduced the signal-to-noise ratio of the white-lines. In addition, the RE M edges overlap, which further impedes a detailed analysis of the ELNES. Figure 5.53a and b show an additional analysis for a single BHO nanoparticle in SmBCO. The BHO position is indicated by a dashed lime in the Sm M_5 white-line intensity map in Fig. 5.53b. The NLLS fit setup consists of a (i) power-law background, (ii) a Sm $M_{4,5}$ Hartree-Slater cross-section model, and (iii) Gaussian functions for the peaks. Note that the Ba M_3 edge starts close to the Sm M_5 edge. The total fit is displayed in black on top of the experimental spectrum in blue.
The NLLS fit was applied to each position in the STEM-EELS spectrum image to extract the Sm $M_{4,5}$ white-line intensities (Fig. 5.53b). The white-line ratio Sm M_4/Sm M_5 was calculated and is also displayed as a map. No appreciable change for Sm M_4/Sm M_5 is observed in the BHO region compared to the surrounding SmBCO matrix. A similar analysis with the same qualitative result is performed for the Gd M_4/Gd M_5 ratio for the GdBCO-BHO film (Fig. 5.53c and d).
For ErBCO, the signal-to-noise ratio in the acquired spectrum images was too low for a precise fit of the Er M_4/Er M_5 ratio. This is because the Er M_4 white-line is comparably weak compared to

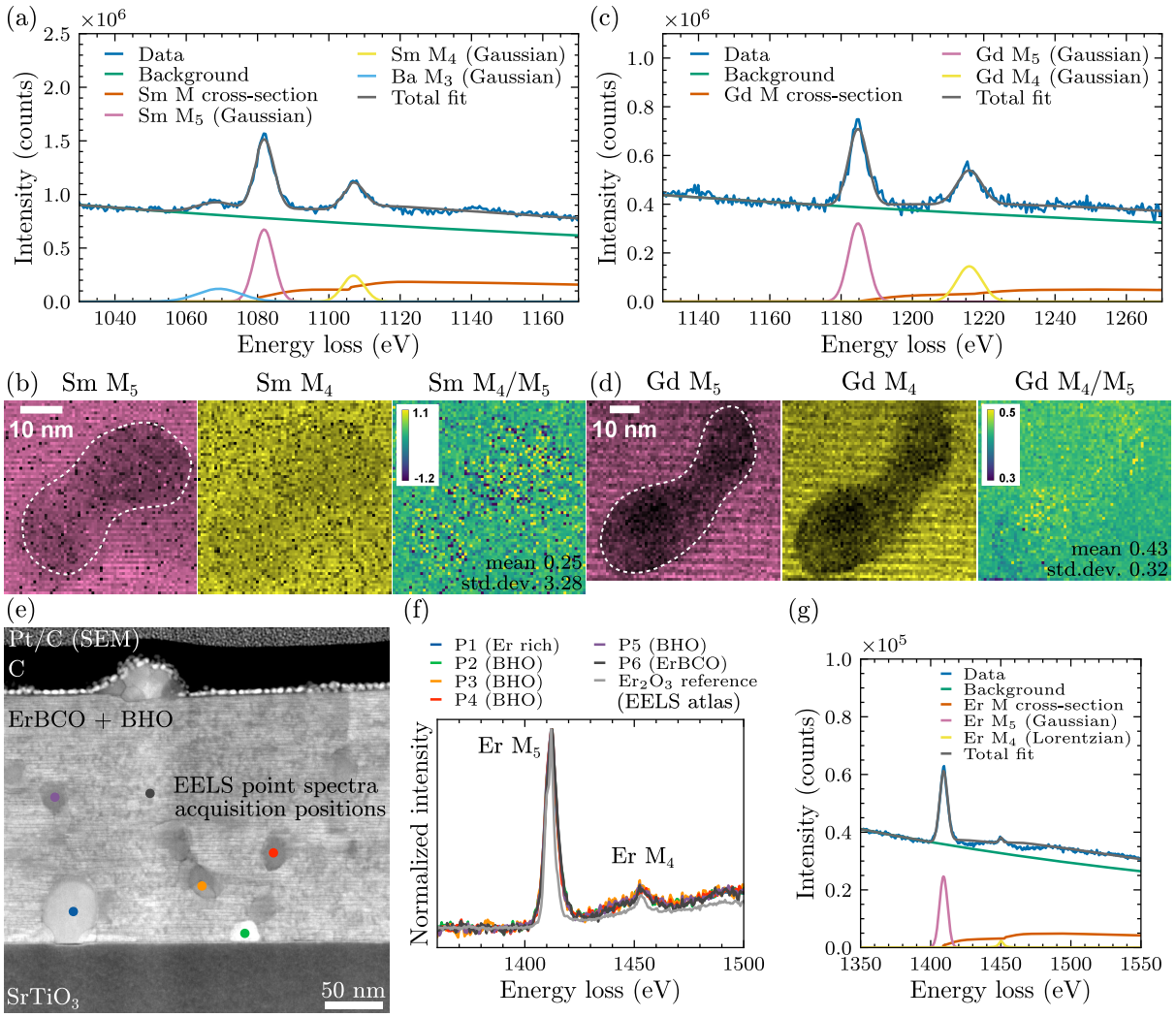

Figure 5.53: Analysis of the M_4/M_5 white-line ratio for (a,b) SmBCO, (c,d) GdBCO, and (e–g) ErBCO. The model setup for non-linear least-squares fitting are displayed in (a), (c), and (g). The extracted M_4/M_5 ratio for (b) SmBCO and (d) GdBCO shows no visible change between the REBCO matrix and the $BaHfO_3$ nanoparticle (the position of the latter is indicated with dashed lines). (e) ADF-STEM image of ErBCO with BHO and overlaid EELS point spectrum acquisition positions. (f) Background-subtracted and normalized experimental Er $M_{4,5}$ signals show no difference between ErBCO (P6), Er_2O_3 (P1), and BHO nanoparticles (P2–P5).

Er M_5. Therefore, EELS point spectra were acquired from the regions shown in the ADF-STEM image in Fig. 5.53e. P1 was taken in an Er-rich precipitate, most likely Er_2O_3. P2 to P5 were acquired on BHO NPs and P6 was taken from the ErBCO matrix. The background-corrected Er $M_{4,5}$ edges were normalized and are plotted in Fig. 5.53f for comparison. All spectra show a similar shape and no white-line shift. A reference spectrum from Er_2O_3 from the EELS atlas[9] by Gatan was also plotted as a further reference for Er^{3+}. The Er M_4/Er M_5 ratio was calculated from the point spectra using the NLLS fit setup shown in Fig. 5.53g. Note that a Lorentzian peak model was used here for the Er M_4 white-line, which gave more reproducible results (regarding the placement of the NLLS fit window in *DigitalMicrograph*).

The M_4/M_5 white line ratios of 0.32 ± 0.02 (Sm, averaged together with the point spectra from Fig. 5.52), 0.44 ± 0.02 (Gd), and 0.10 ± 0.01 (Er) agree with the reported values in the literature for RE^{3+} oxidation states [FB96; KCS21]. All ELNES analyses show no appreciable changes in

[9] `https://eels.info/atlas` (last accessed: 30.03.2022)

the RE M edge ELNES, indicating the same oxidation state RE^{3+} in REBCO and BHO. Note that the effect of the CN of the RE was not considered in these analyses. The CN should – in principle – also affect the ELNES. However, no studies regarding the effect of different CN on the RE $M_{4,5}$ white-lines were found in the literature.

Discussion of RE-BHO intermixing. The next part discusses possible reasons for the experimentally observed RE-dependent mixing of REs into the BHO NPs. An important property for the discussion is the ionic radius of the REs and possible substitution sites in REBCO and BHO (or other nanoparticle materials). Majkic et al. [Maj+21] considered the formation of a $Ba^{2+}(Zr^{4+}_{1-x}RE^{3+}_{x})O_{3-\delta}$ NP compound for BZO NPs in REBCO films, assuming no change for the RE^{3+} oxidation state. This was confirmed here, assuming that a change in oxidation state should affect the RE $M_{4,5}$ ELNES. However, the following discussion partly assumes a change in CN (e.g., from 8 in REBCO to 6 in BHO) for RE^{3+}, which could not be analyzed/confirmed with the presented EELS measurements. The uncertainty in the CN should be considered in the following discussion. Besides BHO, also other barium oxide materials that are typically used for REBCO nanocomposite films are added to the discussion, i.e. $BaZrO_3$ (BHO), $BaTiO_3$ (BTO), $BaSnO_3$ (BSO), and $BaBn_2O_6$ (BNO). These are denoted as BMO (M = Hf, Nb, Sn, Ti, Zr) and most of the materials are perovskites with a stoichiometric formula ABO_3 (A = Ba). The only exception is $BaNb_2O_6$. Regarding the REs, The whole lanthanoid series of the REs from La to Lu is considered in the calculations, even though some of the REs may not form stable REBCO phases.

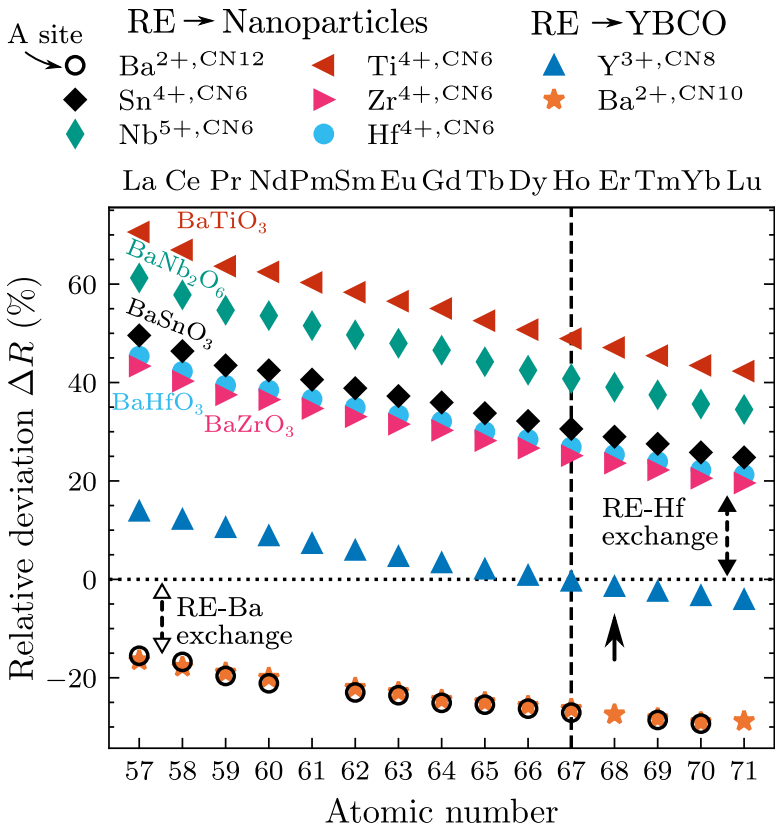

Figure 5.54: Relative deviation ΔR between ionic radii of the the rare-earth ion R_{RE} and different substitution sites in REBCO nanocomposites. A ΔR value closer to 0 is interpreted as a higher substitution probability. The legend above the plot shows the substitution sites. In all cases, an oxidation state RE^{3+} was assumed with the same CN as the substitution site. An enhanced (reduced) RE-BHO intermixing is suggested towards larger (smaller) Z, as indicated by the double-headed arrows. RE-Ba cation substitution becomes more probable for lower Z. The vertical line marks Ho, which has the smallest deviation to Y in YBCO (▲).

First, the relative deviation ΔR between the RE^{3+} atoms and different possible substitution sites x were calculated, e.g. $Y^{3+,CN8}$ in REBCO, $Ba^{2+,CN10}$ in REBCO, $Ba^{2+,CN12}$ in BMO (A-site substitution), and $Hf^{4+,CN6}$ in BHO (B-site substitution). The stable YBCO phase is used as reference compound for a RE substitution into the REBCO matrix [Mac+94]. The

formula

$$\Delta R = \frac{R_{\mathrm{RE}}}{R_x} - 1 \tag{5.8}$$

was used. The values for the ionic radii R were primarily taken from Shannon [Sha76]. Possible missing values were added using the ionic radii from Baloch et al. [Bal+21]. Regarding the here-used $YBa_2Cu_3O_{7-\delta}$ reference phase for $REBa_2Cu_3O_{7-\delta}$, the REs can populate the expected Y site and the Ba site [Mac+94; Mac+06] (so-called RE-Ba cation exchange). The latter becomes more probable for increasing R_{RE} closer to R_{Ba}. For the perovskite NPs, REs can populate the A and B sites [DZ10; Lim+21; TDR01; Jia+09]. For a RE incorporation into the NP materials, a constant REE oxidation state of 3+ and the same CN as the substitution site for the REs is used during the calculations, analogous to [DZ10]. Therefore, the following sites for the REs are considered for a substitution into **REBCO** (here YBCO is used as a reference for REBCO)

- RE $\rightarrow Y^{3+,\mathrm{CN8}}$ (REBCO, Y taken as a reference, ▲)
- RE $\rightarrow Ba^{2+,\mathrm{CN10}}$ (REBCO, ★)

and a substitution into the **BMO nanoparticles**:

- RE $\rightarrow Ba^{2+,\mathrm{CN12}}$ (A-site substitution into BMO, equal R for all NP materials, ○)
- RE $\rightarrow M^{4+,\mathrm{CN6}}$ (B-site substitution into BSO ◆, BHO ●, BZO ▶, BTO ◀)
- RE $\rightarrow Nb^{5+,\mathrm{CN6}}$ (B-site substitution into BNO ⧫)

Note again that there are two different available Ba sites, i.e. (i) $Ba^{2+,\mathrm{CN10}}$ for a RE $\rightarrow$ REBCO substitution and (ii) $Ba^{2+,\mathrm{CN12}}$ for a RE $\rightarrow$ BMO substitution to the A site. The calculated ΔR values are plotted against the RE atomic number in Fig. 5.54. A ΔR value closer to 0 is interpreted as a higher chance of RE substitution. However, the sign of ΔR is not considered in the discussion but may also affect substitution probabilities.

The discussion first focuses on REBCO (▲, ★) and BHO (●, ○). The ΔR values closest to 0 are observed for the expected RE substitution to the Y site (▲) to form the REBCO phase. The ionic radius of Ho is closest to Y and, therefore, shows the smallest deviation to Y (marked with a dashed vertical line at $Z_{\mathrm{Ho}} = 67$). Two general trends are observed. For BHO, the ΔR values get closer to 0 towards larger Z for the Hf sites (●), i.e. a B-site substitution. This increases the chance for a RE-Hf substitution for larger Z (marked by the right double-headed arrow in Fig. 5.54). This observation agrees with the experimentally observed increased tendency for RE-BHO intermixing for REs with larger Z (smaller ionic radii), e.g. shown by EELS (Fig. 5.48 on page 220) or EDXS (Fig. 5.45 on page 217). In contrast, a RE-Ba cation exchange becomes more probable for decreasing Z, as indicated by the left double-headed arrow. The ΔR values for the Ba sites in REBCO (★, CN10) and BMO (○, CN12) are quite similar. Therefore, they can be treated equally.

In the case of BHO, the vertical line at Ho also marks a cross-over point regarding the modulus of ΔR. Here, $|\Delta R|$ is nearly equal for a Ho $\rightarrow$ Hf substitution ($\Delta R = 26.9\,\%$, ●) and Ho $\rightarrow$ Ba substitution in REBCO ($\Delta R = -26.3\,\%$, ★) or BHO ($\Delta R = -27.1\,\%$, ○). The next RE towards higher Z is Er with $Z = 68$ (marked by a vertical arrow). The ΔR values for Er are $\Delta R = 25.4\,\%$ for Er $\rightarrow$ Hf (●) versus $\Delta R = -27.4\,\%$ for Er $\rightarrow$ Ba in REBCO (★). This indicates that an Er substitution to the Hf site in BHO is more likely than an Er substitution to the Ba sites (in REBCO or BHO). Indeed, this observation agrees with the RE concentration in BHO for the 5BCO sample (cf. Fig. 5.48e on Page 220), where a higher Er signal in BHO is observed

compared to the other REs. The Er atoms are preferably incorporated into BHO, whereas the other REs in 5BCO (i.e. Gd, Dy, Ho, Y) have a higher chance to substitute to the Ba site in REBCO instead of a substitution to the Hf site in BHO. However, a higher Er signal in BHO compared to the REBCO matrix was not observed for the other Er-containing samples 3BCO and ErBCO (Fig. 5.50 on page 223). The RE substitution into BHO depends on the exact RE mixture and probably the fabrication parameters and cannot be easily estimated based solely on Fig. 5.54.
The substitution probabilities of Ba sites (A sites) in BMO (○) and REBCO (★) are similar based on Fig. 5.54. However, a significant RE substitution to the Ba sites in BMO (○) can be ruled out from the EDXS (Fig. 5.45 on page 217) and EELS (cf. Fig. 5.48e on Page 220) results. This is because the experimentally observed Gd and Sm signals in BHO are depleted compared to the Gd and Sm signals in REBCO. This indicates that the RE → Ba substitution to the A site of BHO (○) for $Z < 67$ is significantly less probable than a B-site substitution to BHO (Hf sites) for $Z > 67$. The difference in A- and B-site substitution of REs into BHO may be explained by charge compensation, as suggested by Lim et al. [Lim+21]. A RE^{3+} substitution to the Hf^{4+} site generates O vacancies to compensate for the charge of the different oxidation states. This was also suggested by Majkic et al. [Maj+21] for BZO NPs, i.e. $Ba^{2+}(Zr^{4+}_{1-x}RE^{3+}_x)O_{3-\delta}$ with the O non-stoichiometry δ. In contrast, a substitution to the BHO Ba^{2+} site would require cation vacancies (or excess O), and the cations may form precipitates (e.g. HfO_2 or $RE_2Hf_2O_7$ [DZ10]). Such precipitates were not observed experimentally. Hence, here a NP composition $Ba^{2+}(Hf^{4+}_{1-x}RE^{3+}_x)O_{3-\delta}$ is suspected for the NPs analogous to Majkic et al. [Maj+21] for BZO.

The discussion for BHO based on Fig. 5.54 can be extended to other NP materials. As mentioned earlier, the $Ba^{2+,CN12}$ site in BMO nanoparticles (○) is the same for every material and only plotted once. The ΔR data points for all NP materials follow the same trend but are vertically shifted. A RE → B-site substitution becomes more probable for increasing Z (smaller ionic radii), whereas an RE → Ba cation exchange into REBCO is more likely for decreasing Z (larger ionic radii). However, the cross-over point for $|\Delta R|$ (see further above) between these substitution sites shift to another Z compared to $Z = 67$ for BHO. For example, the cross-over points are located at $Z = 66$ (Dy) for BZO and $Z = 69$ (Tm) for BSO. For BNO and BTO, however, no such cross-over point is observed. This suggests that a RE → Ba substitution is more probable (or has a smaller $|\Delta R|$) for *all* REs up to Lu. This would indicate no RE-BMO intermixing for BNO and BTO. However, an Er-BNO intermixing in ErBCO-BNO films was reported by Yamada et al. [Yam+08], which does not agree with the expectation from Fig. 5.54. This exemplifies that the simplified analysis based solely on Fig. 5.54 cannot be used to predict the RE-BMO intermixing. The latter may depend also on the RE mixture, fabrication parameters, the sign of ΔR and other factors.

The Goldschmidt tolerance factor t is another commonly used qualitative metric to evaluate the phase stability of perovskites with the cubic structure ABO_3 [TDR01]. It is defined as

$$t = \frac{R_\mathrm{A} - R_\mathrm{O}}{\sqrt{2}\,(R_\mathrm{B} - R_\mathrm{O})} \quad , \tag{5.9}$$

with the ionic radii R of the different elements in ABO_3. A value $R_\mathrm{O} = 140\,\mathrm{pm}$ was used here for O. A value t closer to 1 is associated with a higher stability of a perovskite for two elements A and B. Therefore, a value closer to 1 is assumed to lead to a higher substitution probability. The t values for the pure NP materials BHO, BZO, BTO, and BSO are shown in Fig. 5.55 as a

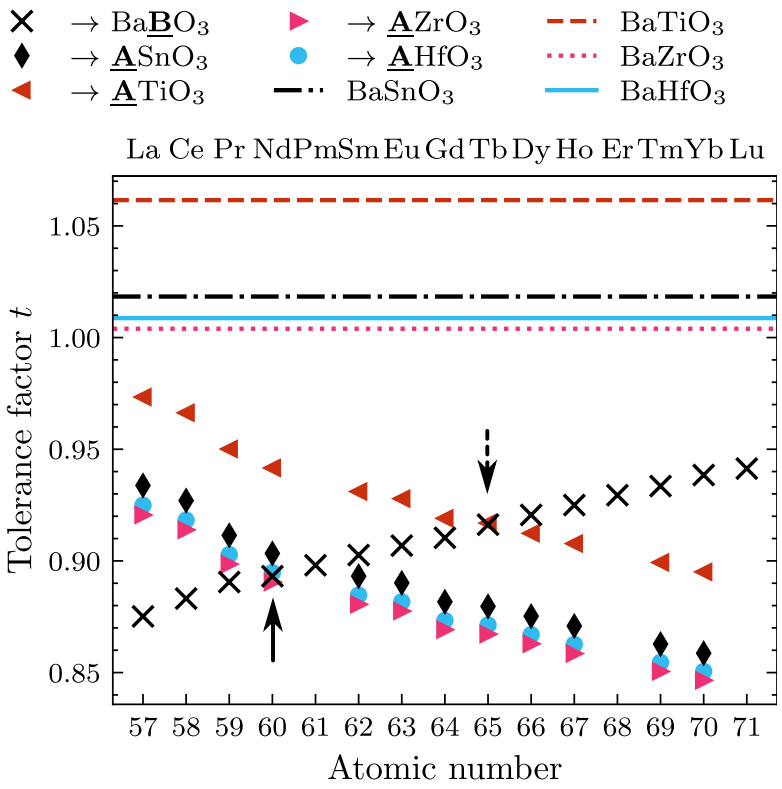

Figure 5.55: Goldschmidt tolerance factors for rare-earth substitution into barium oxide perovskites. A t value closer to 1 is interpreted as a higher substitution probability. The legend above the plot shows the substitution sites. In all cases, an oxidation state RE^{3+} was assumed with the same CN as the substitution site. The horizontal lines mark the t values for the pristine NP materials.

horizontal line. The values are all slightly above 1, with BTO (dashed line) having the largest deviation. Note that $BaNb_2O_6$ is missing in the plot since it is not a perovskite.

The other values in Fig. 5.55 were calculated for different subsitution sites of REs (with RE^{3+}) in the ABO_3 NPs. The same coordination number as the target site is assumed for RE^{3+} in ABO_3, i.e. CN 12 for the A site and CN 6 for the B site. A RE can (i) substitute the B site (×) or (ii) the A site (i.e. Ba site). The substitution sites are underscored in the legend in Fig. 5.55. For case (i), Ba is located on the A site for all investigated NP materials. Hence, the × values are the same for all shown NP materials. In contrast, for case (ii) each NP material has a different element on the B site.

The RE → B-site substitutions (×) show a trend towards $t \to 1$ for increasing Z (i.e. smaller ionic radii). In contrast, the values for a RE → A-site substitution for BHO (●), BZO (▶), BTO (◀), and BSO (⧫) show a higher probability towards smaller Z. This is similar to the trends observed for ΔR in Fig. 5.54. Cross-over points of A- and B-site substitution curves are visible, where the probability for A- and B-site substitution swap. For example, the cross-over point is at $Z = 65$ (Tb, marked by a dashed arrow Fig. 5.55) for BTO and at $Z = 60$ (Nd, marked by a solid arrow) for BHO and BZO. Near the cross-over points, a mixed A- and B-site substitution may be possible [TDR01]. A preferential B-site substitution for REs with $Z > 60$ fits the experimental results for BHO shown in this work and the results of Majkic et al. [Maj+21] for BZO since only REs with $Z > 60$ were investigated (with the exception of Y, which is similar to Ho regarding the ionic radius). As mentioned earlier, an A-site substitution of Ba^{2+} with a RE^{3+} requires the formation of cation vacancies, which may be less probable than the O vacancies for a B-site subsitution of the B^{4+} element. As a result, an A-site substitution with REs may be unlikely, even if the t value for an A-site substitution is closer to 1 than a B-site substitution.

To finish the discussion, it is again emphasized that the plots for ΔR (Fig. 5.54) and t (Fig. 5.55) give only qualitative guidelines for a possible RE intermixing with various NP materials. Further

experiments are required to systematically study the interaction of different REs in single- and multi-RE REBCO nanocomposites with various NP materials.

Conclusions. This section showed analyses for different CSD-grown REBCO-BHO nanocomposite films. All films were optimized regarding the fabrication procedure (e.g. the crystallization temperatures). The CSD method enables high-quality REBCO-film growth for single-RE and multi-RE REBCO films. Only one sample had pores (3BCO), possibly resulting from an insufficient spreading of the precursor solution during spin-coating.
The use of a mixture of several REs in REBCO is of interest for efficient low-T pinning by atomic disorder [Mac+94; Mac+06]. The fabricated films with three and five different REs showed a spatially homogeneous RE mixture in the REBCO films, in contrast to the RE clusters observed by Araki et al. [Ara+18]. This shows that high-quality, "high-entropy" REBCO films can be prepared with the CSD method.
Nanoparticles such as BHO can be added to the REBCO precursor mixture. All CSD-grown films showed a homogeneous distribution of roundish BHO particles with average diameters of about $\sim 20\,\mathrm{nm}$. The nominal BHO concentration is in good agreement with the measured BHO concentrations. However, the size and shape of BHO particles varied slightly between REBCO films with different REs , probably because each RE requires slightly different fabrication parameters to achieve an optimal REBCO phase. Here, different NPs than BHO may be worth investigating for various REBCO films with different REs in future studies.
Another interesting aspect regarding the nanoparticles is their intermixing with REs. For BHO, a higher mixing tendency was found for REs with smaller ionic radii. Here, Er showed the most significant intermixing with BHO. This nanoparticle intermixing should be considered in REBCO-nanoparticle films since part of the REs are "lost" in the nanoparticle material and not available to form the REBCO phase. Here, only BHO was available as a nanoparticle material, but a similar effect was reported for $BaZrO_3$ [Maj+21; Díe+21] or $BaNb_2O_6$ [Yam+08]. Future studies could investigate similar single- and multi-RE REBCO films with other nanoparticle materials. Multi-RE REBCO films are advantageous for these investigations since they provide a direct insight in the RE-dependent intermixing for a given number of REs in the same film produced with the same fabrication parameters. The ionic radius of the REs is a crucial property regarding the RE-nanoparticle intermixing. Here, (i) a simple relative deviation between the ionic radii of the RE and possible substitution sites and (ii) the Goldschmidt tolerance factors were introduced to provide guidelines and predictions for RE-NP intermixing. However, additional experiments and data for the RE-NP intermixing for other NPs and REs are important to get a better understanding of this phenomenon. Besides the relative difference ΔR and the Goldschmidt tolerance factor t, other metrics, e.g. the revised tolerance factor by Bartel et al. [Bar+19], can be used to get a better understanding of RE-NP intermixing.

5.5 Summary

This chapter shows experimental results by SEM and TEM for various REBCO thin films. Three sections present (i) experimental problems (Section 5.1 on page 158) including a detailed investigation regarding the formation of small, nanoscale planar defects in TEM samples (Section 5.2 on page 159), (ii) a microstructural analysis of the effect of an *ex-situ* oxygenation of PLD-grown GdBCO films (Section 5.3 on page 178), and (iii) CSD-grown REBCO-BHO nanocomposite films with a single or a mixture of different REs (Section 5.4 on page 196). The most important findings are summarized in the following.

- The **formation of small planar defects** was observed in nearly all REBCO films, but more pronounced in the CSD-grown films. Most of these planar defects are an artifact of a rapid TEM-sample degradation in air. This requires a careful evaluation of TEM results, since the artificial planar defects are structurally similar to genuine planar defects, i.e. stacking faults. TEM-sample degradation is more severe for thinner TEM samples (or TEM-sample regions). The degradation probably starts at the TEM-sample surface, which is exposed to air during sample transport between the FIB and S/TEM instruments. If technically available, an inert-gas transfer between the instruments should be considered for TEM samples of REBCO. Here, only freshly prepared TEM samples were investigated to minimize the sample-degradation artifacts.

- The ***ex-situ* oxygenation of GdBCO films** grown on MgO substrates has noticeable effects on the microstructure. The GdBCO films were prepared by PLD and fully oxygenated by *ex-situ* annealing in an O atmosphere. Only the oxygenated films show the formation of extended twin-boundaries along the GdBCO$\langle 1\,1\,0\rangle$ directions The twin-boundary spacing of about (40 ± 20) nm (arithmetic average and standard deviation) was similar for all investigated oxygenated films. Different precipitates on the GdBCO surfaces were observed. However, their exact composition could not always be clarified here due to their small lateral size. Some of these precipitates might be Gd_2O_3, which was observed in XRD measurements, but not in TEM cross-section samples. Other microstructural features were found for annealed and unannealed films. For example, misaligned GdBCO grains preferentially form at the MgO substrate surface, probably at larger substrate steps. Such misoriented grains were not observed for CSD-grown REBCO films on STO and LAO. Another observation for all films was the formation of small, plate-like Gd_2CuO_4 precipitates, which grow coherently in the GdBCO films. The Gd_2CuO_4 precipitates are interesting for vortex pinning due to their small size. Regarding the GdBCO-MgO interface, a periodic array of misfit dislocations with a spacing of about 2.4 nm is observed. The growth of *c*-oriented GdBCO starts with the CuO plane of GdBCO.

- High-quality **REBCO-$BaHfO_3$ nanocomposite films** were successfully fabricated with the **CSD method**. The latter is a promising, cost-effective method since no vacuum is required for REBCO fabrication. The added $BaHfO_3$ (BHO) nanoparticles are homogeneously distributed in the REBCO films, as desired for effective flux pinning by the BHO nanoparticles and associated defects (e.g. stacking faults). Small differences in BHO size might be related to different crystallization temperatures required for different REs.
  Multi-RE REBCO films with five, (Y,Gd,Dy,Ho,Er)BCO, and three, (Y,Er,Ho)BCO, different REs were successfully fabricated. Elemental analyses showed a homogeneous distribution of REs in the REBCO films. The formation of RE_2O_3 particles was also observed besides BHO, although with a lower concentration than BHO. The multi-RE REBCO-BHO nanocomposite films are also an ideal sample to study the RE-dependent RE-BHO intermixing. A clear trend was observed for the latter, where REs with smaller ionic radii (such as Er) are more easily incorporated into BHO than REs with larger ionic radii (such as Gd). EELS analyses showed no visible change in the RE M edge ELNES. Hence, the oxidation state of RE^{3+} is probably unchanged in BHO and forms the compound $Ba^{2+}(Hf^{4+}_{1-x}RE^{3+}_{x})O^{2-}_{3-\delta}$.

6. Summary

Analytical electron microscopy provides valuable insights into the structure and chemistry of materials from the micrometer scale down to the atomic scale. This technique was applied in this thesis to study superconducting thin films of the Fe-based superconductor $Ba(Fe_{0.92}Co_{0.08})_2As_2$ (Ba122) and Cu-based superconductors $REBa_2Cu_3O_{7-\delta}$ (REBCO, with RE being Y and/or one or more rare-earth elements from the lanthanoid series). The samples were grown with pulsed laser deposition (PLD) and chemical solution deposition (CSD, only for REBCO). The most important results are summarized in the following.

Results for Ba122 films

The **$Ba(Fe_{0.92}Co_{0.08})_2As_2$ (Ba122) growth rate during PLD** significantly influences secondary-phase formation for Ba122 growth on CaF_2 substrates. A low deposition rate ($0.4\,\text{Å s}^{-1}$) resulted in a high density of planar defects and the formation of BaF_2 as a secondary phase. The latter forms as precipitates at the Ba122-CaF_2 interface, and can grow to large precipitates (even reaching up to the film's surface). BaF_2 grows epitaxially on CaF_2 in various crystalline orientations, but predominantly with $BaF_2[1\,1\,0](0\,0\,1)\|CaF_2[1\,1\,0](0\,0\,1)\|Ba122[1\,0\,0](0\,0\,1)$. In contrast, BaF_2 formation is suppressed for a high deposition rate ($0.9\,\text{Å s}^{-1}$). Fe precipitates with the preferential crystalline orientation $Fe[1\,1\,0](0\,0\,1)\|Ba122[1\,0\,0](0\,0\,1)$ were observed in *all* Ba122 films prepared from stoichiometric Ba122 targets. The number density of Fe precipitates embedded in the films is higher for high deposition rates ($42\,\mu\text{m}^{-2}$) than for low deposition rates ($15\,\mu\text{m}^{-2}$). For both growth rates, the measured Fe-precipitate size at the film surface is similar with around $(80 \pm 20)\,\text{nm}$.
Two types of planar defects were observed. One is a stacking fault at the Ba planes with an in-plane $\langle 1\,0\,0\rangle/2$ shift. The *c*-lattice parameters of the surrounding Ba122 unit-cells are extended by about 4 %. The second planar-defect type increases the local *c*-lattice parameter by about 15 % to 20 % without an in-plane shift. Oxygen (and F) was observed at the stacking faults. Both types of planar defects appear with reduced atomic number (*Z*-)contrast in HAADF-STEM imaging due to O (and possibly F). *Ex-situ* formation of the planar defects can be excluded. Oxidation of Ba122 during film deposition could play an essential role in the planar-defect formation.

Ba122 films with embedded $BaHfO_3$ (BHO), $BaZrO_3$ (BZO), and InAs nanoparticles were grown with quasi-multilayer PLD. No nanoparticles (NPs) were observed for InAs, which is probably the result of (i) the low melting point of InAs (942 °C) and (ii) the high vapor pressure of As at the high deposition temperature (700 °C). Traces of In were measured, which are probably dissolved in the Ba122 matrix. Regarding BHO and BZO, NPs with a size of $\sim 5\,\text{nm}$ were observed in the Ba122 matrix. For a high NP content (about 20 mol %), the NPs aggregate in stacked, interrupted layers on the *ab*-plane. Despite of these high NP concentrations, high-quality Ba122 films were observed. For a low NP content (about 2 mol %), a *c*-oriented alignment (i.e. nanocolumns) was observed. In most cases, crystalline details of the NPs could not be observed, which indicates a disordered NP structure.

Ba122 film growth on $LaAlO_3$ and MgO was found to be less reproducible than on CaF_2 for the used PLD setup. The films on MgO were polycrystalline. A possible solution to this

problem could be a higher deposition rate (>1 Ås^{-1}). Misfit dislocations were observed for selected Ba122 grains with the expected epitaxial relationship Ba122[1 0 0](0 0 1)‖MgO[1 0 0](0 0 1). Ba122 films on $LaAlO_3$ substrates mostly grew epitaxially with the crystalline orientation Ba122[1 0 0](0 0 1)‖$LaAlO_3$[1 0 0](0 0 1). A high concentration of O-rich planar defects was observed. The Ba122-$LaAlO_3$ interface was strongly disordered and partly amorphous, which probably results from TEM-sample preparation.

Measurement artifacts induced by electron- and ion-beam irradiation could be identified. These are especially prominent for the Ba122-CaF_2 system since CaF_2 (and BaF_2) is highly reactive under electron-beam irradiation. This leads to *in-situ* oxidation of BaF_2 and CaF_2 and amorphization of the Ba122-CaF_2 interface. Careful TEM-sample preparation, investigation of freshly prepared TEM samples, and low-dose imaging with high electron energies (300 keV) minimize these problems. Since these artifacts are primarily caused by the CaF_2 substrate, other Fe-based superconductors grown on CaF_2 are most likely affected by similar problems.

Results for REBCO films

***Ex-situ* oxygenated PLD-grown $GdBa_2Cu_3O_{7-\delta}$ (GdBCO) films** were studied to investigate microstructural changes during oxygenation. The oxygenation process is essential to achieve the superconducting REBCO phase with an oxygen deficiency $\delta \approx 0$. The most noticeable microstructural difference after oxygenation is the formation of *c*-oriented twin boundaries during the tetragonal-to-orthorhombic phase transition. The twin boundaries are aligned parallel to the ⟨1 1 0⟩-directions of GdBCO with an observed spacing of about (40±20) nm. Misoriented GdBCO grains were found with the *c*-direction *not* parallel to the growth direction. These misoriented grains grow parallel to the *a*- and *b*-directions of the GdBCO film and preferentially nucleate at surface steps on the MgO substrate. The formation of the Gd_2CuO_4 phase with a plate-like morphology and precipitate sizes of a few nanometers was observed. Gd_2CuO_4 grows coherently inside GdBCO with the crystalline orientation Gd_2CuO_4[1 0 0](0 0 1)‖GdBCO[1 0 0](0 0 1) due to their similar crystal structures. Interestingly, Gd_2O_3 was detected by x-ray diffraction experiments but could not be definitely identified in the (S)TEM analyses. It is possible that (i) some of the plate-like Gd_2CuO_4 precipitates are actually Gd_2O_3 and (ii) that Gd_2O_3 forms as large precipitates with a small number density and are typically missed in extracted TEM samples from random sample regions.

Single- and multi-RE $REBa_2Cu_3O_{7-\delta}$ (REBCO)-BHO nanocomposite films were analyzed regarding their RE distribution and BHO NP concentration (12 mol % BHO). Films with high structural quality were obtained by CSD on $SrTiO_3$ and $LaAlO_3$ substrates because the fabrication parameters for REBCO growth were optimized in earlier experiments. A homogeneous distribution of the REs in the REBCO matrix without the formation of local single-RE REBCO clusters was observed for the multi-RE REBCO films. These medium- ((Y,Er,Ho)BCO, three different REs) and high-entropy REBCO films ((Dy,Gd,Y,Er,Ho)BCO, five different REs) have promising superconducting properties at low temperatures and low external fields due to random atomic-scale defects. The latter were not observed directly by STEM, but this could be a challenging task for future studies. The BHO NPs with a crystalline structure and an average diameter of about 20 nm to 28 nm are homogeneously distributed in the REBCO matrix and generate associated stacking faults. The BHO NPs are randomly oriented in the REBCO matrix. However, BHO preferentially grows with the crystalline orientation BHO[1 0 0](0 0 1)‖$SrTiO_3$[1 0 0](0 0 1) at the REBCO-$SrTiO_3$ interface. The formation of RE_2O_3 NPs in the REBCO films was also observed besides BHO, but with a lower concentration than

BHO. The REBCO-$SrTiO_3$ interface shows epitaxial cube-on-cube growth. In contrast, the REBCO-$LaAlO_3$ interface was more varied with (i) about 1° $\langle 1\,0\,0 \rangle$-tilted growth of REBCO, (ii) different REBCO-$LaAlO_3$ interface structure (cube-on-cube or zigzag alignment), and (iii) the formation of RE_2CuO_4 at the substrate interface.

A **RE-dependent RE-BHO intermixing** was found for the CSD-grown REBCO-BHO nanocomposite films. A clear trend exists because REs with smaller ionic radii are more likely to be incorporated into the BHO nanoparticles. The differences of RE-BHO intermixing for different REs are more pronounced for multi-RE REBCO films than for single-RE REBCO films. The observations indicate substitution of REs for Hf, i.e. $Ba^{2+}(Hf^{4+}_{1-x}RE^{3+}_{x})O^{2-}_{3-\delta}$. The RE-BHO intermixing affects the REBCO composition and is an important aspect of REBCO fabrication. However, more experiments with other REs and NP materials are necessary to improve the understanding of RE-dependent intermixing into barium oxide nanoparticle materials.

Nanoscale planar defects with an extension of about 5 nm to 30 nm in the *ab*-plane were observed in the investigated REBCO films in varying concentrations. These defects are structurally similar to genuine stacking faults in the form of one (or more) extra CuO planes. These genuine planar defects can be distinguished from the artificial nanoscale planar defects by their larger extension in the *ab*-plane. The nanoscale planar defects are most likely caused by rapid TEM-sample degradation during transport in air between different microscopes. A significantly higher density of nanoscale planar defects was observed for CSD-grown REBCO films with BHO NPs compared to PLD-grown GdBCO films. The exact reason for this difference is unclear, but residual molecules from the CSD precursor solution could play a role in the formation of these nanoscale planar defects. The identification of nanoscale planar defects as an artifact and their distinction from genuine extended planar defects is essential for the correlation of the microstructure with the superconducting properties because the nanoscale planar defects would have a desirable size for flux pinning.

Methodology developments

Site-specific TEM-sample preparation by focused-ion-beam milling was required to extract TEM specimens from sample regions with a size of a few ten micrometers. Most (S)TEM studies in this work were performed on cross-section TEM specimens. This bears the disadvantage that only small sample volumes can be analyzed. Plan-view TEM specimens are advantageous in this regard because the analyzed volume is significantly larger. Here, additional **plan-view TEM-sample preparation by focused-ion-beam milling** was used to extract plan-view TEM samples. The combination of cross-section and plan-view imaging geometries results in a more complete picture of the microstructure.

Low-energy energy-dispersive x-ray spectroscopy (EDXS) with electron energies below 5 keV was performed in a scanning electron microscope for thin-film analyses on bulk samples. Here, the use of lower electron energies improves spatial resolution and surface sensitivity. Both aspects are beneficial for the chemical analysis of small surface precipitates with sizes below 100 nm. Monte Carlo simulations of EDXS spectra helped to optimize the primary electron energy in dependence of the film thickness and elements of interest. A drawback of low-energy SEM-EDXS compared to higher electron energies (typically $\geq$ 15 keV) is the significantly reduced x-ray yield.

Therefore, **multivariate statistical analysis** was applied to multidimensional S(T)EM-EDXS (and also STEM-EELS) datasets to (i) improve the signal-to-noise ratio (using principal compo-

nent analysis) and (ii) separate overlapping chemical or crystalline phases (non-negative matrix factorization and independent component analysis).

Outlook

The findings in this work provide starting points for future studies of superconducting thin films. Answers to some questions will also require new directions with regards to electron microscopy. Connecting points to this work could be:

- The reported artifacts induced by electron- and ion-beam irradiation can be used as guidelines for future electron microscopic analyses. The investigated materials are sensitive to air exposure, especially if prepared as thin TEM specimens. Sample transfer under vacuum or an inert gas atmosphere could mitigate artifacts and give a more representative view of the microstructures (e.g. to measure the genuine O concentration in Ba122).
- This work presented applications of more recent SEM data-analysis methods (e.g., automated image segmentation or blind source separation of chemical phases) applied to superconducting films. The use of scanning electron microscopes is advantageous because they are more readily available and accessible in materials science laboratories. The SEM methods should be further developed to enhance data quality, increase sample throughput, analyze larger sample volumes, and reduce the need for time-consuming (and more expensive) TEM analyses. In addition, TEM-sample preparation and subsequent STEM imaging in a combined focused-ion-beam/scanning electron microscope (FIB/SEM) will be a valuable method for reactive samples because sample preparation and sample analysis can be performed in the same instrument without exposing the sample to air.
- Besides advances in methodology, new material-related questions can be deduced from the results of this thesis. For example, the interaction of REs with embedded NPs is an important topic since the addition of NPs is a popular method to enhance the critical current densities in superconducting films.

To conclude, this thesis contains a detailed electron microscopic investigation of Fe- and Cu-based superconducting thin films grown under different conditions. The results provide new insights into the microstructure and growth of these films. This knowledge can be transferred to future studies and improved coated-conductor fabrication with better cost-effectiveness.

List of Figures

List of Tables

Bibliography

Abb73 Abbe, E. *Archiv für Mikroskopische Anatomie* **1873**, *9*, 413–418, DOI: 10.1007/BF02956173 (cit. on p. 12).

Abr04 Abrikosov, A. A. *Reviews of Modern Physics* **2004**, *76*, 975–979, DOI: 10.1103/RevModPhys.76.975 (cit. on p. 7).

Abr57 Abrikosov, A. A. *Journal of Physics and Chemistry of Solids* **1957**, *2*, 199–208, DOI: 10.1016/0022-3697(57)90083-5 (cit. on p. 7).

ACB91 Agostinelli, J. A.; Chen, S.; Braunstein, G. *Physical Review B* **1991**, *43*, 11396–11399, DOI: 10.1103/PhysRevB.43.11396 (cit. on pp. 175, 204).

AR85 Ahn, C. C.; Rez, P. *Ultramicroscopy* **1985**, *17*, 105–115, DOI: 10.1016/0304-3991(85)90003-8 (cit. on pp. 46, 77).

Amb15 Ambrosio, G. *IEEE Transactions on Applied Superconductivity* **2015**, *25*, 1–7, DOI: 10.1109/TASC.2014.2367024 (cit. on p. 1).

Ant+20 Antončík, F.; Jankovský, O.; Hlásek, T.; Bartůněk, V. *Nanomaterials* **2020**, *10*, 1429, DOI: 10.3390/nano10081429 (cit. on p. 10).

Ara+18 Araki, T.; Hayashi, M.; Ishii, H.; Yokoe, D.; Yoshida, R.; Kato, T.; Nishijima, G.; Matsumoto, A. *Superconductor Science and Technology* **2018**, *31*, 065008, DOI: 10.1088/1361-6668/aabb4b (cit. on pp. 2, 196, 203, 231).

AH03 Araki, T.; Hirabayashi, I. *Superconductor Science and Technology* **2003**, *16*, R71–R94, DOI: 10.1088/0953-2048/16/11/R01 (cit. on pp. 10, 11, 179).

Arg+17 Arganda-Carreras, I.; Kaynig, V.; Rueden, C.; Eliceiri, K. W.; Schindelin, J.; Cardona, A.; Sebastian Seung, H. *Bioinformatics* **2017**, *33*, ed. by Murphy, R., 2424–2426, DOI: 10.1093/bioinformatics/btx180 (cit. on pp. 3, 89).

Arz+22 Arzt, M.; Deschamps, J.; Schmied, C.; Pietzsch, T.; Schmidt, D.; Tomancak, P.; Haase, R.; Jug, F. *Frontiers in Computer Science* **2022**, *4*, DOI: 10.3389/fcomp.2022.777728 (cit. on pp. 3, 89).

AB63a Ashby, M. F.; Brown, L. M. *The Philosophical Magazine: A Journal of Theoretical Experimental and Applied Physics* **1963**, *8*, 1083–1103, DOI: 10.1080/14786436308207338 (cit. on pp. 191, 192).

AB63b Ashby, M. F.; Brown, L. M. *The Philosophical Magazine: A Journal of Theoretical Experimental and Applied Physics* **1963**, *8*, 1649–1676, DOI: 10.1080/14786436308207329 (cit. on pp. 191, 192).

AW03 Aßmann, A.; Wendt, M. *Spectrochimica Acta Part B: Atomic Spectroscopy* **2003**, *58*, 711–716, DOI: 10.1016/S0584-8547(02)00274-4 (cit. on p. 106).

Aye+21 Aye, M. M.; Rivasto, E.; Khan, M. Z.; Rijckaert, H.; Palonen, H.; Huhtinen, H.; Driessche, I. V.; Paturi, P. *New Journal of Physics* **2021**, *23*, 113031, DOI: 10.1088/1367-2630/ac3682 (cit. on pp. 2, 124).

Bal+21 Baloch, A. A. B.; Alqahtani, S. M.; Mumtaz, F.; Muqaibel, A. H.; Rashkeev, S. N.; Alharbi, F. H. *Physical Review Materials* **2021**, *5*, 043804, DOI: 10.1103/PhysRevMaterials.5.043804 (cit. on p. 228).

Bar+19 Bartel, C. J.; Sutton, C.; Goldsmith, B. R.; Ouyang, R.; Musgrave, C. B.; Ghiringhelli, L. M.; Scheffler, M. *Science Advances* **2019**, *5*, eaav0693, DOI: 10.1126/sciadv.aav0693 (cit. on p. 231).

Bar18 Barthel, J. *Ultramicroscopy* **2018**, *193*, 1–11, DOI: 10.1016/j.ultramic.2018.06.003 (cit. on p. 27).

Bau12 Baumann, F. H. *Journal of Vacuum Science & Technology B* **2012**, *30*, 041804, DOI: 10.1116/1.4729287 (cit. on p. 31).

BM86 Bednorz, J. G.; Müller, K. A. *Zeitschrift für Physik B Condensed Matter* **1986**, *64*, 189–193, DOI: 10.1007/BF01303701 (cit. on pp. 1, 7).

Bel+02 Belkly, A.; Helderman, M.; Karen, V. L.; Ulkch, P. *Acta Crystallographica Section B: Structural Science* **2002**, *58*, 364–369, DOI: 10.1107/S0108768102006948 (cit. on p. 72).

BZ16 Benedikt, M.; Zimmermann, F. *Journal of the Korean Physical Society* **2016**, *69*, 893–902, DOI: 10.3938/jkps.69.893 (cit. on p. 1).

BBR04 Benzi, P.; Bottizzo, E.; Rizzi, N. *Journal of Crystal Growth* **2004**, *269*, 625–629, DOI: 10.1016/j.jcrysgro.2004.05.082 (cit. on pp. 155, 157).

Ber+19 Bergen, A. et al. *Superconductor Science and Technology* **2019**, *32*, 125006, DOI: 10.1088/1361-6668/ab48d6 (cit. on p. 8).

Ber+14 Berkels, B.; Binev, P.; Blom, D. A.; Dahmen, W.; Sharpley, R. C.; Vogt, T. *Ultramicroscopy* **2014**, *138*, 46–56, DOI: 10.1016/j.ultramic.2013.11.007 (cit. on p. 68).

BL19 Berkels, B.; Liebscher, C. H. *Ultramicroscopy* **2019**, *198*, 49–57, DOI: 10.1016/j.ultramic.2018.12.016 (cit. on p. 68).

Bla+94 Blatter, G.; Feigel'man, M. V.; Geshkenbein, V. B.; Larkin, A. I.; Vinokur, V. M. *Reviews of Modern Physics* **1994**, *66*, 1125–1388, DOI: 10.1103/RevModPhys.66.1125 (cit. on p. 1).

Boe+21 Boeri, L. et al. *Journal of Physics: Condensed Matter* **2021**, DOI: 10.1088/1361-648X/ac2864 (cit. on p. 5).

Bon72 Bonev, I. *Acta Crystallographica Section A: Crystal Physics, Diffraction, Theoretical and General Crystallography* **1972**, *28*, 508–512, DOI: 10.1107/S0567739472001391 (cit. on p. 109).

BN05 Bonnet, N.; Nuzillard, D. *Ultramicroscopy* **2005**, *102*, 327–337, DOI: 10.1016/j.ultramic.2004.11.003 (cit. on pp. 3, 51).

Boo21 Boona, S. R. *Microscopy Today* **2021**, *29*, 42–48, DOI: 10.1017/S1551929520001790 (cit. on p. 39).

Bor+88 Bordet, P.; Chaillout, C.; Chenavas, J.; Hodeau, J. L.; Marezio, M.; Karpinski, J.; Kaldis, E. *Nature* **1988**, *334*, 596–598, DOI: 10.1038/334596a0 (cit. on p. 156).

BW69 Born, M.; Wolf, E., *Principles of Optics: Electromagnetic Theory of Propagation, Interference and Diffraction of Light*, 4th ed; Pergamon Press: Oxford, New York, 1969 (cit. on pp. 22, 28).

Bör+95 Börner, R.; Paulus, W.; Schöllhorn, R.; Kabius, B.; Schubert, J. *Advanced Materials* **1995**, *7*, 55–58, DOI: 10.1002/adma.19950070112 (cit. on pp. 171, 172).

Bou+16 Bouwer, J. C.; Deerinck, T. J.; Bushong, E.; Astakhov, V.; Ramachandra, R.; Peltier, S. T.; Ellisman, M. H. *Advanced Structural and Chemical Imaging* **2016**, *2*, 11, DOI: 10.1186/s40679-016-0025-y (cit. on p. 116).

Boy02 Boyes, E. D. *Microchimica Acta* **2002**, *138*, 225–234, DOI: 10.1007/s006040200026 (cit. on pp. 39, 104).

BCC01 Boyko, V. S.; Chan, S.-W.; Chopra, M. *Physical Review B* **2001**, *63*, 224521, DOI: 10.1103/PhysRevB.63.224521 (cit. on p. 183).

BK04 Boykov, Y.; Kolmogorov, V. *IEEE Transactions on Pattern Analysis and Machine Intelligence* **2004**, *26*, 1124–1137, DOI: 10.1109/TPAMI.2004.60 (cit. on p. 87).

Bra+13 Braccini, V.; Kawale, S.; Reich, E.; Bellingeri, E.; Pellegrino, L.; Sala, A.; Putti, M.; Higashikawa, K.; Kiss, T.; Holzapfel, B.; Ferdeghini, C. *Applied Physics Letters* **2013**, *103*, 172601, DOI: 10.1063/1.4826677 (cit. on pp. 96, 101, 102).

Bro+19 Brodusch, N.; Demers, H.; Gellé, A.; Moores, A.; Gauvin, R. *Ultramicroscopy* **2019**, *203*, 21–36, DOI: 10.1016/j.ultramic.2018.12.015 (cit. on p. 39).

Bus27 Busch, H. *Archiv für Elektrotechnik* **1927**, *18*, 583–594, DOI: 10.1007/BF01656203 (cit. on p. 12).

Cai+05a Cai, C.; Hänisch, J.; Gemming, T.; Holzapfel, B. *IEEE Transactions on Applied Superconductivity* **2005**, *15*, 3738–3741, DOI: 10.1109/TASC.2005.849418 (cit. on pp. 2, 196).

Cai+05b Cai, C.; Hänisch, J.; Hühne, R.; Stehr, V.; Mickel, C.; Gemming, T.; Holzapfel, B. *Journal of Applied Physics* **2005**, *98*, 123906, DOI: 10.1063/1.2148626 (cit. on p. 124).

Can+11 Cantoni, C.; Gao, Y.; Wee, S. H.; Specht, E. D.; Gazquez, J.; Meng, J.; Pennycook, S. J.; Goyal, A. *ACS Nano* **2011**, *5*, 4783–4789, DOI: 10.1021/nn2007628 (cit. on p. 135).

Cat66 Cattell, R. B. *Multivariate Behavioral Research* **1966**, *1*, 245–276, DOI: 10.1207/s15327906mbr0102_10 (cit. on p. 48).

Cav+87 Cava, R. J.; Batlogg, B.; Chen, C. H.; Rietman, E. A.; Zahurak, S. M.; Werder, D. *Nature* **1987**, *329*, 423–425, DOI: 10.1038/329423a0 (cit. on p. 178).

Cav+90 Cava, R. J.; Hewat, A. W.; Hewat, E. A.; Batlogg, B.; Marezio, M.; Rabe, K. M.; Krajewski, J. J.; Peck, W. F.; Rupp, L. W. *Physica C: Superconductivity* **1990**, *165*, 419–433, DOI: 10.1016/0921-4534(90)90376-P (cit. on p. 178).

Cay+ed Cayado, P.; Grünewald, L.; Erbe, M.; Hänisch, J.; Gerthsen, D.; Holzapfel, B. **submitted** (cit. on pp. 54, 196, 203, 205, 207, 265).

Cay+17 Cayado, P.; Mundet, B.; Eloussifi, H.; Vallés, F.; Coll, M.; Ricart, S.; Gázquez, J.; Palau, A.; Roura, P.; Farjas, J.; Puig, T.; Obradors, X. *Superconductor Science and Technology* **2017**, *30*, 125010, DOI: 10.1088/1361-6668/aa8ffe (cit. on p. 197).

Cay16 Cayado, P. Multifunctional Nanostructured Superconductors by Chemical Routes: Towards High Current Conductors, Universitat Autònoma de Barcelona, 2016, DOI: 10.13140/RG.2.2.10659.30246 (cit. on p. 11).

Cay+18 Cayado, P.; Erbe, M.; Kauffmann-Weiss, S.; Jung, A.; Hänisch, J.; Holzapfel, B. *RSC Advances* **2018**, *8*, 42398–42404, DOI: 10.1039/C8RA09188A (cit. on p. 196).

Cay+20 Cayado, P.; Li, M.; Erbe, M.; Liu, Z.; Cai, C.; Hänisch, J.; Holzapfel, B. *Royal Society Open Science* **2020**, *7*, 201257, DOI: 10.1098/rsos.201257 (cit. on p. 10).

Cay+19 Cayado, P.; Rijckaert, H.; Erbe, M.; Langer, M.; Jung, A.; Hänisch, J.; Holzapfel, B. *Nanomaterials* **2019**, *10*, 21, DOI: 10.3390/nano10010021 (cit. on p. 196).

CJW76 Chadderton, L. T.; Johnson, E.; Wohlenberg, T. *Radiation Effects* **1976**, *28*, 111–112, DOI: 10.1080/00337577608233035 (cit. on pp. 93, 98).

CE08 Christen, H. M.; Eres, G. *Journal of Physics: Condensed Matter* **2008**, *20*, 264005, DOI: 10.1088/0953-8984/20/26/264005 (cit. on p. 10).

Chu+16 Chua, E. Y.; Vogirala, V. K.; Inian, O.; Wong, A. S.; Nordenskiöld, L.; Plitzko, J. M.; Danev, R.; Sandin, S. *Nucleic Acids Research* **2016**, *44*, 8013–8019, DOI: 10.1093/nar/gkw708 (cit. on p. 17).

CL75 Cliff, G.; Lorimer, G. W. *Journal of Microscopy* **1975**, *103*, 203–207, DOI: 10.1111/j.1365-2818.1975.tb03895.x (cit. on p. 43).

Con01 Conder, K. *Materials Science and Engineering: R: Reports* **2001**, *32*, 41–102, DOI: 10.1016/S0927-796X(00)00030-9 (cit. on p. 156).

CP11 Cosmus, T. C.; Parizh, M. *IEEE Transactions on Applied Superconductivity* **2011**, *21*, 2104–2109, DOI: 10.1109/TASC.2010.2084981 (cit. on p. 1).

Cox15 Cox, D. C., *Introduction to Focused Ion Beam Nanometrology*; Morgan & Claypool Publishers: 2015, DOI: 10.1088/978-1-6817-4084-3 (cit. on pp. 32, 36).

CS82 Crewe, A. V.; Salzman, D. B. *Ultramicroscopy* **1982**, *9*, 373–377, DOI: 10.1016/0304-3991(82)90098-5 (cit. on p. 27).

Dai+19 Dai, X. H.; Liang, J. T.; Song, J. M.; Zhao, L.; Guo, J. X.; Zhao, H. D.; Wang, Y.; Liu, B. T. *Journal of Superconductivity and Novel Magnetism* **2019**, *32*, 869–875, DOI: 10.1007/s10948-018-4800-y (cit. on pp. 2, 102, 105).

De +16 De Keukeleere, K.; Cayado, P.; Meledin, A.; Vallès, F.; De Roo, J.; Rijckaert, H.; Pollefeyt, G.; Bruneel, E.; Palau, A.; Coll, M.; Ricart, S.; Van Tendeloo, G.; Puig, T.; Obradors, X.; Van Driessche, I. *Advanced Electronic Materials* **2016**, *2*, 1600161, DOI: 10.1002/aelm.201600161 (cit. on p. 202).

dlPeñ+11 De la Peña, F.; Lai, M.-H.; Hochepied, J.-F.; Dynys, F.; Stephan, O.; Walls, M. *Ultramicroscopy* **2011**, *111*, 169–176, DOI: 10.1016/j.ultramic.2010.10.001 (cit. on p. 51).

dlPeñ10 De la Peña, F. Advanced Methods for Electron Energy Loss Spectroscopy Core-Loss Analysis, Orsay: Université Paris-Sud, 2010, p 181 (cit. on p. 46).

dBro25 De Broglie, L. *Annales de Physique* **1925**, *10*, 22–128, DOI: 10.1051/anphys/192510030022 (cit. on p. 12).

dJT06 De Juan, A.; Tauler, R. *Critical Reviews in Analytical Chemistry* **2006**, *36*, 163–176, DOI: 10.1080/10408340600970005 (cit. on p. 51).

Del+90 Dell'Agli, G.; Marino, O.; Mascolo, G.; Pernice, P.; Di Chiara, A.; Pepe, G.; Di Uccio, U. S. *Journal of Materials Science: Materials in Electronics* **1990**, *1*, 20–24, DOI: 10.1007/BF00716011 (cit. on p. 177).

dOud+97 Den Ouden, A.; Wessel, S.; Krooshoop, E.; ten Kate, H. *IEEE Transactions on Applied Superconductivity* **1997**, *7*, 733–738, DOI: 10.1109/77.614608 (cit. on pp. 1, 7).

Díe+21 Díez-Sierra, J.; Rijckaert, H.; Rikel, M.; Hänisch, J.; Sadewasser, M.; Koliotassis, L.; Meledin, A.; López-Domínguez, P.; Falter, M.; Bennewitz, J.; Bäcker, M.; Driessche, I. V. *Superconductor Science and Technology* **2021**, *34*, 114001, DOI: 10.1088/1361-6668/ac2495 (cit. on pp. 2, 216, 231).

Díe+20 Díez-Sierra, J. et al. *ACS Applied Nano Materials* **2020**, *3*, 5542–5553, DOI: 10.1021/acsanm.0c00814 (cit. on p. 202).

DD20 Distante, A.; Distante, C., *Handbook of Image Processing and Computer Vision: Volume 1: From Energy to Image*; Springer International Publishing: Cham, 2020, DOI: 10.1007/978-3-030-38148-6 (cit. on p. 70).

DB12 Dobigeon, N.; Brun, N. *Ultramicroscopy* **2012**, *120*, 25–34, DOI: 10.1016/j.ultramic.2012.05.006 (cit. on p. 49).

Dob+09 Dobigeon, N.; Moussaoui, S.; Coulon, M.; Tourneret, J.-Y.; Hero, A. O. *IEEE Transactions on Signal Processing* **2009**, *57*, 4355–4368, DOI: 10.1109/TSP.2009.2025797 (cit. on p. 51).

DZ10 Dobrowolska, A.; Zych, E. *Chemistry of Materials* **2010**, *22*, 4652–4659, DOI: 10.1021/cm100828v (cit. on pp. 228, 229).

Dre+18 Drees, H.; Müller, E.; Dries, M.; Gerthsen, D. *Ultramicroscopy* **2018**, *185*, 65–71, DOI: 10.1016/j.ultramic.2017.11.005 (cit. on p. 28).

Dro+07 Drouin, D.; Couture, A. R.; Joly, D.; Tastet, X.; Aimez, V.; Gauvin, R. *Scanning* **2007**, *29*, 92–101, DOI: 10.1002/sca.20000 (cit. on p. 44).

Du15 Du, H. *Ultramicroscopy* **2015**, *151*, 62–67, DOI: 10.1016/j.ultramic.2014.11.012 (cit. on p. 119).

Eas06 Eason, R., *Pulsed Laser Deposition of Thin Films: Applications-Led Growth of Functional Materials*; John Wiley & Sons, Inc.: Hoboken, NJ, USA, 2006, DOI: 10.1002/0470052120 (cit. on p. 10).

EFH89 Egdell, R. G.; Flavell, W. R.; Hollamby, P. C. *Journal of Solid State Chemistry* **1989**, *79*, 238–249, DOI: 10.1016/0022-4596(89)90271-5 (cit. on p. 171).

Ege11 Egerton, R., *Electron Energy-Loss Spectroscopy in the Electron Microscope*; Springer US: Boston, MA, 2011, DOI: 10.1007/978-1-4419-9583-4 (cit. on pp. 12, 44, 46, 74, 166, 167).

Ein05 Einstein, A. *Annalen der Physik* **1905**, *322*, 132–148, DOI: 10.1002/andp.19053220607 (cit. on p. 12).

Erb+15 Erbe, M.; Hänisch, J.; Hühne, R.; Freudenberg, T.; Kirchner, A.; Molina-Luna, L.; Damm, C.; Van Tendeloo, G.; Kaskel, S.; Schultz, L.; Holzapfel, B. *Superconductor Science and Technology* **2015**, *28*, 114002, DOI: 10.1088/0953-2048/28/11/114002 (cit. on pp. 54, 197, 207).

Erb+20 Erbe, M.; Cayado, P.; Freitag, W.; Ackermann, K.; Langer, M.; Meledin, A.; Hänisch, J.; Holzapfel, B. *Superconductor Science and Technology* **2020**, *33*, 094002, DOI: 10.1088/1361-6668/ab9aa0 (cit. on pp. 2, 10, 54, 157, 196, 200).

Erb+14 Erbe, M.; Hänisch, J.; Freudenberg, T.; Kirchner, A.; Mönch, I.; Kaskel, S.; Schultz, L.; Holzapfel, B. *Journal of Materials Chemistry A* **2014**, *2*, 4932–4944, DOI: 10.1039/C3TA15243J (cit. on p. 54).

FH07 Faruqi, A. R.; Henderson, R. *Current Opinion in Structural Biology* **2007**, *17*, 549–555, DOI: 10.1016/j.sbi.2007.08.014 (cit. on p. 20).

Fei+21 Feighan, J.; Lai, M. H.; Kursumovic, A.; Zhang, D.; Wang, H.; Lee, J. H.; Moon, S.; MacManus-Driscoll, J. L. *Superconductor Science and Technology* **2021**, *34*, 045012, DOI: 10.1088/1361-6668/abe18d (cit. on pp. 2, 10).

FKM17 Feighan, J. P.; Kursumovic, A.; MacManus-Driscoll, J. L. *Superconductor Science and Technology* **2017**, *30*, 123001, DOI: 10.1088/1361-6668/aa90d1 (cit. on pp. 1, 9, 124).

Fel+10 Feldmann, D. M.; Holesinger, T. G.; Maiorov, B.; Foltyn, S. R.; Coulter, J. Y.; Apodaca, I. *Superconductor Science and Technology* **2010**, *23*, 095004, DOI: 10.1088/0953-2048/23/9/095004 (cit. on p. 192).

Fen+90 Fendorf, M.; Burmester, C. P.; Wille, L. T.; Gronsky, R. *Applied Physics Letters* **1990**, *57*, 2481–2483, DOI: 10.1063/1.103836 (cit. on pp. 160, 161, 173).

Fin+10 Findlay, S. D.; Shibata, N.; Sawada, H.; Okunishi, E.; Kondo, Y.; Ikuhara, Y. *Ultramicroscopy* **2010**, *110*, 903–923, DOI: 10.1016/j.ultramic.2010.04.004 (cit. on p. 119).

FB67 Fischer, D. W.; Baun, W. L. *Journal of Applied Physics* **1967**, *38*, 7 (cit. on p. 106).

Fol+07 Foltyn, S. R.; Civale, L.; MacManus-Driscoll, J. L.; Jia, Q. X.; Maiorov, B.; Wang, H.; Maley, M. *Nature Materials* **2007**, *6*, 631–642, DOI: 10.1038/nmat1989 (cit. on p. 9).

FB96 Fortner, J. A.; Buck, E. C. *Applied Physics Letters* **1996**, *68*, 3817–3819, DOI: 10.1063/1.116627 (cit. on pp. 78, 220, 226).

Fou+99 Fournier, C.; Merlet, C.; Dugne, O.; Fialin, M. *Journal of Analytical Atomic Spectrometry* **1999**, *14*, 381–386, DOI: 10.1039/a807433j (cit. on p. 42).

Fri96 Friel, J. J. *Microscopy Today* **1996**, *4*, 12–13, DOI: 10.1017/S1551929500066979 (cit. on p. 80).

FL06 Friel, J. J.; Lyman, C. E. *Microscopy and Microanalysis* **2006**, *12*, 2–25, DOI: 10.1017/S1431927606060211 (cit. on pp. 80, 84).

Fuj+20 Fujinaka, S.; Sato, Y.; Teranishi, R.; Kaneko, K. *Journal of Materials Science* **2020**, *55*, 8123–8133, DOI: 10.1007/s10853-020-04602-w (cit. on p. 68).

FH08 Fultz, B.; Howe, J. M., *Transmission Electron Microscopy and Diffractometry of Materials*, 3rd ed; Advanced Texts in Physics 1439-2674; Springer: Berlin ; New York, 2008 (cit. on pp. 22, 24).

Gap+05 Gapud, A. A.; Kumar, D.; Viswanathan, S. K.; Cantoni, C.; Varela, M.; Abiade, J.; Pennycook, S. J.; Christen, D. K. *Superconductor Science and Technology* **2005**, *18*, 1502–1505, DOI: 10.1088/0953-2048/18/11/016 (cit. on p. 124).

Gar21 Garrett, J. SciencePlots (v1.0.9), Zenodo, 2021, DOI: 10.5281/zenodo.5512926 (cit. on p. 91).

Gau+17 Gauquelin, N.; van den Bos, K. H. W.; Béché, A.; Krause, F. F.; Lobato, I.; Lazar, S.; Rosenauer, A.; Van Aert, S.; Verbeeck, J. *Ultramicroscopy* **2017**, *181*, 178–190, DOI: 10.1016/j.ultramic.2017.06.002 (cit. on p. 69).

Gau+18 Gautam, B.; Sebastian, M. A.; Chen, S.; Misra, S.; Huang, J.; Javier Baca, F.; Emergo, R.; Haugan, T.; Xing, Z.; Wang, H.; Wu, J. Z. *Applied Physics Letters* **2018**, *113*, 212602, DOI: 10.1063/1.5050616 (cit. on p. 135).

GR16 Gauvin, R.; Rudinsky, S. *Ultramicroscopy* **2016**, *167*, 21–30, DOI: 10.1016/j.ultramic.2016.04.007 (cit. on p. 28).

Gaz+16 Gazquez, J. et al. *Advanced Science* **2016**, *3*, 1500295, DOI: 10.1002/advs.201500295 (cit. on p. 204).

Ger+12 Gerlach, R.; Maazouz, M.; Dingle, T.; Utlaut, M.; McGinn, J. (FEI Company). In-Chamber Electron Detector US Patent, 8164059B2, 2012 (cit. on p. 35).

GR15 Ghosh, N.; Raj, S. In *AIP Conference Proceedings*, 2015; Vol. 1665, p 100009, DOI: 10.1063/1.4918037 (cit. on p. 107).

GS05 Giannuzzi, L. A.; Stevie, F. A., *Introduction to Focused Ion Beams: Instrumentation, Theory, Techniques, and Practice*; Springer: New York, USA, 2005; 357 pp. (cit. on p. 32).

GL09 Ginzburg, V. L.; Landau, L. D. In *On Superconductivity and Superfluidity: A Scientific Autobiography*, Ginzburg, V. L., Ed.; Springer: Berlin, Heidelberg, 2009, pp 113–137, DOI: 10.1007/978-3-540-68008-6_4 (cit. on p. 7).

Gol+18 Goldstein, J. I.; Newbury, D. E.; Michael, J. R.; Ritchie, N. W.; Scott, J. H. J.; Joy, D. C., *Scanning Electron Microscopy and X-Ray Microanalysis*; Springer New York: New York, NY, 2018, DOI: 10.1007/978-1-4939-6676-9 (cit. on pp. 32–34, 39, 44, 85, 104, 142).

Goy+20 Goyal, B.; Dogra, A.; Agrawal, S.; Sohi, B. S.; Sharma, A. *Information Fusion* **2020**, *55*, 220–244, DOI: 10.1016/j.inffus.2019.09.003 (cit. on p. 69).

GS98 Grigis, C.; Schamm, S. *Ultramicroscopy* **1998**, *74*, 159–167, DOI: 10.1016/S0304-3991(98)00040-0 (cit. on p. 167).

GR11 Grillo, V.; Rossi, F. *Journal of Crystal Growth* **2011**, *318*, 1151–1156, DOI: 10.1016/j.jcrysgro.2010.10.180 (cit. on p. 31).

Grü22 Grünewald, L. Data-Analysis Notebooks for the Thesis 'Electron Microscopic Investigation of Superconducting Fe- and Cu-based Thin Films', 2022, DOI: 10.5445/IR/1000144208 (cit. on pp. 53, 72, 76, 81, 87, 89).

Grü+on Grünewald, L.; Cayado, P.; Erbe, M.; Hänisch, J.; Holzapfel, B.; Gerthsen, D. **in preparation** (cit. on p. 265).

Grü+20a Grünewald, L.; Langer, M.; Meyer, S.; Hänisch, J.; Holzapfel, B.; Gerthsen, D. In IBS2app: Iron-based Superconductors: Advances towards Applications, Santa Margherita Ligure, 2020 (cit. on p. 266).

Grü+21a Grünewald, L.; Langer, M.; Meyer, S.; Nerz, D.; Hänisch, J.; Holzapfel, B.; Gerthsen, D. *Superconductor Science and Technology* **2021**, *34*, 035005, DOI: 10.1088/1361-6668/abcecf (cit. on pp. 3, 70, 93, 94, 96, 102, 103, 107, 109–111, 113, 114, 117, 119, 120, 122, 265).

Grü+21b Grünewald, L.; Nerz, D.; Langer, M.; Meyer, S.; Beisig, N.; Cayado, P.; Popov, R.; Hänisch, J.; Holzapfel, B.; Gerthsen, D. In Microscopy Conference (MC 2021), Online, 22.08.2021 – 26.08.2021, 2021, DOI: 10.5445/IR/1000147936 (cit. on p. 266).

Grü+21c Grünewald, L.; Popov, R.; Hänisch, J.; Holzapfel, B.; Gerthsen, D. In Microscopy Conference (MC 2021), Online, 22.08.2021 – 26.08.2021, 2021, DOI: 10.5445/IR/1000143835 (cit. on p. 266).

Grü+21d Grünewald, L.; Cayado, P.; Hänisch, J.; Holzapfel, B.; Gerthsen, D. *Microscopy and Microanalysis* **2021**, *27*, 2876–2879, DOI: 10.1017/S1431927621010023 (cit. on pp. 3, 160, 265).

Grü+21e Grünewald, L.; Langer, M.; Meyer, S.; Hänisch, J.; Holzapfel, B.; Gerthsen, D. In *Proceedings of the European Microscopy Congress 2020*, European Microscopy Congress 2020, Royal Microscopical Society: 2021, DOI: 10.22443/rms.emc2020.67 (cit. on p. 266).

Grü+19a Grünewald, L.; Langer, M.; Meyer, S.; Hänisch, J.; Holzapfel, B.; Gerthsen, D. Structural Properties of Superconducting Ba(Fe,Co)2As2 Thin Films, 2019 (cit. on pp. 145, 149).

Grü+19b Grünewald, L.; Langer, M.; Meyer, S.; Hänisch, J.; Holzapfel, B.; Gerthsen, D. In Microscopy Conference (MC 2019), Berlin, Germany, 01.09.2019 – 05.09.2019, Berlin, Germany, 2019, DOI: 10.5445/IR/1000127055 (cit. on p. 266).

Grü+20b Grünewald, L.; Langer, M.; Meyer, S.; Hänisch, J.; Holzapfel, B.; Gerthsen, D. Supplementary Information for 'Structural and Chemical Properties of Superconducting Co-doped $BaFe_2As_2$ Thin Films Grown on CaF_2', 2020, DOI: 10.5281/zenodo.4058144 (cit. on pp. 95, 98, 266).

Grü+21f Grünewald, L.; Nerz, D.; Langer, M.; Meyer, S.; Beisig, N.; Cayado, P.; Popov, R.; Hänisch, J.; Holzapfel, B.; Gerthsen, D. *Microscopy and Microanalysis* **2021**, *27*, 1056–1058, DOI: 10.1017/S1431927621003986 (cit. on pp. 265, 266).

Gün+99 Günther, W.; Schöllhorn, R.; Epple, M.; Siegle, H.; Thomsen, C.; Kabius, B.; Poppe, U.; Schubert, J.; Zander, W. *Philosophical Magazine A* **1999**, *79*, 449–466, DOI: 10.1080/01418619908210309 (cit. on p. 171).

Gün+96 Günther, W.; Schöllhorn, R.; Siegle, H.; Thomsen, C. *Solid State Ionics* **1996**, *84*, 23–32, DOI: 10.1016/S0167-2738(96)83002-5 (cit. on p. 171).

GS96 Günther, W.; Schöllhorn, R. *Physica C: Superconductivity* **1996**, *271*, 241–250, DOI: 10.1016/S0921-4534(96)00546-1 (cit. on p. 171).

Gup+88 Gupta, A.; Jagannathan, R.; Cooper, E. I.; Giess, E. A.; Landman, J. I.; Hussey, B. W. *Applied Physics Letters* **1988**, *52*, 2077–2079, DOI: 10.1063/1.99752 (cit. on p. 10).

Guz+13 Guzman, R.; Gazquez, J.; Rouco, V.; Palau, A.; Magen, C.; Varela, M.; Arbiol, J.; Obradors, X.; Puig, T. *Applied Physics Letters* **2013**, *102*, 081906, DOI: 10.1063/1.4793749 (cit. on pp. 156, 159, 202).

Guz+17 Guzman, R.; Gazquez, J.; Mundet, B.; Coll, M.; Obradors, X.; Puig, T. *Physical Review Materials* **2017**, *1*, 24801, DOI: 10.1103/PhysRevMaterials.1.024801 (cit. on pp. 159, 169, 216).

Guz13 Guzmán Aluja, R. In-Depth Investigation of the Origin, Evolution and Interaction of Structural Defects in YBCO Nanocomposite Thin Films, Barcelona: Universitat Autònoma de Barcelona, 2013 (cit. on p. 156).

Haa+98 Haage, T.; Zegenhagen, J.; Habermeier, H.-U.; Cardona, M. *Physical Review Letters* **1998**, *80*, 4225–4228, DOI: 10.1103/PhysRevLett.80.4225 (cit. on pp. 175, 204, 209, 212).

Hai+98a Haider, M.; Rose, H.; Uhlemann, S.; Kabius, B.; Urban, K. *Journal of Electron Microscopy* **1998**, *47*, 395–405, DOI: 10.1093/oxfordjournals.jmicro.a023610 (cit. on p. 18).

Hai+98b Haider, M.; Rose, H.; Uhlemann, S.; Schwan, E.; Kabius, B.; Urban, K. *Ultramicroscopy* **1998**, *75*, 53–60, DOI: 10.1016/S0304-3991(98)00048-5 (cit. on p. 18).

Hai+98c Haider, M.; Uhlemann, S.; Schwan, E.; Rose, H.; Kabius, B.; Urban, K. *Nature* **1998**, *392*, 768–769, DOI: 10.1038/33823 (cit. on p. 18).

Hai+14 Haindl, S.; Kidszun, M.; Oswald, S.; Hess, C.; Büchner, B.; Kölling, S.; Wilde, L.; Thersleff, T.; Yurchenko, V. V.; Jourdan, M.; Hiramatsu, H.; Hosono, H. *Reports on Progress in Physics* **2014**, *77*, 046502, DOI: 10.1088/0034-4885/77/4/046502 (cit. on p. 9).

Hai21 Haindl, S., *Iron-Based Superconducting Thin Films*; Springer Series in Materials Science, Vol. 315; Springer International Publishing: Cham, 2021, DOI: 10.1007/978-3-030-75132-6 (cit. on pp. 8, 110, 148, 151).

Hai+16 Haindl, S.; Hanzawa, K.; Sato, H.; Hiramatsu, H.; Hosono, H. *Scientific Reports* **2016**, *6*, 35797, DOI: 10.1038/srep35797 (cit. on p. 102).

Hai+19 Haindl, S.; Kampert, E.; Sasase, M.; Hiramatsu, H.; Hosono, H. *Superconductor Science and Technology* **2019**, *32*, 044003, DOI: 10.1088/1361-6668/aafe3d (cit. on pp. 3, 95, 101, 102, 111, 118).

Hal+09 Hall, M.; Frank, E.; Holmes, G.; Pfahringer, B.; Reutemann, P.; Witten, I. H. *ACM SIGKDD Explorations Newsletter* **2009**, *11*, 10–18, DOI: 10.1145/1656274.1656278 (cit. on p. 89).

Hän+ed Hänisch, J.; Iida, K.; Cayado, P.; Erbe, M.; Grünewald, L.; Hatano, T.; Okada, T.; Gerthsen, D.; Awaji, S.; Holzapfel, B. *Superconductor Science and Technology* **accepted** (cit. on pp. 196, 211, 265).

Hän+22 Hänisch, J.; Iida, K.; Cayado, P.; Erbe, M.; Grünewald, L.; Hatano, T.; Okada, T.; Gerthsen, D.; Awaji, S.; Holzapfel, B. Supplementary Information for 'Microstructure and Pinning Properties of CSD-grown $SmBa_2Cu_3O_{7-\delta}$ Films with and without $BaHfO_3$ Nanoparticles', Zenodo: 2022, DOI: 10.5281/zenodo.6350486 (cit. on p. 266).

Hän+19 Hänisch, J.; Iida, K.; Hühne, R.; Tarantini, C. *Superconductor Science and Technology* **2019**, *32*, 093001, DOI: 10.1088/1361-6668/ab1c00 (cit. on pp. 2, 9, 120, 144, 145).

HI20 Hänisch, J.; Iida, K. In *Superconductivity: From Materials Science to Practical Applications*, Mele, P., Prassides, K., Tarantini, C., Palau, A., Badica, P., Jha, A. K., Endo, T., Eds.; Springer International Publishing: Cham, 2020, pp 269–302, DOI: 10.1007/978-3-030-23303-7_10 (cit. on pp. 1, 145).

Hän+11 Hänisch, J.; Iida, K.; Haindl, S.; Kurth, F.; Kauffmann, A.; Kidszun, M.; Thersleff, T.; Freudenberger, J.; Schultz, L.; Holzapfel, B. *IEEE Transactions on Applied Superconductivity* **2011**, *21*, 2887–2890, DOI: 10.1109/TASC.2010.2100348 (cit. on pp. 2, 102, 105).

Hän+15 Hänisch, J.; Iida, K.; Kurth, F.; Reich, E.; Tarantini, C.; Jaroszynski, J.; Förster, T.; Fuchs, G.; Hühne, R.; Grinenko, V.; Schultz, L.; Holzapfel, B. *Scientific Reports* **2015**, *5*, 1–11, DOI: 10.1038/srep17363 (cit. on pp. 101, 102).

Har+17 Hart, J. L.; Lang, A. C.; Leff, A. C.; Longo, P.; Trevor, C.; Twesten, R. D.; Taheri, M. L. *Scientific Reports* **2017**, *7*, 8243, DOI: 10.1038/s41598-017-07709-4 (cit. on p. 75).

HRT93 Hartmann, A.; Russell, G. J.; Taylor, K. N. R. *Solid State Communications* **1993**, *87*, 857–862, DOI: 10.1016/0038-1098(93)90429-Q (cit. on p. 167).

HS19 *Springer Handbook of Microscopy*; Hawkes, P. W., Spence, J. C. H., Eds.; Springer Handbooks; Springer International Publishing: Cham, 2019, DOI: 10.1007/978-3-030-00069-1 (cit. on pp. 13, 21, 26–28, 31, 43, 206).

Her+87 Hervieu, M.; Domenges, B.; Michel, C.; Heger, G.; Provost, J.; Raveau, B. *Physical Review B* **1987**, *36*, 3920–3922, DOI: 10.1103/PhysRevB.36.3920 (cit. on p. 157).

Hir+14 Hiramatsu, H.; Sato, H.; Katase, T.; Kamiya, T.; Hosono, H. *Applied Physics Letters* **2014**, *104*, 172602, DOI: 10.1063/1.4874609 (cit. on p. 137).

Hir15 Hirel, P. *Computer Physics Communications* **2015**, *197*, 212–219, DOI: 10.1016/j.cpc.2015.07.012 (cit. on pp. 72, 270).

HM21 Hirsch, J. E.; Marsiglio, F. *Nature* **2021**, *596*, E9–E10, DOI: 10.1038/s41586-021-03595-z (cit. on p. 5).

HC20 Holm, J. D.; Caplins, B. W., *STEM in SEM: Introduction to Scanning Transmission Electron Microscopy for Microelectronics Failure Analysis*; ASM International: 2020, DOI: 10.31399/asm.tb.stemsem.9781627082921 (cit. on p. 38).

Hol+92 Holzapfel, B.; Roas, B.; Schultz, L.; Bauer, P.; Saemann-Ischenko, G. *Applied Physics Letters* **1992**, *61*, 3178–3180, DOI: 10.1063/1.107951 (cit. on pp. 10, 143).

Hon69 Honig, R. E. *RCA review* **1969**, *30*, 285–305 (cit. on p. 110).

Hor+21 Horide, T.; Ichinose, A.; Tokura, F.; Matsumoto, K. *Thin Solid Films* **2021**, *733*, 138802, DOI: 10.1016/j.tsf.2021.138802 (cit. on p. 135).

Hor+10 Horny, P.; Lifshin, E.; Campbell, H.; Gauvin, R. *Microscopy and Microanalysis* **2010**, *16*, 821–830, DOI: 10.1017/S1431927610094018 (cit. on p. 15).

Hos+18 Hosono, H.; Yamamoto, A.; Hiramatsu, H.; Ma, Y. *Materials Today* **2018**, *21*, 278–302, DOI: 10.1016/j.mattod.2017.09.006 (cit. on pp. 1, 8, 9).

HTU06 Houben, L.; Thust, A.; Urban, K. *Ultramicroscopy* **2006**, *106*, 200–214, DOI: 10.1016/j.ultramic.2005.07.009 (cit. on p. 25).

HDB98 Howell, P. G. T.; Davy, K. M. W.; Boyde, A. *Scanning* **1998**, *20*, 35–40, DOI: 10.1002/sca.1998.4950200105 (cit. on pp. 115, 127).

HMG19 Hugenschmidt, M.; Müller, E.; Gerthsen, D. *Journal of Microscopy* **2019**, *274*, 150–157, DOI: 10.1111/jmi.12793 (cit. on p. 28).

Hun07 Hunter, J. D. *Computing in Science Engineering* **2007**, *9*, 90–95, DOI: 10.1109/MCSE.2007.55 (cit. on p. 91).

HS92 Hussain, A.; Sayer, M. *Vacuum* **1992**, *43*, 1195–1196, DOI: 10.1016/0042-207X(92)90022-O (cit. on p. 171).

HSK98 Hÿtch, M.; Snoeck, E.; Kilaas, R. *Ultramicroscopy* **1998**, *74*, 131–146, DOI: 10.1016/S0304-3991(98)00035-7 (cit. on p. 212).

HO00 Hyvärinen, A.; Oja, E. *Neural Networks* **2000**, *13*, 411–430, DOI: 10.1016/S0893-6080(00)00026-5 (cit. on p. 51).

Iak+08 Iakoubovskii, K.; Mitsuishi, K.; Nakayama, Y.; Furuya, K. *Microscopy Research and Technique* **2008**, *71*, 626–631, DOI: 10.1002/jemt.20597 (cit. on p. 167).

IY17 Ichino, Y.; Yoshida, Y. *IEEE Transactions on Applied Superconductivity* **2017**, *27*, 1–4, DOI: 10.1109/TASC.2016.2644105 (cit. on p. 135).

Ich+13 Ichinose, A.; Nabeshima, F.; Tsukada, I.; Hanawa, M.; Komiya, S.; Akiike, T.; Imai, Y.; Maeda, A. *Superconductor Science and Technology* **2013**, *26*, 075002, DOI: 10.1088/0953-2048/26/7/075002 (cit. on pp. 96, 99, 101, 102).

Ich+14a Ichinose, A.; Tsukada, I.; Nabeshima, F.; Imai, Y.; Maeda, A.; Kurth, F.; Holzapfel, B.; Iida, K.; Ueda, S.; Naito, M. *Applied Physics Letters* **2014**, *104*, 122603, DOI: 10.1063/1.4869961 (cit. on p. 96).

Ich+14b Ichinose, A.; Tsukada, I.; Nabeshima, F.; Imai, Y.; Maeda, A.; Kurth, F.; Holzapfel, B.; Iida, K.; Ueda, S.; Naito, M. *Applied Physics Letters* **2014**, *104*, 0–5, DOI: 10.1063/1.4869961 (cit. on p. 95).

Iid+10 Iida, K.; Hänisch, J.; Thersleff, T.; Kurth, F.; Kidszun, M.; Haindl, S.; Hühne, R.; Schultz, L.; Holzapfel, B. *Physical Review B* **2010**, *81*, 100507, DOI: 10.1103/PhysRevB.81.100507 (cit. on p. 108).

Iid+11 Iida, K.; Hänisch, J.; Trommler, S.; Matias, V.; Haindl, S.; Kurth, F.; Del Pozo, I. L.; Hühne, R.; Kidszun, M.; Engelmann, J.; Schultz, L.; Holzapfel, B. *Applied Physics Express* **2011**, *4*, 2–5, DOI: 10.1143/APEX.4.013103 (cit. on p. 109).

IHY20 Iida, K.; Hänisch, J.; Yamamoto, A. *Superconductor Science and Technology* **2020**, *33*, 043001, DOI: 10.1088/1361-6668/ab73ef (cit. on p. 9).

Iid+16 Iida, K. et al. *Scientific Reports* **2016**, *6*, 28390, DOI: 10.1038/srep28390 (cit. on pp. 101, 144, 145).

INM17 Imai, Y.; Nabeshima, F.; Maeda, A. *Condensed Matter* **2017**, *2*, 25, DOI: 10.3390/condmat2030025 (cit. on p. 2).

JJK17 Jany, B. R.; Janas, A.; Krok, F. *Nano Letters* **2017**, *17*, 6520–6525, DOI: 10.1021/acs.nanolett.7b01789 (cit. on pp. 3, 56, 104).

Jan19 Jany, B. R. Python Jupyter Notebook to Perform Automatic Microscopic Image Analysis by Moving Window Local Fourier Transform and Machine Learning, 2019, DOI: 10.17632/25x46xjyr5.2 (cit. on p. 72).

JJK20 Jany, B. R.; Janas, A.; Krok, F. *Micron* **2020**, *130*, 102800, DOI: 10.1016/j.micron.2019.102800 (cit. on p. 72).

Jen+91 Jenkins, R.; Manne, R.; Robin, R.; Senemaud, C. *X-Ray Spectrometry* **1991**, *20*, 149–155, DOI: 10.1002/xrs.1300200308 (cit. on p. 41).

JM19 Jha, A. K.; Matsumoto, K. *Frontiers in Physics* **2019**, *7*, DOI: 10.3389/fphy.2019.00082 (cit. on p. 1).

Jia+10 Jia, C. L.; Houben, L.; Thust, A.; Barthel, J. *Ultramicroscopy* **2010**, *110*, 500–505, DOI: 10.1016/j.ultramic.2009.10.006 (cit. on p. 26).

JLU04 Jia, C.-L.; Lentzen, M.; Urban, K. *Microscopy and Microanalysis* **2004**, *10*, 174–184, DOI: 10.1017/S1431927604040425 (cit. on pp. 25, 26).

Jia+13 Jian, H.; Shao, D.; Yang, Z.; Zhu, X.; Sun, Y. *Physica C: Superconductivity* **2013**, *488*, 39–45, DOI: 10.1016/j.physc.2013.03.001 (cit. on p. 196).

Jia+09 Jiang, C.; Fang, L.; Shen, M.; Zheng, F.; Wu, X. *Applied Physics Letters* **2009**, *94*, 071110, DOI: 10.1063/1.3082097 (cit. on p. 228).

Jia16 Jiang, N. *Micron* **2016**, *83*, 79–92, DOI: 10.1016/j.micron.2016.02.007 (cit. on pp. 93, 99).

Jia15 Jiang, N. *Reports on Progress in Physics* **2015**, *79*, 016501, DOI: 10.1088/0034-4885/79/1/016501 (cit. on p. 99).

Jia12 Jiang, N. *Micron* **2012**, *43*, 746–754, DOI: 10.1016/j.micron.2012.02.002 (cit. on pp. 93–95, 98, 99).

JC16 Jolliffe, I. T.; Cadima, J. *Philosophical Transactions of the Royal Society A: Mathematical, Physical and Engineering Sciences* **2016**, *374*, 20150202, DOI: 10.1098/rsta.2015.0202 (cit. on p. 47).

Jon+19 Jones, A.; Lam, S. K. H.; Du, J.; Rubanov, S.; Pan, A. V. *IEEE Transactions on Applied Superconductivity* **2019**, *29*, 1–5, DOI: 10.1109/TASC.2019.2897457 (cit. on p. 209).

Jon16 Jones, L. *IOP Conference Series: Materials Science and Engineering* **2016**, *109*, 012008, DOI: 10.1088/1757-899X/109/1/012008 (cit. on pp. 29, 31).

Jon+17 Jones, L.; Wenner, S.; Nord, M.; Ninive, P. H.; Løvvik, O. M.; Holmestad, R.; Nellist, P. D. *Ultramicroscopy* **2017**, *179*, 57–62, DOI: 10.1016/j.ultramic.2017.04.007 (cit. on pp. 67, 68).

JJ96 Joy, D. C.; Joy, C. S. *Micron* **1996**, *27*, 247–263, DOI: 10.1016/0968-4328(96)00023-6 (cit. on p. 33).

JT14 Jublot, M.; Texier, M. *Micron* **2014**, *56*, 63–67, DOI: 10.1016/j.micron.2013.10.007 (cit. on p. 62).

Kai+07 Kai, H.; Mukaida, M.; Horii, S.; Ichinose, A.; Kita, R.; Kato, S.; Matsumoto, K.; Yoshida, Y.; Teranishi, R.; Yamada, K.; Mori, N. *Physica C: Superconductivity and its Applications* **2007**, *463–465*, 895–899, DOI: 10.1016/j.physc.2007.04.273 (cit. on p. 216).

Kai58 Kaiser, H. F. *Psychometrika* **1958**, *23*, 187–200, DOI: 10.1007/BF02289233 (cit. on p. 51).

Kam+06 Kamihara, Y.; Hiramatsu, H.; Hirano, M.; Kawamura, R.; Yanagi, H.; Kamiya, T.; Hosono, H. *Journal of the American Chemical Society* **2006**, *128*, 10012–10013, DOI: 10.1021/ja063355c (cit. on pp. 1, 8).

Kam+08 Kamihara, Y.; Watanabe, T.; Hirano, M.; Hosono, H. *Journal of the American Chemical Society* **2008**, *130*, 3296–3297, DOI: 10.1021/ja800073m (cit. on p. 8).

Kar+88 Karpinski, J.; Kaldis, E.; Jilek, E.; Rusiecki, S.; Bucher, B. *Nature* **1988**, *336*, 660–662, DOI: 10.1038/336660a0 (cit. on p. 155).

Kat+13 Katase, T.; Hiramatsu, H.; Kamiya, T.; Hosono, H. *New Journal of Physics* **2013**, *15*, 073019, DOI: 10.1088/1367-2630/15/7/073019 (cit. on pp. 2, 102, 105).

Kat+12 Katase, T.; Hiramatsu, H.; Kamiya, T.; Hosono, H. *Superconductor Science and Technology* **2012**, *25*, 084015, DOI: 10.1088/0953-2048/25/8/084015 (cit. on pp. 2, 8, 102, 105).

Kaw+02 Kawanowa, H.; Ozawa, H.; Ohtsuki, M.; Gotoh, Y.; Souda, R. *Surface Science* **2002**, *506*, 87–92, DOI: 10.1016/S0039-6028(01)01802-7 (cit. on p. 209).

KK04 Keenan, M. R.; Kotula, P. G. *Surface and Interface Analysis* **2004**, *36*, 203–212, DOI: 10.1002/sia.1657 (cit. on pp. 47, 49, 83).

KCS21 Kennedy, E.; Choi, C.; Scott, M. C. Comparative Analysis for Meaningful Interpretation of Rare-Earth Oxide $M_{4,5}$energy Loss Edges, 2021 (cit. on p. 226).

Kie+11 Kiessling, A.; Hänisch, J.; Thersleff, T.; Reich, E.; Weigand, M.; Hühne, R.; Sparing, M.; Holzapfel, B.; Durrell, J. H.; Schultz, L. *Superconductor Science and Technology* **2011**, *24*, 055018, DOI: 10.1088/0953-2048/24/5/055018 (cit. on pp. 2, 124).

Kil98 Kilaas, R. *Journal of Microscopy* **1998**, *190*, 45–51, DOI: 10.1046/j.1365-2818.1998.3070861.x (cit. on p. 69).

Kim+14 Kim, Y.-J.; Weiss, J. D.; Hellstrom, E. E.; Larbalestier, D. C.; Seidman, D. N. *Applied Physics Letters* **2014**, *105*, 162604, DOI: 10.1063/1.4898191 (cit. on p. 146).

Kir20 Kirkland, E. J., *Advanced Computing in Electron Microscopy*; Springer International Publishing: Cham, 2020, DOI: 10.1007/978-3-030-33260-0 (cit. on pp. 19, 26, 28).

KT96 Kirkland, E. J.; Thomas, M. G. *Ultramicroscopy* **1996**, *62*, 79–88, DOI: 10.1016/0304-3991(95)00092-5 (cit. on p. 30).

Kla+16 Klamt, C.; Dittrich, A.; Jaquet, B.; Eberl, C.; Döring, F.; Krebs, H.-U. *Applied Physics A* **2016**, *122*, 701, DOI: 10.1007/s00339-016-0234-1 (cit. on pp. 110, 111).

Klu+16 Kluyver, T. et al. *Positioning and Power in Academic Publishing: Players, Agents and Agendas* **2016**, 87–90, DOI: 10.3233/978-1-61499-649-1-87 (cit. on p. 53).

KR32 Knoll, M.; Ruska, E. *Zeitschrift für Physik* **1932**, *78*, 318–339, DOI: 10.1007/BF01342199 (cit. on p. 12).

Koh85 Kohl, H. *Ultramicroscopy* **1985**, *16*, 265–268, DOI: 10.1016/0304-3991(85)90081-6 (cit. on p. 46).

Köh+97 Köhler, A.; Linzen, S.; Kräuβlich, J.; Seidel, P.; Freitag, B.; Mader, W. *Physica C: Superconductivity* **1997**, *282–287*, 571–572, DOI: 10.1016/S0921-4534(97)00371-7 (cit. on p. 175).

Köh+04 Köhler, A.; Zandbergen, H. W.; Linzen, S.; Seidel, P. *Physica C: Superconductivity* **2004**, *408–410*, 842–843, DOI: 10.1016/j.physc.2004.03.215 (cit. on p. 175).

Kon+17 Kondo, Y.; Fukunaga, K.-i.; Okunishi, E.; Endo, N. *Microscopy and Microanalysis* **2017**, *23*, 1790–1791, DOI: 10.1017/S1431927617009618 (cit. on p. 159).

KO14 Kondo, Y.; Okunishi, E. *Microscopy* **2014**, *63*, 391–395, DOI: 10.1093/jmicro/dfu024 (cit. on p. 159).

Kot+14 Kothleitner, G.; Neish, M. J.; Lugg, N. R.; Findlay, S. D.; Grogger, W.; Hofer, F.; Allen, L. J. *Physical Review Letters* **2014**, *112*, 085501, DOI: 10.1103/PhysRevLett.112.085501 (cit. on p. 212).

KK06 Kotula, P. G.; Keenan, M. R. *Microscopy and Microanalysis* **2006**, *12*, 538–544, DOI: 10.1017/S1431927606060636 (cit. on p. 51).

KKvH12 Kotula, P. G.; Klenov, D. O.; von Harrach, H. S. *Microscopy and Microanalysis* **2012**, *18*, 691–698, DOI: 10.1017/S1431927612001201 (cit. on p. 87).

Kra+16 Krause, F. F.; Schowalter, M.; Grieb, T.; Müller-Caspary, K.; Mehrtens, T.; Rosenauer, A. *Ultramicroscopy* **2016**, *161*, 146–160, DOI: 10.1016/j.ultramic.2015.10.026 (cit. on p. 95).

Kra+17 Kraxner, J.; Schäfer, M.; Röschel, O.; Kothleitner, G.; Haberfehlner, G.; Paller, M.; Grogger, W. *Ultramicroscopy* **2017**, *172*, 30–39, DOI: 10.1016/j.ultramic.2016.10.005 (cit. on pp. 79, 80, 139).

Kri+97 Krivanek, O. L.; Dellby, N.; Spence, A. J.; Camps, R. A.; Brown, L. M.; andere In *Institute of Physics Conference Series*, 1997; Vol. 153, pp 35–40 (cit. on p. 18).

Küh+12 Kühn, J.; Hodoroaba, V.-D.; Linke, S.; Moritz, W.; Unger, W. E. S. *Surface and Interface Analysis* **2012**, *44*, 1456–1458, DOI: 10.1002/sia.4974 (cit. on p. 42).

Kum+94 Kumar, D.; Apte, P. R.; Pinto, R.; Sharon, M.; Gupta, L. C. *Journal of The Electrochemical Society* **1994**, *141*, 1611–1616, DOI: 10.1149/1.2054970 (cit. on pp. 11, 171).

Kun+99 Kung, H.; Foltyn, S.; Arendt, P.; Maley, M. *IEEE Transactions on Applied Superconductivity* **1999**, *9*, 2034–2037, DOI: 10.1109/77.784864 (cit. on p. 212).

Kur+13a Kurth, F.; Iida, K.; Trommler, S.; Hänisch, J.; Nenkov, K.; Engelmann, J.; Oswald, S.; Werner, J.; Schultz, L.; Holzapfel, B.; Haindl, S. *Superconductor Science and Technology* **2013**, *26*, 025014, DOI: 10.1088/0953-2048/26/2/025014 (cit. on p. 53).

Kur+13b Kurth, F.; Reich, E.; Hänisch, J.; Ichinose, A.; Tsukada, I.; Hühne, R.; Trommler, S.; Engelmann, J.; Schultz, L.; Holzapfel, B.; Iida, K. *Applied Physics Letters* **2013**, *102*, 1–5, DOI: 10.1063/1.4801312 (cit. on pp. 2, 95, 101, 102).

Kwo+18 Kwon, J.-H.; Meng, Y.; Wu, L.; Zhu, Y.; Zhang, Y.; Selvamanickam, V.; Welp, U.; Kwok, W.-K.; Zuo, J.-M. *Superconductor Science and Technology* **2018**, *31*, 105006, DOI: 10.1088/1361-6668/aad842 (cit. on p. 176).

LP93 LaGraff, J. R.; Payne, D. A. *Physica C: Superconductivity* **1993**, *212*, 478–486, DOI: 10.1016/0921-4534(93)90617-Y (cit. on p. 178).

LP92 LaGraff, J. R.; Payne, D. A. *Ferroelectrics* **1992**, *130*, 87–105, DOI: 10.1080/00150199208019536 (cit. on p. 178).

Lan+19a Langer, M.; Meyer, S.; Ackermann, K.; Grünewald, L.; Kauffmann-Weiss, S.; Aswartham, S.; Wurmehl, S.; Hänisch, J.; Holzapfel, B. In *Journal of Physics: Conference Series*, 2019; Vol. 1293, DOI: 10.1088/1742-6596/1293/1/012014 (cit. on pp. 8, 53).

Lan+19b Langer, M.; Meyer, S.; Ackermann, K.; Grünewald, L.; Kauffmann-Weiss, S.; Aswartham, S.; Wurmehl, S.; Hänisch, J.; Holzapfel, B. *Journal of Physics: Conference Series* **2019**, *1293*, 012014, DOI: 10.1088/1742-6596/1293/1/012014 (cit. on pp. 2, 101, 102, 110, 112, 116, 120, 265).

LC04 Langford, R. M.; Clinton, C. *Micron* **2004**, *35*, 607–611, DOI: 10.1016/j.micron.2004.03.002 (cit. on p. 57).

LBL16 Lazić, I.; Bosch, E. G. T.; Lazar, S. *Ultramicroscopy* **2016**, *160*, 265–280, DOI: 10.1016/j.ultramic.2015.10.011 (cit. on p. 119).

LRM80 Leapman, R. D.; Rez, P.; Mayers, D. F. *The Journal of Chemical Physics* **1980**, *72*, 1232–1243, DOI: 10.1063/1.439184 (cit. on pp. 46, 77).

LeB+10 LeBeau, J. M.; Findlay, S. D.; Allen, L. J.; Stemmer, S. *Ultramicroscopy* **2010**, *110*, 118–125, DOI: 10.1016/j.ultramic.2009.10.001 (cit. on p. 17).

LS08 LeBeau, J. M.; Stemmer, S. *Ultramicroscopy* **2008**, *108*, 1653–1658, DOI: 10.1016/j.ultramic.2008.07.001 (cit. on p. 31).

Leb Lebigot, E. O. Uncertainties: A Python Package for Calculations with Uncertainties (cit. on p. 90).

LS99 Lee, D. D.; Seung, H. S. *Nature* **1999**, *401*, 788–791, DOI: 10.1038/44565 (cit. on p. 49).

Lee+16 Lee, J.; Choi, S.; Oh, W.; Lee, J.; Moon, S.; Yoo, S. *IEEE Transactions on Applied Superconductivity* **2016**, *26*, 1–6, DOI: 10.1109/TASC.2016.2533629 (cit. on pp. 2, 178, 185, 191, 192, 195).

Lee+17 Lee, J.; Jiang, J.; Kametani, F.; Oh, M. J.; Weiss, J. D.; Collantes, Y.; Seo, S.; Yoon, S.; Tarantini, C.; Jo, Y. J.; Hellstrom, E. E.; Lee, S. *Superconductor Science and Technology* **2017**, *30*, 085006, DOI: 10.1088/1361-6668/aa73f5 (cit. on pp. 101, 102, 124, 127, 131, 135).

Lee+13 Lee, S.; Tarantini, C.; Gao, P.; Jiang, J.; Weiss, J. D.; Kametani, F.; Folkman, C. M.; Zhang, Y.; Pan, X. Q.; Hellstrom, E. E.; Larbalestier, D. C.; Eom, C. B. *Nature Materials* **2013**, *12*, 392–396, DOI: 10.1038/nmat3575 (cit. on pp. 124, 135).

Lee+10 Lee, S. et al. *Nature Materials* **2010**, *9*, 397–402, DOI: 10.1038/nmat2721 (cit. on pp. 2, 102, 105, 114).

Lee12 Lee, S. Growth and Characterization of Cobalt-Doped $BaFe_2As_2$ Epitaxial Thin Films and Superlattices, Madison, Wis.: University of Wisconsin-Madison, 2012, 94 pp. (cit. on pp. 102, 118).

Len+02 Lentzen, M.; Jahnen, B.; Jia, C. L.; Thust, A.; Tillmann, K.; Urban, K. *Ultramicroscopy* **2002**, *92*, 233–242, DOI: 10.1016/S0304-3991(02)00139-0 (cit. on p. 24).

Len06 Lentzen, M. *Microscopy and Microanalysis* **2006**, *12*, 191–205, DOI: 10.1017/S1431927606060326 (cit. on pp. 26, 69).

Li+18 Li, C.; Habler, G.; Baldwin, L. C.; Abart, R. *Ultramicroscopy* **2018**, *184*, 310–317, DOI: 10.1016/j.ultramic.2017.09.011 (cit. on p. 62).

Li+19 Li, D.; Lee, K.; Wang, B. Y.; Osada, M.; Crossley, S.; Lee, H. R.; Cui, Y.; Hikita, Y.; Hwang, H. Y. *Nature* **2019**, *572*, 624–627, DOI: 10.1038/s41586-019-1496-5 (cit. on p. 1).

Lim+21 Lim, H.; Jang, S.; Lee, D.-j.; Lee, Y. S. *Journal of the Korean Physical Society* **2021**, *78*, 510–515, DOI: 10.1007/s40042-020-00040-8 (cit. on pp. 228, 229).

LSA01 Limpert, E.; Stahel, W. A.; Abbt, M. *BioScience* **2001**, *51*, 341–352, DOI: 10.1641/0006-3568(2001)051[0341:LNDATS]2.0.CO;2 (cit. on p. 90).

Lin+21 Lin, R.; Zhang, R.; Wang, C.; Yang, X.-Q.; Xin, H. L. *Scientific Reports* **2021**, *11*, 5386, DOI: 10.1038/s41598-021-84499-w (cit. on pp. 190, 208, 209).

Liu21 Liu, J. *Microscopy and Microanalysis* **2021**, 1–53, DOI: 10.1017/S1431927621012125 (cit. on p. 26).

LKS88 Loane, R. F.; Kirkland, E. J.; Silcox, J. *Acta Crystallographica Section A: Foundations of Crystallography* **1988**, *44*, 912–927, DOI: 10.1107/S0108767388006403 (cit. on p. 29).

LLL35 London, F.; London, H.; Lindemann, F. A. *Proceedings of the Royal Society of London. Series A - Mathematical and Physical Sciences* **1935**, *149*, 71–88, DOI: 10.1098/rspa.1935.0048 (cit. on p. 7).

Low+97 Low, B. L.; Xu, S. Y.; Ong, C. K.; Wang, X. B.; Shen, Z. X. *Superconductor Science and Technology* **1997**, *10*, 41–46, DOI: 10.1088/0953-2048/10/1/006 (cit. on p. 179).

Lu+21 Lu, J.; Xin, Y.; Jarvis, B.; Bai, H. *Superconductor Science and Technology* **2021**, *34*, 075004, DOI: 10.1088/1361-6668/abfd0c (cit. on pp. 11, 171).

Mac+94 MacManus-Driscoll, J. L.; Alonso, J. A.; Wang, P. C.; Geballe, T. H.; Bravman, J. C. *Physica C: Superconductivity* **1994**, *232*, 288–308, DOI: 10.1016/0921-4534(94)90789-7 (cit. on pp. 196, 227, 228, 231).

Mac+04 MacManus-Driscoll, J. L.; Foltyn, S. R.; Jia, Q. X.; Wang, H.; Serquis, A.; Civale, L.; Maiorov, B.; Hawley, M. E.; Maley, M. P.; Peterson, D. E. *Nature Materials* **2004**, *3*, 439–443, DOI: 10.1038/nmat1156 (cit. on pp. 1, 2, 216).

Mac+05 MacManus-Driscoll, J. L.; Foltyn, S. R.; Maiorov, B.; Jia, Q. X.; Wang, H.; Serquis, A.; Civale, L.; Lin, Y.; Hawley, M. E.; Maley, M. P.; Peterson, D. E. *Applied Physics Letters* **2005**, *86*, 032505, DOI: 10.1063/1.1851006 (cit. on p. 196).

Mac+06 MacManus-Driscoll, J. L.; Maiorov, B.; Durrell, J.; Foltyn, S.; Jia, Q. X.; Civale, L.; Wang, H.; Kursumovic, A.; Peterson, D. E. *Superconductor Science and Technology* **2006**, *19*, S55–S59, DOI: 10.1088/0953-2048/19/3/008 (cit. on pp. 2, 196, 228, 231).

MW21 MacManus-Driscoll, J. L.; Wimbush, S. C. *Nature Reviews Materials* **2021**, *6*, 587–604, DOI: 10.1038/s41578-021-00290-3 (cit. on pp. 1, 8, 10).

Mae+88 Maeda, H.; Tanaka, Y.; Fukutomi, M.; Asano, T. *Japanese Journal of Applied Physics* **1988**, *27*, L209, DOI: 10.1143/JJAP.27.L209 (cit. on p. 8).

Mae+17 Maeda, T.; Kaneko, K.; Yamada, K.; Roy, A.; Sato, Y.; Teranishi, R.; Kato, T.; Izumi, T.; Shiohara, Y. *Ultramicroscopy* **2017**, *176*, 151–160, DOI: 10.1016/j.ultramic.2016.11.015 (cit. on p. 208).

MKY06 Maekawa, T.; Kurosaki, K.; Yamanaka, S. *Journal of Alloys and Compounds* **2006**, *407*, 44–48, DOI: 10.1016/j.jallcom.2005.06.030 (cit. on p. 268).

Maj+21 Majkic, G.; Jeong, J. S.; Yun, H.; Hernandez, F. C. R.; Galstyan, E.; Pratap, R.; Cheng, H.; Stokes, A.; Mkhoyan, K. A.; Selvamanickam, V. **2021**, *34*, 115002, DOI: 10.1088/1361-6668/ac23ba (cit. on pp. 2, 135, 216, 227, 229–231).

MK17 Mangin, P.; Kahn, R., *Superconductivity*; Springer International Publishing: Cham, 2017, DOI: 10.1007/978-3-319-50527-5 (cit. on pp. 5–7, 10).

Man+87 Mankiewich, P. M.; Scofield, J. H.; Skocpol, W. J.; Howard, R. E.; Dayem, A. H.; Good, E. *Applied Physics Letters* **1987**, *51*, 1753–1755, DOI: 10.1063/1.98513 (cit. on p. 10).

Mar+88 Marsh, P.; Fleming, R. M.; Mandich, M. L.; DeSantolo, A. M.; Kwo, J.; Hong, M.; Martinez-Miranda, L. J. *Nature* **1988**, *334*, 141–143, DOI: 10.1038/334141a0 (cit. on p. 155).

Mat+08 Matsumoto, O.; Utsuki, A.; Tsukada, A.; Yamamoto, H.; Manabe, T.; Naito, M. *Physica C: Superconductivity* **2008**, *468*, 1148–1151, DOI: 10.1016/j.physc.2008.05.019 (cit. on p. 195).

McA+20 McAuliffe, T. P.; Foden, A.; Bilsland, C.; Daskalaki Mountanou, D.; Dye, D.; Britton, T. B. *Ultramicroscopy* **2020**, *211*, 112944, DOI: 10.1016/j.ultramic.2020.112944 (cit. on p. 51).

Meh+12 Mehrtens, T.; Bley, S.; Venkata Satyam, P.; Rosenauer, A. *Micron* **2012**, *43*, 902–909, DOI: 10.1016/j.micron.2012.03.008 (cit. on p. 29).

Men21 Mentel, Ł. Mendeleev - A Python Resource for Properties of Chemical Elements, Ions and Isotopes, version 0.9.0, 2021, DOI: 10.5281/zenodo.5233824 (cit. on p. 224).

Mey21 Meyer, S. Introduction of quasi-multilayer pulsed laser deposition for enhanced superconducting properties of $Ba(Fe_{0.92}Co_{0.08})_2As_2$ thin films, Karlsruhe Institute of Technology (KIT), 2021, DOI: 10.5445/IR/1000127915 (cit. on pp. 2, 53, 54, 124, 125, 130, 135–137, 143–145, 147).

Mey+20 Meyer, S.; Langer, M.; Grünewald, L.; Hänisch, J.; Gerthsen, D.; Holzapfel, B. *Journal of Physics: Conference Series* **2020**, *1559*, 012052, DOI: 10.1088/1742-6596/1559/1/012052 (cit. on pp. 2, 124, 265).

Mey+21 Meyer, T.; Westphal, T.; Kressdorf, B.; Ross, U.; Jooss, C.; Seibt, M. *Ultramicroscopy* **2021**, *228*, 113320, DOI: 10.1016/j.ultramic.2021.113320 (cit. on p. 62).

Mic+98 Michaelis, A.; Irene, E. A.; Auciello, O.; Krauss, A. R. *Journal of Applied Physics* **1998**, *83*, 7736–7743, DOI: 10.1063/1.367947 (cit. on p. 178).

MVC92 Midgley, P. A.; Vincent, R.; Cherns, D. *Philosophical Magazine A* **1992**, *66*, 237–256, DOI: 10.1080/01418619208201554 (cit. on p. 176).

MS05 Mitchell, D.; Schaffer, B. *Ultramicroscopy* **2005**, *103*, 319–332, DOI: 10.1016/j.ultramic.2005.02.003 (cit. on pp. 70, 77).

MN15 Mitchell, D. R.; Nancarrow, M. J. *Microscopy Research and Technique* **2015**, *78*, 886–893, DOI: 10.1002/jemt.22551 (cit. on pp. 79, 112).

Mit+08 Mitchell, N.; Bessette, D.; Gallix, R.; Jong, C.; Knaster, J.; Libeyre, P.; Sborchia, C.; Simon, F. *IEEE Transactions on Applied Superconductivity* **2008**, *18*, 435–440, DOI: 10.1109/TASC.2008.921232 (cit. on pp. 1, 7).

MN21 Miura, K.; Nørrelykke, S. F. *The EMBO Journal* **2021**, *40*, e105889, DOI: 10.15252/embj.2020105889 (cit. on p. 89).

Miu+13 Miura, M.; Maiorov, B.; Kato, T.; Shimode, T.; Wada, K.; Adachi, S.; Tanabe, K. *Nature Communications* **2013**, *4*, 2499, DOI: 10.1038/ncomms3499 (cit. on pp. 124, 131).

Miu+19 Miura, M.; Tsuchiya, G.; Harada, T.; Tanabe, K.; Kiuchi, M.; Matsushita, T. *Superconductor Science and Technology* **2019**, *32*, 064005, DOI: 10.1088/1361-6668/ab0faf (cit. on pp. 124, 127).

Mol+15 Molina-Luna, L.; Duerrschnabel, M.; Turner, S.; Erbe, M.; Martinez, G. T.; Aert, S. V.; Holzapfel, B.; Tendeloo, G. V. *Superconductor Science and Technology* **2015**, *28*, 115009, DOI: 10.1088/0953-2048/28/11/115009 (cit. on pp. 207, 208).

MI11 Momma, K.; Izumi, F. *Journal of Applied Crystallography* **2011**, *44*, 1272–1276, DOI: 10.1107/S0021889811038970 (cit. on p. 91).

Mor+22 Moreira, M.; Hillenkamp, M.; Divitini, G.; Tizei, L. H. G.; Ducati, C.; Cotta, M. A.; Rodrigues, V.; Ugarte, D. *Microscopy and Microanalysis* **2022**, 1–12, DOI: 10.1017/S1431927621013933 (cit. on p. 87).

MCC87 Mory, C.; Colliex, C.; Cowley, J. M. *Ultramicroscopy* **1987**, *21*, 171–177, DOI: 10.1016/0304-3991(87)90083-0 (cit. on p. 28).

MF99 Mott, R. B.; Friel, J. J. *Journal of Microscopy* **1999**, *193*, 2–14, DOI: 10.1046/j.1365-2818.1999.00437.x (cit. on p. 80).

MF20 Moy, A.; Fournelle, J. *Microscopy and Microanalysis* **2020**, *26*, 496–498, DOI: 10.1017/S1431927620014853 (cit. on p. 42).

Mul09 Muller, D. A. *Nature Materials* **2009**, *8*, 263–270, DOI: 10.1038/nmat2380 (cit. on pp. 31, 66).

Mül+92 Müller, O.; Schubert, J.; Zander, W.; Stritzker, B. *Physica C: Superconductivity* **1992**, *191*, 103–107, DOI: 10.1016/0921-4534(92)90635-P (cit. on p. 171).

Mül54 Müller, R. H. *Physical Review* **1954**, *93*, 891–892, DOI: 10.1103/PhysRev.93.891.2 (cit. on p. 127).

Mur+96 Murakami, M.; Sakai, N.; Higuchi, T.; Yoo, S. I. *Superconductor Science and Technology* **1996**, *9*, 1015–1032, DOI: 10.1088/0953-2048/9/12/001 (cit. on p. 196).

MM00 Muralidhar, M.; Murakami, M. *Superconductor Science and Technology* **2000**, *13*, 1315–1321, DOI: 10.1088/0953-2048/13/9/306 (cit. on p. 196).

MS20 Muto, S.; Shiga, M. *Microscopy* **2020**, *69*, 110–122, DOI: 10.1093/jmicro/dfz036 (cit. on pp. 3, 49, 87).

NOM18 Naden, A. B.; O'Shea, K. J.; MacLaren, D. A. *Nanotechnology* **2018**, *29*, 165704, DOI: 10.1088/1361-6528/aaae50 (cit. on pp. 69, 214, 215).

ND08 Nagayama, K.; Danev, R. *Philosophical Transactions of the Royal Society B: Biological Sciences* **2008**, *363*, 2153–2162, DOI: 10.1098/rstb.2008.2268 (cit. on p. 22).

NI95 Nakamura, T.; Iiyama, M. I. M. *Japanese Journal of Applied Physics* **1995**, *34*, 4765, DOI: 10.1143/JJAP.34.4765 (cit. on p. 207).

NP00 Nellist, P. D.; Pennycook, S. J. In *Advances in Imaging and Electron Physics*, Hawkes, P. W., Ed.; Elsevier: 2000; Vol. 113, pp 147–203, DOI: 10.1016/S1076-5670(00)80013-0 (cit. on p. 30).

NB06 Newbury, D. E.; Bright, D. S. *Scanning* **2006**, *27*, 15–22, DOI: 10.1002/sca.4950270104 (cit. on p. 87).

NR13 Newbury, D. E.; Ritchie, N. W. M. *Scanning* **2013**, *35*, 141–168, DOI: 10.1002/sca.21041 (cit. on p. 43).

NR15a Newbury, D. E.; Ritchie, N. W. M. *Journal of Materials Science* **2015**, *50*, 493–518, DOI: 10.1007/s10853-014-8685-2 (cit. on pp. 42, 43).

NR15b Newbury, D. E.; Ritchie, N. W. M. *Microscopy and Microanalysis* **2015**, *21*, 1327–1340, DOI: 10.1017/S1431927615014993 (cit. on p. 42).

Ngo+07 Ngo, V. V.; Hernandez, M.; Roth, B.; Joy, D. C. *Microscopy Today* **2007**, *15*, 12–17, DOI: 10.1017/S1551929500050951 (cit. on pp. 38, 69, 192).

Nik+12 Nikolaichik, V. I.; Sobolev, B. P.; Zaporozhets, M. A.; Avilov, A. S. *Crystallography Reports* **2012**, *57*, 299–307, DOI: 10.1134/S1063774512010087 (cit. on pp. 94–96, 98).

Nor+17 Nord, M.; Vullum, P. E.; MacLaren, I.; Tybell, T.; Holmestad, R. *Advanced Structural and Chemical Imaging* **2017**, *3*, 9, DOI: 10.1186/s40679-017-0042-5 (cit. on p. 72).

NC92 Norton, M. G.; Carter, C. B. *Scanning Microscopy* **1992**, *6* (cit. on pp. 193, 194, 209).

NSC90 Norton, M. G.; Summerfelt, S. R.; Carter, C. B. *Applied Physics Letters* **1990**, *56*, 2246–2248, DOI: 10.1063/1.103246 (cit. on p. 209).

Obr+04 Obradors, X.; Puig, T.; Pomar, A.; Mestres, N.; Sandiumenge, F.; Piñol, S.; Castaño, O.; Cavallaro, A.; Palau, A.; González, J. C.; Coll, M.; Gázquez, J. *Physica C: Superconductivity* **2004**, *408–410*, 913–914, DOI: 10.1016/j.physc.2004.03.160 (cit. on p. 10).

Obr+12 Obradors, X.; Puig, T.; Ricart, S.; Coll, M.; Gazquez, J.; Palau, A.; Granados, X. *Superconductor Science and Technology* **2012**, *25*, 123001, DOI: 10.1088/0953-2048/25/12/123001 (cit. on p. 2).

OP14 Obradors, X.; Puig, T. *Superconductor Science and Technology* **2014**, *27*, 044003, DOI: 10.1088/0953-2048/27/4/044003 (cit. on pp. 1, 8).

Oh+18 Oh, W.; Park, I.; Lee, J.; Lee, H.; Moon, S.; Shinde, K.; Chung, K.; Yoo, S. *IEEE Transactions on Applied Superconductivity* **2018**, *28*, 1–5, DOI: 10.1109/TASC.2018.2814057 (cit. on pp. 2, 178, 195).

Oh+20 Oh, W.-J.; Park, I.; Chung, K.; Lee, J.-H.; Moon, S.-H.; Yoo, S.-I. *Superconductor Science and Technology* **2020**, *33*, 085007, DOI: 10.1088/1361-6668/ab9aa1 (cit. on pp. 2, 178, 195).

Oka+00 Okazaki, T.; Suenaga, K.; Lian, Y.; Gu, Z.; Shinohara, H. *The Journal of Chemical Physics* **2000**, *113*, 9593–9597, DOI: 10.1063/1.1321047 (cit. on p. 224).

Ort+15 Ortel, E.; Kraehnert, R.; Galbert, F.; Hodoroaba, V.-D. *Microscopy and Microanalysis* **2015**, *21*, 1707–1708, DOI: 10.1017/S1431927615009319 (cit. on p. 42).

Ots79 Otsu, N. *IEEE Transactions on Systems, Man, and Cybernetics* **1979**, *9*, 62–66, DOI: 10.1109/TSMC.1979.4310076 (cit. on p. 89).

Ott91 Otten, M. T. *Journal of Electron Microscopy Technique* **1991**, *17*, 221–230, DOI: 10.1002/jemt.1060170209 (cit. on p. 19).

Pak+20 Pak, C.; Su, Y. F.; Collantes, Y.; Tarantini, C.; Hellstrom, E. E.; Larbalestier, D. C.; Kametani, F. *Superconductor Science and Technology* **2020**, *33*, DOI: 10.1088/1361-6668/aba01a (cit. on pp. 53, 94, 145, 146).

Pal+18 Palau, A.; Vallès, F.; Rouco, V.; Coll, M.; Li, Z.; Pop, C.; Mundet, B.; Gàzquez, J.; Guzman, R.; Gutierrez, J.; Obradors, X.; Puig, T. **2018**, *31*, 034004, DOI: 10.1088/1361-6668/aaa65e (cit. on p. 204).

Par+18a Park, I.; Oh, W.; Lee, J.; Moon, S.; Yoo, S. *IEEE Transactions on Applied Superconductivity* **2018**, *28*, 1–5, DOI: 10.1109/TASC.2018.2795244 (cit. on pp. 2, 178, 191, 192, 195).

Par+18b Park, I.; Oh, W.; Lee, J.; Moon, S.; Yoo, S. *Progress in Superconductivity and Cryogenics* **2018**, *20*, 46–49, DOI: 10.9714/PSAC.2018.20.4.046 (cit. on pp. 2, 178, 191, 192, 195).

Pea01 Pearson, K. *The London, Edinburgh, and Dublin Philosophical Magazine and Journal of Science* **1901**, *2*, 559–572, DOI: 10.1080/14786440109462720 (cit. on p. 47).

Ped+11 Pedregosa, F. et al. *Journal of Machine Learning Research* **2011**, *12*, 2825–2830 (cit. on p. 52).

Pen89 Pennycook, S. J. *Ultramicroscopy* **1989**, *30*, 58–69, DOI: 10.1016/0304-3991(89)90173-3 (cit. on pp. 27, 29, 30).

Pen+92 Pennycook, S. J.; Chisholm, M. F.; Jesson, D. E.; Feenstra, R.; Zhu, S.; Zheng, X. Y.; Lowndes, D. J. *Physica C: Superconductivity* **1992**, *202*, 1–11, DOI: 10.1016/0921-4534(92)90288-N (cit. on p. 194).

Pen+96 Pennycook, S. J.; Jesson, D. E.; McGibbon, A. J.; Nellist, P. D. *Journal of Electron Microscopy* **1996**, *45*, 36–43, DOI: 10.1093/oxfordjournals.jmicro.a023410 (cit. on pp. 29, 30).

Phi+12 Phillips, P. J.; De Graef, M.; Kovarik, L.; Agrawal, A.; Windl, W.; Mills, M. J. *Ultramicroscopy* **2012**, *116*, 47–55, DOI: 10.1016/j.ultramic.2012.03.013 (cit. on p. 32).

Pin+20 Pinto, V.; Vannozzi, A.; Angrisani Armenio, A.; Rizzo, F.; Masi, A.; Santoni, A.; Meledin, A.; Ferrarese, F. M.; Orlanducci, S.; Celentano, G. *Coatings* **2020**, *10*, 860, DOI: 10.3390/coatings10090860 (cit. on p. 204).

PB53 Pippard, A. B.; Bragg, W. L. *Proceedings of the Royal Society of London. Series A. Mathematical and Physical Sciences* **1953**, *216*, 547–568, DOI: 10.1098/rspa.1953.0040 (cit. on p. 7).

Ple+13 Plecenik, T.; Gregor, M.; Sobota, R.; Truchly, M.; Satrapinskyy, L.; Kurth, F.; Holzapfel, B.; Iida, K.; Kus, P.; Plecenik, A. *Applied Physics Letters* **2013**, *103*, 052601, DOI: 10.1063/1.4816820 (cit. on p. 107).

Pof+20 Pofelski, A.; Ghanad-Tavakoli, S.; Thompson, D. A.; Botton, G. A. *Ultramicroscopy* **2020**, *209*, 112858, DOI: 10.1016/j.ultramic.2019.112858 (cit. on pp. 69, 214).

Pop+20 Popov, R.; Ackermann, K.; Rijckaert, H.; Hänisch, J.; Driessche, I. V.; Holzapfel, B. *Journal of Physics: Conference Series* **2020**, *1559*, 012038, DOI: 10.1088/1742-6596/1559/1/012038 (cit. on pp. 54, 178).

PLH15 Posen, S.; Liepe, M.; Hall, D. L. *Applied Physics Letters* **2015**, *106*, 082601, DOI: 10.1063/1.4913247 (cit. on p. 7).

Pot17 Potapov, P. *Ultramicroscopy* **2017**, *182*, 191–194, DOI: 10.1016/j.ultramic.2017.06.023 (cit. on p. 49).

Pot16 Potapov, P. *Ultramicroscopy* **2016**, *160*, 197–212, DOI: 10.1016/j.ultramic.2015.10.020 (cit. on pp. 47, 49, 52, 77).

PLO17 Potapov, P.; Longo, P.; Okunishi, E. *Micron* **2017**, *96*, 29–37, DOI: 10.1016/j.micron.2017.02.001 (cit. on p. 82).

PL21a Potapov, P.; Lubk, A. *Microscopy and Microanalysis* **2021**, *27*, 2320–2322, DOI: 10.1017/S1431927621008345 (cit. on p. 68).

PL21b Potapov, P.; Lubk, A. *Micron* **2021**, *145*, 103068, DOI: 10.1016/j.micron.2021.103068 (cit. on p. 51).

Pru+06 Prusseit, W.; Hoffmann, C.; Nemetschek, R.; Sigl, G.; Handke, J.; Lumkemann, A.; Kinder, H. *IEEE Transactions on Applied Superconductivity* **2006**, *16*, 996–998, DOI: 10.1109/TASC.2006.873263 (cit. on p. 178).

Qin+21 Qin, D.; Iida, K.; Hatano, T.; Saito, H.; Ma, Y.; Wang, C.; Hata, S.; Naito, M.; Yamamoto, A. *Physical Review Materials* **2021**, *5*, 014801, DOI: 10.1103/PhysRevMaterials.5.014801 (cit. on p. 101).

Qiu+17 Qiu, W.; Ma, Z.; Patel, D.; Sang, L.; Cai, C.; Shahriar Al Hossain, M.; Cheng, Z.; Wang, X.; Dou, S. X. *ACS Applied Materials and Interfaces* **2017**, *9*, 37446–37453, DOI: 10.1021/acsami.7b11853 (cit. on pp. 96, 101).

Ram+90 Ramesh, R.; Jin, S.; Nakahara, S.; Tiefel, T. H. *Applied Physics Letters* **1990**, *57*, 1458–1460, DOI: 10.1063/1.104126 (cit. on p. 160).

RKH99 Regier, M.; Keskin, E.; Halbritter, J. *IEEE Transactions on Applied Superconductivity* **1999**, *9*, 2375–2379, DOI: 10.1109/77.784949 (cit. on p. 171).

Rei98 Reimer, L., *Scanning Electron Microscopy*; Springer Series in Optical Sciences, Vol. 45; Springer Berlin Heidelberg: Berlin, Heidelberg, 1998, DOI: 10.1007/978-3-540-38967-5 (cit. on pp. 32, 34–36).

RK08 Reimer, L.; Kohl, H., *Transmission Electron Microscopy: Physics of Image Formation*, 5. ed; Springer Series in Optical Sciences 36; Springer: New York, NY, 2008; 587 pp. (cit. on pp. 13, 15, 18, 21, 26, 192).

Ric+17 Richter, S.; Aswartham, S.; Pukenas, A.; Grinenko, V.; Wurmehl, S.; Skrotzki, W.; Buchner, B.; Nielsch, K.; Huhne, R. *IEEE Transactions on Applied Superconductivity* **2017**, *27*, 7–10, DOI: 10.1109/TASC.2016.2633303 (cit. on p. 95).

Rit07 Ritchie, N. *Microscopy and Microanalysis* **2007**, *13*, 160–161, DOI: 10.1017/S1431927607074843 (cit. on p. 86).

Rit09 Ritchie, N. W. M. *Microscopy and Microanalysis* **2009**, *15*, 454–468, DOI: 10.1017/S1431927609990407 (cit. on pp. 40, 44, 56).

Rob03 Roberts, M. C. *Microscopy and Microanalysis* **2003**, *9*, 530–531, DOI: 10.1017/S1431927603442657 (cit. on pp. 56, 81).

RCM82 Roberts, P. T. E.; Chapman, J. N.; MacLeod, A. M. *Ultramicroscopy* **1982**, *8*, 385–396, DOI: 10.1016/0304-3991(82)90061-4 (cit. on p. 20).

Roe+20 Roels, J.; Vernaillen, F.; Kremer, A.; Gonçalves, A.; Aelterman, J.; Luong, H. Q.; Goossens, B.; Philips, W.; Lippens, S.; Saeys, Y. *Nature Communications* **2020**, *11*, 771, DOI: 10.1038/s41467-020-14529-0 (cit. on p. 56).

Ros+10 Rosenzweig, S.; Hänisch, J.; Hühne, R.; Holzapfel, B.; Schultz, L. *Journal of Physics: Conference Series* **2010**, *234*, 012035, DOI: 10.1088/1742-6596/234/1/012035 (cit. on p. 178).

Rot+91 Rothman, S. J.; Routbort, J. L.; Welp, U.; Baker, J. E. *Physical Review B* **1991**, *44*, 2326–2333, DOI: 10.1103/PhysRevB.44.2326 (cit. on p. 171).

RTJ08 Rotter, M.; Tegel, M.; Johrendt, D. *Physical Review Letters* **2008**, *101*, 107006, DOI: 10.1103/PhysRevLett.101.107006 (cit. on p. 8).

Rou+14 Rouco, V.; Palau, A.; Guzman, R.; Gazquez, J.; Coll, M.; Obradors, X.; Puig, T. *Superconductor Science and Technology* **2014**, *27*, 125009, DOI: 10.1088/0953-2048/27/12/125009 (cit. on pp. 202, 204, 216).

Ruf+06 Rufoloni, A.; Augieri, A.; Celentano, G.; Galluzzi, V.; Mancini, A.; Vannozzi, A.; Petrisor, T.; Ciontea, L.; Boffa, V.; Gambardella, U. *Journal of Physics: Conference Series* **2006**, *43*, 199–202, DOI: 10.1088/1742-6596/43/1/050 (cit. on p. 179).

Rup+92 Rupeng, Z.; Goringe, M. J.; Myhra, S.; Turner, P. S. *Philosophical Magazine A* **1992**, *66*, 491–506, DOI: 10.1080/01418619208201571 (cit. on p. 172).

Rus34 Ruska, E. *Zeitschrift für Physik* **1934**, *87*, 580–602, DOI: 10.1007/BF01333326 (cit. on p. 12).

Sac+18 Sachsé, R.; Hertwig, A.; Kraehnert, R.; Hodoroaba, V.-D. *Microscopy and Microanalysis* **2018**, *24*, 762–763, DOI: 10.1017/S1431927618004300 (cit. on p. 42).

SL14 Sang, X.; LeBeau, J. M. *Ultramicroscopy* **2014**, *138*, 28–35, DOI: 10.1016/j.ultramic.2013.12.004 (cit. on p. 68).

Sar+19 Sarkar, A.; Wang, Q.; Schiele, A.; Chellali, M. R.; Bhattacharya, S. S.; Wang, D.; Brezesinski, T.; Hahn, H.; Velasco, L.; Breitung, B. *Advanced Materials* **2019**, *31*, 1806236, DOI: 10.1002/adma.201806236 (cit. on p. 196).

Sat+20 Sato, H.; Hiramatsu, H.; Kamiya, T.; Hosono, H. *ACS Applied Materials & Interfaces* **2020**, *12*, 50096–50104, DOI: 10.1021/acsami.0c12080 (cit. on pp. 120, 144).

SK94 Savvides, N.; Katsaros, A. *Physica C: Superconductivity* **1994**, *226*, 23–36, DOI: 10.1016/0921-4534(94)90473-1 (cit. on p. 188).

SSR12 Schaffer, M.; Schaffer, B.; Ramasse, Q. *Ultramicroscopy* **2012**, *114*, 62–71, DOI: 10.1016/j.ultramic.2012.01.005 (cit. on pp. 60, 165).

Sch49 Scherzer, O. *Journal of Applied Physics* **1949**, *20*, 20–29, DOI: 10.1063/1.1698233 (cit. on pp. 22, 24).

Sch36 Scherzer, O. *Zeitschrift für Physik* **1936**, *101*, 593–603, DOI: 10.1007/BF01349606 (cit. on p. 19).

Sch+12 Schindelin, J. et al. *Nature Methods* **2012**, *9*, 676–682, DOI: 10.1038/nmeth.2019 (cit. on p. 89).

Sch+10 Schlossmacher, P.; Klenov, D.; Freitag, B.; von Harrach, H. *Microscopy Today* **2010**, *18*, 14–20, DOI: 10.1017/s1551929510000404 (cit. on pp. 41, 79, 136).

Sch09 Schou, J. *Applied Surface Science* **2009**, *255*, 5191–5198, DOI: 10.1016/j.apsusc.2008.10.101 (cit. on p. 110).

Sch+03 Schwarz, S. M.; Kempshall, B. W.; Giannuzzi1, L. A.; McCartney, M. R. *Microscopy and Microanalysis* **2003**, *9*, 116–117, DOI: 10.1017/S1431927603441044 (cit. on p. 166).

Sel+15 Selvamanickam, V.; Gharahcheshmeh, M. H.; Xu, A.; Zhang, Y.; Galstyan, E. *Superconductor Science and Technology* **2015**, *28*, 104003, DOI: 10.1088/0953-2048/28/10/104003 (cit. on p. 135).

Señ+91 Señaris-Rodríguez, M. A.; Chippindale, A. M.; Várez, A.; Morán, E.; Alario-Franco, M. A. *Physica C: Superconductivity* **1991**, *172*, 477–480, DOI: 10.1016/0921-4534(91)90216-L (cit. on p. 156).

SO22 Seto, Y.; Ohtsuka, M. *Journal of Applied Crystallography* **2022**, *55*, DOI: 10.1107/S1600576722000139 (cit. on pp. 72, 184).

Sez16 Sezen, M. In *Modern Electron Microscopy in Physical and Life Sciences*, Janecek, M., Kral, R., Eds.; InTech: 2016, DOI: 10.5772/61634 (cit. on pp. 32, 36).

Sha76 Shannon, R. D. *Acta Crystallographica Section A: Crystal Physics, Diffraction, Theoretical and General Crystallography* **1976**, *32*, 751–767, DOI: 10.1107/S0567739476001551 (cit. on p. 228).

Sha21 Sharma, R., *Superconductivity: Basics and Applications to Magnets*; Springer Series in Materials Science, Vol. 214; Springer International Publishing: Cham, 2021, DOI: 10.1007/978-3-030-75672-7 (cit. on p. 5).

ST91 Shi, L. T.; Tu, K. N. *Applied Physics Letters* **1991**, *59*, 2040–2042, DOI: 10/fbhnsg (cit. on p. 171).

Shi+19 Shimada, Y.; Yamamoto, A.; Hayashi, Y.; Kishio, K.; Shimoyama, J. I.; Hata, S.; Konno, T. J. *Superconductor Science and Technology* **2019**, *32*, 084003, DOI: 10.1088/1361-6668/ab0eb6 (cit. on p. 102).

SZ92 Shimizu, R.; Ze-Jun, D. *Reports on Progress in Physics* **1992**, *55*, 487–531, DOI: 10.1088/0034-4885/55/4/002 (cit. on p. 44).

Shl14 Shlens, J. A Tutorial on Principal Component Analysis, 2014 (cit. on p. 47).

Shu+20 Shukunami, Y.; Yamashita, A.; Goto, Y.; Mizuguchi, Y. *Physica C: Superconductivity and its Applications* **2020**, *572*, 1353623, DOI: 10.1016/j.physc.2020.1353623 (cit. on p. 196).

Sie+90 Siegal, M. P.; Phillips, J. M.; van Dover, R. B.; Tiefel, T. H.; Marshall, J. H. *Journal of Applied Physics* **1990**, *68*, 6353–6360, DOI: 10.1063/1.346881 (cit. on p. 145).

Slo+21 Slouf, M.; Skoupy, R.; Pavlova, E.; Krzyzanek, V. *Nanomaterials* **2021**, *11*, 962, DOI: 10.3390/nano11040962 (cit. on p. 39).

Sni+20 Snider, E.; Dasenbrock-Gammon, N.; McBride, R.; Debessai, M.; Vindana, H.; Vencatasamy, K.; Lawler, K. V.; Salamat, A.; Dias, R. P. *Nature* **2020**, *586*, 373–377, DOI: 10.1038/s41586-020-2801-z (cit. on p. 5).

Spi+10 Spiecker, E.; Garbrecht, M.; Jäger, W.; Tillmann, K. *Journal of Microscopy* **2010**, *237*, 341–346, DOI: 10.1111/j.1365-2818.2009.03257.x (cit. on p. 69).

Sta87 Stadelmann, P. A. *Ultramicroscopy* **1987**, *21*, 131–145, DOI: 10.1016/0304-3991(87)90080-5 (cit. on pp. 71, 270).

SZ10 Su, D.; Zhu, Y. *Ultramicroscopy* **2010**, *110*, 229–233, DOI: 10.1016/j.ultramic.2009.11.015 (cit. on pp. 69, 214, 215).

Sug+18 Sugita, Y.; Matsunami, H.; Kawaoka, Y.; Noda, T.; Wolf, M. *Nature* **2018**, *563*, 137–140, DOI: 10.1038/s41586-018-0630-0 (cit. on p. 17).

Sum+14 Sumiya, N.; Kawaguchi, T.; Chihara, M.; Tabuchi, M.; Ujihara, T.; Ichinose, A.; Tsukada, I.; Ikuta, H. *Journal of Physics: Conference Series* **2014**, *507*, 012047, DOI: 10.1088/1742-6596/507/1/012047 (cit. on pp. 102, 111).

Sun+20 Sun, C.; Lux, S.; Müller, E.; Meffert, M.; Gerthsen, D. *Journal of Materials Science* **2020**, *55*, 13824–13835, DOI: 10.1007/s10853-020-04970-3 (cit. on pp. 38, 39).

Sun+19 Sun, C.; Müller, E.; Meffert, M.; Gerthsen, D. *Advanced Structural and Chemical Imaging* **2019**, *5*, 1, DOI: 10.1186/s40679-019-0065-1 (cit. on p. 192).

Tak+12 Takeda, S.; Ueda, S.; Takano, S.; Yamamoto, A.; Naito, M. *Superconductor Science and Technology* **2012**, *25*, 035007, DOI: 10.1088/0953-2048/25/3/035007 (cit. on p. 101).

TT15 Talantsev, E. F.; Tallon, J. L. *Nature Communications* **2015**, *6*, 7820, DOI: 10.1038/ncomms8820 (cit. on p. 6).

Tan+12 Tan, H.; Verbeeck, J.; Abakumov, A.; Van Tendeloo, G. *Ultramicroscopy* **2012**, *116*, 24–33, DOI: 10.1016/j.ultramic.2012.03.002 (cit. on p. 112).

Tar+12 Tarantini, C.; Lee, S.; Kametani, F.; Jiang, J.; Weiss, J. D.; Jaroszynski, J.; Folkman, C. M.; Hellstrom, E. E.; Eom, C. B.; Larbalestier, D. C. *Physical Review B - Condensed Matter and Materials Physics* **2012**, *86*, 214504, DOI: 10.1103/PhysRevB.86.214504 (cit. on p. 135).

Tar+14 Tarantini, C.; Kametani, F.; Lee, S.; Jiang, J.; Weiss, J. D.; Jaroszynski, J.; Hellstrom, E. E.; Eom, C. B.; Larbalestier, D. C. *Scientific Reports* **2014**, *4*, 1–8, DOI: 10.1038/srep07305 (cit. on pp. 94, 95, 101, 102).

Tay64 Taylor, G. I. *Proceedings of the Royal Society of London. Series A. Mathematical and Physical Sciences* **1964**, *280*, 383–397, DOI: 10.1098/rspa.1964.0151 (cit. on p. 36).

TG20 Teng, C.; Gauvin, R. Multivariate Statistical Analysis on a SEM/EDS Phase Map of Rare Earth Minerals Scanning, https://www.hindawi.com/journals/scanning/2020/2134516/ (accessed 01/27/2021) (cit. on p. 3).

Ter+17 Terborg, R.; Kaeppel, A.; Yu, B.; Patzschke, M.; Salge, T.; Falke, M. *Microscopy Today* **2017**, *25*, 30–35, DOI: 10.1017/S1551929517000141 (cit. on p. 41).

The+11 Thersleff, T.; Reich, E.; Iida, K.; Haindl, S.; Trommler, S.; Hänisch, J.; Hühne, R.; Rellinghaus, B.; Schultz, L.; Holzapfel, B. In Microscopy Conference 2011, Kiel, Germany, 2011 (cit. on pp. 96, 102).

The+10 Thersleff, T.; Iida, K.; Haindl, S.; Kidszun, M.; Pohl, D.; Hartmann, A.; Kurth, F.; Hänisch, J.; Hühne, R.; Rellinghaus, B.; Schultz, L.; Holzapfel, B. *Applied Physics Letters* **2010**, *97*, 3–5, DOI: 10.1063/1.3457432 (cit. on pp. 109, 146).

TRU98 Thevenaz, P.; Ruttimann, U.; Unser, M. *IEEE Transactions on Image Processing* **1998**, *7*, 27–41, DOI: 10.1109/83.650848 (cit. on p. 68).

TS89 Thiel, B. L.; Sarikaya, M. *Physica B: Condensed Matter* **1989**, *158*, 568–571, DOI: 10.1016/0921-4526(89)90391-8 (cit. on p. 220).

Tho+21 Thomas, A. A.; Shipulin, I. A.; Holleis, S.; Eisterer, M.; Nielsch, K.; Hühne, R. *Superconductor Science and Technology* **2021**, *34*, 115013, DOI: 10.1088/1361-6668/ac2557 (cit. on pp. 101, 102).

TG14 Thomas, J.; Gemming, T., *Analytical Transmission Electron Microscopy*; Springer Netherlands: Dordrecht, 2014, DOI: 10.1007/978-94-017-8601-0 (cit. on p. 110).

Thu09 Thust, A. *Physical Review Letters* **2009**, *102*, 220801, DOI: 10.1103/PhysRevLett.102.220801 (cit. on p. 20).

Tie+21 Tiesinga, E.; Mohr, P. J.; Newell, D. B.; Taylor, B. N. *Journal of Physical and Chemical Reference Data* **2021**, *50*, 033105, DOI: 10.1063/5.0064853 (cit. on p. xii).

Tie08 Tietz, H. R. *Microscopy and Microanalysis* **2008**, *14*, 804–805, DOI: 10.1017/S1431927608084675 (cit. on p. 20).

Træ+94 Træholt, C.; Wen, J. G.; Svetchnikov, V.; Zandbergen, H. W. *Physica C: Superconductivity* **1994**, *230*, 297–305, DOI: 10.1016/0921-4534(94)90843-5 (cit. on pp. 188, 189, 194).

TE67 Träuble, H.; Essmann, U. *physica status solidi (b)* **1967**, *20*, 95–111, DOI: 10.1002/pssb.19670200108 (cit. on p. 7).

Tre+05 Treacy, M. M. J.; Gibson, J. M.; Fan, L.; Paterson, D. J.; McNulty, I. *Reports on Progress in Physics* **2005**, *68*, 2899–2944, DOI: 10.1088/0034-4885/68/12/R06 (cit. on p. 99).

TD03 Tschumperle, D.; Deriche, R. In *IEEE Computer Society Conference on Computer Vision and Pattern Recognition*, IEEE Comput. Soc: 2003; Vol. 1, pp I-651-I–656, DOI: 10.1109/CVPR.2003.1211415 (cit. on p. 70).

Tsu+98 Tsu, I.-F.; Wang, J.-L.; Kaiser, D. L.; Babcock, S. E. *Physica C: Superconductivity* **1998**, *306*, 163–187, DOI: 10.1016/S0921-4534(98)00361-X (cit. on p. 212).

Tsu+16 Tsukada, I.; Ichinose, A.; Nabeshima, F.; Imai, Y.; Maeda, A. *AIP Advances* **2016**, *6*, 095314, DOI: 10.1063/1.4963646 (cit. on pp. 96, 99, 102).

Tsu+11 Tsukada, I.; Hanawa, M.; Akiike, T.; Nabeshima, F.; Imai, Y.; Ichinose, A.; Komiya, S.; Hikage, T.; Kawaguchi, T.; Ikuta, H.; Maeda, A. *Applied Physics Express* **2011**, *4*, 053101, DOI: 10.1143/APEX.4.053101 (cit. on pp. 101, 102).

TDR01 Tsur, Y.; Dunbar, T. D.; Randall, C. A. *Journal of Electroceramics* **2001**, *7*, 25–34, DOI: 10.1023/A:1012218826733 (cit. on pp. 228–230).

TO90 Tuller, H. L.; Opila, E. *Solid State Ionics* **1990**, *40–41*, 790–794, DOI: 10.1016/0167-2738(90)90122-8 (cit. on p. 178).

Uch15 Uchida, S.-i., *High Temperature Superconductivity*; Springer Series in Materials Science, Vol. 213; Springer Japan: Tokyo, 2015, DOI: 10.1007/978-4-431-55300-7 (cit. on p. 120).

Urb+09 Urban, K. W.; Jia, C. L.; Houben, L.; Lentzen, M.; Mi, S. B.; Tillmann, K. *Philosophical Transactions of the Royal Society A: Mathematical, Physical and Engineering Sciences* **2009**, *367*, 3735–3753, DOI: 10.1098/rsta.2009.0134 (cit. on p. 26).

vdRND93 Van de Riet, E.; Nillesen, C. J. C. M.; Dieleman, J. *Journal of Applied Physics* **1993**, *74*, 2008–2012, DOI: 10.1063/1.354763 (cit. on p. 143).

vdWal+14 Van der Walt, S.; Schönberger, J. L.; Nunez-Iglesias, J.; Boulogne, F.; Warner, J. D.; Yager, N.; Gouillart, E.; Yu, T. *PeerJ* **2014**, *2*, e453, DOI: 10.7717/peerj.453 (cit. on p. 91).

VKA91 Van Tendeloo, G.; Krekels, T.; Amelinckx, S. *Philosophical Magazine Letters* **1991**, *63*, 189–196, DOI: 10.1080/09500839108205990 (cit. on pp. 169, 216).

Vas+93 Vasquez, R. P.; Foote, M. C.; Hunt, B. D.; Barner, J. B. *Physica C: Superconductivity* **1993**, *207*, 266–272, DOI: 10.1016/0921-4534(93)90309-E (cit. on p. 111).

Vas+15 Vasudevan, R. K.; Belianinov, A.; Gianfrancesco, A. G.; Baddorf, A. P.; Tselev, A.; Kalinin, S. V.; Jesse, S. *Applied Physics Letters* **2015**, *106*, 091601, DOI: 10.1063/1.4914016 (cit. on pp. 3, 72).

VV04 Verbeeck, J.; Van Aert, S. *Ultramicroscopy* **2004**, *101*, 207–224, DOI: 10.1016/j.ultramic.2004.06.004 (cit. on pp. 46, 78).

VMK04 Voyles, P. M.; Muller, D. A.; Kirkland, E. J. *Microscopy and Microanalysis* **2004**, *10*, 291–300, DOI: 10.1017/S1431927604040012 (cit. on p. 29).

Wan+16 Wan, Q.; Masters, R. C.; Lidzey, D.; Abrams, K. J.; Dapor, M.; Plenderleith, R. A.; Rimmer, S.; Claeyssens, F.; Rodenburg, C. *Ultramicroscopy* **2016**, *171*, 126–138, DOI: 10.1016/j.ultramic.2016.09.006 (cit. on p. 116).

Wan+21 Wang, H.; Srot, V.; Fenk, B.; Laskin, G.; Mannhart, J.; van Aken, P. A. *Micron* **2021**, *140*, 102979, DOI: 10.1016/j.micron.2020.102979 (cit. on p. 66).

Wan+11 Wang, L.; Ma, Y.; Wang, Q.; Li, K.; Zhang, X.; Qi, Y.; Gao, Z.; Zhang, X.; Wang, D.; Yao, C.; Wang, C. *Applied Physics Letters* **2011**, *98*, 222504, DOI: 10.1063/1.3592580 (cit. on p. 146).

Wan+13 Wang, Y.; Xu, D.; Li, Y.; Liu, L. *Nanoscale Research Letters* **2013**, *8*, 304, DOI: 10.1186/1556-276X-8-304 (cit. on p. 179).

WW99a Watanabe, M.; Williams, D. B. *Ultramicroscopy* **1999**, *78*, 89–101, DOI: 10.1016/S0304-3991(99)00015-7 (cit. on p. 84).

WW99b Watanabe, M.; Williams, D. B. *Microscopy and Microanalysis* **1999**, *5*, 88–89, DOI: 10.1017/S1431927600013763 (cit. on p. 44).

Wer+11 Werfel, F. N.; Floegel-Delor, U.; Rothfeld, R.; Riedel, T.; Goebel, B.; Wippich, D.; Schirrmeister, P. *Superconductor Science and Technology* **2011**, *25*, 014007, DOI: 10.1088/0953-2048/25/1/014007 (cit. on p. 1).

WM05 Weyland, M.; Muller, D. A. *FEI Nanosolutions* **2005**, *1*, 24–35, DOI: 10.48550/arXiv.2008.12870 (cit. on pp. 27, 66).

WC08 Williams, D. B.; Carter, C. B., *Transmission Electron Microscopy: A Textbook for Materials Science*, 2nd ed; Springer: New York, 2008 (cit. on pp. 12, 13, 18, 24, 26).

Wol95 Wold, S. *Chemometrics and Intelligent Laboratory Systems* **1995**, *30*, 109–115, DOI: 10.1016/0169-7439(95)00042-9 (cit. on p. 51).

Wu+87 Wu, M. K.; Ashburn, J. R.; Torng, C. J.; Hor, P. H.; Meng, R. L.; Gao, L.; Huang, Z. J.; Wang, Y. Q.; Chu, C. W. *Physical Review Letters* **1987**, *58*, 908–910, DOI: 10.1103/PhysRevLett.58.908 (cit. on p. 7).

Wu+17 Wu, R. J.; Mittal, A.; Odlyzko, M. L.; Mkhoyan, K. A. *Microscopy and Microanalysis* **2017**, *23*, 794–808, DOI: 10.1017/S143192761700068X (cit. on p. 29).

Xu+17 Xu, A.; Zhang, Y.; Gharahcheshmeh, M. H.; Yao, Y.; Galstyan, E.; Abraimov, D.; Kametani, F.; Polyanskii, A.; Jaroszynski, J.; Griffin, V.; Majkic, G.; Larbalestier, D. C.; Selvamanickam, V. *Scientific Reports* **2017**, *7*, 6853, DOI: 10.1038/s41598-017-06881-x (cit. on p. 135).

XS03 Xu, Y.; Shi, D. *Tsinghua Science and Technology* **2003**, *8*, 342–369 (cit. on p. 8).

Xu+19 Xu, Z.; Zhang, Q.; Fan, F. F.; Gu, L.; Ma, Y. *Superconductor Science and Technology* **2019**, *32*, DOI: 10.1088/1361-6668/ab4f44 (cit. on pp. 95, 124, 131).

Yam+08 Yamada, K.; Mukaida, M.; Kai, H.; Teranishi, R.; Ichinose, A.; Kita, R.; Kato, S.; Horii, S.; Yoshida, Y.; Matsumoto, K.; Toh, S. *Applied Physics Letters* **2008**, *92*, 112503, DOI: 10.1063/1.2894196 (cit. on pp. 2, 216, 229, 231).

Yam+09 Yamamoto, A.; Jaroszynski, J.; Tarantini, C.; Balicas, L.; Jiang, J.; Gurevich, A.; Larbalestier, D. C.; Jin, R.; Sefat, A. S.; McGuire, M. A.; Sales, B. C.; Christen, D. K.; Mandrus, D. *Applied Physics Letters* **2009**, *94*, 062511, DOI: 10.1063/1.3081455 (cit. on p. 7).

YSM21 Yamashita, A.; Shukunami, Y.; Mizuguchi, Y. Improvement of Local Critical Current Density of REBa$_2$Cu$_3$O$_{7-\delta}$ by the Increase in Configurational Entropy of Mixing at the *RE* Site, 2021 (cit. on p. 196).

Yam+18 Yamashita, S.; Kikkawa, J.; Yanagisawa, K.; Nagai, T.; Ishizuka, K.; Kimoto, K. *Scientific Reports* **2018**, *8*, 12325, DOI: 10.1038/s41598-018-30941-5 (cit. on pp. vi, 31).

YBW91 Yan, Y.; Blanchin, M. G.; Wicker, A. *Physica C: Superconductivity* **1991**, *175*, 651–666, DOI: 10.1016/0921-4534(91)90280-C (cit. on pp. 173, 174).

Yan+12 Yang, H. X.; Tian, H. F.; Wang, Z.; Qin, Y. B.; Ma, C.; Li, J. Q.; Cheng, Z. Y.; Yu, R.; Zhu, J. *Journal of Physics: Condensed Matter* **2012**, *24*, 435901, DOI: 10.1088/0953-8984/24/43/435901 (cit. on p. 69).

Yan+14 Yankovich, A. B.; Berkels, B.; Dahmen, W.; Binev, P.; Sanchez, S. I.; Bradley, S. A.; Li, A.; Szlufarska, I.; Voyles, P. M. *Nature Communications* **2014**, *5*, 4155, DOI: 10.1038/ncomms5155 (cit. on p. 68).

Yed+14 Yedra, L.; Xuriguera, E.; Estrader, M.; López-Ortega, A.; Baró, M. D.; Nogués, J.; Roldan, M.; Varela, M.; Estradé, S.; Peiró, F. **2014**, *1*, DOI: 10.1017/S1431927614000440 (cit. on p. 78).

Yip+20 Yip, K. M.; Fischer, N.; Paknia, E.; Chari, A.; Stark, H. *Nature* **2020**, *587*, 157–161, DOI: 10.1038/s41586-020-2833-4 (cit. on p. 17).

Yoo+16 Yoon, S.; Seo, Y.-S.; Lee, S.; Weiss, J. D.; Jiang, J.; Oh, M.; Lee, J.; Seo, S.; Jo, Y. J.; Hellstrom, E. E.; Hwang, J.; Lee, S. *Superconductor Science and Technology* **2016**, *30*, 035001, DOI: 10.1088/1361-6668/30/3/035001 (cit. on pp. 2, 102, 105).

Yu+08 Yu, C.; Scullin, M. L.; Huijben, M.; Ramesh, R.; Majumdar, A. *Applied Physics Letters* **2008**, *92*, 092118, DOI: 10.1063/1.2890493 (cit. on p. 151).

YMS04 Yu, Z.; Muller, D. A.; Silcox, J. *Journal of Applied Physics* **2004**, *95*, 3362–3371, DOI: 10.1063/1.1649463 (cit. on p. 31).

Yua+17 Yuan, P.; Xu, Z.; Wang, D.; Zhang, M.; Li, J.; Ma, Y. *Superconductor Science and Technology* **2017**, *30*, 025001, DOI: 10.1088/0953-2048/30/2/025001 (cit. on pp. 2, 101, 102, 123).

YF89 Yvon, K.; François, M. *Zeitschrift für Physik B Condensed Matter* **1989**, *76*, 413–444, DOI: 10.1007/BF01307892 (cit. on pp. 155, 171).

Zak+96 Zakharov, N. D.; Kästner, G.; Hesse, D.; Lorenz, M. *Applied Physics Letters* **1996**, *69*, 1151–1153, DOI: 10.1063/1.117088 (cit. on p. 172).

Zal21 Zaluzec, N. *Microscopy and Microanalysis* **2021**, *27*, 2070–2074, DOI: 10.1017/S1431927621007492 (cit. on p. 41).

Zan92 Zandbergen, H. W. *Physica C: Superconductivity* **1992**, *193*, 371–384, DOI: 10.1016/0921-4534(92)90959-G (cit. on pp. 160, 163, 171–173, 176, 203).

Zan+91 Zandbergen, H. W.; Cava, R. J.; Krajewski, J. J.; Peck, W. F. *Physica C: Superconductivity* **1991**, *179*, 227–242, DOI: 10.1016/0921-4534(91)90031-S (cit. on p. 172).

Zan+88 Zandbergen, H. W.; Gronsky, R.; Wang, K.; Thomas, G. *Nature* **1988**, *331*, 596–599, DOI: 10.1038/331596a0 (cit. on p. 155).

ZvT90 Zandbergen, H. W.; van Tendeloo, G. *MRS Proceedings* **1990**, *183*, 337, DOI: 10.1557/PROC-183-337 (cit. on p. 183).

Zha+13 Zhang, H.; Gauquelin, N.; Botton, G. A.; Wei, J. Y. T. *Applied Physics Letters* **2013**, *103*, 052606, DOI: 10.1063/1.4813840 (cit. on p. 204).

Zha+18 Zhang, H.; Gauquelin, N.; McMahon, C.; Hawthorn, D. G.; Botton, G. A.; Wei, J. Y. T. *Physical Review Materials* **2018**, *2*, 033803, DOI: 10.1103/PhysRevMaterials.2.033803 (cit. on p. 156).

ZEM12 Zhang, H.-R.; Egerton, R. F.; Malac, M. *Micron* **2012**, *43*, 8–15, DOI: 10.1016/j.micron.2011.07.003 (cit. on pp. 74, 167).

Zha+21a Zhang, Z.; Wang, D.; Wei, S.; Wang, Y.; Wang, C.; Zhang, Z.; Yao, H.; Zhang, X.; Liu, F.; Liu, H.; Ma, Y.; Xu, Q.; Wang, Y. *Superconductor Science and Technology* **2021**, *34*, 035021, DOI: 10.1088/1361-6668/abb11b (cit. on p. 8).

Zha+21b Zhao, Y.; Wu, D.; Zhou, J.; Wen, H.; Liu, Z.; Wang, Q.; Liu, C. *Nanotechnology* **2021**, *32*, 475705, DOI: 10.1088/1361-6528/ac1543 (cit. on pp. 69, 214).

Zhe+19 Zheng, Q.; Chi, M.; Ziatdinov, M.; Li, L.; Maksymovych, P.; Chisholm, M. F.; Kalinin, S. V.; Sefat, A. S. *Journal of Solid State Chemistry* **2019**, *277*, 422–426, DOI: 10.1016/j.jssc.2019.06.040 (cit. on pp. 2, 96, 102, 121).

ZTW13 Zhu, Y.; Tsai, C.-F.; Wang, H. *Superconductor Science and Technology* **2013**, *26*, 025009, DOI: 10.1088/0953-2048/26/2/025009 (cit. on pp. 148, 169, 194, 210, 216).

ZB85 Ziegler, J. F.; Biersack, J. P. In *Treatise on Heavy-Ion Science: Volume 6: Astrophysics, Chemistry, and Condensed Matter*, Bromley, D. A., Ed.; Springer US: Boston, MA, 1985, pp 93–129, DOI: 10.1007/978-1-4615-8103-1_3 (cit. on p. 29).

ZZB10 Ziegler, J. F.; Ziegler, M. D.; Biersack, J. P. *Nuclear Instruments and Methods in Physics Research Section B: Beam Interactions with Materials and Atoms* **2010**, *268*, 1818–1823, DOI: 10.1016/j.nimb.2010.02.091 (cit. on p. 29).

List of Publications

Journal Articles

"Study of the Change in the Composition of $BaHfO_3$ Nanoparticles Embedded in REBCO Films by Scanning Transmission Electron Microscopy"
Grünewald, L., Cayado, P., Erbe, M., Hänisch, J., Holzapfel, B., Gerthsen, D., **in preparation**

"Microstructure, Pinning Properties, and Aging of CSD-grown $SmBa_2Cu_3O_{7-\delta}$ Films with and without $BaHfO_3$ Nanoparticles"
Hänisch, J., Iida, K., Cayado, P., Erbe, M., **Grünewald, L.**, Hatano, T., Okada, T., Gerthsen, D., Awaji, S., Holzapfel, B., *Superconductor Science and Technology* **accepted**

"Critical Current Density Improvement in CSD-grown High-Entropy $REBa_2Cu_3O_{7-\delta}$ Films"
Cayado, P., **Grünewald, L.**, Erbe, M., Hänisch, J., Gerthsen, D., Holzapfel, B., **submitted**

"Structural and Chemical Properties of Superconducting Co-doped $BaFe_2As_2$ Thin Films Grown on CaF_2"
Grünewald, L., Langer, M., Meyer, S., Nerz, D., Hänisch, J., Holzapfel, B., Gerthsen, D., *Superconductor Science and Technology* **2021**, *34*, 035005, DOI: 10.1088/1361-6668/abcecf

"Pulsed Laser Deposition of Quasi-Multilayer Superconducting $Ba(Fe_{0.92}Co_{0.08})_2As_2$-$BaHfO_3$ Nanocomposite Films"
Meyer, S., Langer, M., **Grünewald, L.**, Hänisch, J., Gerthsen, D., Holzapfel, B., *Journal of Physics: Conference Series* **2020**, *1559*, 012052, DOI: 10.1088/1742-6596/1559/1/012052

"On the Growth of Co-doped $BaFe_2As_2$ Thin Films on CaF_2"
Langer, M., Meyer, S., Ackermann, K., **Grünewald, L.**, Kauffmann-Weiss, S., Aswartham, S., Wurmehl, S., Hänisch, J., Holzapfel, B., *Journal of Physics: Conference Series* **2019**, *1293*, 012014, DOI: 10.1088/1742-6596/1293/1/012014

Conference Contributions

Microscopy & Microanalysis 2021 (online)

Contributed Talk (15 min):
"Structural and Chemical Properties of Superconducting Rare-Earth Barium Copper Oxide/$BaHfO_3$ Nanocomposites with Rare-Earth Mixtures"
Grünewald, L., Cayado, P., Hänisch, J., Holzapfel, B., Gerthsen, D., *Microscopy and Microanalysis* **2021**, *27*, 2876–2879, DOI: 10.1017/S1431927621010023

Contributed Talk (15 min):
"Analysis of Superconducting Thin Films in a Modern FIB/SEM Dual-Beam Instrument"

Grünewald, L., Nerz, D., Langer, M., Meyer, S., Beisig, N., Cayado, P., Popov, R., Hänisch, J., Holzapfel, B., Gerthsen, D., *Microscopy and Microanalysis* **2021**, *27*, 1056–1058, DOI: 10.1017/S1431927621003986

Microscopy Conference 2021 (online)

Poster presentation:
"Electron Microscopic Investigation of Post-Annealed Superconducting $GdBa_2Cu_3O_{7-\delta}$ Thin Films on MgO"
Grünewald, L., Popov, R., Hänisch, J., Holzapfel, B., Gerthsen, D., In Microscopy Conference (MC 2021), Online, 22.08.2021 – 26.08.2021, 2021, DOI: 10.5445/IR/1000143835

Poster presentation:
"Analysis of Superconducting Thin Films in a Modern FIB/SEM Dual-Beam Instrument"
Grünewald, L., Nerz, D., Langer, M., Meyer, S., Beisig, N., Cayado, P., Popov, R., Hänisch, J., Holzapfel, B., Gerthsen, D., In Microscopy Conference (MC 2021), Online, 22.08.2021 – 26.08.2021, 2021, DOI: 10.5445/IR/1000147936

Virtual Early Career European Microscopy Congress 2020 (online)

Contributed Talk (15 min):
"Investigation of Superconducting $Ba(Fe,Co)_2As_2$ Thin Films on CaF_2"
Grünewald, L., Langer, M., Meyer, S., Hänisch, J., Holzapfel, B., Gerthsen, D., In *Proceedings of the European Microscopy Congress 2020*, European Microscopy Congress 2020, Royal Microscopical Society: 2021, DOI: 10.22443/rms.emc2020.67

IBS2app: Iron-based Superconductors: advances towards application 2020 (Santa Margherita Ligure, Italy)

Contributed Talk (15 min):
"Structural Properties of Co-doped $BaFe_2As_2$ Thin Films"
Grünewald, L., Langer, M., Meyer, S., Hänisch, J., Holzapfel, B., Gerthsen, D., In IBS2app: Iron-based Superconductors: Advances towards Applications, Santa Margherita Ligure, 2020

Microscopy Conference 2019 (Berlin, Germany)

Poster presentation:
"Structural properties of superconducting $Ba(Fe,Co)_2As_2$ thin films"
Grünewald, L., Langer, M., Meyer, S., Hänisch, J., Holzapfel, B., Gerthsen, D., In Microscopy Conference (MC 2019), Berlin, Germany, 01.09.2019 – 05.09.2019, Berlin, Germany, 2019, DOI: 10.5445/IR/1000127055

Datasets

Grünewald, L., Langer, M., Meyer, S., Hänisch, J., Holzapfel, B., Gerthsen, D., Supplementary Information for 'Structural and Chemical Properties of Superconducting Co-doped $BaFe_2As_2$ Thin Films Grown on CaF_2', 2020, DOI: 10.5281/zenodo.4058144

Hänisch, J., Iida, K., Cayado, P., Erbe, M., **Grünewald, L.**, Hatano, T., Okada, T., Gerthsen, D., Awaji, S., Holzapfel, B., Supplementary Information for 'Microstructure and Pinning Properties of CSD-grown $SmBa_2Cu_3O_{7-\delta}$ Films with and without $BaHfO_3$ Nanoparticles', Zenodo: 2022, DOI: 10.5281/zenodo.6350486

Appendix

Electron microscopes and FIB/SEM instruments

FEI Strata 400S DualBeam
FIB/SEM instrument, Ga^+ LMIS/Schottky FEG, OmniProbe 200 micromanipulator, Bruker X-Flash 5010 EDXS SDD

TFS Helios G4 FX DualBeam
FIB/SEM instrument, Ga^+ LMIS/Schottky FEG, Monochromator, Easylift micromanipulator, Bruker X-Flash 6|60 EDXS SDD, dedicated STEM holder, STEM 4 detector, Bruker OPTIMUS TKD/EBSD detector

FEI Titan^3 80–300
S/TEM instrument, 80 keV to 300 keV, Schottky FEG, Wien-type monochromator (not actively used), CETCOR C_s-corrector (image), TVIPS TemCam XF416 CMOS camera, EDAX Si(Li) EDXS detector, Fischione Model 3000 ADF detector, Gatan GIF 865 ER spectrometer with BF/DF detectors and UltraScan 1000 CCD camera

FEI Tecnai Osiris
S/TEM instrument, 80 keV to 200 keV, Schottky X-FEG, Gatan UltraScan 1000 CCD camera, Super-X (G1) EDXS SDD, Fischione Model 3000 ADF detector

Philips CM200
TEM instrument, 200 keV, Schottky FEG, TVIPS TemCam F416 CMOS camera

Crystal Structures

Table A.1.: Crystal structures used for simulations and crystalline-phase analyses from diffraction patterns and Fourier transforms. Note that RE-containing phases are often structurally similar, e.g. Ho_2O_3 and Y_2O_3.

Material	ICSD Entry	Density (g/cm^{-3})	Comment
$BaFe_2As_2$	169 555	6.48	Ba122, $Ba(Fe_{0.92}Co_{0.08})_2As_2$
BaF_2	64 717	4.89	—
BaO	58 663	5.99	—
BaO_2	24 729	5.43	—
Ba_2As	87 345	5.08	—
$BaAs_2$	414 139	5.48	—
$BaAs_3$	86 402	5.53	—
Ba_2CuO_3	68 217	6.17	—

Continued on next page

Table A.1. – *Continued from previous page*

Material	ICSD Entry	Density (g/cm^{-3})	Comment
$BaCu_2O_2$	9456	5.98	—
$BaCu_3O_4$	65 881	5.50	—
$BaCuO_2$	65 801	5.63	—
$BaFeO_4$	60 662	4.72	—
$BaFeO_3$	262 131	6.40	—
$BaGd_2O_4$	78 484	7.58	—
39320 $BaNb_2O_6$	78 484	6.76	(“BENO”)
$BaCO_3$	91 888	4.31	—
$BaZrO_3$	90 049	6.21	BZO
$BaHfO_3$	—	8.33	BHO, mod. BZO using [MKY06]
C	—	2	amorphous C
CaF_2	82 707	3.18	—
CaO	90 486	3.35	—
CuO	16 025	6.52	—
Cu_2O	172 174	6.11	—
$CuSmO_2$	18 105	6.18	—
Er_2CuO_5	79 430	6.18	—
Er_2O_3	39 185	8.66	—
$ErBa_2Cu_3O_7$	81 176	7.15	ErBCO
Fe	631 736	7.87	α-Fe/Ferrite
Fe_2As	415 628	7.83	—
$FeAs_2$	42 603	7.47	—
FeO	31 081	5.99	—
Fe_2O_3	15 840	5.26	—
Fe_3O_4	35 000	5.22	—
Gd_2CuO_4	65 015	8.16	—
Gd_2BaCuO_5	32 708	7.76	—
Gd_2O_3	181 377	7.61	—
$GdBa_2Cu_3O_7$	56 514	6.97	GdBCO
HfO_2	27 313	10.12	—
Ho_2O_3	80 038	8.41	—
InAs	41 444	5.67	—
$LaAlO_3$	254 051	6.54	LAO
MgO	52 026	3.58	—
Pt	243 678	21.45	—
$SmBa_2Cu_3O_7$	65 391	6.87	SmBCO
Sm_2CuO_4	71 182	7.75	—
Sm_2BaCuO_5	49 812	7.44	—
$Sm_2Ba_4Cu_2O_9$	97 402	6.64	—
Sm_2O_3	34 291	7.74	—
$SrTiO_3$	23 076	5.12	STO
$YBa_2Cu_3O_6$	65 261	6.11	Tetragonal, non-supercond.
$YBa_2Cu_3O_7$	56 507	6.38	RE123, orthorhombic, supercond.
$YBa_2Cu_4O_8$	67 631	6.11	RE124

Continued on next page

Table A.1. – *Continued from previous page*

Material	ICSD Entry	Density (g/cm^{-3})	Comment
$Y_2Ba_4Cu_{6.97}O_{14.89}$	400 090	6.21	RE247
Y_2BaCuO_5	32 707	6.20	—
$Y_2Cu_2O_5$	51 445	5.06	—
Y_2O_3	23 811	5.03	—

Scripts

EDXS spectrum simulation with *DTSA-II*

The following script was used for EDXS spectrum simulation. Alternatively, the *DTSA-II* `Simulation alien...` from the `Tools` menu can be used for quick simulations. Here, the option `Monte Carlo model of a film on a bulk, homogeneous substrate` must be chosen. In the following menu, set the substrate material to `None`. The other options (e.g. beam current) can be adjusted similarly to the script below.

```
# DTSA_simulation.py
# Script to simulate an EDS spectrum from TEM samples with DTSA-II
# Lukas Gruenewald, 2022
# Part of the code is inspired by the code of John Minter, https://github.com/
                                        jrminter
#
# Last tested DTSA-II version: Microscopium 14-9-2021
# Usage:
#   1. Create a folder for your simulation
#   2. Copy this file in the newly created folder
#   3. Adjust user parameters below in a text editor and save (Note that
                                        sample and detector must be defined in
                                        DTSA!)
#   4. Run from the DTSA-II user interface (Command --> Open)

import dtsa2.mcSimulate3 as mc

#Get folder location of this script to store results
from inspect import getsourcefile
from os.path import dirname

simDir = dirname(getsourcefile(lambda:0)) #Directory for results, same as
                                        location of this file

### User parameters

# sample setup
film = material("My-Material") # Material, define before in DTSA-II GUI
tfilm = 100                 # nm (sample thickness)

# beam / acquisition setup
e0      =    200.0          # keV (electron energy)
bs      =    1.0            # nm (beam size, FWHM)
pc      =    1.0            # nA (probe current)
lt      =    60.0         # sec (live time for spectrum collection)
dose    =    pc * lt        # nA*sec
det     =    d203           # Select detector to be used. Must be defined
                                        before in DTSA GUI. Then get detector
```

```
                                        number via "listDetectors()" from the
                                        command window.
#det    =    FindDetector("My detector name") #Alternative to det from above

# simulation parameters
nTraj   =    20000          # number of trajectories to run
imgSize =    2048           # pixel size for images
imgSzNm =    tfilm*2        # image size/field of view in nm
Poisson =    True           # Add Poisson count statistics
charF   =    True           # include characteristic fluorescence (default True
                                        )
bremF   =    True           # include continuum fluorescence  (default True)

#Grab and add x-ray transitions
e2 = film.stoichiometryString().split(',')
e = [tmp.split("(")[0].encode("ascii") for tmp in e2]
estr = ''.join(e)
xrts=mc.suggestTransitions(estr, e0)

wUm     =    5.0        # width microns of line
lUm     =    5.0        # length microns of line
vmrlEl  =    200        # number of el for VMRL

############################
### End of user parameters.
############################


# specify the extra parameters based on user parameters
xtraParams={}
xtraParams.update(mc.configureXRayAccumulators(xrts, charAccum=charF,
                                        charFluorAccum=charF, bremFluorAccum=
                                        bremF))
xtraParams.update(mc.configureBeam(0, 0, 0, bs*1.0e-9)) #beam size
xtraParams.update(mc.configureEmissionImages(xrts, imgSzNm*1.0e-9, imgSize)) #
                                        emission images from detected x-rays
xtraParams.update(mc.configurePhiRhoZ(imgSzNm*1.0e-9))
xtraParams.update(mc.configureTrajectoryImage(imgSzNm*1.0e-9, imgSize, nTraj))
xtraParams.update(mc.configureVRML(nElectrons = vmrlEl))
xtraParams.update(mc.configureOutput(simDir))

#Emission images color palette, default: heat map
#mc.useGrayScalePalette() #Gray scale output
#mc.useHeatMapPalette() #Heat map output, default

sim = mc.multiFilm([[film, tfilm*1e-9]], det, e0, withPoisson=Poisson, nTraj=
                                        nTraj, dose=dose, sf=charF, bf=bremF,
                                        xtraParams=xtraParams)
sim.save(simDir+'\DTSAsim_'+film.getName().encode('ascii')+'_'+str(e0)+'keV_'+
                                        str(tfilm)+'nm.msa')
display(sim)
```

Conversion of .cif files for *JEMS* with *Atomsk*

The following steps can be used for batch conversion of .cif file to *JEMS* [Sta87] .txt files with *Atomsk* [Hir15], e.g. to compare a diffraction pattern or diffractogram to simulated diffraction spots. The following procedure works for Windows 10.

1. Open a command prompt in the folder with the .cif files by clicking into the file-path bar in the Windows explorer, typing `cmd`, and confirming with `ENTER`
2. Create a list of all .cif files in the current folder by running

   ```
   dir /b *.cif > cifs.lst
   ```

   in the command prompt.
3. Run the following command for batch conversion of all .cif files:

   ```
   "C:\Program Files (x86)\Atomsk\atomsk.exe" --list
   cifs.lst -unit A nm JEMS -ignore
   ```

   Note the two dashes (--) before `list`.

Acknowledgments

This PhD thesis was possible through the continuous support of many people I worked with. In no particular order, I want to especially thank...

- Dagmar Gerthsen for the possibility to do my PhD at the LEM, the numerous helpful comments, and feedback throughout the years. I am grateful for the possibility of attending several conferences and the freedom I had in pursuing different scientific questions.
- Bernhard Holzapfel for giving me the opportunity to perform my studies in cooperation with the ITEP and for the helpful comments and suggestions regarding my work. I enjoyed the open and welcoming atmosphere, and our conversations at the IBS2app conference in Santa Margherita Ligure.
- Jens Hänisch for valuable comments, discussions, and careful reading of abstracts and publications. I learned a lot about superconductors and XRD in our discussions.
- My Bachelor student Daniel Nerz for his company in our office and his valuable SEM measurements for this work.
- Marco Langer, Sven Meyer, and Nico Beisig for the fabrication of the IBS films and our fruitful scientific exchanges in your offices at ITEP.
- Pablo Cayado, Manuela Erbe, and Ruslan Popov for providing the REBCO films and the excellent scientific discussions.
- All the people from the "SuSchi" group at ITEP for their welcoming atmosphere, the social meetings and ITEP events, and the patience with me when waiting for results of time-consuming electron-microscopy measurements.
- Erich Müller for *vivid* scientific and non-scientific conversations and his help in FIB/SEM-related questions and problems.
- Michaela Jürgens and Rita Sauter for the organizational matters and the welcoming atmosphere in the LEM administration office.

I want to thank all LEMmings for the pleasant working atmosphere at LEM, scientific and non-scientific exchanges, technical support at the instruments, social events, and the LEM coffee-break group (with Silvia and Patrice at its core).

In addition, I want to acknowledge software and other resources which helped me in creating this thesis:

- The *Practical Electron Microscopy and Database* by Yougui Liao (`https://www.globalsino.com/EM/`) is a valuable resource when learning electron microscopy. I enjoyed clicking through random pages and always learning something new.

– All developers and maintainers of LaTeX, the different LaTeX packages[1], and the team behind *Texmaker*.

– The developers of *ImageJ*/*Fiji* software packages and plugins. The forum is a great place to ask for help and get inspiration for image analyses (`https://forum.image.sc/`).

– Regarding *DigitalMicrograph*, all users who provide their scripts (`https://www.felmi-zfe.at/dm-script/`), especially Dave Mitchell (`http://www.dmscripting.com/`), Christoph T. Koch (`https://www.physik.hu-berlin.de/en/sem/software`), Bernhard Schaffer (`http://digitalmicrograph-scripting.tavernmaker.de/HowToScript_index.htm`), and Pavel Potapov (`http://temdm.com/web/`).

– Nicholas Rudawski for taking the time to create educational videos about the operation of electron microscopes and FIBs (YouTube: `https://www.youtube.com/channel/UCejMCxv5psUKJTrdL2-ZjmQ`).

– Literature sorting and review was a breeze with the *Zotero* software (`https://www.zotero.org/`), and the *Better BibTeX* (`https://retorque.re/zotero-better-bibtex/`) and *ZotFile* (`http://zotfile.com/`) plugins.

Finally, I want to thank my family and friends for their constant support during my studies and PhD journey.

[1] Especially the "amusements" packages (`https://www.ctan.org/topic/amusements`, last accessed 24.03.2022).